



Responsive starch-alginate-containing triazine-based porous organic polymer beads towards hexavalent chromium

Pedro M.C. Matias^{a,1}, Talles B. Costa^{a,b,1}, Dina M.B. Murtinho^a, Derval S. Rosa^b, Artur J.M. Valente^{a,*}

^a Coimbra Chemistry Centre (CQC-IMS), Department of Chemistry, University of Coimbra, 3004-535 Coimbra, Portugal

^b Center for Engineering, Modeling and Applied Social Sciences, Federal University of ABC, 09280-560 Santo André, São Paulo, Brazil

ARTICLE INFO

Keywords:

Starch
Alginate
Porous organic polymers
Gel beads
Potentially toxic metals
Water remediation

ABSTRACT

Some heavy metals (e.g., Cr(VI)), also known as potentially toxic metals, concern the population's health in water due to their persistence, bioaccumulation, and high toxicity. Highly porous materials based on biodegradable and low toxic polysaccharides combined with advanced tailor-made polymers with high surface area and permanent porosity (i.e., porous organic polymers – POPs) are promising technologies for metal sensing, removal, and recovery. In this study, novel starch-alginate-based gel beads containing an imine-linked triazine-based porous organic polymer (IT-POP) were developed, and both the IT-POP and the best beads formulation were applied for sorption and sensing of Cr(VI). Kinetic studies suggested a chemisorption mechanism, explained by electrostatic attractions, and proved the negligible contribution of Cr(VI) to Cr(III) reduction. Thermodynamically, sorption processes were spontaneous and endothermic, leading to increased entropy. The materials also acted as fluorescence chemosensors, undergoing a linear Stern-Volmer fluorescence quenching in the presence of the metal oxyanions. Overall, the results proved that the anchoring of the advanced functional material did not affect its high sorption performance, meaning that composite starch-alginate beads may be an efficient, more economical, and processable alternative for the Cr(VI) remediation.

1. Introduction

Aquatic ecosystems are essential to the biosphere and evolve in synergy with chemical elements and the environment. However, anthropogenic activities lead to the disposal of waste containing toxic compounds and to the contamination of these environments, seriously threatening the balance of biota and environment (Justus et al., 2020; Mendes et al., 2020). Worldwide, 1.7 million deaths per year are linked to water contamination (Sharma et al., 2023). Besides, urban centers hold 55 % of the world's population nowadays, and forecasts point to an increase to 68 % by 2050 (i.e., 9.9 billion people). Therefore, the uncontrolled growth of population can lead to an exponential increase in water contamination due to the demand for consumption (Hachaichi & Egieya, 2023).

Emerging contaminants in hydric resources derive from various sources, such as industry, agriculture, livestock, and domestic waste. They can be pesticides, fertilizers, dyes, solvents, pharmaceuticals,

organic waste, and metal ions (Farid et al., 2019; Morin-Crini et al., 2022; Renu & Singh, 2017; Savassi et al., 2020). Among them, potentially toxic metals (PTMs) are particularly concerned due to their potentially devastating effects on the environment, persistent character, risks of bioaccumulation, and high toxicity (Lopes et al., 2020). Despite environmental protection laws and regulations developed to control the emission of PTMs into water bodies, conventional treatment methods are often insufficient to prevent their impact on ecosystems. Additionally, nonpoint sources of contamination, such as trace metals occurring in soil and atmosphere due to the use of fertilizers, waste disposal, or burning of PTMs-contaminated materials, make pollution control against these elements challenging (Foesch et al., 2020; W. Li & Achal, 2020; A. F. S. Soares & Souza e Souza, 2020; J. S. Soares et al., 2017; Trevizani, 2019).

Chromium (Cr) is one of the most common metallic contaminants in industrial waste from processing, electroplating, alloys, and metallurgy, electronic components manufacturing, and electronic waste recycling

* Corresponding author.

E-mail address: avalente@ci.uc.pt (A.J.M. Valente).

¹ Pedro M.C. Matias and Talles B. Costa equally contributed to this study.

(Avidbegović et al., 2018; Huang et al., 2018; Singh et al., 2022). In particular, Cr(VI) is toxic to plants and animals because it is a strong oxidizing agent and a potentially carcinogenic and genotoxic species. In this regard, the European Union (EU) has limited the amount of total Cr in drinking water to 0.05 mg L⁻¹ (in the European Council Directive 98/83/EC). The World Health Organization suggests a safe level of Cr(VI) in water of up to 0.05 mg L⁻¹. Limits of 1 mg L⁻¹ for Cr(VI) and 5 mg L⁻¹ for total Cr have also been imposed on discharges into the aquatic media in the EU Member States. These countries must also report situations where total chromium discharges into water by a single infrastructure exceed 50 kg per year (Vaipoulou & Gikas, 2020).

Commonly used methods to remove Cr(VI) from water, such as membrane separation, reverse osmosis, ion exchange, coagulation-flocculation, photocatalytic degradation, and reduction followed by chemical precipitation, are typically unsatisfactory due to high costs, the production of large amounts of chemical sludge, and the unsatisfactory removal efficiencies to achieve the required levels in water, especially when Cr(VI) is present at trace levels (Islam et al., 2019; Park et al., 2007). Consequently, adsorption approaches have emerged as a viable, environmentally beneficial, methodologically simple, and cost-effective alternative technology for efficiently remedying water sources contaminated with various hazardous substances.

Nowadays, meso- or microporous materials are up-and-coming for sorption treatment due to their properties (e.g., high surface area, recyclability, and low density) (Ciuffarin et al., 2023; Lam et al., 2018; Y. Wang et al., 2019; Zubair et al., 2019). Furthermore, using biomass to prepare porous sorbent materials offers ecological advantages, highlighting the biodegradability and low toxicity. The main bio-based polymers are cellulose, alginate, pectin, chitosan, and starch (Zhao et al., 2018), which contain various functional groups that allow for the immobilization of PTMs (El-Naggar et al., 2020; Rogovina et al., 2018; Sam et al., 2020; Y. Wang et al., 2019). Sodium alginate is a high-molecular-weight polysaccharide primarily found in the cell walls of brown algae, consisting of β-D-mannuronic and α-L-guluronic acids and bearing both hydroxyl and carboxyl groups that allow the formation of hydrogels via ionotropic gelation (Du et al., 2024; H. Wang et al., 2024). Starch is a noteworthy material employed for the sorption of PTMs due to its richness in hydroxyl groups allowing for effective interactions with many pollutants. Although it can be used independently (with or without functionalization), as a blend or composite, or even in nanoparticles, its potential as an adsorbent is still underestimated (Ahmad et al., 2020; Ahmad & Imran, 2024; Rakotomalala Robinson et al., 2023; Xia et al., 2023).

Our strategy consisted of synthesizing blends of starch-alginate-based beads and POPs (porous organic polymers). POPs are advanced purely organic materials, presenting high stability, surface area, porosity, density of active sites, and low density. Additionally, they show luminescent properties. They comprise many materials with optimized physicochemical properties that show high efficiency, versatility or selectivity, quickness, and reusability for sensing and removing contaminants (Fajal et al., 2023; S. Lu et al., 2021; Matias et al., 2023, 2025). At the best of our knowledge only few bifunctional materials have been developed allowing the simultaneous detection and removal of chromium (Deng et al., 2023; X. Wang, Luo, et al., 2025; Zhou, Chen, et al., 2025).

The present study aims to evaluate the performance of an imine-linked triazine-based porous organic polymer powder (IT-POP) and eco-friendly starch-alginate-containing gels reinforced with different loads of IT-POP for dual application: optical sensing and sorption of Cr(VI). The recovery of this metal, envisioning its reuse at the industrial level, which is environmentally and economically crucial from a circular economy perspective, was also assessed. The hypothesis of this work was formulated on the following criteria: 1) efficient and high sorption capacity, 2) luminescent responsive properties and 3) synergistic effect. The IT-POP has a tendency to agglomerate, which hinders its potential use in practical applications (e.g., continuous flow systems). This can be

overcome by using low-cost natural polymers (sodium alginate and starch) that can be easily processed as beads. Thus, the main objective of the work is to develop a hybrid bifunctional material where both materials can contribute synergistically for the simultaneous removal and detection of Cr(VI) oxyanions. Since the luminescent response is based on interaction phenomena, we can anticipate that the presence of polysaccharides and POP will have a synergistic effect on both desired responses: removal and sensing. We envisage the preparation of a novel, robust, sustainable and more economical and scalable bifunctional architecture for the practical application as an efficient sorbent and sensor towards hexavalent chromium. In this context, the main novelty is the compatibilization of natural materials with a new family of advanced materials – POPs, which is an approach that has still been underexplored to date.

2. Materials and methods

2.1. Materials

In this work, the following materials were used: potato starch ($M_w = (52.9 \pm 8.3) \times 10^3 \text{ g mol}^{-1}$ (more details in section 2.3), 22–26 % amylose and 74–78 % amylopectin (Health Council of the Netherlands: Committee on Updating of Occupational Exposure Limits, 2002), Pan-Reac AppliChem), sodium alginate ($M_w = (23.5 \pm 5.1) \times 10^3 \text{ g mol}^{-1}$ (see section 2.3), mannuronate/guluronate acid ratio of 1.61 (Emami et al., 2018), Sigma-Aldrich), citric acid monohydrate (purity of 99 %, LABCHEM), sodium hydroxide (99.4 % purity, José Manuel Gomes dos Santos – JMGS), calcium chloride (purity ≥ 99 %, PanReac AppliChem), 4-aminobenzonitrile (purity >99 %, Fluorochem), trifluoromethanesulfonic acid (>98 %, Alfa Aesar), 4-hydroxybenzoic acid (99 % purity, Sigma-Aldrich), dimethylsulfoxide (DMSO, purity ≥ 99.5 %, Honeywell), acetic acid (≥ 99.8 %, Honeywell), tetrahydrofuran (THF, purity ≥ 99.9 %, Honeywell), hexamethylenetetramine (HMTA, ≥ 99 %, Riedel-de Haën), trifluoroacetic acid (TFA, 99.9 % purity, abcr GmbH), nitric acid (purity of 69 %, PanReac AppliChem), hydrochloric acid (37 % purity, Chem-Lab), methanol (≥ 99.85 % purity, JMGS), acetone (purity >99.6 %, JMGS), potassium dichromate (purity of 99.5 %, M&B laboratory chemicals), cadmium(II) nitrate tetrahydrate (≥ 99 % purity, Sigma-Aldrich), copper(II) nitrate 2.5aq (≥ 99 % purity, Chem-Lab), nickel(II) nitrate hexahydrate (≥ 96 % purity, Riedel-de Haën), lead(II) nitrate (≥ 99 % purity, Honeywell), zinc(II) nitrate hexahydrate (≥ 98 % purity, Riedel-de Haën), manganese(II) nitrate tetrahydrate (≥ 97 % purity, Riedel-de Haën), standard stock solutions of nickel, lead, cadmium or copper (1000 mg L⁻¹, PanReac AppliChem), chromium standard solution (1000 mg L⁻¹, Chem-Lab), zinc or manganese standards for AAS (1000 mg L⁻¹, Supelco®, Sigma-Aldrich), deuterium oxide (99.9%D, Eurisotop) and deuterated DMSO (DMSO-d₆, 99.8%D, Eurisotop). Distilled and Milli-Q water were used as received. Commercially available chloroform was purified before use, following standard procedures.

2.2. Preparation of IT-POP and starch-alginate-based IT-POP (St-Alg-IT-POP) beads

2.2.1. Synthesis of IT-POP

Imine-linked triazine-based porous organic polymer (IT-POP) was prepared based on a previously reported procedure (Matias et al., 2023, 2024). Briefly, a Schiff base polycondensation reaction between the triamine 1,3,5-tris-(4-aminophenyl)triazine (TAPT, 3.05 mmol, 1.08 g) and the dialdehyde 3,5-diformyl-4-hydroxybenzoic acid (DHA, 4.58 mmol, 0.89 g) was performed in DMSO (20 mL) and CH₃COOH 3 mol dm⁻³ (7.5 mL) at 140 °C under an inert N₂ atmosphere for 48 h. The precipitate was filtered under gravity and washed with THF, acetone, and methanol. Then, the polymer was neutralized by dropwise addition of a NaOH solution and recovered by filtration and washing with water and acetone. The neutral form was used in subsequent synthetic and

application procedures. Furthermore, TAPT and DHA monomers were prepared before the polymer synthesis, starting from 4-aminobenzonitrile (Abuzeid et al., 2019) and 4-hydroxybenzoic acid (Alqarni, 2018), respectively.

2.2.2. Synthesis of St-Alg-IT-POP gel beads

Starch-alginate-based IT-POP gel beads (St-Alg-IT-POP) were synthesized according to the methodologies proposed by Abhari et al. (Abhari et al., 2017), Camani et al. (Camani et al., 2021), and Costa et al. (Barcelos da Costa et al., 2021). First, potato starch (3.50 g) and sodium alginate (1.00 g) were suspended in distilled water (50 mL). After, sodium hydroxide (5.00 mmol, 0.20 g) was added, and the system's temperature was maintained at 60 °C for 3 h. The mixture was continuously stirred until gelatinization was achieved due to the opening of the starch grains and solubilization of the biopolymers. Then, citric acid (3.57 mmol, 0.75 g) was added, and the mixture was kept under stirring at 60 °C for 1 h to allow esterification and covalent crosslinking. At this time, a certain amount of IT-POP (0, 5, 10, or 15 wt%, POP:starch) was sonicated in distilled water (5 mL) for 30 min. The resulting IT-POP suspension was added to the reaction mixture under stirring, and the temperature was increased to 90 °C and maintained for 1 h to complete the crosslinking process. Subsequently, the starch-alginate-based gels were dropped into a Ca(II) crosslinking solution (35 g L⁻¹) to promote external gelation. To ensure complete ionotropic crosslinking, the beads were kept under stirring in the Ca(II) solution for 2 h. Moreover, St-Alg or St-Alg-IT-POPx% (x = 5, 10, or 15 %) beads were washed with distilled water until pH \cong 6.0. Finally, the beads were frozen overnight and freeze-dried at -54 °C for 24 h. Fig. 1 summarizes the bead preparation steps.

2.3. Physicochemical characterization methods

The weighted average molecular masses (M_w) of starch and sodium alginate (section 2.1) were determined by DOSY NMR spectroscopy using a Bruker Avance III spectrometer, 400 MHz, equipped with a 5-mm high power ¹H Bruker DiffBB diffusion probe (gradient strength up to 17 T m⁻¹). For the experiments, 5.0 mg mL⁻¹ starch and sodium alginate solutions were prepared in DMSO-*d*₆:D₂O (9:1, v/v) and D₂O, respectively, and the spectra were acquired at 25 °C in 5-mm NMR test tubes. Pulsed gradient stimulated echo (PGStE) sequence was applied, with $\gamma = 26,752 \text{ rad s}^{-1} \text{ G}^{-1}$, $\delta = 0.01 \text{ s}$ and $\Delta = 0.10 \text{ s}$, and the self-diffusion coefficients, $D \text{ (m}^2 \text{ s}^{-1}\text{)}$, of both polysaccharides were determined through the measured echo intensity, using an average of 16

scans (Valente et al., 2005). Then, the molecular weights and respective errors were estimated by a polymer-independent universal calibration reported elsewhere (Tooley et al., 2024), knowing the self-diffusion coefficients of starch ($D = (1.15 \pm 0.08) \times 10^{-11} \text{ m}^2 \text{ s}^{-1}$) and alginate organic moiety ($D = (4.36 \pm 0.08) \times 10^{-11} \text{ m}^2 \text{ s}^{-1}$) and the bulk viscosities, $\eta \text{ (mPa s}^{-1}\text{)}$, of D₂O ($\eta = 1.097 \text{ mPa s}^{-1}$) (Ibuki & Nakahara, 1991) and DMSO-*d*₆:D₂O (9:1, v/v) mixture ($\eta \approx 2.379 \text{ mPa s}^{-1}$) (Evans et al., 2013; Valente & Söderman, 2019). The molecular weight values for alginate were corrected to include the contribution of the counterion.

The materials were characterized by Fourier-transform infrared spectroscopy (FTIR), thermogravimetric analysis (TGA), absorption and fluorescence spectroscopies, ζ -potential measurements, scanning electron microscopy (SEM), and energy-dispersive X-ray spectroscopy (EDX). FTIR spectra of the samples (at 5 %, w/w, dispersed in KBr) were carried out on a Thermo Fisher Scientific Nicolet 6700 spectrometer (Waltham, Massachusetts, USA) between 4000 and 400 cm⁻¹. TGA was performed between (25–800) °C on a Netzsch Tarsus TG 209 F3 thermogravimetric (Selb, Germany), employing a N₂ flow rate of 50 mL min⁻¹ and a heating rate of 10 °C min⁻¹. The absorption spectra of the powdered samples were recorded in the 277–900 nm range, using an integration time of 25 s and an average of 10 measurements on an Avantes Sensline spectrometer (AvaSpec-ULLS-TEC). This system consisted of a UV-Vis-NIR light source (Mikropack DH-2000-BAL) and a 1.3 mm diameter fiber optic probe (FCR-UVIR 200/600-2-IND). The probe was positioned in a metal holder to maintain a consistent distance from the surface and was oriented perpendicular to the samples during measurement. An empty crucible served as the blank for calibration. Emission spectra were obtained using a Horiba-Jobin-Yvon Spex Fluorog 3–22 fluorimeter (New Jersey, USA), selecting proper excitation wavelengths for each system (430 nm or 351 nm). ζ -potential of the polymeric particles as a function of pH was measured using a Malvern Zetasizer NanoZS analyzer and 0.5 mg mL⁻¹ polymer dispersions in milli-Q water at 25 °C. The ζ -potential values were determined through the Smoluchowski equation by assessing the electrophoretic mobility of the particles in each sample. pH adjustments were made with aqueous NaOH and HNO₃ solutions using a Radiometer Copenhagen MeterLab PHM240 pH meter equipped with a WTW Sentix-MicB microelectrode. The morphology of the polymers was observed using a field-emission scanning electron microscope (Merlin Compact/VPCompact FE-SEM, Carl Zeiss Microscopy GmbH, Jena, Germany) at 1.5 kV. The surface chemical composition analyses were performed on the FE-SEM coupled with an EDX spectrometer (X-MaxN Silicon Drift EDX Detector, Oxford Instruments, Abingdon, UK).

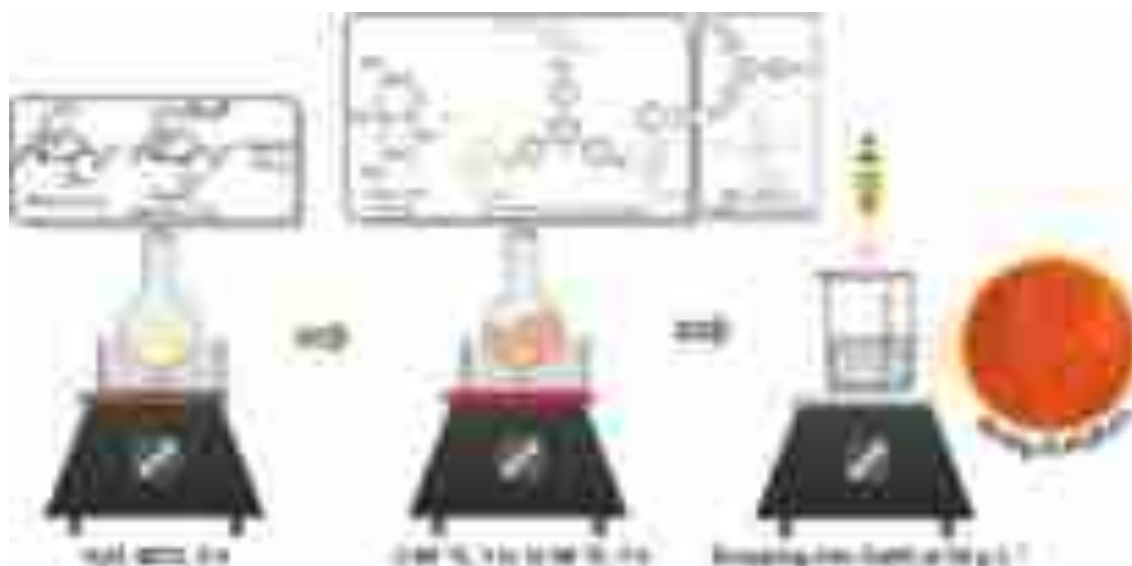


Fig. 1. Schematic representation of the preparation steps of starch-alginate-based-IT-POP beads (St-Alg-IT-POPx%).

2.4. Sorption assays

Sorption assays for both the IT-POP powder and the St-Alg-IT-POPx % beads were carried out by stirring a given mass of each sorbent in model Cr(VI) solutions at 120 rpm in a LABWIT ZWY-100H incubator. The pH of the solution, initial concentration of Cr(VI) (C_0), solid-liquid ratio (R_{S-L}), temperature (T), and contact time (t) were varied between (2–8), (0.1–8.0) mM, (0.5–4.0) mg mL⁻¹ (for IT-POP) or (1.5–10.0) mg mL⁻¹ (for St-Alg-IT-POP), (25–55) °C, and (5–1440) minutes, respectively.

Cr(VI) concentrations were quantified using ultraviolet-visible (UV-vis) spectroscopy (Shimadzu UV-2600i), from absorbances recorded at 351 nm. Additionally, a Thermo Scientific iCE 3500 spectrometer was employed to carry out flame-atomic absorption spectroscopy (F-AAS) studies using an air/acetylene flame and a hollow cathode lamp for the direct determination of total Cr content in aqueous solutions at 358 nm. A chromium standard solution of 1000 mg L⁻¹ in 0.5 M HNO₃ was used to calibrate the measurements performed by F-AAS. Before quantification, the sorbent-containing samples were filtered through nylon syringe filters of 0.22 μm pore size. Once Cr concentrations were known both at $t = 0$ (C_0) and after a time t ($C_t = C_e$ at equilibrium), the sorption performance was evaluated by calculating the sorption efficiency (Q , %, eq. (1)) and sorption capacity ($q_t = q_e$ at equilibrium, mmol g⁻¹, eq. (2)),

$$Q = \left(\frac{C_0 - C_t}{C_0} \right) \times 100 \quad (1)$$

$$q_t = \frac{(C_0 - C_t) \times V}{m} \quad (2)$$

where V (L) and m (g) are the volume of the Cr(VI) solution and the mass of the sorbent, respectively.

For IT-POP and the best-performing gel beads (St-Alg-IT-POP15%, see section 3.2.1.), sorption isotherms and kinetics were studied under optimized experimental conditions, i.e., pH = 2 (Fig. 2F, section 3.1.), $R_{S-L} = 0.5$ mg mL⁻¹ (IT-POP) or 3.3 mg mL⁻¹ (St-Alg-IT-POP15%)

(Fig. S1, in the supplementary material), $t = 24$ h (for isotherms), and C_0 (total Cr) = 0.60 mM and $T = 25$ °C (for kinetics). Non-linear kinetic and equilibrium data modeling was performed to investigate the sorption mechanisms. For that, the pseudo-first-order (PFO) and pseudo-second-order (PSO) kinetic (Vareda et al., 2016) and the Langmuir, Freundlich, and Sips isotherm models (J. Wang & Guo, 2020) (see Table S1 in supplementary material – from Eq. S1 to S5, respectively) were fitted to the obtained Cr(VI) oxyanions sorption profiles. The model's goodness was evaluated by the coefficient of determination (R^2) and the Akaike information criterion (AIC) (Filho et al., 2018) (Table S2, Eqs. S6 and S7, respectively).

Sorption isotherms were performed at different temperatures in order to assess the thermodynamic parameters of sorption, the change of: Gibbs energy (ΔG^0 , kJ mol⁻¹), enthalpy (ΔH^0 , kJ mol⁻¹), and entropy (ΔS^0 , J K⁻¹ mol⁻¹) (Table S3, Eqs. S8 – S10). The values of equilibrium constants (K_e) were calculated from the equilibrium constants obtained by the sorption isotherm model, which best described the experimental data at each T , using Eq. S11 (Table S3) (Lima et al., 2019).

Multicomponent sorption assays were carried out at 25 °C starting from equimolar aqueous solutions containing 0.15 mmol L⁻¹ of each of seven different metal ions: Pb(II), Cu(II), Cd(II), Zn(II), Mn(II), Ni(II), and Cr(VI), and using a polymer dose of 0.5 mg mL⁻¹ (IT-POP) and 3.3 mg mL⁻¹ (St-Alg-IT-POP15%). After the 24 h selectivity sorption tests, all samples were filtered using 0.22 μm nylon syringe filters, and the metal ions in each filtrate were separated and quantified by UV-vis (Cr(VI) anions) and F-AAS (with an air/acetylene flame and using hollow cathode lamps for the direct quantification of Zn, Pb, Cd, Ni, Mn, Cu or total Cr at 214, 217, 229, 232, 280, 325 or 358 nm, respectively). Then, sorption efficiencies (Q , %) and capacities at equilibrium (q_e , mmol g⁻¹) were estimated by eqs. (1) and (2), respectively, and the selectivity parameter (S , %) was calculated by eq. (3), where n_I , n_{II} , n_{III} , n_{IV} , n_V , n_{VI} and n_{VII} (mmol) are the chemical quantity sorbed of each of the seven metals.

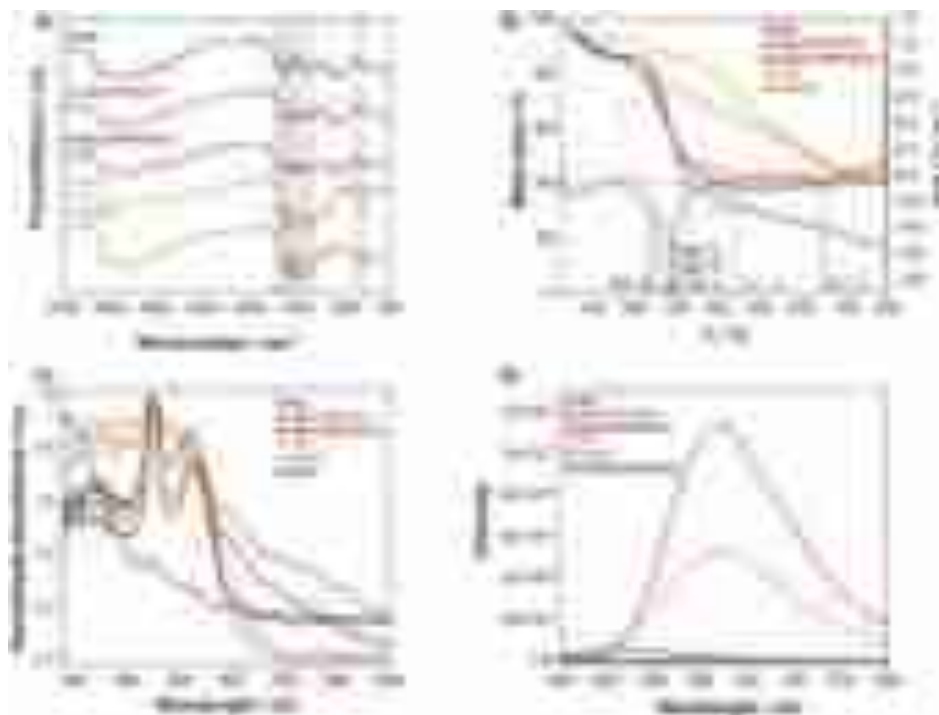


Fig. 2. A) FTIR spectra, B) Thermograms and derivatives (dTGs), C) Absorption spectra and D) Emission spectra of St-Alg (blue), St-Alg-IT-POP15% (red), St-Alg-IT-POP15%/Cr (wine), IT-POP (orange), IT-POP/Cr (dark yellow), and K₂Cr₂O₇ salt or 8.0 mM Cr(VI) solution (black). (For interpretation of the references to colour in this figure legend, the reader is referred to the web version of this article.)

$$S (\%) = \frac{n_I}{n_{\text{total}}} \times 100 = \frac{n_I}{n_I + n_{II} + n_{III} + n_{IV} + n_V + n_{VI} + n_{VII}} \times 100 \quad (3)$$

2.5. Fluorescence measurements

The capacity of the materials to detect Cr(VI) in water was evaluated through steady-state fluorescence studies. For that, IT-POP ($R_{S-L} = 0.5 \text{ mg mL}^{-1}$) or St-Alg-IT-POP15% ($R_{S-L} = 3.3 \text{ mg mL}^{-1}$), both in powder form, were stirred in aqueous Cr(VI) solutions at C_0 ranging from 0 to 5.0 mM, pH = 2.0 and 25 °C, placed in 1 cm optical path quartz cuvettes. Subsequently, the fluorescence of the materials was monitored over time ($t = 5\text{--}1440 \text{ min}$), between 440 and 800 nm, after excitation at 430 nm. Control experiments of the Cr(VI) solution (at 8.0 mM) in the absence of the powder materials were carried out by exciting at 430 nm, and the absorbance maximum of Cr(VI) in water (351 nm), and no fluorescence was observed for the dissolved metal.

To get information about the quenching mechanism of the fluorescence of IT-POP and St-Alg-IT-POP15% powders, the experimental data relating the quotient between the fluorescence intensity in the absence (I_0) and in the presence (I) of Cr(VI) oxyanions, at 600 nm (IT-POP) and 615 nm (St-Alg-IT-POP15%), were analyzed by using the linear Stern-Volmer equation (eq. (4)),

$$\frac{I_0}{I} = 1 + K_S[\text{Cr(VI)}] \quad (4)$$

where $K_S \text{ (M}^{-1}\text{)}$ is the static quenching constant related to the formation of the non-fluorescent ground-state complex between the fluorophore entities and the Cr(VI) quencher species (Lakowicz, 2006).

3. Results and discussion

3.1. Synthesis and physicochemical characterization

IT-POP was synthesized through the Schiff base formation reaction between the primary amine groups of TAPT triamine and the formyl groups of DHA dialdehyde, resulting in a porous polymer containing triazine rings, imine bonds and a richness in hydroxyl and carboxyl groups. IT-POP powder was also incorporated into a polymeric matrix of starch and alginate crosslinked with citric acid to obtain gel beads. The most promising IT-POP-containing beads (St-Alg-IT-POP15%, see section 3.2.1.), the pure beads (St-Alg) and IT-POP were considered for characterization purposes.

FTIR characterization (Fig. 2A) showed a new band in the St-Alg beads at 1735 cm^{-1} (not present in pure starch and alginate, see Fig. S2), attributed to C=O elongation of the ester group formed by the covalent crosslinking reaction of starch and alginate with citric acid (Lipatova & Yusova, 2021). In addition, C—H bending vibrations (845 and 752 cm^{-1}), C—O—C bending from anhydroglucose ring (937 cm^{-1}), C—O stretching (1152 cm^{-1}) and O—H bending of starch/alginate + asymmetric stretching of carboxyl C=O bonds of alginate (1620 cm^{-1}) were observed. IT-POP also presents characteristic peaks in the infrared spectrum, which also appear in IT-POP-containing beads, proving the anchoring of the polymer. These bands include C—N bending (815 cm^{-1}), C—N stretching (1360 cm^{-1}), C=C stretching of aromatic rings (1505 cm^{-1}), C=N of triazine moieties (1607 cm^{-1}), and the stretching of C=N bond (1660 cm^{-1}) resulting from the polymerization reaction between TAPT and DHA. For IT-POP, a shoulder was also observed at 1735 cm^{-1} , assigned to C=O stretching of its carboxyl groups. Additionally, peaks at 2925 and 3360 cm^{-1} can be attributed to C—H and O—H elongations of the hydroxyl and carboxyl groups. Slight differences were noted by comparing the FTIR spectra of the IT-POP and IT-POP-containing beads before and after sorption, proving their interaction with Cr(VI). For both materials, shifts towards higher wavenumbers of the bands centered at 1360 and 1505 cm^{-1} were observed, as well as an increase in the relative intensity of the band at 1505 cm^{-1} compared

to that at 1607 cm^{-1} , showing the involvement of the amine groups and (hetero)aromatic rings in Cr(VI) sorption, possibly by coordination, hydrogen bonds or electrostatic interactions (since for pH < 7.0, N atoms of the triazine rings are protonated (Hynes et al., 2020; Matias et al., 2023)). The sorption of Cr(VI) by IT-POP also seems to mask the presence of carboxyl groups in the polymer structure, as evidenced by the disappearance of the shoulder at around 1735 cm^{-1} . Additionally, the band related to the esterification of starch and alginate shows a slight wavenumber shift due to the presence of Cr(VI) in St-Alg-IT-POP15% beads.

The thermograms (Fig. 2B) showed two degradation steps centered at 252 °C (of alginate) and 297 °C (of starch) for St-Alg beads. At the same time, St-Alg-IT-POP15% only presented one decomposition step centered at intermediate values to those of the native beads (i.e., 272 °C). The decrease from 297 °C to 272 °C may be justified by the lowest degree of crosslinking with citric acid in St-Alg-IT-POP15% (compared to St-Alg), probably due to IT-POP. Additionally, IT-POP polymer proved to be significantly more stable than the beads, showing a mass loss centered at 447 °C , due to the degradation of TAPT. After sorption, both materials increased their thermal stability from $447 \text{ °C} \rightarrow 647 \text{ °C}$ (for IT-POP) and $272 \text{ °C} \rightarrow 287 \text{ °C}$ (for St-Alg-IT-POP15%), which can be explained by the sorbed Cr(VI) promoting further crosslinking of polymer chains, increasing their compaction. The more significant increase in the thermal stability of IT-POP/Cr may be associated with IT-POP interacting with a more considerable number of metal oxyanions.

The optical properties of IT-POP and St-Alg-IT-POP15%, both in powdered form were evaluated by solid-state absorption and emission spectroscopies. The absorption spectra (Figs. 2C) showed maximum wavelengths at $\lambda^{\text{abs}} = 338, 450$ and 510 nm for both IT-POP and St-Alg-IT-POP15%, possibly assigned to $\pi \rightarrow \pi^*$ transitions involving the (hetero)aromatic rings and the conjugated structure of IT-POP, and $n \rightarrow \pi^*$ due to the presence of nitrogen and oxygen atoms, respectively, from low to high wavelengths (Matias et al., 2024). These peaks differ significantly from the absorption spectra of St-Alg beads (with a more intense absorption band at 295 nm and a less intense one at 448 nm) and provide evidence of the incorporation of IT-POP into the St-Alg polymer matrix. After sorption, the spectra of IT-POP and St-Alg-IT-POP15% with Cr(VI) sorbed (IT-POP/Cr and St-Alg-IT-POP15%/Cr, respectively) were similar to the absorption spectra of $\text{K}_2\text{Cr}_2\text{O}_7$, with maximum wavelengths at $\lambda^{\text{abs}} = 450$ and 525 nm , confirming the presence of Cr on the surfaces of the materials. Furthermore, the fluorescence spectra (Fig. 2D) also allowed us to infer about Cr(VI) sorption since IT-POP is fluorescent (while St-Alg is not), and both IT-POP and IT-POP-containing beads reduced to powder emit radiation at 625 nm upon excitation in the visible region. The interaction of the two materials with Cr(VI) resulted in quenching the emission of the polymers, which opens the door for their application as probes/sensors, as will be discussed in section 3.3.

The SEM micrographs showed that IT-POP (Fig. 3A) presented a homogeneous, spherical, and diffuse morphology, and some roughness, characteristic of porous materials. A highly porous network regarding St-Alg beads was observed (Fig. S3). After addition of IT-POP to form St-Alg-IT-POP15% beads (Fig. 3B), it was observed a good anchoring and dispersion of IT-POP, since an IT-POP-like morphology was identified across the smooth surface of the beads (see also Fig. S4), as well as the pore availability in the St-Alg polymer matrix. On the other hand, after sorption of Cr(VI), a reduction of empty pores (coupled with an increase in compaction) was observed for both the IT-POP (Fig. 3C) and the St-Alg-IT-POP15% (Fig. 3D), indicating their occupancy by Cr(VI) species. Furthermore, the SEM-EDX surface mapping confirmed the presence of Cr(VI) homogeneously and uniformly distributed and sorbed over the surface of IT-POP (Fig. 3E) and St-Alg-IT-POP15% (Fig. 3F).

According to the results of the EDX technique (Table S4 and Fig. S5), neat St-Alg beads presented the elements C (49.4 wt%), O (47.7 wt%), Si (0.1 wt%), and Ca (2.8 wt%) in their composition; the presence of Ca(II)

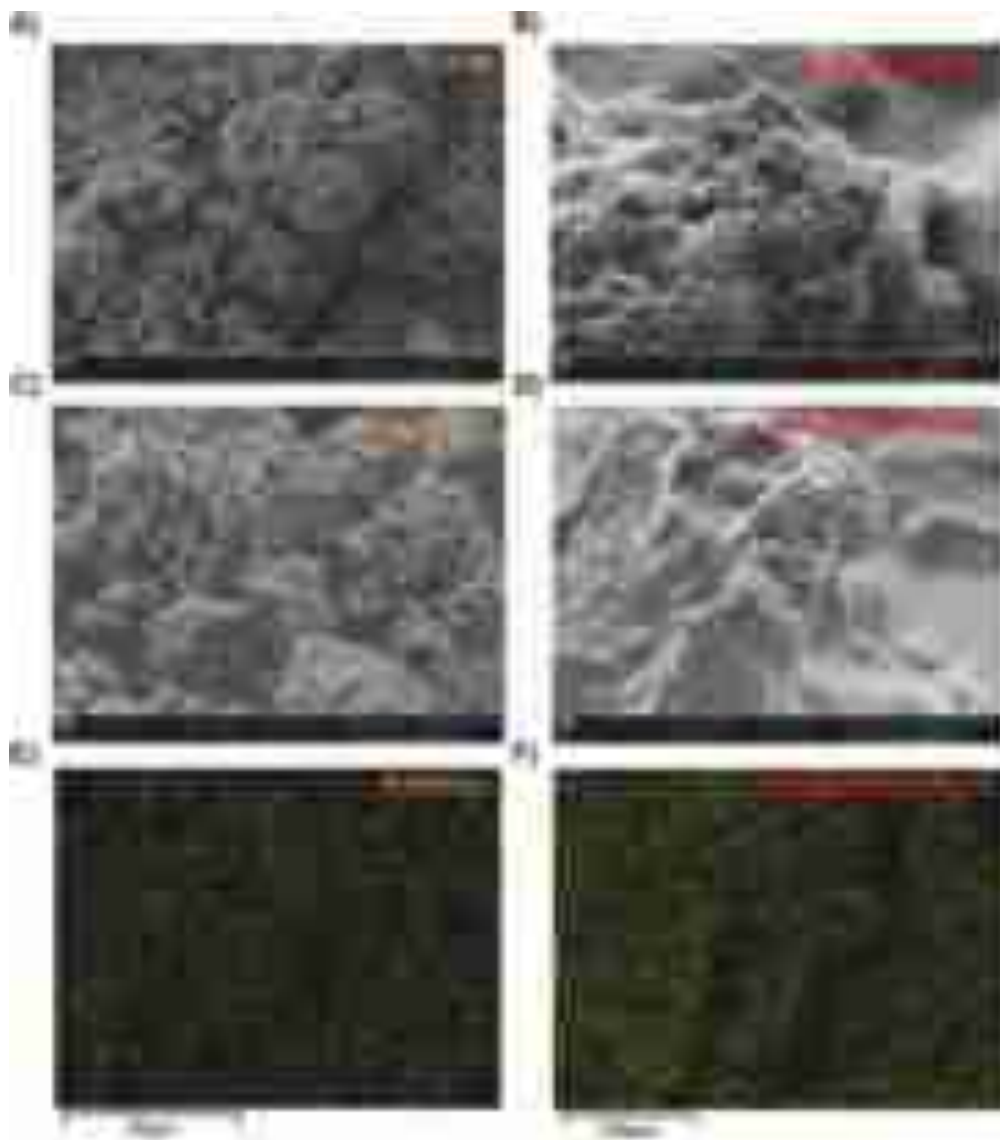


Fig. 3. SEM micrographs of A) IT-POP, B) St-Alg-IT-POP15%, C) IT-POP/Cr, D) St-Alg-IT-POP15%/Cr (10,000 \times magnification); and SEM-EDX surface mapping of Cr (VI) for E) IT-POP/Cr and F) St-Alg-IT-POP15%/Cr.

is related with the ionotropic gelation involving the exchange of Na(I) by Ca(II). The presence of Si can be attributed to traces of diatoms and unicellular organisms, whose shells contain SiO₂, in the commercial sodium alginate (da Costa et al., 2024). IT-POP presented 72.6 wt% of C (because of its aromatic structure and C=N bonds), 15.8 wt% of N (associated with the triazine rings and imine bonds), 1.1 wt% of S (due to the residual content of DMSO retained in its structure), and 10.6 wt% of O (owing to residual DMSO, and hydroxyl and carboxyl groups). After anchoring IT-POP into the St-Alg-IT-POP15% beads, despite the C, O, and Ca elements, a 1.4 wt% of N was detected, confirming the presence of POP on the polymeric matrix of the beads (in a content of around 11 wt%). Upon Cr(VI) sorption, a reduction of N and Ca contents or even the disappearance of these elements was observed in IT-POP/Cr and St-Alg-IT-POP15%/Cr surfaces, indicating the involvement of these elements in the sorption mechanism. Additionally, the presence of K was derived from the use of potassium dichromate salt as a Cr(VI) source, while the contents of Cr on the surface of both post-sorption materials (10.0 wt% for IT-POP/Cr and 0.6 wt% for St-Alg-IT-POP15%/Cr) proved that there was, in fact, Cr(VI) sorption.

3.2. Sorption of hexavalent chromium

3.2.1. Preliminary studies of Cr(VI) sorption

IT-POP showed a significant sorption capacity for Cr(VI) removal (Fig. S1A), which was much higher than that found for pure starch-alginate beads (Fig. S1B). Regarding IT-POP-containing beads composition, an IT-POP loading of 15 wt% led to a greater approximation to the remarkable sorption performance of the pure IT-POP, due to the higher anchoring of the porous organic polymer and, consequently, the greater availability of active sites capable of interacting with Cr(VI). Furthermore, the proximity between the sorption efficiencies of IT-POP and St-Alg-IT-POP15% materials was even more noticeable when the $R_{S-L} = 3.3$ mg mL⁻¹ was selected for the St-Alg-IT-POP-15% beads. Although, in this condition, the amount of IT-POP within the beads was lower than the equivalent of IT-POP powder at the selected R_{S-L} of 0.5 mg mL⁻¹ (for which the best relationship between Q and q_e was obtained), a compromise was reached to avoid using an extremely large amount of material while maintaining a good Q vs. q_e ratio. Thus, these results showed that the loading dose of IT-POP with high sorptive capacity is a fundamental factor in improving the removal potential of the sorbent.

The surface charge of the materials (see Fig. S6A), the chemical

speciation of the metal species in water, and the ability to establish electrostatic interactions between a sorbate and a sorbent can vary as a function of the pH, thus it is a significant indicator that influences sorption performance. In the systems under study, the poor efficacy of both IT-POP and St-Alg-IT-POP15% for removing of Cr(VI) oxyanions with increased pH is observed (Fig. S6B). This is attributed to the fact that the materials have an isoelectric point at pH = 4.7 (IT-POP) and 3.4 (for St-Alg-IT-POP15%, which is as expected closer to that of neat St-Alg beads, at pH = 2.4), meaning that above these pH values their surfaces are negatively charged and repulsive electrostatic effects with the anionic Cr(VI) species in solution will predominate. Therefore, pH = 2 was selected for further studies; at this pH, the predominant Cr(VI) species are $[\text{HCrO}_4]^-$ oxyanions (Alvarez-Galvan et al., 2022) and the sorbents are positively charged promoting the establishment of electrostatic interactions.

3.2.2. Effect of concentration and temperature on Cr(VI) removal: Sorption isotherms and thermodynamics parameters

Fig. 4A and D show that IT-POP and St-Alg-IT-POP15% have excellent removal efficiencies, i.e., close to or above 90 % for the lowest C_0 (0.1 and 0.5 mM). The sorption efficiencies decrease when the initial concentrations increase due to the saturation of the active sites of the polymeric materials. It is also possible to observe that the increase in temperature up to 55 °C improved the performance of both materials. In particular, at $T = 55$ °C, the removal efficiencies increased from $C_0 = 0.1$ mM to $C_0 = 0.5$ mM, as a result of the increase in the concentration gradient between the solid and liquid phases and then decreased with the increase in C_0 for IT-POP; and stabilized between 0.5 and 2.0 mM and only start to decline for $C_0 > 2.0$ mM for St-Alg-IT-POP15%, indicating the occurrence of material saturation for higher concentrations.

The sorption isotherms obtained for IT-POP and St-Alg-IT-POP15% at different temperatures are depicted in Fig. 4B and E, respectively. Among the three isotherm equations (Langmuir, Freundlich and Sips) used to model the experimental profiles, the one that best described all the systems was the Sips isotherm (see Table S5). According to this

equation, maximum sorption capacities (q_{ms}) equal to (3.3 ± 0.3) mmol g^{-1} (25 °C) and (4.7 ± 0.3) mmol g^{-1} (55 °C) were obtained for IT-POP and (0.71 ± 0.04) mmol g^{-1} (25 °C) and (1.07 ± 0.07) mmol g^{-1} (55 °C) for St-Alg-IT-POP15%, indicating that sorption is favored at higher temperatures, being an endothermic and entropy-controlled process. In addition, values of $n_S < 1$ (for IT-POP at all temperatures, and St-Alg-IT-POP15% at $T = 25$ and 30 °C) show some heterogeneity of the material and a non-cooperative chemisorption process (Foo & Hameed, 2010; Matias et al., 2024). In contrast, for St-Alg-IT-POP15% at $T = 35$ and 55 °C, n_S values increased and approach 1 ((0.9 ± 0.1) and (1.1 ± 0.3) , respectively), indicating that with the increase of temperature, the sorption behavior of Cr(VI) by St-Alg-IT-POP15% approaches to the Langmuir model and a homogeneous system, suggesting spontaneous monolayer sorption processes (J. Wang & Guo, 2020).

To check the availability of IT-POP sorption sites when anchored into the beads, the quotients between the maximum sorption capacities obtained for IT-POP powder and St-Alg-IT-POP15% beads were calculated for each temperature. Depending on temperature conditions, there was a reduction in the sorption capacity of the beads of 4.4 to 5.3 folds compared to the pure IT-POP powder. However, it is essential to emphasize that only around (9–11)% of the total mass of the beads corresponds to IT-POP polymer, so if the sorption result were proportional, the sorption capacity of the beads should have decreased by 10-fold. Therefore, it can be stated that the formulation of IT-POP in beads seems beneficial, as it reduces of the amount of IT-POP by ca. 2 folds to achieve the same result as in powder form. In addition, although the sorptive capacity of IT-POP powder was comparable and even superior to other POPs and polysaccharide-based composite materials, it should be emphasised that the St-Alg matrix, in itself presenting an innocuous sorptive effect of Cr(VI), can deagglomerate the IT-POP powder, making its capacity inside the bead superior to those obtained in most of the studies reported in the literature (Table 1). Thus, the strategy developed will enable the reduction of costs in the development of the material (since IT-POP is the most expensive component), while is obtained a more easily scalable and effective architecture for day-to-day

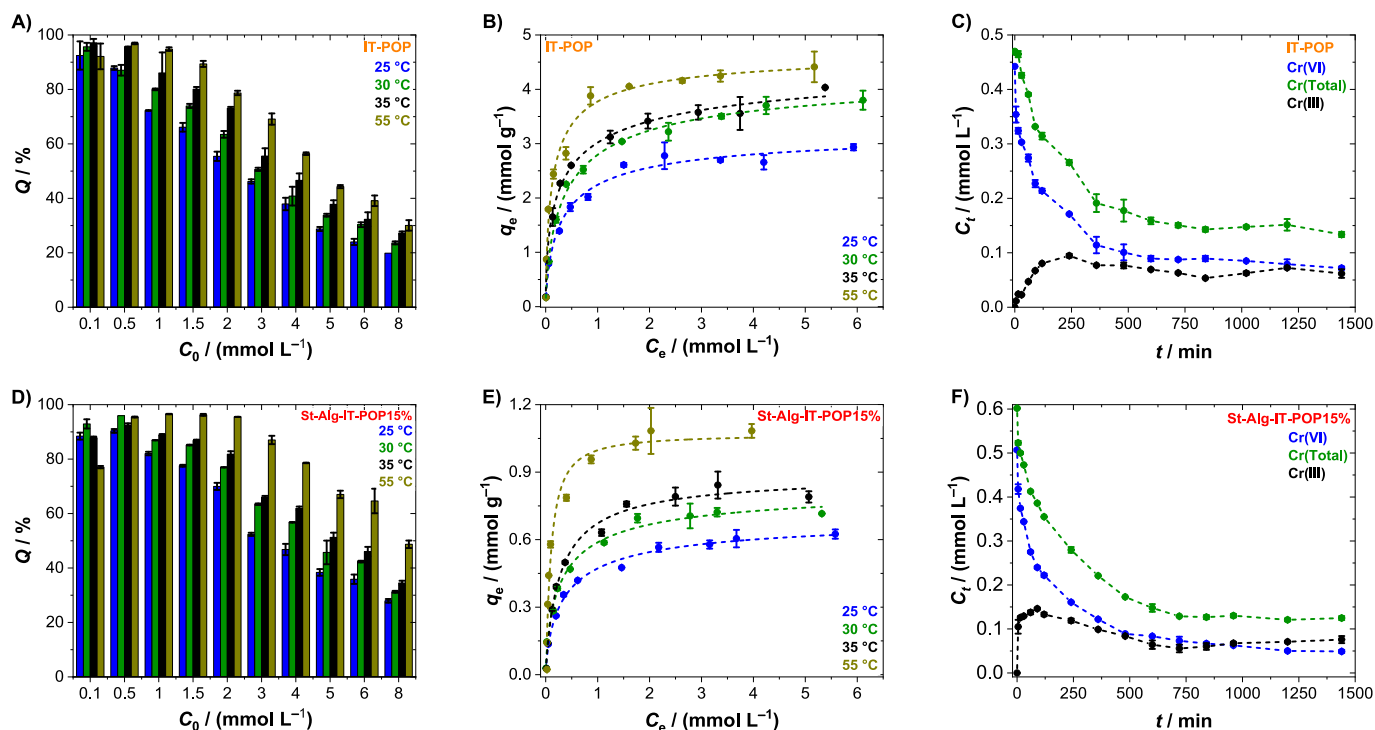


Fig. 4. Removal of Cr(VI) by IT-POP and St-Alg-IT-POP15%: A) and D) removal efficiencies as a function of the initial Cr(VI) concentration and temperature; B) and E) equilibrium isotherms (dashed lines represent the fits of Sips model); C) and F) Profiles of Cr(Total), Cr(VI), and Cr(III) concentration over time for $C_0 = 0.60$ mM (Cr(Total)) at 25 °C, pH = 2, $R_{S-L} = 0.5$ mg mL^{-1} (IT-POP) and $R_{S-L} = 3.3$ mg mL^{-1} (St-Alg-IT-POP15%).

Table 1

Maximum sorption capacity reported for Cr(VI) removal using different sorbents recently reported in the literature.

Sorbent	q_{\max} / (mg g ⁻¹)	pH	T / °C	Reference
IT-POP	171 223	2	25 55	This study
St-Alg-IT-POP15%	37 (369 per g _{IT-POP}) 57 (574 per g _{IT-POP})		25 55	
S-BC	26	3	45	(Ma et al., 2024)
S-PC	884	2	25	(Liang, Wu, et al., 2024)
MAST	165	7	25	(Tan et al., 2024)
M-SGC	37	6	25	(H. Li et al., 2024)
CS-SQDs	186	2	r.t.*	(Deng et al., 2023)
PAA-CNF-W	174	2	25	(X. Wang, Luo, et al., 2025)
NAH	169	> 4	25	(Zhou, Chen, et al., 2025)
SCG	93	2	30	(X. Li et al., 2025)
PBP@NaAlg	47	2	r.t.*	(Boyle et al., 2025)
G-LDH	472	7	20	(X. Wang, Wu, et al., 2025)
MPAC	115	1	20	(Zhou, Du, et al., 2025)
MAB	370	2	25	(Parlayıcı & Baran, 2025b)
Ca@AlgCs	11	3	30–50	(Venkatrajan et al., 2024)
Zr@AlgCs	15	3	30–50	
NAF	257	2	25	(Parlayıcı & Baran, 2025a)
HG-CNS _{5%}	4	3	r.t.*	(Alves et al., 2024)
CCD-PCP	432	3.5	r.t.*	(Daliran et al., 2023)
TET-BPB	530	–	r.t.*	(M. Lu et al., 2025)
ImIP1	423	–	r.t.*	(Y.-S. Wang, Yuan, et al., 2025)
HCNT-C4	191	2	25	(X. Liu et al., 2024)
TAPT-Bd-POP	16	5–6	25	(Machado et al., 2024)
CTF500	98	5	25	(S. Zhou et al., 2022)
PCPD	205	2	25	(H. Liu et al., 2022)
COP-NH2	305	3	–	(Kong et al., 2022)
iCON-5	266	7	r.t.*	(Chandra et al., 2022)
iPOP-ANT	331	–	–	(Sarkar et al., 2022)
iPOP-5(F)	301	7	25	(Mandal et al., 2022)
CON-LDU5	369	5–6	r.t.*	(Z.-J. Li et al., 2022)
DA-POP-1	341	2	25	(Cao et al., 2022)
PTPA-PIP	230	2–6	r.t.*	(Pan et al., 2024)
Fe ₃ O ₄ @COF-MT@PPy	429	2	25	(Liang, Liu, et al., 2024)

* r.t. means room temperature.

applications.

The increase in the sorption capacity with the temperature generally implies that chemical mechanisms can be involved in the capture of Cr(VI) by IT-POP and St-Alg-IT-POP15%, because ΔG can be lower than -20 kJ mol⁻¹, and ΔH is positive (Húmpola et al., 2013; Tran et al., 2016). However, given the magnitude of ΔG values (between -26 and -18 kJ mol⁻¹ see Table 2), physisorption seems more significant than chemisorption (Húmpola et al., 2013). The thermodynamic parameters (obtained from the linear fit of Fig. S7) showed that the Cr(VI) sorption processes on both materials are spontaneous (negative ΔG values), endothermic in nature ($\Delta H = (23 \pm 3)$ kJ mol⁻¹ for IT-POP and (55 ± 6)

Table 2

Thermodynamic parameters obtained for Cr(VI) sorption on IT-POP and St-Alg-IT-POP15% beads.

Parameters	T (°C)	IT-POP	St-Alg-T-POP15%
ΔG / (kJ mol ⁻¹)	25	$-18 (\pm 4)$	$-19 (\pm 8)$
	30	$-19 (\pm 4)$	$-20 (\pm 8)$
	35	$-20 (\pm 4)$	$-21 (\pm 8)$
	55	$-23 (\pm 4)$	$-26 (\pm 9)$
ΔS / (J mol ⁻¹ K ⁻¹)		$140 (\pm 9)$	$246 (\pm 19)$
ΔH / (kJ mol ⁻¹)		$23 (\pm 3)$	$55 (\pm 6)$
R^2		0.9712	0.9779

kJ mol⁻¹ for St-Alg-IT-POP15%), and led to an entropy increase ($\Delta S = (140 \pm 9)$ J mol⁻¹ K⁻¹ for IT-POP and (246 ± 19) J mol⁻¹ K⁻¹ for St-Alg-IT-POP15%). These positive entropy variations can indicate the increase in the disorder of the molecules at the solid/fluid interface, the occurrence of structural changes in the sorbate and sorbent, the displacement of the sorbed water molecules by the sorbate, and the high affinity of Cr(VI) oxyanions for the two sorbents (Húmpola et al., 2013). Furthermore, the sorbate–sorbent affinity also seems to increase with the temperature since as the temperature rises, the sorption capacities increase, and ΔG values become more negative.

3.2.3. Effect of contact time and sorption kinetics

The kinetic profiles showed that the equilibrium time was reached more quickly for IT-POP powder (360 min) than for St-Alg-IT-POP15% beads (480 min), possibly because the anchorage of IT-POP powder in the polymer matrix (i.e., beads) increased the mass transfer resistance of the Cr(VI) oxyanions in the external film, slowing down external diffusion and delaying the contact with the active sites of IT-POP in St-Alg-T-POP15% beads (Fig. 4C and F). Additionally, acidic media (due to its high redox potential) and the active sites of the sorbent can promote the reduction of Cr(VI) oxyanions to Cr(III). To assess these possibilities, each point of the sorption kinetics of Cr by the two sorbents was analyzed using UV–Vis spectroscopy and F-AAS to determine the concentration of Cr(VI) and total Cr, respectively. The difference between the total Cr and Cr(VI) concentrations allowed us to infer about the Cr(III) concentration in solution. The initial concentrations of total Cr and Cr(VI) at pH = 2 were 0.60 mM and (0.44–0.51) mM, which shows a reduction capacity of the acidic medium of (16–27)%. Subsequently, there was a slight decrease of Cr(III) concentration over time using IT-POP powder, showing that it cannot reduce Cr(VI) to Cr(III) and only sorbs a residual amount of Cr(III) initially present in the medium. For St-Alg-IT-POP15% beads, a slight increase in Cr(III) concentration was observed up to $t = 90$ min, possibly due to a minor involvement of the reduction process coupled with sorption promoted by the polymer matrix that anchors IT-POP polymer (Park et al., 2007). For longer contact times, residual sorption of Cr(III) by St-Alg-IT-POP15% was also observed, resulting in a decrease of Cr(III) concentration. In general, these results suggest not only the occurrence of sorption of Cr(VI) oxyanions by the positively charged materials through electrostatic attractions, but also the negligible roles of both the reduction process and the Cr(III) sorption.

The experimental data of the sorption of Cr(VI) and total Cr by the two materials were modeled using PFO and PSO kinetic models (Table 3 and Fig. S8). The higher R^2 values and lower AIC values were observed for the fits of PSO model, suggesting that surface reactions govern Cr(VI) sorption processes.

3.2.4. Selectivity performance

To investigate the ability of the two polymers to selectively sorb metal ions, multicomponent sorption assays were carried out starting from a heptacomponent metal ion solution, containing 0.15 mmol L⁻¹ of each of seven different metal ions: Pb(II), Cu(II), Cd(II), Zn(II), Mn(II), Ni(II), and Cr(VI) (Fig. 5). The two materials maintained high removal efficiencies of Cr(VI) oxyanions (between 91–95%) and a low reduction to Cr(III) (total Cr efficiencies >89 %) (Fig. 5A). Regarding the divalent cations, IT-POP did not sorb them, while St-Alg-IT-POP15% showed removal efficiencies between (10–53)%, due to the presence of hydroxyl and carboxyl groups in the structure of starch and alginate, with a high capacity to coordinate with divalent cations. This trend was also confirmed by Fig. 5B, showing that in the presence of coexisting divalent cations, IT-POP has a high selectivity for Cr(VI) anions (89 %), whereas St-Alg-T-POP15% presents a lower Cr(VI) selectivity (38 %). Despite this, the incorporation of IT-POP made the beads more selective to Cr(VI) than to the other coexisting divalent cations.

Table 3
Fit parameters of the kinetic models.

Model	Parameters	IT-POP		St-Alg-IT-POP15%	
		Cr(VI)	Cr(Total)	Cr(VI)	Cr(Total)
PFO	$q_e / (\text{mmol g}^{-1})$	0.69 (± 0.02)	0.86 (± 0.03)	0.126 (± 0.004)	0.137 (± 0.004)
	$k_1 / (\text{min}^{-1})$	0.011 (± 0.002)	0.011 (± 0.002)	0.012 (± 0.002)	0.007 (± 0.001)
	R^2	0.9285	0.9169	0.9472	0.9638
	AIC	-34.9	-30.7	-55.9	-56.6
PSO	$q_e / (\text{mmol g}^{-1})$	0.75 (± 0.02)	0.94 (± 0.03)	0.138 (± 0.003)	0.156 (± 0.004)
	$k_2 / (\text{g mmol}^{-1} \text{min}^{-1})$	0.022 (± 0.004)	0.017 (± 0.003)	0.12 (± 0.02)	0.055 (± 0.008)
	R^2	0.9644	0.9542	0.9813	0.9814
	AIC	-39.7	-34.8	-62.6	-61.0

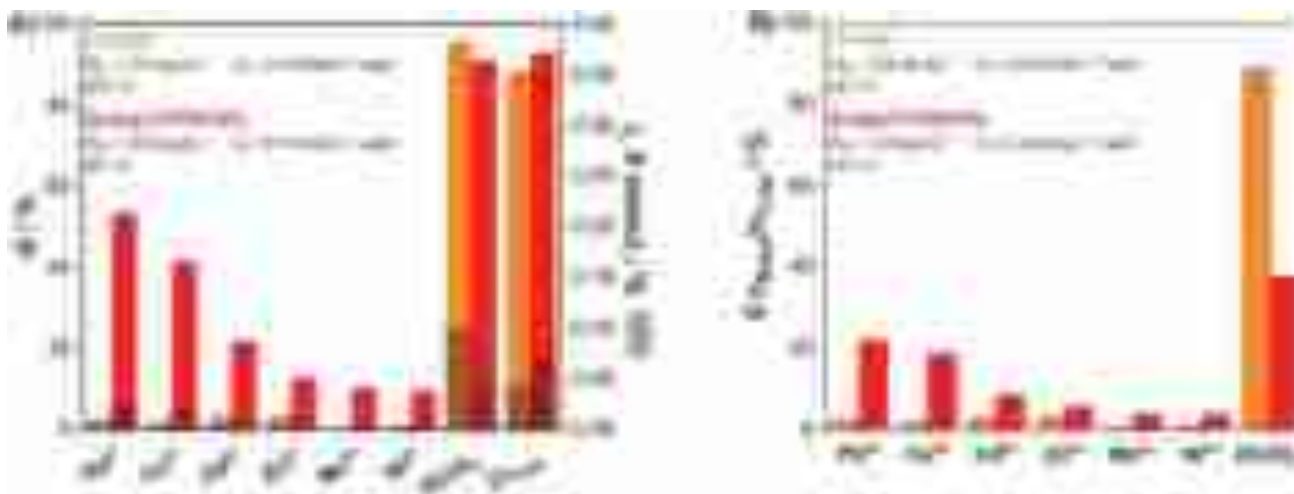


Fig. 5. Multicomponent sorption tests using IT-POP and St-Alg-IT-POP15: A) sorption efficiencies and capacities at equilibrium, and B) selectivity percentages for Pb(II), Cu(II), Cd(II), Zn(II), Mn(II), Ni(II), and Cr(VI) removal at 0.15 mmol L^{-1} each, $R_{S-L} = 0.5 \text{ mg mL}^{-1}$ (IT-POP) or 3.3 mg mL^{-1} (St-Alg-IT-POP15%), pH = 2.0 and 25°C .

3.3. Fluorescence assays

The ability of IT-POP and St-Alg-IT-POP15% to act as fluorescent probes for Cr(VI) detection in water was assessed by placing in contact a dose of each material in aqueous solutions with different initial concentrations of Cr(VI) at pH = 2. The fluorescence signal of both the IT-POP powder and the St-Alg-IT-POP15% beads reduced to powder was monitored over time and stabilized after 6 h of contact (Figs. S9A and S9B, respectively), which coincides with the equilibrium time determined in sorption kinetics, particularly for IT-POP. For $t = 6 \text{ h}$, the fluorescence spectra of each dispersion as a function of the initial

concentration of Cr(VI) are depicted in Figs. 6A (IT-POP) and 6B (St-Alg-IT-POP15%).

It was observed that the increase of Cr(VI) concentration promoted the quenching of fluorescence of both materials, due to the formation of non-fluorescent ground-state complexes between the fluorophore species and the Cr(VI) quencher. Linear Stern-Volmer plots were represented for both cases of fluorescence quenching in Fig. 6C, from the fluorescence intensities at the wavelength at which they are maximal for $t = 6 \text{ h}$ (600 nm for IT-POP and 615 nm for St-Alg-IT-POP15%). The applied Stern-Volmer equation (eq. (4)) correctly modeled both systems, showing $R^2 = 0.9921$ (IT-POP) and 0.9891 (St-Alg-IT-POP15%), and

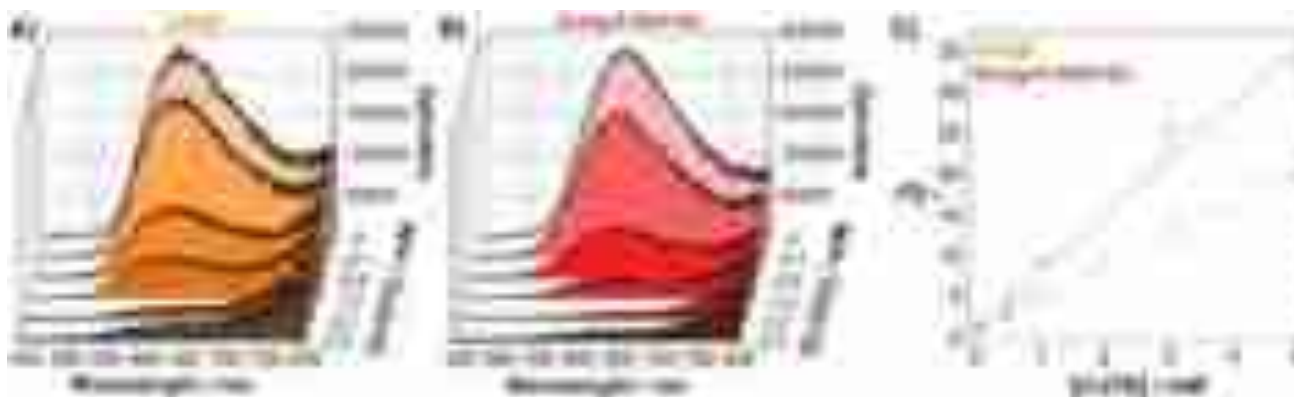


Fig. 6. Representation of the fluorescence emission profiles of IT-POP and St-Alg-IT-POP15% as a function of the initial Cr(VI) concentration for A) IT-POP and B) St-Alg-IT-POP15% powders; C) Linear Stern–Volmer fits for the fluorescence quenching of IT-POP (at $\lambda_{em} = 600 \text{ nm}$) and St-Alg-IT-POP15% (at $\lambda_{em} = 615 \text{ nm}$) in contact with Cr(VI) solutions. The materials were excited at $\lambda_{exc} = 430 \text{ nm}$.

indicating that the two materials have a single population of fluorophores, all with identical accessibility to the quencher metal species (Matias et al., 2024).

The slope values obtained from the Stern-Volmer fittings are the association constants, K_S , for the formation of IT-POP–Cr(VI) and St-Alg-IT-POP15%–Cr(VI) non-fluorescent complexes, which were $3995 (\pm 156) \text{ M}^{-1}$ and $7054 (\pm 314) \text{ M}^{-1}$, respectively. These values follow the same trend and are of the same order of magnitude as the equilibrium constants obtained by sorption studies, at 298,15 K (i.e., 1621 and 1716, respectively). The higher value of K_S obtained for St-Alg-IT-POP15% may be due to the use of a greater mass of beads ($6.7\times$ superior to that of IT-POP powder), possibly leading to a larger macromolecule surface and to an increase in the availability and exposure of fluorophores for the formation of non-emissive complexes (which can occur, e.g., due to the presence of the quencher in the vicinity of the fluorophore during excitation).

The IT-POP and St-Alg-IT-POP15% initial fluorescence intensity is quenched by 50 % at Cr(VI) concentrations of 0.25 and 0.14 mM, respectively, showing again a more appreciable quenching of St-Alg-IT-POP15% fluorescence. The same conclusion can be drawn by comparing the decrease profiles of the fluorescence intensity (i.e., $\frac{I_0}{I}$) as a function of quencher concentration for the two materials (Fig. S9C). Although both are described by first-order exponential decay, the decrease in fluorescence intensity is more abrupt for St-Alg-IT-POP15%. Furthermore, after the decay, the plateau is reached for an initial Cr(VI) concentration close to 1.5 and 2.3 mM for St-Alg-IT-POP and IT-POP, respectively. This indicates that the equilibrium of the interaction with Cr(VI) occurs at higher concentrations for the pure IT-POP polymer, meaning that it achieves saturation after interacting with a more significant number of Cr(VI) oxyanions, as proved by the sorption studies that showed a higher maximum sorption capacity of Cr(VI) for IT-POP.

In summary, both materials present an ability not only to remove/recover Cr(VI) from water but also to detect it by varying the fluorescence response when in contact with Cr(VI)-contaminated aqueous

media, through an interaction mechanism based on hydrogen bonding, electrostatic interactions and coordination exchange, as proposed in Fig. 7. In this sense, they can be considered a new generation of innovative materials since they have a dual application. Furthermore, it is worth noting that the limits of detection (LODs) and quantification (LOQs) for the sensing of Cr(VI) were 0.85 and 2.58 mM for IT-POP, and 0.98 and 2.96 mM for St-Alg-IT-POP15% probes, respectively. These values were estimated by the linear plots of $\left(\frac{I_0}{I} - 1\right)$ as a function of Cr(VI) concentration for the maximum emission wavelengths at $t = 6$ h, and allow us to infer that improvements may be made to the materials to decrease analytical thresholds and to overcome the limitation of the fluorescence changes not being detectable to the naked eye.

4. Conclusions

This study provided valuable insights into the performance and interaction mechanism of two materials, IT-POP and IT-POP-containing St-Alg beads (St-Alg-IT-POP15%), for the remediation of Cr(VI) from water by combining sorption and fluorescence studies. The sorption results showed that the IT-POP polymer presented a higher sorption capacity than St-Alg-IT-POP15% ($(3.3 \pm 0.3) \text{ mmol g}^{-1}$ vs. $(0.71 \pm 0.04) \text{ mmol g}^{-1}$ at 25 °C and pH = 2.0). However, considering that only around 10 % of the bead's mass is IT-POP, it can be concluded that the reduction in capacities was only 4.4 to 5.3 times, showing that St-Alg-IT-POP15% could be around 2 folds more advantageous than IT-POP powder alone. The occurrence of chemisorption, explained by electrostatic interactions, as well as other types of physical interactions, such as coordination or hydrogen bonds, was inferred to be the most probable mechanism, and no significant reduction of Cr(VI) to Cr(III) by the materials was observed. Furthermore, sorption processes were spontaneous, entropically favorable as well as endothermic since the maximum sorption capacities increased up to $(4.7 \pm 0.3) \text{ mmol g}^{-1}$ (IT-POP) and $(1.07 \pm 0.07) \text{ mmol g}^{-1}$ (St-Alg-IT-POP15%) with the temperature

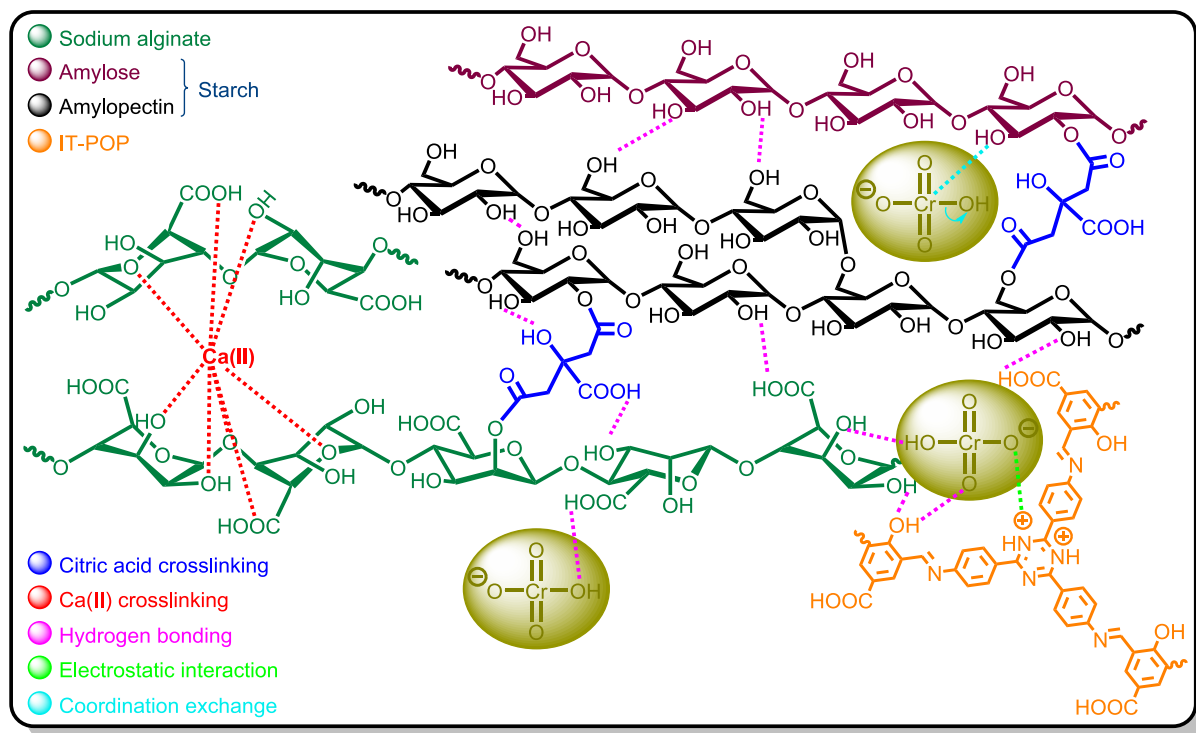


Fig. 7. Representation of the chemical structure of St-Alg-IT-POP beads, containing possible hydrogen bonds, covalent and ionic crosslinking between starch, alginate, citric acid and Ca(II); schematic representation of the hypothesised interaction mechanism for the sorption and fluorescent response of IT-POP and St-Alg-IT-POP towards Cr(VI) anions.

increase up to 55 °C. Fluorescence studies showed that Cr(VI) led to the quenching of fluorescence of both materials acting as probes. This quenching was described by the linear Stern-Volmer model, due to the formation of ground-state non-fluorescent complexes with association constants of 3995 (± 156) M^{-1} and 7054 (± 314) M^{-1} resulting from the collision of Cr(VI) oxyanions with the fluorescence sites or the presence of metal species in the vicinity of the fluorophores. In these studies, LODs and LOQs of 0.85–0.98 mM and 2.58–2.96 mM were obtained, respectively. Overall, this work offers a valuable contribution to materials science in the field of environmental remediation, since IT-POP is a novel advanced functional material and the formulation of St-Alg-IT-POP15% is a very efficient, economical and easier to scale up approach.

CRedit authorship contribution statement

Pedro M.C. Matias: Writing – review & editing, Writing – original draft, Methodology, Investigation, Formal analysis, Data curation, Conceptualization. **Talles B. Costa:** Writing – review & editing, Writing – original draft, Methodology, Investigation, Formal analysis, Data curation, Conceptualization. **Dina M.B. Murтинho:** Writing – review & editing, Supervision, Resources, Methodology, Conceptualization. **Derval S. Rosa:** Writing – review & editing, Validation, Supervision, Resources, Project administration, Conceptualization. **Artur J.M. Valente:** Writing – review & editing, Writing – original draft, Validation, Supervision, Resources, Project administration, Conceptualization.

Declaration of competing interest

The authors declare that they have no known competing financial interests or personal relationships that could have appeared to influence the work reported in this paper.

Acknowledgements

This work was funded by the Coimbra Chemistry Centre (CQC), which is supported by the Fundação para a Ciência e a Tecnologia (FCT, Portugal) through the programs UIDB/00313/2025 and UIDP/00313/2025. Pedro M. C. Matias thanks FCT (Portugal) for the PhD Grant number 2022.12425.BD. This study was also financed, in part, by the São Paulo Research Foundation (FAPESP, Brazil) through Process Numbers #2022/11133-0, #2023/11783-8, and #2020/13703-3. The authors also thank the UC-NMR facility for obtaining the NMR data (<https://www.uc.pt/uc-nmr> (accessed on 21st March 2025)). We would also like to thank Mr. Pedro Cruz for his assistance with the NMR experiments.

Appendix A. Supplementary data

Supplementary data to this article can be found online at <https://doi.org/10.1016/j.carbpol.2025.123788>.

Data availability

The data that support the findings of this study are available from the corresponding author upon reasonable request.

References

- Abhari, N., Madadlou, A., & Dini, A. (2017). Structure of starch aerogel as affected by crosslinking and feasibility assessment of the aerogel for an anti-fungal volatile release. *Food Chemistry*, 221, 147–152. <https://doi.org/10.1016/j.foodchem.2016.10.072>
- Abuzeid, H. R., EL-Mahdy, A. F. M., Ahmed, M. M. M., & Kuo, S.-W. (2019). Triazine-functionalized covalent benzoxazine framework for direct synthesis of N-doped microporous carbon. *Polymer Chemistry*, 10(44), 6010–6020. <https://doi.org/10.1039/C9PY01231A>
- Ahamad, T., Naushad, M., Mousa, R. H., & Alshehri, S. M. (2020). Fabrication of starch-salicylaldehyde based polymer nanocomposite (PNC) for the removal of pollutants

- from contaminated water. *International Journal of Biological Macromolecules*, 165, 2731–2738. <https://doi.org/10.1016/j.ijbiomac.2020.10.170>
- Ahmad, S., & Imran, S. (2024). Synthesis of gum tragacanth-starch hydrogels for water purification. *Materials Advances*, 5(22), 8812–8825. <https://doi.org/10.1039/D4MA00536H>
- Alqarni, S. A. A. (2018). *Synthesis and characterization of Schiff-base complexes as medical imaging precursors [degree of master of diagnostic radiography]*. University of Hull.
- Alvarez-Galvan, Y., Minofar, B., Futera, Z., Francoeur, M., Jean-Marius, C., Brehm, N., ... Gaspard, S. (2022). Adsorption of hexavalent chromium using activated carbon produced from *Sargassum* spp.: Comparison between lab experiments and molecular dynamics simulations. *Molecules*, 27(18), 6040. <https://doi.org/10.3390/molecules27186040>
- Alves, D. F., Camani, P. H., Souza, A. G., & Rosa, D. S. (2024). A novel sustainable composite hydrogel containing nanocellulose to remove potentially toxic metals from contaminated water. *Polymer Bulletin*, 81(7), 5939–5966. <https://doi.org/10.1007/s00289-023-04986-0>
- Avdibegović, D., Regadio, M., & Binnemans, K. (2018). Efficient separation of rare earths recovered by a supported ionic liquid from bauxite residue leachate. *RSC Advances*, 8, 11886–11893. <https://doi.org/10.1039/C7RA13402A>
- Barcelos da Costa, T., Carlos da Silva, M. G., & Adeodato Vieira, M. G. (2021). Development of a natural polymeric bioadsorbent based on sericin, alginate and poly(vinyl alcohol) for the recovery of ytterbium from aqueous solutions. *Journal of Cleaner Production*, 279, Article 123555. <https://doi.org/10.1016/j.jclepro.2020.123555>
- Boyle, O., Xiao, B., & Mangwandi, C. (2025). Valorization of Banana Peel waste into advanced adsorbent beads for the removal of emerging pollutants from wastewater. *Materials*, 18(5), 1084. <https://doi.org/10.3390/ma18051084>
- Camani, P. H., Gonçalo, M. G. M., Barbosa, R. F. S., & Rosa, D. S. (2021). Comprehensive insight of crosslinking agent concentration influence on starch-based aerogels porous structure. *Journal of Applied Polymer Science*, 138(34), 1–12. <https://doi.org/10.1002/app.50863>
- Cao, Z., Wang, M., Gao, H., Li, L., & Ren, S. (2022). Porous organic polymers via Diels-Alder reaction for the removal of Cr(VI) from aqueous solutions. *ACS Macro Letters*, 11(4), 447–451. <https://doi.org/10.1021/acsmacrolett.2c00052>
- Chandra, S., Hassan, A., Prince, A. A., & Das, N. (2022). Rapid and efficient removal of diverse anionic water contaminants using a guanidium-based ionic covalent organic network (iCON). *ACS Applied Polymer Materials*, 4(9), 6630–6641. <https://doi.org/10.1021/acscpm.2c00989>
- Ciuffarin, F., Négrier, M., Plazzotta, S., Libralato, M., Calligaris, S., Budtova, T., & Manzocco, L. (2023). Interactions of cellulose cryogels and aerogels with water and oil: Structure-function relationships. *Food Hydrocolloids*, 140, Article 108631. <https://doi.org/10.1016/j.foodhyd.2023.108631>
- da Costa, T. B., da Silva, T. L., da Silva, M. G. C., & Vieira, M. G. A. (2024). Selectivity of lanthanum and ytterbium in binary and multi-component system by modified sericin/alginate/poly(vinyl alcohol) adsorbent beads. *Journal of Environmental Chemical Engineering*, 12(2), Article 112329. <https://doi.org/10.1016/j.jece.2024.112329>
- Daliran, S., Oveisi, A. R., Khajeh, M., Barkhordar, A., & Dhakshinamoorthy, A. (2023). Zirconium-based cyclodextrin porous coordination polymer for highly efficient uptake of Cr(VI) species. *Polyhedron*, 237, Article 116392. <https://doi.org/10.1016/j.poly.2023.116392>
- Deng, S., Long, J., Dai, X., Wang, G., & Zhou, L. (2023). Simultaneous detection and adsorptive removal of Cr(VI) ions by fluorescent sulfur quantum dots embedded in chitosan hydrogels. *ACS Applied Nano Materials*, 6(3), 1817–1827. <https://doi.org/10.1021/acsnm.2c04768>
- Du, M., Wang, Y., Cao, Y., Tang, W., & Li, Z. (2024). Defect-engineered MOF-801/sodium alginate aerogel beads for boosting adsorption of Pb(II). *ACS Applied Materials & Interfaces*, 16(42), 57614–57625. <https://doi.org/10.1021/acscami.4c08928>
- El-Naggar, M. E., Othman, S. I., Allam, A. A., & Morsy, O. M. (2020). Synthesis, drying process and medical application of polysaccharide-based aerogels. *International Journal of Biological Macromolecules*, 145, 1115–1128. <https://doi.org/10.1016/j.ijbiomac.2019.10.037>
- Emami, Z., Ehsani, M., Zandi, M., & Foudazi, R. (2018). Controlling alginate oxidation conditions for making alginate-gelatin hydrogels. *Carbohydrate Polymers*, 198, 509–517. <https://doi.org/10.1016/j.carbpol.2018.06.080>
- Evans, R., Deng, Z., Rogerson, A. K., McLachlan, A. S., Richards, J. J., Nilsson, M., & Morris, G. A. (2013). Quantitative interpretation of diffusion-ordered NMR spectra: Can we rationalize small molecule diffusion coefficients? *Angewandte Chemie International Edition*, 52(11), 3199–3202. <https://doi.org/10.1002/anie.201207403>
- Fajal, S., Dutta, S., & Ghosh, S. K. (2023). Porous organic polymers (POPs) for environmental remediation. *Materials Horizons*, 10(10), 4083–4138. <https://doi.org/10.1039/D3MH00672G>
- Farid, I., Abbas, M., Bassouny, M., Gameel, A., & Abbas, H. (2019). Indirect impacts of irrigation with low quality water on the environmental safety. *Egyptian Journal of Soil Science*, 60(1), 1–15. <https://doi.org/10.21608/ejss.2019.15434.1294>
- Filho, C. M. C., Bueno, P. V. A., Matsushita, A. F. Y., Rubira, A. F., Muniz, E. C., Durães, L., ... Valente, A. J. M. (2018). Synthesis, characterization and sorption studies of aromatic compounds by hydrogels of chitosan blended with β -cyclodextrin- and PVA-functionalized pectin. *RSC Advances*, 8(26), 14609–14622. <https://doi.org/10.1039/C8RA02332H>
- Foesch, M. D. S., Francelino, M. R., Rocha, P. A., & Gomes, A. R. L. (2020). River water contamination resulting from the Mariana disaster. *Brazil. Floresta e Ambiente*, 27(4), 1–10. <https://doi.org/10.1590/2179-8087.013218>
- Foo, K. Y., & Hameed, B. H. (2010). Insights into the modeling of adsorption isotherm systems. *Chemical Engineering Journal*, 156(1), 2–10. <https://doi.org/10.1016/j.cej.2009.09.013>

- Hachaichi, M., & Egieya, J. (2023). Water-food-energy Nexus in global cities: Addressing complex urban interdependencies. *Water Resources Management*, 37(4), 1811–1825. <https://doi.org/10.1007/s11269-023-03455-7>
- Health Council of the Netherlands: Committee on Updating of Occupational Exposure Limits. (2002). Starch (CAS reg no: 9005-25-8, 9005-84-9); Health-based Reassessment of Administrative Occupational Exposure Limits. In *The Hague: Health Council of the Netherlands*, 2000/15OSH/038.
- Huang, Z., Fan, M., & Tiand, H. (2018). Coal and coal byproducts: A large and developable unconventional resource for critical materials – Rare earth elements. *Journal of Rare Earths*, 36(4), 337–338. <https://doi.org/10.1016/j.jre.2018.01.002>
- Húmpola, P. D., Odetti, H. S., Fertitta, A. E., & Vicente, J. L. (2013). Thermodynamic analysis of adsorption models of phenol in liquid phase on different activated carbons. *Journal of the Chilean Chemical Society*, 58(1), 1541–1544. <https://doi.org/10.4067/S0717-97072013000100009>
- Hynes, L., Montiel, G., Jones, A., Riel, D., Abdulaziz, M., Viva, F., ... Trevani, L. (2020). Melamine adsorption on carbon materials: Impact of carbon texture and surface chemistry. *Materials Advances*, 1(2), 262–270. <https://doi.org/10.1039/D0MA00097C>
- Ibuki, K., & Nakahara, M. (1991). Solvent isotope effect on the viscosity coefficient B for monovalent ions in water at 25 and 40°C. *Zeitschrift Für Naturforschung A*, 46(1–2), 127–130. <https://doi.org/10.1515/zna-1991-1-221>
- Islam, M. A., Angove, M. J., & Morton, D. W. (2019). Recent innovative research on chromium (VI) adsorption mechanism. *Environmental Nanotechnology, Monitoring & Management*, 12, Article 100267. <https://doi.org/10.1016/j.enmm.2019.100267>
- Justus, C. M., Pasini, A., Raminelli, J. A., Gonçalves, L. S. A., & Celligoi, A. (2020). Chemical elements in the water of the São Pedro river basin. *Faxinal - Paraná. Semina: Ciências Agrárias*, 41(3), 743. <https://doi.org/10.5433/1679-0359.2020v41n3p743>
- Kong, K., Cheng, B., Liang, J., Guo, Y., & Wang, R. (2022). The aminated covalent organic polymers for reversible removal of concurrent perfluorooctane sulfonate and dichromate. *Chemical Engineering Journal*, 446, Article 137343. <https://doi.org/10.1016/j.cej.2022.137343>
- Lakowicz, J. R. (2006). *Principles of fluorescence spectroscopy*. Springer.
- Lam, B., Déon, S., Morin-Crini, N., Crini, G., & Fievet, P. (2018). Polymer-enhanced ultrafiltration for heavy metal removal: Influence of chitosan and carboxymethyl cellulose on filtration performances. *Journal of Cleaner Production*, 171, 927–933. <https://doi.org/10.1016/j.jclepro.2017.10.090>
- Li, H., Wang, S., Yuan, Z., Wang, X., Yao, K., & Pang, Z. (2024). Synthesis of magnetic N-Vinylformamide grafted starch and its application in heavy metals adsorption. *Macromolecular Chemistry and Physics*, 225(12). <https://doi.org/10.1002/macp.202400010>
- Li, W., & Achal, V. (2020). Environmental and health impacts due to e-waste disposal in China – A review. *Science of the Total Environment*, 737, Article 139745. <https://doi.org/10.1016/j.scitotenv.2020.139745>
- Li, X., Bi, C., Wang, Y., Peng, C., Li, Y., Yang, S., & Tao, E. (2025). Gallic acid-functionalized chitosan composite for efficient removal of hexavalent chromium in aqueous. *International Journal of Biological Macromolecules*, 305, Article 141240. <https://doi.org/10.1016/j.ijbiomac.2025.141240>
- Li, Z.-J., Liu, J.-Y., Yu, Y., Chang, K.-J., Wang, H., Li, Y.-J., & Gai, K. (2022). Rational Design of High-Performance Cationic Organic Network Adsorbents. *ACS Applied Materials & Interfaces*, 14(20), 23868–23876. <https://doi.org/10.1021/acsami.2c03119>
- Liang, H., Wu, H., Fang, W., Ma, K., Zhao, X., Geng, Z., ... Hu, H. (2024). Two-stage hydrothermal oxygenation for efficient removal of Cr(VI) by starch-based polyporous carbon: Wastewater application and removal mechanism. *International Journal of Biological Macromolecules*, 264, Article 130812. <https://doi.org/10.1016/j.ijbiomac.2024.130812>
- Liang, P., Liu, S., Li, M., Xiong, W., Yao, X., Xing, T., & Tian, K. (2024). Effective adsorption and removal of Cr(VI) from wastewater using magnetic composites prepared by synergistic effect of polypyrrole and covalent organic frameworks. *Separation and Purification Technology*, 336, Article 126222. <https://doi.org/10.1016/j.seppur.2023.126222>
- Lima, E. C., Hosseini-Bandegharai, A., Moreno-Piraján, J. C., & Anastopoulos, I. (2019). A critical review of the estimation of the thermodynamic parameters on adsorption equilibria. Wrong use of equilibrium constant in the Van't Hoff equation for calculation of thermodynamic parameters of adsorption. *Journal of Molecular Liquids*, 273, 425–434. <https://doi.org/10.1016/j.molliq.2018.10.048>
- Lipatova, I. M., & Yusova, A. A. (2021). Effect of mechanical activation on starch crosslinking with citric acid. *International Journal of Biological Macromolecules*, 185, 688–695. <https://doi.org/10.1016/j.ijbiomac.2021.06.139>
- Liu, H., Wu, P., Hou, L., Zhang, X., Zheng, H., Niu, B., ... Fu, J. (2022). A cyclophosphazene-derived porous organic polymer with P-N linkage for environmental adsorption applications. *Colloids and Surfaces A: Physicochemical and Engineering Aspects*, 654, Article 130162. <https://doi.org/10.1016/j.colsurfa.2022.130162>
- Liu, X., Zhu, Z., Wang, X., Yang, J., Zhang, Y., Yan, X., ... Qin, S. (2024). Construction of controlled hyper-crosslinked nanofibrous tubes for Cr(VI) removal: Response surface, kinetics, and isotherm. *Environmental Research*, 263, Article 119980. <https://doi.org/10.1016/j.envres.2024.119980>
- Lopes, T. O. M., Passos, L. S., Vieira, L. V., Pinto, E., Dorr, F., Scherer, R., ... Gomes, L. C. (2020). Metals, arsenic, pesticides, and microcystins in tilapia (*Oreochromis niloticus*) from aquaculture parks in Brazil. *Environmental Science and Pollution Research*, 27(16), 20187–20200. <https://doi.org/10.1007/s11356-020-08493-x>
- Lu, M., Sun, L., Yang, D., Nie, Z., & Gong, W. (2025). New Viologen-based ionic porous organic polymers for efficient removal of anionic dyes and hexavalent chromium (Cr(VI)) from water. *Molecules*, 30(5), 1123. <https://doi.org/10.3390/molecules30051123>
- Lu, S., Liu, Q., Han, R., Guo, M., Shi, J., Song, C., ... Ma, D. (2021). Potential applications of porous organic polymers as adsorbent for the adsorption of volatile organic compounds. *Journal of Environmental Sciences*, 105, 184–203. <https://doi.org/10.1016/j.jes.2021.01.007>
- Ma, R., Xu, X., Zhang, Y., Zhang, D., Xiang, G., Chen, Y., ... Yi, S. (2024). Synergistic effects of adsorption and chemical reduction towards the effective Cr(VI) removal in the presence of the sulfur-doped biochar material. *Environmental Science and Pollution Research*, 31(6), 8538–8551. <https://doi.org/10.1007/s11356-023-31654-7>
- Machado, T. F., Valente, A. J. M., Serra, M. E. S., & Murtinho, D. (2024). Triazine-linked porous organic polymers for heterogeneous catalysis and pollutant adsorption. *ACS Applied Polymer Materials*, 6(7), 4171–4185. <https://doi.org/10.1021/acscapm.4c00225>
- Mandal, L., Fajal, S., Mollick, S., Shirokhar, M. M., More, Y. D., Saurabh, S., ... Ghosh, S. K. (2022). Unveiling the impact of diverse morphology of ionic porous organic polymers with mechanistic insight on the ultrafast and selective removal of toxic pollutants from water. *ACS Applied Materials & Interfaces*, 14(17), 20042–20052. <https://doi.org/10.1021/acscami.2c02174>
- Matias, P. M. C., Murtinho, D., & Valente, A. J. M. (2023). Triazine-based porous organic polymers: Synthesis and application in dye adsorption and catalysis. *Polymers*, 15(8), 1815. <https://doi.org/10.3390/polym15081815>
- Matias, P. M. C., Rodrigues, B., & A. C., Nunes, S. C. C., Canelas Pais, A. A. C., Murtinho, D., & Valente, A. J. M. (2024). Assessing interactions between antibiotics and triazine porous organic polymeric sorbents by photophysics. *Environmental Pollution*, 363, Article 125197. <https://doi.org/10.1016/j.envpol.2024.125197>
- Matias, P. M. C., Nunes, S. C. C., Rodrigues, A. C. B., Ltayef, M., Sellaoui, L., Mbarek, M., ... Valente, A. J. M. (2025). Efficient removal of sulfonamide and tetracycline antibiotics using triazine-based porous organic polymers. *Separation and Purification Technology*, 355, Article 129731. <https://doi.org/10.1016/j.seppur.2024.129731>
- Mendes, S. A., Gonçalves, E. V., Frância, L. S., Correia, L. B. C., Nicola, J. V. N., Pestana, A. C. Z., ... Peron, A. P. (2020). Quality of natural waters surrounding Campo Mourão, state of Paraná, southern Brazil: Water resources under the influences from urban and agricultural activities. *Water, Air, & Soil Pollution*, 231(8), 415. <https://doi.org/10.1007/s11270-020-04795-5>
- Morin-Crini, N., Lichtfouse, E., Liu, G., Balaram, V., Ribeiro, A. R. L., Lu, Z., ... Crini, G. (2022). Worldwide cases of water pollution by emerging contaminants: A review. *Environmental Chemistry Letters*, 20(4), 2311–2338. <https://doi.org/10.1007/s10311-022-01447-4>
- Pan, L., Liu, Z., Hernandez, M. V., Schroeder, B. C., Sun, Y., & Faul, C. F. J. (2024). Poly(amine)-based cationic porous organic polymers for fast and efficient anion-exchange-driven capture of Cr₂O₇²⁻. *ACS Applied Polymer Materials*, 6(11), 6416–6424. <https://doi.org/10.1021/acscapm.4c00658>
- Park, D., Lim, S.-R., Yun, Y.-S., & Park, J. M. (2007). Reliable evidences that the removal mechanism of hexavalent chromium by natural biomaterials is adsorption-coupled reduction. *Chemosphere*, 70(2), 298–305. <https://doi.org/10.1016/j.chemosphere.2007.06.007>
- Parlayıcı, Ş., & Baran, Y. (2025a). Fruit peel incorporated alginate based magnetic hydrogel bio-composite beads for removal of hexavalent chromium. *International Journal of Biological Macromolecules*, 284, Article 137946. <https://doi.org/10.1016/j.ijbiomac.2024.137946>
- Parlayıcı, Ş., & Baran, Y. (2025b). Removal of hexavalent chromium from aqueous solutions using nano-Fe₃O₄/waste banana peel/alginate hydrogel biobeads as adsorbent. *Biomass Conversion and Biorefinery*. <https://doi.org/10.1007/s13399-025-06489-6>
- Rakotomalala Robinson, M., Abdelmoula, M., Mallet, M., & Coustel, R. (2023). The role of starch in nano-magnetite formation: A spectrometric and structural investigation. *Materials Chemistry and Physics*, 297, Article 127285. <https://doi.org/10.1016/j.matchemphys.2022.127285>
- Renu, A., & Singh, K. (2017). Heavy metal removal from wastewater using various adsorbents: A review. *Journal of Water Reuse and Desalination*, 7(4), 387–419. <https://doi.org/10.2166/wrd.2016.104>
- Rogovina, S., Aleksanyan, K., Vladimirov, L., Prut, E., Ivanushkina, N., & Berlin, A. (2018). Development of novel biodegradable polysaccharide-based composites and investigation of their structure and properties. *Journal of Polymers and the Environment*, 26(4), 1727–1736. <https://doi.org/10.1007/s10924-017-1069-3>
- Sam, D. K., Sam, E. K., Durairaj, A., Lv, X., Zhou, Z., & Liu, J. (2020). Synthesis of biomass-based carbon aerogels in energy and sustainability. *Carbohydrate Research*, 491, Article 107986. <https://doi.org/10.1016/j.carres.2020.107986>
- Sarkar, S., Chakraborty, A., Ranjan, R., Nag, P., Vennapusa, S. R., & Mukhopadhyay, S. (2022). A bifunctional imidazolium-functionalized ionic porous organic polymer in water remediation. *Materials Chemistry Frontiers*, 6(20), 3070–3083. <https://doi.org/10.1039/D2QM00636G>
- Savassi, L. A., Paschoalini, A. L., Arantes, F. P., Rizzo, E., & Bazzoli, N. (2020). Heavy metal contamination in a highly consumed Brazilian fish: Immunohistochemical and histopathological assessments. *Environmental Monitoring and Assessment*, 192(8), 542. <https://doi.org/10.1007/s10661-020-08515-8>
- Sharma, M. D., Gupta, P., Chauhan, S., Panwar, R., Singh, S., Kumar, P., & Kulshrestha, S. (2023). Seasonal impact on microbiological quality of drinking water in Solan City of Himachal Pradesh, India. *Environmental Monitoring and Assessment*, 195(8), 930. <https://doi.org/10.1007/s10661-023-11510-4>
- Singh, A., Chauhan, S., Varjani, S., Pandey, A., & Bhargava, P. C. (2022). Integrated approaches to mitigate threats from emerging potentially toxic elements: A way forward for sustainable environmental management. *Environmental Research*, 209, Article 112844. <https://doi.org/10.1016/j.envres.2022.112844>

- Soares, A. F. S., & Souza e Souza, L. P. (2020). Contaminação das águas de abastecimento público por poluentes emergentes e o direito à saúde. *Revista de Direito Sanitário*, 20(2), 100–133. <https://doi.org/10.11606/issn.2316-9044.v20i2p100-133>
- Soares, J. S., Rocha, F. R., & Fávoro, D. I. T. (2017). *Metal and trace element concentration evaluation in sediment profiles of the Tietê River, State of São Paulo, by INAA and ICP OES techniques*.
- Tan, J., Kong, L., Fang, J., Liang, X., & Yin, Y. (2024). Synthesis of a starch-composite magnetic material modified with polyethyleneimine for enhanced adsorption of diclofenac sodium, methyl orange, Amaranth, and hexavalent chromium. *Environmental Advances*, 15, Article 100489. <https://doi.org/10.1016/j.envadv.2024.100489>
- Tooley, O., Pointer, W., Radmall, R., Hall, M., Beyer, V., Stakem, K., ... Haddleton, D. (2024). MaDDOSY (mass determination diffusion ordered spectroscopy) using an 80 MHz bench top NMR for the rapid determination of polymer and macromolecular molecular weight. *Macromolecular Rapid Communications*, 45(8). <https://doi.org/10.1002/marc.202300692>
- Tran, H. N., You, S.-J., & Chao, H.-P. (2016). Thermodynamic parameters of cadmium adsorption onto orange peel calculated from various methods: A comparison study. *Journal of Environmental Chemical Engineering*, 4(3), 2671–2682. <https://doi.org/10.1016/j.jece.2016.05.009>
- Trevizani, T. H. (2019). *Bioacumulação e biomagnificação de metais pesados em teias tróficas de estuários do sul-sudeste do Brasil* [Tese, Universidade de São Paulo]. doi: 10.11606/T.21.2019.tde-01022019-141450.
- Vaiopoulou, E., & Gikas, P. (2020). Regulations for chromium emissions to the aquatic environment in Europe and elsewhere. *Chemosphere*, 254, Article 126876. <https://doi.org/10.1016/j.chemosphere.2020.126876>
- Valente, A. J. M., & Söderman, O. (2019). Do the solvent properties affect the propensity for self-association of α -cyclodextrin? Insights from NMR self-diffusion. *Journal of Molecular Liquids*, 295, Article 111869. <https://doi.org/10.1016/j.molliq.2019.111869>
- Valente, A. J. M., Nilsson, M., & Söderman, O. (2005). Interactions between n-octyl and n-nonyl β -D-glucosides and α - and β -cyclodextrins as seen by self-diffusion NMR. *Journal of Colloid and Interface Science*, 281(1), 218–224. <https://doi.org/10.1016/j.jcis.2004.08.018>
- Varela, J. P., Valente, A. J. M., & Durães, L. (2016). Heavy metals in Iberian soils: Removal by current adsorbents/amendments and prospective for aerogels. *Advances in Colloid and Interface Science*, 237, 28–42. <https://doi.org/10.1016/j.cis.2016.08.009>
- Venkatrajan, G., Venkatesan, J., Madankumar, N., Nirmala, & Pushparaju, S. (2024). Effective chromium removal of metal anchored alginate-chitosan binary bio-composites. *International Journal of Biological Macromolecules*, 264, 130408. <https://doi.org/10.1016/j.ijbiomac.2024.130408>
- Wang, H., Dai, K., Xiang, H., Kou, J., Guo, H., Ying, H., & Wu, J. (2024). High adsorption capacities for dyes by a pH-responsive sodium alginate/sodium lignosulfonate/carboxylated chitosan/polyethyleneimine adsorbent. *International Journal of Biological Macromolecules*, 278, Article 135005. <https://doi.org/10.1016/j.ijbiomac.2024.135005>
- Wang, J., & Guo, X. (2020). Adsorption isotherm models: Classification, physical meaning, application and solving method. *Chemosphere*, 258, Article 127279. <https://doi.org/10.1016/j.chemosphere.2020.127279>
- Wang, X., Luo, S., Luo, J., Liu, L., Hu, Y., Li, Z., ... Qin, H. (2025). Fluorescent cellulose nanofibrils hydrogels for sensitive detection and efficient adsorption of Cu²⁺ and Cr⁶⁺. *Carbohydrate Polymers*, 347, Article 122748. <https://doi.org/10.1016/j.carbpol.2024.122748>
- Wang, X., Wu, J., Zhou, J., Zhang, L., Shen, Y., Wu, J., & Hao, C. (2025). Effective removal of Congo red and hexavalent chromium from aqueous solutions by guar gum/sodium alginate/mg/Al-layered double hydroxide composite microspheres. *International Journal of Biological Macromolecules*, 293, Article 139385. <https://doi.org/10.1016/j.ijbiomac.2024.139385>
- Wang, Y., Su, Y., Wang, W., Fang, Y., Riffat, S. B., & Jiang, F. (2019). The advances of polysaccharide-based aerogels: Preparation and potential application. *Carbohydrate Polymers*, 226, Article 115242. <https://doi.org/10.1016/j.carbpol.2019.115242>
- Wang, Y.-S., Yuan, X.-N., Gou, X.-X., Song, X.-T., Wang, X., Guo, L., ... Han, Y.-F. (2025). Imidazolium-based ionic polymers for fast and efficient anion-exchange driven capture of Cr^{2O7}-. *Science China Chemistry*. <https://doi.org/10.1007/s11426-024-2401-5>
- Xia, H., Zhang, Y., Chen, Q., Liu, R., & Wang, H. (2023). Unraveling adsorption characteristics and removal mechanism of novel Zn/Fe-bimetal-loaded and starch-coated corn cobs biochar for Pb(II) and Cd(II) in wastewater. *Journal of Molecular Liquids*, 391, Article 123375. <https://doi.org/10.1016/j.molliq.2023.123375>
- Zhao, S., Malfait, W. J., Guerrero-Alburquerque, N., Koebel, M. M., & Nyström, G. (2018). Biopolymer aerogels and foams: Chemistry, properties, and applications. *Angewandte Chemie International Edition*, 57(26), 7580–7608. <https://doi.org/10.1002/anie.201709014>
- Zhou, J., Du, X., Lu, K., & Xiao, A. (2025). MXene@polydopamine/oxidized sodium alginate modified collagen composite aerogel as sustainable bio-adsorbent for heavy metal ion adsorption and solar driven water evaporation. *Separation and Purification Technology*, 354, Article 129045. <https://doi.org/10.1016/j.seppur.2024.129045>
- Zhou, M., Chen, M., Wang, Y., Mao, C., Zhang, Y., Liu, J., ... Yang, X. (2025). Construction of carbon dot-embedded fluorescent hydrogels based on oxidized gum arabic-gelatin Schiff base for Cr(VI) detection applications. *International Journal of Biological Macromolecules*, 294, Article 139466. <https://doi.org/10.1016/j.ijbiomac.2025.139466>
- Zhou, S., Zhou, Z., Zhu, D., Jiang, H., Qi, Y., Wang, S., ... Wang, W. (2022). Preparation of covalent triazine-based framework for efficient Cr(VI) removal from water. *Colloids and Surfaces A: Physicochemical and Engineering Aspects*, 632, Article 127757. <https://doi.org/10.1016/j.colsurfa.2021.127757>
- Zubair, N. A., Abouzari-Lotf, E., Mahmoud Nasef, M., & Abdullah, E. C. (2019). Aerogel-based materials for adsorbent applications in material domains. *E3S Web of Conferences*, 90, 01003. <https://doi.org/10.1051/e3sconf/20199001003>



Contents lists available at ScienceDirect

Colloids and Surfaces A: Physicochemical and Engineering Aspects

journal homepage: www.elsevier.com/locate/colsurfaSustainable solutions for Cr⁶⁺ removal using carbon-based adsorbentsJulia D. Perluxo^a, Fillip Cortat Alves^b, Lana S. Maia^c, Maria Ismênia S.T. Faria^d, Daniel M. de Oliveira^e, Edson Cochieri Botelho^b, Derval S. Rosa^c, Daniella R. Mulinari^{e,*}^a Rio de Janeiro State University (UERJ), Faculty of Technology (FAT), Department of Chemistry and Environmental, Resende, RJ, Brazil^b São Paulo State University (UNESP), School of Engineering (FEG), Department of Materials and Technology, Guaratinguetá, SP, Brazil^c Center for Engineering, Modeling, and Applied Social Sciences (CECS), Federal University of ABC (UFABC), Santo André, SP, Brazil^d University of São Paulo (EEL/USP), Department of Materials Engineering (DEMAR), Lorena, SP, Brazil^e Rio de Janeiro State University (UERJ), Faculty of Technology (FAT), Department of Mechanics and Energy, Resende, RJ, Brazil

GRAPHICAL ABSTRACT



ARTICLE INFO

Keywords:

Cr⁶⁺ adsorption
Graphene
Biochar
Printex
Carbon-based adsorbents
Life cycle assessment

ABSTRACT

Removing potentially toxic elements (PTEs), such as hexavalent chromium (Cr⁶⁺), from water presents a significant challenge, especially given the increasing global demand for potable water. This study evaluated the effectiveness of three carbon-based structures — graphene, printex, and biomass-derived biochar — for Cr⁶⁺ adsorption in water, aiming to identify efficient and sustainable solutions for wastewater treatment. To investigate the influence of different carbon-based structures on Cr⁶⁺ adsorption, the physical, chemical, morphological, and thermal properties, as well as particle sizes, were evaluated. Adsorption experiments were conducted under varying conditions of contact time, initial Cr⁶⁺ concentration, and adsorbent dosage, with responses optimized through response surface methodology. Additionally, a Life Cycle Assessment (LCA) was conducted to evaluate the environmental impacts of the developed process, providing a broader sustainability perspective compared to conventional methods. Results indicated significant adsorption efficiencies for all materials: biochar achieved 85.1 % removal of Cr⁶⁺ under optimal conditions (using a 100 mg dosage, at a concentration of 1 mmol.L⁻¹, over 30 min of contact time); Printex reached 85.4 %, and graphene recorded the highest removal rate at 89 %. Adsorption isotherms were best described by the Langmuir model, with maximum capacities of

* Corresponding author.

E-mail addresses: dmulinari@hotmail.com, daniella.mulinari@fat.uerj.br (D.R. Mulinari).<https://doi.org/10.1016/j.colsurfa.2025.137881>

Received 15 May 2025; Received in revised form 20 July 2025; Accepted 25 July 2025

Available online 26 July 2025

0927-7757/© 2025 Elsevier B.V. All rights are reserved, including those for text and data mining, AI training, and similar technologies.

67.7 mg g⁻¹ for graphene, 30.4 mg g⁻¹ for Printex, and 13.3 mg g⁻¹ for biochar. The structural properties of each material influenced this difference in adsorption capacity. The layered structure of graphene and the rough morphology of printex contributed to its performance, while the porous morphology and surface functional groups of biochar also favored adsorption. Nevertheless, this study identifies biochar as a promising and cost-effective material derived from biomass waste, aligning with sustainability goals. The proposed LCA scenarios reinforce this advantage, demonstrating reduced environmental impacts — particularly in terms of human toxicity and aquatic ecotoxicity — and benefits from a circular economic perspective. Importantly, this work provides a direct and systematic comparison of three commonly used carbon-based materials under identical experimental conditions, thereby addressing a key gap in literature and guiding more effective selection of adsorbents for environmental applications.

1. Introduction

Escalating water scarcity in many regions worldwide has reached alarming levels due to the combined pressures of global warming, surging population growth, rapid urbanization, and inefficient management of water resources [1]. Water pollution typically results from the release of waste by the industrial, agricultural, and domestic sectors. This compromises its quality and availability, making adequate wastewater treatment before disposal essential [2].

In this context, potentially toxic elements (PTEs), such as heavy metals, are present in water because of the inadequate disposal of industrial effluents, mainly from the processing and manufacturing of chemicals, minerals, steel, leather tanning, textile dyeing, electroplating, cement production, metallurgy, and others [3]. Among heavy metals, Chromium (Cr) represents a serious environmental problem, and its contamination can primarily enter the human body through drinking water [4]. Chromium (Cr) is the 24th most abundant element, occurring naturally in the Earth's crust in both trivalent and hexavalent forms [5]. It does not undergo biodegradation and can accumulate at toxic levels in aquatic organisms, affecting the health of ecosystems and putting human life at risk [6]. Therefore, the World Health Organization (WHO) has established a permissible level of Cr⁶⁺ in drinking water of no more than 0.05 mg.L⁻¹ [4].

Numerous physical and chemical techniques have been developed for treating water contaminated with Cr⁶⁺, such as ion exchange [7], reverse osmosis [8] membrane filtration [9] chemical reactions involving reduction and precipitation [10] and adsorption [11]. Among the various promising remediation approaches, adsorption stands out as an effective method, including (i) a chemisorption mechanism involving the formation of chemical bonds and (ii) a physisorption mechanism characterized by weaker interactions. In general, this procedure is a practical, effective, and low-cost strategy that is based on capturing molecules on porous surfaces (interactions between analyte-adsorbent materials) during this process [12]. Currently, this method plays a significant role in various fields, such as remediation, surface chemistry, and catalysis [13,14].

Many adsorbent materials have been investigated as possible adsorbents for the removal of Cr⁶⁺ from aqueous solutions, such as biomass [15], beads [5], aerogels [16], hydrogels [17], membranes [18], biochar [19], graphene [12], and graphite [20]. However, carbon-based materials can be classified as highly emerging, efficient adsorbents for removing Cr⁶⁺ from contaminated water due to the diverse functional groups within their structure [21]. These materials are notable for their extensive surface area, many active sites, π - π interactions, high conductivity, and ability to be modified for optimized adsorption [22]. Studies indicate that chemical modification of these surfaces can further increase the resistance of the materials to specific impurities, such as PTEs and industrial dyes [22–24].

Among carbonaceous materials, biochar from agro-industrial residues, graphene, and Printex stand out because they differ significantly in their structure and how these differences influence their ability to adsorb Cr⁶⁺ (hexavalent chromium). Biochar is a porous, carbon-rich material derived from the pyrolysis of biomass, offering a large surface area for adsorption [19,25,26]. Graphene, a two-dimensional

material, possesses a high surface area and unique electronic properties due to its single-layer structure, comprising hexagonally arranged carbon atoms [25]. Commercial carbon material is Printex L6 (Degussa), an alkaline pigment of furnace type with a primary particle size of 18 nm and a BET surface area of 265 m². g⁻¹, a density of 1.8 g.cm⁻³, and primary use in organic degradation [27,28].

These materials have shown significant potential for effectively removing hexavalent chromium (Cr⁶⁺) from wastewater through adsorption and/or reduction mechanisms. However, assessing the environmental impact associated with their production is crucial to ensure their cost-effectiveness and promote their implementation as environmentally friendly solutions [29]. Although individual studies have reported promising results for some carbonaceous materials, a lack of comparative evaluations remains regarding their effectiveness and environmental impacts in Cr⁶⁺ removal. Specifically, the literature has not reported on the effects of various types of carbonaceous materials—such as biochar, graphene, and Printex—on the removal of hexavalent chromium ions. Additionally, there is a lack of summarized information regarding freshwater ecotoxicity, freshwater eutrophication, global warming, human carcinogenic toxicity, human non-carcinogenic toxicity, marine ecotoxicity, marine eutrophication, and territorial ecotoxicity. Furthermore, the effective removal of hexavalent chromium ions from contaminated water environments with these materials has not been systematically documented in prior studies.

This study will assess the environmental impact of removing hexavalent chromium using three carbon-based sorbents (biochar, graphene, and Printex), employing response surface methodology (RSM) to find an efficient and sustainable solution for wastewater treatment. This research aims to contribute to global efforts in environmental preservation and resource protection.

2. Materials and methods

2.1. Materials

The carbonaceous materials were purchased from different suppliers. Nanoplatelet provided Graphene (99.9%, 3 nm, S.A:800 m².g⁻¹ Dia: 1.5 μ m). Orion Carbons (Degussa) provided Carbon Printex L6. Biochar was produced from pineapple top waste collected at a street market in Lorena, São Paulo, Brazil, as this material is generated in large quantities and frequently discarded as waste at markets and fairs without efficient use. Initially, the waste was dried at 80 °C for 48 h to remove moisture. The dried material was then crushed, ground in a mill, and sieved to obtain particles smaller than 35 mesh.

2.2. Synthesis of biochar from pineapple crown residue (BPCR)

The biochar from pineapple crown residue was prepared as follows: the dried residue was impregnated with a water solution of NaOH at 80 g.L⁻¹, maintaining a ratio of 1:3 (residue: alkaline solution/active agent) at room temperature for 24 h. After that, the sample was dried at 100 °C for 24 h, resulting in a material known as activated pineapple crown fiber. The activated fiber was pyrolyzed at 600 °C for 1.5 h in a muffle furnace under an argon atmosphere, with a flow rate of 100 mL.

min^{-1} argon flow. Finally, the biochar was washed with distilled water until reaching a pH of 7 and then dried at $80\text{ }^{\circ}\text{C}$ for 24 h, obtaining the biochar from pineapple crown residue.

2.3. Characterization of carbonaceous materials

The adsorption capacity can be influenced by various factors, including pH, surface area, porosity, type of adsorbent material, and temperature [30,31]. Thus, to understand the influence of different types of carbonaceous materials on the adsorption capacity of Cr^{6+} , the physicochemical, morphological, and thermal properties were tested.

The elemental composition of the materials was analyzed to determine the weight fractions of carbon (C), hydrogen (H), nitrogen (N), and oxygen (O) using a Thermo Scientific Elemental Analyzer, model Flash EA 1112.

The density of the samples was measured using a helium gas pycnometer (Ultrapyc 1200e, Quantachrome Instruments, Boynton Beach, FL, USA) at room temperature. Before the analysis, the samples were dried in an oven at $35\text{ }^{\circ}\text{C}$ for 24 h to eliminate residual moisture. Each density value represents the average of three measurements performed for each sample.

The chemical structures of the materials were analyzed using Fourier-transform infrared spectroscopy (FTIR) (Frontier 94942 Model, PerkinElmer Inc., Massachusetts, USA) with an attenuated total reflectance (ATR) diamond accessory. The data was gathered through 64 scans, with a spectral resolution of 4 cm^{-1} in the range of $4000\text{--}500\text{ cm}^{-1}$.

The physical structures of the materials were evaluated using X-ray diffraction with a diffractometer (Rigaku, model Miniflex II). The measuring conditions were: CuK α radiation with a graphite monochromator, 30 kV voltage, and 40 mA electric current. The patterns were obtained in $10\text{--}50^{\circ}$ angular intervals with 0.05° steps and a 1 s counting time. Bragg's law was applied to calculate the interplanar distance, based on Eq. (1), and the dimensions of the crystallites were determined using the Scherrer equation, as expressed in Eq. (2).

$$n\lambda = 2d\sin\theta \quad (1)$$

$$D = \frac{K\lambda}{\beta\cos\theta} \quad (2)$$

Where: λ represents the wavelength of the radiation, n is the diffraction order (an integer: 1, 2, 3), d refers to the distance between atomic planes, θ represents the orientation of these planes relative to the beam, D refers to the average particle diameter, K is the constant that depends on the shape of the particles, and β is the full width at half maximum (FWHM) of the diffraction peak.

Biochar from pineapple crown residue morphology was analyzed using Scanning Electron Microscopy (SEM) with FEG Schottky electron emission on MEV-FEG TESCAN Mira 4. The fiber was affixed to carbon tape within a sample holder. This analysis employed secondary electron mode (SE) and backscattered electron mode (BSE) at an accelerating voltage of 5 keV. Furthermore, ImageJ software was applied to analyze and stabilize the sample's pore structure.

A laser particle size analyzer (Bettersize Instruments Ltd., China) was used to measure the particle size of the samples. The samples were dispersed in distilled water under constant agitation (1600 rpm). Testing was performed in triplicate, and average values were calculated. The D90 indicates the diameter where 90 % of the distribution is a smaller particle size.

The thermogravimetric analysis (TGA) was performed using a TG/DTA 6200 thermobalance from SII Nanotechnology – SEIKO. Samples weighing around 5 mg were placed in alumina pans, with alumina powder as the reference material. The experiment followed the ASTM E2250 standard, employing a temperature range of $30\text{--}800\text{ }^{\circ}\text{C}$, a heating rate of $10\text{ }^{\circ}\text{C}\cdot\text{min}^{-1}$, and a continuous synthetic air flow of 100 mL

min^{-1} . The temperature range used in the experiment was chosen based on satisfactory results presented in other studies, which demonstrated its suitability for thermogravimetric analysis of similar materials [32–34]. The analysis aimed to assess mass loss as a function of temperature and determine the thermal decomposition temperature (T_{onset}). The T_{onset} was determined from the TG curve as the temperature at which a deflection is first observed from the established baseline before the thermal event.

Zero point charge is an essential parameter for predicting the exact mechanism of adsorption by varying the pH of the reaction mixture. The study measured the Zeta potential of the materials, specifically focusing on their point of zero charge (pH_{ZPC}). For this purpose, samples were introduced into a 50 mL solution of $0.1\text{ mol}\cdot\text{L}^{-1}$ NaCl. The pH of the solution was adjusted within a range of 2.0–10.0 using $0.1\text{ mol}\cdot\text{L}^{-1}$ NaOH and $0.1\text{ mol}\cdot\text{L}^{-1}$ HCl. The final pH values were recorded after the system had equilibrated for 24 h. ZPC corresponds to the point at which the initial and final pH values of the solution are equal after the reaction.

2.4. Adsorption analysis for design of experiments (DOE)

An experimental design was conducted to optimize the adsorption conditions of $\text{Cr}6+$ using carbon-based sorbents (biochar, graphene, and Printex), investigating the influence of three primary parameters: contact time, solution concentration, and adsorbent material dosage. Each parameter was explored at three different levels: i) The contact time between the adsorbent materials and the adsorbate solution was evaluated for 10, 60, and 90 min; ii) The initial adsorbate concentration in the solution was studied at: 0.5, 1, and 3 $\text{mmol}\cdot\text{L}^{-1}$; iii) The adsorbent material dosage used in the solution varied at 10, 50 and 100 mg.

The study planning was conducted using Design Expert software and involved a surface response method, comprising a total of 14 experiments. Each experiment was performed in triplicate, with a specific amount of each material added to an Erlenmeyer flask containing 10 mL of the adsorbed solution at the defined concentration. The vials were shaken on an orbital shaker at 150 rpm for the specified contact time. After the shaking time, the samples were filtered, and the residual adsorbate concentrations were determined using UV-Vis spectrophotometry at 420 nm. Removal efficiency (%) and adsorption capacity (q_e), were calculated by Eqs. (3) and (4).

$$\%R = \left(\frac{C_0 - C_e}{C_0} \right) \bullet 100 \quad (3)$$

Where: C_0 is the PTEs metals initial concentration ($\text{mmol}\cdot\text{L}^{-1}$); C_e is the PTEs metals concentration at equilibrium ($\text{mmol}\cdot\text{L}^{-1}$).

$$q_e = \frac{(C_0 - C_e)V}{W} \quad (4)$$

Where: q_e represents adsorption capacity at any time, $\text{mg}\cdot\text{g}^{-1}$; V denotes volume of solution, L; and W represents the weight of carbon-based sorbents, $\text{g}\cdot\text{L}^{-1}$.

All measurements were carried out in duplicate and reported as mean \pm standard deviation. One-way analysis of variance (ANOVA) was performed using Design Expert software with a 95 % confidence level.

2.5. Kinect study

A kinetic adsorption study was conducted to evaluate the effect of contact time on adsorption capacity while maintaining a constant adsorbate concentration and adsorbent dosage until equilibrium was reached. Based on the results of optimization experiments conducted using Design-Expert® software, a dosage of 10 mg and an initial adsorbate concentration of $1\text{ mmol}\cdot\text{L}^{-1}$ were selected. The experiments were carried out by agitating the flasks on an orbital shaker at 150 rpm for various contact times, including 10, 30, 60, 90, 120, 150, 180, and

210 min. The amount of adsorbate adsorbed at each interval (q_e) was measured, which allowed for the construction of the adsorption kinetics curve. The pseudo-first-order model, is defined by the differential Eq. (5):

$$\frac{dq_t}{dt} = k_1(q_e - q_t) \quad (5)$$

which, upon integration under appropriate initial conditions, yields the linear form described by Eq. (6):

$$\ln(q_e - q_t) = \ln(q_e) - k_1 t \quad (6)$$

Where: q_t is the amount of adsorbate at time t ; q_e is the amount adsorbed at equilibrium; k_1 is the rate constant of pseudo-first-order adsorption.

The pseudo-second-order model assumes that the adsorption rate is proportional to the square of the number of unoccupied sites, and is described by Eq. (7):

$$\frac{dq_t}{dt} = k_2(q_e - q_t)^2 \quad (7)$$

Its linearized form can be expressed by Eq; (8):

$$\frac{t}{qt} = \frac{1}{k_2 q_e^2} + \frac{t}{q_e} \quad (8)$$

Where: $k_2 \left(\frac{g}{mg \cdot min} \right)$ is the pseudo-second-order rate constant.

2.6. Adsorption isotherms

The study of sorption through adsorption isotherms can provide insights into how Cr^{6+} is adsorbed, as well as estimate the maximum metal ion capacity of the carbon-based sorbents (biochar, graphene, and printex). Accordingly, the samples were exposed to solutions with varying concentrations of Cr^{6+} (0.5, 1.0, 2.0, 3.0, 4.0, 5.0, 10.0, 20.0, 30.0 and 40.0 $mmol L^{-1}$) for 180 min. Samples were stirred at 150 rpm to assess the fit to the isotherm models. The sorption isotherm models applied were the Langmuir and the Freundlich models.

The Langmuir isotherm is one of the most widely used for adsorption, which considers that the adsorption process occurs in a single layer of molecules on the surface of the adsorbent, without this process occurring at the adsorbed sites, and can be described by Eq. (9).

$$q_e = \frac{q_m K_L C_e}{1 + K_L C_e} \quad (9)$$

Where: q_m sorbent monolayer capacity; K_L : sorption free energy constant; C_e equilibrium concentration; q_e equilibrium dye concentration of the sorbent.

The parameters q_m and K_L are obtained through a linear fit using the values of C_e/q_e versus C_e . Additionally, the adsorption tendency and suitability of the Langmuir model can be assessed using a dimensionless constant called the separation factor (RL), as shown in Eq. (10).

$$RL = \frac{1}{1 + K_L C_e} \quad (10)$$

Where: RL represents the process favourability. If $RL > 1$, the process is unfavorable. If $RL = 1$, linear. If $0 < RL < 1$, favorable. If $RL = 0$, irreversible.

Freundlich is an empirical model, which consider multilayer adsorption, where the surface of the adsorbent has heterogeneous sites, and can be described by Eq. (11):

$$q_e = K_F C_e^{1/n} \quad (11)$$

Where: K_F : sorption capacity constant; n : sorption intensity constant.

If $n = 1$, it is a linear sorption process. If $n < 1$, chemical process. If $n > 1$, physical process. K_F and n can be calculated by Eq. (12):

$$\log_{10} \frac{1}{n} \log_{10} C_e + \log K_F \quad (12)$$

2.7. Desorption and regeneration

Desorption and regeneration studies were conducted to assess the reusability and efficiency of biochar alone as a biosorbent for Cr^{6+} . For Printex and graphene, this was not possible because the particle size is smaller, making this study impossible. To evaluate the number of viable cycles of biochar, Cr^{6+} oxyanion solutions were selected due to their higher sorption potential. The adsorbents were subjected to three consecutive runs under optimal conditions determined from adsorption test analyses (1.0 $mmol L^{-1}$ for 30 min, with 100 mg of the material). The absorbance was recorded during these runs using UV-Vis spectroscopy to calculate the concentration of Cr^{6+} in the material and assess its reusability. The biochar was chemically regenerated using HNO_3 after each cycle. In this technique, the regeneration efficiency depends on the solubility of the adsorbates in the solvent, which can alter the chemical structure of the adsorbent [35].

2.8. Life Cycle Assessment (LCA)

According to the directives prescribed by the International Standards ISO 14,040/14,044, the LCA was conducted using the open-source software OpenLCA 1.9, the Ecoinvent 3.4 databases, and the ReCiPe 2019 Midpoint (H) method for data interpretation. The selected environmental categories were Freshwater ecotoxicity, Freshwater eutrophication, Global warming, Human carcinogenic toxicity, Human non-carcinogenic toxicity, Marine ecotoxicity, Marine eutrophication, and Territorial ecotoxicity. Background data were obtained from literature, expert knowledge, and estimations from similar processes. Foreground data, including energy consumption, were obtained directly from the development carried out.

3. Results and discussion

3.1. Elemental composition and density

The elemental composition of the carbon-based sorbents was evaluated to determine the amount of C, H, N, and O in the samples studied. In general, the materials presented a difference in elemental analysis, which can actively impact interactions with the adsorbate, either through chemical bonds (chemical adsorption) or electrostatic interactions (physical adsorption) [36], as shown in Table 1.

Graphene exhibited the highest carbon content (74.8 %), reflecting its highly graphitic structure [37]. Biochar had an intermediate carbon content (71.2 %) and was the only material to contain nitrogen (0.964 %), evidenced by its carbonaceous character due to its lignocellulosic origin [1]. Printex, despite having the minor carbon content (68.4 %), stood out for its high oxygen content (31.0 %) and the highest C/H ratio (131), indicating a highly aromatic and functionalized structure [29]. The C/O ratios reinforce the structural differences between the materials: graphene had the highest value (3.20), suggesting a lower degree of oxidation compared to biochar (2.80) and printex (2.20) [37].

Based on the density values, graphene exhibited the highest average density (2.92 $g \cdot cm^{-3}$), followed by Printex (2.70 $g \cdot cm^{-3}$) and biochar

Table 1
Summary of density and elemental composition data for graphene, Printex, and biochar.

Samples	Density (g. cm^{-3})	Elemental composition (wt% %)					
		C	N	H	O	C/H	C/O
Graphene	2.92 ± 0.08	74.8	0.00	1.43	23.7	52.2	3.20
Printex	2.70 ± 0.05	68.4	0.00	0.524	31.0	131	2.20
Biochar	2.17 ± 0.09	71.2	0.964	2.21	25.7	32.2	2.80

($2.17 \text{ g}\cdot\text{cm}^{-3}$). These results reflect the differences in the material's composition and structure. The superior density of graphene is linked to its highly crystalline structure, characterized by tightly packed atomic arrangements and minimal porosity, which contribute to its high bulk density. Printex displayed a lower density as an industrial carbon black due to its less ordered microstructure, which contains fewer crystalline regions and greater void spaces. In contrast, biochar showed the lowest density, consistent with its biomass-derived origin. This material is notably porous, with a significant fraction of micropores and a heterogeneous internal architecture, factors that reduce its overall density. This trend is consistent with literature findings, which note that increased density can be attributed to changes in pore volume, optimized macroporosity, and improved surface area [33,34].

3.2. Attenuated total reflectance Fourier-transform infrared spectroscopy (ATR-FTIR) and X-ray diffraction (XRD)

The FTIR spectra of biochar, graphene, and printex are presented in Fig. 1a, with the main peaks highlighted. A clearer assignment of the spectral bands to functional groups is provided below, along with their implications for Cr^{6+} adsorption behavior.

The FTIR spectrum of graphene exhibits a relatively constant curve without notable peaks, indicating the absence of significant functional groups [37]. This is characteristic of highly crystalline and pure materials, limiting chemisorption. The low intensity or absence of a peak near 3000 cm^{-1} , typically associated with C–H stretching of aliphatic groups, further confirms the lack of surface functionalities, which is often a result of purification or controlled oxidation processes [40]. Despite this, graphene retains high physisorption capacity, mainly due to its extensive surface area, which allows weak electrostatic interactions with Cr^{6+} species in solution [38,39], making it suitable for applications such as sensors and catalytic support materials.

The Printex spectrum is also nearly flat, indicating that it is a homogeneous material, revealing few detectable chemical functionalities [40]. The slight presence of aliphatic C–H stretching bands near $2920\text{--}2850 \text{ cm}^{-1}$ may be linked to amorphous carbon structures — typical of industrial carbon blacks — although surface reactivity remains low [41]. However, Printex presents a high surface area and disordered structure, which supports physisorption processes, possibly through van der Waals forces or electrostatic interactions with adsorbate species, contributing moderately to Cr^{6+} retention.

In contrast, biochar shows well-defined peaks, indicating the presence of several surface functional groups. The broadband around 3000 cm^{-1} corresponds to C–H stretching vibrations of aliphatic

hydrocarbons, likely from biomass residues. The peak in the $1700\text{--}1600 \text{ cm}^{-1}$ region is associated with C=O stretching of carbonyl groups, while intense features between $1500\text{--}1000 \text{ cm}^{-1}$ correspond to C–O stretching in ethers, alcohols, and phenolic compounds [41]. These polar groups significantly enhance the surface reactivity of biochar, enabling chemisorption via complexation or ion exchange mechanisms with Cr^{6+} species [38]. Combined with its porous structure, biochar exhibits a dual adsorption mechanism — physisorption and chemisorption — making it particularly efficient for removing Cr^{6+} from aqueous media.

X-ray diffractometry (XRD) was used to analyze the crystalline structure and organization of the materials. The primary differences observed in the XRD patterns of these materials are attributed to the degree of crystallization, the arrangement of carbon layers, and the presence of amorphous phases or specific structural features. Biochar and printex presented similar structures, unlike graphene, as evidenced in Fig. 1b.

For graphene, its main peak appears near $2\theta \approx 26^\circ$, corresponding to the basal plane (002), which reflects the spacing between graphene layers. Through this analysis, using Bragg's law, it was determined that the interplanar distance of graphene is approximately 0.342 nm . The XRD technique also enabled the determination of the average particle diameter of graphene. Using the Scherrer equation, it was found that the material has an average diameter of 3.62 nm . Therefore, it can be concluded that the material consists of approximately 10 graphene nanolayer pyrolysis, making it a composition rich in organic functional groups [42]. These differences reflect the intrinsic structural characteristics of each material.

Printex showed two peaks, the first at $2\theta = 25.5^\circ$, corresponding to the basal plane (002), and the second one at $2\theta = 42.6^\circ$, which corresponds to SO_2 , according to JCPDF #73-2096 [27]. The printex sample exhibited a behavior similar to that of biochar, a material with an amorphous and heterogeneous structure. The absence of defined peaks indicates that the material has a low degree of organization.

Biochar, being a carbonaceous material obtained through biomass pyrolysis, generally has a highly amorphous and heterogeneous structure. As observed in Fig. 1b, a broader and more intense amorphous halo is present near $2\theta \approx 25^\circ$, corresponding to the (002) plane characteristic of graphitic structures and carbonaceous materials. This broadening originates from the small dimensions of the crystallites perpendicular to the aromatic layers [43]. Its XRD pattern shows a low degree of organization, as there are no well-defined peaks of crystalline planes, as seen in graphene, due to its disordered structure. This indicates low crystallinity and the presence of amorphous carbon, a pattern also observed in

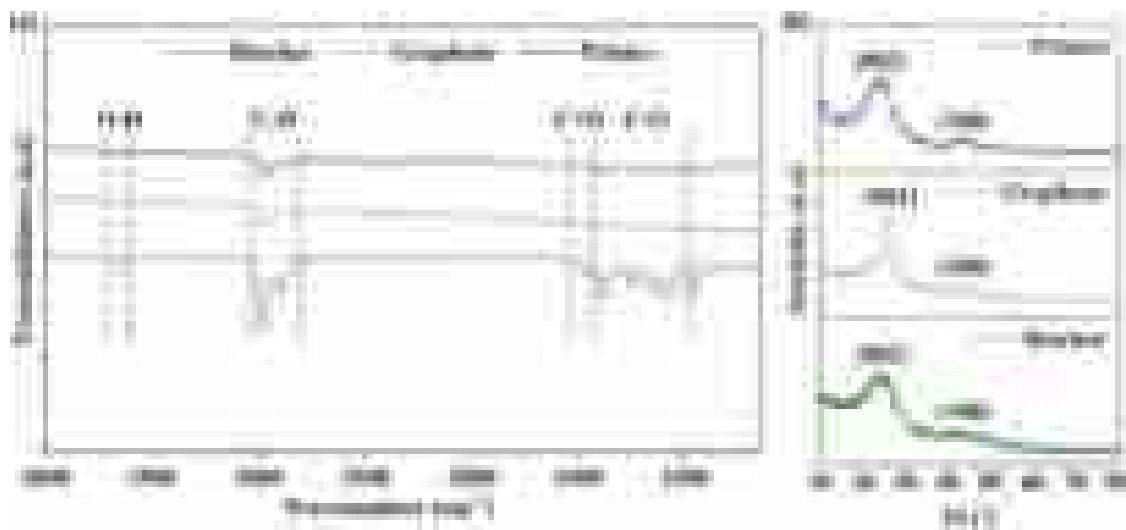


Fig. 1. FTIR spectra of graphene, Printex, and biochar (a) and XRD patterns of graphene, printex, and biochar (b).

other studies, such as that by Pórto et al. [44]. For pyrolyzed materials at higher temperatures, around 600–700 °C, a second halo of lower intensity can be observed near $2\theta \approx 43^\circ$, corresponding to the (100) plane, also characteristic of graphitic structures and carbon materials [44].

3.3. Scanning electron microscopy (SEM) and particle size

The morphology of the adsorbent material has a significant influence on its ability and efficiency in adsorbing metal ions [45]. The surface area, pore size distribution, and the presence of functional groups on the surface are crucial morphological factors that determine the number of available adsorption sites and, therefore, the amount of metal ions that

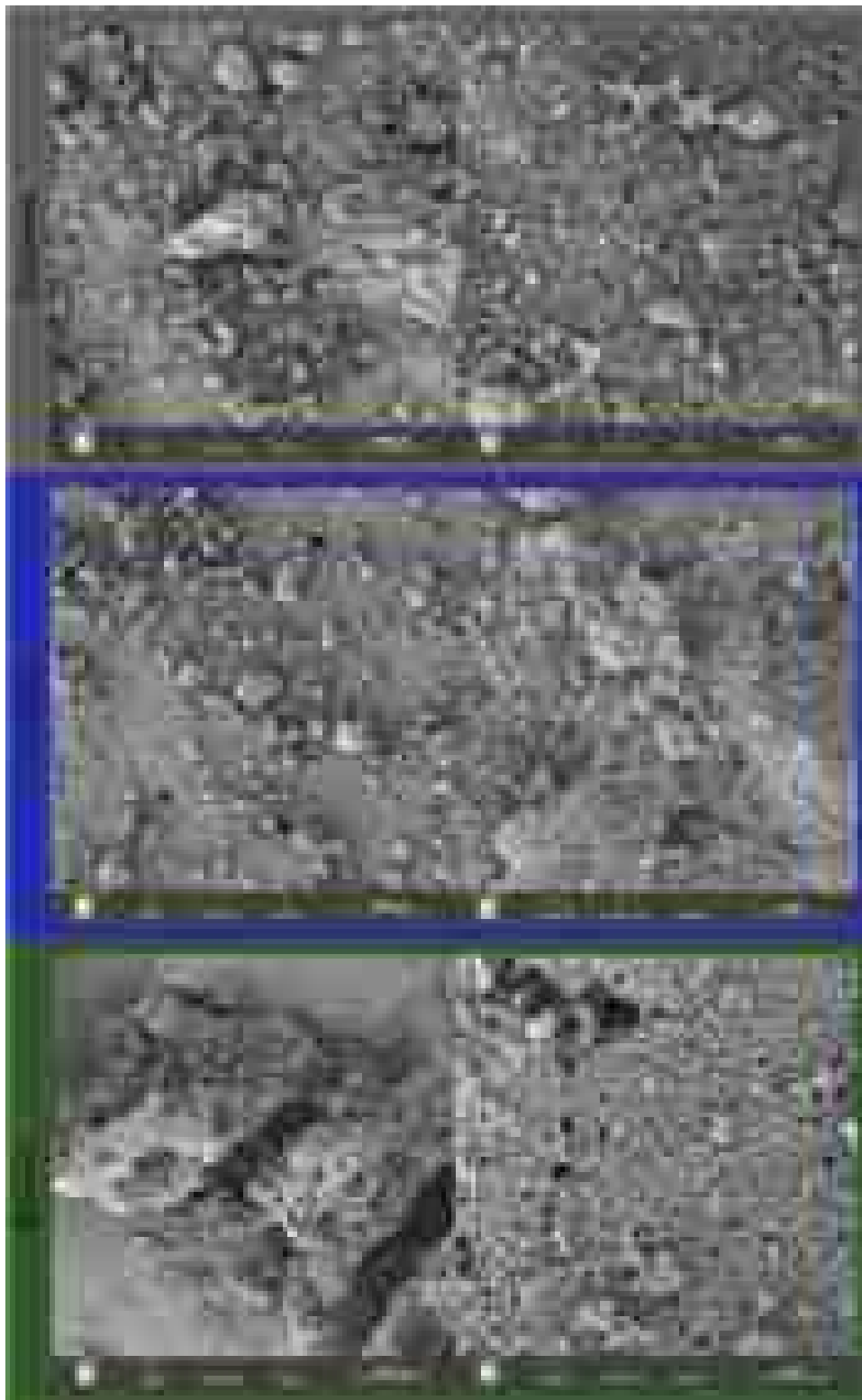


Fig. 2. SEM images of biochar, graphene, and printex with magnifications of 500X and 10000X.

can be removed from a solution [30,31]. Fig. 2 shows the morphologies of carbonaceous materials (biochar, graphene, and Printex) obtained by SEM-FEG.

Biochar from pineapple crown residue morphology evidenced a porous structure, which can be associated with removing volatiles during the pyrolysis process, leading to the formation of a fixed carbon mass with a high density of pores of varying sizes [48]. The SEM images of graphene showed a rough structure with hierarchical pores and a wide size distribution, making it a preferable site for PTE binding [46]. However, graphene originally had a layered structure. Printex displays that the carbonaceous material exhibits a rough structure and particles with irregular shapes, similar to the morphology of graphene. Silva et al. also demonstrated identical morphology when they proposed a new sensor based on a glassy carbon electrode (GCE) modified with Printex 6 L carbon (Printex6L/GCE) [47].

Although biochar presented a different morphology compared to printex and graphene, the materials have similar particle size distributions, as shown in Fig. 3. It is noteworthy that from the images, it is possible to observe that the porous structure presented by biochar has more visible pores on its surface, which can favor interaction processes and enhance the removal of contaminants. In addition, the sustainable aspect presented by this material, along with its lower cost, are other attractive factors for potential application in environmental solutions.

The differences in the size and shape of the particles in the materials can be observed in the images with magnifications of 500X and 10000X (Fig. 2). The particle size of the studied samples was measured, yielding the following values: 0.823 μm for graphene, 0.820 μm for Printex, and 0.860 μm for biochar. Compared to printex and biochar, graphene has a slightly smaller particle size, and the aggregates formed are closely related. This fact could favor the adsorption process.

The particle size directly influences the exposed surface area, as smaller particles generally have a larger specific surface area, thereby increasing interaction with adsorbates and potentially leading to increased adsorption activity and faster reaction rates [48]. Gora et al. evaluated the effect of particle size on the adsorption rates and capacities of Spent coffee grounds (SCGs) for Pb^{2+} , Cu^{2+} , Zn^{2+} , and Ni^{2+} under alkaline conditions. The initial adsorption rates for all four metal ions were 8–12 times higher for the smallest particle size compared to the largest. Slower initial adsorption rates with increasing particle size were due to intraparticle diffusion of metal ions into the porous structure [49]. Muthuraja et al. investigated the adsorption mechanisms of Pb^{2+} and Cu^{2+} ions on both pristine and artificially aged microplastics (MPs) made of polystyrene (PS) and polypropylene (PP). Furthermore, the influence of MP size on the adsorption capacity under different environmental conditions was evaluated. The experimental results highlight the significantly higher adsorption ability of smaller [50].

Bukka and Sarin studied the effect of particle size of zeolite and clinoptilolite on gas adsorption (GA). For comparison, similar evaluations were conducted for natural porous zeolite with interconnected micro-, meso-, and macropores. GA studies revealed that even with a particle size reduction to 212 μm , isolated pores were found inaccessible. Size reduction in materials with interconnected pores, however, was not shown to impact the evaluation of pore structure using GA [51].

3.4. Thermogravimetric analysis (TGA)

Thermogravimetric analysis (TGA) and its derivative (DTG) curves were employed to evaluate the thermal stability of carbon-based materials (biochar, graphene, and Printex) and to investigate their potential applications in environmental and industrial processes. Fig. 4 presents the TG and DTG curves for the three materials.

The TG curves revealed distinct thermal behaviors among the samples, reflecting the differences in their composition and structure. Graphene exhibited an onset decomposition temperature (T_{onset}) of 240 $^{\circ}\text{C}$, indicating the initiation of thermal decomposition associated with the decomposition of less stable carbon structures and the release of volatile

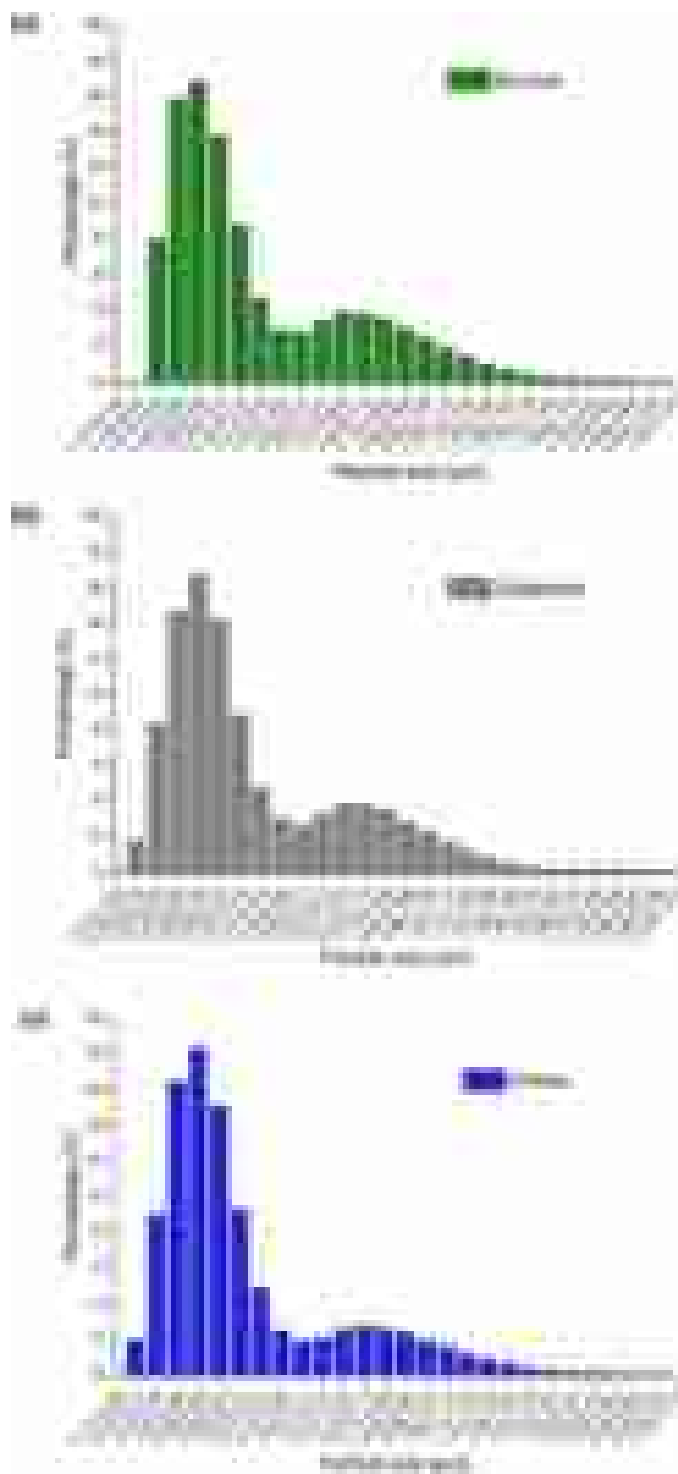


Fig. 3. Particle size distribution of biosorbents, where (a) Biochar, (b) Graphene, and (c) Printex.

compounds. The DTG curve for graphene displayed two significant thermal events: the first, occurring below 100 $^{\circ}\text{C}$, corresponded to moisture loss due to the hydrophilic nature of the material, while the second, a dominant peak between 240 and 700 $^{\circ}\text{C}$, reflected the near-total decomposition of its structured carbon framework. At 800 $^{\circ}\text{C}$, the residue was 4 %, suggesting a high purity level with minimal inorganic content [52].

Biochar demonstrated a higher T_{onset} of 300 $^{\circ}\text{C}$. The DTG analysis highlighted two significant events. The first, below 100 $^{\circ}\text{C}$, was

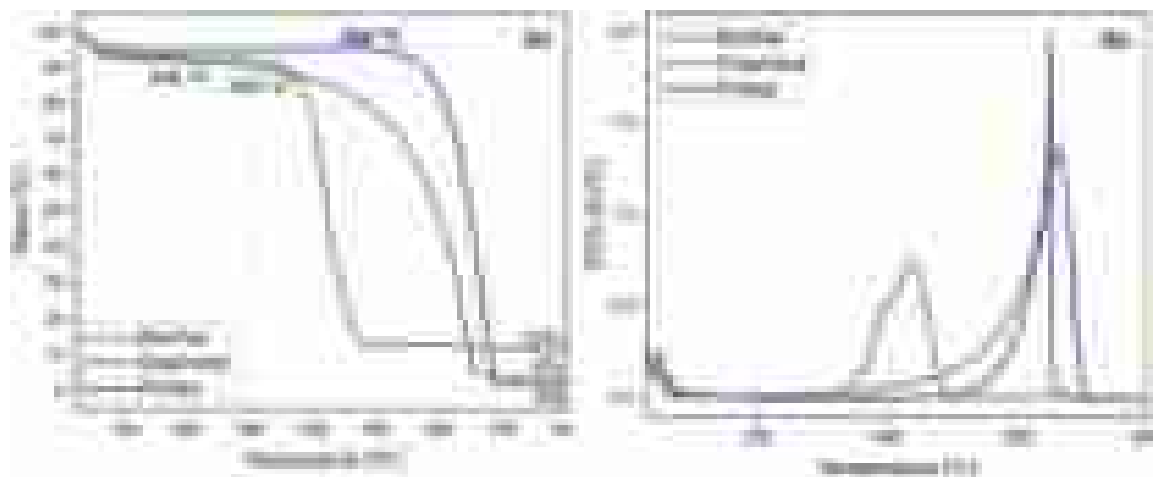


Fig. 4. TG (a) and DTG (b) curves for biochar, graphene, and Printex, showing thermal behavior and decomposition peaks.

attributed to moisture loss, while the second, between 300 and 500 °C, corresponded to the primary decomposition of organic matter, such as hemicellulose and cellulose. The residue at 800 °C was 12 %, attributed to the ash content and residual inorganic components present due to its biomass origin [33,34].

Printex displayed the highest thermal stability, with a T_{onset} of 480 °C, indicative of its highly crystalline and reticulated carbon structure. Its DTG curve also showed two distinct events. The initial moisture loss occurred below 100 °C, followed by a prominent and sharp decomposition peak between 480 and 710 °C, representing the nearly complete oxidation of its organized carbon framework. The residue at 800 °C was only 2 %, consistent with its high purity and minimal inorganic impurities [53].

Table 2 summarizes the thermogravimetric data, including the onset degradation temperature (T_{onset}), decomposition intervals, and residue percentages analyzed at 800 °C.

The decomposition intervals and residue levels observed are consistent with those reported in previous studies. As Bredin et al. highlighted, Printex’s higher T_{onset} and lower residue indicate its highly crystalline and reticulated carbon structure. The combustion of Printex begins around 400 °C, peaks at approximately 500 °C, and is completed by 580 °C, reflecting its superior thermal stability and minimal inorganic content [53]. This behavior is consistent with the results presented by Farivar et al. (2021), who demonstrated that the distinct DTG peaks and T_{max} values of graphene reflect their high structural purity and thermal stability, as well as their minimal inorganic content [52]. These findings support that materials with more ordered structures, such as Printex and graphene, exhibit enhanced thermal resistance.

In contrast, Biochar exhibited a broader decomposition range, spanning from 383 to 800 °C, underscoring its heterogeneous composition and the presence of diverse functional groups. This observation aligns with Schultz et al. [54] and Montalvo et al. [55], who also noted the varying thermal stability of biochar depending on the activation methods and the biomass source. The broader decomposition profile and higher residue content (12 %) observed for biochar are attributed to the

complex mixture of organic and inorganic components that result from its biomass origin, further supporting the understanding that materials with higher impurity levels and structural heterogeneity tend to decompose over a wider temperature range.

These results emphasize the distinct thermal properties of each material and their relevance for specific applications. Printex’s high thermal stability and minimal residue are ideal for high-temperature industrial processes and catalytic applications. Biochar, with its high residue content and broader decomposition profile, shows promise in environmental applications, such as adsorbents for water and wastewater treatment. Meanwhile, graphene’s moderate T_{onset} and low residue highlight its versatility for high-purity applications, including electronics and composite reinforcement.

These findings underscore the importance of tailoring carbon-based materials to specific applications based on their unique thermal properties. Future studies could explore chemical modifications or functionalization strategies to further enhance the performance of these materials in industrial and environmental applications.

3.5. Determination of the zero-charge point (ZPC)

The point of zero charge (PZC) significantly influences adsorption processes, particularly by determining the surface charge of a material

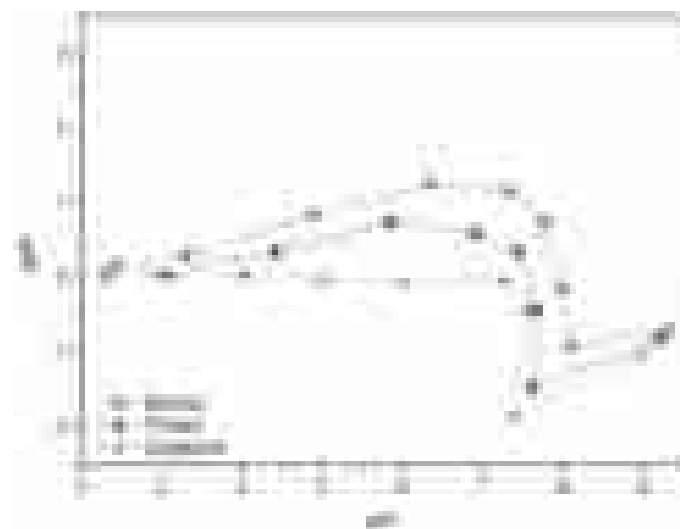


Fig. 5. Comparison of charge as a function of point of zero charge (pH_{ZPC}) of Biochar, Printex, and Graphene.

Table 2
Summary data from thermogravimetric analysis for Graphene, Biochar, and Printex, including T_{onset} , decomposition intervals, and residue percentages at 800 °C.

Samples	T_{onset} (°C)	Decomposition interval (°C)	Residue at 800°C
Graphene	240	240–700	4
Biochar	300	300–500	12
Printex	480	480–710	2

and how it interacts with charged molecules in a solution [56]. Analysis of Fig. 5 reveals the zero charge point (pH_{ZPC}) for each material. The results showed distinct surface charge behaviors depending on the material. Biochar exhibits a higher pH_{ZPC} of approximately 7.5, indicating a greater presence of carboxylic and phenolic groups. This promotes protonation and deprotonation at slightly alkaline pH levels [57]. In contrast, Printex has a pH_{ZPC} close to 6, which is less alkaline and associated with a carbon-loving nature and low functional reactivity. Graphene, with a pH_{ZPC} ranging from 4 to 5, exhibits an acidic character due to the predominance of oxygenated groups, such as hydroxyls and epoxides, which facilitate protonation in acidic media [58]. Moreover, it is essential to note that maintaining pH levels around 2 and 3 can contribute to favorable adsorption outcomes. These findings are consistent with previous observations by Bento et al. (2025), who reported a point of zero charge (pH_{ZPC}) of approximately 7 for pinecone residues used in the adsorption of Cr^{6+} [59].

For this reason, a highly acidic pH value was chosen for the adsorption process, as it is highly efficient in removing metallic contaminants under these conditions. In acidic environments, the high concentration of H^+ ions promotes the protonation of the functional

groups present on the surface of the adsorbent, which increases the positive charge and favors the attraction of anionic species, such as Cr^{6+} [60]. This ensures that the scientific properties in DOE analyses remain consistent and that the results are reliable.

3.6. Adsorption analysis for design of experiments (DOE)

Investing in studies that evaluate the development of technologies for treating water contaminated with metal ions is crucial for addressing environmental challenges and ensuring water security. Therefore, the present study proposes comparing the performance of Cr^{6+} removal from water by the surfaces of biochar, graphene, and Printex samples. Three-dimensional curves were plotted to clarify the effects of the process variables (dosage, initial concentration, and contact time). The impact of initial concentration-contact time (Fig. 6), time-dosage (Figure S1), and initial concentration-dosage (Figure S2) on Cr^{6+} adsorption by biochar was assessed and displayed as response surface plots.

Fig. 6 demonstrates that varying the dosage significantly impacts the efficiency of Cr^{6+} removal from water on the samples of biochar,

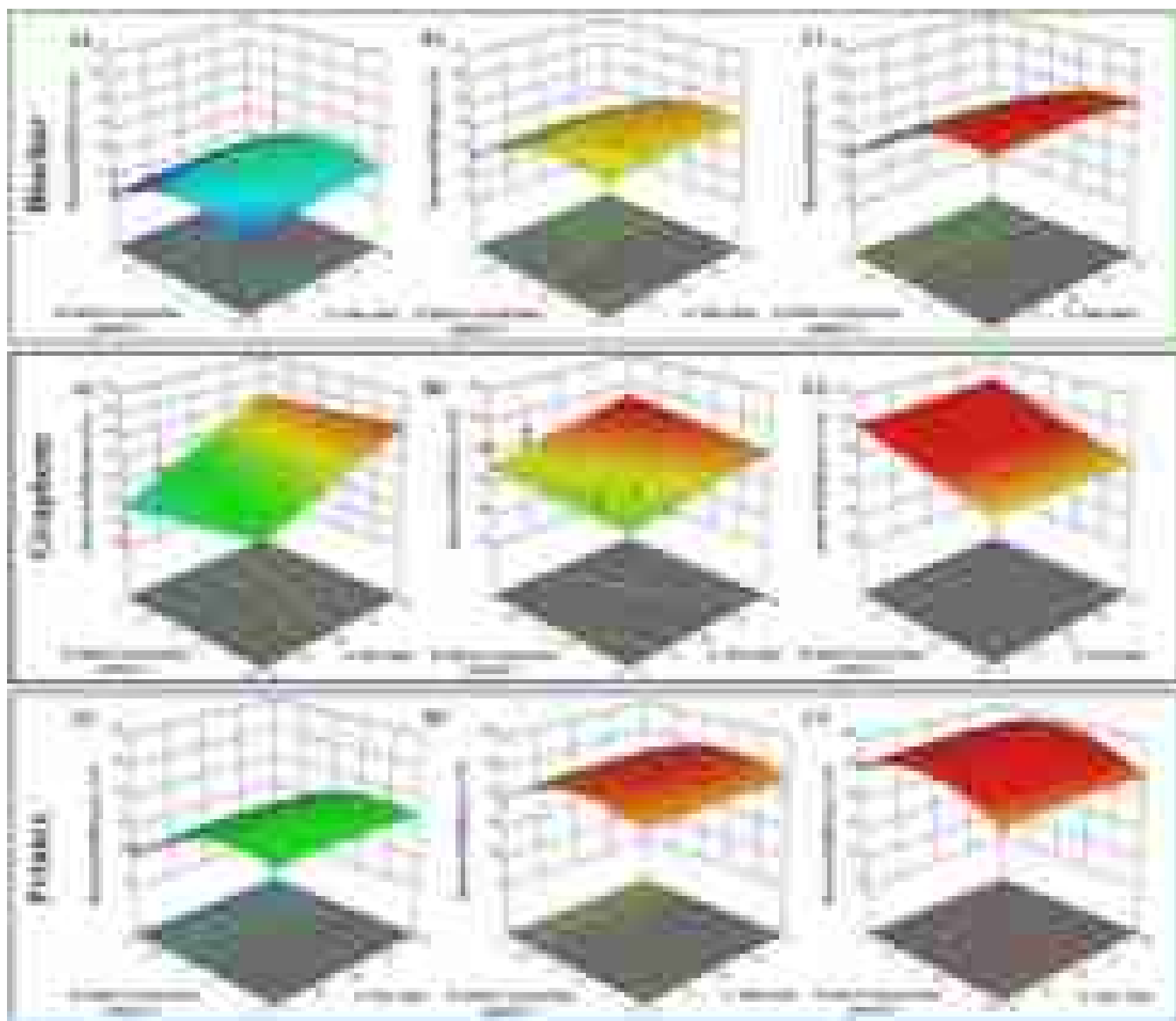


Fig. 6. Response surface plot of time and initial concentration where (a1, a2, and a3) dosage = 10 mg; (b1, b2, and b3) dosage = 50 mg; and (c1, c2, and c3) dosage = 100 mg). (The color changes from blue to red, indicating that the removal rate gradually increases.).

graphene, and printex surfaces, as the slope of the dosage response surface is steeper than that of the initial concentration and contact time. The plots revealed that as the adsorbent dosage increased from 10 to 100 mg, the Cr^{6+} removal rate gradually increased.

Biochar exhibited a maximum removal capacity of 85.1 % ($8.87 \text{ mg} \cdot \text{g}^{-1}$), achieved with a dosage of 100 mg, a contact time of 30 min, and an initial concentration of 1 mmol/L. Graphene achieved a maximum removal percentage of 89.0 % ($55.5 \text{ mg} \cdot \text{g}^{-1}$) under 50 mg, 30 min, and $3 \text{ mmol} \cdot \text{L}^{-1}$ conditions. Finally, Printex demonstrated a maximum removal capacity of 85.4 % ($17.8 \text{ mg} \cdot \text{g}^{-1}$), comparable to biochar, using 50 mg, 30 min, and $1 \text{ mmol} \cdot \text{L}^{-1}$. The structural properties of each material influenced the difference in adsorption capacity. The layered structure of graphene and the rough morphology of Printex enhanced its performance, as shown by XDR and SEM techniques. Additionally, the porous structure and surface functional groups of biochar also promoted effective adsorption.

According to the studies, this observed trend by dosage can be attributed to the increase in active sites on the biochar surface with higher dosages, which enhances adsorption performance [46,61–63].

Yussult et al. reported similar behavior when evaluating response surface modeling and optimization of Cr^{6+} adsorption onto eucalyptus tree bark-derived pristine and chemically modified biochar, affirming that the amount of adsorbent has a significant effect on the removal efficiency of Cr^{6+} ions [64]. Rajani et al. synthesized carbonaceous nickel ferrite ($\text{NiFe}_2\text{O}_4/\text{C}$) for Cr^{6+} removal, and it was found that at an equilibrium time of 60 min, nearly 85 % of the chromium was removed using 0.01 g [65].

Regarding the effect of contact time, the results suggest that the active sites present on the surface of all samples were cumulatively saturated after 30 min of testing. This trend was also observed by Vaghela et al. when evaluating the potential for Pb^{2+} ion removal using biochar derived from wheat straw [66].

The ANOVA analysis helps to determine the statistical significance of the disparity between the mean values. Table 3 presents the ANOVA statistical analysis comparing the removal efficiency of Cr^{6+} . The results indicate that biochar and Printex are significant model terms, as evidenced by a p-value of less than 0.05. Additionally, yield coefficients (R^2) approaching one were achieved, ensuring adequate analysis.

A slight difference in the removal efficiency of the ion of interest by each adsorbent material explored was observed, showing the potential for using biochar obtained from pineapple crowns as an adsorbent material in the removal of Cr^{6+} from real industrial effluents. Given the abundance of agro-industrial waste and biomass available, reusing these materials for biochar production represents a unique opportunity to align the treatment of contaminated water with sustainable waste management practices. Investing in research that explores the potential of this waste is crucial for creating environmentally responsible and economically viable solutions, thereby contributing to the mitigation of global environmental problems and promoting the circular economy.

3.7. Kinetic study

The kinetic study of hexavalent chromium (Cr^{6+}) adsorption using Biochar, Graphene, and Biochar reveals distinct behaviors among the materials, as shown in Fig. 7.

Table 3

Results of analysis of variance (ANOVA), showing the sum of squares, mean square, and P-value using a single factor to consider the efficiency of the samples studied.

Samples	Sum of Squares	D_r	Mean Square	F-value	p-value	R^2
Biochar	9413.6	9	1046	19.4	0.006	0.978
Graphene	2409.6	6	401.6	2.77	0.105	0.704
Printex	5424.7	9	602.7	22.7	0.004	0.981

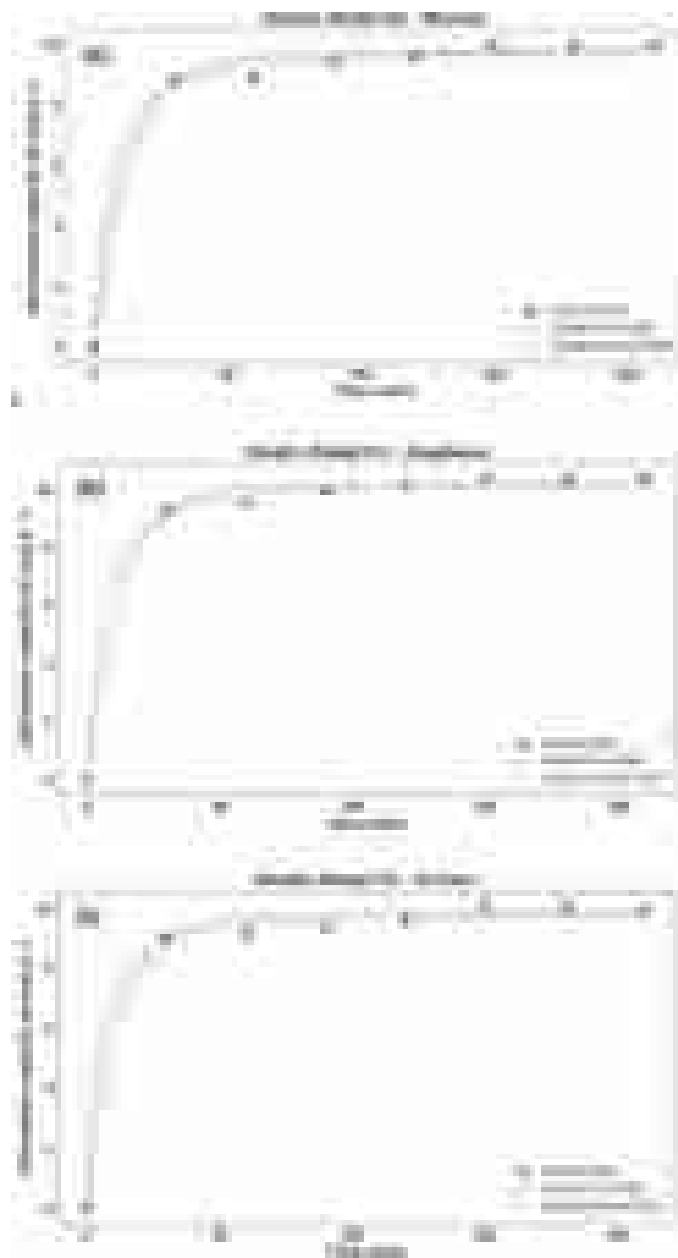


Fig. 7. Pseudo First Order and Pseudo Second Order Kinetic models for Cr^{6+} adsorption onto carbonaceous materials: biochar (a), graphene (b), and printex (c).

The results primarily align with the pseudo-second-order model, suggesting that in all three cases, the adsorption process is predominantly influenced by chemical interactions. Graphene presented excellent performance, with values of $R^2 = 0.9974$ for the pseudo-second-order model and 0.9936 for the pseudo-first-order model, reaching equilibrium quickly due to its high surface area and the presence of functional groups such as hydroxyls ($-\text{OH}$), carboxyls ($-\text{COOH}$) and carbonyls ($\text{C}=\text{O}$), which promote chemical bonds with Cr^{6+} species [67]. Printex, in turn, exhibited a significant fit to the pseudo-second-order model ($R^2 = 0.9948$), slightly surpassing the fit to the pseudo-first-order model ($R^2 = 0.9912$). This behavior is attributed to its surface containing similar oxygenated functional groups, which favor electrostatic interactions and bonds through electron pair donation [68]. Biochar demonstrated efficient kinetics, with rapid initial adsorption followed by gradual stabilization, as indicated by R^2 values of 0.9939 for the pseudo-second-order model and 0.9885 for the

pseudo-first-order model. This behavior reflects the presence of a variety of functional groups, including phenols, lactones, quinones, and carboxyls, as well as the possible participation of redox mechanisms associated with the conversion of Cr^{6+} to Cr^{3+} , as reported by Peng et al. [69]. Although graphene and Printex present satisfactory kinetic results, biochar stands out as an emerging alternative, exhibiting an excellent fit to the pseudo-second-order model and maintaining constant performance over time, which indicates efficient and stable adsorption, even without structural modifications or the addition of reducing agents.

3.8. Adsorption isotherms

Adsorption isotherms are crucial for comprehending the adsorption process, as they elucidate the interaction mechanisms between the adsorbate and the adsorbent surface. In this study, the Langmuir and Freundlich isotherm models were employed to determine which best characterizes the adsorption mechanism of Cr^{6+} on biochar, graphene, and printex. Fig. 8 illustrates the fits of the adsorption isotherms to the experimental data.

For graphene and printex, the Langmuir model demonstrated a fit ($R^2 > 0.40$), indicating a predominantly monolayer adsorption on homogeneous surfaces with finite and identical adsorption sites [70,71]. Specifically, graphene exhibited a maximum adsorption capacity ($q_e = 67.7 \text{ mg}\cdot\text{g}^{-1}$) with a Langmuir constant ($K_L = 0.0014 \text{ L}\cdot\text{mg}^{-1}$), reflecting high affinity and exceptional performance. Printex also showed effective adsorption, with $q_e = 30.4 \text{ mg}\cdot\text{g}^{-1}$ and a notably high affinity constant ($K_L = 0.014 \text{ L}\cdot\text{mg}^{-1}$). For biochar, the Freundlich model also provided a good fit ($R^2 = 0.66$), with $q_e = 13.3 \text{ mg}\cdot\text{g}^{-1}$ and an exceptionally high affinity constant ($K_L = 0.085 \text{ L}\cdot\text{mg}^{-1}$), reinforcing that adsorption occurs primarily through monolayer coverage despite the inherently more heterogeneous nature of biochar, as similarly observed for other bio-based materials [72].

Thus, the adsorption isotherms obtained for the three carbon-based materials reveal specific characteristics, reflecting their different structures and active surfaces. The graphene synthesized in this study exhibited behavior compatible with the Langmuir model, in agreement with Khdoor et al. (2024) characterized by monolayer adsorption on a superficial surface and uniform adsorption energy [73]. Printex presented a maximum adsorption capacity of approximately 30 mg/g , a value compatible with that reported by Yolshina et al. [74], reinforcing its well-established performance under similar conditions [74]. On the other hand, biochar stands out for following the Freundlich model, as also observed by Tho et al. (2021), reflecting a heterogeneous surface with adsorption sites of different energies [75]. In addition to presenting the technical performance of inventive materials, biochar stands out as an environmentally sustainable alternative obtained from biomass waste with a low environmental impact. Its economic and ecological predictions reinforce its potential as a promising adsorbent material in future prospective applications for effluent treatment and environmental remediation.

On the other hand, none of the experimental data fit the Temkin model for any of the studied systems, suggesting that the heat of adsorption does not decrease linearly with surface coverage or that the model assumptions do not adequately capture the interactions between Cr^{6+} and the surfaces of these adsorbents [76]. These results highlight that while graphene and printex exhibit strong adsorption capabilities, biochar also performs remarkably well in the Langmuir model, reinforcing its potential as a highly effective, sustainable, and low-cost adsorbent for practical applications.

3.9. Desorption and regeneration

The regeneration of adsorbents after contaminant capture represents a significant challenge, mainly when nanoparticles are used. In the case of materials such as graphene and Printex, this challenge is amplified due to the tendency of these particles to form agglomerates, a

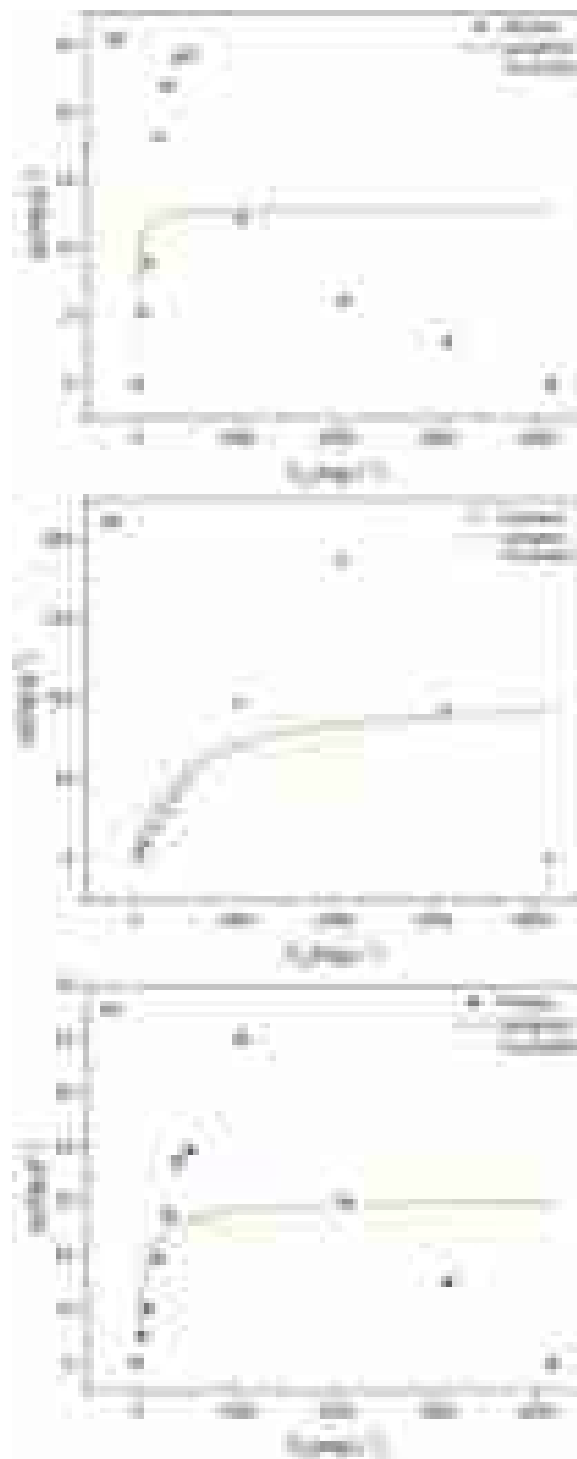


Fig. 8. Non-linear fitting of Langmuir and Freundlich isotherm models to the experimental equilibrium data for Cr^{6+} adsorption onto carbonaceous materials: biochar (a), graphene (b), and printex (c).

consequence of the strong interaction between them and pollutants. This phenomenon compromises the desorption efficiency and limits the reuse of the adsorbent material [77]. On the other hand, biochar is a promising alternative for adsorption and desorption processes due to its high contaminant removal capacity and ease of regeneration. Furthermore, biochar is considered a sustainable option, since it is produced from organic waste, and is an environmentally friendly solution for the treatment of contaminated water [78]. Effective regeneration of adsorbents is crucial to ensure the sustainability and economic viability of

large-scale adsorption processes [79].

In the study of biochar reusability, Cr^{6+} solutions were used due to their high adsorption potential. The adsorbents underwent three consecutive cycles under ideal conditions established in the adsorption test ($1.0 \text{ mmol}\cdot\text{L}^{-1}$ for 30 min, with 100 mg of material). Between cycles, chemical regeneration with HNO_3 was performed, the effectiveness of which depends on the solubility of the adsorbates in the solvent, which can alter the chemical structure of the adsorbent. Fig. 10 illustrates the adsorption percentages in each desorption cycle.

The removal of Cr^{6+} showed a considerable reduction, going from 85 % to 21 % after the second chemical regeneration cycle. This decrease can be attributed to the loss of biochar mass during the repeated filtration and drying processes, which reduce the number of active adsorption sites and compromise the material's effectiveness. In addition, the difficulty in recovering Cr^{6+} ions, which remain strongly adsorbed on the surface of the biochar, can be explained by the electrostatic interaction between the positively charged biochar and the ions, favoring the desorption of the contaminant and making the process even less effective [78,79].

3.10. Life cycle assessment

Considering the samples studied, which present a direct environmental application field—the bioremediation process—impact assessment is essential for understanding the ecological impacts associated with their production and use. In this context, Life Cycle Assessment (LCA) is a powerful tool that quantifies the environmental impacts associated with all stages of a product's life cycle, from raw material extraction to end-of-life, considering a sustainable perspective [80,81].

Previous studies have reported poor quality data for the graphite/graphene production chain in the existing LCA's examined [82,83]. However, these studies have also shown that production, primarily via conventional or synthetic routes, is often associated with significant energy consumption, greenhouse gas emissions, and the use of hazardous chemicals, which raises concerns regarding their overall environmental performance [82]. According to Surovtseva et al. [70], current inventories suggest that greenhouse gas emissions, such as CO_2 , and energy consumption for synthetic graphite may be more than double the values reported in prior work, achieving values of $13.8 \text{ kg CO}_2\text{eq/kg}$ and 45.9 MJ/kg , respectively.

In the present study, recognizing the potential of biochar prepared, LCA was conducted to assess the environmental impacts of its production, and Fig. 11 shows the LCA results considering the impact categories of Freshwater ecotoxicity, Freshwater eutrophication, Global warming, Human carcinogenic toxicity, Human non-carcinogenic toxicity, Marine

ecotoxicity, Marine eutrophication, and Territorial ecotoxicity. Two scenarios were considered: the production of biochar (represented by the black bar) and a similar process incorporating waste treatment and carbon credits (represented by the green bar). The waste treatment credit is related to avoiding impacts due to the non-disposal of pineapple residue for treatment in municipal landfills. In contrast, the carbon credit is attributed exclusively to the amount of CO_2eq to carbon sequestered by the mass fraction of pineapple residue converted into biochar [29].

Freshwater ecotoxicity (FEco) and eutrophication (FEu) refer to the impact of toxic substances or excess nutrients released into the environment on freshwater organisms. In contrast, Marine ecotoxicity (MEco) and eutrophication (MEu) reflect this impact on the marine organisms [81]. The results evidenced a significant decrease for FEco and MEco and a slight change for FEu and MEu. This behavior can be attributed to substituting fossil resources for biomass in the production of activated carbon, thereby reducing landfill disposal.

Global warming is an indicator of potential global warming due to emissions of greenhouse gases into the air [81]. Although analysis shows a slight reduction in carbon retention from biomass and a reduction in emissions in other processes, there is evidence that the pineapple crown-based biochar production process contributes to mitigating the potential for global warming. Another category with a similar effect was territorial ecotoxicity, which refers to toxicity in land ecosystems [81].

Human carcinogenic or non-carcinogenic toxicity involves the impact on humans of toxic substances emitted to the environment [81]. The results reflected a high environmental benefit, and this behavior is possibly related to replacing fossil resources with biomass and the non-disposal of biomass in landfills, which minimizes or avoids the release of toxic substances into water, air, and soil.

Overall, the analysis reveals that when considering the environmental credits associated with using biochar, such as the valorization of pineapple crown residue and carbon capture, environmental impacts are significantly reduced in several categories, particularly human toxicity and ecotoxicity. These results highlight the potential of biochar as an environmentally advantageous alternative for environmental remediation compared to graphene and Printex, whose production generally involves high energy consumption and gas emissions.

4. Conclusions

This research investigates the adsorption capacity of chromium (Cr^{+6}) using three carbon-based materials: graphene, printex, and biomass-derived biochar. The study evaluates the influence of the physicochemical, morphological properties, and particle size of these materials, as well as their life cycle impacts. The results showed high efficiencies for all adsorbents: biochar removed 85.1 % of Cr^{6+} under optimal conditions (100 mg dosage, $1 \text{ mmol}\cdot\text{L}^{-1}$ concentration, 30 min contact time); printex achieved 85.4 %, and graphene demonstrated the highest removal rate of 89 %. The adsorption isotherms were best described by the Langmuir model, with maximum capacities of $67.7 \text{ mg}\cdot\text{g}^{-1}$ for graphene, $30.4 \text{ mg}\cdot\text{g}^{-1}$ for Printex, and $13.3 \text{ mg}\cdot\text{g}^{-1}$ for biochar. This variation in adsorption capacity is linked to the structural properties of each material. Biochar's superior porosity and surface functionality enable it to match or exceed synthetic materials like graphene and printex in adsorption efficiency (%), positioning it as a cost-effective and sustainable alternative. Furthermore, under production scenarios using pineapple residues and assessed through the ReCiPe 2016 Midpoint (H) method, biochar exhibited significantly lower environmental impacts—especially in terms of human toxicity and aquatic ecotoxicity—when compared to traditional materials. Notably, biochar stands out as a sustainable and cost-effective option derived from biomass waste, aligning with environmental objectives. This study provides an integrated evaluation of physicochemical properties, adsorption efficiency, and life cycle impacts of carbon-based adsorbents. The multi-criteria approach addresses a key gap in the literature by

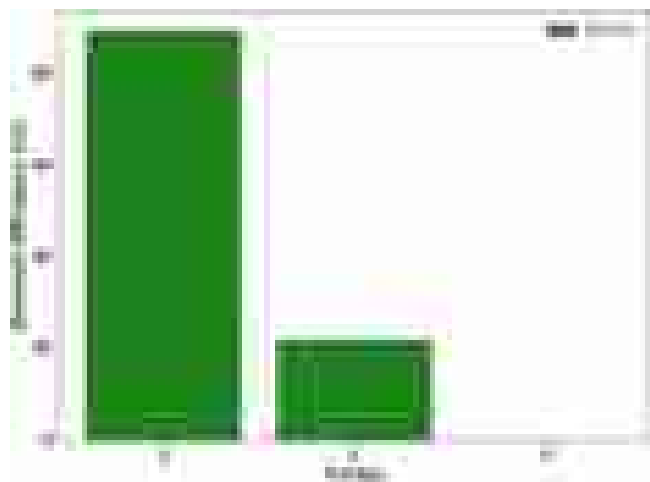


Fig. 10. Adsorption percentage of Cr^{6+} of biochar in reuse cycles (sorption: dose of $10 \text{ g}\cdot\text{L}^{-1}$; $\text{C}_0 = 1.0 \text{ mmol}\cdot\text{L}^{-1}$ and $T = 25 \text{ }^\circ\text{C}$).

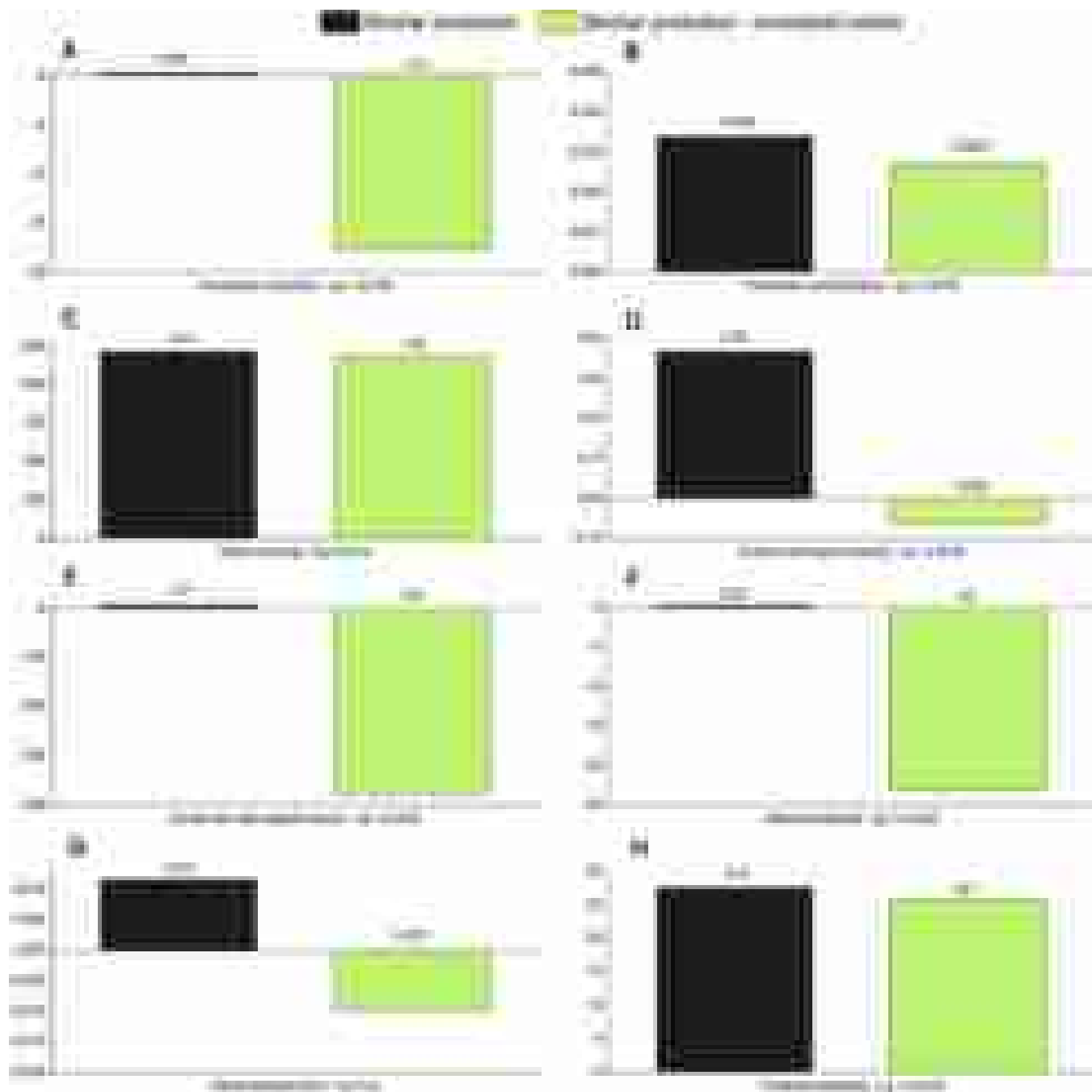


Fig. 11. Life Cycle Assessment results of biochar, considering the base production and production with considered waste treatment and carbon credits, concerning a Freshwater ecotoxicity (A), Freshwater eutrophication (B), Global warming (C), Human carcinogenic toxicity (D), Human non-carcinogenic toxicity (E), Marine ecotoxicity (F), Marine eutrophication (G), and Territorial ecotoxicity (H).

offering a holistic comparison and establishing direct structure–property–performance relationships under controlled conditions. The findings offer practical guidance for material selection in Cr⁶⁺ remediation and contribute to the advancement of more sustainable adsorption technologies.

CRedit authorship contribution statement

Perluxo Julia: Writing – original draft, Resources, Methodology, Investigation, Formal analysis, Data curation, Conceptualization. **Fillip Cortat Alves:** Writing – review & editing, Writing – original draft, Resources, Methodology, Investigation, Formal analysis, Data curation, Conceptualization. **Rosa Derval:** Writing – review & editing, Validation,

Supervision, Project administration, Methodology, Funding acquisition, Data curation. **Mulinari Daniella Regina:** Writing – review & editing, Validation, Supervision, Resources, Project administration, Methodology, Investigation, Funding acquisition, Formal analysis, Data curation. **Maia Lana Siqueira:** Writing – review & editing, Writing – original draft, Resources, Methodology, Investigation, Formal analysis, Data curation, Conceptualization. **Faria Maria Ismênia S.D.:** Writing – review & editing, Validation, Methodology, Investigation, Formal analysis, Data curation, Conceptualization. **Oliveira Daniel:** Writing – original draft, Validation, Methodology, Data curation, Conceptualization. **Botelho Edson:** Writing – review & editing, Validation, Resources, Investigation, Formal analysis.

Declaration of Competing Interest

The authors declare that they have no known competing financial interests or personal relationships that could have appeared to influence the work reported in this paper.

Acknowledgments

FAPERJ, Brazil funded this research (E-26/210.019/2024, E-26/201.092/2022, and E-26/210.450/2021), FAPESP, Brazil (2020/13703-3, 2021/14714-1, 2023/14598-7, and 2024/23595-4) and Conselho Nacional de Desenvolvimento Científico e Tecnológico - CNPq, Brazil (308053/2021-4 and 403934/2021-4). The authors thank the UFABC, CAPES (code 001), and REVALORES Strategic Unit. and Multiuser Central Facilities (CEM - UFABC), and FINEP (01.18.0071.00/0476/16).

Statements & Declarations

It is not applicable.

Appendix A. Supporting information

Supplementary data associated with this article can be found in the online version at [doi:10.1016/j.colsurfa.2025.137881](https://doi.org/10.1016/j.colsurfa.2025.137881).

Data availability

Data will be made available on request.

References

- [1] A. Biswas, S. Sarkar, S. Das, S. Dutta, M.R. Choudhury, A. Giri, B. Bera, K. Bag, B. Mukherjee, K. Banerjee, D. Gupta, D. Paulet, Water scarcity: A global hindrance to sustainable development and agricultural production – a critical review of the impacts and adaptation strategies, *Camb. Prism. Water* 13 (2025) e4, <https://doi.org/10.1017/wat.2024.16>.
- [2] H. Baocheng, A. Jamil, M. Bellaoulah, A. Mukhtar, N.K. Clauvis, Impact of climate change on water scarcity in Pakistan. Implications for water management and policy, *J. Water Clim. Change* 15 (2024) 3602–3623, <https://doi.org/10.2166/wcc.2024.710>.
- [3] K. Mariappan, S. Sakthinathan, S. Chen, T. Chiu, Cubic engineering approached a novel needle-structured cobalt-doped zinc oxide interconnected with carbon nanofiber as a composite for the determination of toxic 4-nitrophenol in environmental water samples, *Colloids Surf. A Physicochem. Eng. Asp.* 685 (2024) 133147, <https://doi.org/10.1016/j.colsurfa.2024.133147>.
- [4] E.M. Abd El-Monaem, A.M. Omer, H.A. Hamad, A.S. Eltaweil, Construction of attapulgite decorated cetylpyridinium bromide/cellulose acetate composite beads for removal of Cr (VI) ions with emphasis on mechanistic insights, *Sci. Rep.* 14 (2024) 12164, <https://doi.org/10.1080/s41598-024-62378-4>.
- [5] P. Sharma, S.P. Singh, S.K. Parakh, Y.W. Tong, Health hazards of hexavalent chromium (Cr (VI)) and its microbial reduction, *Bioengineered* 13 (2022) 4923–4938, <https://doi.org/10.1080/21655979.2022.2037273>.
- [6] Y. Zhigalenok, A. Tazhibayeva, S. Kokhmetova, A. Starodubtseva, T. Kan, D. Isbergenova, F. Malchik, Hexavalent chromium at the crossroads of science, environment and public health, *RSC Adv.* 15 (2025) 21439–21464, <https://doi.org/10.1039/D5RA03104D>.
- [7] S. Ozkul, O. Arbazadeh, R.J.M. Bisselink, N.J.M. Kuipers, H. Bruning, H.H. M. Rijnaarts, J.E. Dykstra, Selective adsorption in ion exchange membranes: the effect of solution ion composition on ion partitioning, *Water Res.* 254 (2024) 121382, <https://doi.org/10.1016/j.watres.2024.121382>.
- [8] R. Engstler, J. Reipert, S. Karimi, J.L. Vukušić, F. Heinzler, P. Davies, M. Ulbricht, S. Barbe, A reverse osmosis process to recover and recycle trivalent chromium from electroplating wastewater, *Membranes (Basel)* 12 (2022) 12090853, <https://doi.org/10.3390/membranes12090853>.
- [9] S. Imdad, R.K. Dohare, M. Agarwal, A. Srivastava, Efficient removal of Cr (VI) from wastewater using recycled polymer-based supported ionic liquid membrane technology, *Sep Purif. Technol.* 327 (2023) 124908, <https://doi.org/10.1016/j.seppur.2023.124908>.
- [10] C. Wu, J. Zhou, S. Pang, L. Yang, E. Lichtfouse, H. Liu, S. Xia, B.E. Rittmann, Reduction and precipitation of chromium(VI) using a palladium membrane biofilm reactor, *Water Res.* 249 (2024) 120878, <https://doi.org/10.1016/j.watres.2023.120878>.
- [11] F. Zahakifar, M. Dashtinejad, H. Sepehrian, M. Samadfam, J. Fasihi, A. Yadollahi, Intensification of Cr(VI) adsorption using activated carbon adsorbent modified with ammonium persulfate, *Sci. Rep.* 14 (2024) 16949, <https://doi.org/10.1038/s41598-024-68105-3>.
- [12] S. Singh, A.G. Anil, B. Uppara, S.K. Behera, B. Nath, N. Pavithra, S. Bhati, J. Singh, N.A. Khan, P.C. Ramamurthy, Adsorption and DFT investigations of Cr(VI) removal using nanocrystals decorated with graphene oxide, *NPJ Clean. Water* 7 (2024) 17, <https://doi.org/10.1038/s41545-024-00306-9>.
- [13] Y. Zhao, F. Liu, M. Yang, K. Qi, A. Zada, J. Pan, Removal of bisphenol A (BPA) from aqueous solution by potassium carbonate modified wetland plant biochars, *Colloids Surf. A Physicochem. Eng. Asp.* 703 (1) (2024) 35184, <https://doi.org/10.1016/j.colsurfa.2024.135184>.
- [14] Y. Zhao, M. Yang, K. Qi, J. Pan, The adsorption of bisphenol A by biochars modified with potassium phosphate, *Desal Water Treat.* 319 (2024) 100444, <https://doi.org/10.1016/j.dwt.2024.100444>.
- [15] C. Zhang, H.X. Ren, C.Q. Zhong, D. Wu, Biosorption of Cr(VI) by immobilized waste biomass from polyglutamic acid production, *Sci. Rep.* 10 (2020) 3705, <https://doi.org/10.1038/s41598-020-60729-5>.
- [16] J. Flores-Gómez, V.H. Romero-Arellano, M. Vazquez-Lepe, Á. de, J. Martínez-Gómez, J. Morales-Rivera, Modeling and optimization of the adsorption of Cr (VI) in a chitosan-resole aerogel using response surface methodology, *Gels* 9 (3) (2023) 197, <https://doi.org/10.3390/gels9030197>.
- [17] A. Solis-Ceballos, R. Roy, A. Golsztajn, J.R. Tavares, M.J. Dumont, Selective adsorption of Cr(III) over Cr(VI) by starch-graft-itaconic acid hydrogels, *J. Hazard Mater. Adv.* 10 (2023) 100255, <https://doi.org/10.1016/j.hazadv.2023.100255>.
- [18] N. Wang, D. Xiao, Electrospinning PVA/PEI/rGO Fibrous Membrane and Its Adsorption of Cr(VI) and Congo Red in Water, *Ind. Eng. Chem. Res.* 62 (2023) 21237–21250, <https://doi.org/10.1021/acs.iecr.3c03254>.
- [19] Y. Tan, J. Wang, L. Zhan, H. Yang, Y. Gong, Removal of Cr(VI) from aqueous solution using ball mill modified biochar: multivariate modeling, optimization and experimental study, *Sci. Rep.* 14 (2024) 4853, <https://doi.org/10.1038/s41598-024-55520-9>.
- [20] D. Coetzee, T. Rojviroon, S. Niamlang, J. Militký, J. Wiener, J. Večerník, J. Melicherková, J. Müllerová, Effects of expanded graphite's structural and elemental characteristics on its oil and heavy metal sorption properties, *Sci. Rep.* 14 (2024) 13716, <https://doi.org/10.1038/s41598-024-64695-0>.
- [21] R.H. Krishna, M.N. Chandrababha, K. Samrat, T.P. Krishna Murthy, C. Manjunatha, S.G. Kumar, Carbon nanotubes and graphene-based materials for adsorptive removal of metal ions – a review on surface functionalization and related adsorption mechanism, *Appl. Surf. Sci. Adv.* 16 (2023) 100431, <https://doi.org/10.1016/j.apsadv.2023.100431>.
- [22] D.R. Rout, H.M. Jena, O. Baigenzenov, A. Hosseini-Bandegharai, Graphene-based materials for effective adsorption of organic and inorganic pollutants: a critical and comprehensive review, *Sci. Total Environ.* 863 (2023) 160871, <https://doi.org/10.1016/j.scitotenv.2022.160871>.
- [23] X.T. Zhen, Y.L. Yu, M.Z. Shi, S.C. Zhu, T.C. Yan, Z.X. Yue, Y.X. Gu, H. Zheng, J. Cao, Activated carbon derived from hawthorn kernel waste for rapid adsorption of fungicides, *Surf. Interfaces* 28 (2022) 101700, <https://doi.org/10.1016/j.surfint.2021.101700>.
- [24] W. Hayat, X. Du, Z. Hua Liu, I. Hussain, K. Naseem, Y. Zhang, Removal of methomyl in water by leaves-generated biochar: effect of metallic coating, kinetics, and important role of hydroxyl radical, *Surf. Interfaces* 48 (2024) 104306, <https://doi.org/10.1016/j.surfint.2024.104306>.
- [25] M.M. Sabzehmeidani, S. Mahnaee, M. Ghaedi, H. Heidari, V.A.L. Roy, Carbon based materials: A review of adsorbents for inorganic and organic compounds, *Mater. Adv.* 2 (2021) 598–627, <https://doi.org/10.1039/d0ma00087f>.
- [26] S. Bhattacharya, P. Das, A. Bhowal, A. Saha, Thermal chemical and ultrasonic assisted synthesis of carbonized Biochar and its application for reducing Naproxen: Batch and Fixed bed study and subsequent optimization with response surface methodology (RSM) and artificial neural network (ANN), *Surf. Interfaces* 26 (2021) 101378, <https://doi.org/10.1016/j.surfint.2021.101378>.
- [27] M.H.M.T. Assumpção, R.F.B. De Souza, D.C. Rascio, J.C.M. Silva, M.L. Calegario, I. Gaubeur, T.R.L.C. Paixão, P. Hammer, M.R.V. Lanza, M.C. Santos, A comparative study of the electrogeneration of hydrogen peroxide using Vulcan and Printex carbon supports, *Carbon* 49 (2011) 2842–2851, <https://doi.org/10.1016/j.carbon.2011.03.014>.
- [28] P.J.M. Cordeiro-Junior, R. Gonçalves, T.T. Guaraldo, R. da Silva Paiva, E. C. Pereira, M.R.V. Lanza, Oxygen reduction reaction: Semi-empirical quantum mechanical and electrochemical study of Printex L6 carbon black, *Carbon* 156 (2020) 1–9, <https://doi.org/10.1016/j.carbon.2019.09.036>.
- [29] P.H.F. Pereira, L.S. Maia, A.I.C. da Silva, B.A.R. Silva, F.R. Pinhati, S.A. de Oliveira, D.S. Rosa, D.R. Mulinari, Prospective Life Cycle Assessment Prospective (LCA) of Activated Carbon Production, Derived from Banana Peel Waste for Methylene Blue Removal, *Adsorption* 30 (2024) 1081–1101, <https://doi.org/10.1007/s10450-024-00485-4>.
- [30] X. Guo, L. Yang, Z. Du, H. Zhou, L. Li, W. Zhu, L. Dai, Co-effects from inorganic and organic fractions in dissolved components of biochar on its adsorption behavior: taking uranium adsorption as an example, *Colloids Surf. A Physicochem. Eng. Asp.* 713 (2025) 136546, <https://doi.org/10.1016/j.colsurfa.2025.136546>.
- [31] S. Goyal, S. Chaudhary, *Syzygium cumini* derived biochar as sustainable adsorbent: Synthesis, parametric optimization with experimental and theoretical sketch, *Colloids Surf. A Physicochem. Eng. Asp.* 718 (2025) 136945, <https://doi.org/10.1016/j.colsurfa.2025.136945>.
- [32] L.S. Maia, A.I.C. da Silva, E.S. Carneiro, F.M. Monticelli, F.R. Pinhati, D. R. Mulinari, Activated carbon from palm fibres used as an adsorbent for methylene blue removal, *J. Polym. Environ.* 29 (2021) 1162–1175, <https://doi.org/10.1007/s10924-020-01951-0>.

- [33] A.I.C. da Silva, G. Paranha, L.S. Maia, D.R. Mulinari, Development of activated carbon from pineapple crown wastes and its potential use for removal of methylene blue, *J. Nat. Fibers* 19 (2022) 5211–5226, <https://doi.org/10.1080/15440478.2021.1875365>.
- [34] L.S. Maia, L.D. Duizit, F.R. Pinhatio, D.R. Mulinari, Valuation of banana peel waste for producing activated carbon via NaOH and pyrolysis for methylene blue removal, *Carbon Lett.* 31 (2021) 749–762, <https://doi.org/10.1007/s42823-021-00226-5>.
- [35] J. Wang, X. Guo, Adsorption isotherm models: Classification, physical meaning, application and solving method, *Chemosphere* 258 (2020) 127279, <https://doi.org/10.1016/j.chemosphere.2020.127279>.
- [36] P. Zhang, D. O'Connor, Y. Wang, L. Jiang, T. Xia, L. Wang, D.C.W. Tsang, Y.S. Ok, D. Hou, A green biochar/iron oxide composite for methylene blue removal, *J. Hazard Mater.* 384 (2020) 121286, <https://doi.org/10.1016/j.jhazmat.2019.121286>.
- [37] E.M. Aliyev, M.M. Khan, A.M. Nabiye, R.M. Alosmanov, I.A. Bunyad-zadeh, S. Shishatskiy, V. Filiz, Covalently modified graphene oxide and polymer of intrinsic microporosity (PIM-1) in mixed matrix thin-film composite membranes, *Nanoscale Res Lett.* 13 (2018) 359, <https://doi.org/10.1186/s11671-018-2771-3>.
- [38] Z. Liu, T. Lu, Q. Chen, An sp-hybridized all-carboatomic ring, cyclo[18]carbon: Bonding character, electron delocalization, and aromaticity, *Carbon* 165 (2020) 468–475, <https://doi.org/10.1016/j.carbon.2020.04.099>.
- [39] Q. Dong, G. Li, F. Liu, J. Ren, H. Wang, R. Wang, Cu nanoclusters activating ultrafine Fe₃N nanoparticles via the Mott-Schottky effect for rechargeable zinc-air batteries, *Appl. Catal. B* 326 (2023) 122415, <https://doi.org/10.1016/j.apcath.2023.122415>.
- [40] L.A.M. Mahmoud, J.L. Rowlandson, D.J. Fermin, V.P. Ting, S. Nayak, Porous carbons: a class of nanomaterials for efficient adsorption-based hydrogen storage, *RSC Adv.* 15 (2025) 25–55, <https://doi.org/10.1039/D4FM000215F>.
- [41] S. Ügdüler, T. Van Laere, T. De Somer, S. Gusev, K.M. Van Geem, A. Kulawig, R. Leineweber, M. Defoin, H. Van den Bergen, D. Bontinck, S. De Meester, Understanding the complexity of deinking plastic waste: An assessment of the efficiency of different treatments to remove ink resins from printed plastic film, *J. Hazard Mater.* 452 (2023) 131239, <https://doi.org/10.1016/j.jhazmat.2023.131239>.
- [42] A.H. Fahmi, A.W. Samsuri, H. Jol, D. Singh, Physical modification of biochar to expose the inner pores and their functional groups to enhance lead adsorption, *RSC Adv.* 8 (2018) 38270–38280, <https://doi.org/10.1039/c8ra06867d>.
- [43] Y. Liu, X. Zhao, J. Li, D. Ma, R. Han, Characterization of bio-char from pyrolysis of wheat straw and its evaluation on methylene blue adsorption, *Desalin. Water Treat.* 46 (2012) 115–123, <https://doi.org/10.1080/19443994.2012.677408>.
- [44] T.P. Pôrto, J.C. Lourenço, B. Nogueira, N.P. de Moraes, R. da Silva Souto, A. F. Siqueira, L.A. Rodrigues, M.R. de, V. Lanza, R. da Silva Rocha, Synthesis of activated carbon from sugarcane bagasse using blends of hydroxides for maximizing reaction targeted at obtaining hydrogen peroxide, *Biomass. Bioenergy* 191 (2024) 107438, <https://doi.org/10.1016/j.biombioe.2024.107438>.
- [45] A.G. Paes Júnior, G.C. Maciel, P.L.N. Carvalho, A.C.M. Almeida, N.F. da P. Ribeiro, Remoção de tolueno via processo de adsorção utilizando lama vermelha, *Braz. J. Dev.* 6 (2020) 11387–11416, <https://doi.org/10.34117/bjdv6n3-126>.
- [46] N.K. Mondal, S. Chakraborty, Adsorption of Cr(VI) from aqueous solution on graphene oxide (GO) prepared from graphite: equilibrium, kinetic and thermodynamic studies, *Appl. Water Sci.* 10 (2020) 61, <https://doi.org/10.1007/s13201-020-1142-2>.
- [47] L.P. Silva, F.C. Vicentini, B.C. Lourencao, G.G. Oliveira, M.R.V. Lanza, O. Fatibello-Filho, A new sensor architecture based on carbon Printex 6L to the electrochemical determination of ranitidine, *J. Solid State Electrochem* 20 (2016) 2395–2402, <https://doi.org/10.1007/s10008-016-3143-5>.
- [48] P.V. Mane, R.M. Rego, P.L. Yap, D. Losic, M.D. Kurkuri, Unveiling cutting-edge advances in high surface area porous materials for the efficient removal of toxic metal ions from water, *Prog. Mater. Sci.* 146 (2024) 101314, <https://doi.org/10.1016/j.pmatsci.2024.101314>.
- [49] E.H. Gora, S.G. Saldana, L.M. Casper, V.C. Sijercic, O.A. Giza, R.L. Sanders, Effect of Exhausted Coffee Ground Particle Size on Metal Ion Adsorption Rates and Capacities, *ACS Omega* 7 (2022) 38600–38612, <https://doi.org/10.1021/acsomega.2c04058>.
- [50] R. Muthuraja, B. Ou, M. Thangavelu, T.N. Narayanan, N. Chittamart, D. Janjaroen, Effects of particle size and aging on heavy metal adsorption by polypropylene and polystyrene microplastics under varying environmental conditions, *Chemosphere* 369 (2024) 143843, <https://doi.org/10.1016/j.chemosphere.2024.143843>.
- [51] V.V.R. Bukka, P. Sarin, Effects of particle size reduction on the pore structure and accessibility in natural porous materials, *Energ. Fuels* 38 (2024) 9578–9587, <https://doi.org/10.1021/acs.energyfuels.4c00194>.
- [52] F. Farivar, P.L. Yap, K. Hassan, T.T. Tung, D.N.H. Tran, A.J. Pollard, D. Losic, Unlocking thermogravimetric analysis (TGA) in the fight against “Fake graphene” materials, *Carbon* 179 (2021) 505–513, <https://doi.org/10.1016/j.carbon.2021.04.064>.
- [53] A. Bredin, A.V. Larcher, B.J. Mullins, Thermogravimetric analysis of carbon black and engine soot - Towards a more robust oil analysis method, *Tribol. Int* 44 (2011) 1642–1650, <https://doi.org/10.1016/j.triboint.2011.06.002>.
- [54] J. Schultz, G. Capobianco, P.A. da Silva Veiga, M.R. Fornari, A.R. Antonangelo, S. M. Tebcherani, A.S. Mangrich, S.A. Pianaro, Sustainable activated carbon obtained as a by-product of the sugar and alcohol industry for removal of amoxicillin from aqueous solution, *Energy Ecol. Environ.* 5 (2020) 433–443, <https://doi.org/10.1007/s40974-020-00173-3>.
- [55] J. Montalvo Andia, A. Larrea, J. Salcedo, J. Reyes, L. Lopez, L. Yokoyama, Synthesis and characterization of chemically activated carbon from *Passiflora ligularis*, *Inga feuillei* and native plants of South America, *J. Environ. Chem. Eng.* 8 (2020) 103892, <https://doi.org/10.1016/j.jece.2020.103892>.
- [56] M. Kosmulski, The pH dependent surface charging and points of zero charge. X. Update, *Adv. Colloid Interface Sci.* 319 (2023) 102973, <https://doi.org/10.1016/j.cis.2023.102973>.
- [57] Q. Fang, B. Chen, Y. Lin, Y. Guan, Aromatic and hydrophobic surfaces of wood-derived biochar enhance perchlorate adsorption via hydrogen bonding to oxygen-containing organic groups, *Environ. Sci. Technol.* 48 (2014) 279–288, <https://doi.org/10.1021/es403711y>.
- [58] L. Zuccaro, J. Krieg, A. Desideri, K. Kern, K. Balasubramanian, Tuning the isoelectric point of graphene by electrochemical functionalization, *Sci. Rep.* 5 (2015) 11794, <https://doi.org/10.1038/srep11794>.
- [59] J.G.S. Bento, L.F. Senra, L.S. Maia, L.S. Almeida, L.M. Ferreira, M.I.S.T. Faria, D. S. Rosa, D.R. Mulinari, Prediction of Cr⁶⁺ removal on the biosorbent from pine cone residue with machine learning simulations, *Surf. Interfaces* 65 (2025) 106460, <https://doi.org/10.1016/j.surfint.2025.106460>.
- [60] K. Das, U. Sukul, J.S. Chen, R.K. Sharma, P. Banerjee, G. Dey, M. Taharia, C. J. Wijaya, C.I. Lee, S.L. Wang, N.H.K. Nuong, C.Y. Chen, Transformative and sustainable insights of agricultural waste-based adsorbents for water defluoridation: Biosorption dynamics, economic viability, and spent adsorbent management, *Heliyon* 10 (8) (2024) e29747, <https://doi.org/10.1016/j.heliyon.2024.e29747>.
- [61] P. Brender, R. Gadiou, J.C. Rietsch, P. Fioux, J. Dentzer, A. Ponche, C. Vix-Guterl, Characterization of carbon surface chemistry by combined temperature programmed desorption with in situ X-ray photoelectron spectrometry and temperature programmed desorption with mass spectrometry analysis, *Anal. Chem.* 84 (2012) 2147–2153, <https://doi.org/10.1021/acs.102244b>.
- [62] F.H. Emamy, A. Bumajdad, J.P. Lukaszewicz, Adsorption of hexavalent chromium and divalent lead ions on the nitrogen-enriched chitosan-based activated carbon, *Nanomaterials* 11 (2021) 1907, <https://doi.org/10.3390/nano11081907>.
- [63] S. Mortazavian, H. An, D. Chun, J. Moon, Activated carbon impregnated by zero-valent iron nanoparticles (AC/nZVI) optimized for simultaneous adsorption and reduction of aqueous hexavalent chromium: Material characterizations and kinetic studies, *Chem. Eng. J.* 353 (2018) 781–795, <https://doi.org/10.1016/j.cej.2018.07.170>.
- [64] A.S. Yusuff, L.T. Popoola, A.I. Igbafe, Response surface modeling and optimization of hexavalent chromium adsorption onto eucalyptus tree bark-derived pristine and chemically-modified biochar, *Chem. Eng. Res. Des.* 182 (2022) 592–603, <https://doi.org/10.1016/j.cherd.2022.04.007>.
- [65] M.R. Rajani, R. Ravishanker, S. R. M. K. Asha, C. Vidya, G.R. Suma, K. Prashantha, Effective removal of Cr(VI) from an aqueous solution using a carbon coated NiFe₂O₄ nano-adsorbent, *Colloids Surf. A Physicochem Eng. Asp.* 693 (2024) 134012, <https://doi.org/10.1016/j.colsurfa.2024.134012>.
- [66] D.R. Vaghela, A. Pawar, N.L. Panwar, D. Sharma, Modelling and Optimization of Biochar-Based Adsorbent Derived from Wheat Straw Using Response Surface Methodology on Adsorption of Pb²⁺, *Int J. Environ. Res. Pub.* 17 (2023) 9, <https://doi.org/10.1007/s41742-022-00498-3>.
- [67] T. Naseem, F. Bibi, S. Arif, M. Waseem, S. Haq, M.N. Azra, T. Liblik, I. Zekker, Adsorption and kinetics studies of Cr(VI) by graphene oxide and reduced graphene oxide-zinc oxide nanocomposite, *Molecules* 27 (2022) 7152, <https://doi.org/10.3390/molecules27217152>.
- [68] F. Bin, S. Wenzhong, S. Liyi, Q. Shijie, Adsorption of hexavalent chromium by polyacrylonitrile-based porous carbon from aqueous solution, *R. S. Open Sci.* 5 (2018), <https://doi.org/10.1098/rsos.171662>.
- [69] H. Peng, J. Guo, H. Qiu, C. Wang, C. Zhang, Z. Hao, Y. Rao, Y. Gong, Efficient Removal of Cr(VI) with Biochar and Optimized Parameters by Response Surface Methodology, *Processes* 9 (2021) 889, <https://doi.org/10.3390/pr9050889>.
- [70] Y. Wang, Y. Chen, F. Shan, T. Zhang, Z. Zhang, M. Liu, L-glutamic acid-functionalized graphene oxide with characteristic of anti-stacking towards efficient adsorption-reduction removal of Cr(VI), *J. Environ. Chem. Eng.* 12 (2024) 114764, <https://doi.org/10.1016/j.jece.2024.114764>.
- [71] A.B. Arbuzov, I.V. Muromtsev, I.V. Rezanov, M.V. Trenikhin, A.V. Lavrenov, Influence of the structure of carbon black on its electrical conductivity and adsorption properties, *J. Mater. Sci.* 59 (37) (2024) 17517–17530, <https://doi.org/10.1007/s10853-024-10245-y>.
- [72] H. Li, L. Yu, Z. Chen, B. Xiao, K. Jin, The characteristics of adsorption Cr(VI) by iron-modified and iron-doped phosphorus-based biochar biochar, *Green. Chem. Lett. Rev.* 17 (1) (2024), <https://doi.org/10.1080/17518253.2024.2329607>.
- [73] Z. Khdoor, S. Makharza, M. Qurie, F. Fohely, A.A. Taha, S. Hampel, Removal of toxic hexavalent chromium via graphene oxide nanoparticles: study of kinetics, isotherms, and thermodynamics, *RSC Adv.* 14 (2024) 24345–24351, <https://doi.org/10.1039/D4RA03697B>.
- [74] V.A. Yolshina, L.A. Yolshina, V.I. Pryakhina, SEM and XPS Study of Cr⁶⁺ Removal from Wastewater via Reduction and Adsorption by Hierarchically Structured Carbon Composite in Neutral Media, *J. Inorg. Organomet Polym.* 31 (2021) 1–12, <https://doi.org/10.1007/s10904-021-02003-3>.
- [75] P.T. Tho, H.T. Van, L.H. Nguyen, T.K. Hoang, T.N.H. Tran, T.T. Nguyen, T.B. H. Nguyen, V.Q. Nguyen, H.L. Sy, V.N. Thai, Q.B. Tran, S.M. Sadehghzadeh, R. Asadpour, P.Q. Thang, Enhanced simultaneous adsorption of As(III), Cd(II), Pb(II) and Cr(VI) ions from aqueous solution using cassava root husk-derived biochar loaded with ZnO nanoparticle, *RSC Adv.* (31) (2021) 18881–18897, <https://doi.org/10.1039/D1RA01599K>.
- [76] S.S. Gabr, M.F. Mubarak, M. Keshawy, I.E. Sayed, T.A. Moghny, Linear and nonlinear regression analysis of phenol and P-nitrophenol adsorption on a hybrid

- nanocarbon of ACTF: kinetics, isotherm, and thermodynamic modeling, *Appl. Water Sci.* 13 (2023) 230, <https://doi.org/10.1007/s13201-023-02018-w>.
- [77] B.G. Fouda-Mbanga, O. Onotu, Z. Tywabi-Ngeva, Advantages of the reuse of spent adsorbents and potential applications in environmental remediation: a review, *Green. Anal. Chem.* 11 (2024) 100156, <https://doi.org/10.1016/j.greeac.2024.100156>.
- [78] M. Masuku, J.F. Nure, H.I. Atagana, N. Hlongwa, T.T.I. Nkambule, Pinecone biochar for the Adsorption of chromium (VI) from wastewater: Kinetics, thermodynamics, and adsorbent regeneration, *Environ. Res.* 258 (2024) 119423, <https://doi.org/10.1016/j.envres.2024.119423>.
- [79] R. Sinha, R. Kumar, P. Sharma, N. Kant, J. Shang, T.M. Aminabhavi, Removal of hexavalent chromium via biochar-based adsorbents: State-of-the-art, challenges, and future perspectives, *J. Environ. Manag.* 317 (2022) 115356, <https://doi.org/10.1016/j.jenvman.2022.115356>.
- [80] Z. Jiang, O.E. Ozbulut, G. Arce, L.M. Colosi, Accounting for decarbonization impacts across the full life cycle of alternative concrete materials: a case-study for graphene-amended cementitious composites, *J. Clean. Prod.* 482 (2024) 144186, <https://doi.org/10.1016/j.jclepro.2024.144186>.
- [81] X. Zhu, C. Labianca, M. He, Z. Luo, C. Wu, S. You, D.C.W. Tsang, Life-cycle assessment of pyrolysis processes for sustainable production of biochar from agro-residues, *Bioresour. Technol.* 360 (2022) 127601, <https://doi.org/10.1016/j.biortech.2022.127601>.
- [82] P. Engels, F. Cerdas, T. Dettmer, C. Frey, J. Hentschel, C. Herrmann, T. Mirfabrikkar, M. Schueler, Life cycle assessment of natural graphite production for lithium-ion battery anodes based on industrial primary data, *J. Clean. Prod.* 336 (2022) 130474, <https://doi.org/10.1016/j.jclepro.2022.130474>.
- [83] D. Surovtseva, E. Crossin, R. Pell, L. Stamford, Toward a life cycle inventory for graphite production, *J. Ind. Ecol.* 26 (2022) 964–979, <https://doi.org/10.1111/jiec.13234>.



An ecofriendly pectin-co-montmorillonite composite hydrogel for the separation of contaminant metal ions from water

João Gabriel Ribeiro^a, Rizia Maria Raimondi^b, Alana Gabrieli de Souza^a,
Derval dos Santos Rosa^a, Alexandre Tadeu Paulino^{b,c,*}

^a Centro de Engenharia, Modelagem e Ciências Sociais Aplicadas, Universidade Federal do ABC, Av. dos Estados, 5001, Bairro Bangu, 09210-580 Santo André, SP, Brazil

^b Santa Catarina State University, Postgraduate Program in Applied Chemistry, Rua Paulo Malschitzki, 200, Zona Industrial Norte, 89219-710 Joinville, SC, Brazil

^c Santa Catarina State University, Department of Chemistry, Rua Paulo Malschitzki, 200, Zona Industrial Norte, 89219-710 Joinville, SC, Brazil

ARTICLE INFO

Editor: Jingming Duan

Keywords:

Pectin
Hydrogel
Montmorillonite
Sorption
Potentially toxic elements

ABSTRACT

The aim of this study was to investigate the synthesis, characterization, and sorption performance of ecofriendly pectin-co-montmorillonite composite hydrogels for the separation of potentially toxic elements (PTEs) from water. Hydrogels were synthesized using an environmentally friendly method, incorporating montmorillonite (MMT) at proportions ranging from 0 to 10 % in the tridimensional pectin (PC) network. The composite hydrogels were characterized by Fourier-transform infrared spectroscopy (FT-IR), scanning electron microscopy (SEM), and thermogravimetric analysis (TGA). Batch sorption studies were conducted to investigate the capacity to separate copper (Cu^{2+}), nickel (Ni^{2+}), manganese (Mn^{2+}), zinc (Zn^{2+}), cadmium (Cd^{2+}), and hexavalent chromium (Cr^{6+}) ions from water. Higher PTE separation efficiencies were found with hydrogels containing 1 % MMT, with greater selectivity for Cu^{2+} ions. An exhaustive sorption study revealed that the separation process of Cu^{2+} fits the pseudo-second-order kinetic model and Langmuir isotherm, with maximum sorption capacity (q_{max}) of ~ 36.8 mg of hydrogel per g of PTE. This indicates that PC-co-MMT composite hydrogels are efficient alternative sorbents for the selective separation of PTEs from water, with potential application in ecofriendly water purification systems.

1. Introduction

PC is a multifunctional biodegradable polysaccharide with a heterogeneous chemical structure containing large amounts of anionic groups [1]. PC is found in banana peel, apple pomace, pomelo, passion fruit rind, and citrus peel. Its chemical structure contains α -(1,4)-linked D-galacturonic acid residues coupled to 1–4 glycosidic bonds [2]. This polysaccharide can be applied in the human diet [3], the treatment of illnesses [4], drug delivery systems [5], the food industry [6], and tissue engineering. Studies have focused on the use of PC as a biosorbent for the treatment of water contaminated with potentially toxic elements (PTEs) and different organic pollutants [1,2].

There is an increasing concern with the contamination of water-bodies by PTEs due to the harmful effects for the climate, environment, and society [7]. Although the environment has an intrinsic capacity to mitigate pollutants via biodegradation and biotransformation processes,

PTEs are environmentally persistent and difficult to remove [8]. Water contaminated by PTEs is a major problem due to the growing number of people around the world in need of drinking water [9]. Water of inadequate quality can cause diseases that overwhelm healthcare systems and lead to numerous deaths [10–12]. The different types of PTEs include copper (Cu), iron (Fe), arsenic (As), cobalt (Co), mercury (Hg), manganese (Mn), molybdenum (Mo), zinc (Zn), and lead (Pb) [7]. As these species are carcinogenic and teratogenic, environmental pollution-controlling institutions have established maximum concentration limits in the environment to avoid social impacts. Main PTEs found in wastewater, human health effects, and maximum concentration limits permitted by the World Health Organization (WHO) [13–16] can be seen in the supplementary material (Table 1S).

Many green biomaterials and technologies have been studied for the purification of water and wastewater due to capacity of remediating PTEs in different media [17]. Currently, the most common technologies

* Corresponding author at: Santa Catarina State University, Postgraduate Program in Applied Chemistry, Rua Paulo Malschitzki, 200, Zona Industrial Norte, 89219-710 Joinville, SC, Brazil.

E-mail address: alexandre.paulino@udesc.br (A.T. Paulino).

<https://doi.org/10.1016/j.jwpe.2024.106629>

Received 25 July 2024; Received in revised form 16 November 2024; Accepted 19 November 2024

Available online 26 November 2024

2214-7144/© 2024 Elsevier Ltd. All rights reserved, including those for text and data mining, AI training, and similar technologies.

include membrane-filtration, ion exchange, oxidation-reduction, sedimentation, algal-sorption, and biotransformation processes [18,19]. However, most technologies are expensive or complex, which limits their application in developing countries [20]. Hydrogels are potential sorbents for the removal and separation of different pollutants from water due to their porous structure and three-dimensional network [8,21]. In general, a hydrogel must have a large surface area, good mechanical stability, and active surface sites for efficient sorption processes [17].

PC hydrogels are excellent candidates for water purification processes due to their affinity for PTEs and capacity to bind physically to divalent cations, forming an egg-box structure [22]. Several works have demonstrated the effect of PC hydrogels for water treatment. For instance, Arachchige et al. prepared PC materials for the sorption of Pb^{2+} and reported sorption capacity of 263 mg g^{-1} due to the functional groups of the biopolymer (COO- and O-H), cation exchange, and electrostatic interactions [23]. Shao et al. prepared chitosan/PC gel beads for the removal of Cd^{2+} , Cu^{2+} , Pb^{2+} , and Hg^{2+} , with sorption capacities of 177, 169, 266, and 208 mg g^{-1} , respectively. In this case, the sorption process was attributed to interactions between PTEs and carboxyl groups, in addition to the large specific surface area of the composite beads [24].

Although PC has available carboxyl groups to interact with metal ions, Martínez-Sabando et al. reported that this biopolymer has a heterogeneous chemical composition and physicochemical properties that vary in terms of galacturonic acid content, degree of esterification, and molecular weight [2]. In addition to the outstanding performance of PC in different applications, the development of composites can provide a more stable structure that increases the pollutant sorption and desorption, expanding the multifunctionality of the material [25,26]. For instance, Zhang et al. (2023) prepared PC/lignin composites, confirming high tensile strength, water barrier properties, and hydrophobic stability [27]. The literature shows a trend of combining PC with other biopolymers or active nanoparticles to enhance the sorption capacity and optimize water decontamination processes [20]. Khampala et al. (2023) studied a composite biofilm of microalgal and PC for Pb^{2+} removal, with maximum sorption capacity of 122 mg g^{-1} [28]. Hassan et al. (2024) prepared PC composites containing Cu/Fe nanoparticles for methylene blue degradation, increasing the removal efficiency from 24 for pure PC to 97 % for the composite [29]. Lessa et al. (2020) reported that cellulose functional groups favor the sorption of PTEs, enabling the reusability of the final material due to the greater stability [30].

Clay minerals have been studied as reinforcing agents for increasing the mechanical strength, thermal stability, barrier property, and amount of available active sites of composite materials [31]. Beigi et al. prepared a PC hydrogel containing Fe_3O_4 and bentonite as a nanoadsorbent of crystal violet [32]. Gamboni et al. prepared PC-co-brea gum-co-MMT hydrogels for the sorption of methylene blue. Rehmat et al. developed PC-functionalized clay hydrogels for drug delivery and controlled release [33,34]. Fernandes Filho et al. developed PC hydrogels modified with MMT for the removal of dyes and herbicides from water [35].

In this work, PC composite hydrogels containing MMT were prepared as advanced, useful, functional sorbents for the treatment of water contaminated with PTEs. As PC and MMT are environmentally friendly, the composite hydrogel was also considered eco-friendly compared to materials commonly employed in water purification systems. Although PC hydrogels are described in the literature, studies investigating the combination of PC and different clay minerals are important to determining the synergic effects of both materials in the removal and separation of PTEs from water. The affinity of the hydrogel synthesized in this work for six coexisting PTEs [Cu^{2+} , Ni^{2+} , Mn^{2+} , Zn^{2+} , Cd^{2+} , and Cr^{6+} ions] was investigated. Some results have exhibited the remarkable versatility and sustainability of the composite biomaterials for applications in water treatment systems. This not only enables enhancing the general efficiency of water purification processes for contaminated sites, but also contributes to minimizing the environmental impacts associated

with the disposal of conventional sorbents.

2. Material and methods

2.1. Materials

PC hydrogels were prepared using potassium persulfate and citric PC from Dynamics Contemporary Chemistry Ltda. (São Paulo, Brazil). Acrylamide, glycidyl methacrylate (GMA), and montmorillonite (MMT) were purchased from Sigma-Aldrich Corporation (São Paulo, Brazil). All materials were used as received. The materials used for the sorption study were nickel nitrate (99 % purity) and zinc nitrate (98 % purity) purchased from Dynamics Contemporary Chemistry Ltda. (São Paulo, Brazil), cadmium nitrate (98 % purity) from Neon Chemistry Ltda. (São Paulo, Brazil), potassium dichromate (99 % purity) from ECIBRA Analytical Reagents Ltda. (São Paulo, Brazil), copper nitrate (99 % purity) and citric acid (99.5 % purity) from Synth Reagents Ltda. (São Paulo, Brazil), and manganese nitrate (98 % purity) from Sigma Aldrich Corporation (São Paulo, Brazil).

2.2. Hydrogel preparation

The PC hydrogel was synthesized in two steps. PC was first modified with GMA with the aim of adding reactive vinyl groups to the polysaccharide structure [36]. For such, 12 g of PC were dissolved in a glass flask containing 500 mL of Milli-Q® water at $60 \text{ }^\circ\text{C}$, with the pH of the final solution adjusted to 3.5. Next, 9.456 mmol (1.25 mL) of GMA were added. The system was left under constant stirring at $50 \text{ }^\circ\text{C}$ for 24 h. The modified polysaccharide was dried in a forced-air circulation oven at $60 \text{ }^\circ\text{C}$ for 24 h. In the second step, 7 g of modified PC were dissolved in 50 mL of Milli-Q® water at $50 \text{ }^\circ\text{C}$. Next, 0.0211 mol (1.495 g) of acrylamide and 0.5215 mmol (0.141 g) of potassium persulfate were added. The resulting solution was homogenized, transferred to plastic syringes, and left in a forced-air circulation oven at $65 \text{ }^\circ\text{C}$ for 6 h with the aim of completing the chemical crosslinking. The formed cross-linked hydrogel was placed in a distilled water bath for 24 h and dried in oven at $60 \text{ }^\circ\text{C}$ for 24 h before characterization and application. The PC composite hydrogel containing MMT was synthesized by adding 1, 5, and 10 wt-% of clay mineral during the solubilization of acrylamide and potassium persulfate. A schematic drawing of this synthesis is presented in Fig. 1. The PC hydrogel was denominated HPC and the composite hydrogel was denominated HCx%, with x varying according to the MMT content.

2.3. Sorption of PTEs

The PTE sorption capacity of the PC-co-MMT composite hydrogels was investigated in multielement assays with different concentrations of Cu^{2+} , Ni^{2+} , Mn^{2+} , Zn^{2+} , Cd^{2+} , and Cr^{6+} ions. Simulated water samples were prepared in the laboratory using distilled water at pH 6.8. Total PTE concentrations ranged from 0.3 mmol L^{-1} (0.05 mmol L^{-1} of each contaminant) to 3.0 mmol L^{-1} (0.50 mmol L^{-1} of each contaminant). PTE concentrations in the water samples after sorption, kinetic, and isotherm studies were determined using a Vario ion chromatograph equipped with an UV/Vis detector (Metrohm, Switzerland). PTE concentrations were calculated by using standard calibration curves, with linearity ranging from 0.10 to 10 ppm and a coefficient of determination (R^2) of ~ 0.99 . Accuracies of the calibration curves were checked weekly with standard solutions. All PTE measurements were performed in triplicate to ensure statistical reliability and minimize variability, enabling reliable discussions of the sorption, kinetic, and isotherm results.

Briefly, 50 mg of hydrogel were added to an Erlenmeyer flask containing 50 mL of simulated water sample contaminated with Cu^{2+} , Ni^{2+} , Mn^{2+} , Zn^{2+} , Cd^{2+} , and Cr^{6+} ions. The solution pH was adjusted to 4.0 using nitric acid (0.10 mol L^{-1}), when necessary. The flask was placed



Fig. 1. Illustration of hydrogel synthesis and preparation.

on a Solab SL-180 shaker (Solab, Brazil) operating at 120 rpm for 24 h before measuring the PTE concentrations by ion chromatography. Sorption assays for studying isotherm models were only performed with the Cu^{2+} ion (species with the best affinity for the hydrogel in the multielemental selectivity assay) using 50 mg of hydrogel and 50 mL simulated water samples with six different metal concentrations (0.10, 0.25, 0.50, 1.00, 2.00, and 3.00 mmol L^{-1}). Isotherm parameters were not determined for Ni^{2+} , Mn^{2+} , Zn^{2+} , Cd^{2+} , and Cr^{6+} ions due to the lower sorption capacities compared to that of Cu^{2+} ions in the multielement selectivity assay. Sorption assays for studying kinetic models were only performed with Cu^{2+} ion considering the same justification previously described for the isotherm assays. In this case, 800 mg of hydrogel were placed in a beaker containing 800 mL of 0.5- mmol L^{-1} metal ion solution under magnetic stirring at 120 rpm. Aliquots of this solution (4 mL) were collected at different contact times (5, 10, 15, 20, 25, 30, 45, 60, 120, 240, 360, 1440, and 2880 min) for the determination of the sorption capacity of Cu^{2+} ions as a function of time. Sorption capacity was determined using Eq. (1):

$$q_e = \frac{C_0 - C_e}{m} \cdot V \quad (1)$$

in which, m (g) is the mass of the dried hydrogel, C_0 and C_e (mg L^{-1}) are the initial and equilibrium concentrations of PTEs in the solution, and V (L) is the volume of the solution.

2.4. SEM images

SEM images were recorded to analyze the microstructural properties of the PC-co-MMT composite hydrogels. Such images were recorded using fractured surfaces of dried samples to provide a detailed view of the internal morphology and porous structure. The equipment employed for this study was a JSM-6010LA, JEOL scanning electron microscope (Massachusetts, USA) operating at an acceleration voltage of 10 kV and spot size of 4 nm. All hydrogels were previously covered with a thin gold film (25 nm) using an EM ACE 200 sputtering device (Leica Microsystems, Germany) before recording the images.

2.5. FT-IR spectra

FT-IR spectra were recorded using a PerkinElmer® Inc. spectrometer (Massachusetts, USA) equipped with attenuated total reflectance (ATR), operating in transmittance mode from 650 to 4000 cm^{-1} , with a spectral resolution of 4 cm^{-1} .

2.6. Thermogravimetric analysis (TGA)

Thermograms for TGA were recorded using a STA 6000 PerkinElmer TGA equipment (PerkinElmer, USA) operating from 30 to 600 $^{\circ}\text{C}$ at a heating rate of 10 $^{\circ}\text{C min}^{-1}$ and under a nitrogen atmosphere at a flow rate of 20 mL min^{-1} .

2.7. Recovery studies

The hydrogels used for the Cu^{2+} ion sorption, isotherm, and kinetic studies were dried in an oven at 40°C . Next, 50 mg of the dried hydrogels containing the metal were mixed with a $0.10\text{ mol L}^{-1}\text{ HNO}_3$ solution in glass flasks. These systems were left under stirring at 120 rpm for 6 h. The Cu^{2+} ion concentration remaining in solution was measured by ion chromatography for the determination of the recovery efficiency (%) using Eq. (2):

$$\text{Recovery Efficiency (\%)} = \frac{n_{\text{Cu}^{2+}\text{desorbed}}}{n_{\text{Cu}^{2+}\text{adsorbed}}} \times 100 \quad (2)$$

in which, $n_{\text{Cu}^{2+}\text{desorbed}}$ is the amount of Cu^{2+} ion desorbed from the hydrogel and $n_{\text{Cu}^{2+}\text{adsorbed}}$ is the amount of Cu^{2+} sorbed in the hydrogel.

3. Results and discussion

3.1. Sorption of PTEs

Fig. 2 displays the separation percentages (%) of Cu^{2+} , Ni^{2+} , Mn^{2+} , Zn^{2+} , Cd^{2+} , and Cr^{6+} ions from water in a multielement study using different PC-based hydrogels. Separation percentages ranged from 40 to 100 % for Cu^{2+} , Ni^{2+} , Mn^{2+} , Zn^{2+} , and Cd^{2+} ions (exception: Cr^{6+}), indicating that PC-co-MMT composite hydrogels are potential sorbents for water purification processes. The lowest separation efficiency was found using the PC-based hydrogel without MMT due to lower amount of active sorption sites in the three-dimensional polymer network, which increases the saturation rate. The sorption of PTEs in/on natural polysaccharide-based networks normally takes place through coordination bonds in electron-rich centers ($-\text{COO}^-$, $-\text{OH}$, and $-\text{CONH}$ groups) [37,38]. This may explain the lower separation efficiency of Cr^{6+} ions, as this species is normally found in aqueous media in the anionic form (CrO_4^{2-} , $\text{Cr}_2\text{O}_7^{2-}$, HCrO_4^-), generating electrostatic repulsion forces between the PTE and polymer network [39].

The presence of MMT in the polymer network increased the separation percentages due to the increase in specific surface area, with complete removal of Cu^{2+} and Zn^{2+} ions from water under the experimental conditions of the study. The sorption affinity of the PTEs studied for the PC-based hydrogels was observed in the following order: $\text{Cu}^{2+} > \text{Zn}^{2+} > \text{Ni}^{2+} > \text{Cd}^{2+} > \text{Mn}^{2+} > \text{Cr}^{6+}$. It is important to highlight that Cr^{6+} ion was considered a cationic species but can be found in the anionic form in aqueous media, as mentioned above. Similar results were described for PC/graphene oxide composites, with the following

affinity order: $\text{Cr}^{3+} > \text{Cu}^{2+} > \text{Mn}^{2+} > \text{Hg}^{2+} > \text{Co}^{2+} > \text{Mg}^{2+} > \text{Fe}^{3+} > \text{Ni}^{2+} > \text{Zn}^{2+} > \text{Cd}^{2+}$ [40]. Doping PC with graphene increases the sorption capacity at different pH values, altering the PTE affinity order [41,42]. This takes place due to the possibility of complex formation between electron donor groups in the sorbent structure and PTEs [43], making the sorption process and affinity order pH-dependent [44]. Moreover, it is important to control the solution pH during sorption studies, as Pb^{2+} and Zn^{2+} ions can form $\text{Pb}(\text{OH})_2$ and $\text{ZnO}/\text{Zn}(\text{OH})_2$ at pH ranging from 3 to 6, affecting the sorption capacity [45]. The sorption efficiency of PTEs in/on different materials can also depend on the ionic radius and reactivity of the atomic orbitals involved in the reaction [46]. This may also explain the lower separation efficiency of the Cr^{6+} ion, which has a stable electronic configuration half-filled at the t_{2g} level (d_{xy} , d_{yz} , and d_{zx} sub d-orbitals), resulting in lower reactivity.

Some 0.30 mol L^{-1} selectivity assays were nonconclusive, since Cu^{2+} and Zn^{2+} ions were both completely removed from the water using $\text{HCl}1\%$. Therefore, a selectivity assay was performed with a PTE concentration of 3.00 mmol L^{-1} , as displayed in Fig. 3. Higher separation percentages were also found for Cu^{2+} ions, with a maximum of $\sim 57.7\%$ using $\text{HCl}1\%$ and a minimum of $\sim 45.7\%$ using $\text{HCl}5\%$. The high Cu^{2+} affinity decreased the sorption capacity of Zn^{2+} , Ni^{2+} , Mn^{2+} , Cd^{2+} , and Cr^{6+} ions due to partial or total occupation of the active sorption sites available in/on the hydrogel network [47]. The higher Cu^{2+} affinity may be attributed to stronger interactions with oxygen atoms and the carbon-rich structures of PC, enabling easier coordination reactions. In this case, the reaction mechanism may take place by i) cation-exchange, in which H^+ ions are replaced with Cu^{2+} ions, ii) complexation with oxygen-containing chemical groups in the hydrogel network, iii) electrostatic interactions, and iv) the chelation of Cu^{2+} with carbon atoms [48]. Moreover, PC-co-MMT composite hydrogels are expected to have suitable pore sizes, reticulation degree, and swelling degree of the polymer network to sorb PTEs. The swelling degree for $\text{HCl}1\%$ is normally lower than that for $\text{HCl}5\%$ and $\text{HCl}10\%$, as previously described by our research group [49]. However, this parameter did not significantly affect the sorption and separation capacities of Cu^{2+} from water due to stronger interactions between the PTE and chemical groups of the three-dimensional polymer network.

3.1.1. Sorption isotherms

Sorption isotherms were studied to determine the interactions between $\text{HCl}1\%$ and Cu^{2+} ions due to higher affinity for this PTE in the selectivity assays. The data were validated using coefficient of determination (R^2) values with the experimental parameters displayed in Table 1.

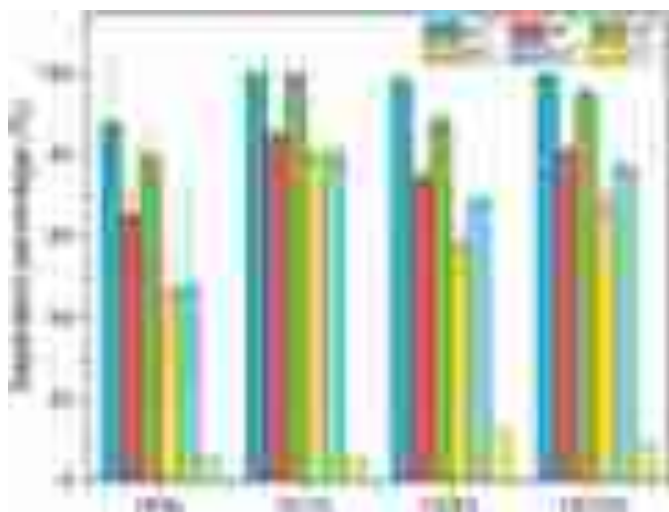


Fig. 2. Separation percentages (%) of Cu^{2+} , Ni^{2+} , Mn^{2+} , Zn^{2+} , Cd^{2+} , and Cr^{6+} ions from water in multielement study using different hydrogels.

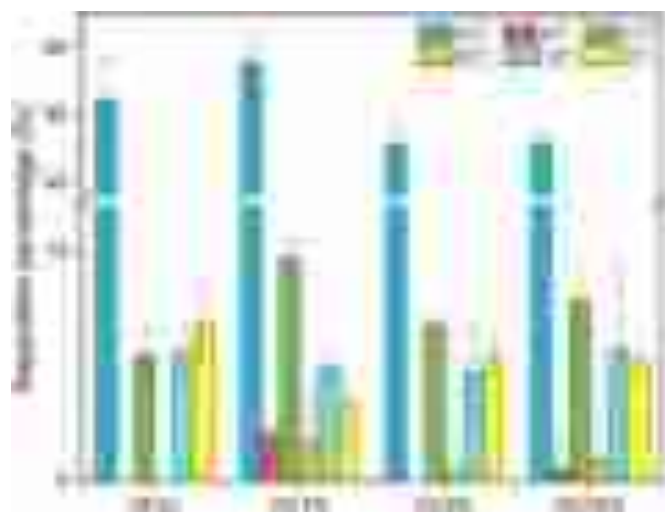


Fig. 3. Separation percentages (%) of Cu^{2+} , Ni^{2+} , Mn^{2+} , Zn^{2+} , Cd^{2+} , and Cr^{6+} ions from water in multielement study using different hydrogels.

Table 1
Langmuir, Freundlich, and Temkin isotherm parameters for sorption of Cu²⁺ in HC1% hydrogel.

Isotherm model	Parameters
Langmuir	K _l : 11.45 q _m : 0.5798 R _l : 0.025 R ² : 0.9880
Freundlich	K _f : 0.5067 n _f : 2.624 R ² : 0.5594
Temkin	K _t : 238.4 b _t : 26066.0 R ² : 0.8263

Fig. 4 displays the Langmuir, Freundlich, and Temkin isotherm plots for the sorption of Cu²⁺ ions in the HC1% hydrogel. The coefficient of determination (R²) was higher for the Langmuir isotherm (R² = 0.9880) compared to the Freundlich (R² = 0.5594) and Temkin (R² = 0.8263) isotherms. This indicates that Cu²⁺ sorption in HC1% takes place by the formation of a monolayer on a homogeneous surface. Thus, PTEs can be homogeneously sorbed to the active sites with uniform distribution on the surface of the hydrogel [50]. Moreover, there are no mutual interactions or steric hindrances among PTE ions sorbed to adjacent active sites [51,52]. The R_l parameter also indicated that the sorption process is favorable, since 0 < R_l < 1 [53]. The Langmuir q_m (maximum sorption capacity) value was 37.4 mg g⁻¹, which is similar to values reported elsewhere for different materials [54,55]. Table 2 displays the sorption results of PTEs in different polysaccharide-based hydrogels for the purposes of comparison with the results of the present study.

3.1.2. Sorption kinetics

The pseudo-first-order kinetic model is commonly employed for explaining physical sorption processes taking place between a sorbent and sorbate, whereas the pseudo-second-order kinetic model is commonly employed for explaining physicochemical sorption processes. In both cases, it is possible to detect ion exchange as well as electron transfer and sharing between pollutants and active sorption sites of the hydrogel during water treatment process [64]. The pseudo-second-order kinetic model plot for the sorption of Cu²⁺ in HC1% is displayed in Fig. 5. The coefficient of determination for this result was 0.9967, demonstrating a better kinetic fit compared to the pseudo-first-order kinetic model. The kinetic parameters are displayed in Table 3.

From these results, we conclude that active sorption sites of PC and MMT are chemically adsorbing Cu²⁺ ions during the sorption process. In

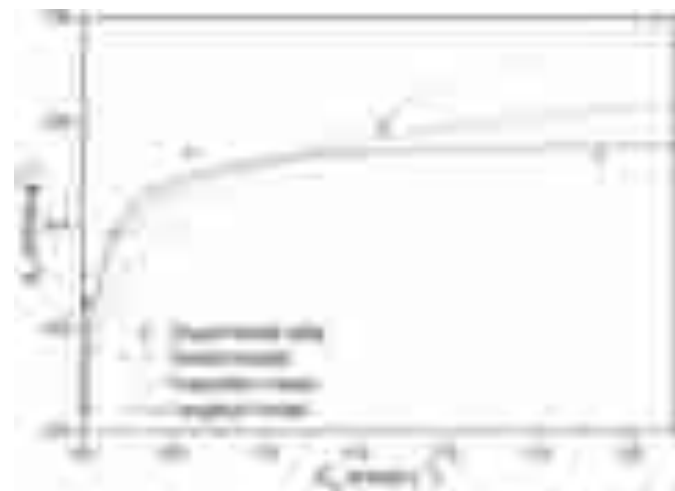


Fig. 4. Langmuir, Freundlich, and Temkin isotherm plots for sorption of Cu²⁺ ion to HC1%.

Table 2
Sorption results found in the literature for sorption of PTEs using polysaccharide-based hydrogels.

Polysaccharide	PTEs	Sorption values	Reference
Agar	Fe ³⁺ , Cr ³⁺ , Ni ²⁺ and Mn ²⁺	97, 24, 43, and 55 %	[46]
Tragacanth gum	Co ²⁺ , Zn ²⁺ , Cr ³⁺ , and Cd ²⁺	100, 77, 71, and 67 mg g ⁻¹	[56]
Carboxymethyl cellulose	Cr ⁶⁺	6 mmol g ⁻¹	[57]
Thiophene-chitosan	Hg ²⁺	20.5 mg g ⁻¹	[58]
Diethylaminoethyl dextran	Mn ²⁺ , Pb ²⁺ , and Cd ²⁺	133, 35, and 2 mg g ⁻¹	[59]
Chitosan/calcium alginate/bentonite	Cu ²⁺ and Cd ²⁺	115 and 102 mg g ⁻¹	[60]
Carboxymethyl cellulose/chitosan/alginate acid	Cr ⁶⁺ , Cu ²⁺ , and Ni ²⁺	247, 271, and 240 mg g ⁻¹	[61]
Cellulose	Cu ²⁺	52.3 mg g ⁻¹	[62]
Pectin	Cu ²⁺	81 mg g ⁻¹	[22]
Starch	Cu ²⁺	33 mg g ⁻¹	[63]

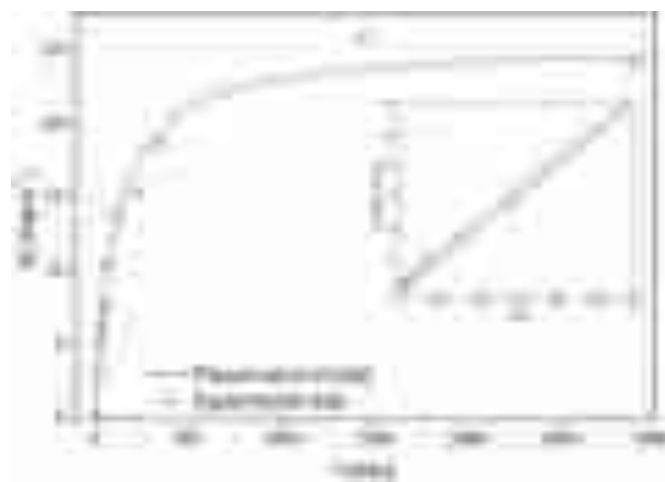


Fig. 5. Pseudo-second-order kinetic model plot for sorption of Cu²⁺ ion to HC1%.

Table 3
Kinetic parameters for sorption of Cu²⁺ ions in HC1% hydrogel.

Kinetic model	Parameters
Pseudo 1st order	k ₁ : -4.76 × 10 ⁻⁷ q _e : 16.59 R ² : 0.5477
Pseudo 2nd order	k ₂ : 3.69 × 10 ⁻⁴ q _e : 25.52 R ² : 0.9967

k₁ = pseudo 1st order rate constant (min⁻¹); k₂ = pseudo 2nd order rate constant (g mg⁻¹ min⁻¹); q_e = sorption capacity at equilibrium (mg g⁻¹); R² = coefficient of determination.

this case, the kinetic fitting curve reveals three situations: i) rapid movement of Cu²⁺ ions from bulk solution to the hydrogel structure in the initial minutes of contact, ii) a decrease in the sorption rate over time due to the gradual occupation of active sites, and iii) saturation of active sites [54]. The q_e values were higher than those previously reported by our research group [35], confirming that this type of hydrogel is more efficient for the separation of PTEs than organic species from water, probably due to different affinities. Similar results were found for PC/carboxymethyl cellulose/PEG hydrogels prepared for anionic and cationic dye separation from aqueous solutions [65].

3.2. SEM images

The porosity of biomaterials and composites is crucial for environmental applications. The presence of interconnected pores in polymer-based materials increases the available surface area, favoring interactions with different chemical compounds [66]. As can be seen in the SEM images displayed in Fig. 6, PC-co-MMT composite hydrogels have porous structures with interconnected pores ranging from 20 to 40 μm . This type of morphology indicates the presence of thin sheetlike structures that resemble the middle lamellas of plant cell walls [67], such as those found in PC. A detailed analysis of Fig. 6a–b indicates structures with larger pore sizes. Fig. 6c–d shows pore clusters with smaller sizes in addition to smoother and less porous structures. This morphology is expected due to the tendency of MMT to form agglomerates during the synthesis of the composite hydrogel [68,69]. These differences in morphology may be the result of the variation in crosslinking density, as MMT serves as crosslinking points in the hydrogel network. This increases the network density due to the space occupied by MMT when filling the cavities of the hydrogel [70]. This variation in morphology alters the porous structure, affecting the sorption and separation of PTEs from water. As MMT tends to form strong intermolecular interactions with PC, a high MMT content can compete with PTEs for interactions with the hydrogel matrix during the sorption and separation of compounds from aqueous solutions [35].

3.3. FT-IR spectra

The FT-IR spectra of HPEc, HC1%, HC5%, and HC10% before and after sorption of PTEs are displayed in Fig. 7. Briefly, all hydrogels exhibited absorption bands at 3283 and 3448 cm^{-1} due to O–H and N–H group stretching. The absorption band found at 2961 cm^{-1} was assigned to the C–H asymmetrical stretching, whereas the band at 1410

cm^{-1} was assigned to the COO^{-1} symmetrical stretching of PC. C–O bonds of ester groups were recorded at 1257 and 1020 cm^{-1} . Moreover, the absorption bands at 1624 and 1739 cm^{-1} were associated with the axial deformation of vinylic groups of the glycidyl methacrylate and ester groups, respectively. The absorption band at 1655 cm^{-1} was assigned to either C=O or -NH vibrations contained in amide I and amide II groups, indicating the efficiency of the crosslinking process [71,50]. Other vibrations found at 1320 and 1010 cm^{-1} were assigned to C–O and O bending. The absorption band at 550 cm^{-1} was associated with C–H bending [72]. An absorption band at 1070 cm^{-1} recorded for the composite hydrogels named HC1%, HC5%, and HC10% was attributed to the Si–O group. The absorption bands at 850, 790, 527, and 473 cm^{-1} were assigned to the OH–MgAlOH, OH–Fe₂Fe₃OH, Si–O–Al, and Al–O groups, respectively. These signals appeared in the FTIR spectra due to chemical structure of MMT, in which contains silicon bound to tetrahedral sites and aluminum bound to octahedral sites [73]. Some changes in the peak heights and positions occurred after synthesizing the PC-co-MMT composite hydrogels due to the reactivity of the polysaccharide and clay mineral [50,32].

Overall, the sorption of PTEs in hydrogel networks changes the peak heights and positions of FT-IR spectra due to coordination reactions among carboxyl, amine, amide groups, and metals, forming coordination complexes [84]. The HPEc and HC1% spectra were similar before and after the sorption of Cu^{2+} , with small changes in band intensities. However, some changes were noticed when comparing HC5% and HC10%: MMT peaks at 3628 cm^{-1} assigned to Al–OH groups and the peaks at 1991 cm^{-1} disappeared [74], indicating coordination between hydroxyl groups and PTEs [75]. Moreover, changes in NH_2 vibrations occurred due to the transference of electrons from nitrogen to PTEs during the coordination reactions [24]. Several changes were also observed in the region from 1800 to 700 cm^{-1} , as displayed in Fig. 8. This may be attributed to covalent bonds forming between PTEs and

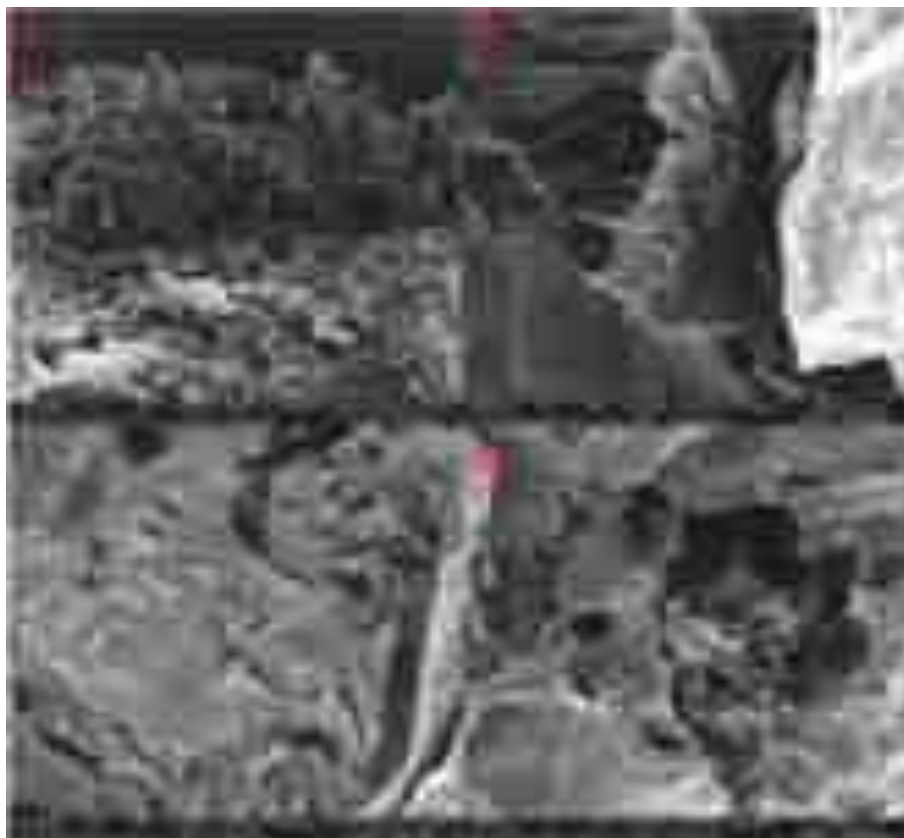


Fig. 6. SEM images of following hydrogels: a) HPEc, b) HC1%, c) HC5%, d) HC10%.

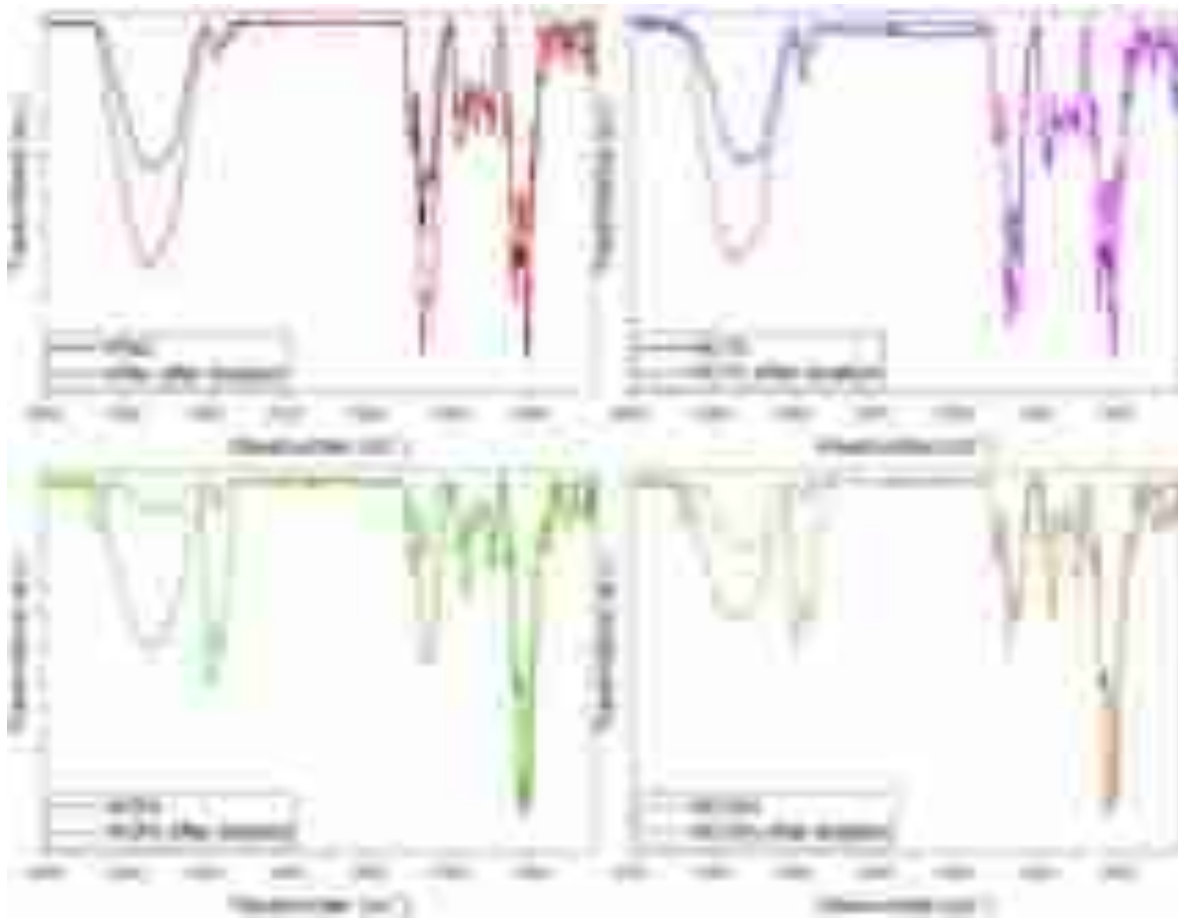
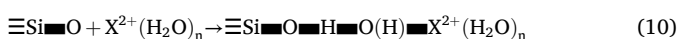
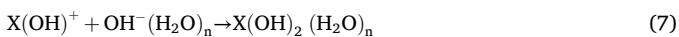
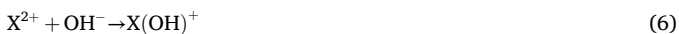


Fig. 7. FTIR spectra of HPEc, HC1%, HC5%, and HC10% before and after sorption of Cu²⁺ ion.

oxygen-containing functional groups, especially MMT. The bands from 1700 to 1550 cm⁻¹ associated with the -COO⁻ vibration modes in PC were shifted to higher wavenumber values, with changes in shape after the sorption of Cu²⁺ due to interaction with oxygen atoms. Larger absorption bands without clear definition were noticed from 1464 to 1210 cm⁻¹ after the sorption of Cu²⁺, indicating that -COOH groups are potential active sites in ion exchange processes, whereas free hydroxyl groups play a secondary role [76]. Changes in the intensities and positions of Si-O group bands and the appearance of new signals in their spectral regions could be associated with stretching vibrations of bonds formed between MMT and metals [77]. Such bonds may take place due to either electrostatic interactions, complexation, hydroxylation, or self-polarization [78]. Sorption processes between MMT and other species normally follow Eqs. (3) to (11), with X being the contaminant species.



The FT-IR spectra recorded in this work confirm the visual analysis of the hydrogel samples after the PTE sorption assays. In this case, the color of the hydrogel changed drastically from pale yellow to dark green in presence of Cu²⁺ and the light blue Cu²⁺ solution turned colorless. This color change is associated with the sorption process and formation of metallic complexes, altering the electronic structure of the metal [79]. For instance, the formation of copper carboxylates in the hydrogel network changes the color of the polymer structure from yellow to dark green [80–82]. A schematic drawing of the Cu²⁺ sorption process in the PC-co-MMT composite hydrogel structures – representing the present work – is displayed in Fig. 9.

3.4. Thermogravimetric analysis and derivative thermogravimetry

TGA and DTG curves for the PC hydrogels before and after sorption of Cu²⁺ ions are displayed in Figs. 10 and 11, respectively. Four weight loss events were identified at temperatures ranging from 25 to 600 °C. The first weight loss stage occurred up to 150 °C due to dehydration of the polymer network. The second stage occurred between 150 and 300 °C due to polysaccharide depolymerization and decomposition. Other events taking place in this situation were the decarboxylation and dehydration of saccharide rings [83]. The third thermal event was related to polysaccharide backbone degradation, whereas the fourth thermal event was associated with the generation of carbonaceous residues. The comparison of T_{5%} values for HPEc, HC1%, HC5%, and HC10% revealed that the presence of MMT in the polymeric hydrogel networks increased the initial temperature of thermal decomposition [22]. However, the peaks highlighted in the DTG curves indicated that

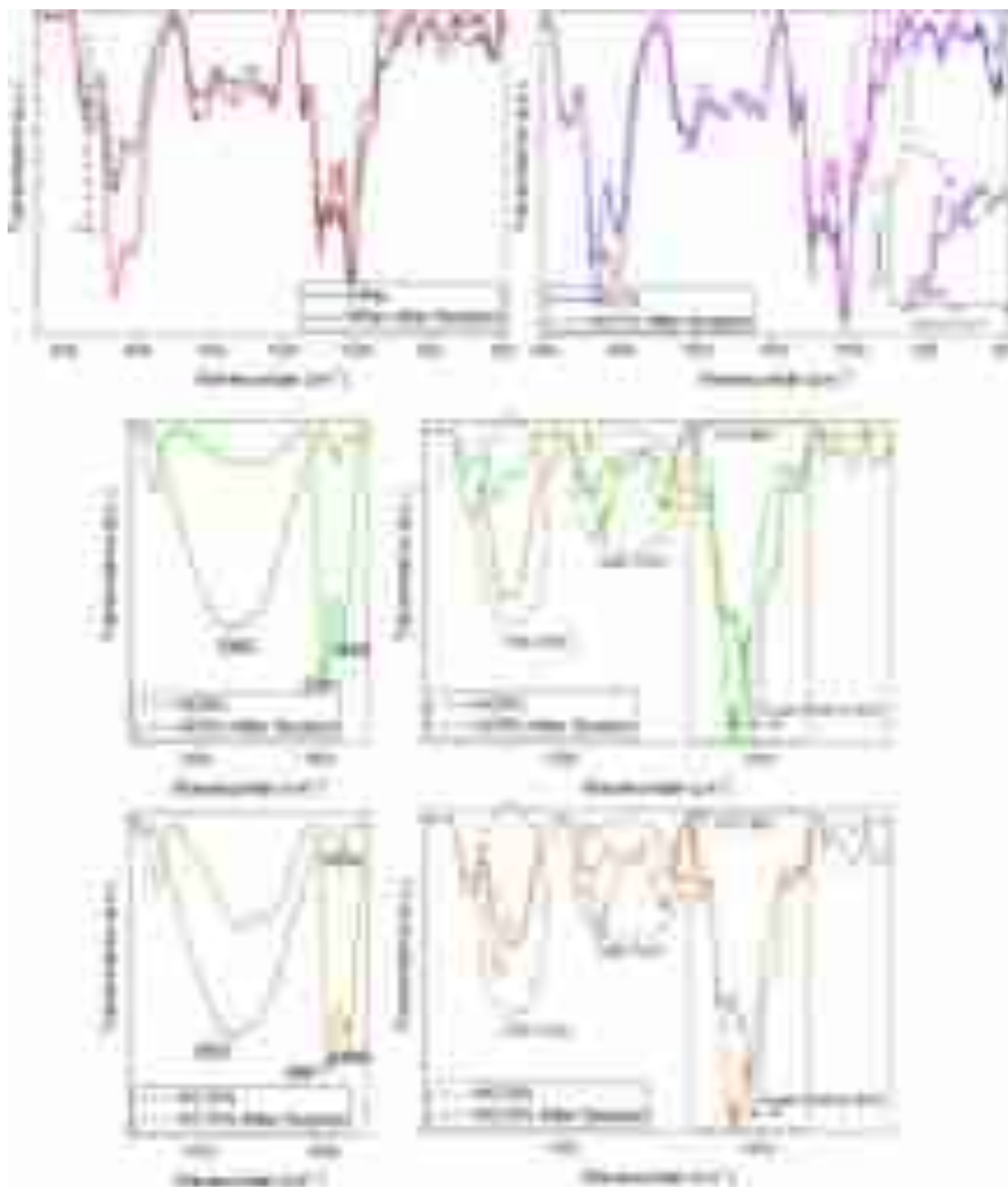


Fig. 8. FTIR spectra in different spectral regions before and after sorption of Cu^{2+} ion.

much higher amounts of MMT can decrease thermal stability due to the destabilization of effective hydrogel networks among the PC chains present in the branched polymeric hydrogel networks [84]. The thermal resistance of hydrogels tends to decrease with conversions of $-\text{COOH}$ groups into $-\text{COO}^-$ ions in aqueous solutions. However, this was surpassed by either ionic or coordination bonds between $-\text{COO}^-$ ions and Cu^{2+} ions [85]. Higher signal values for HC10% in the DTG curves after the sorption of Cu^{2+} indicate an increase in the interaction intensity with the increase in the MMT content in the hydrogel network. This is the result of stronger interactions between functional chemical groups of the hydrogel structure and the PTE [86].

3.5. Hydrogel and PTE regeneration

Desorption studies performed using PC-co-MMT hydrogel containing Cu^{2+} ions sorbed in the polymer network indicated a recovery efficiency of $\sim 93\%$ with the $0.10 \text{ mol L}^{-1} \text{ HNO}_3$ solution. This high recovery rate indicates potential reusability of the hydrogel in successive sorption-desorption cycles. This result is crucial for proposing sustainable water purification processes. Desorption processes employing an HNO_3 solution as solvent facilitate the protonation of carboxylate and hydroxyl groups in the hydrogel structure, releasing PTE ions from functional groups of the polymer network [87]. This recovery is also facilitated with the deswelling of the hydrogel in acid solutions due to the weakening

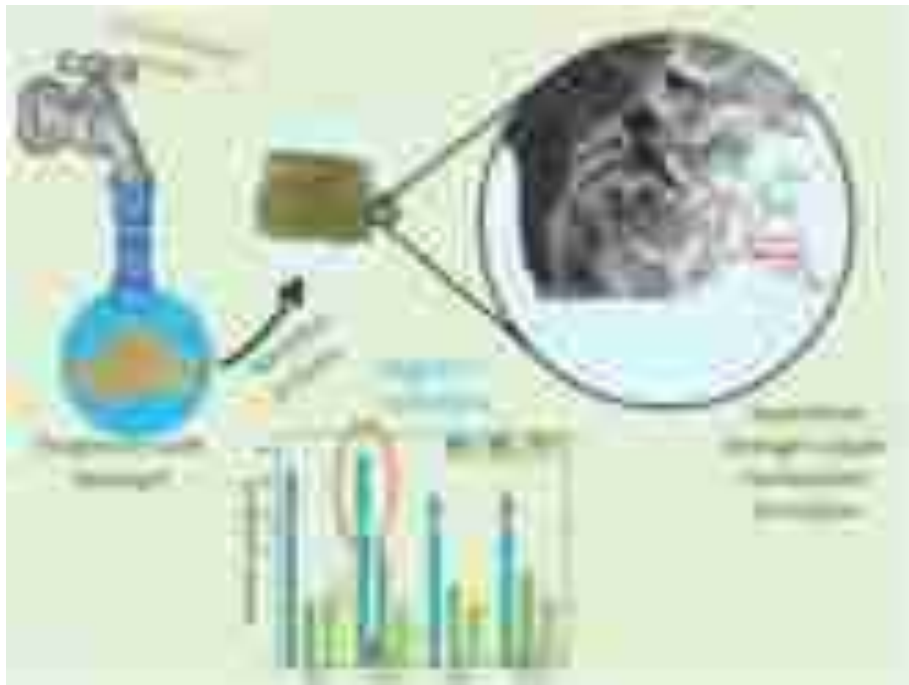


Fig. 9. Scheme illustrating sorption process of Cu^{2+} ion to pectin-co-MMT composite hydrogel structure.

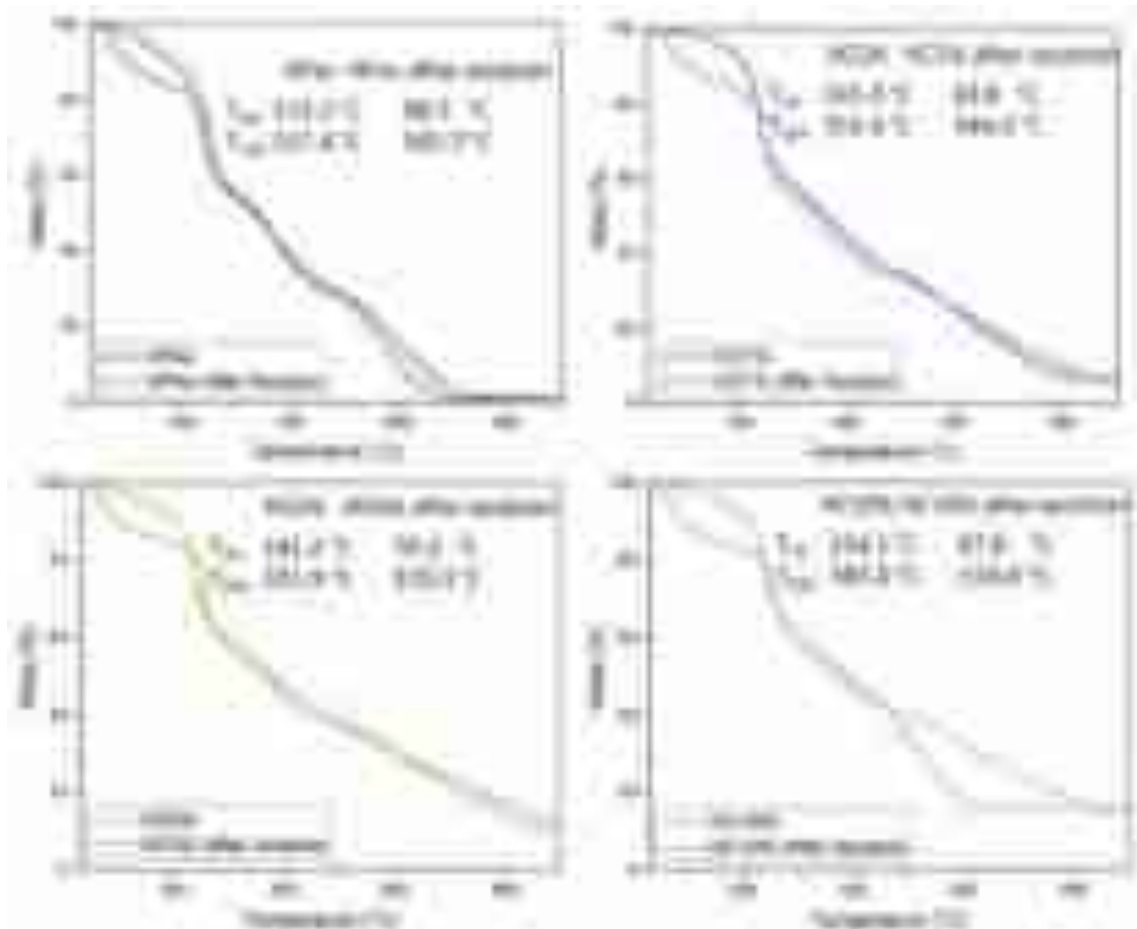


Fig. 10. TGA curves for pectin hydrogels before and after sorption of Cu^{2+} ion.

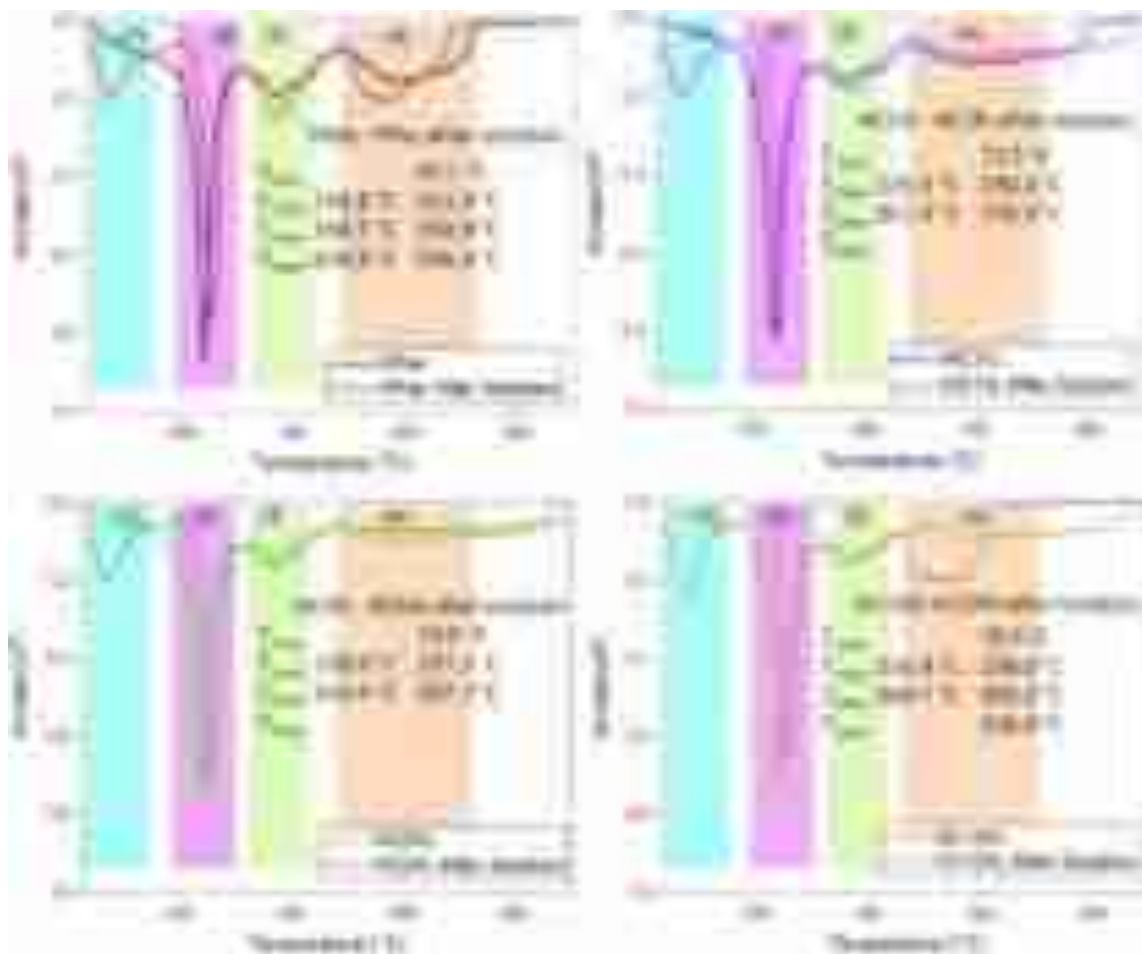


Fig. 11. DTG curves for pectin hydrogels before and after sorption of Cu^{2+} ion.

of the electrostatic repulsion forces among protonated carboxyl groups in the polymer network [88]. Several factors affect the desorption processes of PTEs from hydrogels, including sorbent-sorbate interaction intensity, type of solvent, and properties of the polymer matrix [89]. This work indicates that strong interactions between Cu^{2+} ions and carboxylate groups contribute to higher sorption capacities. In contrast, HNO_3 successfully disrupts these types of bonds, enabling the recovery of the hydrogel and PTEs. The results presented here are similar to those described elsewhere for the recovery of Cd^{2+} and Pb^{2+} ions from soybean residue hydrogel [90]. Desorption efficiency varies depending on the type of polymer matrix employed in the sorption studies, as previously described for green hydrogels during the recovery of Ag^+ , Cu^{2+} , Ni^{2+} , Zn^{2+} , and Pb^{2+} ions using $4.0 \text{ mol L}^{-1} \text{ HNO}_3$ [91].

4. Conclusions

PC-co-MMT composite hydrogels were prepared for the separation of PTEs from water with the aim of proposing alternative water treatment methods. The morphologies of these hydrogels indicated porous structures depending on the MMT content in the polymeric networks. For instance, higher MMT contents led to smaller pore sizes due to the increase in crosslinking points and intermolecular interactions in the hydrogel chain. The simultaneous sorption assays of some PTEs confirmed the following affinity order by the hydrogel network: $\text{Cu}^{2+} > \text{Zn}^{2+} > \text{Ni}^{2+} > \text{Cd}^{2+} > \text{Cr}^{6+}$. The sorption of Cu^{2+} was efficiently explained by the Langmuir isotherm model, inferring a favorable process with interactions taking place at homogeneous surface-active sites. The pseudo-second-order kinetic model was suitable to infer that the Cu^{2+} sorption phenomenon in the PC-co-MMT composite hydrogel takes

place predominately via chemical reactions. FT-IR spectra confirmed the formation of three-dimensional polymer hydrogel networks as well as the sorption process of Cu^{2+} . All hydrogels exhibited suitable thermal stabilities to be employed in water treatment process. Overall, we have presented here an environmentally friendly alternative for the high-performance separation of PTEs from water.

Supplementary data to this article can be found online at <https://doi.org/10.1016/j.jwpe.2024.106629>.

CRedit authorship contribution statement

João Gabriel Ribeiro: Writing – original draft, Formal analysis, Data curation. **Rizia Maria Raimondi:** Methodology, Formal analysis, Data curation. **Alana Gabrieli de Souza:** Writing – original draft, Resources, Data curation. **Derval dos Santos Rosa:** Supervision, Resources, Funding acquisition. **Alexandre Tadeu Paulino:** Writing – review & editing, Supervision, Project administration, Funding acquisition, Data curation, Conceptualization.

Declaration of competing interest

The authors declare that they have no known competing financial interests or personal relationships that could have appeared to influence the work reported in this paper.

Acknowledgments

ATP thanks Fundação de Amparo à Pesquisa e Inovação do Estado de Santa Catarina (FAPESC, Brazil) for the financial support (Grant

number: 2023/TR331) and Conselho Nacional de Desenvolvimento Científico e Tecnológico (CNPq, Brazil) for the research productivity fellowship (Grant number: 313064/2022-9). DSR thanks CNPq (Grant number: 308053/2021-4 and 403934/2021-4) and Fundação de Amparo à Pesquisa do Estado de São Paulo (FAPESP, Brazil) for research support (Grant numbers: 2022/01382-3, 2021/14714-1, and 2020/13703-3). This work was partially supported by the Brazilian agencies MCTIC/CNPq (Grant number: 406973/2022-9) and by Coordenação de Aperfeiçoamento de Pessoal de Nível Superior (CAPES, Brazil – Finance Code 001) and Multiuser Central Facilities (CEM - UFABC).

Data availability

No data was used for the research described in the article.

References

- [1] M. Elma, N. Kadek Devi Ananda Saraswati, P. Fransiska Afrida Simatupang, R. Febriyanti, A. Rahma, F. Ria Mustalifah, Hydrogel derived from water hyacinth and pectin from banana peel as a membrane layer, *Mater Today Proc* 87 (2023) 13–17. doi:<https://doi.org/10.1016/j.matpr.2023.01.368>.
- [2] J. Martínez-Sabando, F. Coin, J.H. Melillo, S. Goyanes, S. Cervený, A review of pectin-based material for applications in water treatment, *Materials* 16 (2023) 2207. <https://doi.org/10.3390/ma16062207>.
- [3] V. Chandel, D. Biswas, S. Roy, D. Vaidya, A. Verma, A. Gupta, Current advancements in pectin: extraction, properties and multifunctional applications, *Foods* 11 (2022) 2683. <https://doi.org/10.3390/foods11172683>.
- [4] A. Morgan, D. Darby, T. Bruce, A. Romero, K. Cooksey, Development of an antimicrobial coating containing nisin and pectin for deli meat turkey bologna, *LWT* 159 (2022) 113210. <https://doi.org/10.1016/j.lwt.2022.113210>.
- [5] D. Li, J. Li, H. Dong, X. Li, J. Zhang, S. Ramaswamy, F. Xu, Pectin in biomedical and drug delivery applications: a review, *Int. J. Biol. Macromol.* 185 (2021) 49–65. <https://doi.org/10.1016/j.ijbiomac.2021.06.088>.
- [6] C.M.P. Freitas, J.S.R. Coimbra, V.G.L. Souza, R.C.S. Sousa, Structure and advancements of pectin in food, biomedical, and pharmaceutical industry: a review, *Coatings* 11 (2021) 922. <https://doi.org/10.3390/coatings11080922>.
- [7] A. Mohammadpour, Z. Emadi, M.R. Samaei, K. Ravindra, S.M. Hosseini, M. Amin, M. Samiei, L. Mohammadi, R. Khaksefidi, A. Allah Zarei, M. Motamed-Jahromi, A. Mousavi Khaneghah, The concentration of potentially toxic elements (PTEs) in drinking water from Shiraz, Iran: a health risk assessment of samples, *Environ. Sci. Pollut. Res.* 30 (2022) 23295–23311. doi:<https://doi.org/10.1007/s11356-022-23535-2>.
- [8] A. Spoiälä, C.-I. Ilie, D. Ficai, A. Ficai, E. Andronescu, Chitosan-based nanocomposite polymeric membranes for water purification—a review, *Materials* 14 (2021) 2091. <https://doi.org/10.3390/ma14092091>.
- [9] Z. Xie, Y.-P. Peng, L. Yu, C. Xing, M. Qiu, J. Hu, H. Zhang, Solar-inspired water purification based on emerging 2D materials: status and challenges, *Sol. RRL* 4 (2020). <https://doi.org/10.1002/solr.201900400>.
- [10] O.A. Diegtiar, V.H. Hornyk, S.O. Kravchenko, V.V. Karlova, T.V. Shtal, Improving public water resources policy in Ukraine: municipal and environmental issues, *Journal of Environmental Management and Tourism* 11 (2020) 672. [https://doi.org/10.14505/jemt.11.3\(43\).20](https://doi.org/10.14505/jemt.11.3(43).20).
- [11] B.M. Onyegeme-Okerenta, O.L. West, Toxicological evaluation of contamination by potentially toxic elements (PTEs) and related risks in the surface waters of three tidal streams of the Niger Delta, Nigeria, *Asian Journal of Environ. Ecol.* 20 (2023) 67–83. <https://doi.org/10.9734/ajece/2023/v20i4448>.
- [12] L.P. Padhye, P. Srivastava, T. Jasemizad, S. Bolan, D. Hou, S.M. Shaheen, J. Rinklebe, D. O'Connor, D. Lamb, H. Wang, K.H.M. Siddique, N. Bolan, Contaminant containment for sustainable remediation of persistent contaminants in soil and groundwater, *J. Hazard. Mater.* 455 (2023) 131575. <https://doi.org/10.1016/j.jhazmat.2023.131575>.
- [13] Md.R. Awwal, Md.M. Hasan, A. Islam, A.M. Asiri, M.M. Rahman, Optimization of an innovative composited material for effective monitoring and removal of cobalt (II) from wastewater, *J. Mol. Liq.* 298 (2020) 112035. <https://doi.org/10.1016/j.molliq.2019.112035>.
- [14] H.M. Queiroz, S.C. Ying, M. Abernathy, D. Barcellos, F.A. Gabriel, X.L. Otero, G. N. Nóbrega, A.F. Bernardino, T.O. Ferreira, Manganese: the overlooked contaminant in the world largest mine tailings dam collapse, *Environ. Int.* 146 (2021) 106284. <https://doi.org/10.1016/j.envint.2020.106284>.
- [15] S. Velusamy, A. Roy, S. Sundaram, T. Kumar Mallick, A review on heavy metal ions and containing dyes removal through graphene oxide-based adsorption strategies for textile wastewater treatment, *Chem. Rec.* 21 (2021) 1570–1610. <https://doi.org/10.1002/trc.202000153>.
- [16] T.A. Saleh, M. Mustaqeem, M. Khaled, Water treatment technologies in removing heavy metal ions from wastewater: a review, *Environ Nanotechnol Monit Manag* 17 (2022) 100617. <https://doi.org/10.1016/j.enmm.2021.100617>.
- [17] R. Gusain, N. Kumar, S.S. Ray, Recent advances in carbon nanomaterial-based adsorbents for water purification, *Coord. Chem. Rev.* 405 (2020) 213111. <https://doi.org/10.1016/j.ccr.2019.213111>.
- [18] S.K. Read, A.J.C. Semião, M.C. Graham, M. Ross, Live algal sorbents for the removal of potentially toxic elements: a review, *Applied Phycology* 4 (2023) 15–33. <https://doi.org/10.1080/26388081.2022.2158132>.
- [19] N. Gul, B. Khan, A.H.A. Khan, T. Nawaz, F. Wahid, C.A.T. Toloza, E. Alzahrani, R. A. Hauser-Davis, S. Khan, A novel assessment of potentially toxic elements (PTEs) in water and sediment samples from the Indus River, Pakistan: an ecological risk assessment approach, *Mar. Pollut. Bull.* 205 (2024) 116657. <https://doi.org/10.1016/j.marpolbul.2024.116657>.
- [20] A.M. Tischer, R.R. Ferreira, J.G. Ribeiro, D. dos Santos Rosa, A.T. Paulino, Green synthesis of an advanced composite membrane for the purification of water contaminated with potentially toxic metals, *Journal of Water, Process. Eng.* 61 (2024) 105239. <https://doi.org/10.1016/j.jwpe.2024.105239>.
- [21] Q. Sun, B. Aguila, Y. Song, S. Ma, Tailored porous organic polymers for task-specific water purification, *Acc. Chem. Res.* 53 (2020) 812–821. <https://doi.org/10.1021/acs.accounts.0c00007>.
- [22] W. Zhang, J. Song, Q. He, H. Wang, W. Lyu, H. Feng, W. Xiong, W. Guo, J. Wu, L. Chen, Novel pectin based composite hydrogel derived from grapefruit peel for enhanced Cu(II) removal, *J. Hazard. Mater.* 384 (2020) 121445. <https://doi.org/10.1016/j.jhazmat.2019.121445>.
- [23] M.P. Mudugamuwa Arachchige, T. Mu, M. Ma, Effect of high hydrostatic pressure-assisted pectinase modification on the Pb²⁺ adsorption capacity of pectin isolated from sweet potato residue, *Chemosphere* 262 (2021) 128102. <https://doi.org/10.1016/j.chemosphere.2020.128102>.
- [24] Z. Shao, J. Lu, J. Ding, F. Fan, X. Sun, P. Li, Y. Fang, Q. Hu, Novel green chitosan-pectin gel beads for the removal of Cu(II), Cd(II), Hg(II) and Pb(II) from aqueous solution, *Int. J. Biol. Macromol.* 176 (2021) 217–225. <https://doi.org/10.1016/j.ijbiomac.2021.02.037>.
- [25] C. Xia, X. Li, Y. Wu, S. Suharti, Y. Unpaprom, A. Pugazhendhi, A review on pollutants remediation competence of nanocomposites on contaminated water, *Environ. Res.* 222 (2023) 115318. <https://doi.org/10.1016/j.envres.2023.115318>.
- [26] K.-G. Liu, F. Bigdeli, Z. Sharifzadeh, S. Gholizadeh, A. Morsali, Role of metal-organic framework composites in removal of inorganic toxic contaminants, *J. Clean. Prod.* 404 (2023) 136709. <https://doi.org/10.1016/j.jclepro.2023.136709>.
- [27] S. Zhang, X. Cheng, Q. Fu, Y. Li, P. Wu, Y. Qiao, J. Yan, L. Si, G.I.N. Waterhouse, H. Li, S. Ai, Pectin-nanocellulose composite films with water resistance, UV resistance, and antibacterial activity, *Food Hydrocoll* 143 (2023) 108783. <https://doi.org/10.1016/j.foodhyd.2023.108783>.
- [28] S. Khampala, S. Sopasin, C. Puchongkwarin, C. Umpuch, An experimental design approach for lead (II) ion removal in an aqueous environment using a composite biofilm from microalgal biomass and pectin, *Chem. Eng. Commun.* 211 (2024) 743–762. <https://doi.org/10.1080/00986445.2023.2296041>.
- [29] F. Hassan, U. Talib, S. Saif, P. Akhter, F. Ali, M. Abbas, U. Younas, K. Ashraf, S. Alamri, Q. uz Zaman, Pectin functionalized with Cu/Fe nanoparticles for enhanced degradation of methylene blue from wastewater, *Front Sustain Food Syst* 8 (2024). doi:<https://doi.org/10.3389/fsufs.2024.1395730>.
- [30] E.F. Lessa, A.L. Medina, A.S. Ribeiro, A.R. Fajardo, Removal of multi-metals from water using reusable pectin/cellulose microfibrils composite beads, *Arab. J. Chem.* 13 (2020) 709–720. <https://doi.org/10.1016/j.arabjc.2017.07.011>.
- [31] F.M. Ibrahim, M.A. El-Liethy, R. Abouzeid, A.M. Youssef, S.Z.A. Mahdy, E.S. El Habbasha, Preparation and characterization of pectin/hydroxyethyl cellulose/clay/TiO₂ bionanocomposite films for microbial pathogen removal from contaminated water, *Int. J. Biol. Macromol.* 274 (2024) 133511. <https://doi.org/10.1016/j.ijbiomac.2024.133511>.
- [32] P. Beigi, F. Ganjali, F. Hassanzadeh-Afruz, M.M. Salehi, A. Maleki, Enhancement of adsorption efficiency of crystal violet and chlorpyrifos onto pectin hydrogel@Fe₃O₄-bentonite as a versatile nanoadsorbent, *Sci. Rep.* 13 (2023) 10764. <https://doi.org/10.1038/s41598-023-38005-z>.
- [33] J.E. Gamboni, M.A. Bertuzzi, A.M. Slavutsky, Methylene blue sorption phenomena onto pectin, brea gum, montmorillonite based hydrogels: kinetic and thermodynamic assessment, *J Polym Environ* 30 (2022) 4710–4725. <https://doi.org/10.1007/s10924-022-02546-7>.
- [34] S. Rehmat, N.B. Rizvi, S.U. Khan, A. Ghaffar, A. Islam, R.U. Khan, A. Mehmood, H. Butt, M. Rizwan, Novel stimuli-responsive pectin-PVP-functionalized clay based smart hydrogels for drug delivery and controlled release application, *Front Mater* 9 (2022). <https://doi.org/10.3389/fmats.2022.823545>.
- [35] W.B.F. Filho, S.T.R. Agassin, K.P. Naidek, A.T. Paulino, Pectin hydrogels modified with montmorillonite: case studies for the removal of dyes and herbicides from water, *J. Environ. Chem. Eng.* 11 (2023) 110846. <https://doi.org/10.1016/j.jece.2023.110846>.
- [36] D.C. Hanauer, A.T. Paulino, Anchoring lactase in pectin-based hydrogels for lactose hydrolysis reactions, *Process Biochem.* 122 (2022) 50–59. <https://doi.org/10.1016/j.procbio.2022.08.026>.
- [37] P. Kulal, V. Badalamoole, Magnetite nanoparticle embedded pectin-graft-poly(N-hydroxyethylacrylamide) hydrogel: evaluation as adsorbent for dyes and heavy metal ions from waste water, *Int. J. Biol. Macromol.* 156 (2020) 1408–1417. <https://doi.org/10.1016/j.ijbiomac.2019.11.181>.
- [38] Z. Sekhavat Pour, M. Ghaemy, Removal of dyes and heavy metal ions from water by magnetic hydrogel beads based on poly(vinyl alcohol)/carboxymethyl starch-g-poly(vinyl imidazole), *RSC Adv.* 5 (2015) 64106–64118. <https://doi.org/10.1039/c5ra08025h>.
- [39] T.V. Toledo, C.R. Bellato, K.D. Pessoa, M.P.F. Fontes, Remoção de cromo (VI) de soluções aquosas utilizando o composto magnético calcinado hidrotalcita-óxido de ferro: estudo cinético e de equilíbrio termodinâmico, *Quim Nova* 36 (2013) 419–425. <https://doi.org/10.1590/S0100-40422013000300012>.

- [40] S. Kaushal, N. Kaur, M. Kaur, P.P. Singh, Dual-responsive pectin/graphene oxide (Pc/GO) nano-composite as an efficient adsorbent for Cr (III) ions and photocatalyst for degradation of organic dyes in waste water, *J. Photochem. Photobiol. A Chem.* 403 (2020), <https://doi.org/10.1016/j.jphotochem.2020.112841>.
- [41] M.T. Kartel, L.A. Kupchik, B.K. Veisov, Evaluation of Pectin Binding of Heavy Metal Ions in Aqueous Solutions, 1999.
- [42] H. Zhang, M. Shi, J. Ma, M. Xia, F. Wang, C. Liao, The interaction and mechanism between threonine-montmorillonite composite and Pb²⁺ or Cu²⁺: experimental study and theory calculation, *J. Mol. Liq.* 326 (2021) 115243, <https://doi.org/10.1016/j.molliq.2020.115243>.
- [43] Y. Chu, M.A. Khan, F. Wang, M. Xia, W. Lei, S. Zhu, Kinetics and equilibrium isotherms of adsorption of Pb(II) and Cu(II) onto raw and arginine-modified montmorillonite, *Adv. Powder Technol.* 30 (2019) 1067–1078, <https://doi.org/10.1016/j.apt.2019.03.002>.
- [44] B. Baeyens, M.H. Bradbury, Contaminant Hydrology a Mechanistic Description of Ni and Zn Sorption on Na-montmorillonite Part I: Titration and Sorption Measurements, 1997.
- [45] L. De Pablo, M.L. Chávez, M. Abatal, Adsorption of heavy metals in acid to alkaline environments by montmorillonite and Ca-montmorillonite, *Chem. Eng. J.* 171 (2011) 1276–1286, <https://doi.org/10.1016/j.cej.2011.05.055>.
- [46] G.U. Rani, A.K. Konreddy, S. Mishra, Novel hybrid biosorbents of agar: swelling behaviour, heavy metal ions and dye removal efficacies, *Int. J. Biol. Macromol.* 117 (2018) 902–910, <https://doi.org/10.1016/j.ijbiomac.2018.05.163>.
- [47] M. Ben Amar, K. Walha, V. Salvador, Valorisation of pine cone as an efficient biosorbent for the removal of Pb(II), Cd(II), Cu(II), and Cr(VI), *Adsorpt. Sci. Technol.* 2021 (2021), <https://doi.org/10.1155/2021/6678530>.
- [48] M. Fu, X. Tuo, X. Yan, D. Li, H. Zhu, S. Gao, X. Han, J. Zhou, D. Mou, J. Xiu, Adsorption performance and mechanism of pectin modified with β -cyclodextrin for Zn²⁺ and Cu²⁺, *Int. J. Biol. Macromol.* 274 (2024) 133563 <https://doi.org/10.1016/j.ijbiomac.2024.133563>.
- [49] W.B.F. Filho, S.T.R. Agassin, K.P. Naidek, A.T. Paulino, Pectin hydrogels modified with montmorillonite: case studies for the removal of dyes and herbicides from water, *J. Environ. Chem. Eng.* 11 (2023) 110846, <https://doi.org/10.1016/j.jece.2023.110846>.
- [50] S.T. Maleki, P. Beigi, M. Babamoradi, Synthesis of pectin hydrogel/Fe₃O₄/Bentonite and its use for the adsorption of Pb (II), Cu (II), and Cd (II) heavy metals from aqueous solutions, *Mater. Sci. Eng. B* 298 (2023) 116899, <https://doi.org/10.1016/j.mseb.2023.116899>.
- [51] M.R. Abukhadra, M. Mostafa, Effective decontamination of phosphate and ammonium utilizing novel muscovite/phillipsite composite; equilibrium investigation and realistic application, *Sci. Total Environ.* 667 (2019) 101–111, <https://doi.org/10.1016/j.scitotenv.2019.02.362>.
- [52] O. Abid, E. Ahmed, H. Shehza, A. Sharif, Z.H. Farooqi, Z. Liu, L. Zhou, J. Ouyang, R. Begum, A. Irfan, A.R. Chaudhry, M.I. Din, Competitive recovery of copper ions using ethyl acetoacetate modified chitosan/organo-functionalized alginate hydrogel beads: kinetics and isothermal sorption studies, *Colloids Surf. A Physicochem. Eng. Asp.* 675 (2023) 132019, <https://doi.org/10.1016/j.colsurfa.2023.132019>.
- [53] Z. Sayyar, Z. Hosseini, P. Mohammadzadeh Pakdel, A. Hassani, Preparation of novel and low-cost chitosan modified with montmorillonite/ZnO hydrogel nanocomposite for adsorption of ciprofloxacin from water, *Journal of Water, Process. Eng.* 63 (2024) 105449, <https://doi.org/10.1016/j.jwpe.2024.105449>.
- [54] L. Yang, L. Bao, T. Dong, H. Xie, X. Wang, H. Wang, J. Wu, C. Hao, Adsorption properties of cellulose/guar gum/biochar composite hydrogel for Cu²⁺, Co²⁺ and methylene blue, *Int. J. Biol. Macromol.* 242 (2023) 125021, <https://doi.org/10.1016/j.ijbiomac.2023.125021>.
- [55] T.S. Hamidon, M.H. Hussin, Improved p-chlorophenol adsorption onto copper-modified cellulose nanocrystal-based hydrogel spheres, *Int. J. Biol. Macromol.* 233 (2023) 123535, <https://doi.org/10.1016/j.ijbiomac.2023.123535>.
- [56] A. Masoumi, M. Ghaemy, Removal of metal ions from water using nanohydrogel tragacanth gum-g-polyamidoxime: isotherm and kinetic study, *Carbohydr. Polym.* 108 (2014) 206–215, <https://doi.org/10.1016/j.carbpol.2014.02.083>.
- [57] L. Song, F. Liu, C. Zhu, A. Li, Facile one-step fabrication of carboxymethyl cellulose based hydrogel for highly efficient removal of Cr(VI) under mild acidic condition, *Chem. Eng. J.* 369 (2019) 641–651, <https://doi.org/10.1016/j.cej.2019.03.126>.
- [58] S. Maity, N. Naskar, B. Jana, S. Lahiri, J. Ganguly, Fabrication of thiophene-chitosan hydrogel-trap for efficient immobilization of mercury (II) from aqueous environs, *Carbohydr. Polym.* 251 (2021) 116999, <https://doi.org/10.1016/j.carbpol.2020.116999>.
- [59] C. Demirbilek, C.Ö. Dinç, Synthesis of diethylaminoethyl dextran hydrogel and its heavy metal ion adsorption characteristics, *Carbohydr. Polym.* 90 (2012) 1159–1167, <https://doi.org/10.1016/j.carbpol.2012.06.068>.
- [60] Z. Lin, Y. Yang, Z. Liang, L. Zeng, A. Zhang, Preparation of chitosan/calcium alginate/bentonite composite hydrogel and its heavy metal ions adsorption properties, *Polymers (Basel)* 13 (2021) 1891, <https://doi.org/10.3390/polym13111891>.
- [61] R. Zhang, B. Liu, J. Ma, R. Zhu, Preparation and characterization of carboxymethyl cellulose/chitosan/alginate acid hydrogels with adjustable pore structure for adsorption of heavy metal ions, *Eur. Polym. J.* 179 (2022) 111577, <https://doi.org/10.1016/j.eurpolymj.2022.111577>.
- [62] Y.H. Teow, L.M. Kam, A.W. Mohammad, Synthesis of cellulose hydrogel for copper (II) ions adsorption, *J. Environ. Chem. Eng.* 6 (2018) 4588–4597, <https://doi.org/10.1016/j.jece.2018.07.010>.
- [63] Q. Chen, X. Zheng, L. Zhou, Y. Zhang, Adsorption of Cu(II) and methylene blue by succinylated starch nanocrystals, *Starch-Stärke* 71 (2019), <https://doi.org/10.1002/star.201800266>.
- [64] E.H. Gürkan, B. İlyas, Y. Tibet, Adsorption performance of heavy metal ions from aqueous solutions by a waste biomass based hydrogel: comparison of isotherm and kinetic models, *Int. J. Environ. Anal. Chem.* 103 (2023) 1343–1360, <https://doi.org/10.1080/03067319.2021.1873314>.
- [65] H. Zhu, S. Chen, H. Duan, J. He, Y. Luo, Removal of anionic and cationic dyes using porous chitosan/carboxymethyl cellulose-PEG hydrogels: optimization, adsorption kinetics, isotherm and thermodynamics studies, *Int. J. Biol. Macromol.* 231 (2023) 123213, <https://doi.org/10.1016/j.ijbiomac.2023.123213>.
- [66] R.K. Mishra, A.B.A. Majeed, A.K. Banthia, Development and characterization of pectin/gelatin hydrogel membranes for wound dressing, *Int. J. Plast. Technol.* 15 (2011) 82–95, <https://doi.org/10.1007/s12588-011-9016-y>.
- [67] L. Liu, P.H. Cooke, D.R. Coffin, M.L. Fishman, K.B. Hicks, Pectin and polyacrylamide composite hydrogels: effect of pectin on structural and dynamic mechanical properties, *J. Appl. Polym. Sci.* 92 (2004) 1893–1901, <https://doi.org/10.1002/app.20174>.
- [68] M.P.M. da Costa, I.L. de Mello Ferreira, M.T. de Macedo Cruz, New polyelectrolyte complex from pectin/chitosan and montmorillonite clay, *Carbohydr. Polym.* 146 (2016) 123–130, <https://doi.org/10.1016/j.carbpol.2016.03.025>.
- [69] J. Kurczewska, Chitosan-montmorillonite hydrogel beads for effective dye adsorption, *Journal of Water Process Engineering* 48 (2022) 102928, <https://doi.org/10.1016/j.jwpe.2022.102928>.
- [70] R. Sun, Z. Lv, Y. Wang, Y. Gu, Y. Sun, X. Zeng, Z. Gao, X. Zhao, Y. Yuan, T. Yue, Preparation and characterization of pectin-alginate-based microbeads reinforced by nano montmorillonite filler for probiotics encapsulation: improving viability and colonic colonization, *Int. J. Biol. Macromol.* 264 (2024) 130543, <https://doi.org/10.1016/j.ijbiomac.2024.130543>.
- [71] M.R. Guilherme, A.V. Reis, A.T. Paulino, T.A. Moia, L.H.C. Mattoso, E. B. Tamborgi, Pectin-based polymer hydrogel as a carrier for release of agricultural nutrients and removal of heavy metals from wastewater, *J. Appl. Polym. Sci.* 117 (2010) 3146–3154, <https://doi.org/10.1002/app.32123>.
- [72] S. Pirsfa, F. Asadzadeh, I. Karimi Sani, Synthesis of magnetic gluten/pectin/Fe₃O₄ nano-hydrogel and its use to reduce environmental pollutants from Lake Urmia sediments, *J. Inorg. Organomet. Polym. Mater.* 30 (2020) 3188–3198, <https://doi.org/10.1007/s10904-020-01484-y>.
- [73] B. Tyagi, C.D. Chudasama, R.V. Jasra, Determination of structural modification in acid activated montmorillonite clay by FT-IR spectroscopy, *Spectrochim. Acta A Mol. Biomol. Spectrosc.* 64 (2006) 273–278, <https://doi.org/10.1016/j.saa.2005.07.018>.
- [74] W. Wang, Y. Zhao, H. Yi, T. Chen, S. Kang, T. Zhang, F. Rao, S. Song, Pb(II) removal from water using porous hydrogel of chitosan-2D montmorillonite, *Int. J. Biol. Macromol.* 128 (2019) 85–93, <https://doi.org/10.1016/j.ijbiomac.2019.01.098>.
- [75] D. Wang, H. Xu, J. Ma, X. Lu, J. Qi, S. Song, Strong promoted catalytic ozonation of atrazine at low temperature using tourmaline as catalyst: influencing factors, reaction mechanisms and pathways, *Chem. Eng. J.* 354 (2018) 113–125, <https://doi.org/10.1016/j.cej.2018.07.032>.
- [76] I. Abdelfattaha, W. Abdelwahab, A.M. El-Shamy, Montmorillonitic clay as a cost effective, eco-friendly and sustainable adsorbent for physicochemical treatment of contaminated water, *Egypt J Chem* 65 (2022) 687–695.
- [77] X. Sheng, C. Qin, B. Yang, X. Hu, C. Liu, M.G. Waigi, X. Li, W. Ling, Metal cation saturation on montmorillonites facilitates the adsorption of DNA via cation bridging, *Chemosphere* 235 (2019) 670–678, <https://doi.org/10.1016/j.chemosphere.2019.06.159>.
- [78] Y. Chen, S. Wang, Y. Li, Y. Liu, Y. Chen, Y. Wu, J. Zhang, H. Li, Z. Peng, R. Xu, Z. Zeng, Adsorption of Pb(II) by tourmaline-montmorillonite composite in aqueous phase, *J. Colloid Interface Sci.* 575 (2020) 367–376, <https://doi.org/10.1016/j.jcis.2020.04.110>.
- [79] E.A. Hassan, W.S. Abou Elseoud, M.T. Abo-Elfadl, M.L. Hassan, New pectin derivatives with antimicrobial and emulsification properties via complexation with metal-terpyridines, *Carbohydr. Polym.* 268 (2021) 118230, <https://doi.org/10.1016/j.carbpol.2021.118230>.
- [80] S. Švarcová, D. Hradil, J. Hradilová, Z. Čermáková, Pigments—copper-based greens and blues, *Archaeol. Anthropol. Sci.* 13 (2021) 190, <https://doi.org/10.1007/s12520-021-01406-0>.
- [81] Y. Kondratenko, A.A. Zolotarev, I. Ignatyev, V. Ugolkov, T. Kochina, Synthesis, crystal structure and properties of copper(II) complexes with triethanolamine and carboxylic acids (succinic, salicylic, cinnamic), *Transit. Met. Chem.* 45 (2020) 71–81, <https://doi.org/10.1007/s11243-019-00359-7>.
- [82] R. Scatena, S. Massignani, A.E. Lanza, F. Zorzi, M. Monari, F. Nestola, C. Pettinari, L. Pandolfo, Synthesis of coordination polymers and discrete complexes from the reaction of copper(II) carboxylates with pyrazole: role of carboxylates basicity, *Cryst. Growth Des.* 22 (2022) 1032–1044, <https://doi.org/10.1021/acs.cgd.1c00861>.
- [83] J.F. Mendes, J.T. Martins, A. Manrich, A.R. Sena Neto, A.C.M. Pinheiro, L.H. C. Mattoso, M.A. Martins, Development and physical-chemical properties of pectin film reinforced with spent coffee grounds by continuous casting, *Carbohydr. Polym.* 210 (2019) 92–99, <https://doi.org/10.1016/j.carbpol.2019.01.058>.
- [84] L.D.C.B. Araújo, H.K. de Matos, D.P. Facchi, D.A. de Almeida, B.M.G. Gonçalves, J. P. Monteiro, A.F. Martins, E.G. Bonafé, Natural carbohydrate-based thermosensitive chitosan/pectin adsorbent for removal of Pb(II) from aqueous solutions, *Int. J. Biol. Macromol.* 193 (2021) 1813–1822, <https://doi.org/10.1016/j.ijbiomac.2021.11.014>.
- [85] M. Karmakar, H. Mondal, M. Mahapatra, P.K. Chattopadhyay, S. Chatterjee, N.R. Singha, Pectin-grafted terpolymer superadsorbent via N-H activated strategic

- protrusion of monomer for removals of Cd(II), Hg(II), and Pb(II), *Carbohydr. Polym.* 206 (2019) 778–791. doi:<https://doi.org/10.1016/j.carbpol.2018.11.032>.
- [86] N.R. Singha, M. Karmakar, M. Mahapatra, H. Mondal, A. Dutta, M. Deb, M. Mitra, C. Roy, P.K. Chattopadhyay, An in situ approach for the synthesis of a gum ghatti-g-interpenetrating terpolymer network hydrogel for the high-performance adsorption mechanism evaluation of Cd(II), Pb(II), Bi(III) and Sb(III), *J Mater Chem A Mater* 6 (2018) 8078–8100, <https://doi.org/10.1039/c8ta01106k>.
- [87] P.B. Vilela, A. Dalalibera, V.A. Becegato, A.T. Paulino, Single-component and multi-component metal abatement in water using a hydrogel based on chitosan: characterization, isotherm, kinetic, and thermodynamic results, *Water Air Soil Pollut.* 231 (2020), <https://doi.org/10.1007/s11270-020-04873-8>.
- [88] K. Varnier, T. Vieira, M. Wolf, L.A. Belfiore, E.B. Tambourgi, A.T. Paulino, Polysaccharide-based hydrogels for the immobilization and controlled release of bovine serum albumin, *Int. J. Biol. Macromol.* 120 (2018) 522–528, <https://doi.org/10.1016/j.ijbiomac.2018.08.133>.
- [89] Z. Darban, S. Shahabuddin, R. Gaur, I. Ahmad, N. Sridewi, Hydrogel-based adsorbent material for the effective removal of heavy metals from wastewater: a comprehensive review, *Gels* 8 (2022) 263, <https://doi.org/10.3390/gels8050263>.
- [90] M. Zhang, Q. Yin, X. Ji, F. Wang, X. Gao, M. Zhao, High and fast adsorption of Cd (II) and Pb(II) ions from aqueous solutions by a waste biomass based hydrogel, *Sci. Rep.* 10 (2020) 3285, <https://doi.org/10.1038/s41598-020-60160-w>.
- [91] T.N. Dharmapriya, D. Li, Y.-C. Chung, P.-J. Huang, Green synthesis of reusable adsorbents for the removal of heavy metal ions, *ACS Omega* 6 (2021) 30478–30487, <https://doi.org/10.1021/acsomega.1c03879>.



Prediction of Cr⁶⁺ removal on the biosorbent from pine cone residue with machine learning simulations

Joaquim G.G.S. Bento^a, Luidy F. Senra^a, Lana S. Maia^b, Luana Souza Almeida^c,
Lucas M. Ferreira^d, Maria Ismênia S.T. Faria^e, Derval S. Rosa^b, Daniella R. Mulinari^{f,*}

^a Rio de Janeiro State University (UERJ), Faculty of Technology (FAT), Department of Chemistry and Environmental, Resende, RJ, Brazil

^b Center for Engineering, Modeling, and Applied Social Sciences (CECS), Federal University of ABC (UFABC), Santo André, SP, Brazil

^c Rio de Janeiro State University (UERJ), Faculty of Technology (FAT), Department of Industrial Engineering, Resende, RJ, Brazil

^d University of São Paulo (EEL/USP), Department of Materials Engineering (DEMAR), Lorena, SP, Brazil

^e Federal University of Rio de Janeiro (UFRJ), Rio de Janeiro, RJ, Brazil

^f Rio de Janeiro State University (UERJ), Faculty of Technology (FAT), Department of Mechanic and Energy, Resende, RJ, Brazil

ARTICLE INFO

Dataset link: [Machine learning models and dataset for the prediction of Cr⁶⁺ removal of aqueous solutions using the pine cone residue \(Original data\)](#)

Keywords:

Machine learning
Biosorbent
Pine cone residue
Adsorption

ABSTRACT

This study investigates the revalorization of pine cone residue as an efficient, low-cost, and eco-friendly biosorbent for the removal of hexavalent chromium (Cr⁶⁺) from aqueous solutions. The material was characterized using techniques, including Brunauer-Emmett-Teller (BET) analysis, Attenuated Total Reflectance Fourier Transform Infrared Spectroscopy (ATR-FTIR), X-ray Diffraction (XRD), and Scanning Electron Microscopy (SEM). The adsorption conditions were optimized through experimental design, focusing on the effects of contact time, initial solution concentration, and pH. Furthermore, three machine learning models—multiple linear regression, decision tree regression, and random forest regression—were employed to predict the efficiency of Cr⁶⁺ removal. The optimized conditions resulted in a maximum removal efficiency of 90.84 % within a short contact time. Among the models tested, the decision tree regression achieved the highest predictive accuracy, with a correlation coefficient (R²) of 0.978. These findings underscore the potential of machine learning in modeling adsorption processes and highlight the importance of biosorbents in sustainable water treatment and revalorization of agricultural waste.

1. Introduction

Heavy metals, known as Potentially toxic metals (PTEs), pose a significant threat to human life and aquatic ecosystems due to their non-biodegradability and tendency to accumulate in living organisms. They are toxic and can be carcinogenic. Various industries, including metal plating facilities, mining operations, fertilizer production, tanneries, battery manufacturing, paper production, and pesticide application, contribute significantly to the release of these metals into the environment. Chromium, in particular, exists in two forms in water: trivalent (Cr³⁺) and hexavalent (Cr⁶⁺). Cr⁶⁺ is generally more harmful to human health than Cr³⁺, as it can cause a range of health issues. Symptoms can range from mild skin irritation to severe conditions such as lung cancer, kidney failure, and liver failure. The International Agency for Research on Cancer (IARC) classifies Cr⁶⁺ compounds as “carcinogenic to humans”. The World Health Organization has

established a maximum allowable limit of 50 µg L⁻¹ of total chromium in drinking water [1–4].

Effluents contaminated with Cr⁶⁺ can be treated using various methods and techniques including adsorption, photodegradation, coagulation, reduction and precipitation, and ion exchange [5–9]. Among these options, adsorption is often preferred due to its ease of operation and affordability, especially since it can utilize low-cost materials [3].

Several materials have been utilized in the literature to remove Cr⁶⁺ from water. These include earth-based materials such as gravel, clay, zeolite, lime rock, seashell (*Diplodonta*) [10], pomegranate peel [11], and raw marine green alga [12].

Several studies have explored the use of waste materials for their ability to absorb Cr⁶⁺ and other heavy metals. Velinov et al. [13] synthesized a sorbent from woodchip residue and assessed its effectiveness in simultaneously removing Cr⁶⁺ and Cr³⁺ from water, achieving

* Corresponding author.

E-mail address: daniella.mulinari@fat.uerj.br (D.R. Mulinari).

<https://doi.org/10.1016/j.surfin.2025.106460>

Received 26 December 2024; Received in revised form 8 April 2025; Accepted 10 April 2025

Available online 11 April 2025

2468-0230/© 2025 Elsevier B.V. All rights reserved, including those for text and data mining, AI training, and similar technologies.

adsorption capacities of 16.18 and 83.52 mg g⁻¹, respectively. In another study, Velinov et al. [14] used another wood residue, sawdust, to synthesize a sorbent capable of removing Cr⁶⁺ from water, which showed an impressive adsorption capacity of 104.2 mg g⁻¹. These findings suggest that lignocellulosic residues are effective for chromium removal. Additionally, employing waste materials in adsorption processes for wastewater treatment presents several advantages, including low cost, abundant availability, ease of operation, and high effectiveness [13,14].

In this context of natural and lignocellulosic residues, pine cones emerge as a promising material due to their effective adsorption potential. Thaçi et al. [15] conducted a study on untreated pine cones, demonstrating their ability to remove Pb²⁺ and Cd²⁺ from aqueous solutions. While pine trees are cultivated in various industrial applications, pine cones, the seed-bearing organ of the tree, are regarded as forestry waste with limited industrial use [16–18]. As a result, these residues can be obtained at a very low cost and in abundant supply.

Adsorption is influenced by several factors, like initial concentration, contact time, pH, and adsorbent mass [19]. These variables affect the adsorption process in different ways, making it difficult to analyze the process mechanistically. As a result, non-mechanistic models can be more straightforward to apply for understanding adsorption. In this context, artificial intelligence models are promising options. Machine Learning, a subset of artificial intelligence, has been utilized across various fields such as material science, aerospace, energy, environmental modeling, chemistry, and physics [20]. Therefore, implementing a machine learning model can be invaluable when studying the adsorption capacity of a biosorbent. This approach can potentially minimize the number of experiments required to explore the impact of these multiple variables on adsorption. Furthermore, machine learning can help predict the optimal conditions under which the studied material will perform best, thereby enhancing its efficiency in removing contaminants [20,21].

Machine learning models are used to understand the behavior of biosorbents and predict their adsorption capacity for removing specific substances. Iftikhar et al. [22] compiled data from previous studies on the removal capacity of industrial dyes using carbon-based materials. They extracted experimental conditions, such as synthesis conditions and physical properties from these experiments to serve as inputs for their model. The output of the model is the predicted adsorption capacity, which is then compared to the actual adsorption capacity observed in the experiments. Their study identifies the key features that most significantly influence the adsorption capacity of these materials. Iftikhar et al. [23] utilized a similar methodology, focusing on the adsorption capacity of PO₄(III) ions using biochar-based materials and employing five probabilistic machine learning models. Additionally, Jaffari et al. [24] and Jaffari et al. [25] adopted the same approach. The former developed ten tree-based machine learning models to predict the adsorption capacity of biochar materials for various emerging contaminants, such as personal care products, pharmaceuticals, endocrine-disrupting compounds, fungicides, and pesticides, in aqueous solutions. The latter developed various machine learning and three deep learning (DL) models to study the removal of heavy metal ions from wastewater using biochar adsorbents [22–25].

The literature has developed predictive models using machine learning to study the adsorption of toxic elements PTE's [26–28]. For example, Guo et al. [26] investigated the adsorption capacity of bentonite and developed an accurate prediction model for the material's ability to adsorb heavy metals. Similarly, Zhao et al. [27] used artificial intelligence models to predict the adsorption capacity of hydrochar when treating a water solution containing Pb²⁺, Zn²⁺, and Cd²⁺. Liu et al. [28] developed a machine learning model to predict adsorption efficiency on iron (oxy)hydroxides based on a database that includes adsorption from 11 heavy metals.

Supervised machine learning models used for regression can effectively predict a targeted response by analyzing the impact of various

variables [29,30]. This study aims to utilize three regression-supervised machine learning models (multiple linear regression, decision tree regressor, and random forest regression) to estimate the adsorption of Cr⁶⁺ from water using untreated pine cone residue, contributing to sustainable environmental solutions. The application of machine learning in this context is valuable as it provides insights that can significantly enhance the adsorption process. Additionally, it reduces the need for extensive experimental trials and offers a more efficient framework for optimization.

2. Materials and methods

2.1. Materials

Pine cone residue was collected at the Faculty of Technology (FAT) Campus at Rio de Janeiro State University (UERJ) in Resende, Rio de Janeiro, Brazil. The geographical coordinates of the pinecone sampling sites are 22°27'08" S and 44°22'47" W, as illustrated in Figure S1.

2.2. Obtain of biosorbent

The pine cone residue was crushed, ground, and sieved using 35 mesh screens. It was then dried at 80 °C for 24 h to remove moisture, resulting in a sustainable pine cone biosorbent, as shown in Fig. 1.

2.3. Characterization of pine cone residue

The moisture content of the pine cone residue was determined using a moisture analyzer, model MOC63u, from Shimadzu. The surface area, pore size, and volume were measured using the Sorb2800 analyzer (GoldAPPIstruments) with nitrogen isotherms. The chemical structures of pine cone residue were analyzed using Fourier-transform infrared spectroscopy (FTIR) with a Frontier 94,942 Model, PerkinElmer Inc., Massachusetts, USA. This analysis employed an attenuated total reflectance (ATR) diamond accessory, a spectral resolution of 4 cm⁻¹, and covered the range of 4000–650 cm⁻¹ with 64 scans.

A Shimadzu diffractometer (model XDR-6100) was used to evaluate the physical structure of the pine cone residue. The analysis was conducted under the following conditions: CuK α radiation with graphite monochromator, 30 kV voltage, and 40 mA, with patterns in the range 10–50°, 0.05 steps, and 1 s of counting time.

The morphology of the pine cone residue was examined using Scanning Electron Microscopy (SEM) with FEG Schottky electron emission on a MEV-FEG TESCAN Mira 4. The residue was affixed to carbon tape on a sample holder, employing both secondary electron mode (SE) and backscattered electron mode (BSE) at 5 keV. Additionally, ImageJ software was utilized to analyze and stabilize the pore structure of the sample.

The study conducted Zeta potential measurements, focusing specifically on the point of zero charge (pH_{ZPC}) of the pine cone residue. These measurements were performed by adding samples to a 50 mL solution of 0.1 mol L⁻¹ NaCl. The pH of the solution was simultaneously adjusted within the range of 2.0 to 10.0 using 0.1 mol L⁻¹ NaOH and 0.1 mol L⁻¹ HCl solutions. The solution's final pH values were measured after allowing 24 h for the reaction to occur. The ZPC represents the point where the initial pH of the solution matches the final pH after the reaction.

2.4. Adsorption analysis for design of experiments (DOE)

An experimental design was conducted to optimize the adsorption conditions of Cr⁶⁺ using biosorbent. This study focused on three main parameters: contact time, initial solution concentration, and pH. Each parameter was examined at three different levels: i) The contact time between the adsorbent materials and the adsorbate solution was assessed at 10, 60, and 90 min; ii) The initial concentration of the

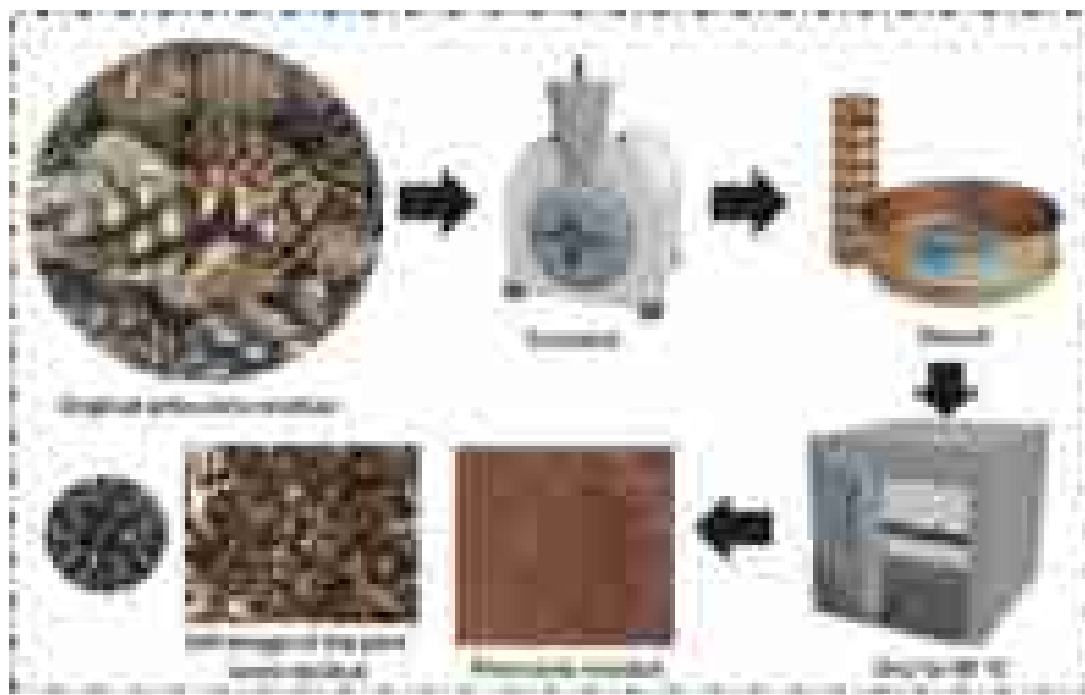


Fig. 1. Methodology illustration of the process of obtaining biosorbent from pine cone residue.

adsorbate in the solution was tested at 50, 588, and 800 mg L⁻¹; iii) The pH were varied at 0, 2, and 4 values. These levels were chosen based on recent articles in the literature, including studies by Maia et al. [31]. The pH values were maintained at acidic levels, as chromium is more efficiently adsorbed in acidic environments, as demonstrated by Singh et al. [32].

The study design was developed using Design Expert software and utilized a three-factorial approach, resulting in a total of 27 experiments. Each experiment was performed in triplicate, where a specific amount of adsorbent material was added to an erlenmeyer flask containing 20 mL of a solution with the defined concentration. The flasks were shaken on an orbital shaker at a speed of 150 rpm for the specified contact time. Following the shaking time, the samples were filtered, and the residual concentrations of the adsorbate were measured using a UV-visible spectrophotometer (NI 1600UV, Nova Instruments). This measurement was referenced against a standard curve for Cr⁶⁺ in the range of 25–800 mg L⁻¹, derived from a stock aqueous solution of K₂Cr₂O₇, at a maximum wavelength of 420 nm. The removal rates (%) were calculated using Eq. (1).

$$\%R = \left(\frac{C_0 - C_e}{C_0} \right) \cdot 100 \quad (1)$$

Where:

- C₀ is the PTEs metals initial concentration (mmol.L⁻¹).
- C_e is the PTEs metals concentration at equilibrium (mmol.L⁻¹).

2.5. Desorption and regeneration study

Desorption and regeneration studies were conducted to assess the reusability and efficiency of the pine cone residue as a biosorbent for Cr⁶⁺. Each adsorption-desorption cycle involved a 20 mL solution of K₂Cr₂O₇ with an initial concentration of 800 mg L⁻¹ of dichromate (282.8 mg L⁻¹ of Cr⁶⁺) mixed with 0.1 g of the biosorbent. The adsorption process was carried out under agitation for 1.5 h at a controlled temperature.

After the adsorption process, the Cr⁶⁺-loaded material was dried in

an oven at 60 °C. The desorption process involved adding 0.1 g of the Cr⁶⁺-loaded material to 40 mL of a 0.1 mol L⁻¹ HNO₃ solution (with a dosage of 5.0 g L⁻¹) under agitation for 1.5 h.

Following desorption, the regenerated material was thoroughly washed with distilled water until the pH approached neutrality (~5.0) and then dried again 60 °C before being reused in the next cycle.

At the end of each adsorption-desorption cycle, liquid phase samples were collected, filtered, and analyzed using a UV-visible spectrophotometer (NI 1600UV, Nova Instruments) to determine the residual Cr⁶⁺ concentration. The desorption capacity (q_{el}), recovery rate (%), and adsorption capacity (q_e) were calculated using Eqs. (2), (3), and (4) respectively:

$$q_{el} = \frac{(C_{el} \cdot V_{el})}{m} \quad (2)$$

$$\text{Recovery rate} = \frac{q_{el}}{q_e} \quad (3)$$

$$q_e = \frac{(C_e \cdot V_e)}{m} \quad (4)$$

2.6. Machine learning models

This study employs three regression models to estimate the percentage of Cr⁶⁺ adsorption from water using the pine cone residue. Details about these models are provided in SubSections 2.6.1, 2.6.2, and 2.6.3. The training set includes independent variables such as contact time (x₁), pH (x₂) and the adsorbate concentration (x₃), as well as the dependent variable, which is the percentage of Cr⁶⁺ adsorption (y). This data was collected from 27 experiments described in SubSection 2.4. The performance of the machine learning models is compared based on their determination coefficient (R²), which verifies the model's accuracy concerning experimental values. The R² ranges from 0 to 1, and higher values suggest a high model precision [33,34].

The regression models are coded on Python (version 3.9.7) and organized with the Pandas library (version 2.1.4). The graphs and figures are plotted with Plotly (version 5.9.0), and the codes are executed on an AMD Ryzen 5 Microsoft Surface (R) Edition with 8GB of RAM.

Python's Scikit-learn library (version 1.3.0) is used to pre-process the data, construct and plot the models, and calculate their determination coefficient.

The models are created as follows. First, the "StandardScaler" function of the Scikit-learn library is used to scale the data to unit variance. Then, the data is split into training and testing, following the proportion of 80 % for training and 20 % for testing. The model is trained, and the test subset is used to score the model. The machine learning models and the results of the 27 experiments can be retrieved at Bento et al. [35].

2.6.1. Multiple linear regression

In this context of multiple linear regression, the dependent variable (y) is approximated with a linear function of x_1 , x_2 , and x_3 , as described by the model in Eq. (5). The θ_0 coefficient is the intercept, and θ_1 , θ_2 , and θ_3 are the contact time, pH, and adsorbate concentration coefficients. In this research, the Statsmodels library (version 0.14.0) is used to find the coefficients of the model in Eq. (5) using the Ordinary Least Squares regression method.

$$y = \theta_0 + \theta_1 x_1 + \theta_2 x_2 + \theta_3 x_3 \quad (5)$$

Aside from the determination coefficient, the second analysis is the F-test, which checks whether a relationship exists between the dependent and independent variables (Siegel, 2016). In this test, the null hypothesis is that all model coefficients are equal to zero (i.e., $H_0: \theta_0 = \theta_1 = \theta_2 = \theta_3 = 0$) [35]. Considering the number of experiments, if the F value is greater than two, the null hypothesis is rejected, and at least one coefficient is nonzero [35]. Additionally, a hypothesis test (p-test) is used to determine whether each coefficient is different. The p-value ranges from 0 to 1, and in this study, if the p-value of 0.05 or less is considered evidence that the parameter is nonzero [33].

2.6.2. Decision tree regression

The second model is decision tree regression [36], which is a hierarchical model designed for supervised learning [37]. This method is suitable for both linear and non-linear problems [38]. However, this approach is less intuitive than Eq. (5), as the algorithm employs a divide-and-conquer strategy by splitting the training data into several branches [39–41].

The Decision Tree regressor processes the data to create rules that divide the tree while minimizing the tree's entropy [39,42], which represents the model's uncertainty. The primary goal of the regressor is to reduce the variance from the top of the tree towards the bottom, where the leaf vertices are located [43]. For a comprehensive understanding of Decision Tree Regression, the authors recommend consulting the works Alpaydin [37] and Zhou [39].

2.6.3. Random forest regression

Random Forest Regression is an ensemble learning technique that involves creating and combining multiple decision trees using the bagging bootstrap aggregation method [42,44]. This method generates several decision trees, and at each split, a random subset of features (such as contact time, pH, and adsorbate concentration) is selected. This randomness helps to create trees [45], which are combined to form the output tree. One of the main advantage of ensemble learning is its ability to reduce the likelihood of poor model selections, minimizing biases and preventing overfitting. The objective of Random Forest Regression is to minimize entropy; however, it also aims to reduce variance by averaging the entropies of the decision trees that make up the forest [43].

3. Results and discussion

3.1. Moisture content and Brunauer-Emmett-Teller (BET)

The moisture content of the crushed and milled sample was characterized with an average value of 16.41 ± 0.287 , which means 16.41 g of water per 100 g of pine cone residue. This value is considered high,

but this determination was essential to know the actual value of the pine cone residue sample to be included in the sorption tests. Hellum [46] evidenced similar behavior when evaluating the cone moisture and relative humidity effects on seed release from lodgepole pine cones from Alberta.

The results of the surface area, pore size, and pore volume of pine cones are shown in Table 1. These characteristics are of the mesoporous solid, according to the International Union of Pure and Applied Chemistry (IUPAC) classification [47]. The mesoporous nature of pine cones significantly affects the adsorption capacity. The surface area of the sample was not high. However, the pore size and volume can favor the binding between the chromium pollutant and the material surface, which is advantageous for wastewater treatment. Several authors showed similar results, such as $6.60 \text{ m}^2 \text{ g}^{-1}$ [48], $0.58 \text{ m}^2 \text{ g}^{-1}$ [49], $6.01 \text{ m}^2 \text{ g}^{-1}$ [50], $2.22 \text{ m}^2 \text{ g}^{-1}$ [51], and $2.00 \text{ m}^2 \text{ g}^{-1}$ [52].

3.2. Attenuated total reflectance fourier-transform infrared spectroscopy (ATR-FTIR), X-ray diffraction (XRD), and scanning electron microscopy (SEM)

The spectra of the pine cone residue were evaluated, as shown in Fig. 2a, revealing the presence of various functional groups on the pine cone residue surface. The $3500\text{--}3200 \text{ cm}^{-1}$ broadband corresponds to O–H stretching vibrations, characteristic of hydroxyl groups in cellulose, hemicellulose, and lignin. A peak at 2927 cm^{-1} was attributed to the side chains' C–H vibrations in aromatic methoxyl and methylene groups. Additionally, the band at 1615 cm^{-1} corresponds to C = C stretching vibrations in aromatic rings, a hallmark of lignin's structure. Another notable peak at 1512 cm^{-1} is attributed to the aromatic skeletal vibrations of lignin, while the band at 1447 cm^{-1} represents C–H deformation vibrations in lignin macromolecules. The peak at 1370 cm^{-1} is associated with C–H bending vibrations in polysaccharides, and the band at 1247 cm^{-1} corresponds to C = O stretching vibrations of acetyl groups present in hemicellulose. Furthermore, the peak observed at 1160 cm^{-1} is assigned to the asymmetric stretching of C–O–C bonds in cellulose, and the band at 1020 cm^{-1} is linked to C–C stretching vibrations in the pyranose ring of the cellulose chain. Finally, the weak peak at 879 cm^{-1} corresponds to glycosidic bonds in cellulose [53,54].

The identified hydroxyl and carbonyl groups play a prominent role in adsorption mechanisms. The high polarity of hydroxyl groups promotes hydrogen bonding and electrostatic interactions, making these sites ideal for capturing metal ions. This is especially relevant for Cr^{6+} adsorption, as hydroxyl groups enhance the material's ability to bind this metal effectively [55].

Similarly, carbonyl groups act as electron donors, facilitating the formation of bonds with metal cations. This chelating capacity enables the biomass to retain potentially toxic metals more stably. Moreover, nitro groups contribute negative charges to the pine cone residue surface, intensifying the electrostatic attraction between the biomass and metal species such as Cr^{6+} [56].

This analysis demonstrates that the functional groups identified in pine cone biomass are highly significant for adsorption processes. These groups confer selectivity, electron-donation capacity, and affinity for specific metal ions, highlighting the potential of this natural material to serve as an efficient adsorbent for environmental remediation applications.

The XRD study of the raw pine cone residues of pine cone was carried

Table 1

Moisture content, Surface Area (SA), Pore size (S), and Volume pore (V) for the pine cone sample.

n	Moisture content	SA ($\text{m}^2 \text{ g}^{-1}$)	S (nm)	V ($\text{cm}^3 \text{ g}^{-1}$)
Pine cone residue	16.4 ± 0.3	2.72	2.64 - 2.64	0.59

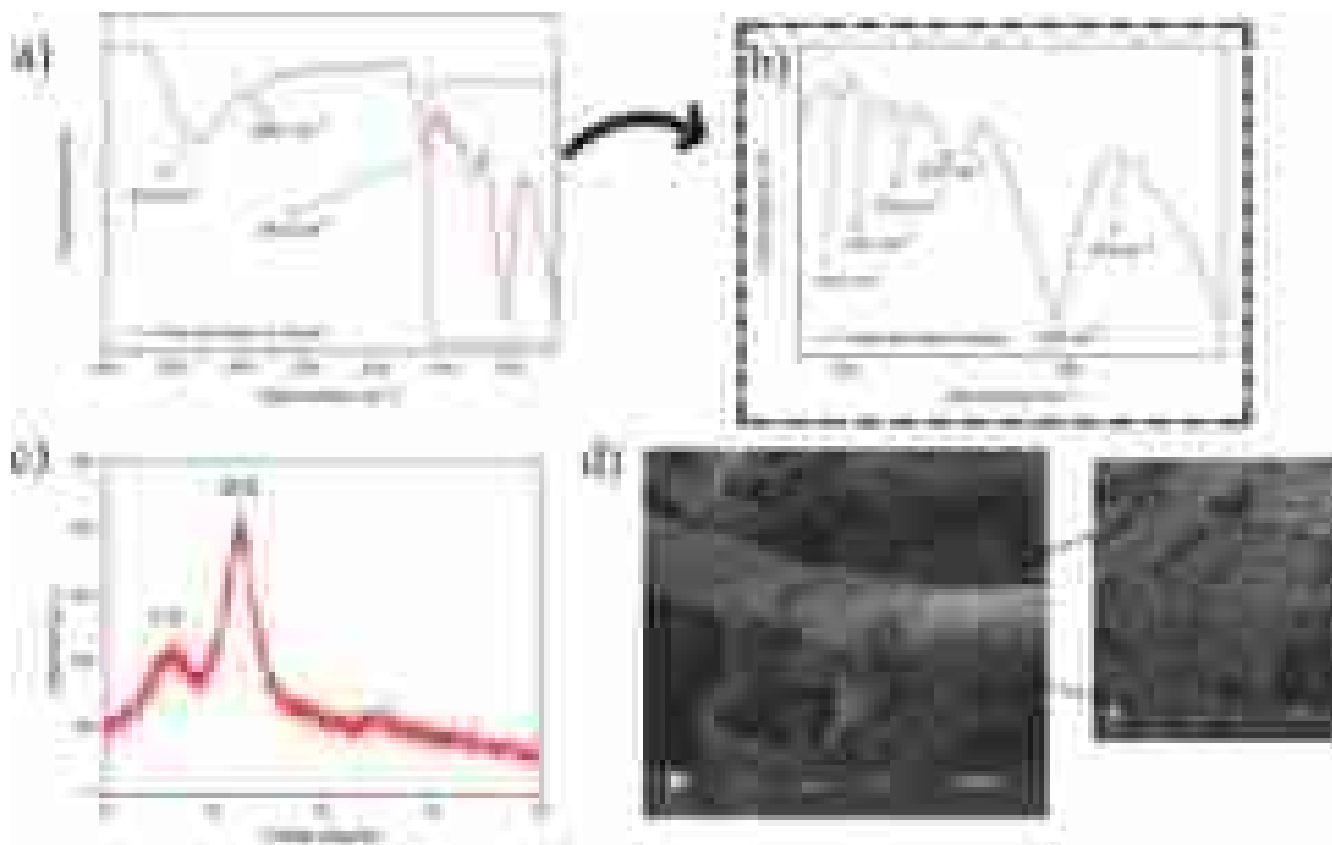


Fig. 2. Pine cone residue characterization results: a) FTIR spectra in wavenumber 4000 to 650 cm^{-1} and b) FTIR spectra in wavenumber 1600 to 650 cm^{-1} ; c) XRD patterns; d) Photomicroscopy, obtained by SEM with magnification 2000X, highlighting on the right, the magnification of 10000X.

out to assess the crystalline structure of the pine cone residues, as shown in Fig. 2c. It can be observed that pine cone residue exhibited three characteristic peaks at $2\theta = 16^\circ$ and 22° , which correspond to the 110 and 200 crystallographic planes, respectively [57]. Baatache et al. [58] cite that these peaks are likely related to the diffraction of a protein constituent enveloped by other components, such as polysaccharides and polyphenols with a more amorphous pattern. Also, these components can remove several heavy metals from water by coagulation, using

Pine cones as a natural coagulant.

The morphology of pine cone powder consists of a heterogeneous and disordered texture with cavities, irregular pores, and a porous structure, as shown in Fig. 2d. The particle size, calculated from the SEM images, was $0.39 \pm 0.14 \mu\text{m}$, and the deviation shown highlights the particle's heterogeneity. The SEM picture of the Pine cone biomass shows the availability of pores and internal surfaces, which can facilitate the removal of Cr^{6+} in water. Chebbi et al. [59] evidenced similar

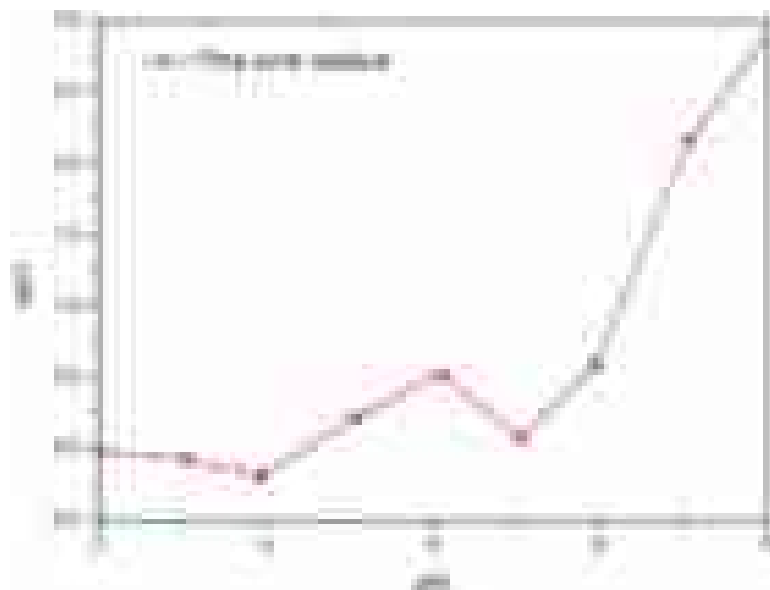


Fig. 3. Comparison of charge as a function of pH and point of zero charges of the pine cone residue.

morphology when studying the pine cone adsorbent to remove prednisolone and pre-treatment medical lab wastewater.

3.3. Determination of the zero-charge point (ZPC)

From the analysis of Fig. 3, a zero-charge point is observed for the studied pine cone residue at a more neutral pH, around 7. This is attributed to several factors, including the pine cone residue's chemical composition. Furthermore, acidic pH values, such as 2 and 4, remain slightly altered, guaranteeing good adsorption results.

As previously analyzed through FTIR, the pine cone residue's composition reveals functional groups that can protonate or deprotonate. However, at a neutral pH of approximately 7, these groups are in equilibrium between protonation and deprotonation, resulting in a net charge close to zero [60]. As the pH of the solution decreases, the surface becomes increasingly positively charged.

Regarding adsorption, it was planned to work at low pH values such as 0, 2, and 4, avoiding significant modifications at these acidic extremes as they could negatively affect the results for removing metallic contaminants. Cr^{6+} adsorption is favored in acidic environments [32], and as observed in Fig. 3, at very low pH levels, where the H^+ concentration is extremely high, the pine cone residue's surface does not significantly alter the pH. This ensures that the properties studied in the DOE analyses remain consistent and that the results are reliable.

3.4. Adsorption analysis for design of experiments (DOE)

Based on the analysis of Fig. 4, a clear trend of optimal conditions for Cr^{6+} adsorption can be observed across the three studied planes.

For the pH x concentration combination (Fig. 4a), it is noted that as the solution's pH decreases and the concentration of Cr^{6+} increases, adsorption tends to rise, reaching over 90 % adsorption for the best combination: an extremely acidic pH of 0 and a high salt concentration of 800 mg.L^{-1} . The pattern increases for the concentration x time combination (Fig. 4b) as the contact time between the Cr^{6+} solution and the adsorbent extends. Similarly to the pH x concentration pattern, higher concentrations result in higher adsorption capacity for Cr^{6+} ions, but it stops increasing at 800 mg.L^{-1} salt. A combination of 90 min and 800 mg.L^{-1} of potassium dichromate concentration yielded the same adsorption efficiency of 90.84 %. Finally, for the pH x time combination (Fig. 4c), the plane's peak predictably indicates optimal conditions around a pH 0 and extended contact time, specifically 90 min. Maximum adsorption of approximately 90 % was also consistent in this case.

The behavior obtained by the pine cone residue can be associated with its surface charge and chemical composition. The ZPC (Fig. 3) confirmed that the pine cone residue surface was positively charged under the acidic conditions employed. Furthermore, the hydroxyl and carbon-based groups on the residue surface indicated by FTIR (Fig. 2a) are known to become protonated under acidic conditions. These groups are available to capture the ion of interest, performing an interesting

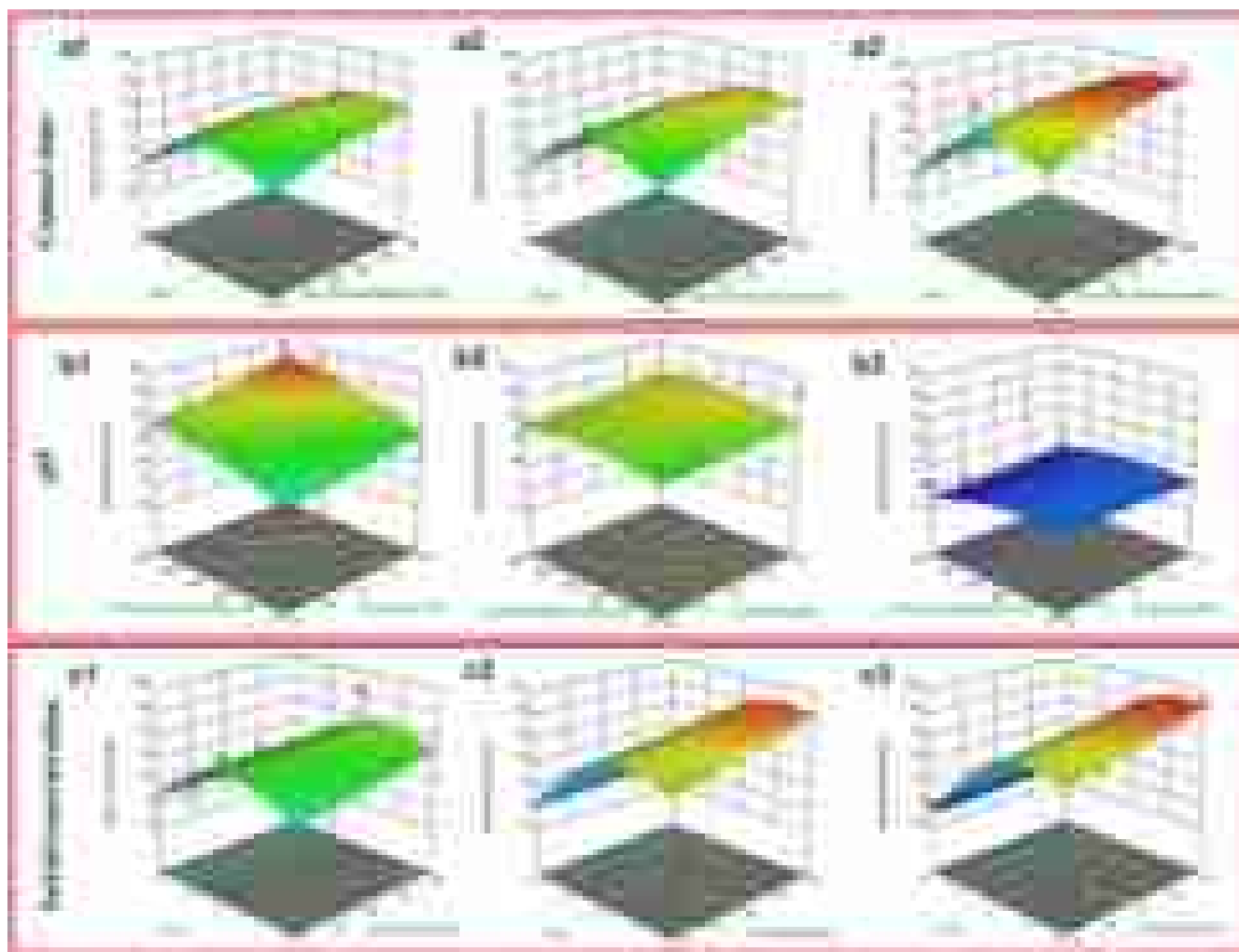


Fig. 4. Response surface plot of time and initial concentration where: Contact time (a1: 10 min; a2: 30 min, and a3: 90 min; pH (b1: 0; b2: 2, and b3: 4); and Initial concentration (c1: 50 mmol.L^{-1} ; c2: 588 mmol.L^{-1} , and c3: 800 mmol.L^{-1}). (The color changes from blue to red, indicating the removal rate gradually increases).

removal even at high concentrations. In aqueous media, Cr^{6+} ions tend to be found in the form of oxyanions (CrO_4^{2-} , $\text{Cr}_2\text{O}_7^{2-}$, or HCrO_4^-), and the capture of these species can occur through electrostatic interactions [61, 62]. In this sense, the good affinity of the biosorbent for Cr^{6+} oxyanions can be attributed to the positive charge and availability of the functional groups (or active sites) on the material's surface, which acts attractively for negative charges by an electrostatic mechanism. Therefore, it can be concluded that the best conditions studied for working with this metal involve a combination of the three key factors: an acidic pH of 0, a concentration of 800 mg.L^{-1} to be adsorbed, and a maximum contact time of 90 min, the latter being responsible for the adsorption peak.

Based on the experiments, the efficiency presented by the pine cone residue shows that the material can be a promising alternative, especially when compared to other materials (biochar or pine cone treated) since the material is used without any type of treatment to improve the contact surface [58,63–65]. In addition, the proposed material can be associated with complementary water treatment processes since the potability limit established by CONAMA, considering the hexavalent chromium content, is up to 0.5 mg.L^{-1} [CONAMA (2005) Resolução CONAMA n° 357/2005. 1–24] [66].

Fig. 5

The study of the chemical composition of the biosorbent is important to confirm the presence of metallic ions during the sorption process. Considering the best adsorbent material under optimal conditions (pH 0, concentration of 800 and 1000 mg.L^{-1} , and 90 min), the SEM with EDX shown in Figs. 6 and 7 shows Chromium's presence on the pine cone residue's surface, confirming that adsorption occurred.

Furthermore, FTIR analysis (Fig. 7) showed significant chemical modifications in the pine cone residue after adsorption. A comparison between the spectra before and after adsorption reveals changes in the functional groups associated with the interaction with Cr^{6+} ions. Notably, the reduction in intensity and band shifts played a fundamental role in adsorption. The differences in the bands generally indicate an interaction between the Cr^{6+} ions and the functional groups present in the biosorbent and that these groups were directly involved in the adsorption mechanism. Similar results were observed by Oliveira Júnior et al. [67], who used FTIR to analyze the pod shell of *Libidibia ferrea* before and after Cr^{6+} adsorption, evidencing changes in the functional groups of the biosorbent after interaction with metal ions. It's possible to see a decrease in intensity of the O—H stretching vibrations, which suggests that this functional group could be involved in the interaction with the Chromium ions [68] This observation was made by other studies as well, such as Shi et al. [69] and Singh and Mishra [70]. Similarly, the C = O vibrations peak had their intensity attenuated, this can be attributed to acetyl groups present in hemicellulose, which may interact with the chromium ions. This tendency is followed by C—H vibrations and C—O—C bonds at 1447 cm^{-1} and 1160 cm^{-1} , respectively. Thus, it's possible to assume that all these groups play a role in the phenomenon of chromium adsorption by this material. Additionally, it's possible to propose that the surface complexation of chromium ions is happening on this material [71].

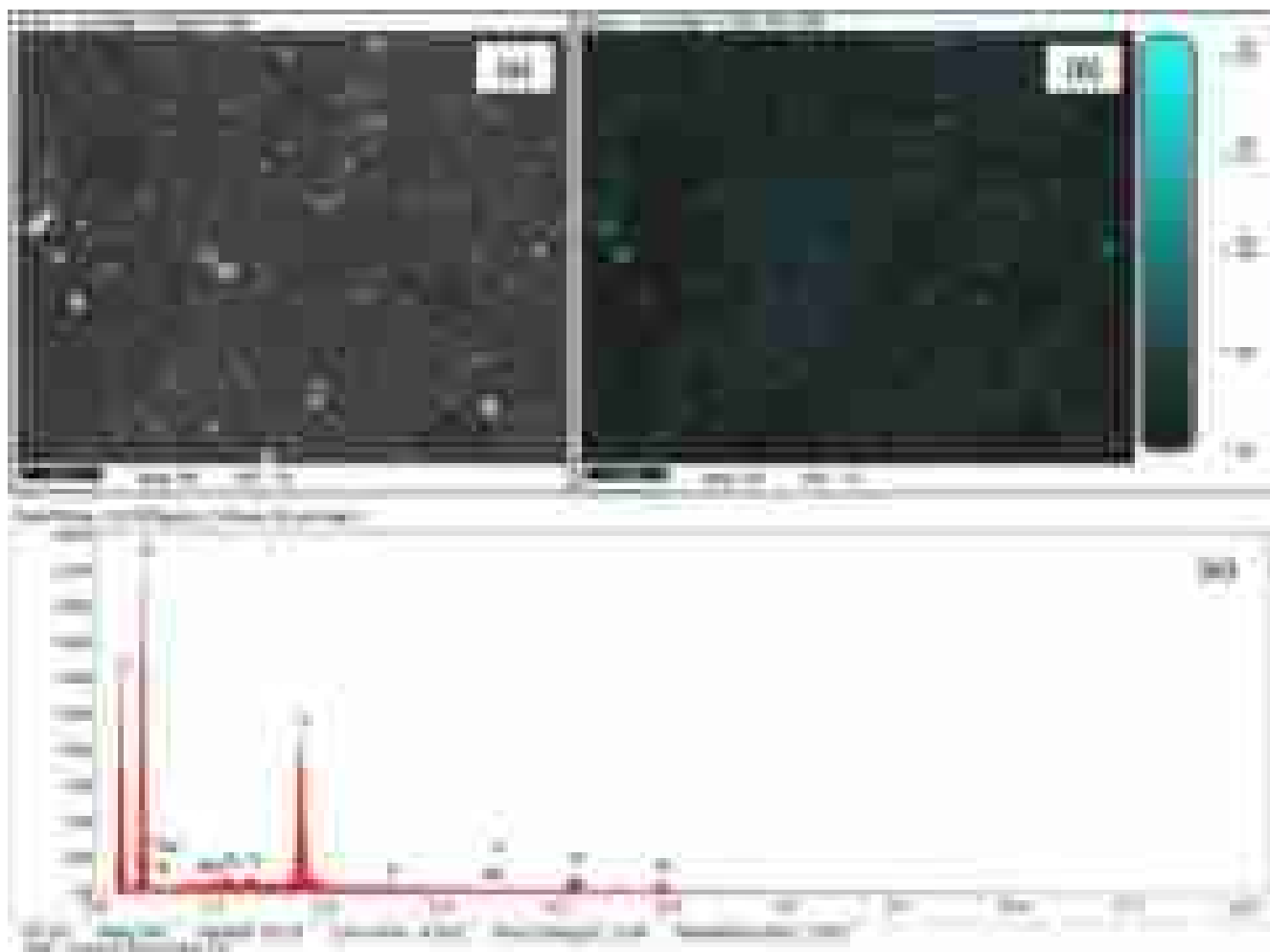


Fig. 5. EDX and SEM images of the selected pine cone residue under optimal conditions after adsorption (800 ppm).

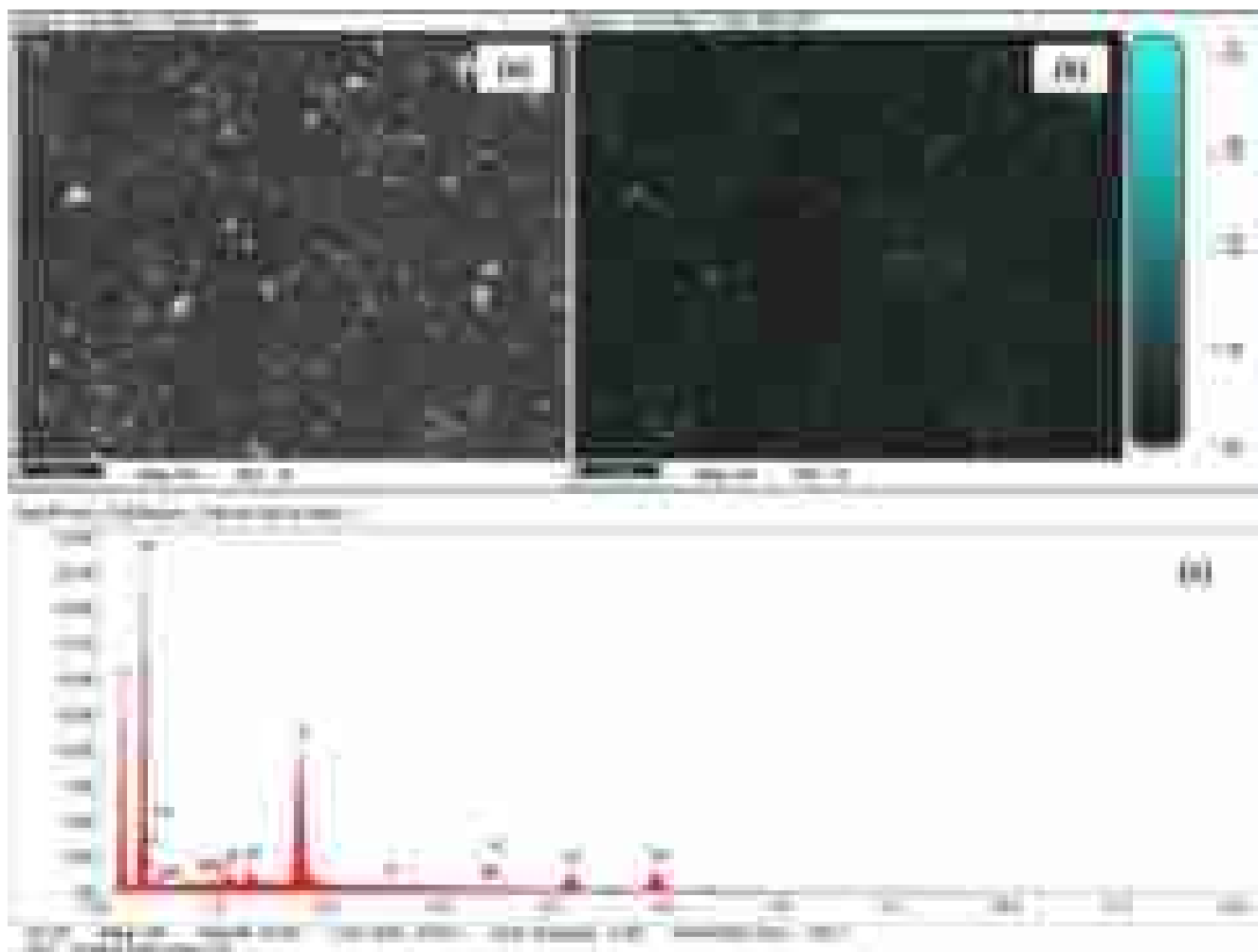


Fig. 6. EDX and SEM images of the selected pine cone residue under optimal conditions after adsorption (1000 ppm).

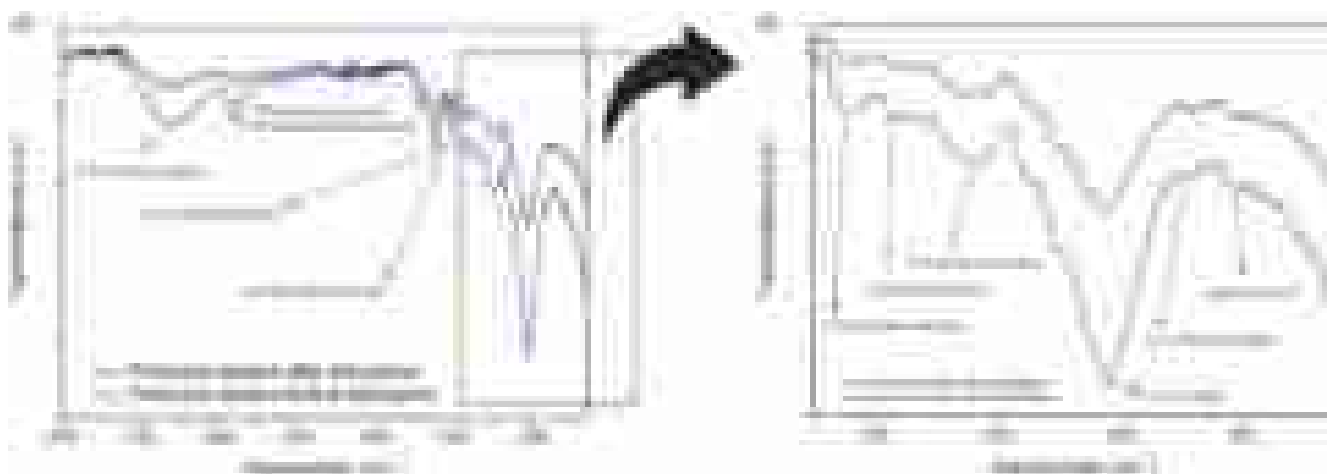


Fig. 7. FTIR comparative analysis: a) FTIR spectra of pinecone residue after and before adsorption in wavenumber 4000 to 650 cm^{-1} and b) FTIR spectra in wavenumber 1600 to 650 cm^{-1} .

3.5. Desorption and regeneration

The performance of the better adsorbent and its subsequent use can be done through the regeneration process proposed by Maia et al. [31]. Results showed that the pine cone residue remains highly efficient even

after multiple adsorption/desorption cycles, as displayed in Fig. 6. In the first experiment, the pine cone demonstrated an adsorption capacity of 49.3 mg.g^{-1} of Cr^{6+} . After the first desorption, 14 mg of Chromium per liter of the nitric acid solution was recovered, with a q_{el} coefficient of 2.08 mg.g^{-1} and a recovery rate of 4.22% , as shown in Fig. 8.

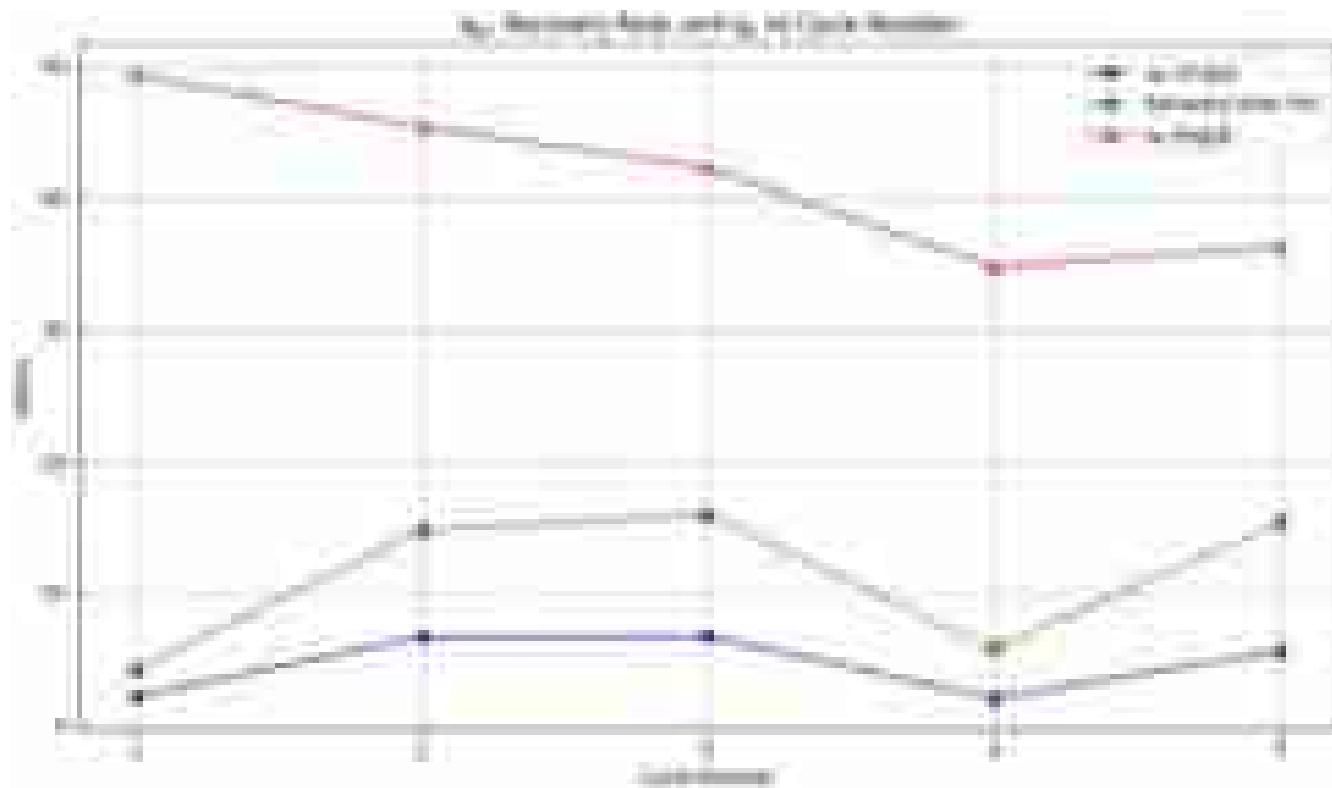


Fig. 8. Adsorption percentage of Cr⁶⁺ and pine cone residue recovery rate in reuse cycles.

In the following cycles, the adsorption capacity of the pine cone remained high, with values of 45.4, 42.3, 34.7, and 36.32 mg.g⁻¹ in cycles 2 to 5, respectively, demonstrating that even after five desorption cycles, the material still maintains its efficiency. The recovery rate increased after the first cycle, reaching a maximum of 15.91 % in the third cycle. This indicates that the pine cone was more willing to desorb Chromium after the first cycle and did not maintain a decreasing desorption trend. The desorption capacity, described by the q_{el} coefficient, also increased, peaking at 6.73 mg.g⁻¹ in the third cycle.

Thus, the pine cone residue, in addition to being a low-cost, natural, and unmodified waste material, can withstand numerous adsorption/desorption cycles, demonstrating its exceptional efficiency in removing contaminants like Cr⁶⁺. Katiyara and Katiyarb [72] evidenced two cycles without much difference in performance when evaluating the bio-sorption potential of magnetic pine cone hydrochar (MPHC) for chromium removal from wastewater.

3.6. Machine learning models

As explained in SubSection 2.6, this research aims to (i) identify a machine learning model capable of predicting the pine cone residue adsorption and (ii) to understand the behavior of the fiber under different experimental conditions.

The multiple linear regression model obtained from the experimental data is presented in Eq. (6), and the results are depicted in the parallel coordinate plot in Fig. 9. Each horizontal line in the plot represents the combination of attributes [i.e., contact time (x₁), pH (x₂) and the adsorbate concentration (x₃)] and the result [i.e., the percentage of Cr⁶⁺ adsorption (y)]. The colors of the horizontal lines indicate the percentage of Cr⁶⁺. Therefore, green horizontal lines represent a higher adsorption, and red lines a lower adsorption. Fig. 9 suggests that experiments with a pH of 4 have lower adsorption and should be avoided. Moreover, the contact time of 90 min has higher adsorption.

$$y = 0.5132 + 0.0018x_1 - 0.1378x_2 + 0.0001x_3 \tag{6}$$

The F-value is 9.989, and the hypothesis that all coefficients in the



Fig. 9. Comparison between the experimental data and the values estimated with multiple linear regression.

multiple linear regression are equal to zero can be rejected. Therefore, one can assume that there is a relation between the variables. The determination coefficient of the model in Eq. (6) is 0.541, which is relatively low. Moreover, the graph in Fig. 10 compares the experimental results (black line) with the linear regression estimates (red line). The red and the black lines in Fig. 10 are far from each other, which confirms the low accuracy of the multiple linear regression as indicated by the determination coefficient.

The standard deviation of the linear regression coefficients, their respective confidence interval, and p-value are presented in Table 2. The pH coefficient is negative, suggesting an inverse correlation with the percentage of Cr^{6+} adsorption. In other words, increasing the pH implies reducing the adsorption, which was also observed in the graph of Fig. 9. Moreover, the time coefficient is greater than the adsorbate concentration coefficient ($\theta_1 > \theta_3$), suggesting that increasing the time has a greater contribution to increasing the percentage of Cr^{6+} . The intercept (θ_0) and the pH (θ_2) have a p-value smaller than 0.05, implying that these two coefficients (θ_0 and θ_2) are different than zero.

Even though this first model was proven not to be the most accurate, it has provided meaningful insights on how to tune the experiment's parameters to potentially achieve better results. For instance, in a previous study, Zhu et al. [20] found that increasing the adsorbate concentration and decreasing the pH were the two most important factors to increase the adsorption of the pine cone residue. Nonetheless, in this study, we have identified that time also plays an important role when designing the experiment.

The second machine learning model is the decision tree regression, illustrated in Fig. 11. The decision tree shows the standardized values, as explained in SubSection 2.6.2, and the sequence of splits performed in the data. As can be seen, the pH (x_2) is the first variable used to split the data, confirming this attribute's importance as identified in the multiple linear regression. The determination coefficient of the decision tree regression is 0.978, suggesting a high accuracy of this approach. Fig. 11 compares the experimental data (black line) and the decision tree estimation (red line). The estimation seems to be precise except for the conditions with a time of 10 min, pH of 2, and a concentration of 588 ppm (point 10, 2, 588) and time of 30 min, pH of 0, and a concentration of 588 ppm (point 30, 0, 588).

Fig. 12

The last machine learning model tested is the random forest regression, with results shown in Fig. 13. Similar to the decision tree, this model is accurate as the determination coefficient is 0.921, and the experimental data (black line) and the random forest regressor (red line) in Fig. 13 are close to each other. Even though the random forest regression has a determination coefficient close to 1, the decision tree's coefficient is higher. Therefore, the decision tree obtained the best estimates for the pine cone residue adsorption of Cr^{6+} among the three machine learning models. Rather than conducting several experiments to predict the pine cone residue adsorption, future studies could save

Table 2

Statistical analysis of the linear regression coefficients.

Coefficient name	Coefficient value	Standard deviation	P-value	Confidence interval	
				Lower bound (2.5 %)	Upper bound (97.5 %)
Intercept (θ_0)	0.5132	0.110	0.000	0.285	0.741
Time (θ_1)	0.0018	0.001	0.175	-0.001	0.004
pH (θ_2)	-0.1378	0.027	0.000	-0.193	-0.083
Adsorbate concentration (θ_3)	0.0001	0.000	0.290	-0.000	0.000

time and use the decision tree model proposed in this research. Moreover, another avenue for future research is to use optimization methods (e.g., genetic algorithm, particle swarm optimization, greedy randomized adaptive search procedure) to find the best combination of the three attributes that maximize the pine cone residue adsorption of Cr^{6+} .

The results obtained in this research suggest that the relationship between the three attributes (i.e., contact time, pH, and adsorbate concentration) and the pine cone residue adsorption of Cr^{6+} is non-linear. Future studies could use non-linear machine learning models (e.g. decision trees, artificial neural networks) to estimate the pine cone residue adsorption of Cr^{6+} , considering other attributes, such as temperature and dosage. In addition, the objective of the machine learning models could be to increase the equilibrium adsorption capacity (q_e) instead of the percentage of Cr^{6+} adsorption.

In sum, this work highlights the dual benefit of environmental remediation and waste reuse, demonstrating that pine cone residues, coupled with machine learning models, can serve as an effective and scalable alternative for Cr^{6+} removal in aqueous systems. Future studies may explore additional process optimizations, such as adsorption efficiency (q_e), alternative machine learning approaches, use of the model judged as best for this type of prediction concluded in this study, reuse of the biosorbent in continuous adsorption cycles to increase practical applicability further, and the practical study of the application of pine cone residue in water treatment plants.

4. Conclusions

This study comprehensively evaluated the potential of pine cone waste as a sustainable and low-cost biosorbent for Cr^{6+} removal from aqueous solutions. By optimizing the adsorption conditions through an experimental design, we investigated the influence of contact time, initial adsorbate concentration, and pH on the removal efficiency. The results demonstrated that the maximum Cr^{6+} removal efficiency reached 90.84 %, even at short exposure times. The optimized adsorption conditions were identified as a biosorbent dosage of 51.38 mg.g^{-1} , a contact time of 90 min, and an acidic environment.



Fig. 10. Comparison between the experimental data and the values estimated with multiple linear regression.

To further improve the adsorption prediction, we applied three machine learning models: multiple linear regression, decision tree regression, and random forest regression. The decision tree regression model exhibited the highest predictive accuracy, with a correlation coefficient (R^2) of 0.978, confirming its suitability for modeling adsorption processes. This result highlights the potential of machine learning as a powerful tool for adsorption studies, reducing the need for extensive experimental trials and improving predictive capabilities.

In addition, this study highlights the value of agricultural residues by converting abundant and underutilized waste material into an efficient adsorbent for removing potentially toxic metal. The findings contribute to the development of environmentally friendly water treatment solutions, supporting global sustainability goals and strategies for managing industrial wastewater.

Ethical statements

It is not applicable.

CRediT authorship contribution statement

Joaquim G.G.S. Bento: Writing – original draft, Resources, Methodology, Investigation, Formal analysis, Data curation, Conceptualization. **Luidy F. Senra:** Writing – original draft, Validation, Software, Methodology, Investigation, Formal analysis, Data curation, Conceptualization. **Lana S. Maia:** Writing – original draft, Visualization, Methodology, Investigation, Formal analysis, Data curation, Conceptualization. **Luana Souza Almeida:** Writing – original draft, Software, Resources, Project administration, Methodology, Formal analysis. **Lucas M. Ferreira:** Resources, Methodology, Formal analysis. **Maria Ismênia S.T. Faria:** Writing – review & editing, Validation, Supervision, Resources, Methodology, Investigation, Formal analysis. **Derval S. Rosa:** Writing – review & editing, Validation, Supervision, Project administration, Investigation, Funding acquisition, Data curation, Conceptualization. **Daniella R. Mulinari:** Writing – review & editing, Validation, Supervision, Project administration, Investigation, Funding acquisition, Formal analysis, Data curation, Conceptualization.

Declaration of competing interest

The authors declare that they have no known competing financial interests or personal relationships that could have appeared to influence the work reported in this paper.

Acknowledgments

This research was funded by FAPERJ, Brazil (E-26/010.101232/2018, E-26/010/002530/2019, E-26/210.450/2021, and E-26/210.029/2024), FAPESP, Brazil (2020/13703-3, 2021/14714-1 and 2023/14598-7) and Conselho Nacional de Desenvolvimento Científico e Tecnológico - CNPq, Brazil (308053/2021-4 and 403934/2021-4). The authors thank the UFABC, CAPES (code 001), and REVALORES Strategic Unit. and Multiuser Central Facilities (CEM - UFABC), and FINEP (01.18.0071.00/0476/16).

Supplementary materials

Supplementary material associated with this article can be found, in the online version, at [doi:10.1016/j.surfin.2025.106460](https://doi.org/10.1016/j.surfin.2025.106460).

Data availability

Data will be made available on request.

Machine learning models and dataset for the prediction of Cr6+ removal of aqueous solutions using the pine cone residue (Original data) (Mendeley Data)

References

- [1] A. Fetimi, O. Kebiche-Senhadj, Y. Benguerba, G.S. Albakri, M.A. Alreshidi, M. Abbas, M. Hamachi, M. Bahita, S. Merouani, K.K. Yadav, Enhancing predictive accuracy for Cr(VI) removal in polymer inclusion membranes: a comparative study of machine learning models, *Inorganica Chim. Acta* 567 (2024) 122050, <https://doi.org/10.1016/j.ica.2024.122050>.
- [2] F. Fu, Q. Wang, Removal of heavy metal ions from wastewaters: a review, *J. Environ. Manage.* 92 (3) (2010) 407–418, <https://doi.org/10.1016/j.jenvman.2010.11.011>.
- [3] R. Ishtiaq, N. Zahra, S. Iftikhar, F. Rubab, K. Sultan, A. Abbas, S. Lam, Z.H. Jaffari, K.Y. Park, Adsorption of Cr(VI) ions onto fluorine-free niobium carbide (MXene) and machine learning prediction with high precision, *J. Environ. Chem. Eng.* 12 (2) (2024) 112238, <https://doi.org/10.1016/j.jece.2024.112238>.
- [4] Guidelines for drinking-water quality: fourth edition incorporating the first and second addenda www.who.int/publications/i/item/9789240045064.
- [5] M. Balamurali, M. Rajan, Coconut shells based MrGO@CMC adsorbent for the chromium (VI) ion removal from contaminated water through batch adsorption method, *Results Surf. Interfaces* 17 (2024) 100346, <https://doi.org/10.1016/j.rsurfi.2024.100346>.
- [6] N.S. Hassan, A.A. Jalil, M.B. Bahari, N.M. Izzuddin, N.A.F.M. Fauzi, N.W.C. Jusoh, M.F.A. Kamaruddin, R. Saravanan, H. Tehubijuluw, A critical review of MXene-based composites in the adsorptive and photocatalysis of hexavalent chromium removal from industrial wastewater, *Environ. Res.* 259 (2024) 119584, <https://doi.org/10.1016/j.envres.2024.119584>.
- [7] D. Mahringer, M. Lutz, M. Klumbies, S. Pabst, A.S. Ruhl, Reduction, coagulation and biotic filtration (RCbF) for Cr(VI) groundwater remediation – a case study, *J. Water. Process. Eng.* 65 (2024) 105867, <https://doi.org/10.1016/j.jwpe.2024.105867>.
- [8] P.B. Sujiritha, V.L. Vikash, G. Ponesakki, N. Ayyadurai, N.R. Kamini, Microbially induced carbonate precipitation with arthrobacter creatinolyticus: an eco-friendly strategy for mitigation of chromium contamination, *J. Environ. Manage* 365 (2024) 121300, <https://doi.org/10.1016/j.jenvman.2024.121300>.
- [9] M. Tan, S. Yang, C. Song, Z. He, J. Wang, Y. Liu, F. Liu, Y. Zhang, Selective removal of chromium and chloride by flow electrode capacitive deionization (FCDI) with carrier-facilitated ion exchange membrane, *Chem. Eng. J.* (2024) 156182, <https://doi.org/10.1016/j.cej.2024.156182>.
- [10] Y.H. Fseha, J.O. Eniola, B. Sizirici, S. Stephen, I. Yildiz, A. Khaleel, A. Adamson, Application of natural earth-based materials as adsorbents for the treatment of Chromium (VI)-contaminated tannery wastewater: box-Behnken and fixed-bed column optimization, *Sustain. Chem. Environ.* 7 (2024) 100127, <https://doi.org/10.1016/j.sceenv.2024.100127>.
- [11] F.A. Salam, A. Narayanan, Biosorption - a case study of hexavalent chromium removal with raw pomegranate peel, *Desalination Water Treat.* 156 (2019) 278–291, <https://doi.org/10.5004/dwt.2019.23554>.
- [12] A.H. Shobier, M.M. El-Sadaawy, G.F. El-Said, Removal of hexavalent chromium by ecofriendly raw marine green alga ulva fasciata: kinetic, thermodynamic and isotherm studies, *Egypt. J. Aquatic Res.* 46 (4) (2020) 325–331, <https://doi.org/10.1016/j.ejar.2020.09.003>.
- [13] N. Velinov, M. Petrović, V. Radović, K. Miljana, M. Miloš, B. Jelena, Danijela, A. Bojić, Characterization and application of wood-ZrO₂ sorbent for simultaneous removal of chromium (III) and chromium (VI) from binary mixture, *Nord. Pulp. Paper. Res. J.* 36 (2) (2021) 373–385, <https://doi.org/10.1515/npprj-2020-0082>.
- [14] N. Velinov, M. Radović Vučić, M. Petrović, M. Kostić, D. Bojić, A. Hurt, A. Bojić, Ultrasonic-assisted synthesis of wood-aluminium-based sorbents: comparison with conventional preparation and evaluation of chromium removal, *Wood. Mater. Sci. Eng.* 18 (3) (2023) 1065–1075, <https://doi.org/10.1080/17480272.2022.2105660>.
- [15] B. Taçi, S. Gashi, N. Daci, F. Podvorica, F. Sopaj, A versatile study of single and binary removals of Pb(II) and Cd(II) ions from aqueous solutions using pine cone as biosorbent, *Desalination Water Treat.* 319 (2024) 100465, <https://doi.org/10.1016/j.dwt.2024.100465>.
- [16] C. Kim, S. Lee, S. Park, Efficient micropore sizes for carbon dioxide physisorption of pine cone-based carbonaceous materials at different temperatures, *J. CO₂ Utiliz.* 54 (2021) 101770, <https://doi.org/10.1016/j.jcou.2021.101770>.
- [17] A. Banerjee, K. Jha, M. Petru, R. Kumar, S. Sharma, M.S. Saini, K.A. Mohammed, A. Kumar, M. Abbas, E.M. Tag-Eldin, Fabrication and characterization of weld attributes in hot gas welding of alkali treated hybrid flax fiber and pine cone fibers reinforced poly-lactic acid (PLA) based biodegradable polymer composites: studies on mechanical and morphological properties, *J. Mater. Res. Technol.* 27 (2023) 272–297, <https://doi.org/10.1016/j.jmrt.2023.09.252>.
- [18] H.S. Altundogan, A. Topdemir, M. Çakmak, N. Bahar, Hardness removal from waters by using citric acid modified pine cone, *J. Taiwan. Inst. Chem. Eng.* 58 (2015) 219–225, <https://doi.org/10.1016/j.jtice.2015.07.002>.
- [19] M. Abewaa, A. Arka, T. Haddis, A. Mengistu, T. Takele, E. Adino, Y. Abay, N. Bekele, G. Andualem, H. Girmay, Hexavalent chromium adsorption from aqueous solution utilizing activated carbon developed from Rumex abyssinicus, *Results. Eng.* 22 (2024) 102274, <https://doi.org/10.1016/j.rineng.2024.102274>.
- [20] X. Zhu, X. Wang, K. Liu, S. Zhou, U.F. Alqsair, A. El-Shafay, Machine learning simulation of Cr (VI) separation from aqueous solutions via a hierarchical nanostructure material, *J. Mol. Liq.* 350 (2022) 118565, <https://doi.org/10.1016/j.molliq.2022.118565>.
- [21] I. Maamoun, M.A. Rushdi, O. Falyouna, R. Eljamal, O. Eljamal, Insights into machine-learning modeling for Cr(VI) removal from contaminated water using nano-nickel hydroxide, *Sep. Purif. Technol.* 308 (2022) 122863, <https://doi.org/10.1016/j.seppur.2022.122863>.

- [22] S. Iftikhar, N. Zahra, F. Rubab, R. Abrar, F.A. Sumra, M.B. Khan, A. Abbas, Z. H. Jaffari, Artificial neural networks for insights into adsorption capacity of industrial dyes using carbon-based materials, *Sep. Purif. Technol.* 326 (2023) 124891, <https://doi.org/10.1016/j.seppur.2023.124891>.
- [23] S. Iftikhar, R. Ishtiaq, N. Zahra, F. Ruba, Z. Lam, A. Abbas, Z.H. Jaffari, Probabilistic prediction of phosphate ion adsorption onto biochar materials using a large dataset and online deployment, *Chemosphere* 370 (2025) 144031, <https://doi.org/10.1016/j.chemosphere.2024.144031>.
- [24] Z.H. Jaffari, H. Jeong, J. Shin, J. Kwak, C. Son, Y. Lee, S. Kim, K. Chon, K.H. Cho, Machine-learning-based prediction and optimization of emerging contaminants' adsorption capacity on biochar materials, *Chem. Eng. J.* 466 (2023) 143073, <https://doi.org/10.1016/j.ccej.2023.143073>.
- [25] Z.H. Jaffari, A. Abbas, C. Kim, J. Shin, J. Kwak, C. Son, Y. Lee, S. Kim, K. Chon, K. H. Cho, Transformer-based deep learning models for adsorption capacity prediction of heavy metal ions toward biochar-based adsorbents, *J. Hazard. Mater.* 462 (2024) 132773, <https://doi.org/10.1016/j.jhazmat.2023.132773>.
- [26] L. Guo, X. Xu, C. Niu, Q. Wang, J. Park, L. Zhou, H. Lei, X. Wang, X. Yuan, Machine learning-based prediction and experimental validation of heavy metal adsorption capacity of bentonite, *Sci. Total Environ.* 926 (2024) 171986, <https://doi.org/10.1016/j.scitotenv.2024.171986>.
- [27] F. Zhao, L. Tang, H. Jiang, Y. Mao, W. Song, H. Chen, Prediction of heavy metals adsorption by hydrochars and identification of critical factors using machine learning algorithms, *Bioresour. Technol.* 383 (2023) 129223, <https://doi.org/10.1016/j.biortech.2023.129223>.
- [28] J. Liu, J. Zhao, J. Du, S. Peng, S. Tan, W. Zhang, X. Yan, H. Wang, Z. Lin, Machine learning predicts heavy metal adsorption on iron (oxyhydr)oxides: a combined insight into the adsorption efficiency and binding configuration, *Sci. Total Environ.* 950 (2024) 175370, <https://doi.org/10.1016/j.scitotenv.2024.175370>.
- [29] O. Baatache, K. Derbal, A. Benalia, A. Khalifaoui, R. Bouchareb, A. Panico, A. Pizzi, Use of Pine cone as bio-coagulant for heavy metal removal from industrial wastewater: use of Box-Behnken design, *Ind. Crops. Prod.* 210 (2024) 118185, <https://doi.org/10.1016/j.indcrop.2024.118185>.
- [30] K. Faceli, A.C. Lorena, J. Gama, T.A. de Almeida, A.C.P.L.F. de Carvalho, *Inteligência Artificial: Uma abordagem de Aprendizado De Máquina, 2nd ed., LTC, 2023.*
- [31] L.S. Maia, P.H.F. Pereira, A.I.C. Da Silva, T.B. Da Costa, D.R. Mulinari, D.D.S. Rosa, A novel starch-based composite hydrogel enhanced by activated charcoal from the banana peel for water decontamination, *J. Appl. Polym. Sci.* 141 (29) (2024), <https://doi.org/10.1002/app.55685>.
- [32] K. Singh, R. Rastogi, S. Hasan, Removal of Cr(VI) from wastewater using rice bran, *J. Colloid. Interface Sci.* 290 (1) (2005) 61–68, <https://doi.org/10.1016/j.jcis.2005.04.011>.
- [33] D.C. Montgomery, G.C. Runger, *Estatística Aplicada e Probabilidade Para Engenheiros, 2nd ed., LTC, 2003.*
- [34] M. Zhang, H. He, Y. Huang, R. Huang, Z. Wu, X. Liu, H. Deng, Machine learning integrated high quantum yield blue light carbon dots for real-time and on-site detection of Cr(VI) in groundwater and drinking water, *Sci. Total Environ.* 904 (2023) 166822, <https://doi.org/10.1016/j.scitotenv.2023.166822>.
- [35] J. Bento, L. Senra, L. Maia, L. Souza Almeida, L. Ferreira, M.I. Faria, D. Rosa, D. Mulinari, Machine learning models and dataset for the prediction of Cr6+ removal of aqueous solutions using the pine cone residue, *Mendeley Data V1* (2025), <https://doi.org/10.17632/6b5pjk7bg.1>.
- [36] R. Kiseell, J. Poserina, *Regression models.* Elsevier Ebooks, 2017, pp. 39–67, <https://doi.org/10.1016/b978-0-12-805163-4.00002-5>.
- [37] E. Alpaydin, *Introduction to Machine Learning, 3rd edition,* MIT Press, 2014.
- [38] M. Khajavian, A. Haseli, Modeling the adsorption of ibuprofen on the Zn-decorated S,P,B co-doped C2N nanosheet: machine learning and central composite design approaches, *J. Industr. Eng. Chem.* 137 (2024) 583–592, <https://doi.org/10.1016/j.jiec.2024.04.002>.
- [39] Z.-Hua Zhou, *Machine learning.* Springer Nature eBook, 1st ed. 2021, Springer Singapore, 2021, <https://doi.org/10.1007/978-981-15-1967-3>.
- [40] N.S.S.V.S. Rao, S.J.J. Thangaraj, Flight ticket prediction using random forest regressor compared with decision tree regressor, in: 2023 Eighth International Conference on Science Technology Engineering and Mathematics (ICONSTEM), 2023, pp. 1–5, <https://doi.org/10.1109/ICONSTEM56934.2023.10142260>.
- [41] M.J. Amiri, M. Bahrami, S. Rajabi, Assessment of M5 model tree for prediction of azithromycin antibiotic removal by multi-wall carbon nanotubes in a fixed-bed column system, *AQUA – Water Infrastruct., Ecosyst. Society* 71 (4) (2022) 533–545, <https://doi.org/10.2166/aqua.2022.157>.
- [42] J. Prateek, *Artificial Intelligence with Python : a Comprehensive Guide to Building Intelligent Apps for Python Beginners and Developers,* Packt Publishing, 2017.
- [43] M. Bahrami, M.J. Amiri, S. Rajabi, M. Mahmoudi, The removal of methylene blue from aqueous solutions by polyethylene microplastics: modeling batch adsorption using random forest regression, *Alexandria Eng. J.* 95 (2024) 101–113, <https://doi.org/10.1016/j.aej.2024.03.100>.
- [44] Avila, J., & Hauck, T. (2017). *Scikit-Learn Cookbook - Second Edition.*
- [45] B. Beigzadeh, M. Bahrami, M.J. Amiri, M.R. Mahmoudi, A new approach in adsorption modeling using random forest regression, bayesian multiple linear regression, and multiple linear regression: 2,4-D adsorption by a green adsorbent, *Water Sci. Technol.* 82 (8) (2020) 1586–1602, <https://doi.org/10.2166/wst.2020.440>.
- [46] A.K. Hellum, Cone moisture and relative humidity effects on seed release from lodgepole pine cones from Alberta, *Can. J. Forest Res.* 12 (1) (1982) 102–105, <https://doi.org/10.1139/x82-015>.
- [47] R. Amen, M. Yaseen, A. Mukhtar, J.J. Klemes, S. Saqib, S. Ullah, A.G. Al-Sehemi, S. Raffiq, M. Babar, C.L. Fatt, M. Ibrahim, S. Asif, K.S. Qureshi, M.M. Akbar, A. Bokhari, Lead and cadmium removal from wastewater using eco-friendly biochar adsorbent derived from rice husk, wheat straw, and corncob, *Clean. Eng. Technol.* 1 (2020) 100006, <https://doi.org/10.1016/j.clet.2020.100006>.
- [48] N. Van Vinh, M. Zafar, S.K. Behera, H. Park, Arsenic(III) removal from aqueous solution by raw and zinc-loaded pine cone biochar: equilibrium, kinetics, and thermodynamics studies, *Int. J. Environ. Sci. Technol.* 12 (4) (2014) 1283–1294, <https://doi.org/10.1007/s13762-014-0507-1>.
- [49] M.R. Yazdani, N. Duimovich, A. Tiraferri, P. Laurell, M. Borghei, J.B. Zimmerman, R. Vahala, Tailored mesoporous biochar sorbents from pinecone biomass for the adsorption of natural organic matter from lake water, *J. Mol. Liq.* 291 (2019) 111248, <https://doi.org/10.1016/j.molliq.2019.111248>.
- [50] L. Gao, Z. Li, W. Yi, L. Wang, P. Zhang, Z. Wan, Y. Li, Quantitative contribution of minerals and organics in biochar to Pb(II) adsorption: considering the increase of oxygen-containing functional groups, *J. Clean. Prod.* 325 (2021) 129328, <https://doi.org/10.1016/j.jclepro.2021.129328>.
- [51] Y. Cai, J. Yang, Z. Ran, F. Bu, X. Chen, M. Shaaban, Q. Peng, Optimizing Typha biochar with phosphoric acid modification and ferric chloride impregnation for hexavalent chromium remediation in water and soil, *Chemosphere* 354 (2024) 141739, <https://doi.org/10.1016/j.chemosphere.2024.141739>.
- [52] W. Huang, R. Wu, J. Chang, S. Juang, D. Lee, Pristine and manganese ferrite modified biochars for copper ion adsorption: type-wide comparison, *Bioresour. Technol.* 360 (2022) 127529, <https://doi.org/10.1016/j.biortech.2022.127529>.
- [53] A. Kumar, V. Gupta, K.K. Gaikwad, Microfibrillated cellulose from pine cone: extraction, properties, and characterization, *BioMass Convers. Biorefin.* 13 (17) (2021) 1–8, <https://doi.org/10.1007/s13399-021-01794-2>.
- [54] I.L. Costa, P.H. Pereira, A.M. Claro, N.C.D. Amaral, H. Da Silva Barud, R.B. Ribeiro, D.R. Mulinari, 3D-printing pen from valorization of pine cone residues as reinforcement in acrylonitrile butadiene styrene (ABS): microstructure and thermal properties, *J. Thermoplast. Compos. Mater.* 36 (2) (2021) 535–554, <https://doi.org/10.1177/0892705721101273557>.
- [55] S.Z.N. Ahmad, W.N.W. Salleh, A.F. Ismail, N. Yusof, M.Z.M. Yusof, F. Aziz, Adsorptive removal of heavy metal ions using graphene-based nanomaterials: toxicity, roles of functional groups and mechanisms, *Chemosphere* 248 (2020) 126008, <https://doi.org/10.1016/j.chemosphere.2020.126008>.
- [56] H. Atmani, S. Zazouli, F.E. Bakkardouch, L. Laallam, A. Jouaiti, Insights into interactions of cellulose acetate and metal ions (Zn²⁺, Cu²⁺, and Ag⁺) in aqueous media using DFT study, *Comput.Theor. Chem* 1202 (2021) 113322, <https://doi.org/10.1016/j.comptc.2021.113322>.
- [57] J. Trifol, D.C.M. Quintero, R. Moriana, Pine Cone Biorefinery: integral valorization of residual biomass into lignocellulose nanofibrils (LCNF)-reinforced composites for packaging, *ACS. Sustain. Chem. Eng.* 9 (5) (2021) 2180–2190, <https://doi.org/10.1021/acscuschemeng.0c07687>.
- [58] O. Baatache, K. Derbal, A. Benalia, A. Khalifaoui, R. Bouchareb, A. Panico, A. Pizzi, Use of Pine cone as bio-coagulant for heavy metal removal from industrial wastewater: use of Box-Behnken design, *Ind. Crops. Prod.* 210 (2024) 118185, <https://doi.org/10.1016/j.indcrop.2024.118185>.
- [59] M. Chebbi, S. Ounoki, L. Youcef, F.N. Chergui, A. Amrane, Sustainable pine cone adsorbent: removal of prednisolone and pre-treatment of a medical lab wastewater, *Sustain. Chem. Pharm.* 39 (2024) 101565, <https://doi.org/10.1016/j.scp.2024.101565>.
- [60] A.E. Ofomaja, E.B. Naidoo, S.J. Modise, Kinetic and pseudo-second-order modeling of lead biosorption onto pine cone powder, *Ind. Eng. Chem. Res.* 49 (6) (2010) 2562–2572, <https://doi.org/10.1021/ie901150x>.
- [61] R. Garg, R. Garg, M. Sillanpää, N. Alimuddin, M.A. Khan, N.M. Mubarak, Y.H. Tan, Rapid adsorptive removal of chromium from wastewater using walnut-derived biosorbents, *Sci. Rep.* 13 (1) (2023), <https://doi.org/10.1038/s41598-023-33843-3>.
- [62] B.D. Pant, D. Neupane, D.R. Paudel, P.C. Lohani, S.K. Gautam, M.R. Pokhrel, B. R. Poudel, Efficient biosorption of hexavalent chromium from water by modified arcanut leaf sheath, *Heliyon* 8 (4) (2022) e09283, <https://doi.org/10.1016/j.heliyon.2022.e09283>.
- [63] N.K. Mondal, S. Chakraborty, Adsorption of Cr(VI) from aqueous solution on graphene oxide (GO) prepared from graphite: equilibrium, kinetic and thermodynamic studies, *Appl. Water. Sci.* 10 (2) (2020), <https://doi.org/10.1007/s13201-020-1142-2>.
- [64] M. Masuku, J.F. Nure, H.I. Atagana, N. Hlongwa, T.T. Nkambule, Pinecone biochar for the adsorption of chromium (VI) from wastewater: kinetics, thermodynamics, and adsorbent regeneration, *Environ. Res.* 258 (2024) 119423, <https://doi.org/10.1016/j.envres.2024.119423>.
- [65] M.B. Amar, K. Walha, V. Salvadó, Valorisation of pine cone as an efficient biosorbent for the removal of Pb(II), Cd(II), Cu(II), and Cr(VI), *Adsorption Sci. Technol.* 2021 (2021), <https://doi.org/10.1155/2021/6678530>.
- [66] Conselho Nacional do Meio Ambiente (CONAMA). (2005). Resolução nº 357, de 17 de março de 2005. https://www.icmbio.gov.br/cepsul/images/stories/legislacao/Resolucao/2005/res_conama_357_2005.classificacao_corpos_agua_rtfda_altrd_res_393_2007_397_2008_410_2009_430_2011.pdf.
- [67] J.A. Oliveira Júnior, R.R. de Souza, C.C. Nascimento, Evaluation of *Libidibia ferrea* (Fabaceae) pod skin as chromium adsorbent applied to a synthetic tanner effluent, *Scientia Plena* 20 (2024) 011701, <https://doi.org/10.14808/sci.plena.2024.011701>.
- [68] A.H.J. Aké, N. Rochdi, M. Jemo, M. Hafidi, Y. Ouhdouch, L. El Fels, Cr(VI) removal performance from wastewater by *microflora* isolated from tannery effluents in a semi-arid environment: a SEM, EDX, FTIR and zeta potential study, *Front. Microbiol.* 1 (15) (2024) 1423741, <https://doi.org/10.3389/fmicb.2024.1423741>.

- [69] X. Shi, B. Gong, S. Liao, J. Wang, Y. Liu, T. Wang, J. Shi, Removal and enrichment of Cr(VI) from aqueous solutions by lotus seed pods, *Water Environ. Res.* 92 (1) (2020) 84–93, <https://doi.org/10.1002/wer.1187>.
- [70] V. Singh, V. Mishra, Sustainable reduction of Cr (VI) and its elemental mapping on chitosan coated *citrus limetta* peels biomass in synthetic wastewater, *Sep. Sci. Technol.* 57 (10) (2021) 1609–1626, <https://doi.org/10.1080/01496395.2021.1993921>.
- [71] M. Masuku, J.F. Nure, H.I. Atagana, N. Hlongwa, T.T.I. Nkambule, Pinecone biochar for the adsorption of chromium (VI) from wastewater: kinetics, thermodynamics, and adsorbent regeneration, *Environ. Res.* 258 (2024) 119423, <https://doi.org/10.1016/j.envres.2024.119423>.
- [72] S. Katiyar, R. Katiyar, A parametric optimization for leveraging the potential of ammonia modified magnetic pine cone hydrochar for Cr (VI) contaminated wastewater treatment, *Biocatal. Agric. Biotechnol.* 60 (2024) 103286, <https://doi.org/10.1016/j.bcab.2024.103286>.

Exploring the Potential of Multiple Brazilian Clays as Adsorbents in Corn Starch Hydrogels for the Removal of Potentially Toxic Metal

Rafaela R. Ferreira,^[a] Lana S. Maia,^[a] Paulo H. F. Pereira,^[b] Romualdo R. Menezes,^[c] Daniella R. Mulinari,^[b] and Derval S. Rosa^{*[a]}

Modern industrialization has led to heavy metal contamination of vital natural resources for animals and humans. This study explores eco-friendly strategies to address this issue, focusing on synthesizing a starch hydrogel (SH) composite reinforced with six clays: brasgel (B), chocobofo (Cb), cloisite 20A (C20A), chocolate (Ch), palygorskite (P), and treated palygorskite (Tp). Physical–chemical, morphological, and thermal properties of the hydrogels were evaluated, along with their capacity to remove metallic ions (Cr(VI), Cd(II), Ni(II), Mn(II), Zn(II), and Cu(II)) via ion chromatography. FTIR confirmed successful clay incorporation into the hydrogel structure, with Van der Waals interactions most prominent with Ch clay. The clays enhanced three-dimensional

(3D) porous structures with accessible functional groups, improving ion removal. All hydrogels showed increased d-spacing of clays (except Cb), indicating intercalated/exfoliated composites, which improved water absorption and thermal resistance. Sorption data revealed significant metal ion absorption, particularly Cr(VI) oxyanions. For divalent ions, the affinity order was Mn(II) > Zn(II) > Cu(II) > Cd(II) > Ni(II). Notably, SH-Cb and SH-Ch hydrogels excelled in metal ion adsorption, proving their effectiveness. Overall, clay-reinforced hydrogels effectively treated contaminated effluents, offering a promising solution to heavy metal pollution.

1. Introduction

Water is the most necessary and significant element for all life, but water resources have been plagued by pollution from both organic and inorganic sources, which originates from industrial, agricultural, and everyday waste, leading to an increasing scarcity of water.^[1] Water pollution has wide-ranging environmental impacts, including ecosystem degradation, biodiversity loss, and risks to human health.^[2] These activities release pollutants such as heavy metals, chemicals, and other hazardous substances into water bodies.^[3–5] In this context, heavy metal ions are transferred between animals and plants through the food chain and can also cause serious harm to humans.^[6] The metal elements Hg, Cd, Cu, Pb, Zn, Ni, Co, Sb, Cr, and the metalloid with a specific gravity greater than 5.0 g cm⁻³, com-

monly known as potentially toxic elements (PTEs), are present at significant levels in wastewater from various sources, including industrial and agricultural sources.^[7–9] Therefore, finding an efficient and sustainable method to treat emerging PTEs in wastewater is urgent. Advanced oxidation processes (AOPs), such as photocatalysis,^[10] microwave catalysis,^[11] coagulation,^[12] and photo-remediation,^[13] are commonly used for treating industrial effluent. However, specific techniques are applied to remove metallic ions from wastewater. These techniques include solvent extraction,^[14,15] reverse osmosis,^[16] ion exchange,^[17] chemical precipitation,^[18] membrane filtration,^[19] electrochemistry,^[20] bio-electrochemical methods,^[21] and adsorption.^[22,23] Among these methods, adsorption is a simple process for removing pollutants and has been observed to be advantageous over other wastewater treatment methods due to its simplicity, economic viability, high performance, and the possibility of reusing the adsorbent.^[22,24] It is considered the most effective method for treating low concentrations of contaminants.^[25]

Adsorption has been extensively studied as an efficient technique for removing PTEs from wastewater, employing various adsorbent materials.^[26–28] Numerous studies have demonstrated the effectiveness of different materials in removing metallic ions, such as Cr(VI), Cu(II), Cd(II), Ni(II), Mn(II), and Zn(II). For example, natural clays are effective in removing Cu(II), Zn(II), and Cd(II) ions.^[29,30] At the same time, activated carbon has shown promising results in removing Pb(II) and Hg(II) from water samples.^[31] Cryogels made of polyethyleneimine (PEI) have been successfully utilized to remove Cd(II), Cr(VI), Ni(II), and Zn(II) ions from wastewater.^[32] Additionally, biochar derived from fruit residues is effective in removing Pb(II), Cd(II), and Ni(II) from wastewater.^[33] These materials exhibit significant potential for application in removing PTEs from industrial effluents. Further research in

[a] R. R. Ferreira, L. S. Maia, D. S. Rosa

Center for Engineering, Modeling, and Applied Social Sciences (CECS), Federal University of ABC (UFABC), Rua Catequese, 242, Santo André-SP, Bairro Jardim CEP: 09090-400, Brazil
E-mail: dervalrosa@yahoo.com.br

[b] P. H. F. Pereira, D. R. Mulinari

State University of Rio de Janeiro (UERJ), Department of Mechanic and Energy, Rua Fonseca Teles, 121, 2nd floor, Resende, Rio de Janeiro CEP 20940-903, Brazil

[c] R. R. Menezes

Laboratory of Materials Technology (LTM), Department of Materials Engineering, Federal University of Campina Grande (UFCG), Av. Aprígio Veloso 882, State of Paraíba, Campina Grande 58429-900, Brazil

© 2025 The Author(s). ChemistrySelect published by Wiley-VCH GmbH. This is an open access article under the terms of the [Creative Commons Attribution](#) License, which permits use, distribution and reproduction in any medium, provided the original work is properly cited.

this field could lead to the development of more efficient and sustainable methods for wastewater treatment.

Recently, using novel adsorbents with high efficiency, fast rates, and easy regeneration has attracted significant attention. For the adsorbent materials, the amount and accessibility of active sites on the surface play an essential role in obtaining an ideal adsorbent for the adsorption process.^[34] The most common adsorbents are activated charcoal,^[35] polymers,^[35] carbon nanotubes,^[36] biomass,^[37] hydrogels.^[23,28] Bekchanov et al. present a comprehensive review of the scientific advances of the last decade in the development of green adsorbents, with a focus on cellulose and starch-based functional materials for the efficient removal of heavy metal ions from aqueous solutions.^[38] Among several materials, polysaccharide-based hydrogels are a type of polymer material with a three-dimensional (3D) network porous structure with a high specific surface area, high porosity, and surface activity (functional groups) for removing PTEs in wastewater.^[26,39–42] Additionally, hydrogels possess processing simplicity, high selectivity, high performance, proper mechanical strength, excellent biocompatibility and biodegradability, and easy recyclability.^[34,41–44] Regarding the adsorption properties, the performance of hydrogels can be improved by incorporating fillers into their structure.^[45,46] Various reinforcements can be used, such as cellulose nanofibrils,^[47] activated charcoal,^[48] carbon nanotubes,^[49] clays, and clay nanotubes.^[50–52]

Pure starch and other polysaccharide-based materials underperform advanced adsorbents due to low surface areas. A promising strategy to improve these adsorbents is to incorporate inorganic lamellar materials, such as clays and clay minerals, into the crosslinked starch network.^[53] Clays are formed primarily from a negatively charged layer of aluminosilicate/silica minerals and are known as high-potential cationic adsorbents due to their relatively large surface areas.^[54] Ion exchange reactions are the main mechanisms of adsorption of heavy metal ions that occur through the formation of inner-sphere complexes through the Si-O- and Al-O- groups on the edges of clay particles.^[55] This approach is feasible and cost-effective, potentially improving starch-based adsorbents. In a previous study, we individually characterized several clays regarding their physicochemical and adsorptive properties.^[56] In the present work, we advanced this research by incorporating these natural clays into starch-based hydrogels. We aim to evaluate how their inclusion modifies the hydrogel's structure, stability, and metal removal efficiency. This combined strategy—integrating well-characterized natural clays into a biodegradable hydrogel matrix—has not been sufficiently explored in literature. Our approach enhances the material's properties and offers a cost-effective and environmentally friendly solution for multi-metal removal from industrial effluents.

2. Materials and Methods

2.1. Materials

Corn starch (Amidex 3001%–27% wt. by mass of amylose and 73% wt. by mass of amylopectin) was purchased from Ingre-

dion Incorporated (São Paulo, Brazil). Sodium hydroxide (NaOH, 98%), zinc nitrate ($\text{Zn}(\text{NO}_3)_2 \cdot 6\text{H}_2\text{O}$, 98%), and nickel nitrate ($\text{Ni}(\text{NO}_3)_2 \cdot 6\text{H}_2\text{O}$, 99%) were purchased from Dynamics Contemporary Chemistry, cadmium nitrate ($\text{Cd}(\text{NO}_3)_2 \cdot 4\text{H}_2\text{O}$, 98%) was acquired from Neon Chemistry, potassium dichromate ($\text{K}_2\text{Cr}_2\text{O}_7$, 99%) was obtained from ECIBRA Analytical Reagents, copper nitrate ($\text{Cu}(\text{NO}_3)_2 \cdot 3\text{H}_2\text{O}$, 99%), and citric acid ($\text{C}_6\text{H}_8\text{O}_7$, 99.5%) were acquired from Synth. Manganese nitrate ($\text{Mn}(\text{NO}_3)_2 \cdot 4\text{H}_2\text{O}$, 98%) was acquired from Sigma-Aldrich. The standard stock solutions of 1000 mg L⁻¹, 99.9% purity (hexavalent chromium, copper, cadmium, manganese, nickel, and zinc) were acquired from Specscol. The clays brasgel (B), chocobofo (Cb), and chocolate (Ch) were supplied by the company BENTONISA–Bentonita do Nordeste S.A., located in the city of Boa Vista/PB. Cloisite 20A (C20A) was purchased from Southern Clay Products, TX, USA. The palygorskite (P) and treated palygorskite (Tp) used were supplied by União Brasileira de Mineração SA (UBM, Guadalupe, Piauí, Brazil).

2.2. Hydrogels Synthesis

For neat starch hydrogel (SH) synthesis, an adequate amount of starch was dispersed in a predetermined amount of distilled water with a mixing rate of 280 rpm. This solution was heated at 40 °C and maintained in constant agitation to achieve complete dissolution. Then, the NaOH was added to the solution, and after 3 h, citric acid ($\text{C}_6\text{H}_8\text{O}_7$) was added, resulting in the hydrogels' immediate crosslinking. After 17 h, the hydrogels were submitted to the water bath at 90 °C for 1 h to ensure complete crosslinking of the new bonds. Later, the prepared materials were poured into plastic molds and dried in an oven at 70 °C for 48 h.

For the synthesis of SH composites filled with clay, a similar procedure was realized. The difference is in the insertion of clays indicated by the name starch-based hydrogels (SH-5%X). The X represents six clays studied: brasgel (B), chocobofo (Cb), chocolate (Ch), cloisite 20A (C20A), palygorskite (P), and treated palygorskite (TP). The clays were added along with starch to facilitate dissolution in distilled water. Figure 1 illustrates the methodology for obtaining hydrogels.

2.3. Characterization

2.3.1. Attenuated Total Reflectance Fourier-Transform Infrared Spectroscopy (ATR-FTIR)

A Fourier-transform infrared spectrophotometer (Spectrum 100, Perkin Elmer, Inc., Massachusetts, USA) equipped with an attenuated total reflectance accessory (ATR) was used to investigate the sample's functional groups and their attributed vibrations. The spectrophotometer was operated in transmittance mode, covering the wavenumbers in a range of 650 to 4000 cm⁻¹, with a spectral resolution of 4 cm⁻¹.

2.3.2. Scanning Electron Microscopy (SEM)

The SEM technique obtained morphology, structure, and pore size (FEI Quanta 250, Thermo Fisher Scientific, USA). The mate-



Figure 1. Methodology adopted for obtaining neat hydrogel (a) and hydrogel composite (b).

rials were fractured in liquid N_2 to analyze the fracture region. Samples were covered with a thin layer of gold with a thickness of 25 nm (Sputtering Leica EM ACE200, Leica Microsystems, Germany). The micrographs were obtained under the conditions: current of 50 pA, voltage of 10 kV, and spot size of 4 nm. Pore size distribution of SHs was performed using ImageJ software.

2.3.3. X-Ray Diffraction (XRD)

Crystallinity and structural changes in starch-based hydrogels were evaluated by XRD. Thus, a diffractometer STOE-STADI P, varying the range in 2θ , from 10 to 80.735, a pass of 0.015 was used. Curve monochromator of Germanium (111) and radiation of $CuK\alpha 1$ was used, with a wavelength of 1.54 nm and an integration time of 60s for a kind of 1.05. The d-spacing was calculated using Bragg's law as described by Equation (1):^[57]

$$d = \frac{n\lambda}{2\sin\theta} \quad (1)$$

where:

- D is the spacing of the diffracting planes in Å.
- λ is the wavelength of the incident X-ray (1.5406 Å).
- θ is the peak position in radians.
- n is the order of diffraction ($n = 1$).

2.3.4. Thermogravimetric Analysis (TGA)

TGA was realized to detect the samples' thermal stability and decomposition temperature using an SDT Q600 thermogravi-

metric analyzer from TA Instruments. The temperature range was 30 °C–700 °C under an N_2 atmosphere (10 mL min^{-1}) at a heating rate of 10 °C min^{-1} . The data acquired through TGA generated a TG curve, from which its derivative (DTG) was derived. The TG graph offered insights into T_{ONSET} (°C), residue (%), and DTG values representing the T_{MAX} (°C) of the samples. The study of the heat-resistance index was made using Equation (2):

$$T_{\text{HRI}} = 0.49 \times [T_{5\%} + 0.6 \times (T_{30\%} - T_{5\%})] \quad (2)$$

where:

- T_{HRI} is the heat resistance in °C.
- $T_{5\%}$ is the temperature at 5% weight loss in °C.
- $T_{30\%}$ the temperature at 30% weight loss in °C.

2.3.5. Degree of Swelling

The hydrogel's degree of swelling (DS) was evaluated using Equation (3). The SH and their hydrogel composites were weighed on an analytical balance to obtain the dry mass. Then, the dried sample pieces were submerged in 40 mL of distilled water at room temperature, considering the time range of 0 to 2880 min. For each defined time, the samples were taken out in distilled water, and with the auxiliary paper tissue, all the water present on the surface was removed. Then, the specimens were weighed and immersed again. The experiments were realized in triplicate.

$$DS = \frac{m_f - m_i}{m_i} \cdot 100 \quad (3)$$

where M_t is the swollen hydrogel mass at a time t in grams and M_i is the dried hydrogel mass ($t = 0$) in grams. The water diffusion mechanism was estimated following Equation (4), where W_t and W_e are the water masses diffused in the hydrogel network at time t and equilibrium e , respectively, k is a constant, and n is a parameter that describes the diffusion mechanism.

$$\frac{W_t}{W_e} = kt^n \quad (4)$$

2.3.6. PTEs Sorption

PTEs are found in wastewater samples with other organic and inorganic contaminants.^[58] The affinity of clays, neat hydrogel, and its hydrogel composite was investigated in simulated effluent containing six coexisting ions (Cr(VI), Cd(II), Ni(II), Mn(II), Zn(II), and Cu(II)). Metal solutions were prepared by dissolving the metal salts ($K_2Cr_2O_7$, $Cd(NO_3)_2 \cdot 4H_2O$, $Ni(NO_3)_2 \cdot 6H_2O$, $Mn(NO_3)_2 \cdot 4H_2O$, $Zn(NO_3)_2 \cdot 6H_2O$, and $Cu(NO_3)_2 \cdot 3H_2O$) in ultra-pure water at pH 3.5–4.0. The total concentration of competing ions (Cr(VI), Cd(II), Ni(II), Mn(II), Zn(II), and Cu(II)) was $0.963 \text{ mmol L}^{-1}$ ($0.161 \pm 0.024 \text{ mmol L}^{-1}$ each). The tests were carried out under stirring ($\sim 150 \text{ rpm}$) at room temperature ($\sim 25 \text{ }^\circ\text{C}$), with a dosage of 1.0 g L^{-1} and pH 3.5–4.0 in Erlenmeyer flasks (125 mL). After 24 h, the metals' concentrations were measured by ion chromatography, IC (940 Professional IC Vario, Metrohm, Switzerland). Removal rates (%) were calculated by Equation (5):

$$\%R = \left(\frac{C_0 - C_e}{C_0} \right) \cdot 100 \quad (5)$$

where:

- C_0 is the PTEs metals initial concentration (mmol L^{-1}).
- C_e is the PTEs metals concentration at equilibrium (mmol L^{-1}).

3. Results and Discussion

3.1. Attenuated Total Reflectance Fourier-Transform Infrared Spectroscopy (ATR-FTIR)

FTIR analysis was employed to evaluate the crosslinking process during hydrogel production, and the obtained spectrum is presented in Figure 2a. The starch showed several characteristic peaks that were identified at 3300, 2934, 1640, 1456, and 1337 cm^{-1} , which can be associated with specific vibrations: the stretching vibration of O–H groups,^[59] the stretching vibration of the C–H bond present in aliphatic methyl ($-\text{CH}_3$) or methylene ($-\text{CH}_2$) groups,^[60] to the vibrational elongation of the carbonyl group ($\text{C}=\text{O}$),^[61] and water molecules are contained within the starch structure,^[62] respectively. The peaks at 1456 cm^{-1} and 1337 cm^{-1} are related to the twisting and shearing of carbon atoms ($-\text{CH}_2$), respectively.^[63] The hydrogel sample spectrum presented similar peaks at 3300 and 2934 cm^{-1} , but a change between 1500 and 1250 cm^{-1} was observed, which can be attributed to aliphatic bonds, indicating conformational changes of the carbon–carbon bonds,

resulting in the crosslinking process, correlating with the retrogradation and reorganization of the amylose to amylopectin chains.^[64,65] This reaction involves the interaction between the crosslinking agents and the hydroxyl groups present in the chemical structure of starch.^[66] Thus, a mechanism can be proposed for the action of citric acid during the crosslinking reaction to produce the SHs, as shown in Figure 2b. Camani and coworkers also prepared corn-starch-based aerogels using trisodium citrate. They observed a similar trend: the crosslinking agent formed an interconnected network through the reaction with amylose and amylopectin chains (starch retrogradation).^[67]

Figure 3 presents the FTIR spectra of various clays in the mid-infrared region and their hydrogels. Evaluating the clay spectra, samples B, Cb, Ch, and C20A exhibited bands at $3630\text{--}3387 \text{ cm}^{-1}$, corresponding to the axial stretching vibration of the –OH group and water adsorbed between their lamellae. All spectra showed changes in the bands close to 3300 cm^{-1} , with an increase in the intensity of this band for Cb and Ch clays. The B clay exhibits a band at 1630 cm^{-1} related to water deformation and characteristic Si–O–Si bonds in the $1116\text{--}1004 \text{ cm}^{-1}$ and $915\text{--}523 \text{ cm}^{-1}$ regions.^[68] Moreover, Cb and Ch showed bands related to symmetric and asymmetric stretching vibrations of Si–O–Si groups.^[68,69] The clay C20A exhibits a doublet at 2920 and 2852 cm^{-1} for CH_2 asymmetric and symmetric stretching, respectively. It also shows peaks at 1637 cm^{-1} (H–O–H bending), 1468 cm^{-1} (CH_2 plane scissoring), 1011 cm^{-1} (silicate Si–O bond stretching), and 796 cm^{-1} (CH bending out of plane).^[70,71] The bands at $3680\text{--}3698 \text{ cm}^{-1}$, corresponding to Mg3-OH groups, confirmed that clays B, Cb, Ch, and C20A possess smectite structures.^[72]

Regarding P and Tp clays, bands at 3625 and 3404 cm^{-1} were associated with water molecules coordinated to the magnesium atom at the edge of the octahedral sheet. Furthermore, additional bands at 1654 and 1434 cm^{-1} were assigned to water's bending and carbonates' asymmetric stretching vibration, respectively.^[73] The band at 1191 cm^{-1} is considered specific to fibrous clay minerals (palygorskite) due to the inversion of Si–O–Si bonds between the tetrahedra. A shift from 1654 to 1649 cm^{-1} was observed in the organo-functionalized Tp sample, with decreased intensity after treatment. Notably, new bands at 1517 and 1386 cm^{-1} were also observed, likely attributed to asymmetric and symmetric stretching of the carboxyl group, indicating interactions between the active sites and the surface of functionalized clays.^[74,75]

For all systems, the pure and clay-containing hydrogel spectra were very similar, with no drastic changes or new peaks in the fingerprint region, indicating that no new bonds were involved besides those of hydrogel crosslinking. However, evaluating the hydroxyl band, it was possible to observe an intensity reduction in the spectra of the SH-B, SH-C20A, SH-P, and SH-Tp samples, comparing them with the neat hydrogel spectrum (SH). One of the possible hypotheses is that during the 17 h crosslinking process, the clay available in the system becomes trapped and crosslinked. Dai et al. and Ghafelebashi et al. suggest that the incorporation of clays may serve as a physical crosslinking agent, promoting the formation of crosslinked hydrogels

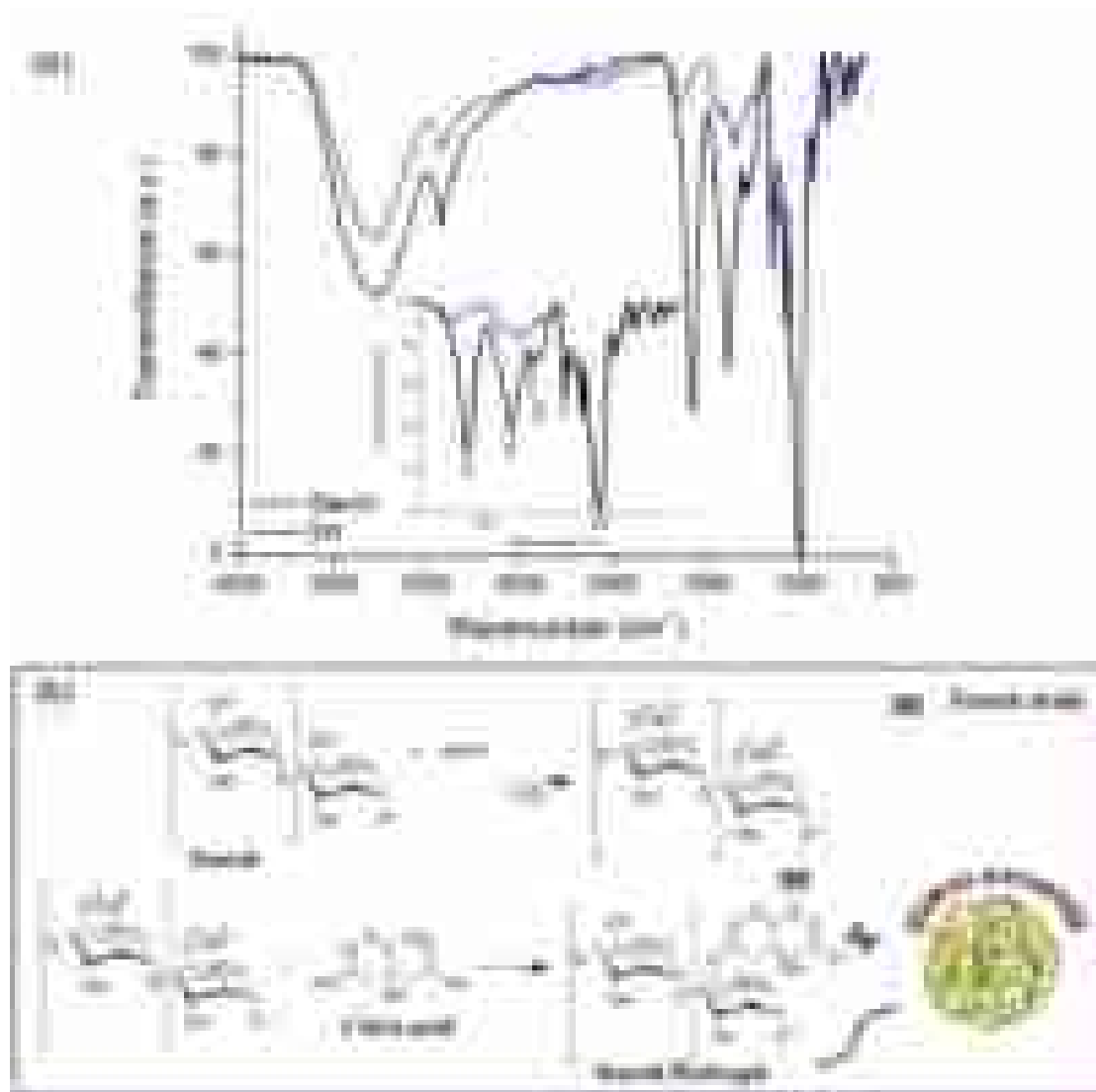


Figure 2. Fourier transform infrared spectroscopy (FTIR) spectra: a) for starch and SH. b) Illustration of equations referring to the synthesis route of SHs and showing possible covalent crosslinking.

through hydrogen bonding interactions,^[76,77] which may happen due to increased interaction between the unreacted acid and the hydroxyl groups present in both the starch structure and the clay.^[78] Another hypothesis would be that the clay was internally retained in the hydrogel structure and crosslinked during the process, consuming the hydroxyls of both the hydrogel and the clay, which could restrict the mobility of silicate groups that have variable charges, which are responsible for the adsorption of anions by clay minerals. This may influence the sorption results due to the lower availability of functional groups.^[79]

The SH-Cb and SH-Ch hydrogels had different behavior, where an increase in the band's intensity was observed, referring to the hydroxyls present in the material. This behavior can be attributed to the structure of the smectite clay, composed of an octahedral alumina layer between two opposite tetrahedral layers of silica. This structure may allow the functional groups of these clays to interact less strongly during

the reticulation process, allowing greater surface availability in the obtained material. These behaviors may increase the availability of both the hydrogel and clay functional groups, which may influence sorption capabilities. It is worth mentioning that SH-Cb clay had a more significant change in the FTIR spectrum, with sudden changes in peaks such as the appearance of peaks at 1453, 1294, 1257 cm⁻¹, doublet formation at 1153 and 1135 cm⁻¹, and 937, 917, 754, 729 cm⁻¹. The appearance of peaks in these regions may indicate the presence of Cb clay, as highlighted by Silva, Scheibler, and Rodrigues, who observed peaks at 1050 cm⁻¹ and around 920 cm⁻¹, related to the vibrations of the Si-O groups -Si from the silicate tetrahedral layers and to the Al-OH-Al groups from the alumina octahedral layers.^[80] All these results indicated the successful incorporation of the clays into the SH structure, which presented distinct behaviors depending on the clay's natural composition.

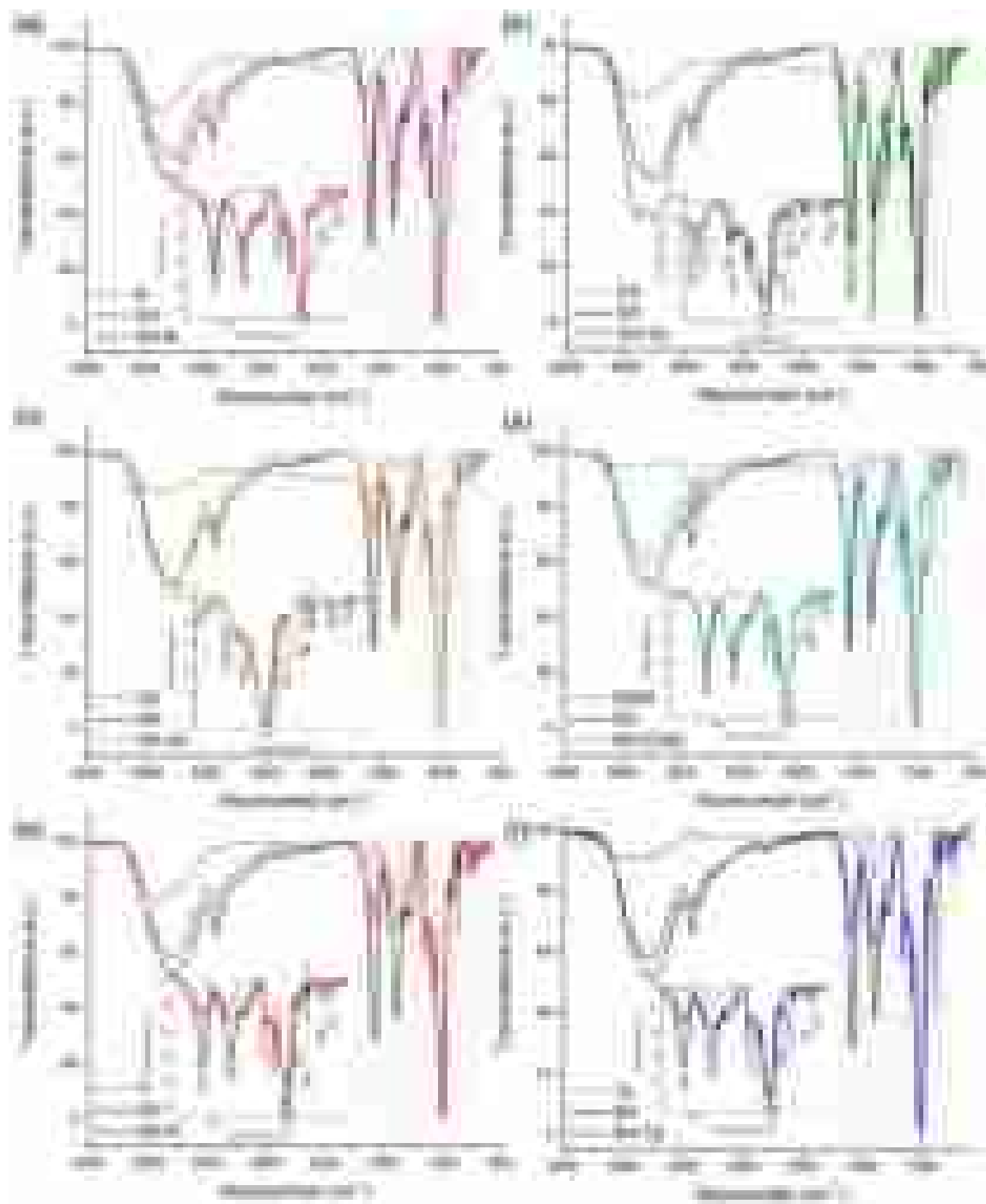


Figure 3. Fourier transform infrared spectroscopy (FTIR) spectra SH composites containing the different clays: a) SH-B; b) SH-Cb; c) SH-Ch; d) SH-C20A; e) SH-P; and f) SH-TP.

3.2. Scanning Electron Microscopy (SEM)

The changes in the morphology of SH promoted by the addition of clays were investigated through SEM images, as shown in Figure 4.

As shown in Figure 4a, SH showed an irregular structure of smooth surface, agglomeration, and a few pores. The average pore diameter is approximately $123 \pm 57 \mu\text{m}$. A similar trend was reported by Zhang et al., when developing sugar beet

pulp cellulose/starch-based hydrogel.^[39] The addition of clays resulted in hydrogel composites, a porous 3D network structure (Figure 4b–g) with greater pore volume and smaller pore size, ranging from $57\text{--}115 \mu\text{m}$. SH-B, SH-Cb, SH-Ch, SH-C20A, SH-P, and SH-Tp hydrogels showed average pore diameters of $57 \pm 19 \mu\text{m}$, $67 \pm 46 \mu\text{m}$, $115 \pm 77 \mu\text{m}$, $81 \pm 57 \mu\text{m}$, $109 \pm 62 \mu\text{m}$, and $73 \pm 46 \mu\text{m}$, respectively. When incorporating 5% clay in the SH, the internal rearrangement of the starch molecules was induced, fully revealing the physical and chemical crosslinked network

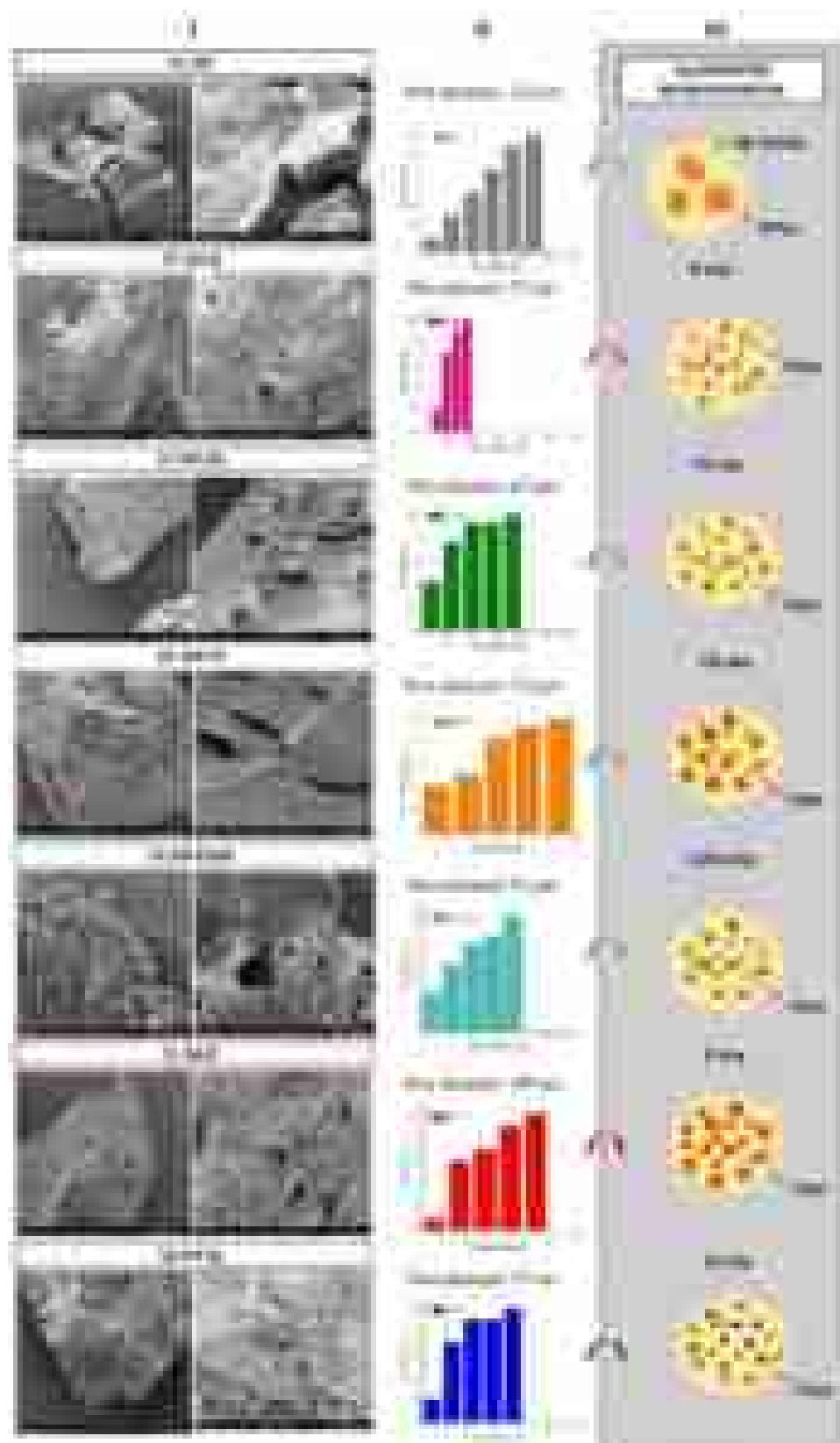


Figure 4. SEM images of neat SHs and SH composites containing the different clays: a) SH; b) SH-B; c) SH-Cb; d) SH-Ch; e) SH-C20A; f) SH-P; and g) SH-Tp, where the images on the left are magnified 100x and those on the right, 500x (I), diameter distribution histograms (II), and illustration representative of pores size (III).

structure inside the hydrogel and favoring the heterogeneous distribution of clays in SH, forming a rough surface.^[81] Based on the SEM images, there is a significant difference in the number/shape and distribution of pores within the polymeric matrix. It is worth noting that the SH-Cb, SH-Ch, and SH-Tp hydrogels had a more well-defined pore structure when compared to the other prepared samples. When fabricating and characterizing a superabsorbent hydrogel composite based on starch (St)- graft-poly (acrylic acid (AA)-co-acrylamide (AM))/polyvinyl alcohol (PVA) and cellulose nanocrystals (CNC), Olad and coworkers also reported that the porous structure was created due to the physical crosslinking of PVA chains with the and the grafted polymeric structure.^[82] As discussed in FTIR, the inclusion of clay in the hydrogel favors the creation of new interactions and the break of some junctions in the polymeric matrix. This behavior directly affects the surface morphology of the hydrogel samples.^[82] The formation of porous architecture favors an increase in the surface area and capillary effect, making the possible transportation of the water into/through the samples as well as trapping more PETs contaminants in the active site.^[28,83,84] Although BET surface area and porosity were not directly measured for these starch-clay hydrogels, a previous study conducted by our group on starch-based hydrogels, Costa et al., reported a macro- and mesoporous architecture with a specific surface area of 4.01 m²/g. These results support the role of porosity and surface area in facilitating water transport and enhancing contaminant adsorption in the hydrogels studied here.^[85]

3.3. X-ray Diffraction (XRD)

Dispersion of different clay particles within neat SH was also evidenced using XRD patterns. Besides, XRD analysis was used to identify mineralogical constituents (e.g., minerals or inorganic compounds) of clays samples.^[86] Figure 5 presents the neat SH and hydrogel composites (SH-X) XRD diffractograms.

From the diffractograms of the clays, it was observed that studied clays are mainly comprised of crystalline materials such as quartz (Qz), kaolinite (K), illite (It), and anatase (An). Similar composition was reported by Villalba et al.^[87] and Byun et al.^[57] For Qz, the sharpest peak at $2\theta \sim 27^\circ$ was highlighted for B (27.1°), P (26.8°), and Tp (26.8°) clays. This peak indicates the presence of high Qz content with fewer impurities.^[88] Ch, Cb, and C20A clays also contain Qz, but to a lesser extent due to lower intensity peaks observed at 27.6°, 26.9°, and 27.9°, respectively.^[88] For K, the significant peaks appear in Cb (17.5°, 20.1°, and 21.6°), Ch (20.1°, and 24.1°), C20A (20.1°), and B (20.1°, and 21.0°) clays; and smooth peaks were revealed in P (20.2°, 21.2°, and 23.4°), and Tp (23.0°) clays. Regarding It, all the clays show intensity peaks such as Ch (35.1° and 44.1°), Cb (35.4°), B (35.1° and 36.8°), C20A (35.2°), P (36.1° and 43.5°), Tp (36.4°, 39.6°, and 43.5°). Last, for An, the peaks mainly appear in Ch (38.1°), C20A (38° and 44.4°), P (39.5°), Tp (47.8° and 48.9°).^[89]

These compositions imply that the fillers employed primarily consist of clay minerals from the smectite group.^[90] Thus,

endowing them with a high hydration potential.^[91] The diffractograms of B, Cb, Ch, and C20A clays exhibit diffraction peaks at specific 2θ values, indicating the presence of smectite clay mineral characteristics. Smectite clays structure (layer type 2:1) is composed of an octahedral alumina sheet sandwiched between two opposing tetrahedral silica sheets. The P clay shows distinct diffraction peaks at 2θ values, whereas the Tp clay, functionalized with a cationic surfactant, shows similar peaks with a slight increase in quartz peaks due to the stability of quartz in organic media. P clay, a natural mineral clay, has a structure formed by tetrahedra arranged in a ribbon (chain layer type 2:1) extending in the a-axis direction, with an average b-axis width of three linked tetrahedral chains in sepiolite and two linked chains in palygorskite.^[92,93]

The d-spacing of the clay samples was measured from the most intense peak through Bragg's equation, as related by Barus et al.^[84] shows obtained d spacing values of clays, SH, and hydrogel composites.

The XRD pattern of the SH exhibited a characteristic semi-crystalline structure, evidenced by the presence of distinct broad peaks at $2\theta = 10.2^\circ, 15.1^\circ, 18.2^\circ, 20.1^\circ,$ and 23.3° . According to the literature, these peaks represent the simultaneous presence of partially crystalline amylopectin molecules and amorphous amylose molecules.^[94,95]

Incorporating clays in the matrix caused significant changes in the diffraction patterns compared to the SH. In the hydrogel composites patterns, shifts in peak positions and changes in peak intensities were observed. For all the hydrogel composites, the increased intensity of lower 2θ angle values was noted, such as SH-B (10.3° and 11.0°), SH-Cb (10.1° and 11.0°), SH-Ch (10.0° and 10.7°), SH-C20A (11.4°), SH-P (10.1° and 12.1°), and SH-Tp (10.5° and 10.8°). This behavior was more significant for SH-Ch, SH-C20A, SH-P, and SH-Tp samples. Besides, after the formation of the hydrogel composite, some characteristic peaks of clays were found to shift, decrease or disappear in the XRD patterns of composites such as SH-B ($2\theta = 25^\circ\text{--}30^\circ$), SH-Cb ($2\theta = 20^\circ\text{--}25^\circ$), SH-Ch ($2\theta = 20^\circ\text{--}25^\circ$), SH-C20A ($2\theta = 20^\circ\text{--}25^\circ$), SH-P ($2\theta = 25^\circ\text{--}30^\circ$), and SH-Tp ($2\theta = 25^\circ\text{--}30^\circ$). This behavior is mainly due to the disappearance of the regular/periodic structure of clays in the SH, indicating dispersion and intercalation of clays in the polymeric matrix.^[77,76,96] Based on Table 1, it is possible to state that the SH-P hydrogel is an exfoliated structure material; SH-B, SH-Ch, SH-C20A, and SH-Tp hydrogels are intercalated structure materials; and SH-Cb is a conventional composite structure material. Eldin and Ibrahim, 2021,^[97] reported a similar trend confirming the intercalated-exfoliated structure formation when developing plasticized starch/montmorillonite clay/chitosan blends.

An increase in d-spacing is expected in hydrogel composites, as reported by Ghafelebashi and coworkers when developing a novel polyvinyl alcohol (PVA)/bentonite nanocomposite hydrogel. The authors affirmed that the increase in the d-spacing is due to the homogeneous dispersion and exfoliation of bentonite in the PVA matrix after the formation of the nanocomposites.^[76] In general, these changes in d-spacing values may indicate alterations in the internal structure of clays and SH, such as modifications in chemical bonds or rearrangement of molecules.^[98,99]

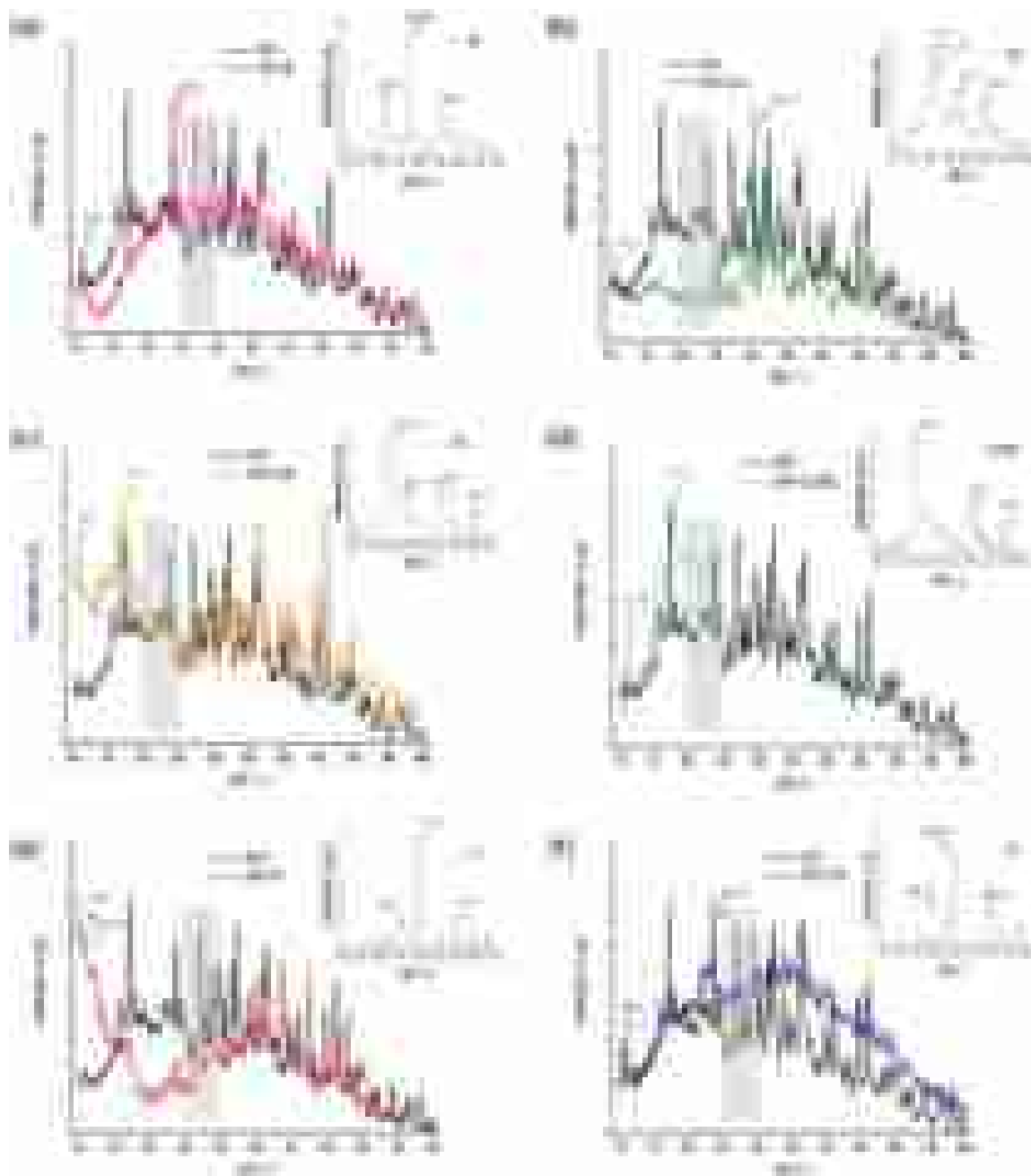


Figure 5. XRD curves for pure clays, neat SH and SH composites containing the different clays: a) SH-B; b) SH-Cb; c) SH-Ch; d) SH-C20A, e) SH-P; and f) SH-Tp.

The mentioned alterations can mean that there were new strong interactions (ionic and hydrogen bonds) between the polysaccharide chains and clays, proofing the presence of clays in the hydrogel matrix. Khairuddin et al.^[100] developed cassava-derived starch composites reinforced with different types of commercial clay (Cloisite Na, Cloisite 15A, PGV, and Nanofill 116 C). The authors affirmed that the modifications in the patterns caused by the incorporation of the fillers suggested the presence of hydrogen bond interactions between the hydroxyl groups present in the starch's polymeric chains and on the clays' surface. Taking together with the FTIR results, it can be inferred

the formation of hydrogen bonding and the interactions among SH and clays. These alterations may result in improved thermal properties of the hydrogel, as confirmed by Khairuddin et al.^[100] Besides, the free *d* spacing values and hydrated ionic diameters also influence the penetration potential of ions into the SH matrix. Based on the studied hydrated ions, the diameters in increasing order are Cr(VI) (3.75 Å) < Ni(II) (4.04 Å) < Cu(II) (4.19 Å) < Cd(II) (4.26 Å) < Zn(II) (4.30 Å) < Mn(II) (4.38 Å). Thus, it is possible to observe that hydrogel composites, mainly SH-Ch hydrogel, exhibit favorable nanochannels (active sites) for trapping ions.^[101] Similar behavior was reported by Arshadi and

Samples	Angle (°)	<i>d</i> spacing (Å)
B	26.9	3.23
Cb	20.1	4.31
Ch	20.1	4.31
C20A	20.1	4.32
P	29.7	2.93
TP	29.6	2.94
SH	36.4	2.40
SH-B	23.7	3.66
SH-Cb	30.3	2.88
SH-Ch	17.1	5.04
SH-C20A	17.6	4.91
SH-P	10.1	8.57
SH-TP	23.2	3.73

coworkers, in which the number of ions passing through the adsorbent material nanochannels increases with increasing the free interlayer spacing of the layers.^[101]

3.4. Thermogravimetric Analysis (TG/DTG)

TG analysis was carried out to evaluate the changes in weight as a function of temperature for SH and SH with different clays. TG and DTG curves of SH, SH-B, SH-Cb, SH-Ch, SH-C20A, SH-P, and SH-TP are depicted in Figure 6a,b, and the data are compiled in Tables 2 and 3.

Based on the findings, the DTG curve referring to SH displayed three thermal events (Table 2). The first stage occurred around 100 °C with 3.9% weight loss, and T_{MAX} equals 77 °C, which can be attributed to the starting of evaporation of water molecules or other small molecular substances in the hydrogel network structure.^[39,102] The second stage was observed at the temperature range of 155 °C–230 °C with 8.6%–17.9% weight

loss and T_{MAX} equals 173 °C, which can be related to the thermal decomposition of unreacted citric acid and adsorbed water. Hazrol et al. found a similar result when investigating the thermal analysis of fiber-reinforced starch-based hybrid composites. In their study, the thermal behavior using starch showed a decrease in mass loss due to the thermal decomposition of unreacted citric acid and adsorbed water in the second stage between (150 °C–170 °C).^[103] The third stage was noted at the temperature range of 230 °C–360 °C with 18.2%–63.0% weight loss, and T_{MAX} equals 280 °C which could be attributed to the thermal degradation of the starch crosslinked structure.^[104] After exposing the sample to 700 °C, a certain level of stability was observed in terms of mass loss, and a residue corresponding to 26.4% in mass was formed, which could be due to the presence of inorganic material.

Some changes were observed in composite hydrogel patterns when incorporating different clays into the SH matrix. Overall, the thermal behavior exhibited slight differences between the samples, which could be attributed to other clays, indicating that the clays influence the degree of reticulation.^[105] It was possible to note that only SH-B and SH-P hydrogels obtained thermal stability compared with SH and other hydrogel composites. For the SH-B hydrogel, two thermal events of weight loss were registered (Table 1). The first stage occurred at 170 °C–220 °C with T_{MAX} equal to 182 °C, corresponding to the thermal decomposition of unreacted citric acid.^[103] The second stage was observed between 230 °C–355 °C with a T_{MAX} equal to 280 °C, suggesting the occurrence of a dihydroxylation process, i.e., breaking the bonds of hydroxyl groups (OH) that are strongly linked in the structure of the clays.^[103,104] It is worth mentioning that the insertion of B clay favored the reduction of weight loss rate at 700 °C, generating greater residue (30.3%) compared to the SH (26.4%). Regarding SH-P hydrogel, this sample showed two thermal events: the first stage (155 °C–225 °C) with a T_{MAX} of 177 °C, corresponding to the thermal decomposition of unreacted citric acid and the second stage (225 °C–360 °C) with a T_{MAX} of 280 °C, indicating the dehydroxylation process.^[106] This sample obtained 27.3% residue at 700 °C, a higher residue value than

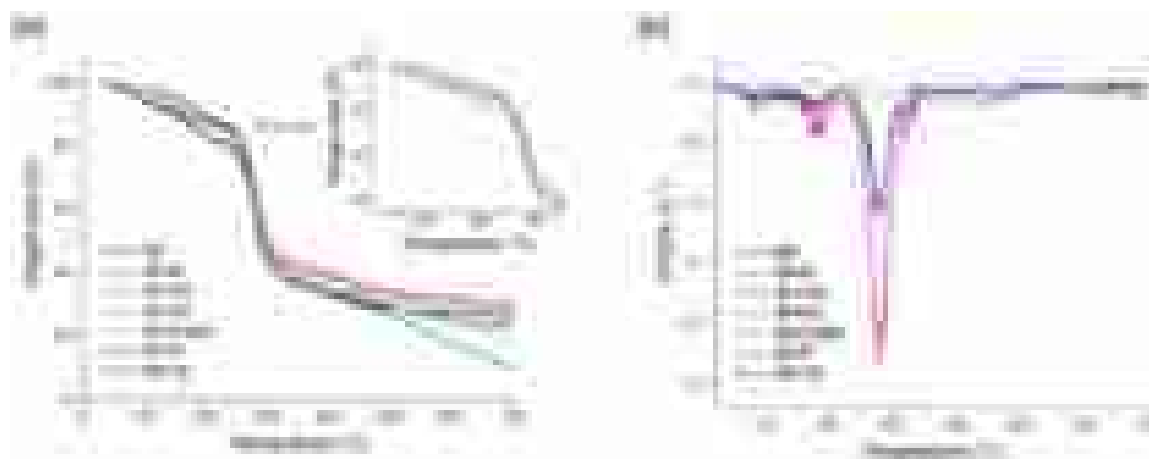


Figure 6. TG/DTG curves for neat SH and SH composites containing the different clays SH-B, SH-Cb, SH-Ch, SH-C20A, SH-P, and SH-TP: a) TG curves and b) DTG curves.

Table 2. T_{ONSET} , values of $T_{5\%}$ and $T_{30\%}$ of loss weight from TG curves and T_{MAX} of thermal degradation events are present in the DTG curves of SH, SH-B, SH-Cb, SH-Ch, SH-C20A, SH-P, and SH-Tp.

Samples	Weight Loss (%)							Residue 700 °C	T_{ONSET} °C	$T_{\text{MAX} 1}$ °C	$T_{\text{MAX} 2}$ °C	$T_{\text{MAX} 3}$ °C
	100 °C	200 °C	300 °C	400 °C	500 °C	600 °C	700 °C					
SH	3.9	14.8	46.8	65.5	71.2	72.7	73.6	26.2	265	77	173	280
SH-P	1.8	8.7	41.9	59.2	65.4	67.8	69.7	26.9	260	–	182	280
SH-Tp	4.1	11.5	48.8	66.7	72.5	81.4	89.6	22.4	260	–	–	280
SH-Cb	1.3	9.8	46.6	62.5	68.2	71.8	76.5	9.79	258	–	166	280
SH-Ch	1.5	8.2	47.3	64.3	69.9	75.6	81.1	23.1	265	–	184	280
SH-C20A	1.8	9.6	44.2	60.9	66.6	69.0	72.7	18.4	255	–	177	278
SH-B	3.8	15.2	50.8	65.3	70.5	73.8	77.1	30.1	261	85	162	280

Table 3. $T_{5\%}$ and $T_{30\%}$ values were used to obtain the heat-resistance index (T_{HRI}) of SH, SH-B, SH-Cb, SH-Ch, SH-C20A, SH-P, and SH-Tp.

Samples	$T_{5\%}$ (°C)	$T_{30\%}$ (°C)	T_{HRI} (°C)
SH	113.0	282.4	105.2
SH-B	162.5	287.8	116.5
SH-Cb	109.9	282.2	104.5
SH-Ch	175.4	285.2	118.2
SH-C20A	163.6	284.1	115.6
SH-P	156.1	286.4	114.8
SH-Tp	106.5	279.1	102.9

the SH. Both behaviors can confirm the strong interaction of the clay with the -OH groups of the SH, delaying its breakdown in an initial recording stage.^[105,106]

For the SH-Cb hydrogel, only one thermal event was noted at the temperature range of 230 °C–360 °C with a T_{MAX} of 280 °C; and for the SH-Ch hydrogel, two thermal events were observed: first stage (130–230 °C) with a T_{MAX} of 166 °C and second stage (230–360 °C) with a T_{MAX} of 280 °C. Similar to the SH-Ch composite, the SH-C20A hydrogel showed two thermal events: the first stage (130–230 °C) with a T_{MAX} of 184 °C and the second stage (230 °C–360 °C) with a T_{MAX} of 278 °C. The SH-Tp hydrogel obtained three thermal events: the first stage (30–130 °C) with a T_{MAX} of 85 °C, the second stage (130–230 °C) with a T_{MAX} of 162 °C and the third stage (230 °C–360 °C) with a T_{MAX} of 280 °C (Table 2). The 30 °C–130 °C temperature suggested the volatilization of weakly bound water and small organic compounds.^[107] A temperature range of 130 °C–230 °C evidenced physical dehydration, i.e., evaporation of the moisture entrapped within the entangled polymer chain.^[77,84] When achieving at the temperature of 230 °C, the breakdown of the starch carbon skeleton as well as the internal structure, can be observed.^[103,108] These samples obtained lower thermal stability compared to SH, showing residue percentages of 10.4, 23.5, 18.9, and 22.9%, respectively. Another interesting way to assess the thermal stability of SH and hydrogel composite is to calculate the heat resistance index. The heat resistance index refers to the temperature at which a polymer can tolerate physical heat. This is determined using the method proposed by Icdyugu et al.^[109] Table 3 provides the values for the heat resistance index (T_{HRI}) of all samples, calculated

from thermograph data for the 5% ($T_{5\%}$) and 30% ($T_{30\%}$) weight losses of Figure 6. An increase in the thermal resistance of hydrogel composites was noted compared to SH after the insertion of clays in the matrix, except for SH-Cb and SH-Tp. This fact demonstrates that clays addition in the SH matrix promotes the creation of a stronger 3D network structure and higher thermal stability at temperatures reaching 30% of weight loss for hydrogel composites.

3.5. Degree of Swelling

One of the hydrogels' most significant properties is their remarkable absorption capacity, especially for water decontamination. To investigate the swelling phenomenon in hydrogels, an experiment was conducted involving the immersion of these materials in distilled water for different intervals over 2800 min to achieve the swelling equilibrium state. Figure 7 illustrates the expansion levels observed in starch-based hydrogels reinforced with various clays at a 5% ratio. A rapid initial expansion was observed in all cases, stabilizing after 1440 min. This behavior indicates the saturation of all active absorption sites within the hydrophilic 3D matrix. The values related to the water absorption capacity for each hydrogel are presented in Table 4.

Sample SH exhibited a degree of swelling (DS) of 84.6%, indicating a more substantial water absorption due to its free hydroxyl groups compared to clay-loaded samples. This observation highlights that SH possesses hydrophilic characteristics, enabling its -OH groups to interact with water molecules.^[81] According to Kaur et al., the water absorption mechanism undergoes two stages, where initially, the hydrophilic groups on the hydrogel surface strongly interact with water, promoting the swelling of the hydrogel structure, which exposes other groups within the structure that can lead to further interactions over time. However, the swelling of the structure is constrained by the degree of crosslinking, which limits the expansion capacity of the network.^[110]

With the incorporation of clays into the starch structure, a reduction in absorption capacity is observed, following the sequence SH-B, SH-Ch, SH-Tp, SH-Cb, SH-C20A, and SH-P, with DS values of 84.5%, 84.2%, 64.9%, 65.0%, 55.8%, and 21.4%, respectively. This reduction likely occurred due to the crosslinking and grafting processes, increasing the crosslinking density of the

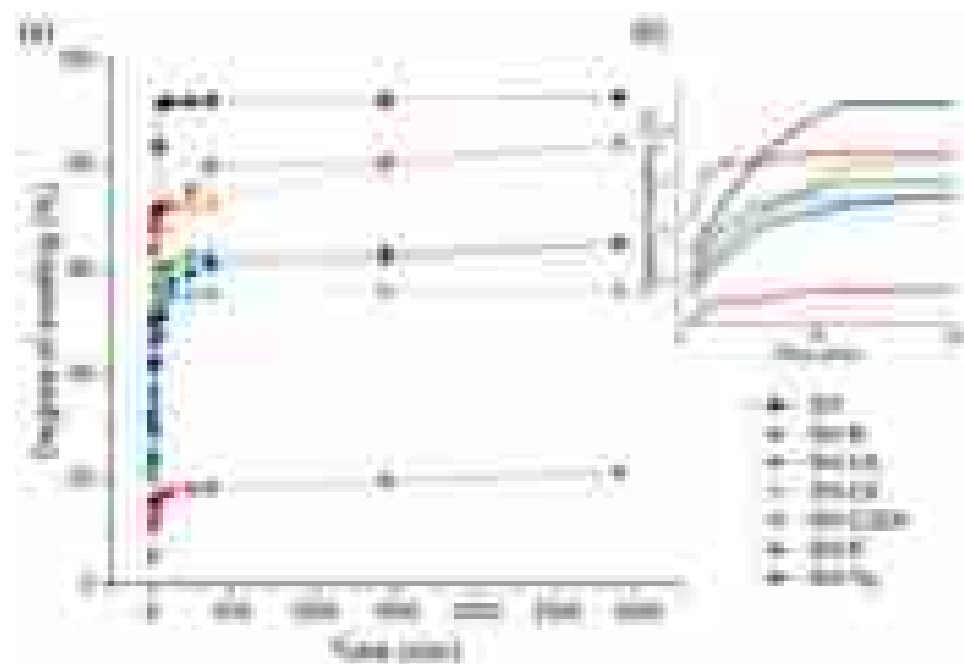


Figure 7. Degree of water swelling of the neat SH and their SHs containing the different clays. a) Degree of swelling of different hydrogel variants during 2880 min–SH, SH-B, SH-Cb, SH-Ch, SH-C20A, SH-P, and SH-Tp. b) Zoomed-in range from 5 to 120 min.

Table 4. Degree of swelling of the developed SHs and Fick's diffusion coefficients.

Samples	DS (%)	n	k	R^2
SH	92.8	0.095	0.617	0.843
SH-B	84.5	0.021	0.853	0.915
SH-Cb	65.0	0.061	0.722	0.830
SH-Ch	84.2	0.914	0.581	0.912
SH-C20A	55.8	0.059	0.741	0.818
SH-P	21.4	0.025	0.857	0.845
SH-Tp	64.9	0.072	0.659	0.910

composite hydrogels, which is one of the most relevant structural parameters affecting water absorption capacity and fluid retention. Nevertheless, the spacing between crosslinks remains suitable for water molecule absorption, resulting in increased water absorption.^[111]

The water absorption data were adjusted according to Equation (3) to evaluate Fick diffusion, which concerns the diffusion and random movement of solvent molecules in the hydrogel's polymeric network. Table 4 shows the results obtained.

According to Fick's Law, when R^2 values are greater than 0.9, it indicates a proper fit for Fick's model. In this context, only the SH-Ch sample demonstrates a satisfactory fit. When analyzing the " n " values, when " n " is less than 0.5, the diffusion process is classified as Fickian. In this scenario, it is observed that the SH, SH-B, SH-Cb, SH-C20A, SH-P, and SH-Tp samples exhibit such behavior. When $0.5 < n < 1$, an anomalous diffusion process occurs, characterized by simultaneous diffusion and relaxation of polymeric chains. This occurs, for example, in the SH-Ch sample. Last, when " n " Equation (3), the process is predominantly

influenced by the relaxation of the polymeric chains. None of the samples demonstrated this specific behavior.^[112,113] Furthermore, higher values of k during water absorption in hydrogels confirmed a faster swelling kinetics, with equilibrium reached in shorter absorption times. This affects the absorption of inorganic and organic pollutants in water and wastewater.^[114]

3.6. PTE's Sorption

Due to their abundance and high toxicity, PTEs pose a significant environmental concern. The persistent presence of metals in aquatic ecosystems has negative consequences for human and fauna health, increasing the urgency of developing effective methods for their removal from water.^[115] Therefore, we evaluated the performance of hydrogels with and without the different clays in synthetic effluents containing six coexisting ions (Cu(II), Cd(II), Zn(II), Ni(II), Mn(II), and Cr(VI)), as shown in Figure 8. Evaluating the absorption of divalent cations (Cu(II), Cd(II), Zn(II), Ni(II), and Mn(II)), we observed an improvement in the removal when the hydrogels were incorporated with the different clays, as shown in Figure 8 and as well as the removal rate data presented in Table 5. The divalent cations showed the following order of metal affinity: Mn(II) (SHCh) > Zn(II) (SHCb) > Cu(II) (SHCh) > Cd(II) (SHCb) > Ni(II) (SHCb), resulting in removals of 17.3%, 13.5%, 10.8%, 10.1%, and 6.6%, respectively. The results indicate an increase in the potential for the removal of bivalent metals with the inclusion of clays. However, limited removal of these ions was still observed. The order of metal affinity observed (Mn(II) > Zn(II) > Cu(II) > Cd(II) > Ni(II)) can be explained based on the ionic properties of the metals, such as their hydrated ionic radii and hydration energies. Mn(II) and Zn(II) possess lower hydration energies and larger radii, facilitat-

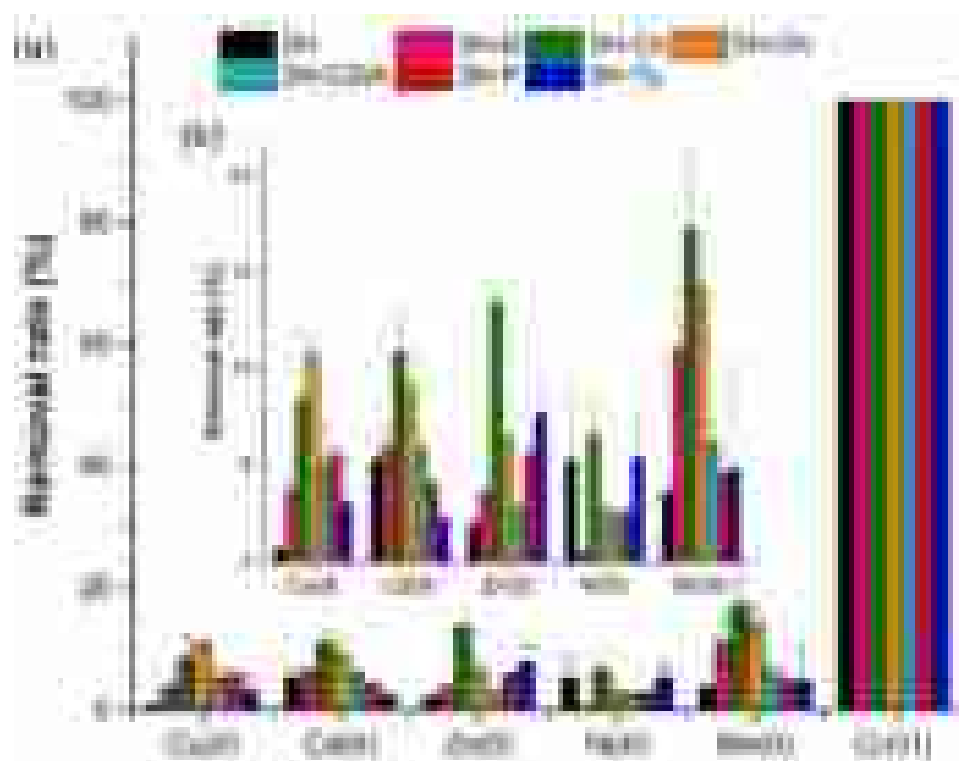


Figure 8. a) Sorption selectivity of PTEs by neat SH and SHs containing different clays (dosage of 1.0 g/L; $C_0 = 0.161 \pm 0.024 \text{ mmol L}^{-1}$ each; pH controlled: 3.5–4.0; stirring of $\sim 150 \text{ rpm}$; temperature of $\sim 25 \text{ }^\circ\text{C}$; contact time of 24 h). b) Zoomed-in range from Cu(II) to Mn(II).

Table 5. The adsorption removal rate (%) of Cu(II), Cd(II), Zn(II), Ni(II), Mn(II), and Cr(VI) ions in SH composites containing the different clays.

Samples	Removal (%)					
	Cu(II)	Cd(II)	Zn(II)	Ni(II)	Mn(II)	Cr(VI)
SH	0.7 ± 0.3	5.3 ± 1.7	2 ± 1.4	3.7 ± 5.3	3.7 ± 2.7	100 ± 0
SH-B	3.8 ± 0.8	6 ± 0.9	3.7 ± 2	0.5 ± 0.1	11.1 ± 3.8	100 ± 0
SH-Cb	8.5 ± 3.5	10.9 ± 1.8	13.5 ± 9.7	6.6 ± 4.1	17.3 ± 4	100 ± 0
SH-Ch	10.8 ± 0.7	9.1 ± 1.9	6.5 ± 1.9	2.8 ± 1.2	14.3 ± 2.8	100 ± 0
SH-C20A	5.2 ± 1.9	5.9 ± 0.8	2.9 ± 1	2.6 ± 0	6.3 ± 1.2	100 ± 0
SH-P	5.6 ± 0.4	0.4 ± 4.1	5.6 ± 0.4	1.6 ± 2.6	3.9 ± 4.6	100 ± 0
SH-Tp	3.1 ± 2.4	1.5 ± 2.3	3.7 ± 2.8	5.4 ± 2.5	4.9 ± 5.6	100 ± 0

ing their diffusion and interaction with the active sites.^[116] Cu(II) exhibits strong complexation with donor atoms like oxygen, justifying its intermediate affinity. Ni(II), with higher hydration energy and smaller radius, showed the lowest affinity.

Considering the evaluated systems, the hydrogels containing clays with a smectite structure (layer type 2:1) showed better results than the hydrogels with clays with palygorskite structure (chain layer type 2:1).^[117] This structural difference can influence the swelling capacity, which can affect the sorption capacity of the clay. Lalji et al. showed that smectite minerals are more susceptible to swelling as the interlamellar spacing between their structures is relatively larger, in contrast to other clay minerals.^[118] Among the studied smectites, it is noteworthy that the SHCb and SHCh samples showed the best results, possibly

because they retained their active sites after the crosslinking process. Additionally, removing metal ions is associated with ion exchange processes and complexation. The release of native cations (Na^+ , K^+ , Ca^{2+} , and Mg^{2+}) from the clay structure during the adsorption confirms ion exchange, whereas the presence of hydroxyl groups ($-\text{OH}$) in starch and negatively charged sites such as $\text{Si}-\text{O}^-$ and $\text{Al}-\text{O}^-$ on the clays are responsible for the formation of inner-sphere complexes with metal ions.^[56]

Comparing the removal capacity of the hydrogels for Cr(VI) and divalent cations, we noticed a remarkably high affinity for chromium. This is because Cr(VI) in aqueous medium exists as oxyanions (CrO_4^{2-} , $\text{Cr}_2\text{O}_7^{2-}$, or HCrO_4). On the other hand, divalent metal nitrates predominate in cationic form, with no competitive sorption relationship between oxyanions and diva-

Table 6. Comparison between polymeric adsorbents for heavy metal removal.

Samples	Heavy metal	Adsorption capacity (%)	Experimental conditions	Multimetallic system?/renewable source?	References
SHCb (this study)	Cr(VI)	100%	pH 5, 25 °C, 24h	Yes/Yes	This work
	Mn(II)	17.3%			
	Zn(II)	13.5%			
SHCh (this study)	Cu(II)	10.9%	pH 5, 25 °C, 24h	Yes/Yes	This work
	Mn(II)	14.3%			
Natural clay	Cu(II)	71.1%	pH 5, 16 °C, 27min	Yes/Yes	[29]
	Zn(II)	69.0%			
PEI cryogels	Zn(II)	83%–98%	pH 4, 25 °C, 90min	Yes/No	[32]
PBAT membrane without and with cellulose nanostructure	Cr(VI)	6%–71%	pH 5, 25 °C, 3h	No/Yes	[6]

lent cations.^[119] For the samples developed, comparing with SH and with the inclusion of different clays in the structure, we observed a removal capacity of 100%. Studies indicate that Cr(VI) can be easily adsorbed on adsorbents through electrostatic interaction,^[120] complexation with functional groups^[121] or in alkaline conditions.^[108] Given the methodology adopted for developing the hydrogel, a strong base (NaOH) was used to deprotonate the hydroxyl groups present in the starch. Subsequently, it is believed that part of these deprotonated hydroxyls participated in a nucleophilic attack on a carbonyl group of citric acid (CA), resulting in the crosslinking of the starch and, consequently, in the formation of the hydrogel. However, because the CA concentration is low, some of the deprotonated hydroxyls likely remain unreacted with the CA. As a result, these unreacted hydroxyls can form ionic bonds with sodium (Na⁺), giving the hydrogel an alkaline character. In this context, it is possible to hypothesize that this alkaline characteristic of the hydrogel can explain why the results obtained for the divalent metals were not so favorable. Samples with a positive charge would tend to repel the divalent cations, which could negatively influence the removal efficiency. On the other hand, considering that chromium has a negative charge, it would be natural for it to be attracted to the surface of the hydrogel. Thus, the results demonstrated a greater sorption affinity between hydrogels and Cr(VI) oxyanions. In this way, further studies of kinetic, equilibrium, thermodynamic, desorption/reuse, and fixed-bed column for scale-up are strongly recommended to understand the sorption process deeply.

Table 6 compares other adsorbents reported in the literature to highlight the efficiency of the synthesized starch-based hydrogels. This allows a broader understanding of the removal capacities under similar experimental conditions.

It is important to highlight that, unlike some comparative studies, the experiments presented here were conducted in a synthetic solution containing six coexisting metal ions, reflecting more realistically the complexity of industrial effluents. Although the individual adsorption capacity is reduced in this type of system, the hydrogels reinforced with natural clays demonstrated satisfactory performance, especially against Cr(VI), with 100%

removal. In addition, the materials developed are biodegradable, low-cost and obtained from renewable sources, which reinforces their environmental and technological potential for sustainable applications in contaminated water treatment.

4. Conclusion

This study investigated the potential of several Brazilian clays as adsorbents in corn SHs, aiming to remove potentially toxic metals. The hydrogel composites, incorporating different types of clay, were efficiently synthesized and submitted to evaluate their physical–chemical, morphological, thermal, and sorption properties. The FTIR spectroscopy revealed that the SH–B, SH–C20A, SH–P, and SH–Tp hydrogels were internally retained in the hydrogel matrix and underwent crosslinking during the process, affecting the mobility of the silicate groups. On the other hand, the SH–Cb and SH–Ch hydrogels showed an increase in the intensity of the band corresponding to the hydroxyls of the material, showing peaks at 1050 cm⁻¹ (Si–O–Si) and approximately 920 cm⁻¹ (Al–OH–Al), indicating a successful incorporation of clays into the SH structure. The hydrogels revealed 3D porous structures with accessible functional groups, whereas the average pore sizes reached approximately 89.3 μm, favoring water penetration into the interior of the samples. Swelling showed a reduction in water absorption in the presence of clays, probably due to the increase in the crosslinking density of the composite hydrogels. Additionally, only in the SH–Ch, favoring an anomalous diffusion process, marked by simultaneous diffusion and relaxation of the polymeric chains. Both non-reinforced and clay-reinforced hydrogels showed a promising adsorption capacity for metal ions, especially Cr(VI) oxyanion ions. Regarding divalent ions, the order of metal affinity was Mn(II) > Zn(II) > Cu(II) > Cd(II) > Ni(II).

These findings emphasize the significant role of clay type in enhancing the adsorption performance of starch-based hydrogels. In this context, the SH–Cb and SH–Ch hydrogels demonstrated a remarkable ability to adsorb metal ions, highlighting their effectiveness. Incorporating natural and modified clays pro-

vided structural and functional advantages that improved the sorption capacity of the materials. Such results indicate that these hybrid hydrogels are low-cost, environmentally friendly alternatives for the treatment of industrial effluents containing multiple coexisting metal ions. Such results demonstrate the potential of these materials for removing contaminants from effluents. In future perspectives, further analyses will be explored to understand the physical-chemical structure and adsorption mechanism better.

Acknowledgments

This research was funded by CNPq (308053/2021-4 and 403934/2021-4) and FAPESP (2024/08105-0, 2024/23595-4, 2023/14598-7, 2022/01382-3, 2021/14714-1, and 2020/13703-3). The authors thank the UFABC, CAPEScode 001); REVALORES Strategic Unit, CAPES (001); and Multiuser Central Facilities (CEM-UFABC). The authors thank the FAPERJ (E-26/203.905/2022, E-26/210.092/2022, and E-26/210.450/2021).

Conflict of Interests

The authors declare no conflict of interest.

Data Availability Statement

The data that support the findings of this study are available from the corresponding author upon reasonable request.

Keywords: Brazilian clays · Metallic ions adsorption mechanism · Starch hydrogel (SH)


- [1] Y. Gong, Y. Wang, N. Lin, R. Wang, M. Wang, X. Zhang, *Environ. Poll.* **2022**, *299*, 118871.
- [2] B. S. Rath, P. S. Kumar, D.-V. N. Vo, *Sci. Total Environ.* **2021**, *797*, 149134.
- [3] M. Zhang, Y. Zhou, F. Wang, Z. Chen, X. u Zhao, W. Duan, G. Yin, X. Yang, J. Li, Q. Yin, M. Zhao, *Front. Chem.* **2022**, *10*, <https://doi.org/10.3389/fchem.2022.1054286>.
- [4] G. Zhou, J. Luo, C. Liu, L. Chu, J. Crittenden, *Water Res.* **2018**, *131*, 246–254.
- [5] N. A. A. Qasem, R. H. Mohammed, D. U. Lawal, *NPJ Clean Water* **2021**, *4*, 36.
- [6] R. F. S. Barbosa, A. G. Souza, H. F. Maltez, D. S. Rosa, *Chem. Eng. J.* **2020**, *395*, 125055.
- [7] H. Xiang, X. Min, C.-J. Tang, M. Sillanpää, F. Zhao, *J. Water Proc. Eng.* **2022**, *49*, 103023.
- [8] Q. Zhou, N. Yang, Y. Li, B. Ren, X. Ding, H. Bian, X. Yao, *Glob. Ecol. Conserv.* **2020**, *22*, e00925.
- [9] S. Pan, J. Shen, Z. Deng, X. Zhang, B. Pan, *J. Hazard. Mater.* **2022**, *423*, 127158.
- [10] S. Ahmed, F. S. A. Khan, N. M. Mubarak, M. Khalid, Y. H. Tan, S. A. Mazari, R. R. Karri, E. C. Abdullah, *J. Environ. Chem. Eng.* **2021**, *9*, 106643.
- [11] G. Yuan, K. Li, J. Zhang, Z. Huang, F. Li, H. Zhang, J. Wang, S. Zhang, Q. Jia, *J. Hazard. Mater.* **2023**, *443*, 130211.
- [12] R. Lin, Y. Li, T. Yong, W. Cao, J. Wu, Y. Shen, *J. Environ. Manage.* **2022**, *306*, 114460.
- [13] X. Luo, C. Wu, Y. Lin, W. Li, M. Deng, J. Tan, S. Xue, *Environ. Sci.* **2023**, *125*, 662–677.
- [14] S. Wang, J. Li, H. Narita, M. Tanaka, *Miner. Eng.* **2021**, *172*, 107132.
- [15] Z. Ying, Y. Song, K. Zhu, G. Wu, Y. Ju, Q. Wei, X. Ren, *J. Environ. Chem. Eng.* **2022**, *10*, 107384.
- [16] F. Qiu, R. Chen, T.-S. Chung, Q. Ge, *Desalination* **2022**, *539*, 115924.
- [17] S. Tamizharasan, R. Muralidharan, N. Abirami, H. Leelavathi, A. Siva, A. Kumarasamy, R. Arulmozhi, *Optik (Stuttg)* **2023**, *283*, 170930.
- [18] D. a Li, X. Zhang, X. Liang, W. Liu, K. Guo, Z. Zhang, S. Wang, Y. Xing, Z. Li, J. Li, H. Wang, *Arab. J. Chem.* **2023**, *16*, 104836.
- [19] M. Liu, Q. Lu, W. Yu, *Chemosphere* **2023**, *324*, 138297.
- [20] L. Lu, Y. Xie, Z. Yang, B. Chen, *J. Hazard. Mater.* **2023**, *442*, 130021.
- [21] S. Wang, A. Adekunle, V. Raghavan, *J. Environ. Manage.* **2022**, *317*, 115333.
- [22] Z. Darban, S. Shahabuddin, R. Gaur, I. Ahmad, N. Sridewi, *Gels* **2022**, *8*, 263.
- [23] H. Zhu, S. Chen, Y. Luo, *J. Agric. Food Res.* **2023**, *12*, 100552.
- [24] N. Chowdhury, Solaiman, C. K. Roy, S. H. Firoz, T. Foyez, A. B. Imran, *ACS Omega* **2021**, *6*, 836–844.
- [25] B. S. Rath, P. S. Kumar, *Environ. Poll.* **2021**, *280*, 116995.
- [26] N. A. Abd El-Ghany, M. H. A. Elella, H. M. Abdallah, M. S. Mostafa, M. Samy, *J. Polym. Environ.* **2023**, *31*, 2792–2825.
- [27] M. Banza, H. Rutto, *Can. J. Chem. Eng.* **2023**, *101*, 1906–1918.
- [28] M. Srikaew, P. Jumpapaeng, P. Suwanakood, C. Kaiyasuan, V. Promarak, S. Saengsuwan, *J. Industr. Eng. Chem.* **2023**, *118*, 53–69.
- [29] A. Es-Said, L. El Hamdaoui, F. E. Ennoukh, H. Nafai, N. Zerki, G. Lamzougui, R. Bchitou, *Phosphor. Sulfur Silicon Relat. Elem.* **2023**, *198*, 424–434.
- [30] M. G. Mukhamediev, D. Z. Bekchanov, M. M. Juraev, P. Lieberzeit, D. A. Gafurova, *Russ. J. Appl. Chem.* **2021**, *94*, 1594–1601.
- [31] A. A. Alswat, A. M. Ashmali, T. M. Alqasmi, H. R. Alhassani, F. T. Alshorifi, *Heliyon* **2023**, *9*, e14301.
- [32] S. Bagdat, F. Tokay, S. Demirci, S. Yilmaz, N. Sahiner, *J. Environ. Manage.* **2023**, *329*, 117002.
- [33] Z. Ding, Y. Ge, S. C. Gowd, E. Singh, V. Kumar, D. Chaurasia, V. Kumar, K. Rajendran, P. C. Bhargava, P. Wu, F. Lin, S. Harirchi, V. Ashok kumar, R. Sirohi, R. Sindhu, P. Binod, M. J. Taherzadeh, M. K. Awasthi, *Bioresour. Technol.* **2023**, *376*, 128903.
- [34] M. Ahmadian, M. Jaymand, *Coord. Chem. Rev.* **2023**, *486*, 215152.
- [35] B. Wang, J. Lan, C. Bo, B. Gong, J. Ou, *RSC Adv.* **2023**, *13*, 4275–4302.
- [36] A. Abutaleb, M. Imran, N. Zouli, A. H. Khan, S. Hussain, M. A. Ali, O. Bakather, M. A. Gondal, N. A. Khan, H. Panchal, S. Zahmatkesh, *Chemosphere* **2023**, *316*, 137824.
- [37] K. A. Adegoke, S. O. Akinawo, T. A. Adebuseyi, O. A. Ajala, R. O. Adegoke, N. W. Maxakato, O. S. Bello, *Int. J. Environ. Sci. Technol.* **2023**, *20*, 1615–11644.
- [38] D. Bekchanov, M. Mukhamediev, D. Eshtursunov, P. Lieberzeit, X. Su, *Polym. Adv. Technol.* **2024**, *35*, e6207.
- [39] X. Zhang, Q. Liu, S. Zhu, M. Yu, *Mater. Today Commun.* **2022**, *33*, 104355.
- [40] W. Chen, S. Yuan, J. Shen, Y. Chen, Y. Xiao, *Front. Bioeng. Biotechnol.* **2021**, *8*, <https://doi.org/10.3389/fbioe.2020.627351>.
- [41] J. Alam, A. K. Shukla, F. A. A. Ali, O. Daoud, M. Alhoshan, *The Treatment of Pharmaceutical Wastewater*, Elsevier, **2023**, pp. 347–365, <https://doi.org/10.1016/B978-0-323-99160-5.00007-2>.
- [42] D. Bekchanov, M. Mukhamediev, S. Yarmenov, P. Lieberzeit, A. Mujahid, *Carbohydr. Polym.* **2024**, *323*, 121397.
- [43] N. Kumar, R. Gusain, S. Pandey, S. S. Ray, *Adv. Mater. Interf.* **2023**, *10*, 2201375.
- [44] M. M. El Sayed, *J. Polym. Environ.* **2023**, *31*, 2855–2879.
- [45] L. Li, J. Guo, C. Kang, H. Song, *Polym. (Basel)* **2023**, *15*, 1765.
- [46] A. Rezgui, E. Guibal, T. Boubakera, *Can. J. Chem. Eng.* **2017**, *95*, 775–782.
- [47] D. Park, J. W. Kim, K. Shin, J. W. Kim, *Carbohydr. Polym.* **2021**, *272*, 118459.
- [48] L. Cao, N. Li, *Int. J. Biol. Macromol.* **2021**, *177*, 383–391.
- [49] M. Mihajlovic, M. Mihajlovic, P. Y. W. Dankers, R. Masereeuw, R. P. Sijbesma, *Macromol. Biosci.* **2019**, *19*, 1800173.
- [50] K. A. B. Pereira, K. L. N. P. Aguiar, P. F. Oliveira, B. M. Vicente, L. G. Pedroni, C. R. E. Mansur, *ACS Omega* **2020**, *5*, 4759–4769.
- [51] S. Ma, H. Zheng, Y. Chen, J. Zou, C. Zhang, Y. Wang, *J. Wuhan Univ. Technol.-Mater. Sci. Ed.* **2020**, *35*, 287–292.
- [52] B. Huang, M. Liu, C. Zhou, *Carbohydr. Polym.* **2017**, *175*, 689–698.
- [53] S. P. Santos, A. Kurniawan, A. E. Angkawijaya, H. Shuwanto, I. D. A. A. Warmadewanthi, C.-W. Hsieh, H.-Y. Hsu, F. E. Soetaredjo, S. Ismadji, K.-C. Cheng, *Chem. Eng. J.* **2023**, *452*, 139261.
- [54] J. Boruah, D. Chowdhury, *Minerals* **2022**, *13*, 26.

- [55] H. Ghasemi, M. Afshang, T. Gilvari, B. Aghabarari, S. Mozaffari, *Res. Surf. Interf.* **2023**, *10*, 100097.
- [56] R. R. Ferreira, T. B. da Costa, R. F. D. S. Barbosa, P. H. Camani, R. R. Menezes, D. D. S. Rosa, *Adsorption* **2024**, *30*, 2113–2133.
- [57] Y. Byun, C. Seo, T. Yun, Y. Joo, H. o Young Jo, *Geoderma* **2023**, *430*, 116294.
- [58] T. B. da Costa, M. G. C. da Silva, M. G. A. Vieira, *J. Rare Earths* **2020**, *38*, 339–355.
- [59] N. Nordin, S. H. Othman, S. A. Rashid, R. K. Basha, *Food Hydrocoll.* **2020**, *106*, 105884.
- [60] C. Cagnin, B. M. Simões, F. Yamashita, A. C. Andrello, G. M. de Carvalho, M. V. E. Grossmann, *J. Appl. Polym. Sci.* **2021**, *138*, 50194.
- [61] B. Debnath, P. Duarah, D. Haldar, M. K. Purkait, *Food Packag. Shelf Life* **2022**, *34*, 100937.
- [62] Y. Mao, P. Li, J. Yin, Y. Bai, H. Zhou, X. Lin, H. Yang, L. Yang, *J. Mater. Sci. Technol.* **2021**, *63*, 228–235.
- [63] Y. Yuan, H. Chen, *Food Packag. Shelf Life* **2021**, *30*, 100718.
- [64] I. Gonenc, F. Us, *Starch–Stärke* **2019**, *71*, 1800046.
- [65] A. Mohammadi, J. Moghaddas, *Turk. J. Chem.* **2020**, *44*, 614–633.
- [66] L. Wang, M. Sánchez-Soto, T. Abt, M. L. Maspocho, O. O. Santana, *Polym. Int.* **2016**, *65*, 899–904.
- [67] P. H. Camani, M. G. M. Gonçalves, R. F. S. Barbosa, D. S. Rosa, *J. Appl. Polym. Sci.* **2021**, *138*, 50863.
- [68] E. Antonio, M. K. M. De, E. M. Araújo, R. d. S. B. Ferreira, S. S. L. Oliveira, V. d. N. Medeiros, *Mater. Res. Expr.* **2019**, *6*, 12.
- [69] L. N. R. de Paula, G. M. de Paula, M. G. F. Rodrigues, *Ceramica* **2020**, *66*, 269–276.
- [70] Y. Zhu, S. Kottarath, J. O. Iroh, R. A. Vaia, *Energ. (Basel)* **2022**, *15*, 5366.
- [71] Y. Zhu, J. O. Iroh, R. Rajagopalan, A. Aykanat, R. Vaia, *Energ. (Basel)* **2022**, *15*, 1291.
- [72] G. Georgopoulos, E. Badogiannis, S. Tsivilis, M. Perraki, *Appl. Clay Sci.* **2021**, *215*, 106306.
- [73] Y. Yahia, F. García-Villén, A. Djelad, L. S. Belaroui, R. Sanchez-Espejo, M. Sassi, A. López-Galindo, C. Viseras, *Appl. Clay Sci.* **2019**, *180*, 105169.
- [74] A. Santana, J. L. S. Sobrinho, S. F. E. C. da, L. C. C. Nunes, *Mater. Sci. Eng. C* **2017**, *73*, 245–251.
- [75] M. U. Sousa, A. M. Rodrigues, M. E. B. Araujo, R. R. Menezes, G. A. Neves, H. L. Lira, *Materials* **2022**, *15*, 2708.
- [76] A. Ghafelbashi, S. Khosravani, M. H. Kazemi, F. Rajabi, M. C. Amiri, *Coll. Surf. A Physicochem. Eng. Asp.* **2022**, *650*, 129580.
- [77] H. Dai, Y. Huang, H. Huang, *Carbohydr. Polym.* **2018**, *185*, 1–11.
- [78] S. Datta Chaudhuri, A. Mandal, A. Dey, D. Chakrabarty, *Appl. Clay Sci.* **2020**, *185*, 105405.
- [79] M. Arif, G. Liu, B. Yousaf, R. Ahmed, S. Irshad, A. Ashraf, M. Zia-ur-Rehman, M. S. Rashid, *J. Clean Prod.* **2021**, *310*, 127548.
- [80] J. V. do. N. Silva, J. R. Scheibler, M. G. F. Rodrigues, *Mater. Sci. Forum* **2015**, *820*, 539–544.
- [81] R. Lin, R. Xu, H. Chen, B. o Liu, C. Yuan, L. i Guo, B. o Cui, Y. Fang, *Carbohydr. Polym.* **2023**, *316*, 121044.
- [82] A. Olad, F. Doustdar, H. Gharekhani, *Coll. Surf. A Physicochem. Eng. Asp.* **2020**, *601*, 124962.
- [83] B. Salahuddin, S. Aziz, S. Gao, Md. S. A. Hossain, M. Billah, Z. Zhu, N. Amiralian, *Polym. (Basel)* **2022**, *14*, 5074.
- [84] D. A. Barus, S. Humaidi, R. T. Ginting, J. Sitepu, *Environ. Nanotechnol. Monit. Manag.* **2022**, *17*, 100650.
- [85] T. B. da Costa, P. H. Camani, R. R. Ferreira, A. G. Souza, M. G. A. Vieira, D. D. S. Rosa, *Int. J. Biol. Macromol.* **2025**, *317*, 144710.
- [86] N. I. A. Acevedo, M. C. G. Rocha, L. C. Bertolino, *Cerâmica* **2017**, *63*, 253–262.
- [87] J. C. Villalba, V. R. L. Constantino, F. J. Anaissi, *J. Coll. Interf. Sci.* **2010**, *349*, 49–55.
- [88] N. Saxena, A. Kumar, A. Mandal, *J. Pet. Sci. Eng.* **2019**, *173*, 1264–1283.
- [89] W. R. Mohamed, N. M. Sami, S. S. Metwally, E. A. Saad, *Hydrometallurgy* **2022**, *208*, 105816.
- [90] I. A. Silva, D. S. Silva, M. U. Sousa, R. R. Menezes, H. S. Ferreira, G. A. Neves, *Clean Technol. Environ. Pol.* **2020**, *22*, 2163–2176.
- [91] G. L. R. Leal, A. I. C. Garnica, R. R. Silva, L. R. Viana, A. C. B. Júnior, J. C. O. Freitas, F. D. S. Curbelo, *J. Pet. Sci. Eng.* **2022**, *215*, 110562.
- [92] X. Wang, Y. Li, H. Wang, *Minerals* **2020**, *10*, 347.
- [93] Y. Lu, A. Wang, *Micropor. Mesopor. Mater.* **2022**, *333*, 111765.
- [94] A. Sayed, M. Yasser, A.-r. ME, R. Mohsen, *Chem. Pap.* **2022**, *76*, 5119–5132.
- [95] M. R. Area, B. Montero, M. Rico, L. Barral, R. Bouza, J. López, *Int. J. Biol. Macromol.* **2022**, *202*, 345–353.
- [96] A. A. Keirudin, N. Zainuddin, N. A. Yusof, *Polym. (Basel)* **2020**, *12*, 2465.
- [97] H. M. Nizam El-Din, D. M. Ibraheim, *Int. J. Biol. Macromol.* **2021**, *192*, 151–160.
- [98] J. Strankowska, L. Piszczyk, M. Strankowski, M. Danowska, K. Szutkowski, S. Jurga, J. Kwela, *Eur. Phys. J. Spec. Top.* **2013**, *222*, 2179–2186.
- [99] S. Lee, M. Kim, J. Choi, S. Y. Kim, *Mater. Today Chem.* **2023**, *29*, 101434.
- [100] P. C. Khairuddin, A. Z. Nawangratri, T. Pham, *J. Phys. Conf. Ser.* **2019**, *1153*, 012091.
- [101] F. Arshadi, M. Mohammad, E. Hosseini, H. Ahmadi, M. Asadnia, Y. Orooji, A. H. Korayem, A. Noorbakhsh, A. Razmjou, *J. Memb. Sci.* **2021**, *639*, 119752.
- [102] X. Su, C. Xiao, C. Hu, *Int. J. Biol. Macromol.* **2018**, *115*, 1189–1193.
- [103] M. D. Hazrol, S. M. Sapuan, R. A. Ilyas, E. S. Zainudin, M. Y. M. Zuhri, N. I. Abdul, *Heliyon* **2023**, *9*, e15153.
- [104] S. Xu, Z. Zhou, Z. Liu, P. Sharma, *Sci. Adv.* **2023**, *9*, <https://doi.org/10.1126/sciadv.ade3240>.
- [105] Y. Wang, M. Lin, W. Dai, Y. Zhou, Z. Xie, K. Liu, L. Gao, *Coll. Polym. Sci.* **2020**, *298*, 1533–1541.
- [106] H. Peidayesh, Z. Ahmadi, H. A. Khonakdar, M. Abdouss, I. Chodák, *Polym. Adv. Technol.* **2020**, *31*, 1256–1269.
- [107] H. Liu, T. Chen, D. Chang, C. Qing, D. Kong, D. Chen, J. Xie, R. L. Frost, *J. Coll. Interf. Sci.* **2013**, *393*, 87–91.
- [108] M. Khan, I. M. C. Lo, *Water Res.* **2016**, *106*, 259–271.
- [109] M. G. Icduygu, M. Asilturk, M. A. Yalcinkaya, Y. K. Hamidi, M. C. Altan, *Materials* **2019**, *12*, 1387.
- [110] P. Kaur, H. B. Bohidar, D. R. Nisbet, F. M. Pfeffer, A. Rifai, R. Williams, R. Agrawal, *Cellulose* **2023**, *30*, 2713–2730.
- [111] M. Shahzamani, S. Taheri, A. Roghanizad, N. Naseri, M. Dinari, *Int. J. Biol. Macromol.* **2020**, *147*, 187–193.
- [112] J. S. Marciano, R. R. Ferreira, A. G. de Souza, R. F. S. Barbosa, A. J. de Moura Junior, D. S. Rosa, *Int. J. Biol. Macromol.* **2021**, *181*, 112–124.
- [113] M. B. Sordi, M. C. Fredel, A. C. C. da Cruz, P. T. Sharpe, R. de Souza Magini, *Clin. Oral Investig.* **2022**, *27*, 125–137.
- [114] T. Vieira, S. E. S. Artifon, C. T. Cesco, P. B. Vilela, V. A. Becegato, A. T. Paulino, *Coll. Polym. Sci.* **2021**, *299*, 649–662.
- [115] C. J. C. Nocheseda, F. P. Liza, A. K. M. Collera, E. B. Caldona, R. C. Advincola, *Addit. Manuf.* **2021**, *48*, 102380.
- [116] Y. Marcus, *J. Chem. Soc., Faraday Trans.* **1991**, *87*, 2995–2999.
- [117] S. Gu, X. Kang, L. Wang, E. Lichtfouse, C. Wang, *Environ. Chem. Lett.* **2019**, *17*, 629–654.
- [118] S. M. Lalji, S. I. Ali, R. Ahmed, S. Hashmi, Z. U. I. H. Awan, Y. Jawed, *Arab. J. Geosci.* **2022**, *15*, 864.
- [119] C. Xu, Y. Xu, D. Zhong, H. Chang, J. Mou, H. Wang, H. Shen, *Carbohydr. Polym.* **2022**, *296*, 119872.
- [120] Y. Xu, J. Chen, R. Chen, P. Yu, S. Guo, X. Wang, *Water Res.* **2019**, *160*, 148–157.
- [121] L. Zhang, W. Xia, X. Liu, W. Zhang, *J. Mater. Chem. A Mater.* **2015**, *3*, 331–340.

Manuscript received: March 31, 2025

RESEARCH ARTICLE OPEN ACCESS

Chitosan Hydrogels Crosslinked With Glutaraldehyde for Potential Toxic Elements Removal: Batch and Purification Device Analysis

Rennan F. S. Barbosa¹ | Sudip Shyam² | Sirshendu Misra² | Sushanta K. Mitra² | Derval S. Rosa¹ 

¹Center for Engineering, Modeling, and Applied Social Sciences (CECS), Federal University of ABC (UFABC), Santo André, SP, Brazil | ²Micro & Nano-Scale Transport Laboratory, Waterloo Institute for Nanotechnology, Department of Mechanical and Mechatronics Engineering, University of Waterloo, Waterloo, Ontario, Canada

Correspondence: Derval S. Rosa (derval.rosa@ufabc.edu.br)

Received: 17 September 2024 | **Revised:** 27 May 2025 | **Accepted:** 19 June 2025

Funding: This work was supported by Fundação de Amparo à Pesquisa do Estado de São Paulo (2020/13703-3, 2021/08296-2, 2021/14714-1) and Conselho Nacional de Desenvolvimento Científico e Tecnológico (403934/2021-4, 308053/2021-4), and Mitacs (IT30489).

Keywords: adsorption | gels | polysaccharides | swelling

ABSTRACT

The presence of toxic metal ions in contaminated wastewater raises significant concerns for human health. Three-dimensional porous systems like hydrogels are being explored for contaminant removal. Still, there is a lack of understanding of their production parameters and performance. Therefore, the present work investigates the production parameters of chitosan hydrogels using the design of experiments methodology. Hydrogels were developed by solubilizing chitosan in acetic acid solution and cross-linked using glutaraldehyde, varying its proportions. The formulation containing 2% chitosan and 1% glutaraldehyde has water absorption superior to 300% and potential for metal removal, particularly copper and chromium. Crosslinking was validated by FTIR analysis, and the obtained hydrogel presented a highly porous structure. Kinetic studies showed a better fit to a pseudo-second order, and the Langmuir isotherm presented the best fit, showing sorption capacities of 0.422 and 1.143 mmol g⁻¹ for copper and chromium, respectively. Filtration tests demonstrated that a 0.25 mL/min flow rate provided the best performance, with an initial fast removal that stabilizes. In addition, the weight and design used directly influence the adsorption properties. Results show that chitosan-based hydrogels can potentially remove metal contaminants. A filtering system is a feasible alternative for developing a low-cost, efficient, and environmentally friendly system.

1 | Introduction

Water contamination is one of modern society's most worrying environmental impacts, presenting a considerable public health threat [1]. Potentially toxic elements (PTEs) such as agricultural pesticides, fertilizers, herbicides, dyes, solvents, drugs, organic waste, and traces of metal ions discharged without adequate treatment by industries have raised significant concerns about their continued impact along the trophic chain, as they have long-term effects [2]. The presence of metal ions is particularly aggravating since they are nonbiodegradable and toxic even at

low concentrations and may undergo bioaccumulation and biomagnification along the food chain [3].

Different technologies have been studied to treat effluents to PTEs from water, the most common being solvent extraction [4], ion exchange [5], chemical precipitation [6], and reverse osmosis [7]. However, these methods suffer from some drawbacks like high use of reagents and energy, limited removal potential at low concentrations, generation of toxic by-products, and long treatment times [8, 9]. Thus, new alternatives have been investigated, and the use of adsorption has emerged as one potential

This is an open access article under the terms of the [Creative Commons Attribution](https://creativecommons.org/licenses/by/4.0/) License, which permits use, distribution and reproduction in any medium, provided the original work is properly cited.

© 2025 The Author(s). *Journal of Applied Polymer Science* published by Wiley Periodicals LLC.

process to meet the demands of metal removal, presenting low cost, smooth and flexible operating parameters, low energy consumption, and high efficiency [10].

The adsorption is based on the presence of binding sites on the surface of the adsorbent material, which makes it a process highly influenced by surface groups and the surface area of the material [11]. The use of biopolymers like chitosan for adsorption is appealing due to their abundance, biodegradability, low cost, and functional surface and backbone with hydroxyl (—OH) and amine (—NH₂) groups, which makes their application competitive against usual processes [1, 12]. Upadhyay and collaborators reported that these groups guarantee the chitosan hydrogel's capacity to remove metal ions [13].

Furthermore, to promote systems with increased surface area, the development of polymeric structures like hydrogels, which exhibit high hydrophilicity and the ability to absorb large volumes of water, is an interesting approach to enhancing adsorption properties [14]. The reaction of chitosan with glutaraldehyde undergoes a condensation reaction with the free amino groups through a Schiff's base reaction, known as crosslinking, and promotes a three-dimensional network with elevated surface area and porosity [12].

The structure's crosslinking is interesting because it increases the stability of the chitosan and allows it to be recovered and reused. However, the surface functional groups are consumed during this reaction, which can compromise their properties and application. Furthermore, the practical use of hydrogels in filtering systems is still scarce, so the materials developed have not been evaluated in simulations of real systems.

Therefore, to evaluate the impact of the concentration of chitosan and the crosslinking agent used in forming hydrogels to remove metal ions and propose their application, this work systematically investigates the fabrication and characterization of chitosan hydrogels. The hydrogels were evaluated for their capacity to absorb water and remove metal ions in experiments. The best formulation was then evaluated using FIB-SEM and flow tests to develop a device for application in filtering systems.

2 | Materials and Methods

2.1 | Materials

In this study, chitosan was provided by Polymar (Brazil). Glutaraldehyde was used as a reticulation agent, and analytical standards of the target metal ions (Cd(II), Cr(VI), Cu(II), Mn(II), Zn(II), and Ni(II)) were employed for the sorption assays. All reagents were purchased from Labsynth Produtos para Laboratórios (Brazil). Poly(dimethylsiloxane) (PDMS) Sylgard 184, a silicone elastomer base, was obtained from Dow Corning (USA).

2.2 | Chitosan Hydrogel Development

For the development of chitosan hydrogels, a systematic study was carried out in order to select the optimal conditions for

hydrogel production. Figure 1a illustrates the obtaining process of the hydrogel. Briefly, the chitosan was solubilized in a solution of acetic acid (2% v/v) in different concentrations (1%, 2%, and 3% w/v). For hydrogel formation, glutaraldehyde was used as a crosslinking agent at various concentrations (1% to 10% v/w). Response surface planning was employed to evaluate the effect of the proportion of chitosan and the crosslinking agent, and 18 formulations were generated, as presented in Table S1 (Supporting Information). After preparation, the samples were washed in 3 cycles to remove noncrosslinked glutaraldehyde and then stored for characterization.

2.3 | Development of a Model Filtering Device

A 3D printer (model Form 3B, Formlabs, USA) was used to develop a mold containing flow channels, with an internal cavity for inserting the hydrogel, to simulate a filtering system with a solution flow. Different geometric characteristics were considered to evaluate variables related to mold development, illustrated in Figure 1. Initially, a rectangular structure was evaluated to accommodate the hydrogel, as shown in Figure 1b, which has dimensions of 3 mm by 2 mm in the inner cavity. A similar mold was developed to complement this system, but with dimensions of 10 mm by 2 mm, as shown in Figure 1c. It was also considered a system composed of an internal cavity with internal angles, maintaining the rectangular section of 10 mm by 2 mm but composed of angled walls, as shown in Figure 1d. These aspects were important for assessing the impact on the sorption process, as illustrated in Figure 1 and presented in more detail in the characterization section below.

After obtaining the mold, a PDMS solution was prepared, mixing the silicone solution with a curing agent at a ratio of 10:1, respectively. The resulting mixture was then degassed in a desiccator to remove the air bubbles, poured into the mold, and cured for 4 h in an oven at 80°C [15]. After this, the PDMS system was removed from the mold, the hydrogel was placed inside, and the system, along with a glass slide, was treated with O₂ plasma (Plasma Etch PE25-JW Plasma Cleaner) to destroy the surface chemistry and allow its bonding for sealing.

2.4 | Characterization

2.4.1 | Degree of Swelling

The water absorption capacity of the samples was evaluated by immersion in distilled water at room temperature, in triplicate. The samples were taken at regular intervals, the excess water was removed with the help of a tissue, and then weighed using an electronic scale. The weight before and after water immersion was then evaluated to determine the absorption capacity. This parameter can be defined as follows:

$$DS = \frac{m_f - m_i}{m_i} \times 100 \quad (1)$$

Where m_i is the initial dry mass of hydrogels at $t=0$ (g) and m_f is the swollen mass of hydrogels at time t (g).

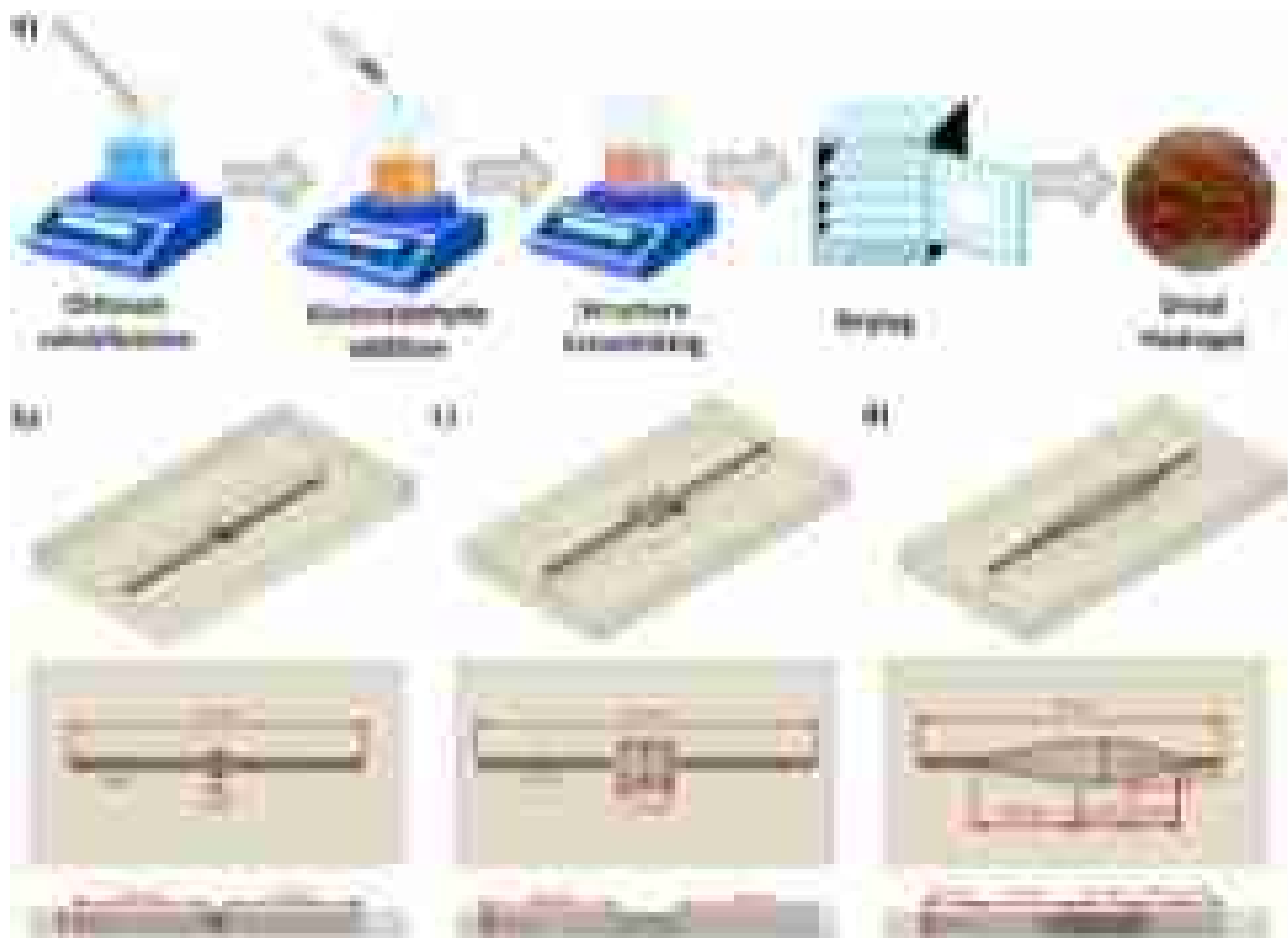


FIGURE 1 | (a) Illustration of the chitosan hydrogel production process; and representation of the filtering system with an illustration of the molds used showing the three-dimensional designs, top view, and side view, (b) rectangular design with internal cavity of 3 mm by 2 mm, (c) rectangular design with internal cavity of 10 mm by 2 mm, (d) angular design with internal cavity of 10 mm by 2 mm. [Color figure can be viewed at [wileyonlinelibrary.com](https://onlinelibrary.wiley.com)]

2.4.2 | Sorption Assays in the Batch System: Hydrogels Affinity

The affinity test of the developed hydrogels for Cu^{2+} , Ni^{2+} , Zn^{2+} , Cd^{2+} , Mn^{2+} , and Cr^{6+} was performed by adding 0.1 g of hydrogels and 25 mL of metal ions solution (0.17 mmol/L each) in Erlenmeyer flasks (125 mL). The solution pH was maintained at 4 with an HNO_3 solution. The sorption affinity assays were conducted in a shaker incubator (SL-180/A, Solab, Brazil) at 150 rpm at room temperature ($\sim 25^\circ\text{C}$). After 24 h, the metal ion concentrations were determined by ion chromatography (940 Professional IC Vario, Metrohm, Switzerland), and the data were processed using MagIC Net 4.0 Software.

2.4.3 | Fourier-Transform Infrared Spectroscopy (FTIR)

Fourier transform infrared spectroscopy (FTIR) was performed in a Frontier 94,942 Spectrophotometer (PerkinElmer, USA) to evaluate the chemical changes in the structure of the cellulose and hydrogels formed, using the attenuated total reflectance accessory. The analysis was performed with a resolution of 4 cm^{-1} , using 64 scans and a scanning range of $4000\text{--}600\text{ cm}^{-1}$.

2.4.4 | Microstructure Imaging—FIB-SEM

A Zeiss Crossbeam 350 with Laser was used to perform the FIB-SEM analysis, which combines a regular SEM microscope with a laser cannon that can remove surface material and produce a flat 2D surface for the material evaluation [16, 17]. The sample was mounted with carbon tape. Then, the femtosecond laser was used to ablate the material using a 30 kV voltage and a current of 10 nA to obtain a cavity to explore the interior porous, and a final beam current of 50 pA was used to polish the internal structure of the hydrogel sample. After this procedure, the SEM images were obtained with a voltage of 4 kV and a current of 50 pA. The pore size distribution was evaluated using ImageJ software.

2.4.5 | Sorption Assays in the Batch System: Kinetic Study

The kinetic sorption of chitosan matrix toward specific metal ions (Cu^{2+} and Cr^{6+}) was evaluated using mono-element solutions to investigate the performance without competing ions. Therefore, a solution containing individually Cu^{2+} or Cr^{6+} at 1 mmol L^{-1} was prepared at pH 4, and a dosage of 1 g L^{-1} was employed.

The sorption assay was conducted using an orbital shaker table SL-180/A (Solab, Brazil) at 150 rpm at room temperature ($\sim 25^{\circ}\text{C}$). Samples of the liquid phase were collected at determined times (0–24 h), and the solution was filtered using a $22\ \mu\text{m}$ filter to remove the particulate sample, and the obtained solution was analyzed using Ion Chromatography.

2.4.6 | Sorption Essays in the Batch System: Equilibrium Study

The effect of metal ion concentration was investigated. Different metal ion solutions with concentrations ranging from 0.1 to $2\ \text{mmolL}^{-1}$ were prepared. The adsorbent material was then added using a $1\ \text{gL}^{-1}$ dosage.

The experiment was conducted using an orbital shaker table at 150 rpm at room temperature ($\sim 25^{\circ}\text{C}$) for 24 h. Then, the solution was filtered using a $22\ \mu\text{m}$ filter to remove the particulate sample, and the obtained solution was analyzed using Ion Chromatography. The experimental data were fitted according to Langmuir and Freundlich Isotherms using the nonlinear equations.

3 | Results and Discussion

3.1 | Hydrogel Characterization

The crosslinking of glutaraldehyde with chitosan is a favorable reaction due to the high reactivity of aldehyde groups toward amine groups. This promotes the formation of an imine bond, also known as Schiff bases [18]. This reaction occurs through a nucleophilic attack of the amine group's free electrons toward the aldehyde group's carbon, followed by a proton transfer from the amine to oxygen, forming a hydroxyl group. Then, the protonation of this hydroxyl occurs, promoting the release of water by creating a $\text{C}=\text{N}$ linkage. After this, deprotonation occurs from the nitrogen atom, neutralizing the molecule's charge [19].

Figure 2 presents the proposed cross-linking mechanism responsible for producing chitosan hydrogels. It illustrates the interaction of a chitosan chain with one side of a glutaraldehyde molecule. For the complete cross-linking process, another chitosan chain is expected to interact with the other aldehyde group, forming a complex polymeric network.

The obtained chitosan hydrogels after crosslinking were then evaluated to understand the influence of concentration on the crosslinking process and the impact of their properties on their potential applications.

A typical characteristic of hydrogels is their swelling capacity due to water absorption, which may be affected by the crosslinking degree, the hydroxyl content, and hydrated groups [20]. Therefore, to assess the hydrogels' swelling capacity, the water absorption test was carried out for 1 and 7 days, and the results are shown in Figure 3. The individual data are presented in Table S2 (Supporting Information).

Figure 3 shows that all the hydrogels showed a high degree of water absorption, greater than 100%, after 1 day of testing.

Furthermore, it is observed that some samples stood out with more than 200% absorption, and some samples surpassed 300% water absorption. Wei and co-workers, who investigated using different molecular weights of chitosan and citric acid, observed water absorption of around 20% [21]. Liu and co-workers obtained hydrogels based on chitosan and gelatin that presented a swelling degree of around 60% [22]. Wei and co-workers developed a PVA/chitosan hydrogel film that presented a swelling degree of 260% and showed great potential to remove dye from water solutions [21]. Therefore, the obtained hydrogels have higher absorption values, indicating their potential for intended application in removing metal ions.

Comparing the response surface curve shapes, it is observed that a similar profile is present, and it is possible to identify a behavior trend for which the lower glutaraldehyde content implies greater water absorption. This result may be associated with the extent of the crosslinking of the chitosan chain with glutaraldehyde. It is expected that glutaraldehyde reacts with the available amine groups in the chitosan structure [23]. Therefore, free amino groups are reduced, and the conformational entanglement may promote new interactions through hydrogen bonds. This process promotes a reduction of available groups able to absorb water and may also impact the potential removal of contaminants [24, 25]. In addition, increasing the chitosan content does not clearly benefit the absorption properties, indicating that the combination of lower concentrations of chitosan and glutaraldehyde shows the best response in the space studied.

To evaluate the potential application of the developed hydrogels as an adsorption material, they were tested using a selectivity assay containing six metal ions with equimolar concentration. The response surfaces presenting the removal rate obtained are shown in Figure 4, and the individual data are presented in Table S3 (Supporting Information).

Figure 4 shows that the hydrogels removed metal ions with distinct behavior, which indicates the affinity of chitosan's chemical structure with the ions evaluated. The adsorption process is affected by both test conditions, like pH, concentration, dosage, temperature, and agitation, while the metal ions interaction may be influenced by hydrated ionic radius, surface charge, electronegativity, and competition in a multi-component solution [26, 27]. Evaluating the surface profiles, the removal of nickel and cadmium showed a similar trend, with higher removal observed in the intermediate region of the evaluated experimental space. On the other hand, the removal of zinc and manganese showed better removal in the corner regions of the curve. In contrast, the removal of copper and chromium had a linear correlation between the property and the formulations evaluated.

As reported in the literature, chitosan hydrogels are expected to interact with metallic ions through functional groups that include hydroxyls and amines at the chitosan chemical structure [28, 29]. However, the crosslinking process promotes the formation of covalent bonds, reducing the availability of these groups and possibly impacting the sorption capacity of the hydrogels developed [21]. It is worth noting that the hydrogels presented a significant removal potential for copper and chromium.

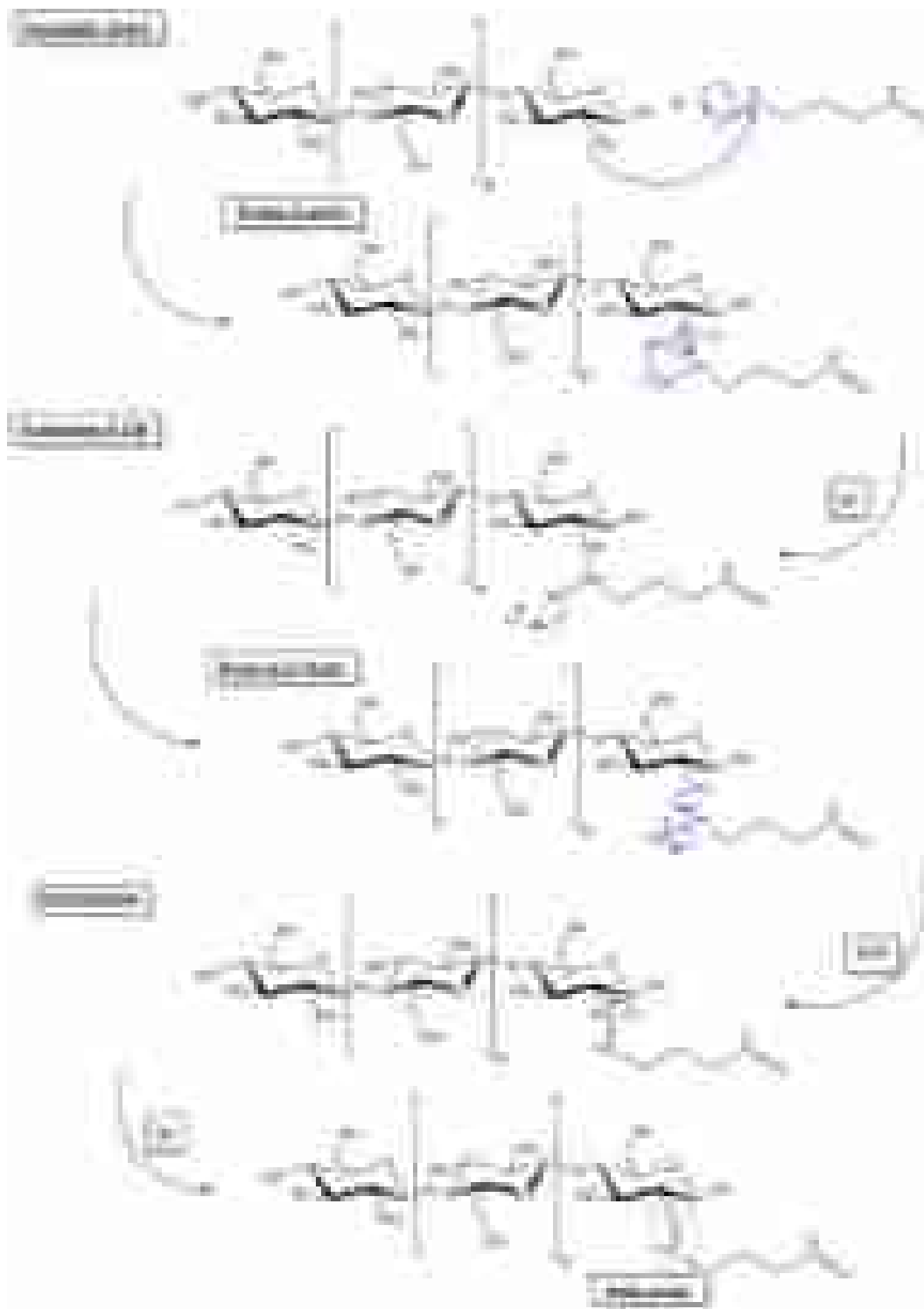


FIGURE 2 | Crosslinking mechanism reaction of chitosan and glutaraldehyde responsible for promoting the hydrogel polymeric network. [Color figure can be viewed at [wileyonlinelibrary.com](https://onlinelibrary.wiley.com/doi/10.1002/app.57539)]

In the case of copper removal, a significant variation in removal was observed depending on the composition employed, which indicates that the degree of hydrogel crosslinking directly influences the groups available for interaction and removal of the metal ion. It is possible to notice that the lower chitosan and glutaraldehyde content combined provided the hydrogel with higher copper removal. Mallik and collaborators also highlighted the potential of chitosan for copper removal using chitosan-based adsorbents [30].

Regarding chromium removal, a total removal was observed under the test conditions, considering the deviation between the samples, indicating that the chitosan matrix presents a high affinity for chromium removal. Possibly, under the test conditions, the saturation of active sites for chromium removal was not obtained. The literature corroborates this result, for which the removal is associated with interaction with hydroxyls and protonated amine groups [31]. Wang and co-workers highlighted

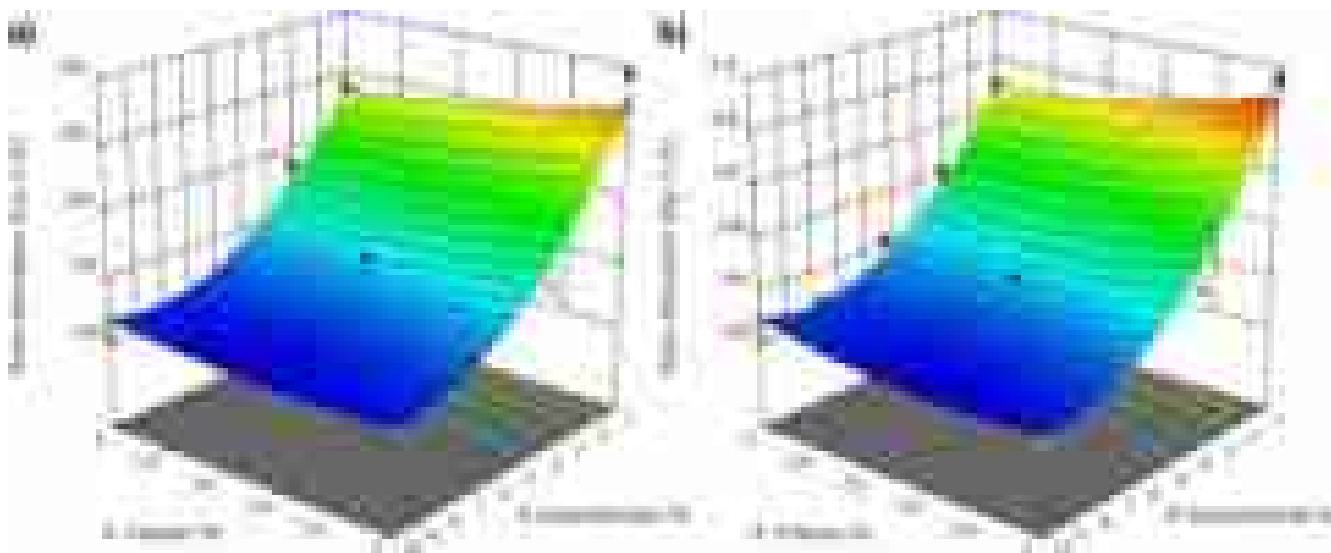


FIGURE 3 | Response surface and contour plot of water absorption concerning chitosan and glutaraldehyde concentrations in (a) 1 day and (b) 7 days of water contact. [Color figure can be viewed at [wileyonlinelibrary.com](https://onlinelibrary.wiley.com)]

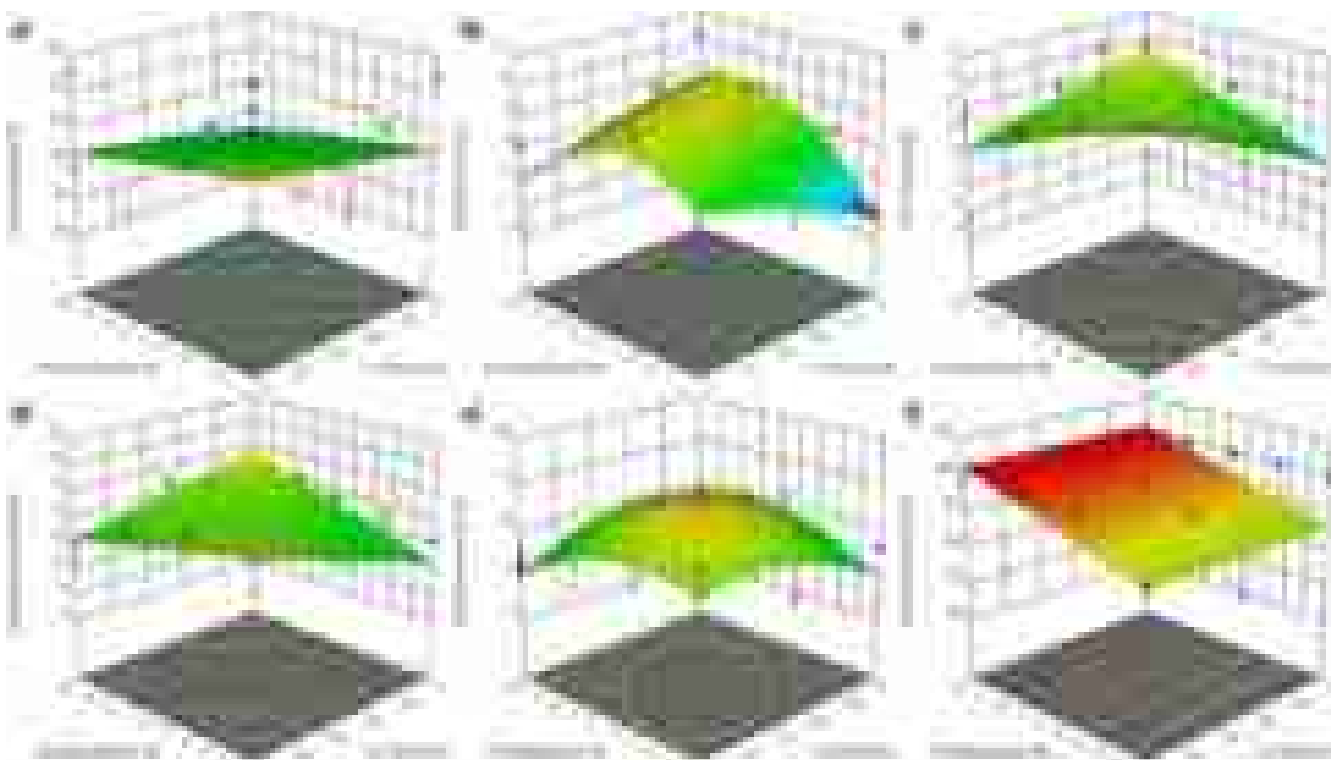


FIGURE 4 | Response surface and contour plot concerning chitosan and glutaraldehyde concentrations for the removal of (a) copper, (b) nickel, (c) zinc, (d) manganese, (e) cadmium, and (f) chromium. [Color figure can be viewed at [wileyonlinelibrary.com](https://onlinelibrary.wiley.com)]

the potential application of chitosan aerogels for chromium removal, even in the presence of competing contaminants [32].

Water absorption and metal ions removal results were used as response parameters to the experimental planning developed to select the better hydrogel preparation condition, enhancing the properties obtained. The results were analyzed using the Design Expert software, defining the condition that the concentration of chitosan was in the range used in the formulations and that the glutaraldehyde concentration was minimized. Based on this

condition, the software highlighted that the hydrogel developed with 2% chitosan and 1% glutaraldehyde showed the best sorption potential. Thus, this condition was selected as the optimal condition for hydrogel development, named CH for chitosan hydrogel, and further evaluated.

The CH matrix was investigated using the FTIR technique to analyze the functional groups in chitosan and the impact promoted by the cross-linking reaction. The obtained spectra are presented in Figure 5.

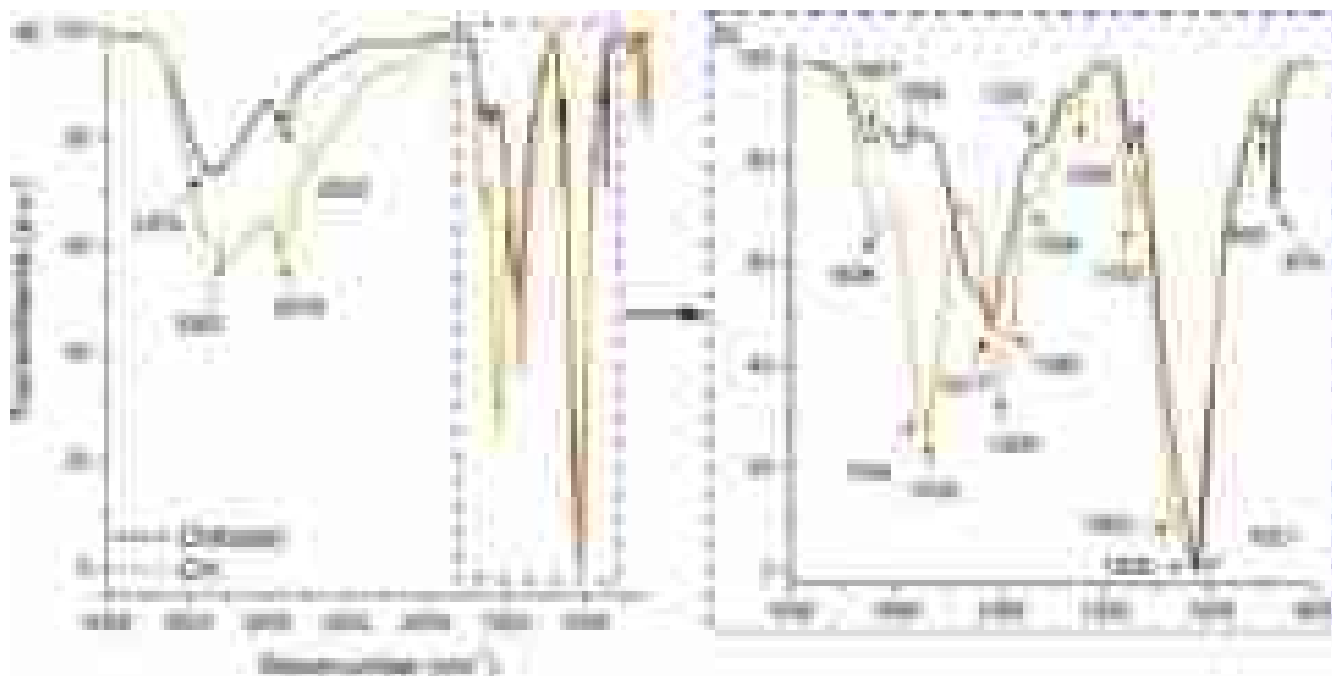


FIGURE 5 | FTIR spectra with highlighted peaks of chitosan and chitosan hydrogel (CH) with (a) full FTIR spectra and (b) zoom at 1800–800 range to illustrate the main differences in the fingerprint region. [Color figure can be viewed at [wileyonlinelibrary.com](https://onlinelibrary.wiley.com)]

From the FTIR spectra, characteristic chitosan peaks can be observed. A vast band at 3374cm^{-1} is related to the overlapped stretching of hydroxyl and amine groups. The peak at 2922cm^{-1} is associated with the $-\text{CH}$ stretching. It is also observed amid I from chitosan acetylated rings and amines of deacetylated rings at 1647 and 1588cm^{-1} peaks, respectively [33]. The strong band around 1417cm^{-1} is associated with $\text{C}-\text{N}$ deformation. The peak at 1152cm^{-1} is also related to the $\text{C}-\text{O}-\text{C}$ glycoside structure [34].

Regarding the chitosan hydrogel (CH), it is observed that the spectra changed considerably, specifically in the fingerprint region (from 1800 to 800cm^{-1} range). It is worth noting the change in the 1636cm^{-1} region with the presence of a single peak, which may be associated with the imine group ($\text{C}=\text{N}$), indicating the success of cross-linking of the hydrogel [35, 36]. It is also observed a shift for the band of $\text{C}-\text{N}$ to 1406cm^{-1} , reinforcing the interaction promoted in this region [37]. It also highlighted the appearance of bands at 1554 and 1383cm^{-1} , which are associated with $\text{C}-\text{H}$ stretching, related to the glutaraldehyde chain, and are reinforced by the increased intensity of the 2919cm^{-1} band [38, 39]. These results validate the cross-linking of the chitosan structure previously mentioned.

The metal adsorption and water absorption are intrinsically linked to the porous structure of the hydrogel. Therefore, scanning electron microscopy was used to evaluate the selected chitosan hydrogel structure. However, since removing the water within the hydrogel during the sample preparation process is essential, it is expected to observe the pores will collapse at the surface structure. This behavior was observed by Mohamed and co-workers [40] and Anigor and co-workers [41]. Therefore, the FIB-SEM technique was employed to properly evaluate the hydrogel porous structure. It is worth highlighting the importance of the method used, which can make a laser cut in the sample and reveal the internal structure, being extremely valuable for evaluating the hydrogel's

internal porous structure without compromising it during sample preparation [17, 42]. Figure 6a shows the obtained FIB-SEM image revealing a highly porous structure, corroborating the observed properties. The pores observed are within the macroporous in size [43], with values of $23.6 \pm 6.8\mu\text{m}$ and, as can be seen in Figure 6b, there is a concentration of pores in the $20\text{--}25\mu\text{m}$ range, followed by the $25\text{--}30$ and $15\text{--}20\mu\text{m}$ ranges, concentrating around 74% of the pores observed.

The time required for the adsorption process to occur is an important parameter. Therefore, the kinetic study of adsorption for the most promising metal ions removed using the chitosan hydrogel (copper and chromium) was performed, and the obtained curves are presented in Figure 7.

The kinetic curve shown in Figure 7 indicates that the chitosan hydrogel has a high initial sorption rate, which reduces over time as the available sites become saturated, while internal sites become available as the hydrogel structure swells, as reported by Vieira and collaborators [44]. The removal was significant in the first hours, reaching 86% and 89% removal rates at 6 h for copper and chromium, respectively, of the total adsorbed amount in 24 h.

The pseudo-first order (PFO) and pseudo-second order (PSO) kinetic models were used to fit the obtained data, and the fit parameters are presented in Table 1.

It is observed that the PSO model presented a better fit for copper and chromium, showing a higher R^2 and lower red- χ^2 value. According to Ferreira and co-workers, this model indicates that the sorption rate is associated with the number of sites available in the adsorbent structure, which may suggest that chemisorption is the key sorption process [45]. Yu and co-workers also indicated that chemisorption is the dominant rate-limiting step

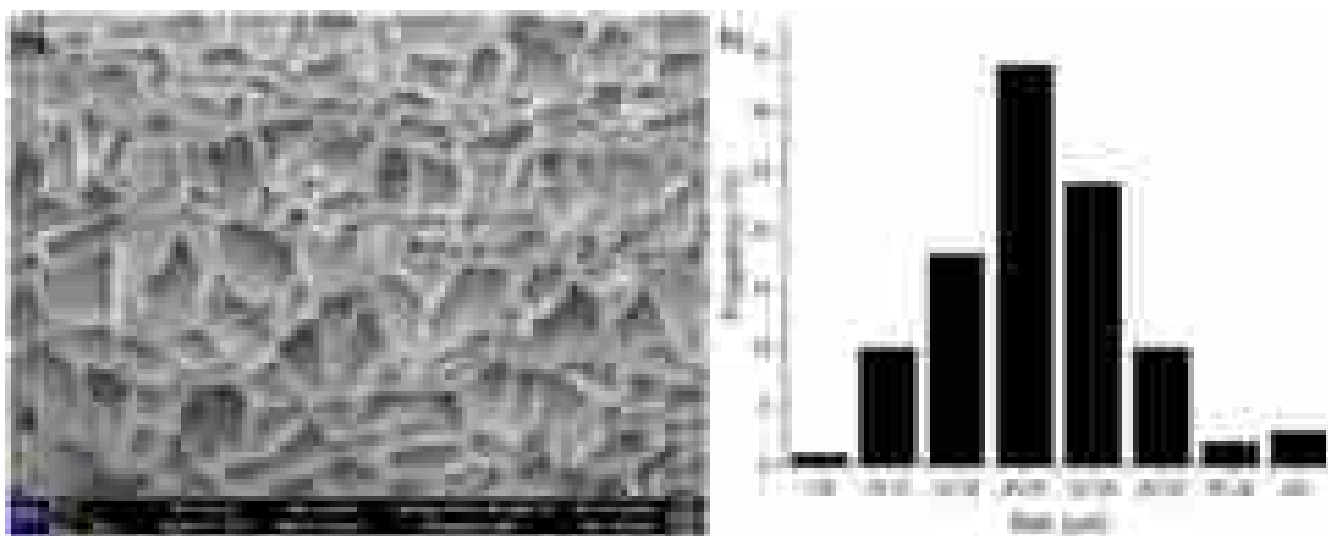


FIGURE 6 | (a) Chitosan hydrogel porous structure obtained after FIB milling followed by SEM analysis, (b) pore size histogram distribution. [Color figure can be viewed at [wileyonlinelibrary.com](https://onlinelibrary.wiley.com)]

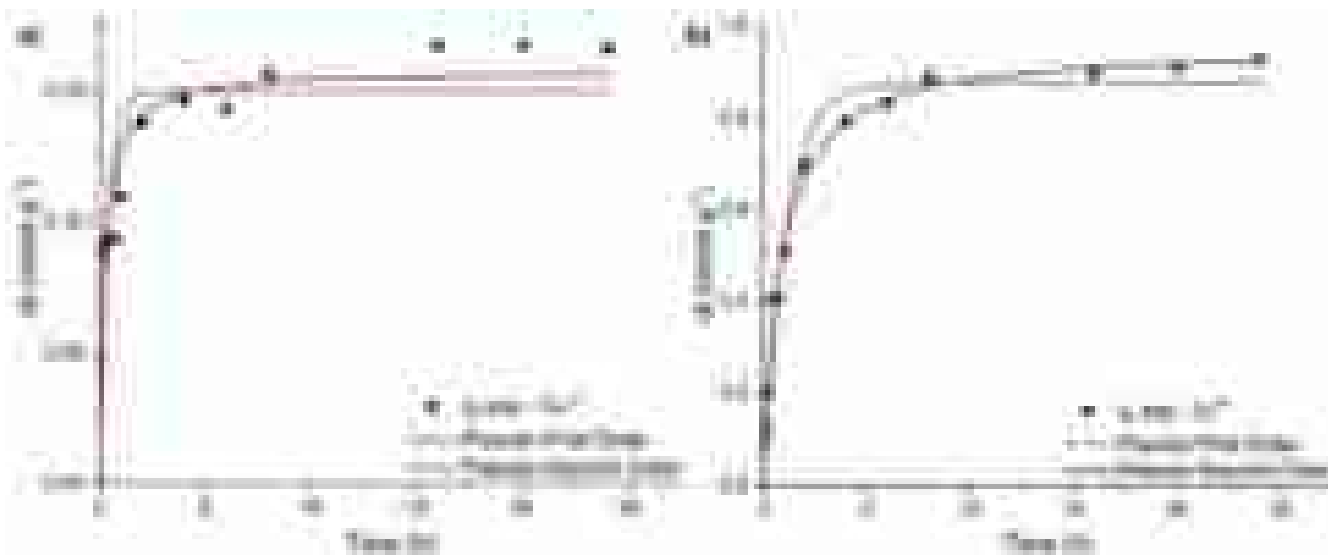


FIGURE 7 | Kinetic curve for chitosan hydrogel in removing (a) copper and (b) chromium. [Color figure can be viewed at [wileyonlinelibrary.com](https://onlinelibrary.wiley.com)]

of magnetic chitosan–iron(III) hydrogels [46]. Vilela and co-workers also reported a similar finding working with chitosan-based hydrogel, suggesting that the active-binding site number governs the sorption of chromium [47].

The isotherm study was performed to understand the CH performance further and measure the matrix adsorption capacity. Figure 8 presents the experimental data points and fitted isotherm models for copper and chromium adsorption by CH. The fitted parameters are presented in Table 2.

As shown in Table 2, the Langmuir isotherm model presented a better fit for removing copper and chromium due to its higher R^2 and lower χ^2 than the Freundlich model, which reinforces that possibly chemisorption is associated with the metal ions adsorption process.

From q_{\max} values reported by the Langmuir fit, it is observed that the chitosan matrix presents a considerable removal of

chromium, which is possibly associated with hydroxyl and amine groups present at the chitosan structure. According to Lv, the adsorption capacity of hydrogels is associated with the synergistic effect of the three-dimensional porous structures and the presence of binding sites for metal adsorption [48]. Moreover, it highlights that the crosslinking concentration employed did not hinder the available sites from promoting the effective adsorption process.

Table 3 shows the adsorption capacity of recently published hydrogels, fibers, and other adsorbents, as well as the results obtained in this study, allowing comparison with the literature.

From the adsorption capacity, it is observed that several works presented adsorption capacity around the range of $0.50\text{--}2.0\text{ mmol g}^{-1}$, which was close to the values observed in the chitosan hydrogel developed in the presented study. Notably, some reports from the literature present superior adsorption

TABLE 1 | Fit parameters of the kinetics models of Cu²⁺ and Cr⁶⁺ sorption by chitosan hydrogel (CH).

Metal	Model	Parameters		Model	Parameters	
Copper	Pseudo-first order (PFO)	q _e (mmol g ⁻¹)	0.15	Pseudo-second order (PSO)	q _e (mmol g ⁻¹)	0.158
		k ₁ (min ⁻¹)	2.485		k ₂ (g mmol ⁻¹ min ⁻¹)	25.13
		R ²	0.836		R ²	0.929
		red-χ ²	4.41E+04		red-χ ²	1.90E-04
Chromium	Pseudo-first order (PFO)	q _e (mmol g ⁻¹)	0.874	Pseudo-second order (PSO)	q _e (mmol g ⁻¹)	0.957
		k ₁ (min ⁻¹)	0.904		k ₂ (g mmol ⁻¹ min ⁻¹)	1.216
		R ²	0.985		R ²	0.995
		red-χ ²	1.77E-03		red-χ ²	6.01E-04

**FIGURE 8** | Adsorption isotherms for Cr⁶⁺ according to Langmuir and Freundlich models for (a) CH, (b) CH-5% CN, (c) CH-3% CN-Suc, and (d) CH-10% CN-EDTA. [Color figure can be viewed at [wileyonlinelibrary.com](https://onlinelibrary.wiley.com)]**TABLE 2** | Fit parameters of the isotherm models of Cu²⁺ and Cr⁶⁺ sorption for pure chitosan hydrogel and composites containing nanocellulose without and with modification.

Model		Copper	Chromium
Langmuir	q _{max} (mmol g ⁻¹)	0.422	1.143
	K _L (L mmol ⁻¹)	9.318	27.384
	R ²	0.994	0.979
	red-χ ²	1.99E-04	4.63E-03
Freundlich	K _F (mmol g ⁻¹) (L mmol ⁻¹)	0.363	1.144
	n	3.704	5.044
	R ²	0.966	0.967
	red-χ ²	1.09E-03	7.46E-03

capacities, showing room for improvement of the developed hydrogel, which could be attained with the chemical functionalization of chitosan or the addition of highly adsorbent nanostructures.

3.2 | Hydrogel Application in Filtering Device

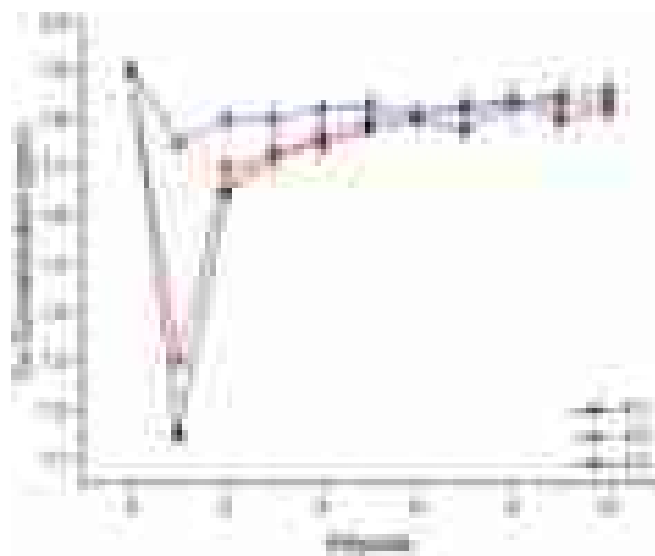
One of the main drawbacks of developing a new formulation is evaluating its effectiveness in simulating a real condition. This happens since the adsorption tests are usually performed in batch conditions, which are difficult to correlate with dynamic conditions where a solution flow is present. Therefore, the development of a filtering device was investigated using the selected chitosan hydrogel sample. To prepare the filtering system, a 3D printer was employed to obtain a mold for the device production using PDMS.

An initial design, as presented in Figure 1b, was established considering a small cavity for inserting the hydrogel, and then a system flow test was carried out. The system showed promising potential for the intended application, as presented in the video in the [Supporting Information](#). It is worth noticing in the video that the hydrogel's swelling process can be observed, which occurs instantaneously and corroborates the water absorption results observed previously.

Different variables were considered to optimize the metal ion removal process and analyze the application potential of the developed system. The first evaluation was to determine the test

TABLE 3 | Comparison of adsorption capacity presented in published results with the present work.

Adsorbent material	Adsorption capacity (mmol g ⁻¹)		References
	Cu ²⁺	Cr ⁶⁺	
Alginate-based composite beads	1.01	—	[49]
CS/PVA/PVP composite hydrogel	0.52	—	[50]
Humus chitosan hydrogel	—	1.22	[51]
Kaolin/CNTs/PAM hydrogel	1.52	—	[52]
Zwitterionic plastic-hydrogel	—	1.64	[53]
S2-intercalated layered double hydroxide	—	0.67	[54]
Teff straw-based activated carbon	—	0.95	[55]
Carboxymethylated chitosan hydrogel beads	2.05	—	[56]
Chitosan–cellulose hydrogel beads	0.84	—	[57]
Chitosan-based hydrogel		1.41	[47]
Chitosan hydrogel	0.44	1.14	This work

**FIGURE 9** | Temporal evaluation of copper removal using initial square design and different flow rates (F1 = 0.05 mL/min, F2 = 0.25 mL/min, F3 = 0.5 mL/min). In the x-axis, 0 represents the initial metal concentration (before passing through the filtering device). The number indicates the solution samples obtained sequentially after passing through the filtering device developed. [Color figure can be viewed at [wileyonlinelibrary.com](https://onlinelibrary.wiley.com)]

flow since a small flow can be a prolonged and unfeasible process. In contrast, a very high flow can present pressure, leakage problems, and low contact time for interaction. Therefore, a study using copper ions as a reference was carried out due to the considerable removal observed with hydrogels. Different flow rates, named F1 (0.05 mL/min), F2 (0.25 mL/min), and F3 (0.5 mL/min), were established to evaluate metal removal from the medium.

For this, the removal of copper with flow was considered due to its intermediate removal rates, lower than chromium but superior to other metal ions. Figure 9 shows the results observed for removal over time. It is possible to observe that the flow applied directly impacted the removal of copper ions, for which the lowest flow rate showed the highest removal, around 39%, for the first sample, while the intermediate flow rate had a removal of 31%. On the other hand, the fastest flow rate showed little removal, limited to 8%.

This behavior is consistent with the need for a minimum period of interaction between the solution and the surface of the material, allowing the contaminant of interest to interact with the chemical groups present [58]. In addition, the diffusion process to the internal regions of the hydrogel tends to take place and requires time, as it is associated with the swelling of the hydrogel structure, so a lower flow rate allows greater contact with the structure, ensuring its expansion and interaction [59]. The highest flow used had a low removal potential, which may indicate that the ions had little time to interact with the hydrogel structure and are not efficiently removed from the medium. It is worth noting that the intermediate flow still showed considerable removal and a time gain compared to the lower flow and was therefore selected as the ideal flow for further tests.

Evaluating the results, it was also possible to observe that the samples taken consecutively showed a reduction in the contaminant removal potential, which may be associated with the saturation of the structure's most available surface groups. Even so, the material continues to remove the metal from the medium, as over time, the hydrogel structure also swells with the diffusion of water and allows new internal groups to be exposed. Overall, it was observed that after five sequential samples, the values showed little variation for subsequent samples, which is interesting, as it indicates that the system has a consistent adsorption property. Only five samples were taken in the additional experiments since the system presented stability beyond that point.

It was also observed that due to the swelling nature of the hydrogel, it expanded considerably, spreading beyond the original area of the designed device. Moreover, the size of the initial design would limit the hydrogel weight to be included in the device cavity. A new mold design was prepared using larger dimensions, as shown in Figure 1c, to solve these issues. Another variation considered was an alternative design with an internal angle between the walls to accommodate water flow during system use better, as presented in Figure 1d. Both systems were evaluated to apply the hydrogel to remove metal ions.

Therefore, a new batch was prepared, and different weights of the developed hydrogel were evaluated during its application in the filtering device. Figure 10 shows the removal results

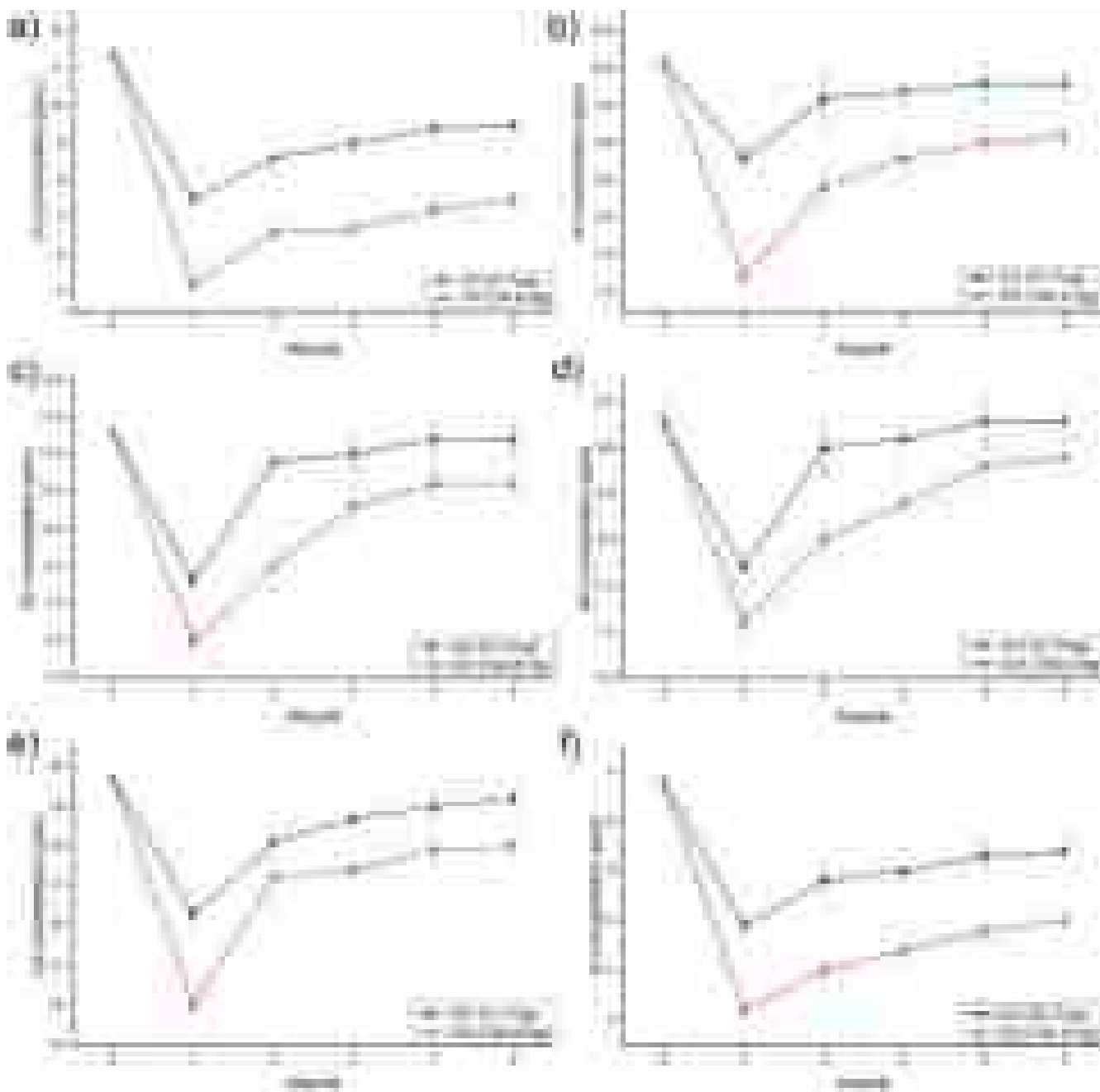


FIGURE 10 | Temporal evaluation of metal removal in a multielemental solution using the filtering device based on the square design using different hydrogel weights. In the x-axis, 0 represents the initial metal concentration (before passing through the filtering device). The number indicates the solution samples obtained sequentially after passing through the filtering device developed for each metal: (a) Copper, (b) Nickel, (c) Zinc, (d) Manganese, (e) Cadmium, and (f) Chromium. [Color figure can be viewed at [wileyonlinelibrary.com](https://onlinelibrary.wiley.com)]

using the multielement solution, demonstrating that higher chitosan hydrogel weight during the sorption tests promoted a higher removal for each metal ion. Hidayat and co-workers observed a similar trend, indicating that the increase in adsorption sites helps to promote a higher removal [60]. Additionally, it is possible to notice that copper and chromium were the main removed metal ions, as previously observed in the batch test performed.

Further evaluating the results, it is possible to notice that, unlike the previous batch test, the chromium removal using the filtering device was incomplete, which possibly occurred due to the

shorter contact time resulting from the dynamic test employed. However, the result shows high initial removal and continuous removal capacity over time, highlighting the potential of the developed material.

In addition, weight values higher than 100 mg were not considered for the tests due to the highly expansive nature of the hydrogel and the observation that there was no linear gain in the degree of removal with increasing mass. This observation is consistent with isotherm studies, which indicate that there is an optimum dosage for the adsorption process, so increasing the amount of adsorbent material used after some condition does

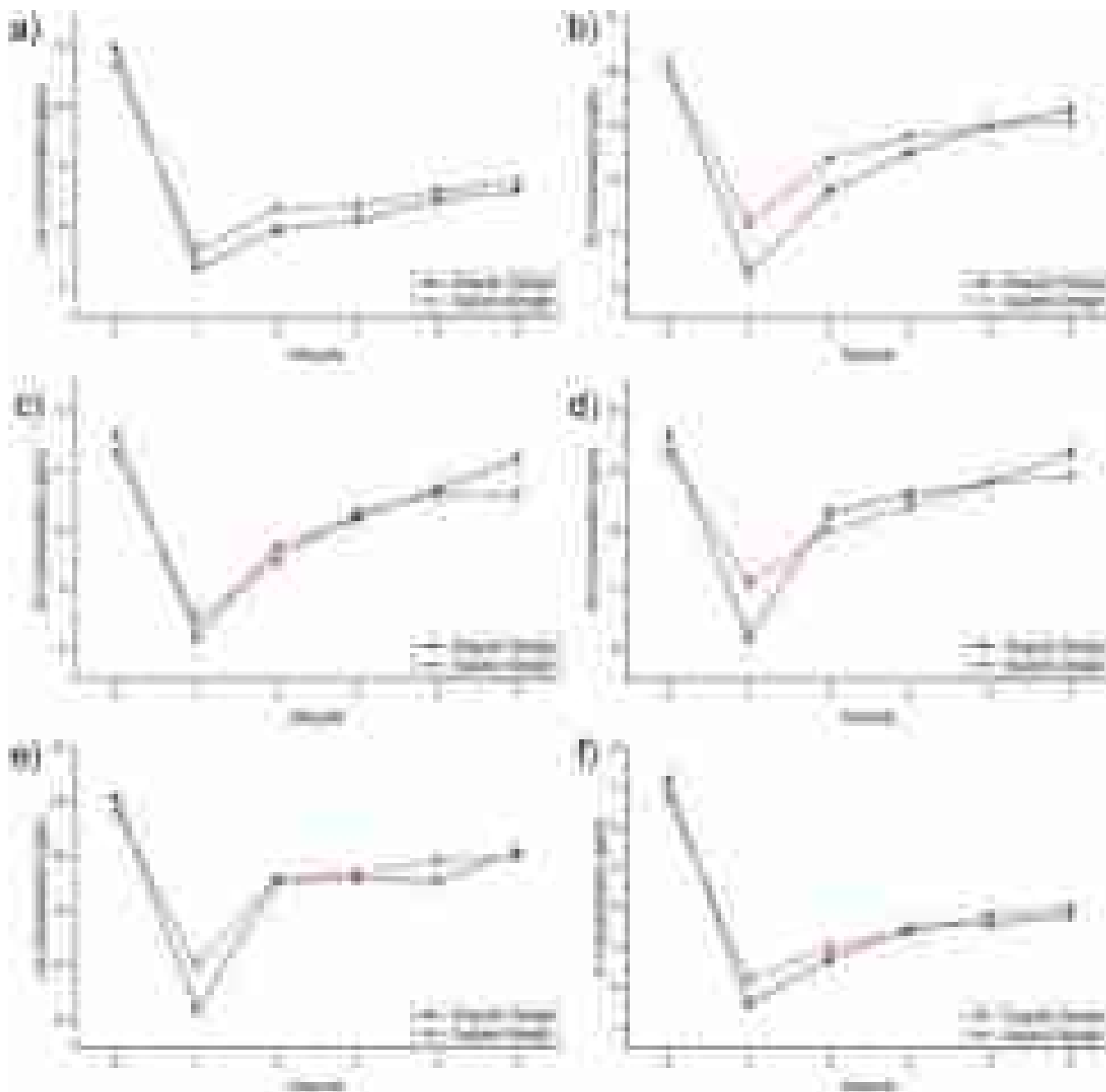


FIGURE 11 | Temporal evaluation of metal removal in a multielemental solution using the filtering device using similar chitosan hydrogel weights and varying between the square and angular design for the filtering channel. In the x-axis, 0 represents the initial metal concentration (before passing through the filtering device). The number indicates the solution samples obtained sequentially after passing through the filtering device developed for each metal: (a) Copper, (b) Nickel, (c) Zinc, (d) Manganese, (e) Cadmium, and (f) Chromium. [Color figure can be viewed at [wileyonlinelibrary.com](https://onlinelibrary.wiley.com/doi/10.1002/app.57539)] [wileyonlinelibrary.com](https://onlinelibrary.wiley.com/doi/10.1002/app.57539)]

not promote significant gains for the system, especially considering a dynamic flow.

To evaluate the removal potential of the system developed, the effect of changing the mold was evaluated by comparing the use of the square system and the angular system with similar hydrogel weights. The removal results using the multielement solution are shown in Figure 11.

Evaluating the results shown in the Figure 11, it can be seen that changing the system to use an angular design promoted greater initial removal of metal ions, which may be associated

with better accommodation of the solution in the system, allowing more gradual contact with the hydrogel structure and ensuring sufficient interaction time to promote its removal. However, with subsequent samples, there was an approximation to the removal shown by the square design. This suggests that a similar interaction condition is reached over time, so the hydrogel performs similarly, regardless of the design used. It should also be noted that some metals (especially zinc and manganese) showed a higher concentration in the last measurements using the angular design than the square design, which may suggest faster saturation of the hydrogel's functional groups.

Thus, the result suggests that a change in design may enhance the removal of metal ions and is notable for promoting greater removal in shorter time intervals, which is a desirable characteristic for producing quick application systems. Although complete metal removal was not achieved under the conditions tested, the results indicate the potential use of chitosan hydrogels for metal removal, considering a continuous solution flow, which is not commonly investigated. The application of the system for removing isolated contaminants has even greater potential since there would be no effect of competition for functional groups. In addition, there is potential to enhance the properties of the hydrogels developed by including chelating nanoparticles within the hydrogel structure, which can enhance metal removal by adsorption and allow an efficient, low-cost, and renewable system for purifying contaminated water.

4 | Conclusion

In this work, the design of experiments methodology was used to produce chitosan hydrogels and evaluate the relationship between the concentration of chitosan and crosslinking agent with the water absorption and metal removal properties of hydrogels. Eighteen different formulations were produced, and it was possible to note that the increase in the concentration of crosslinking agent reduces the water absorption properties, and the samples with 2% crosslinking agent stood out with absorption higher than 300%. In addition, the metal ion removal properties are also impacted in this process due to the lower availability of active groups. The hydrogels developed stood out for chromium and copper removal, reaching removals of 100% and 75%, respectively, for the conditions studied. The sample using 2% chitosan and 1% glutaraldehyde was selected through the response surface analysis as the best formulation for preparing the hydrogels. The hydrogel crosslinking was validated by FTIR analysis, which showed the appearance of peaks related to imine groups from the reaction of amine groups from chitosan with aldehyde present in glutaraldehyde. The hydrogel sample presented a highly porous structure with a pore size of $23.6 \pm 6.8 \mu\text{m}$. Kinetic data indicated a better fit to the pseudo-second-order model. In comparison, isotherm studies presented a better fit to the Langmuir model, which suggests chemisorption may be present during metal ion removal, with an adsorption capacity of 0.422 and 1.143 mmol g^{-1} for copper and chromium, respectively. The simulation using a filtering device indicated that the flow rate directly influenced the system capacity to remove metal ions, and using a flow of 0.25 mL/min aligned the process time and removal capacity. The adsorption process followed two steps, with an initial high removal and stabilization over time. A direct influence of weight and system design on removal properties was also observed. Overall, the results indicate a potential application of chitosan hydrogel in filtering devices to remove metal ions, presenting an alternative approach to water decontamination.

Author Contributions

Rennan F. S. Barbosa: conceptualization (lead), data curation (lead), formal analysis (lead), investigation (lead), methodology (lead), writing – original draft (lead), writing – review and editing (equal). **Sudip Shyam:** formal analysis (supporting), investigation (supporting),

methodology (supporting), validation (equal), writing – review and editing (supporting). **Sirshendu Misra:** formal analysis (supporting), investigation (supporting), methodology (supporting), validation (supporting), writing – review and editing (supporting). **Sushanta K. Mitra:** conceptualization (equal), funding acquisition (equal), methodology (equal), project administration (equal), supervision (lead), writing – review and editing (equal). **Derval S. Rosa:** conceptualization (equal), funding acquisition (lead), methodology (equal), project administration (lead), validation (equal), writing – review and editing (lead).

Acknowledgments

This research was funded by Fundação de Amparo à Pesquisa do Estado de São Paulo (2020/13703–3, 2021/08296–2, and 2021/14714–1), Conselho Nacional de Desenvolvimento Científico e Tecnológico (403934/2021–4 and 308053/2021–4), Mitacs Globalink Research Award (Ref. No. IT30489), Waterloo Institute for Nanotechnology, Multi-user Experimental Centers (CEM-UFABC), and REVALORES Strategic Unit. The Article Processing Charge for the publication of this research was funded by the Coordenação de Aperfeiçoamento de Pessoal de Nível Superior - Brasil (CAPES) (ROR identifier: 00x0ma614).

Conflicts of Interest

The authors declare no conflicts of interest.

Data Availability Statement

Data will be made available on request.

References

1. H. E. Al-Hazmi, J. Łuczak, S. Habibzadeh, et al., “Polysaccharide Nanocomposites in Wastewater Treatment: A Review,” *Chemosphere* 347 (2024): 140578, <https://doi.org/10.1016/j.chemosphere.2023.140578>.
2. V. Masindi and K. L. Muedi, “Environmental Contamination by Heavy Metals,” in *Heavy Metals* (InTech, 2018), <https://doi.org/10.5772/intechopen.76082>.
3. R. F. S. Barbosa, A. G. Souza, H. F. Maltez, and D. S. Rosa, “Chromium Removal From Contaminated Wastewaters Using Biodegradable Membranes Containing Cellulose Nanostructures,” *Chemical Engineering Journal* 395 (2020): 125055, <https://doi.org/10.1016/j.cej.2020.125055>.
4. H. Peng, J. Guo, B. Li, H. Huang, W. Shi, and Z. Liu, “Removal and Recovery of Vanadium From Waste by Chemical Precipitation, Adsorption, Solvent Extraction, Remediation, Photo-Catalyst Reduction and Membrane Filtration. A Review,” *Environmental Chemistry Letters* 20 (2022): 1763–1776, <https://doi.org/10.1007/s10311-022-01395-z>.
5. X. Guan, X. Yuan, Y. Zhao, et al., “Application of Functionalized Layered Double Hydroxides for Heavy Metal Removal: A Review,” *Science of the Total Environment* 838 (2022): 155693, <https://doi.org/10.1016/j.scitotenv.2022.155693>.
6. M. C. Benalia, L. Youcef, M. G. Bouaziz, S. Achour, and H. Menasra, “Removal of Heavy Metals From Industrial Wastewater by Chemical Precipitation: Mechanisms and Sludge Characterization,” *Arabian Journal for Science and Engineering* 47 (2022): 5587–5599, <https://doi.org/10.1007/s13369-021-05525-7>.
7. R. Wang, S. Guan, A. Sato, et al., “Nanofibrous Microfiltration Membranes Capable of Removing Bacteria, Viruses and Heavy Metal Ions,” *Journal of Membrane Science* 446 (2013): 376–382, <https://doi.org/10.1016/j.memsci.2013.06.020>.
8. F. Fu and Q. Wang, “Removal of Heavy Metal Ions From Wastewaters: A Review,” *Journal of Environmental Management* 92 (2011): 407–418, <https://doi.org/10.1016/j.jenvman.2010.11.011>.

9. M. M. Lakouraj, F. Hasanzadeh, and E. N. Zare, "Nanogel and Super-Paramagnetic Nanocomposite of Thiacalix[4]Arene Functionalized Chitosan: Synthesis, Characterization and Heavy Metal Sorption," *Iranian Polymer Journal* 23 (2014): 933–945, <https://doi.org/10.1007/s13726-014-0287-y>.
10. L. Joseph, B. M. Jun, J. R. V. Flora, C. M. Park, and Y. Yoon, "Removal of Heavy Metals From Water Sources in the Developing World Using Low-Cost Materials: A Review," *Chemosphere* 229 (2019): 142–159, <https://doi.org/10.1016/j.chemosphere.2019.04.198>.
11. S. Rajendran, A. K. Priya, P. Senthil Kumar, et al., "A Critical and Recent Developments on Adsorption Technique for Removal of Heavy Metals From Wastewater-A Review," *Chemosphere* 303 (2022): 135146, <https://doi.org/10.1016/j.chemosphere.2022.135146>.
12. A. Balakrishnan, S. Appunni, M. Chinthala, et al., "Chitosan-Based Beads as Sustainable Adsorbents for Wastewater Remediation: A Review," *Environmental Chemistry Letters* 21 (2023): 1881–1905, <https://doi.org/10.1007/s10311-023-01563-9>.
13. U. Upadhyay, I. Sreedhar, S. A. Singh, C. M. Patel, and K. L. Anitha, "Recent Advances in Heavy Metal Removal by Chitosan Based Adsorbents," *Carbohydrate Polymers* 251 (2021): 117000, <https://doi.org/10.1016/j.carbpol.2020.117000>.
14. C. Zhao, G. Liu, Q. Tan, et al., "Polysaccharide-Based Biopolymer Hydrogels for Heavy Metal Detection and Adsorption," *Journal of Advanced Research* 44 (2023): 53–70, <https://doi.org/10.1016/j.jare.2022.04.005>.
15. F. Zhao, S. Mitra, A. R. Kim, et al., "Determining Effective Refractive Index and Elasticity of Nanoscale Metal - Thin, Soft Polymer Bilayers Using Interference Signatures of a Glass Probe," *Colloids and Surfaces A: Physicochemical and Engineering Aspects* 674 (2023): 131861, <https://doi.org/10.1016/j.colsurfa.2023.131861>.
16. B. Bera, S. K. Mitra, and D. Vick, "Understanding the Micro Structure of Berea Sandstone by the Simultaneous Use of Micro-Computed Tomography (Micro-CT) and Focused Ion Beam-Scanning Electron Microscopy (FIB-SEM)," *Micron* 42 (2011): 412–418, <https://doi.org/10.1016/j.micron.2010.12.002>.
17. K. M. Gerke, E. V. Korostilev, K. A. Romanenko, and M. V. Karanina, "Going Submicron in the Precise Analysis of Soil Structure: A FIB-SEM Imaging Study at Nanoscale," *Geoderma* 383 (2021): 114739, <https://doi.org/10.1016/j.geoderma.2020.114739>.
18. A. Webster, M. D. Halling, and D. M. Grant, "Metal Complexation of Chitosan and Its Glutaraldehyde Cross-Linked Derivative," *Carbohydrate Research* 342 (2007): 1189–1201, <https://doi.org/10.1016/j.carres.2007.03.008>.
19. A. Woźniak and M. Biernat, "Methods for Crosslinking and Stabilization of Chitosan Structures for Potential Medical Applications," *Journal of Bioactive and Compatible Polymers* 37 (2022): 151–167, <https://doi.org/10.1177/08839115221085738>.
20. F. Valipour, E. Z. Rahimabadi, and H. Rostamzad, "Preparation and Characterization of Wound Healing Hydrogel Based on Fish Skin Collagen and Chitosan Cross-Linked by Dialdehyde Starch," *International Journal of Biological Macromolecules* 253 (2023): 126704, <https://doi.org/10.1016/j.ijbiomac.2023.126704>.
21. B. Wei, J. Zou, Q. Pu, K. Shi, B. Xu, and Y. Ma, "One-Step Preparation of Hydrogel Based on Different Molecular Weights of Chitosan With Citric Acid," *Journal of the Science of Food and Agriculture* 102 (2022): 3826–3834, <https://doi.org/10.1002/jsfa.11732>.
22. Y. Liu, R. Wang, D. Wang, et al., "Development of a Food Packaging Antibacterial Hydrogel Based on Gelatin, Chitosan, and 3-Phenylactic Acid for the Shelf-Life Extension of Chilled Chicken," *Food Hydrocolloids* 127 (2022): 107546, <https://doi.org/10.1016/j.foodhyd.2022.107546>.
23. N. R. Kildeeva, P. A. Perminov, L. V. Vladimirov, V. V. Novikov, and S. N. Mikhailov, "About Mechanism of Chitosan Cross-Linking With Glutaraldehyde," *Russian Journal of Bioorganic Chemistry* 35 (2009): 360–369, <https://doi.org/10.1134/S106816200903011X>.
24. X. Wan, Z. Rong, K. Zhu, and Y. Wu, "Chitosan-Based Dual Network Composite Hydrogel for Efficient Adsorption of Methylene Blue Dye," *International Journal of Biological Macromolecules* 222 (2022): 725–735, <https://doi.org/10.1016/j.ijbiomac.2022.09.213>.
25. T. S. Machado, L. Crestani, G. Marchezi, et al., "Synthesis of Glutaraldehyde-Modified Silica/Chitosan Composites for the Removal of Water-Soluble Diclofenac Sodium," *Carbohydrate Polymers* 277 (2022): 118868, <https://doi.org/10.1016/j.carbpol.2021.118868>.
26. Z. Liu, D. Xu, S. Gao, Y. Zhang, and J. Jiang, "Assessing the Adsorption and Diffusion Behavior of Multicomponent Ions in Saturated Calcium Silicate Hydrate Gel Pores Using Molecular Dynamics," *ACS Sustainable Chemistry & Engineering* 8 (2020): 3718–3727, <https://doi.org/10.1021/acssuschemeng.9b06817>.
27. B. L. Zhang, W. Qiu, P. P. Wang, et al., "Mechanism Study About the Adsorption of pb(II) and cd(II) With Iron-Trimesic Metal-Organic Frameworks," *Chemical Engineering Journal* 385 (2020): 123507, <https://doi.org/10.1016/j.cej.2019.123507>.
28. M. J. Ahmed, B. H. Hameed, and E. H. Hummadi, "Review on Recent Progress in Chitosan/Chitin-Carbonaceous Material Composites for the Adsorption of Water Pollutants," *Carbohydrate Polymers* 247 (2020): 116690, <https://doi.org/10.1016/j.carbpol.2020.116690>.
29. J. F. Chin, Z. W. Heng, H. C. Teoh, W. C. Chong, and Y. L. Pang, "Recent Development of Magnetic Biochar Crosslinked Chitosan on Heavy Metal Removal From Wastewater – Modification, Application and Mechanism," *Chemosphere* 291 (2022): 133035, <https://doi.org/10.1016/j.chemosphere.2021.133035>.
30. A. K. Mallik, S. F. Kabir, F. B. A. Rahman, M. N. Sakib, S. S. Efty, and M. M. Rahman, "Cu(II) Removal From Wastewater Using Chitosan-Based Adsorbents: A Review," *Journal of Environmental Chemical Engineering* 10 (2022): 108048, <https://doi.org/10.1016/j.jece.2022.108048>.
31. S. Sethi, S. Thakur, D. Sharma, et al., "Malic Acid Cross-Linked Chitosan Based Hydrogel for Highly Effective Removal of Chromium (VI) Ions From Aqueous Environment," *Reactive and Functional Polymers* 177 (2022): 105318, <https://doi.org/10.1016/j.reactfunctpolym.2022.105318>.
32. Q. Wang, W. Zuo, Y. Tian, et al., "An Ultralight and Flexible Nanofibrillated Cellulose/Chitosan Aerogel for Efficient Chromium Removal: Adsorption-Reduction Process and Mechanism," *Chemosphere* 329 (2023): 138622, <https://doi.org/10.1016/j.chemosphere.2023.138622>.
33. Y. Luo, Z. Hu, X. Lei, Y. Wang, and X. Guo, "Fluorescent Magnetic Chitosan-Based Hydrogel Incorporating Amino-Functionalized Fe₃O₄ and Cellulose Nanofibers Modified With Carbon Dots for Adsorption and Detection of Cr (VI)," *Colloids and Surfaces A: Physicochemical and Engineering Aspects* 658 (2023): 130673, <https://doi.org/10.1016/j.colsurfa.2022.130673>.
34. M. Chen, M. Yu, R. Kang, et al., "Removal of pb (II) and V (V) From Aqueous Solution by Glutaraldehyde Crosslinked Chitosan and Nanocomposites," *Chemosphere* 297 (2022): 134084, <https://doi.org/10.1016/j.chemosphere.2022.134084>.
35. L. Raju, A. R. Stesho Crystalin Lazuli, N. K. Udaya Prakash, and E. Rajkumar, "Chitosan-Terephthaldehyde Hydrogels – Effect of Concentration of Cross-Linker on Structural, Swelling, Thermal and Antimicrobial Properties," *Materialia* 16 (2021): 101082, <https://doi.org/10.1016/j.mtla.2021.101082>.
36. F. Doustdar, A. Olad, and M. Ghorbani, "Effect of Glutaraldehyde and Calcium Chloride as Different Crosslinking Agents on the Characteristics of Chitosan/Cellulose Nanocrystals Scaffold," *International Journal of Biological Macromolecules* 208 (2022): 912–924, <https://doi.org/10.1016/j.ijbiomac.2022.03.193>.




37. B. Li, C. L. Shan, Q. Zhou, et al., "Synthesis, Characterization, and Antibacterial Activity of Cross-Linked Chitosan-Glutaraldehyde," *Marine Drugs* 11 (2013): 1534–1552, <https://doi.org/10.3390/md11051534>.
38. D. Karolina, M. S. Maja, D. S. Magdalena, and Ż. Grażyna, "Identification of Treated Baltic Amber by FTIR and FT-Raman – A Feasibility Study," *Spectrochimica Acta. Part A, Molecular and Biomolecular Spectroscopy* 279 (2022): 121404, <https://doi.org/10.1016/j.saa.2022.121404>.
39. M. P. Arulmoorthy, G. Anbarasi, M. Srinivasan, and B. Vishnupriya, "Biosynthesis and Characterization of Chitosan Based Hydrogel: A Potential In Vitro Wound Healing Agent," *Materials Today: Proceedings* 48 (2019): 263–275, <https://doi.org/10.1016/j.matpr.2020.07.186>.
40. R. R. Mohamed, M. E. Fahim, and M. A. Soliman, "Development of Hydrogel Based on Carboxymethyl Cellulose/Poly(4-Vinylpyridine) for Controlled Releasing of Fertilizers," *BMC Chemistry* 16 (2022): 52, <https://doi.org/10.1186/s13065-022-00846-6>.
41. C. O. Aniagor, G. M. Taha, S. M. Badawy, M. E. El-Naggar, and A. Hashem, "Preparation of a Novel Acrylic Fiber-Based Hydrogel and Its Utilization for the Removal of Aqueous Lead Ion," *Journal of Materials Research and Technology* 18 (2022): 1450–1459, <https://doi.org/10.1016/j.jmrt.2022.03.007>.
42. B. Bera, N. S. K. Gunda, S. K. Mitra, and D. Vick, "Characterization of Nanometer-Scale Porosity in Reservoir Carbonate Rock by Focused Ion Beam-Scanning Electron Microscopy," *Microscopy and Microanalysis* 18 (2012): 171–178, <https://doi.org/10.1017/S1431927611012505>.
43. R. Foudazi, R. Zowada, I. Manas-Zloczower, and D. L. Feke, "Porous Hydrogels: Present Challenges and Future Opportunities," *Langmuir* 39 (2023): 2092–2111, <https://doi.org/10.1021/acs.langmuir.2c02253>.
44. T. Vieira, S. E. S. Artifon, C. T. Cesco, P. B. Vilela, V. A. Becegado, and A. T. Paulino, "Chitosan-Based Hydrogels for the Sorption of Metals and Dyes in Water: Isothermal, Kinetic, and Thermodynamic Evaluations," *Colloid & Polymer Science* 299 (2021): 649–662, <https://doi.org/10.1007/s00396-020-04786-2>.
45. R. R. Ferreira, T. B. da Costa, R. F. S. Barbosa, P. H. Camani, R. R. Menezes, and D. dos S. Rosa, "Brazilian Clays as Natural Cation Exchangers for Copper Sorption in a Batch System," *Adsorption* 30 (2024): 2113–2133, <https://doi.org/10.1007/s10450-024-00543-x>.
46. Z. Yu, X. Zhang, and Y. Huang, "Magnetic Chitosan-Iron(III) Hydrogel as a Fast and Reusable Adsorbent for Chromium(VI) Removal," *Industrial and Engineering Chemistry Research* 52 (2013): 11956–11966, <https://doi.org/10.1021/ie400781n>.
47. P. B. Vilela, A. Dalalibera, E. C. Duminelli, V. A. Becegado, and A. T. Paulino, "Adsorption and Removal of Chromium (VI) Contained in Aqueous Solutions Using a Chitosan-Based Hydrogel," *Environmental Science and Pollution Research* 26 (2019): 28481–28489, <https://doi.org/10.1007/s11356-018-3208-3>.
48. A. Lv and X. Lv, "Porous Chitosan Quaternary Ammonium Salt Hydrogel Embedded With cu, Ni and pd Nanoparticles for Efficient Coupled Adsorption-Catalytic Reduction of Methylene Blue and 4-Nitrophenol," *International Journal of Biological Macromolecules* 282 (2024): 136842, <https://doi.org/10.1016/j.ijbiomac.2024.136842>.
49. D. Zhao, W. Ye, and W. Cui, "Fabrication of Novel Bio-Adsorbent and Its Application for the Removal of cu(II) From Aqueous Solution," *Environmental Science and Pollution Research* 29 (2022): 29613–29623, <https://doi.org/10.1007/s11356-021-17013-4>.
50. Y. Tassanapukdee, P. Prayongpan, and K. Songsrirote, "Removal of Heavy Metal Ions From an Aqueous Solution by CS/PVA/PVP Composite Hydrogel Synthesized Using Microwaved-Assisted Irradiation," *Environmental Technology and Innovation* 24 (2021): 101898, <https://doi.org/10.1016/j.eti.2021.101898>.
51. R. Chen, C. Gan, B. Cai, et al., "Co-Adsorption and Selective-Adsorption of Heavy Metals and Dyes From Aqueous Solution by Bio-Based Humus/Chitosan Hydrogels," *Journal of Environmental Sciences (China)* 145 (2024): 193–204, <https://doi.org/10.1016/j.jes.2023.09.004>.
52. Z. Li, J. Qiu, X. Xu, et al., "Solar Driven Kaolin-Based Hydrogels for Efficient Interfacial Evaporation and Heavy Metal Ion Adsorption From Wastewater," *Separation and Purification Technology* 354 (2025): 129243, <https://doi.org/10.1016/j.seppur.2024.129243>.
53. X. H. Yue, F. S. Zhang, C. C. Zhang, and P. Qian, "Upcycling of Blending Waste Plastics as Zwitterionic Hydrogel for Simultaneous Removal of Cationic and Anionic Heavy Metals From Aqueous System," *Journal of Hazardous Materials* 432 (2022): 128746, <https://doi.org/10.1016/j.jhazmat.2022.128746>.
54. Y. Zhou, Z. Liu, A. Bo, et al., "Simultaneous Removal of Cationic and Anionic Heavy Metal Contaminants From Electroplating Effluent by Hydrotalcite Adsorbent With Disulfide (S₂⁻) Intercalation," *Journal of Hazardous Materials* 382 (2020): 121111, <https://doi.org/10.1016/j.jhazmat.2019.121111>.
55. S. Shewatatek, G. Gonfa, S. M. Hailegiorgis, and B. Tessema, "Response Surface Optimization of Chromium (IV) Removal With Teff Straw-Based Activated Carbon," *Results in Chemistry* 15 (2025): 102168, <https://doi.org/10.1016/j.rechem.2025.102168>.
56. H. Yan, J. Dai, Z. Yang, H. Yang, and R. Cheng, "Enhanced and Selective Adsorption of Copper(II) Ions on Surface Carboxymethylated Chitosan Hydrogel Beads," *Chemical Engineering Journal* 174 (2011): 586–594, <https://doi.org/10.1016/j.cej.2011.09.064>.
57. N. Li and R. Bai, "Copper Adsorption on Chitosan-Cellulose Hydrogel Beads: Behaviors and Mechanisms," *Separation and Purification Technology* 42 (2005): 237–247, <https://doi.org/10.1016/j.seppur.2004.08.002>.
58. J. Qu, Q. Meng, W. Peng, et al., "Application of Functionalized Biochar for Adsorption of Organic Pollutants From Environmental Media: Synthesis Strategies, Removal Mechanisms and Outlook," *Journal of Cleaner Production* 423 (2023): 138690, <https://doi.org/10.1016/j.jclepro.2023.138690>.
59. Z. Qing, L. Wang, X. Liu, Z. Song, F. Qian, and Y. Song, "Simply Synthesized Sodium Alginate/Zirconium Hydrogel as Adsorbent for Phosphate Adsorption From Aqueous Solution: Performance and Mechanisms," *Chemosphere* 291 (2022): 133103, <https://doi.org/10.1016/j.chemosphere.2021.133103>.
60. E. Hidayat, T. Yoshino, S. Yonemura, Y. Mitoma, and H. Harada, "Synthesis, Adsorption Isotherm and Kinetic Study of Alkaline-Treated Zeolite/Chitosan/Fe³⁺ Composites for Nitrate Removal From Aqueous Solution—Anion and Dye Effects," *Gels* 8 (2022): 782, <https://doi.org/10.3390/gels8120782>.

Supporting Information

Additional supporting information can be found online in the Supporting Information section.

RESEARCH ARTICLE OPEN ACCESS

Innovative Use of Brazilian Clays in Porous Aerogels and Hydrogels for Water Dye Purification

Luidy F. Senra¹  | Joaquim G. G. S. Bento¹ | Lana S. Maia² | Maria Ismênia S. T. Faria³ | Daniella R. Mulinari⁴  | Derval S. Rosa² 

¹Rio de Janeiro State University (UERJ), Faculty of Technology (FAT), department of Chemistry and Environmental, Resende, Brazil | ²Center for Engineering, Modeling, and Applied Social Sciences (CECS), Federal University of ABC (UFABC), Santo André, Brazil | ³Department of Materials Engineering (DEMAR), University of São Paulo (EEL/USP), Lorena, Brazil | ⁴Rio de Janeiro State University (UERJ), Faculty of Technology (FAT), department of Mechanic and Energy, Resende, Brazil

Correspondence: Daniella R. Mulinari (daniella.mulinari@fat.uerj.br; dmulinari@hotmail.com)

Received: 26 June 2025 | **Revised:** 16 August 2025 | **Accepted:** 31 August 2025

Funding: This work was supported by Fundação Carlos Chagas Filho de Amparo à Pesquisa do Estado do Rio de Janeiro, Fundação de Amparo à Pesquisa do Estado de São Paulo, Financiadora de Estudos e Projetos, Conselho Nacional de Desenvolvimento Científico e Tecnológico.

Keywords: aerogel | clay | dye adsorption | hydrogel | methylene blue

ABSTRACT

This research focused on the synthesis of starch-based hydrogels and aerogels that were cross-linked with citric acid and sodium hydroxide, and enhanced with chocolate clays—specifically Ch and chocobofo (Cb) at concentrations of 10% and 15% by weight. The primary goal was to evaluate their effectiveness in removing methylene blue (MB) from solutions. The hydrogels and aerogels were characterized using various techniques, including picnometry, scanning electron microscopy, Fourier-transform infrared spectroscopy (FTIR), and thermogravimetric analysis. Additionally, the pH at the zero point charge (pHzpc) was assessed. The adsorption performance of these materials was tested under different conditions, such as varying adsorbent dosages, contact times, and initial dye concentrations to determine the most effective material. This research aims to provide an environmentally sustainable solution to water pollution. FTIR analysis indicated interactions that altered the density, morphology, thermal stability, and pHzpc of the developed hydrogels and aerogels. The results showed that aerogel composites exhibited superior adsorption capabilities compared to hydrogel composites. The maximum adsorption capacity of MB reached 90%, with the aerogel composite containing 15% Cb (SA + 15% Cb) achieving a maximum capacity of 75 mg g⁻¹, according to the isotherm model. The aerogel composites with 15% clay exhibited a better fit to the Langmuir isotherm model, indicating that the removal of the dye is favorable. Therefore, incorporating clays into aerogels can enhance their performance, making them a viable alternative for developing new eco-friendly materials.

1 | Introduction

One of the most pressing global challenges is the lack of clean water caused by continued population growth and rapid industrialization, destroying several ecosystems [1]. Many industries, such as pharmaceutical, paper, textile, food, rubber, and plastic, use dye to color their products, and they are the primary and most significant cause of water pollution [2].

The discharge of several types of dye into the environment is estimated to be 10% to 15% of the 0.8 million tons of dyes produced annually worldwide. Furthermore, the dye business is projected to grow by about 2% to 3% annually in the following years. Therefore, it can be assumed that the amount of residues thrown into the environment will also increase. Due to their non-biodegradable nature and persistence in the environment, these compounds can potentially cause various adverse health

This is an open access article under the terms of the [Creative Commons Attribution](https://creativecommons.org/licenses/by/4.0/) License, which permits use, distribution and reproduction in any medium, provided the original work is properly cited.

© 2025 The Author(s). *Polymer Engineering & Science* published by Wiley Periodicals LLC on behalf of Society of Plastics Engineers.

Summary

- Starch-based hydrogels/aerogels (10 and 15% wt.) with Ch and Cb clays for the removal of MB.
- FTIR confirmed starch cross-linking via the use of citric acid for materials.
- The addition of clays improves properties of the aerogels and hydrogels.
- Aerogels showed superior adsorption performance compared to hydrogels in MB adsorption.
- Aerogels (15% Cb/Ch) fit the Langmuir isotherm model with q_{\max} of 75 and 76 mg g^{-1} .

effects, such as carcinogenicity and mutagenicity in humans [3]. In water bodies, they negatively affect photosynthetic organisms and disrupt aquatic life.

Due to these problems, wastewater from industrial processes that use these problematic dyes confronts pollution control areas, generating an alarming concern [4]. The most frequently studied toxic dyes include methylene blue, methyl orange, and Congo red, all known to have severe ecological and health impacts [5]. Methylene blue, in particular, has become an increasingly prominent research subject. From 1990 to 2018, approximately 17,000 articles were published on the topic, and in just the past 6 years, more than 31,000 have been published showing the effect of the accumulated dye in wastewater; it can cause respiratory issues, vomiting, eye burns, diarrhea, and nausea [6]. This dye also poses significant environmental risks, as it severely impacts aquatic flora and fauna by reducing dissolved oxygen levels and light penetration, thereby hindering photosynthesis [7].

The search for methods to remove these problematic dyes from water bodies grows daily [8]. These methods include filtration [9], flocculation [10], ion exchange [11], reverse osmosis [12], and adsorption [13]. Adsorption is one of the attractive, simple, and inexpensive methods widely used for wastewater treatment. It offers high efficiency for decolorizing dyes and degrading organic and inorganic contaminants [14]. It is a versatile method for tackling a broad spectrum of pollutants by using adsorbent materials that can be custom-made to target particular pollutants [15]. Moreover, the adsorption process is a low-energy consumption technology with easy operation, which is substantially capable of renewal and re-use of employed sorbent materials [16]. This makes it an overall green and efficient solution in many industrial wastewater management areas.

Several adsorbent materials, such as activated carbon [17], seaweed [18], various types of biosorbents, including agricultural wastes [19], chitosan [20], sawdust [21], and fruit peels [22], as well as clay minerals, have been extensively studied for their ability to remove dyes from contaminated water [23]. This is due to their relative ease of operation, availability, selectivity, and potential for large-scale applications.

Eco-friendly aerogels and hydrogels have shown promising adsorption properties. These innovative materials have high porosity and water absorption capacity, can be synthesized to adsorb

specific pollutants, and are highly efficient in treating various contaminants [24]. Hydrophilic polymer chains interconnected by crosslinks form their composition, and their production typically involves monomers' polymerization with crosslinking agents [25]. There are extensive studies on how crosslink agents affect the characteristics of the materials [26]. Their main uses include the removal of contaminants, tissue engineering, and controlled drug release.

With the recent increase in the demand for renewable and eco-friendly materials, research aimed at synthesizing hydrogels and aerogels from biodegradable materials is growing [27], especially starch-based hydrogels, which are cheap and easily synthesized.

Considering the already impressive adsorption capacities and properties of the materials mentioned earlier, recent studies have focused on enhancing their performance by combining them with other materials exhibiting strong adsorption potential. These include activated carbons [28], metals [29], modified clays [30], etc. By integrating these materials, the overall adsorption efficiency can be further improved, allowing for more effective removal of contaminants and expanding the applicability of the adsorbents in diverse environmental conditions [31].

The addition of clay to these materials is a promising study, as it significantly increases the surface area of the material, giving them unique adsorption properties [32] and improving the mechanical stability of these materials [33], making them more effective in diverse environmental conditions. This combination is sustainable and cost-effective, further reinforcing their potential for widespread use in environmental treatment. Despite advances in research on composites incorporating modified clays in hydrogels and aerogels, the literature still needs studies focused on composites reinforced with Chocolate and Chocobofo Brazilian clays from an environmental perspective, especially regarding the evaluation of the addition of Chocobofo. Based on this gap, a search was carried out in the ScienceDirect database, and the number of articles on the topic is shown in Figure 1.

The data indicated that the search for starch hydrogels and aerogels is high, evidenced by the high research on the topics, with 1054 publications. When delving deeper into the composites of these materials, a drop to 613 research studies is evidenced, of which only 139 are focused on the use of clays as the agent to be added. The search for studies on the adsorption of these materials showed a drop to 113 publications, and when specifying studies on dye adsorption, there are 41 studies. Finally, the surprising fact of zero publications using Chocolate or Chocobofo Brazilian clays as an agent to be added to starch hydrogels to increase their dye adsorption results shows a clear gap in this area, which opens opportunities for new work and future publications.

As shown in Figure 1, 41 documents containing the topics "starch hydrogel" "starch aerogel" and "clay" as dye adsorption materials have already been published. Zamani-Babgohari et al. studied the hydrogel's adsorption capacity for removing methylene blue from water. However, their material's synthesis was initiated with the preparation of carboxymethyl starch and subsequent copolymerization with polyacrylic acid and polyacrylamide [34]. Mushtaq and coworkers reviewed the properties

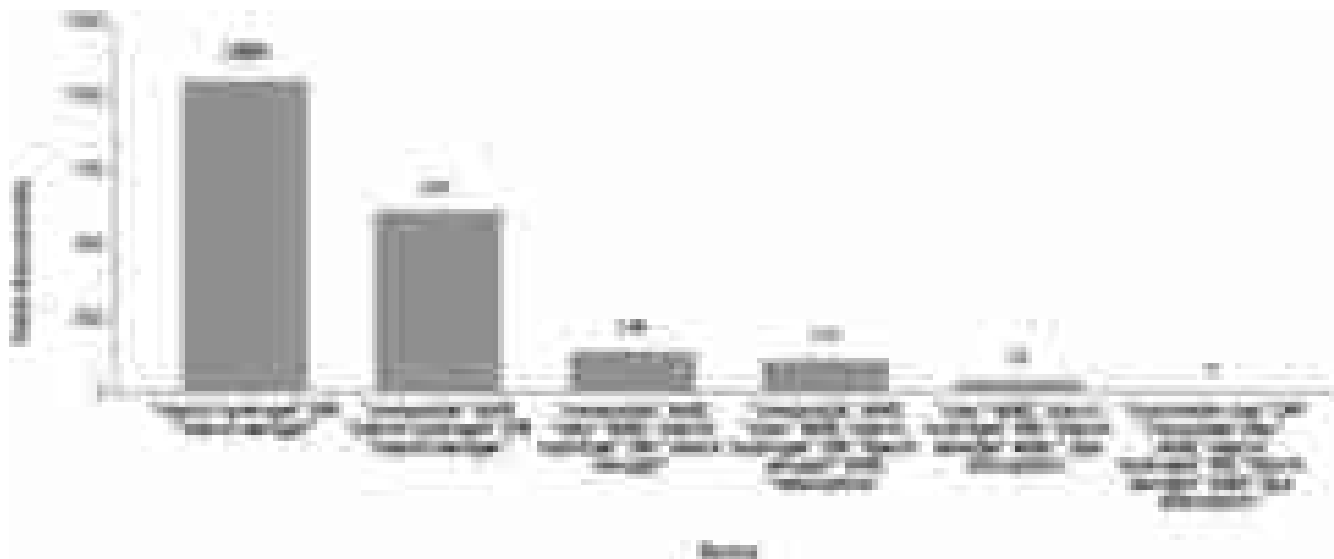


FIGURE 1 | Illustration of the paper number on the topic identified using different expressions related to the article's subject.

and applications of gelatin-based hydrogels in dye adsorption. Gelatin is extracted from collagen, an abundant protein component in animals' skins, bones, and cartilage animals' skins, bones, and cartilage; thus, it is a biodegradable, essential component of adsorption material used in the environment.

Like starch, gelatin can also be found and obtained from natural sources, being a cost-effective material [35]. Hu et al. developed a new aromatic ring-rich polymer adsorbent to improve the adsorption rate. This adsorbent can interact with dye molecules mainly via π - π stacking interactions. Two other reagents (1, 3, 5-triethynylbenzene (TB) and 2, 6-bis(4-iodo-1H-pyrazol-1-yl)pyridine) were synthesized and used for the elaboration of the material [36]. All these works contain similarities with this one, like the adsorbate studied (methylene blue), but the material and methods used for obtaining the adsorbent are different; besides, as already mentioned, no work has been done investigating the effects of dye adsorption for incorporation of chocolate or Cb to starch-based hydrogels/aerogels.

Thus, this research focuses on the synthesis of starch-based hydrogels and aerogels cross-linked with citric acid and sodium hydroxide (formation of trisodium citrate) and enhanced with modified clays of chocolate and chocobofo, typically from Paraíba (BR) [37], for the removal of methylene blue. The sorption performance of these materials was evaluated under different conditions of adsorbent mass, contact time, pH, and initial concentration of the dye, providing an environmentally sustainable solution to water pollution.

2 | Materials and Methods

2.1 | Materials

The chemicals utilized in this study, sodium hydroxide (NaOH, 98% purity), methylene blue (MB), and dye, were purchased from Dynamics Contemporary Chemistry. Citric acid ($C_6H_8O_7$, 99.5% purity) was acquired from Synth. Corn starch (Amidex 3001–27%

wt. by mass of amylose and 73% wt. by mass of amylopectin) was purchased from Ingredion Incorporated (São Paulo, Brazil). The Chocolate Clay (Ch) and Chocobofo Clay (Cb) were supplied by the company BENTONISA—Bentonita do Nordeste S.A. The clays are mainly comprised of crystalline materials such as quartz (Qz), kaolinite (K), illite (It), and anatase (An). The identification of mineralogical constituents (e.g., minerals or inorganic compounds) of clays is presented in the (Figure S1).

2.2 | Synthesis of Hydrogel and Aerogel

The hydrogel was prepared following methodologies previously developed by the research group [38].

For neat aerogels, synthesis was prepared from a 200 mL aqueous solution containing 14 g of starch. After starch dissolution, sodium hydroxide was added and stirred at 280 rpm for 3 h at 40°C. Afterward, citric acid was added to form trisodium citrate, resulting in a gel's immediate crosslinking and formation. This process happened in a closed system under 200 rpm, stirring at 40°C for 17 h. After the stirring process, the obtained gel was heated to 90°C for 60 min in a water bath and then cooled under ambient temperature. Later, the prepared materials were poured into plastic molds and stored in a refrigerator at -5°C for 48 h. The frozen hydrogel was submitted to the freeze-drying process using the Lyophilizer Liotop K105. The lyophilized material was washed with distilled water until it reached a neutral pH (~ 7). After washing, the material was frozen and freeze-dried again, resulting in the aerogel. A similar procedure was used to prepare the hydrogels and aerogels composite with Chocolate (Cb) or Chocobofo (Cb) Brazilian clays, in which 10% and 15% wt. of clays were added to the mixture after the starch was dispersed. The hydrogel composites were named SH + 10% Cb; SH + 10% Ch; SH + 15% Cb; and SH + 15% Ch. The aerogel composites were named SA + 10% Cb; SA + 10% Ch; SA + 15% Cb; and SA + 15% Ch. The schematic procedure for preparing the hydrogel and aerogel is illustrated in Figure 2.

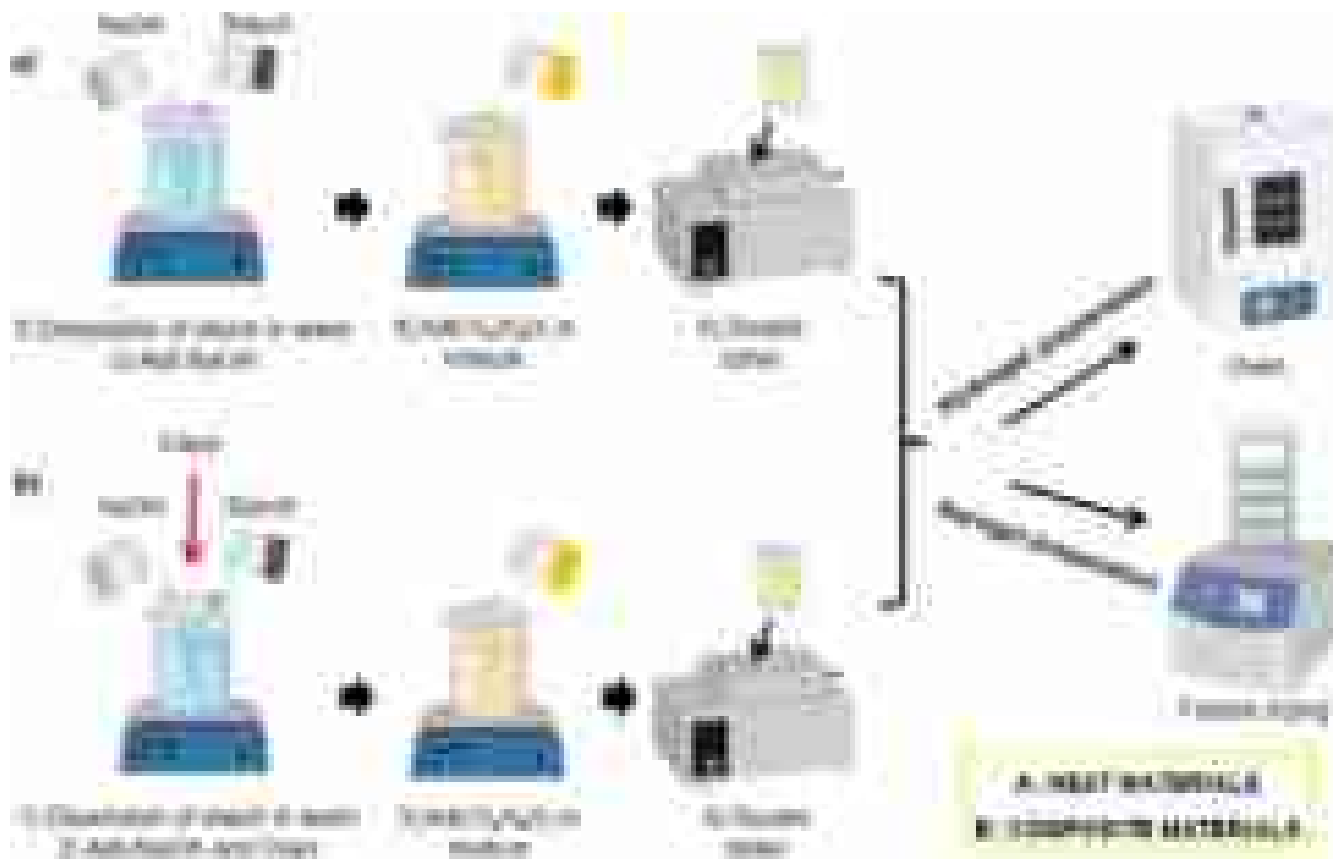


FIGURE 2 | Methodological illustration of the process of hydrogel, aerogel, and their composites, where: (a) Neat materials and (b) Composite materials.

2.3 | Characterization

2.3.1 | Density

The samples' density was measured at room temperature using an Ultrapyc 1200e helium gas pycnometer. A single-factor ANOVA statistical analysis was performed to compare the density (gcm^{-3}) with the percentage of clays (0, 10, and 15wt.%) added to the hydrogel and aerogel.

2.3.2 | Field Emission Scanning Electron Microscopy (FE-SEM)

The morphology of samples (hydrogel, aerogel, and their composites) was examined with scanning electron microscopy (SEM) with FEG Schottky electron emission in MEV-FEG TESCAN Mira 4 in the secondary electron mode (SE) and back-scattered electron mode (BSE) at 5 keV. Before SEM analysis, all samples were oven-dried at 50°C and coated with a thin layer of gold.

2.3.3 | Fourier-Transform Infrared Spectroscopy (ATR-FTIR)

FTIR analyses were performed on samples to investigate their main functional groups. The FTIR spectra were acquired using a Perkin Elmer spectrophotometer (Spectrum 100

Model) operated in the transmittance method with an attenuated total reflection (ATR). Measurements were taken within the range of 400 to 4000 cm^{-1} . Before analysis, all materials were oven-dried at 50°C for 24 h, and the aerogel samples were freeze-dried.

2.3.4 | Thermogravimetric Analysis (TGA)

The thermal properties of samples (hydrogel, aerogel, and their composites) were examined using the SII Nanotechnology INC equipment (Exstar 6000 model, TG/DTA 6200 series). The analysis was conducted under a constant nitrogen flow of 100 mLmin^{-1} , covering a temperature range of 25°C to 900°C with a heating rate of 10°C min^{-1} . Approximately 10 mg of samples at 50°C for 24 h were used for the analysis.

2.3.5 | Determination of the Zero-Charge Point (ZPC)

The study conducted Zeta potential measurements, explicitly focusing on pH_{ZPC} (point of zero charges), using hydrogel, aerogel, and their composites. These measurements were performed by adding samples to a 50 mL solution of 0.1 molL^{-1} NaCl. The pH of the solution was simultaneously adjusted within the range of 2.0 to 10.0 using 0.1 molL^{-1} NaOH and 0.1 molL^{-1} HCl solutions. The solution's final pH values were measured after allowing 24 h for the reaction to occur. The ZPC represents the

point where the initial pH of the solution matches the final pH after the reaction.

2.3.6 | Methylene Blue (MB) Adsorption Tests

Experiments were conducted in triplicate to evaluate the adsorption capacity (mg g^{-1}) and efficiency (%) of the hydrogel, aerogel, and their composites for MB dye removal. The experiment was based on the developed study by [39].

2.3.6.1 | Effect of Material Dosage. The sorption capacities of MB by hydrogel, aerogel, and their composites were investigated under dynamic conditions. In the mass variation experiment, 30 to 200 mg of each material was immersed in 100 mL of MB solution at 50 mg L^{-1} concentration. The mixture was stirred at 150 rpm and kept at 25°C for a predetermined time of 10 min. After the contact time, the MB concentration in the solution was analyzed using a UV-visible spectrophotometer based on the MB standard curve at its maximum wavelength of 665 nm. The amount of dye adsorbed on the adsorbent (q_e , mg g^{-1}) and the removal efficiency (RE, %) were calculated using Equations (1 and 2), respectively.

$$q_e = \frac{(C_i - C_e)}{m} \cdot V \quad (1)$$

$$RE = \frac{(C_i - C_e)}{C_i} \cdot 100 \quad (2)$$

Where q_e is the amount of dye in mg per gram of adsorbent; C_i and C_e are the initial concentration and equilibrium concentration of dye in mg per l, respectively; V is the volume of the solution, and m is the mass of adsorbent in g.

This step will serve to select the best materials for later evaluation. Subsequently, the dye's contact time and initial concentration will be evaluated, identifying which type of clay will influence this adsorption process.

2.3.6.2 | Effect of Contact Time. In this experiment, contact times were pre-determined at 10, 60, 120, 240, and 1440 min. After each time, the MB concentration in the solution was analyzed using a UV-visible spectrophotometer at the same maximum wavelength (665 nm).

2.3.6.3 | Effect of Initial Concentration. The analysis of adsorption isotherms can provide insight into how MB is adsorbed and estimate the maximum amount of dye that the samples (hydrogel, aerogel, and their composites) can absorb. To evaluate the fit of the isotherm models, the samples were exposed to MB solutions with varying concentrations (25, 50, 75, 100, and 150 mg L^{-1}) for 240 min, stirred at 150 rpm, and maintained at 25°C . The sorption isotherm models used were Langmuir and Freundlich.

2.3.6.4 | Adsorption Isotherm. The adsorption isotherm model was studied under optimum conditions. The isotherm models observed along their linearized forms were the Langmuir Equations (3 and 4) and the Freundlich models Equations (5

and 6). These two isotherm models were adapted from previous work by Martins et al. [40].

- Langmuir model

$$q_e = \frac{(q_m \cdot K \cdot L \cdot C_e)}{1 + K_L \cdot C_e} \quad (3)$$

Where: $q_{m\text{max}}$ is the sorbent monolayer capacity; K_L is the sorption free energy constant; C_e is the equilibrium concentration; q_e is the equilibrium dye concentration of the sorbent; q_m and K_L can be determined from linear adjustment using C_e/q_e and C_e data.

$$K_L = \frac{1}{1 + K_F \cdot C_e} \quad (4)$$

Where RL refers to process favorability. If $RL > 1$, the process is unfavorable. If $RL = 1$, linear. If $0 < RL < 1$, favorable. If $RL = 0$, irreversible.

- Freundlich model

$$q_e = K_F + C_e \cdot \frac{1}{n} \quad (5)$$

Where K_F is the sorption capacity constant; n is the sorption intensity constant. If $n = 1$, it is a linear sorption process. If $n < 1$, it is a chemical process. If $n > 1$, it is a physical process. K_F and n can be calculated by Equation 6:

$$\log \log (q_e) = \frac{1}{n} \log \log (C_e) + \log \log (K_F) \quad (6)$$

3 | Results and Discussion

3.1 | Density

Figure 3 shows the density results of the hydrogel, aerogel, and its composite samples. It can be observed that adding clay to the matrix increased their densities, as reported by other articles [41].

It was observed that the aerogel and its composites presented a higher density than the hydrogel and their composites, which can be justified by the crosslinking degree. Also, a higher content of clays increases the crosslinking density inside the aerogel, which will result in an adsorption network space [42].

As the clay content increases in aerogels, the density also increases. This trend is consistent with the hydrogels, indicating that the structural modification induced by clay is similar in both materials. Pure aerogel, although denser than pure hydrogel, still offers a lower density than clay-enriched composites, reinforcing the role of clay in reinforcing and densifying materials.

Pure hydrogel, on the other hand, has the lowest value among all densities. This is an interesting observation, as it provides information about the base structure of the hydrogel without the influence of clay. This behavior is due to differences in the crystalline structure of clays and the fact that clay has metallic

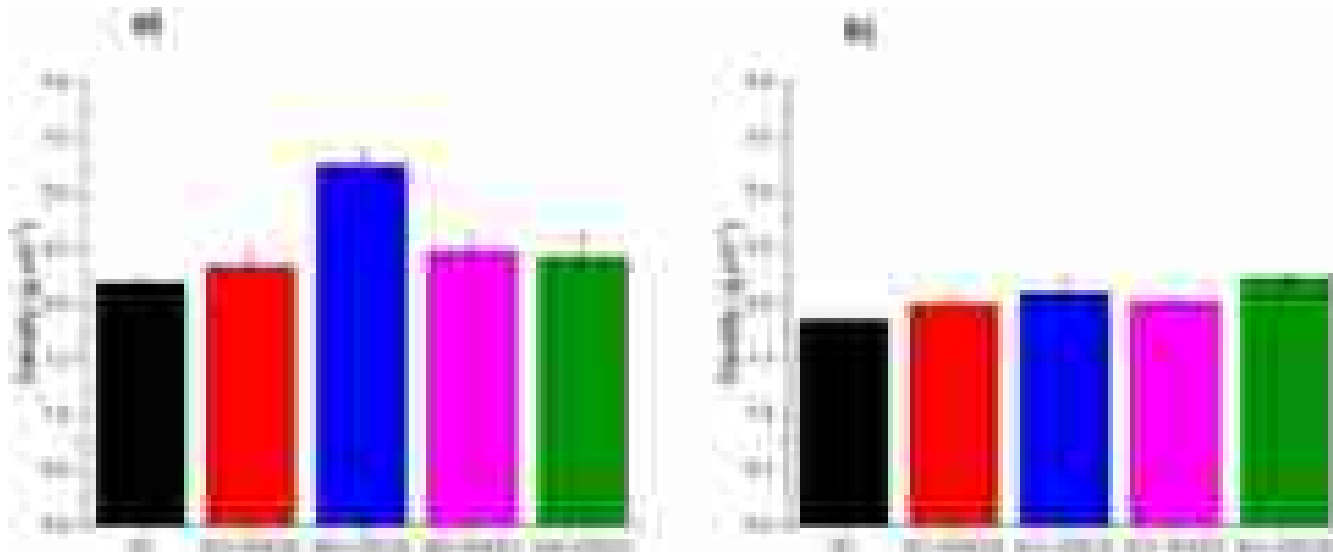


FIGURE 3 | Densities of aerogel, hydrogel, and their composites reinforced with Chocolate (Ch) and Chocobofe (Cb) Brazilian clays, where (a) refers to aerogels and their composites and (b) refers to hydrogels and their composites.

TABLE 1 | Values of Student's *t*-test and *p* compared to hydrogels and aerogels samples.

Samples	Student's <i>t</i> -test	<i>p</i>	Is there a difference?
SH and SA	9.7595	0.00061750	Yes
SH and SA + 10% Cb	4.3474	0.01218210	Yes
SH and SA + 15% Cb	5.1056	0.00695557	Yes
SH and SA + 10% Ch	5.55716	0.00508475	Yes
SH and SA + 15% Ch	1.0077	0.37060804	No

elements, which contribute to the densification of porous materials such as hydrogels and aerogels [43].

According to the *p* values calculated from the Student's *t* values, calculated from the densities and standard deviation, shown in Table 1, there is no statistical difference between the densities of the aerogel and hydrogel composites with 15% wt. chocolate, only because the *p* is greater than 0.05.

3.2 | Field Emission Scanning Electron Microscopy (FE-SEM)

Figure 4 shows micrographs of Brazilian clays—Chocobofe (top row) and Chocolate (bottom row), with magnifications of 100×, 2000×, and 5000× for each row. The SEM images of Cb show a granular morphology with relatively well-dispersed particles of varying sizes. As the magnification increases, a lamellar texture can be noted. Regarding the morphological aspect of Chocolate clay, a granular character is also evident, but the particles appear

less uniform and more compact than in Chocobofe. A more heterogeneous structure is observed at higher magnifications, with agglomerated particles, rougher surfaces, and less evidence of organized lamellae. Similar behavior was reported by Ferreira et al. [44] when investigating Brazilian clays as natural cation exchangers for copper sorption in a batch system.

Figure 5 shows micrographs of aerogels and hydrogels with and without clays— aerogels (on the left) and hydrogels (on the right) - at different magnifications. The neat starch-based aerogels presented a three-dimensional network structure, where it is possible to observe a structure without pores and thin walls [26]. When incorporating clays in the matrix, an improvement in the structural integrity of the aerogel can be noted, as well as the formation of a rougher and more porous surface. The clay content inserted in the matrix influenced the integrity of the composites. It was evident that adding 10% of clays, especially Cb, promoted the development of a rougher structure with a heterogeneous pore distribution and denser.

According to Huang et al. [45], more connection points between the free starch molecules were formed, inducing densification of the internal structure. On the other hand, the insertion of 15% of clays caused the collapse of the pores, and the reason attributed to this is the saturation of the matrix, which induced the weakening of the interactions between the starch chains and functional groups of the clays [46]. In the composites reinforced with Chocolate clay, the insertion of 15% clay allowed the formation of a rougher structure but with broken pores. This behavior can be justified by the fillers' morphological and crystalline structures, as will be discussed in the next sections.

Regarding the micrographs of the starch-based hydrogels, it can be observed that a certain degree of heterogeneity developed after the clays of incorporation. In the hydrogel composites, the pores are encapsulated, and this characteristic may be associated with the drying stage to which they were subjected during manufacture. The presence of encapsulated pores was reported by Hwang et al. [47] when studying the

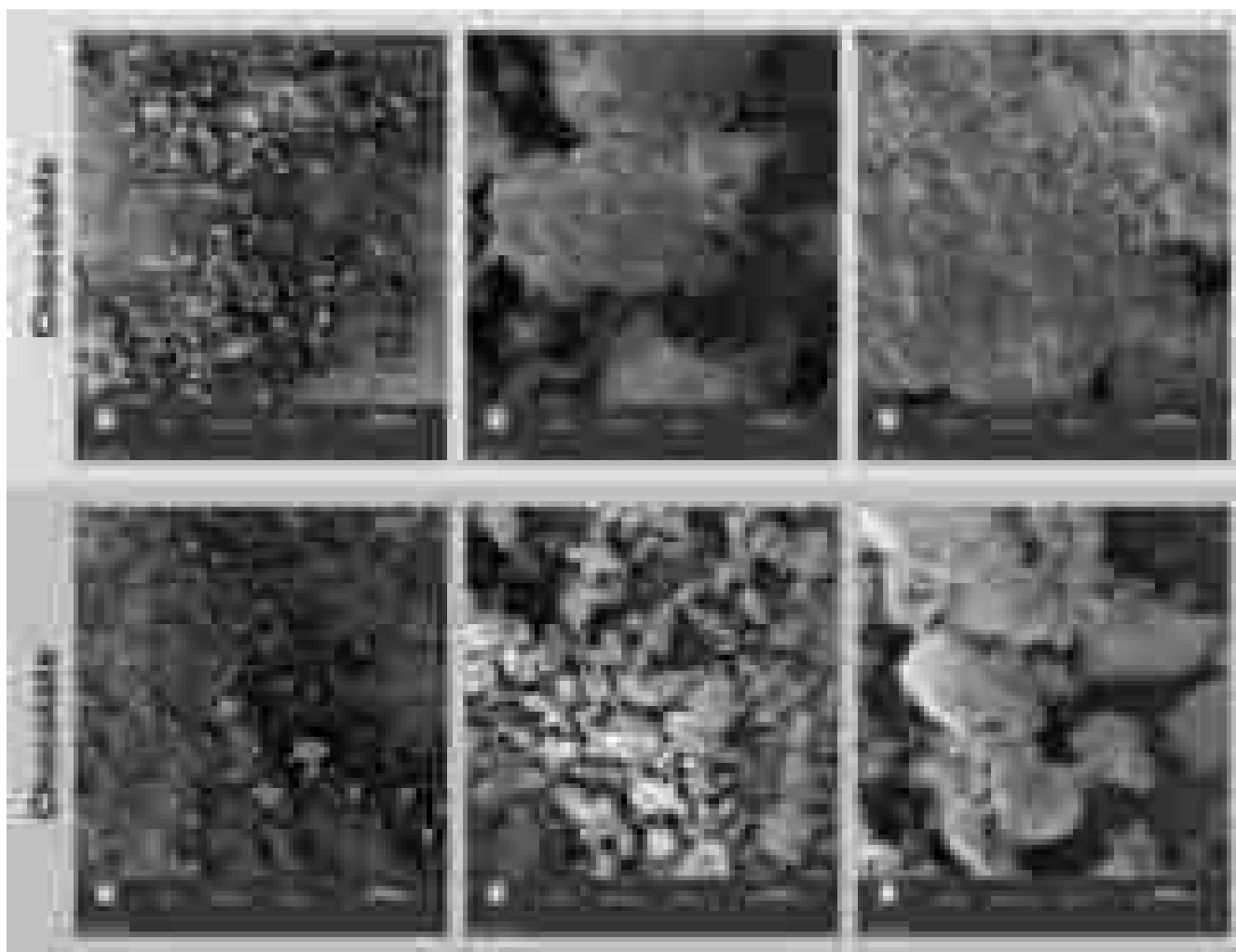


FIGURE 4 | SEM images of brazilian clays (chocobofo and chocolate) were used to reinforce hydrogel and aerogel composites. The top row shows the chocobofo and the bottom the chocolate Clay. On the left, middle, and right, the magnifications are 100 \times , 2000 \times , and 5000 \times , respectively.

manufacture of alginate hydrogels. However, the insertion of Ch (10%) was able to promote the formation of open pores with broken walls.

In general, the materials studied presented an interesting morphology, making them promising adsorbents for treating contaminated water.

3.3 | Fourier-Transform Infrared Spectroscopy (ATR-FTIR)

FTIR analysis was conducted to understand the effect of clays on the structure of hydrogels and aerogels, as shown in Figure 6.

The spectra of aerogels and hydrogels were evaluated (Figure 6a,b), revealing bands at 3284 cm^{-1} (O—H stretching), 2924 cm^{-1} (asymmetric C—H stretching), 1580 cm^{-1} (C=O of the trisodium citrate carboxyl group), 1380 cm^{-1} (O—H bending), 1148 cm^{-1} and 1077 cm^{-1} (C—O stretching), 996 cm^{-1} and 932 cm^{-1} (C—O—C group of the anhydroglucose ring), and 845 cm^{-1} and 760 cm^{-1} (C—H bending) [26]. These peaks confirm the reticulation process, as displayed by Pereira et al. [39].

For the spectra of the clays (Figure 6c,d), a highly similar structure was noted, with chocobofo (Cb) and chocolate (Ch) clays revealing characteristic bands at 1629 cm^{-1} related to the angular deformation of the hydration water, bands at 1382 cm^{-1} , 1112 cm^{-1} , and 1002 cm^{-1} , corresponding to Si—O—Si stretching, bands at 915 cm^{-1} corresponding to Si—OH groups, and, finally, at 796 cm^{-1} is associated with the CH bending out of plane [44]. These bands are typical of aluminosilicates, confirming the smectite nature of these clays and their layered structures.

In the pure hydrogel and aerogel analysis, the peak at 996 cm^{-1} exhibited similar behavior, indicating that both materials contain almost equal amounts of this C—O—C functional group. However, the pure hydrogel presented higher peaks across the other bands, suggesting a greater presence of functional groups associated with the starch matrix, such as hydroxyl and carboxyl groups. This highlights the dense, hydrated network in the hydrogel structure compared to the aerogel.

The materials again exhibited highly similar peaks for the aerogels but with different intensities. The aerogel with 10% Ch presented the most intense peaks, particularly at 996 cm^{-1} (C—O—C

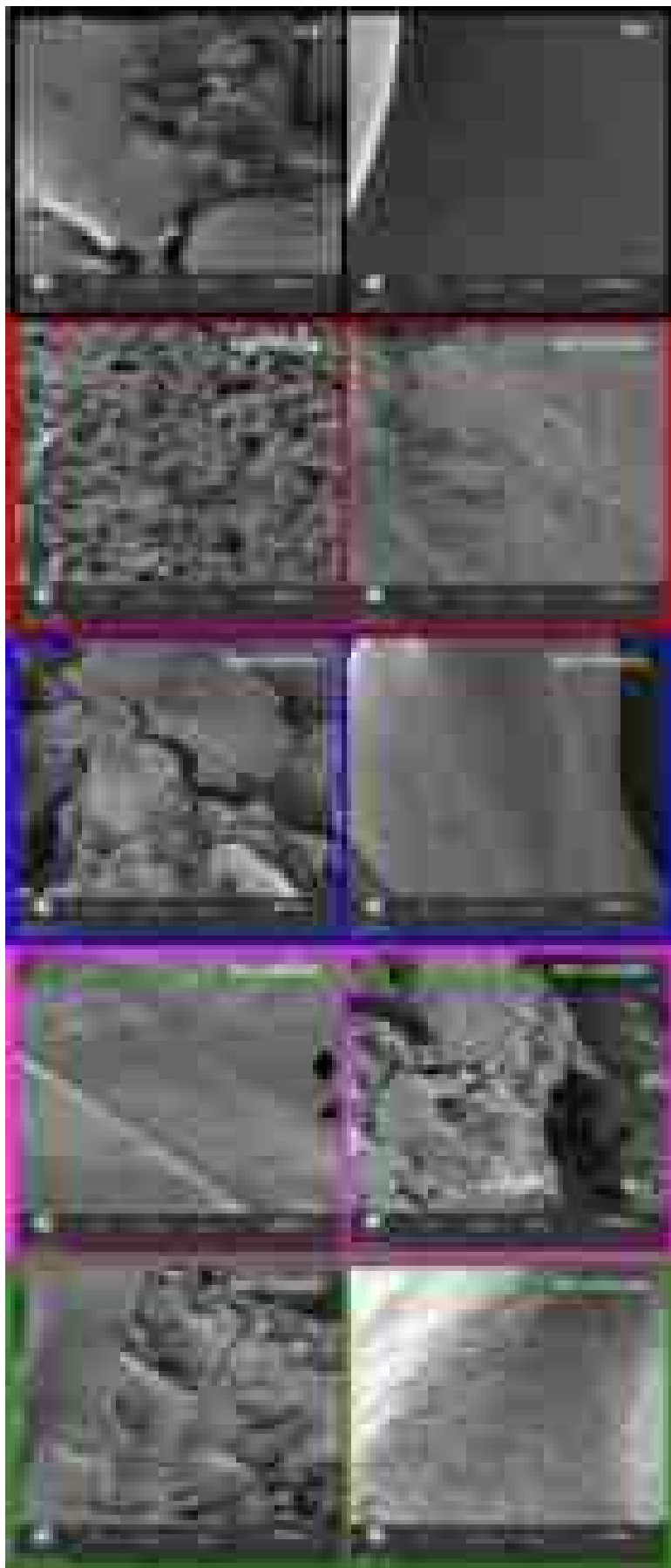


FIGURE 5 | Legend on next page.

FIGURE 5 | SEM images of hydrogel, aerogel, and their composites reinforced with chocolate and chocobofoe brazillian clays. In black: The left SA sample and on the left SH sample; In red: The left SA + 10% Cb sample and on the left SH +10% Cb sample; In blue: The left SA + 15% Cb sample and on the left SH +15% Cb sample; In pink: He left SA + 10% Ch sample and on the left SH +10% Ch sample; In green: The left SA + 15% Ch sample and on the left SH +15% Ch sample.

group stretching). The aerogel with 15% Ch displayed similar behavior, though slightly reduced peak intensities, particularly at 1148 cm^{-1} , 1077 cm^{-1} , 845 cm^{-1} , and 760 cm^{-1} , indicating a stabilization trend as clay concentration increases. Meanwhile, the pure aerogel exhibited the lowest peak intensities across all regions. These results demonstrate a strong interaction between the aerogel matrix and the clay particles, with 10% Ch showing the most significant incorporation and structural modifications.

The results for the hydrogels were more distinct than those for the aerogels. Composites containing higher clay concentrations exhibited more pronounced peaks, especially at 1382 cm^{-1} , 1112 cm^{-1} , and 982 cm^{-1} (Si—O—Si regions), indicating greater interaction between the clay particles and the hydrogel matrix. Conversely, the pure hydrogel presented the lowest peak intensities, confirming the reinforcing effect of clay addition on the polymer matrix.

More intense peaks in aerogels and hydrogels containing clays highlight the incorporation of the clay particles into the matrix and their interaction with the starch-based network. The observed changes, particularly at bands associated with C—O stretching and Si—O—Si groups, suggest that the clays influence the arrangement of polysaccharide chains and contribute to modifications in the porous structure.

Therefore, based on the analysis of Figure 6, a clear trend is observed: the composites containing clays exhibit more intense peaks than the pure materials, demonstrating a strong interaction between the starch matrix and the clay particles. This interaction enhances the structural properties of the aerogels and hydrogels, modifying their functional groups and contributing to their porous architecture, as we have previously highlighted in the SEM analyses. The results also emphasize that the clay type and concentration play a critical role in determining the extent of these changes, with Cb exhibiting slightly superior performance in the hydrogels and Ch showing prominent effects in the aerogels.

3.4 | Thermogravimetric Analysis (TGA)

Figure 7 (a, b, c, and d) depicts the TG and DTG curves of aerogel, hydrogel, and their composite materials with different contents of Chocobofoe and Chocolate. The data are compiled in Table 2.

According to the thermal curves, the thermal decomposition of the neat aerogel and neat hydrogel is similar within two stages of loss mass. In both materials, the first stage presented a mass reduction of around 100°C , attributed to the entrapped water in the polymer [48]. The second stage ($\sim 160^\circ\text{C}$ – 230°C for neat aerogel and $\sim 230^\circ\text{C}$ – 250°C for neat hydrogel) is attributed to the thermal decomposition of the starch chains and initiation of degradation of the starch crosslinked structure. This behavior was discussed by Patric et al. and Chen et al. when studying the properties and morphology of starch aerogels and hydrogels,

respectively. In this context, DTG curves indicated that the main decomposition of the starch aerogel occurs at 260.2°C , and the starch hydrogel is at 274.6°C [49].

After incorporating chocobofoe and chocolate clays into the aerogel and hydrogel structure, the thermal curves exhibited three stages of mass loss the first stage, occurring at a temperature of around 100°C , can be associated with the presence of water and/or volatile compounds [50], and the second stage ($\sim 250^\circ\text{C}$ – 320°C for aerogel and hydrogel composites), can be related to initial decomposition of starch chains (organic compounds) and clays (inorganic compounds) [51]. Lastly, the third stage ($\sim 350^\circ\text{C}$ – 400°C for aerogel and hydrogel composites) can be attributed to the degradation of starch crosslinked structure with the clay (De la Cruz et al. 2023). Another important observation is that the higher the clay content in the structure, the greater the thermal stability, especially in composites containing Cb [52] also noted similar behavior when evaluating the thermal stability of aerogels containing cellulose and sepiolite clay. When the temperature exceeded 300°C , the decomposition rate of hydrogels/aerogels without clay was faster than that of hydrogels/aerogels with clays. According to Wang et al. [53], this can be justified by the formation of noncovalent bond interaction between clay and hydrogel/aerogels, increasing the thermal stability of material composites. This trend was also related to De La Cruz et al. [51] when evaluating gelatin B aerogel with montmorillonite. The authors affirmed that clays provided a shielding effect, favoring a significant decrease in the degradation of composites.

3.5 | Zero-Charge Point (ZPC)

Zero point charge is an important parameter for predicting the exact mechanism of adsorption by varying the pH of the reaction mixture. Figure 8 displays that the material's behavior is similar when considering the pH variation analysis.

Moreover, Figure 8a shows a slightly acidic behavior of the hydrogels, indicating that the pH of the adsorbent surface is almost neutral, with zero charge point values around 6.70. This neutrality is attributed to the synthesis process, which involves cornstarch, an acidic substance, and citric acid, which is also acidic [39]. However, when these interact with sodium hydroxide, a fundamental compound also used in the synthesis, they are neutralized to an almost neutral pH.

In the case of aerogels (Figure 8b), the analysis indicates a slightly basic pH, with zero charge point values around 7.90 for the materials analyzed. Here, sodium hydroxide seems to play a more active role, neutralizing the acids in the synthesis and slightly basifying the medium. As seen in analyses conducted in previous studies, such as that of Liu and coworkers, the adsorption of methylene blue changes very little when the pH is adjusted from 6 up to maximum of 10, as analyzed by the authors [54]. With this in mind, and given that both the hydrogel and the aerogel

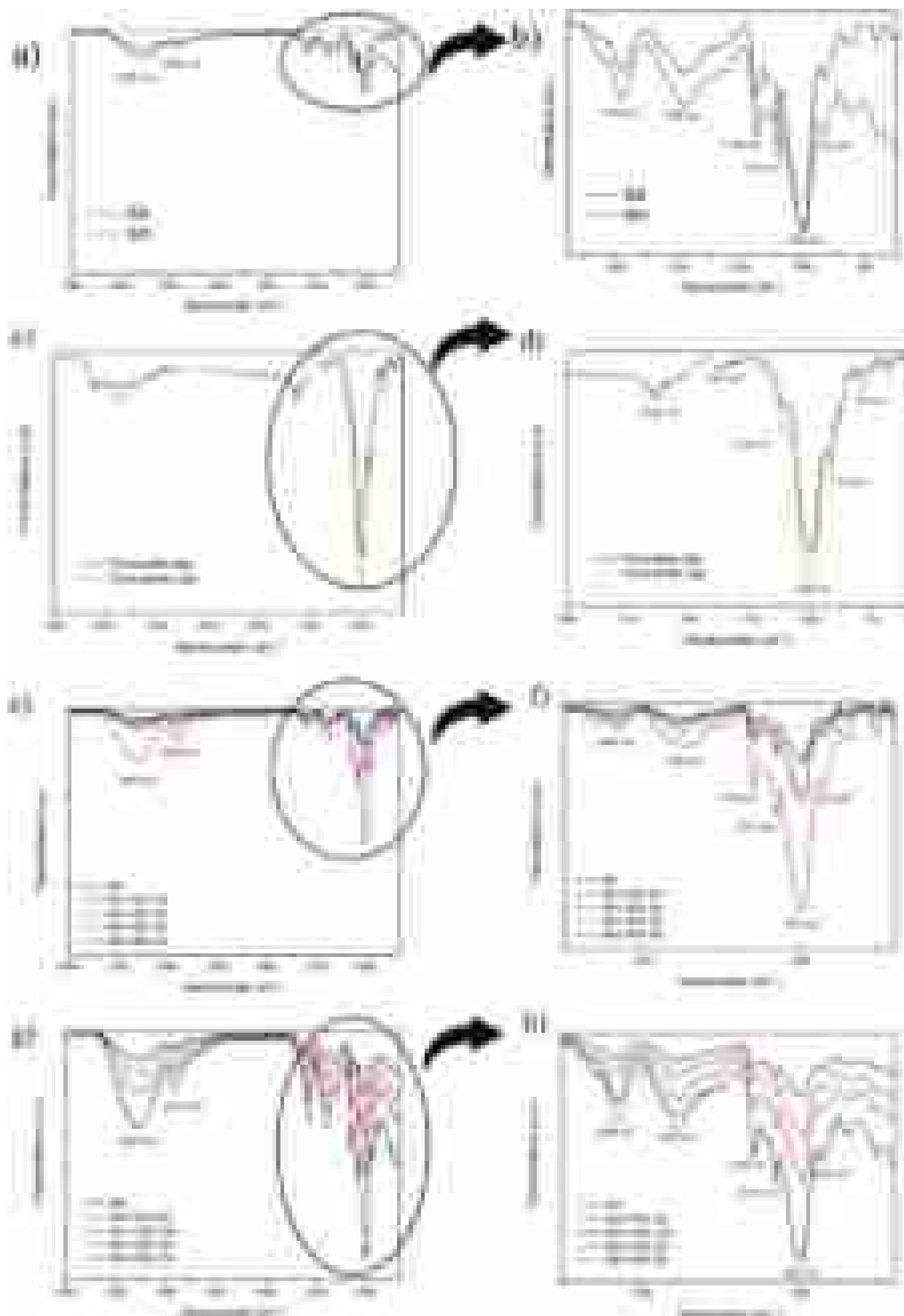


FIGURE 6 | Legend on next page.

FIGURE 6 | FTIR spectra: (a) neat hydrogel and aerogel in the wavenumber range of 4000–650 cm^{-1} , and (b) in the wavenumber range of 1750–650 cm^{-1} ; (c) chocolate and Cbs in the wavenumber range of 4000–650 cm^{-1} , and (d) in the wavenumber range of 2000–650 cm^{-1} (e) neat aerogel and its composites in the wavenumber range of 4000–650 cm^{-1} , and (f) its composites in the wavenumber range of 1750–650 cm^{-1} ; (g) neat hydrogel and its composites in the wavenumber range of 4000–650 cm^{-1} , and (h) its composites in the wavenumber range of 1750–650 cm^{-1} .

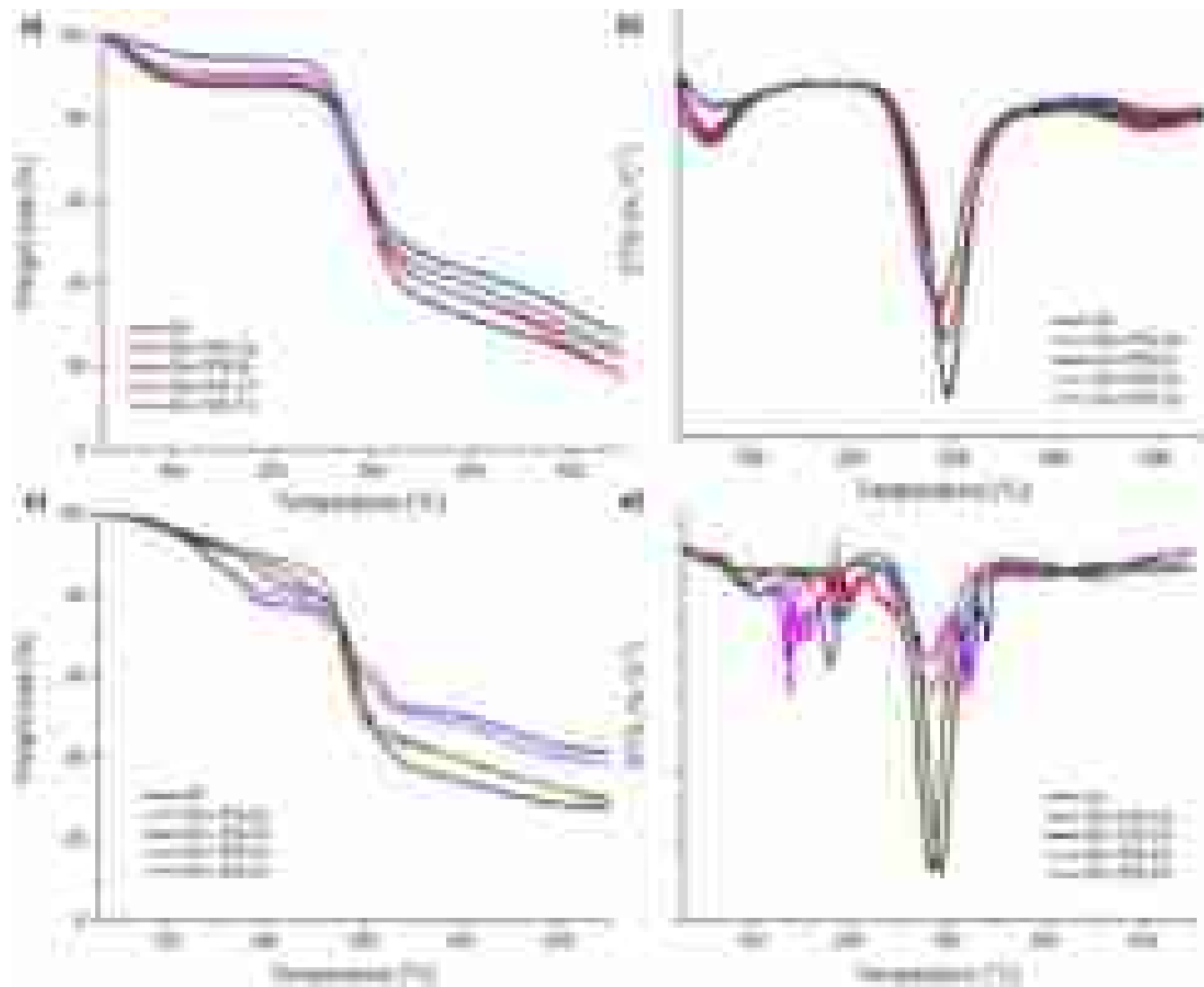


FIGURE 7 | TG/DTG curves for the hydrogel, aerogel, and their composites reinforced with Chocolate and Chocobofoe Brazilian clays: (a) TG and (b) DTG curves of aerogels and their composites; (c) TG and (d) DTG curves of hydrogels and their composites.

exchangers present satisfactory behaviors, as indicated by the analysis of the point of zero charge, no problems should be expected in the adsorption analysis. This ensures that the best possible adsorption values for this problematic dye can be achieved.

3.6 | Adsorption Tests

3.6.1 | Effect of Material Dosage

The study of material dosage's effect on adsorption capacity was carried out, and results can be observed in Figures 9 and 10. The MB adsorption capacity of aerogel and its composites reinforced with Chocolate (Ch) and Chocobofoe (Cb) Brazilian clays was

better compared to the hydrogel and its composites reinforced with Chocolate (Ch) and Chocobofoe (Cb) Brazilian clays.

In the neat hydrogel (Figure 9), very low adsorption was observed using a 30 mg mass of material. As the amount of material dosage increases, the adsorption percentage also rises, reaching a maximum of 6.6%. There is a noticeable improvement in adsorption for the hydrogel composites. However, this enhancement does not justify the more complex synthesis process and greater material cost, as some composites show only slight improvements while others even worsen in performance. For instance, at a 150 mg material mass, comparing the neat hydrogel with the 10% chocolate hydrogel shows improvement, while the composite SH + 10% Ch performs worse.

TABLE 2 | Weight loss values in interval temperature (100°C–550°C), Tonset, and residue present in the TG/DTG curves of neat starch aerogel, neat starch hydrogel, and composite materials with different contents of clays.

Samples	Weight loss (%)					Residue 550°C	T _{onset} , °C	T _{max} , °C
	100°C	200°C	300C	400°C	500°C			
SA	10.2	11.7	43.0	68.3	76.3	18.4	260.2	293.4
SA + 10% Cb	7.90	9.21	40.0	63.6	75.2	18.3	259.5	292.4
SA + 15% Cb	3.91	5.49	38.3	56.9	66.5	28.0	249.4	284.5
SA + 10% Ch	9.39	10.8	44.6	63.4	72.5	22.5	248.6	284.5
SA + 15% Ch	10.8	12.1	41.9	60.1	70.5	24.4	251.5	287.5
SH	3.90	14.8	47.0	65.5	71.2	28.8	274.6	292.5
SH + 10% Cb	2.93	11.8	50.5	60.2	67.2	30.2	260.7	283.5
SH + 15% Cb	3.51	21.7	37.1	49.5	57.0	58.3	255.8	279.8
SH + 10% Ch	2.69	19.0	39.4	52.0	59.8	39.0	257.0	281.3
SH + 15% Ch	3.44	10.1	46.8	60.3	67.2	29.4	262.0	281.3

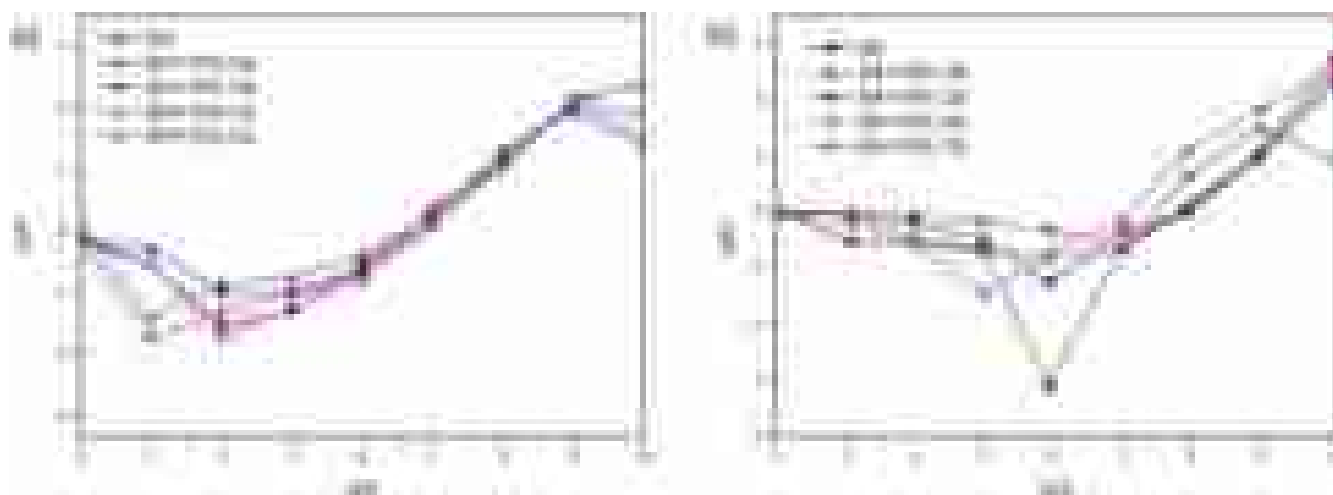


FIGURE 8 | Point of zero charge for the (a) hydrogel and (b) aerogel and their composites reinforced with Chocolate (Ch) and Chocobofoe (Cb) Brazillian clays.

In contrast, aerogels exhibited a significant increase in adsorption capacity when clay was added to the materials, as shown in Figure 10. This is evident in the adsorption percentage using 200 mg of the exchanger, which increased from 16.5% in the neat aerogel to 63.9% in the composite SA + 15% Ch.

Analyzing the q_e values of the materials, measured in mg of dye adsorbed per gram of exchanger, it was observed that aerogel and their composites presented a better q_e than hydrogel and their composites. In hydrogel and their composites, a decrease in q_e makes the synthesis of these materials seem unwise. Therefore, a higher amount of clays in the aerogels can affect the polymerization process. Also, a higher content of clays will increase the crosslinking density inside the aerogel, resulting in an adsorption network space [42]. Thus, the proper weight ratio of clays to aerogel composites is 15%, which was selected in the following studies.

3.6.2 | Effect of Contact Time

The effect of contact time on adsorption behavior was studied to investigate the adsorption capacity of SA + 15% Ch and SA + 15% Cb aerogel composites, as shown in Figure 11. In analyzing the variation of contact time between the material and the dye (MB), it was observed that there was an increase in adsorption percentage up to 2 h for the SA + 15% Ch. At this point, the material appears to reach saturation and can no longer adsorb additional dye. For the SA + 15% Cb, however, this saturation occurs after 4 h of contact time. For each material, these times represent the highest adsorption points.

To refine the analysis with a single chosen contact time, a 4 h contact period could be an effective choice to maximize adsorption efficiency for both materials, even with a slight decrease in adsorption for the SA + 15% Ch (approximately 1.2%).

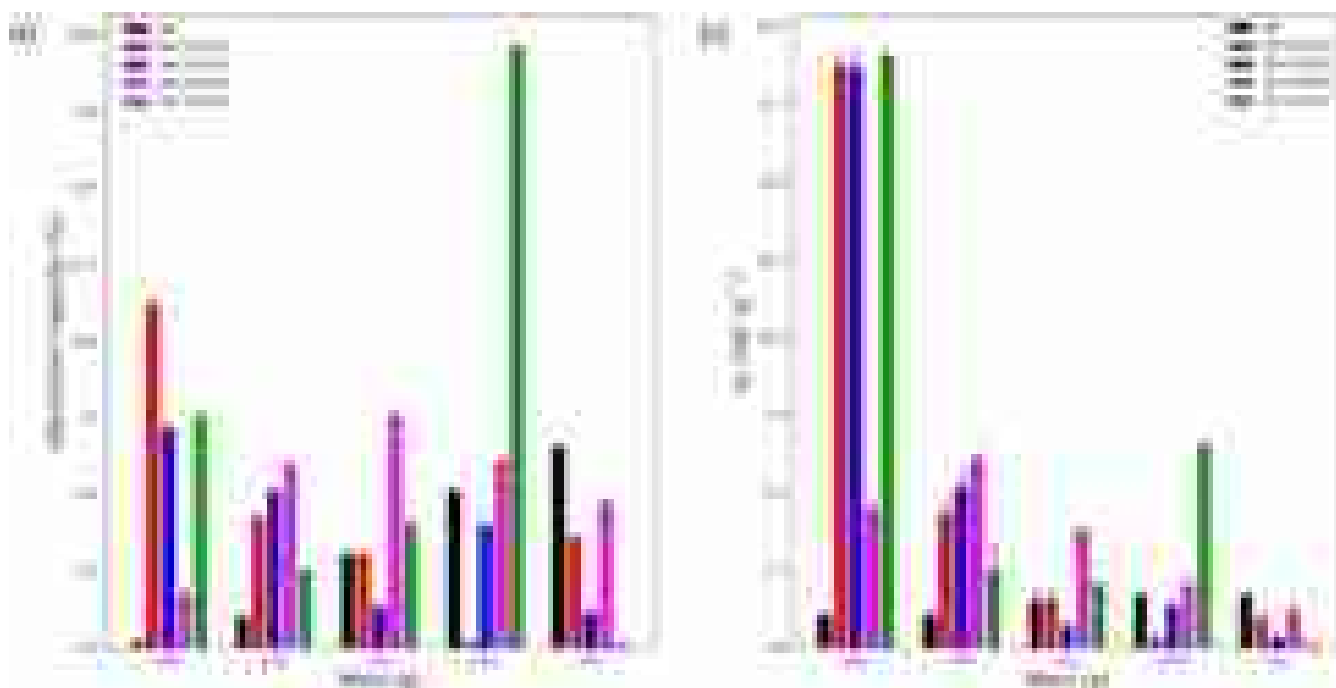


FIGURE 9 | Effect of material dosage in the adsorption capacity (a) and q_e (b) parameter on the hydrogel and their composites (SH, SH + 10% Cb, SH + 15% Cb, SH + 10% Ch and SH + 15% Ch).

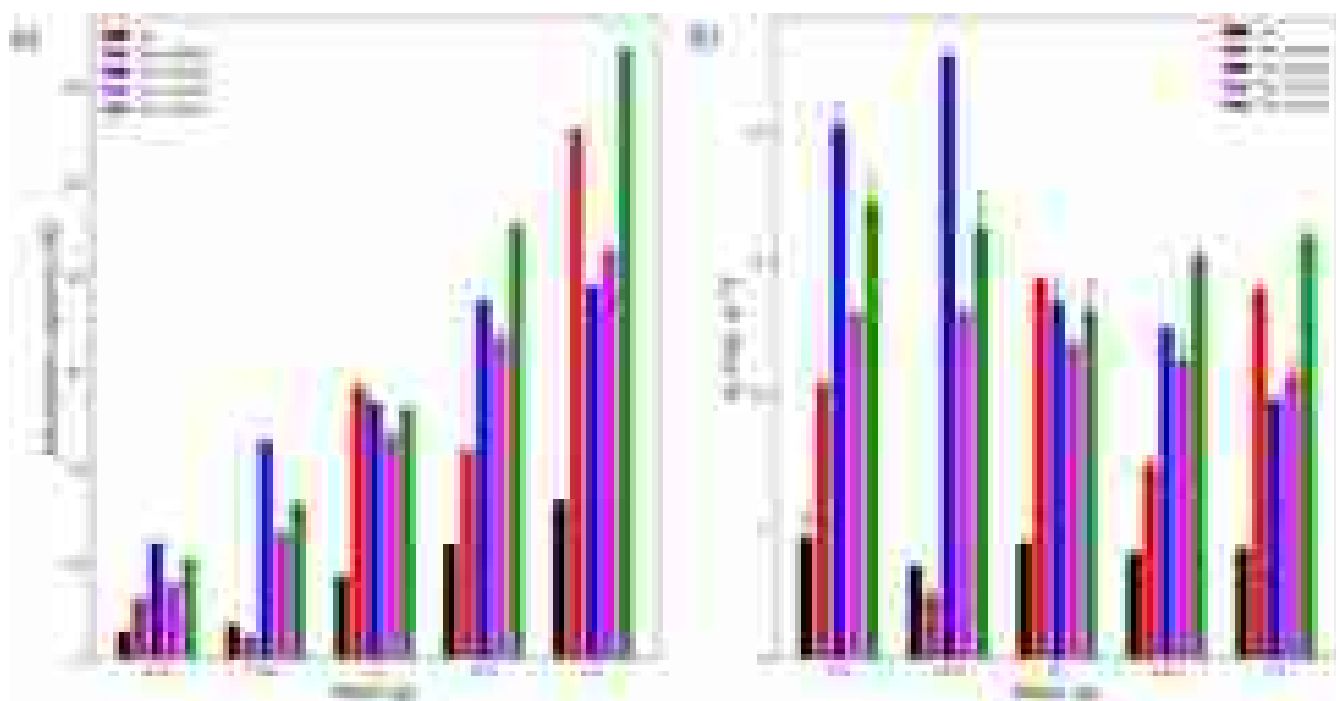


FIGURE 10 | Effect of material dosage on the adsorption capacity (a) and q_e (b) parameter on the aerogel and their composites (SA, SA + 10% Cb, SA + 15% Cb, SA + 10% Ch, and SA + 15% Ch).

In terms of adsorption efficiency, analyzed by q_e , given the same volume and dye concentration and the same mass of adsorbent in contact, the highest adsorption percentages will yield the best q_e coefficients. Therefore, as mentioned earlier, to refine subsequent analyses, the optimal coefficients are achieved with a 4 h contact time between the aerogel and the dye solution, with $47.6 \text{ mg}\cdot\text{g}^{-1}$ to SA + 15% Cb and $42.3 \text{ mg}\cdot\text{g}^{-1}$ to SA + 15% Ch.

3.6.3 | Effect of Initial Concentration

The effect of initial concentration on adsorption behavior was calculated to study the adsorption capacity of SA + 15% Ch and SA + 15% Cb aerogel composites. For the initial concentration effect, it can be seen in Figure 12 that lower dye concentrations result in greater adsorption by the aerogels,

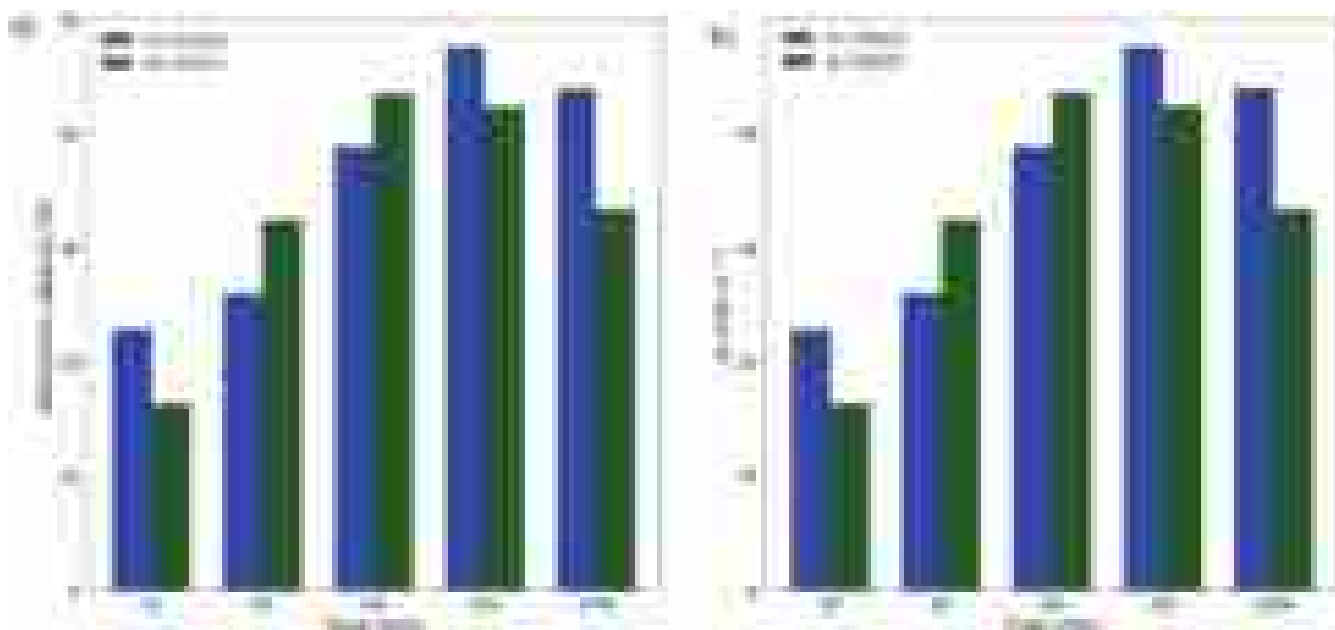


FIGURE 11 | Effect of time contact in the adsorption capacity (a) and q_e parameter (b) on the SA + 15% Cb and SA + 15% Ch.

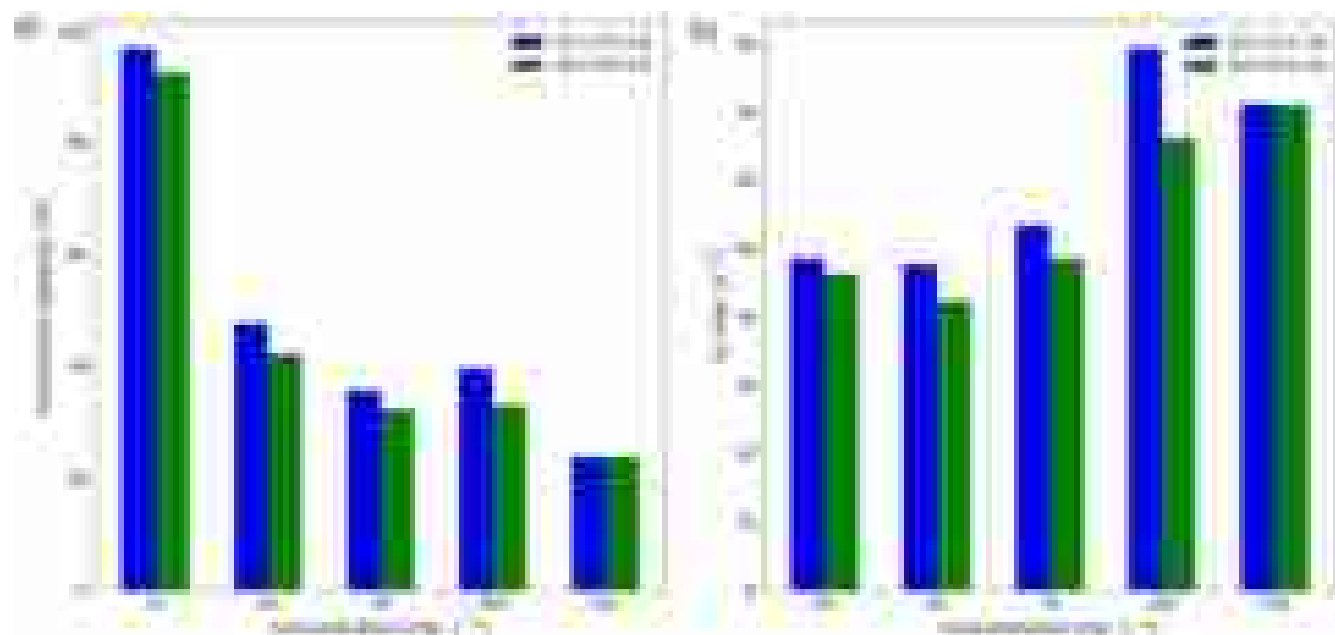


FIGURE 12 | Effect of initial dye concentration on the adsorption capacity (a) and q_e (b) parameter in the SA + 15% Cb and SA + 15% Ch.

which progressively decreases with increasing initial methylene blue concentration. However, this trend does not directly reflect the greater efficiency when analyzing the (q_e) values. According to the data presented, the peak efficiency of one of the aerogels occurs in the range of $100 \text{ mg} \cdot \text{L}^{-1}$, in which the material with 15% Cb presents a value of 79.4 mg of dye adsorbed per gram of composite. The aerogel with 15% Ch slightly improves in the concentration range of $150 \text{ mg} \cdot \text{L}^{-1}$, reaching a (q_e) coefficient of $70.96 \text{ mg} \cdot \text{g}^{-1}$.

In the Langmuir and Freundlich isotherms, shown in Table 3, the analysis of the adsorption process of the materials SA + 15% Cb (chocobofe aerogel) and SA + 15% Ch (chocolate aerogel)

was performed using both models, which provide essential information about the behavior and efficiency of the materials in the adsorption process. The Langmuir model, which assumes monolayer adsorption on a homogeneous surface with energetically equivalent sites, better fits the experimental data. For the SA + 15% Cb, the maximum adsorption capacity (q_{max}) was $75.2 \text{ mg} \cdot \text{g}^{-1}$, with a (K_L) value of 0.126 and a coefficient of determination (R^2) of 0.951. For the SA + 15% Ch, the maximum adsorption capacity was slightly higher, reaching $76.3 \text{ mg} \cdot \text{g}^{-1}$, with (K_L) of 0.124 and (R^2) of 0.933. The high values of (R^2) confirm that the Langmuir model describes the adsorption behavior of the materials well, suggesting the predominance of monolayer adsorption.

TABLE 3 | Estimated MB adsorption capacity for aerogels containing 15% wt of clays using the Langmuir and Freundlich models.

Models	Materials	Parameters	Results
Langmuir isotherm	SA + 15% Cb	$q_{\text{máx}}$	75.2
		K_L	0.126
		R^2	0.951
	SA + 15% Ch	$q_{\text{máx}}$	76.3
		K_L	0.124
		R^2	0.933
Freundlich isotherm	SA + 15% Cb	K_F	46.3
		n	13.4
		R^2	0.393
	SA + 15% Ch	K_F	39.8
		n	11.3
		R^2	0.381

On the other hand, the analysis by the Freundlich model, which considers multilayer adsorption on heterogeneous surfaces, revealed a less accurate description of the materials studied. In the case of the SA + 15% Cb aerogel, the value of (K_F) was 46.3, with (n) equal to 13.4 and a coefficient of determination (R^2) of only 0.393. Similarly, the SA + 15% Ch aerogel presented (K_F) of 39.8, with (n) equal to 11.3 and (R^2) of 0.381. The low values of (R^2) indicate an unsatisfactory fit to the Freundlich model, suggesting that the heterogeneous surfaces hypothesis with multilayer adsorption is not appropriate for the materials in question.

Therefore, the results showed that the Langmuir model is the most appropriate to describe the adsorption behavior of the SA + 15% Cb and SA + 15% Ch aerogels, reinforcing the predominance of monolayer adsorption. Between the two materials, the SA + 15% Ch presented a slightly higher maximum adsorption capacity, while the SA + 15% Cb showed a slightly higher coefficient of determination, indicating better data consistency. These results suggest that clays added to aerogels enhance the adsorption capacity, with a more predictable and efficient behavior for methylene blue removal.

4 | Conclusions

The study evaluated the chemical, thermal, morphological, and adsorptive differences presented by aerogels, starch hydrogels, and their composites with different contents of Chocobofo and Chocolate clays for removing MB dye from water. The results highlighted that the crosslinking process was successfully achieved in all formulations, ensuring materials with dense structures and interesting thermal stability were manufactured. The hydrogel composites presented possible encapsulated pores, while the aerogel composites presented porous and interconnected structures more apparent after incorporating clays, which favor the dye adsorption and absorption processes. The structure obtained by the materials strongly influenced the sorption

capacity. The aerogel composites (SA + 10% Cb and SA + 15% Cb) were responsible for adsorbing 90% of MB and fitting the experimental data to the isothermal models. SA + 15% Cb obtained a q_{max} of 75.2 mg.g⁻¹. Therefore, the study is promising in starch-based aerogels and hydrogels reinforced with Brazilian clays, directly contributing to advances in sustainable materials applied in the treatment of water contaminated with MB dye.

Author Contributions

Luidy F. Senra: resources, conceptualization, writing – original draft, investigation, methodology, visualization, formal analysis, data curation, validation. **Joaquim G. G. S. Bento:** resources, writing – original draft, data curation, formal analysis, validation, visualization, methodology, investigation. **Lana S. Maia:** investigation, methodology, validation, visualization, formal analysis, data curation, resources, writing – original draft, conceptualization. **Maria Ismênia S. T. Faria:** investigation, visualization, methodology, resources, formal analysis. **Daniella R. Mulinari:** funding acquisition, writing – review and editing, conceptualization, validation, visualization, project administration, resources, supervision. **Derval S. Rosa:** supervision, funding acquisition, writing – review and editing, visualization, validation, project administration, conceptualization, resources.

Acknowledgments

This research was funded by FAPERJ, Brazil (E-26/010.101232/2018, E-26/010/002530/2019, E-26/210.450/2021, E-26/202.664/2024, and E-26/210.029/2024), FAPESP, Brazil (2020/13703-3, 2021/14714-1, 2023/14598-7, and 2024/23595-4) and Conselho Nacional de Desenvolvimento Científico e Tecnológico—CNPq, Brazil (308053/2021-4 and 403934/2021-4). The authors thank the UFABC, CAPES (code 001), and REVALORES Strategic Unit, Multiuser Central Facilities (CEM—UFABC), and FINEP (01.18.0071.00/0476/16). The Article Processing Charge for the publication of this research was funded by the Coordenação de Aperfeiçoamento de Pessoal de Nível Superior - Brasil (CAPES) (ROR identifier: 00x0ma614).

Conflicts of Interest

The authors declare no conflicts of interest.

Data Availability Statement

Data will be made available on request.

References

1. E. De Souza Martins Freitas and R. S. Del Gaudio, “Crise ecológica, escassez hídrica e ideologias: uma análise crítica da Carta de 2070,” *Sociedade & Natureza* 27, no. 3 (2015): 439–451, <https://doi.org/10.1590/1982-451320150306>.
2. N. Markandeya, D. Mohan, and S. P. Shukla, “Hazardous Consequences of Textile Mill Effluents on Soil and Their Remediation Approaches,” *Cleaner Engineering and Technology* 7 (2022): 100434, <https://doi.org/10.1016/j.clet.2022.100434>.
3. R. Al-Tohamy, S. S. Ali, F. Li, et al., “A Critical Review on the Treatment of Dye-Containing Wastewater: Ecotoxicological and Health Concerns of Textile Dyes and Possible Remediation Approaches for Environmental Safety,” *Ecotoxicology and Environmental Safety* 231 (2022): 113160, <https://doi.org/10.1016/j.ecoenv.2021.113160>.
4. A. Pugazhendhi, S. Kamarudin, M. A. Alshehri, R. Ganesan, and K. Brindhadevi, “Nanomaterials – A Promising Solution for Textile and Fossil Fuel Generated Pollutants,” *Environmental Research* 258 (2024): 119427, <https://doi.org/10.1016/j.envres.2024.119427>.

5. S. S. Emmanuel, A. A. Adesibikan, E. A. Opatola, and C. O. Olawoyin, "A Pragmatic Review on Photocatalytic Degradation of Methyl Orange Dye Pollutant Using Greenly Biofunctionalized Nanometallic Materials: A Focus on Aquatic Body," *Applied Organometallic Chemistry* 37, no. 7 (2023): e7108, <https://doi.org/10.1002/aoc.7108>.
6. O. S. Bayomie, H. Kandeel, T. Shoeib, H. Yang, N. Youssef, and M. M. H. El-Sayed, "Novel Approach for Effective Removal of Methylene Blue Dye From Water Using Fava Bean Peel Waste," *Scientific Reports* 10, no. 1 (2020): 7824, <https://doi.org/10.1038/s41598-020-64727-5>.
7. I. Khan, K. Saeed, I. Zekker, et al., "Review on Methylene Blue: Its Properties, Uses, Toxicity and Photodegradation," *Water (Basel)* 14, no. 2 (2022): 242, <https://doi.org/10.3390/w14020242>.
8. M. D. Khan, A. Singh, M. Z. Khan, S. Tabraiz, and J. Sheikh, "Current Perspectives, Recent Advancements, and Efficiencies of Various Dye-Containing Wastewater Treatment Technologies," *Journal of Water Process Engineering* 53 (2023): 103579, <https://doi.org/10.1016/j.jwpe.2023.103579>.
9. B. Azimi, S. Sepahvand, S. Ismaeilimoghadam, et al., "Application of Cellulose-Based Materials as Water Purification Filters; A State-Of-The-Art Review," *Journal of Polymers and the Environment* 32, no. 1 (2023): 345–366, <https://doi.org/10.1007/s10924-023-02989-6>.
10. C. Zaharia, C. Musteret, and M. Afrasinei, "The Use of Coagulation–Flocculation for Industrial Colored Wastewater Treatment—(I) the Application of Hybrid Materials," *Applied Sciences* 14, no. 5 (2024): 2184, <https://doi.org/10.3390/app14052184>.
11. M. K. Barman, A. Bhattarai, and B. Saha, "Applications of Ion Exchange Resins in Environmental Remediation," *Vietnam Journal of Chemistry* 61, no. 5 (2023): 533–550, <https://doi.org/10.1002/vjch.202300027>.
12. R. Wang, J. Li, C. Xu, X. Xu, F. Tang, and M. Huang, "Integrating Reverse Osmosis and Forward Osmosis (RO-FO) for Printing and Dyeing Wastewater Treatment: Impact of FO on Water Recovery," *Environmental Science and Pollution Research* 30, no. 40 (2023): 92495–92506, <https://doi.org/10.1007/s11356-023-28853-7>.
13. S. Dwivedi and S. Dey, "Review on Biochar as an Adsorbent Material for Removal of Dyes From Waterbodies," *International Journal of Environmental Science and Technology* 20, no. 8 (2022): 9335–9350, <https://doi.org/10.1007/s13762-022-04364-9>.
14. K. H. D. Tang, N. M. Darwish, A. M. Alkahtani, M. R. AbdelGawwad, and P. Karácsony, "Biological Removal of Dyes From Wastewater: A Review of Its Efficiency and Advances," *Tropical Aquatic and Soil Pollution* 2, no. 1 (2022): 59–75, <https://doi.org/10.53623/tasp.v2i1.72>.
15. N. S. Topare and V. S. Wadgaonkar, "A Review on Application of Low-Cost Adsorbents for Heavy Metals Removal From Wastewater," *Materials Today: Proceedings* 77 (2022): 8–18, <https://doi.org/10.1016/j.matpr.2022.08.450>.
16. J. K. Bediako, V. Apalangya, I. O. Hodgson, I. Anugwom, and E. Repo, "Adsorbents for Water Decontamination: A Recycling Alternative for Fiber Precursors and Textile Fiber Wastes," *Science of the Total Environment* 919 (2024): 171000, <https://doi.org/10.1016/j.scitotenv.2024.171000>.
17. N. Kumar, A. Pandey, N. Rosy, and Y. C. Sharma, "A Review on Sustainable Mesoporous Activated Carbon as Adsorbent for Efficient Removal of Hazardous Dyes From Industrial Wastewater," *Journal of Water Process Engineering* 54 (2023): 104054, <https://doi.org/10.1016/j.jwpe.2023.104054>.
18. X. Cheng, H. Li, D. Jiang, et al., "Insights Into Simultaneous Efficient Removal of Cationic and Anionic Dyes by Nitrogen-Rich Seaweed Carbon Adsorbent," *Process Safety and Environmental Protection* 184 (2024): 38–49, <https://doi.org/10.1016/j.psep.2024.01.067>.
19. A. Hashem, C. O. Aniagor, O. M. Morsy, A. Abou-Okeil, and A. A. Aly, "Apricot Seed Shell: An Agro-Waste Biosorbent for Acid blue193 Dye Adsorption," *Biomass Conversion and Biorefinery* 14, no. 11 (2022): 12283–12296, <https://doi.org/10.1007/s13399-022-03272-9>.
20. P. Bhatt, S. Joshi, G. M. U. Bayram, P. Khati, and H. Simsek, "Developments and Application of Chitosan-Based Adsorbents for Wastewater Treatments," *Environmental Research* 226 (2023): 115530, <https://doi.org/10.1016/j.envres.2023.115530>.
21. Z. Ahamad and A. Nasar, "Utilization of *Azadirachta indica* Sawdust as a Potential Adsorbent for the Removal of Crystal Violet Dye," *Sustainable Chemistry* 4, no. 1 (2023): 110–126, <https://doi.org/10.3390/suschem4010009>.
22. A. K. Tolkou, E. K. Tsoutsas, G. Z. Kyzas, and I. A. Katsoyiannis, "Sustainable Use of Low-Cost Adsorbents Prepared From Waste Fruit Peels for the Removal of Selected Reactive and Basic Dyes Found in Wastewaters," *Environmental Science and Pollution Research* 31, no. 10 (2024): 14662–14689, <https://doi.org/10.1007/s11356-024-31868-3>.
23. G. George, A. M. Ealias, and M. P. Saravanakumar, "Advancements in Textile Dye Removal: A Critical Review of Layered Double Hydroxides and Clay Minerals as Efficient Adsorbents," *Environmental Science and Pollution Research* 31, no. 9 (2024): 12748–12779, <https://doi.org/10.1007/s11356-024-32021-w>.
24. H. Abedpour, J. Moghaddas, M. N. Borhani, and T. N. Borhani, "Separation of Toxic Contaminants From Water by Silica Aerogel-Based Adsorbents: A Comprehensive Review," *Journal of Water Process Engineering* 53 (2023): 103676, <https://doi.org/10.1016/j.jwpe.2023.103676>.
25. S. Montes and H. Maleki, *Aerogels and Their Applications* (Elsevier eBooks, 2019), 337–399, <https://doi.org/10.1016/b978-0-12-813357-6.00015-2>.
26. P. H. Camani, M. G. M. Gonçalo, R. F. S. Barbosa, and D. S. Rosa, "Comprehensive Insight of Crosslinking Agent Concentration Influence on Starch-Based Aerogels Porous Structure," *Journal of Applied Polymer Science* 138, no. 34 (2021): e50863, <https://doi.org/10.1002/app.50863>.
27. Q. Huang, C. Wang, D. Hao, W. Wei, L. Wang, and B. Ni, "Ultra-light Biodegradable 3D-g-C₃N₄ Aerogel for Advanced Oxidation Water Treatment Driven by Oxygen Delivery Channels and Triphase Interfaces," *Journal of Cleaner Production* 288 (2020): 125091, <https://doi.org/10.1016/j.jclepro.2020.125091>.
28. B. M. Thamer, F. A. Al-Aizari, and H. S. Abdo, "Activated Carbon-Incorporated Tragacanth Gum Hydrogel Biocomposite: A Promising Adsorbent for Crystal Violet Dye Removal From Aqueous Solutions," *Gels* 9, no. 12 (2023): 959, <https://doi.org/10.3390/gels9120959>.
29. Z. Ahmadian, F. Kazeminava, M. Afrouz, et al., "A Review on the Impacts of Metal/Metal Nanoparticles on Characteristics of Hydrogels: Special Focus on Carbohydrate Polymers," *International Journal of Biological Macromolecules* 253 (2023): 126535, <https://doi.org/10.1016/j.ijbiomac.2023.126535>.
30. M. M. A. Hameed, F. A. Al-Aizari, and B. M. Thamer, "Synthesis of a Novel Clay/Polyacrylic Acid-Tannic Acid Hydrogel Composite for Efficient Removal of Crystal Violet Dye With Low Swelling and High Adsorption Performance," *Colloids and Surfaces A: Physicochemical and Engineering Aspects* 684 (2024): 133130, <https://doi.org/10.1016/j.colsurfa.2023.133130>.
31. J. Yang, J. Nie, L. Bian, et al., "Clay Minerals/Sodium Alginate/Polyethylene Hydrogel Adsorbents Control the Selective Adsorption and Reduction of Uranium: Experimental Optimization and Monte Carlo Simulation Study," *Journal of Hazardous Materials* 468 (2024): 133725, <https://doi.org/10.1016/j.jhazmat.2024.133725>.
32. M. A. Ruiz-Fresneda, E. González-Morales, C. Gila-Vilchez, et al., "Clay–Polymer Hybrid Hydrogels in the Vanguard of Technological Innovations for Bioremediation, Metal Biorecovery, and Diverse Applications," *Materials Horizons* 11, no. 22 (2024): 5533–5549, <https://doi.org/10.1039/d4mh00975d>.

33. X. Zhai, C. Ruan, J. Shen, et al., "Clay-Based Nanocomposite Hydrogel With Attractive Mechanical Properties and Sustained Bioactive Ion Release for Bone Defect Repair," *Journal of Materials Chemistry B* 9, no. 10 (2021): 2394–2406, <https://doi.org/10.1039/d1tb00184a>.
34. F. Zamani-Babgohari, A. Irannejad, M. K. Pour, and G. R. Khayati, "Synthesis of Carboxymethyl Starch Co (Polyacrylamide/ Polyacrylic Acid) Hydrogel for Removing Methylene Blue Dye From Aqueous Solution," *International Journal of Biological Macromolecules* 269 (2024): 132053, <https://doi.org/10.1016/j.ijbiomac.2024.132053>.
35. F. Mushtaq, Z. A. Raza, S. R. Batool, et al., "Preparation, Properties, and Applications of Gelatin-Based Hydrogels (GHs) in the Environmental, Technological, and Biomedical Sectors," *International Journal of Biological Macromolecules* 218 (2022): 601–633, <https://doi.org/10.1016/j.ijbiomac.2022.07.168>.
36. X. Hu, Z. Li, Y. Ge, S. Liu, and C. Shi, "Enhanced π - π Stacks of Aromatic Ring-Rich Polymer Adsorbent for the Rapid Adsorption of Organic Dyes," *Colloids and Surfaces A: Physicochemical and Engineering Aspects* 643 (2022): 128782, <https://doi.org/10.1016/j.colsurfa.2022.128782>.
37. B. M. A. Brito, J. M. Cartaxo, N. F. C. Nascimento, H. C. Ferreira, G. A. Neves, and R. R. Menezes, "Avaliação de argilas bentoníticas poliacrílicas do estado da Paraíba com aditivos para aplicação em perfuração de poços de petróleo e tintas à base de água," *Cerâmica* 62, no. 361 (2016): 45–54, <https://doi.org/10.1590/0366-69132016623611978>.
38. L. S. Maia, P. H. F. Pereira, A. I. C. Da Silva, T. B. Da Costa, D. R. Mulinari, and D. D. S. Rosa, "A Novel Starch-Based Composite Hydrogel Enhanced by Activated Charcoal From the Banana Peel for Water Decontamination," *Journal of Applied Polymer Science* 141, no. 29 (2024): 106460, <https://doi.org/10.1002/app.55685>.
39. P. H. F. Pereira, A. I. C. Da Silva, R. F. S. Barbosa, V. Arantes, D. R. Mulinari, and D. S. Rosa, "Insights in the Adsorption of Eco-Friendly Starch Hydrogel," *Adsorption* 30, no. 7 (2024): 1685–1702, <https://doi.org/10.1007/s10450-024-00509-z>.
40. L. S. Martins, N. C. Zanini, L. S. Maia, et al., "Crude Oil and S500 Diesel Removal From Seawater by Polyurethane Composites Reinforced With Palm Fiber Residues," *Chemosphere* 267 (2020): 129288, <https://doi.org/10.1016/j.chemosphere.2020.129288>.
41. W. C. Lopes, F. M. Brito, F. E. Neto, et al., "Development of a New Clay-Based Aerogel Composite From Ball Clay From Piauí, Brazil and Polysaccharides," *Polymers* 15, no. 11 (2023): 2412, <https://doi.org/10.3390/polym15112412>.
42. X. Wang, Y. Zheng, L. Zong, et al., "Porous Biochar Composite Hydrogel for Effective Removal of Low-Concentration Methylene Blue From Wastewater," *Journal of Polymer Research* 29, no. 11 (2022): 467, <https://doi.org/10.1007/s10965-022-03295-w>.
43. J. Sun, T. Luo, M. Zhao, et al., "Hydrogels and Aerogels for Versatile Photo-/Electro-Chemical and Energy-Related Applications," *Molecules* 29, no. 16 (2024): 3883, <https://doi.org/10.3390/molecules29163883>.
44. R. R. Ferreira, T. B. Da Costa, R. F. Da Silva Barbosa, P. H. Camani, R. R. Menezes, and D. D. S. Rosa, "Brazilian Clays as Natural Cation Exchangers for Copper Sorption in a Batch System," *Adsorption* 30 (2024): 2113–2133, <https://doi.org/10.1007/s10450-024-00543-x>.
45. J. Huang, J. Gao, L. Qi, Q. Gao, and L. Fan, "Preparation and Properties of Starch–Cellulose Composite Aerogel," *Polymers* 15, no. 21 (2023): 4294, <https://doi.org/10.3390/polym15214294>.
46. Y. Zhao, M. Tian, and P. Huang, "Starch/Clay Aerogel Reinforced by Cellulose Nanofibrils for Thermal Insulation," *Cellulose* 28, no. 6 (2021): 3505–3513, <https://doi.org/10.1007/s10570-021-03750-9>.
47. C. M. Hwang, S. Sant, M. Masaali, et al., "Fabrication of Three-Dimensional Porous Cell-Laden Hydrogel for Tissue Engineering," *Biofabrication* 2, no. 3 (2010): 035003, <https://doi.org/10.1088/1758-5082/2/3/035003>.
48. F. Chen, C. Miao, Q. Duan, et al., "Developing Slow Release Fertilizer Through In-Situ Radiation-Synthesis of Urea-Embedded Starch-Based Hydrogels," *Industrial Crops and Products* 191 (2022): 115971, <https://doi.org/10.1016/j.indcrop.2022.115971>.
49. M. Pantić, M. Nowak, G. Lavrič, Ž. Knez, Z. Novak, and I. Zizovic, "Enhancing the Properties and Morphology of Starch Aerogels With Nanocellulose," *Food Hydrocolloids* 156 (2024): 110345, <https://doi.org/10.1016/j.foodhyd.2024.110345>.
50. X. Wang, Y. Wang, M. Sun, et al., "Aramid Pulp Reinforced Clay Aerogel Composites: Mechanical, Thermal and Combustion Behavior," *Gels* 8, no. 10 (2022): 654, <https://doi.org/10.3390/gels8100654>.
51. L. G. De La Cruz, T. Abt, N. León, and M. Sánchez-Soto, "Properties of Freeze-Dried Gelatin/Clay Aerogel Composites Crosslinked With Tannic Acid," *ACS Applied Polymer Materials* 5, no. 10 (2023): 7774–7785, <https://doi.org/10.1021/acsapm.3c00971>.
52. P. Gupta, C. Verma, and P. K. Maji, "Flame Retardant and Thermally Insulating Clay Based Aerogel Facilitated by Cellulose Nanofibers," *Journal of Supercritical Fluids* 152 (2019): 104537, <https://doi.org/10.1016/j.supflu.2019.05.005>.
53. Z. Wang, T. Li, H. Peng, H. Ren, J. Lin, and C. Lou, "Natural-Clay-Reinforced Hydrogel Adsorbent: Rapid Adsorption of Heavy-Metal Ions and Dyes From Textile Wastewater," *Water Environment Research* 94, no. 4 (2022): e10698, <https://doi.org/10.1002/wer.10698>.
54. T. Liu, Y. Li, Q. Du, et al., "Adsorption of Methylene Blue From Aqueous Solution by Graphene," *Colloids and Surfaces B: Biointerfaces* 90 (2011): 197–203, <https://doi.org/10.1016/j.colsurfb.2011.10.019>.

Supporting Information

Additional supporting information can be found online in the Supporting Information section. **Figure S1:** XRD curves for chocobofe and chocolate clays.



Development of lignin biochar and its incorporation in cellulose hydrogels for water decontamination

Lucas R. Gonçalves¹ · Rafaela R. Ferreira¹ · Alana G. Souza¹ ·
Rennan F. S. Barbosa¹ · Talles B. da Costa¹ · Derval S. Rosa¹

Received: 29 January 2025 / Revised: 3 March 2025 / Accepted: 4 March 2025 /
Published online: 17 March 2025

© The Author(s), under exclusive licence to Springer-Verlag GmbH Germany, part of Springer Nature 2025

Abstract

The presence of toxic elements has raised concern about its effects and the search for new cost-efficient alternatives for its removal, and the use of polysaccharides has stood out for its abundance, properties and low cost. Based on these, this work presents the production of lignin biochar (Bc) for incorporation in cellulose hydrogels obtained from eucalyptus waste. A treatment with biochar was used, which demonstrated the ability to obtain stable biochar with high porosity. Then, cellulose hydrogels were developed employing epichlorohydrin as crosslinking agent loaded with Bc contents of 1, 3 and 5 wt%. FTIR, TGA, and XRD analyses revealed no significant structural changes in the hydrogels after the addition of Bc, and the morphology indicated good dispersion and adhesion of the adsorbent material. The hydrogels exhibited good water absorption capacity, and the swelling ratio was greater than 290% for all samples. The evaluation of the adsorption rate of heavy metals by the cellulose-based hydrogel composites presented the following metallic affinity order: $\text{Cu}^{2+} > \text{Cr}^{6+} > \text{Cd}^{2+} > \text{Zn}^{2+} > \text{Ni}^{2+} > \text{Mn}^{2+}$. The results show that the obtained materials have potential to promote water decontamination with environmentally friendly characteristics.

Keywords Lignin recovery · Lignocellulosic materials · Biochar · Hydrogels · Water treatment · Heavy metals

✉ Derval S. Rosa
dervalrosa@yahoo.com.br

¹ Center for Engineering, Modeling, and Applied Social Sciences (CECS), Federal University of ABC (UFABC), Av. Dos Estados, 5001, Santo André, SP CEP 09210-210, Brazil

Introduction

The presence of pollutants in water is a global concern, and contaminated water can generate extremely dangerous effects, affecting the environment and the living beings that consume it [1]. Among the different pollutants, potentially toxic elements such as lead, cadmium, and chromium stand out due to their harmful effect on human health. Conventional treatments have proven ineffective or expensive to guarantee their removal, so new removal methods have been investigated [2]. In this regard, the adsorption method has gained visibility due to its high efficiency, ease of operation, and low waste generation. Moreover, the possibility of producing low-cost and environmentally friendly adsorbent materials has been highlighted.

Agricultural residues are organic substances discarded during agricultural production, such as plant residues, manure, agricultural secondary products, and rural household residues [3, 4]. The forestry industry is one of the agricultural sectors that generate the highest amount of solid waste during production, with a few million tons of residual fibers. Eucalyptus (*Eucalyptus citriodora*) is one of the main plant species exploited by this industry, and about 20 million hectares of eucalyptus are cultivated in several countries around the world, such as Brazil, India, and China, giving rise to a huge amount of biomass that is wasted and misused every year [5, 6].

This lignocellulosic biomass draws attention due to its biodegradability, low cost, high availability, and carbon neutrality and is composed of three biopolymers: cellulose, hemicellulose, and lignin [7]. Due to these characteristics, biomass emerges as one of the main substitutes for fossil carbon sources, representing the main pollutants causing global warming [8]. High value-added products produced from biomass are increasingly gaining prominence due to their sustainable and carbon-free characteristics, such as biofuels, chemicals, and plastics [9]. By isolating cellulose, hemicellulose, and lignin, low-cost natural polymers are obtained with common characteristics such as biodegradability, low toxicity, and abundance [10]. These different polysaccharides possess different chemical structures, which can be employed for diverse applications, and recently their use for environmental remediation has been highlighted.

The development of hydrogel systems using polysaccharides is an interesting destination, which reevaluates these materials from different residue sources [11]. The hydrogels are a three-dimensional porous network with the ability to absorb considerable water due to the presence of functional groups within its chemical structure. Cellulose hydrogels have been highlighted in the literature due to their available hydroxyl groups and can be employed to retain toxic pollutants from the environment. However, incorporating materials with different functional groups could improve these materials' adsorption properties [12].

Considering the biopolymers also present in biomass residue, lignin presents a complex structure that makes its application difficult, being usually discarded without proper use. Because of this undervaluation of lignin, many studies and scientific articles have been published to highlight its potential for application in

high value-added products by the industry [13]. However, lignin complex structure offers the opportunity to extract new properties based on extraction and treatment performed. One process that has stood out is biochar development, which shows the potential to promote a material with a high surface area and improved adsorption capacity. Thus, using lignin to produce biochar is a cost-efficient alternative to developing new environmentally friendly materials with the reuse of agricultural waste [14, 15].

The development of biochar through the pyrolysis process of lignin is promising because this polysaccharide contains a higher amount of carbon compared to other polysaccharides, making it a potential source for biochar production [16]. Additionally, compared to cellulose and hemicellulose, lignin exhibits a high oxygen content and is rich in functional groups for adsorption, mainly including carboxyl groups and phenolic hydroxyl groups [17]. A large portion of the studies in the literature involve modifications or functionalization of the material to enhance its adsorption capacity; however, many of these processes use chemicals toxic and/or non-biodegradable materials [18–20] making these approaches less environmentally friendly.

The present work aims to evaluate the production of lignin-derived biochar without modification from eucalyptus waste to develop highly adsorbent hydrogels. Cellulose hydrogels were crosslinked using epichlorohydrin with different biochar contents (1, 3 and 5 wt%). The physicochemical, thermal, morphological, water absorption, and heavy metals adsorption properties were evaluated. Thus, the present work presents a destination of a waste source to obtain a material that can assist in environmental decontamination.

Materials and methods

Materials

Eucalyptus (*Eucalyptus citriodora*) residues, in the form of sawdust, obtained from the bark and wood cut after harvesting in Mato Grosso (Brazil), were used as lignocellulosic biomass. The microcrystalline cellulose and the reagents used (sulfuric acid (H_2SO_4), urea ($\text{CH}_4\text{N}_2\text{O}$), epichlorohydrin ($\text{C}_3\text{H}_5\text{ClO}$), and sodium hydroxide (NaOH)) were purchased from Labsynth—Diadema, SP, Brazil.

Methods

Biochar preparation

For each 10 g of eucalyptus residues, 10 mL of 72% H_2SO_4 was added, dissolving the polysaccharide fraction of the lignocellulosic material. After 2 h of acid hydrolysis, distilled water was added to the mixture, and the material remained in a water bath for 4 h. The resulting lignin biochar was filtered using a Buchner funnel and washed with warm distilled water. The biochar obtained after filtration was dried at

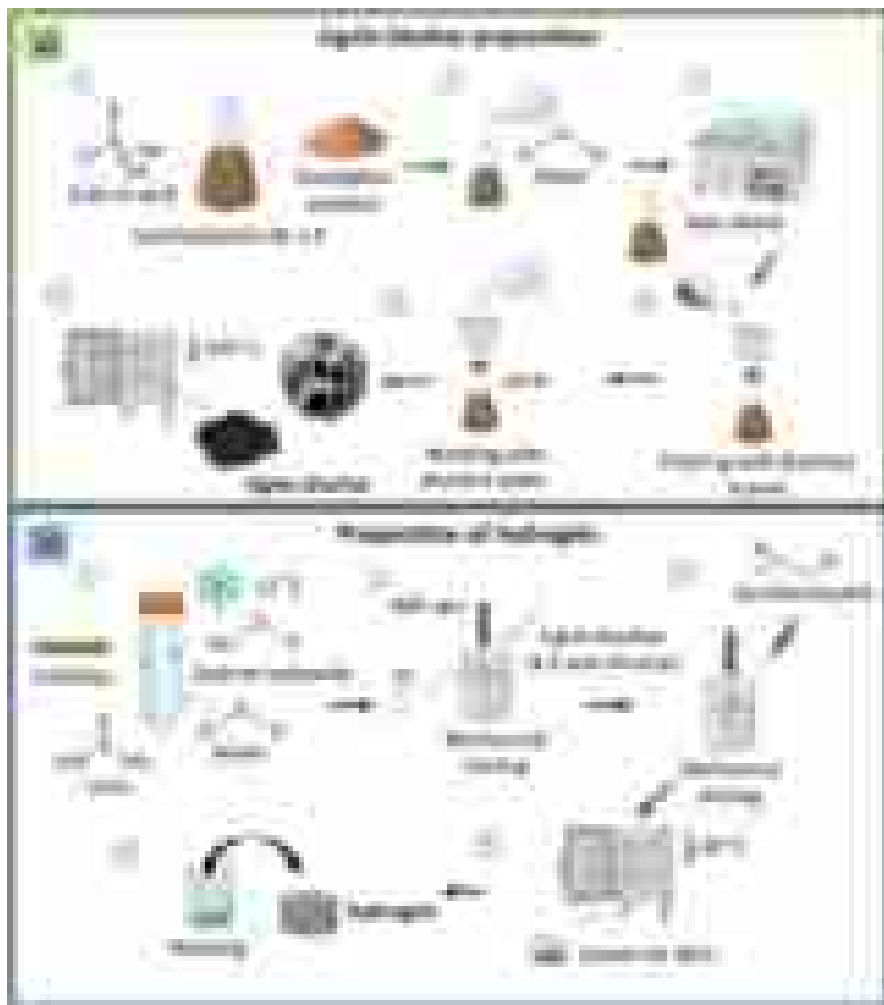


Fig. 1 **a** Lignin biochar (Bc) preparation method and **b** production stages of cellulose hydrogels with the addition of the biochar obtained

103 °C for 24 h in an oven. Figure 1a shows a scheme that illustrates the preparation methodology used for biochar.

Production of cellulose hydrogels containing biochar

Four cellulose hydrogels were produced, one pure without adding biochar (Bc) and three with adding biochar at different concentrations (1, 3 and 5 wt%). To form cellulose hydrogels, 7 g of NaOH, 12 g of $\text{CH}_4\text{N}_2\text{O}$, 3 g of cellulose, and 81 mL of water were used. Urea and sodium hydroxide were dissolved in water, and cellulose was added shortly after dissolution. This mixture was placed in plastic containers

and refrigerated at approximately $-10\text{ }^{\circ}\text{C}$ for 24 h. After this period, the containers were placed at room temperature until the solution was partially liquid so it was possible to shake it. Biochar was added at different concentrations (1, 3, and 5 wt%), and the mechanical stirrer was then used to stir the solution for 30 min at about 900 rpm. After 15 min of agitation, 5 mL of $\text{C}_3\text{H}_5\text{ClO}$ was added to crosslink the hydrogel.

Finally, after stirring, the solutions were placed again in plastic containers and dried in an oven at $60\text{ }^{\circ}\text{C}$ for 48 h. After drying, the hydrogels were washed with water for 72 h to remove $\text{C}_3\text{H}_5\text{ClO}$ residues, which could affect the results, and were again taken to drying in an oven at $60\text{ }^{\circ}\text{C}$ for 24 h. Figure 1b shows a scheme that illustrates the preparation methodology used for hydrogels.

Characterization

Fourier-transform infrared spectroscopy

Fourier-transform infrared spectroscopy (FTIR) was performed on a Frontier 94,942 (PerkinElmer, USA) instrument with an attenuated total reflectance (ATR) accessory. The range from 4000 to 400 cm^{-1} was evaluated with 32 scans, and a resolution of 4 cm^{-1} .

Scanning electron microscopy (SEM)

The samples were submitted to scanning electron microscopy analysis in a JEOL-JCM 600, 20 kV equipment. The samples were previously coated with gold by the sputtering technique (SCANCOAT, PIRANI 501), with 30 nm of gold deposition on the surface [21].

Energy-dispersive X-ray spectroscopy (EDS)

The materials were also characterized by energy-dispersive X-ray spectroscopy (EDS) analysis, before and after heavy metals capture. EDS spectra were obtained from the Compact Scanning Electron Microscope (JSM-6010LA, Jeol System Technology Co., LTD.) using the following conditions: current of 50 pA, voltage of 15 kV, and spot size of 50 nm.

X-ray diffraction (XRD)

The samples were characterized using a polycrystal X-ray diffractometer, model STADI-P (Stoe®, Darmstadt, Germany), operating in transmission mode, with $\text{CuK}\alpha$ radiation ($\lambda = 1.54056\text{ \AA}$), at a step width of 0.01° and counting time of 100 s at each 0.5° , from $2\theta = 10^{\circ}$ to 40° .

Brunauer–Emmett–Teller (BET)

To evaluate the specific surface area and pore size of the samples, the BET method (Quantachrome, model NOVA1200e, Germany) was employed. The samples were subjected to vacuum heating at 100 °C for 2 h to ensure the complete removal of water from all pores within the materials. The full nitrogen adsorption/desorption isotherm was obtained by varying the relative pressure (P/P_0) from 0.1 to 0.99 at a temperature of -196 °C. The micropore and mesopore volumes were determined using the following equations, where V_{mi} represents the specific micropore volume (cm^3/g), V_{me} denotes the specific mesopore volume (cm^3/g), and V_{ads} corresponds to the specific adsorbed volume at a given relative pressure (cm^3/g) [22]:

$$V_{mi} = V_{ads(P/P_0=0.1)} \quad (1)$$

$$V_{me} = V_{ads(P/P_0=0.99)} - V_{ads(P/P_0=0.1)} \quad (2)$$

Thermogravimetric analysis (TGA)

Thermogravimetric analysis was used to analyze the mass loss behavior of the material as a function of a progressive increase in temperature. The Netzsch STA 449 F3 Jupiter model equipment was used in a nitrogen atmosphere with a heating rate of 10 °C min^{-1} , with a temperature of 30–600 °C.

Swelling ratio

The swelling ratio (SR) of the hydrogels was determined by immersion of dry hydrogel fragments of ~ 0.1 g in distilled water, with mass measurements taken at regular intervals within one week (168 h). The experiments were carried out at room temperature, in triplicate, and the SR was calculated using Eq. 3, where $m_s(t)$ is the mass of hydrogel swollen at a time t , and $m(t=0)$ is the dry hydrogel mass (g) [2].

$$\text{DS}(\%) = \frac{m_s(t) - m(t=0)}{m(t=0)} \cdot 100 \quad (3)$$

Heavy metals adsorption

The adsorption experiments were performed in Erlenmeyer flasks where $\sim 0.040 \pm 0.001$ g of each sample (biochar, neat hydrogel, and hydrogel composites) were immersed in 40 mL of heavy metals solution (Cr^{6+} , Cd^{2+} , Ni^{2+} , Mn^{2+} , Zn^{2+} , and Cu^{2+}) containing 0.052 ± 0.011 mmol/L of each. The systems were kept under agitation (~ 150 rpm), pH 4.0–4.5, and room temperature (~ 25 °C). After 24 h, aliquots were collected, and heavy metal concentrations were determined by ion chromatography (940 Professional IC Vario, Metrohm). All measurements were

performed in duplicate. Removal efficiencies ($\%R$) calculated from Eq. 4, where C_0 is the heavy metal initial concentration (mmol/L), and C_e is the heavy metal concentration at equilibrium (mmol/L) [4].

$$\%R = \frac{(C_0 - C_e)}{C_0} \cdot 100 \quad (4)$$

Results and discussion

Biochar (Bc)

FTIR

FTIR is a technique widely used to identify the composition of lignocellulosic materials and the chemical structure of their constituents: cellulose, hemicellulose, and lignin. This technique allows the detection of changes in the chemical structure of these materials, which can occur either due to natural causes, such as aging or caused by chemical treatments [23].

The FTIR results were compared with results obtained in the literature to determine the main bands found in the FTIR spectra of eucalyptus sawdust fiber (treated and pure), and their possible attributions are presented in Table 1.

Figure 2 presents the FTIR spectra of the eucalyptus fiber after treatment with biochar, and it was possible to notice important changes that suggest the impact of treatment on the chemical composition of the eucalyptus fiber. This method proved to be “aggressive,” degrading most of the cellulose and hemicellulose present in the pure eucalyptus fiber. The disappearance of hemicellulose and cellulose is a positive aspect, since the objective of this work is the extraction of lignin; however, it is extremely important that the chemical structure of lignin remains unchanged so that its subsequent applications are successful and that its properties remain unchanged. However, due to the intensity of sulfuric acid, the peaks located in the 1650–1647 and 1260–1235 cm^{-1} intervals related to lignin also underwent significant changes after treatment with biochar.

The peak ranges 3800–3000, 1735–1730, 1462–1457, 1370–1365, 1160–1155, 900–896, and 835–830 cm^{-1} , related to the presence of cellulose and hemicellulose, disappeared in the spectrum of fiber treated with sulfuric acid (Fig. 2a), indicating degradation and disturbance of its chemical structures. Cellulose may have suffered a rupture of its intramolecular hydrogen bonds, which characterizes the changes caused in its crystalline structure [31]. The peaks in the intervals 1650–1647 and 1260–1235 cm^{-1} were considerably impacted, presenting a reduction and shift, which may indicate a loss of lignin and changes in its chemical structure (Fig. 2b). Since other lignin-related peaks remain unchanged, lignin is still present in the structure after treatment, but the structural changes in lignin and the decrease in process yield are points of attention for the procedure. Overall, the biochar method showed satisfactory results for the proposed preparation of biochar based on lignin,

Table 1 Main FTIR bands found in eucalyptus fiber (treated and pure)

Wavenumber (cm ⁻¹)	Assignment	Possible assignments	References
3800–3000	H–O–H intermolecular stretching via hydrogen bonding	Hydroxyl groups in lignin, cellulose and hemicellulose	[23–27]
3000–2850	C–H stretching	Cellulose and hemicelluloses	[24–28]
1735–1730	Stretching C=O	Characteristic of carbonyl and acetyl groups (hemicelluloses)	[24–27, 29]
1650–1647	Aromatic rings present in Lignin	Lignin	[24–28]
1595–1592	Skeletal vibration of the C=C phenolic ring	Lignin	[23–27]
1510–1500			
1462–1457	Stretching –C–O–C	Cellulose I, lignin and hemicelluloses	[24–27, 30]
1425–1420	Symmetrical bending δ CH ₂ (Weaker peak near 1420 cm ⁻¹)	Crystallized cellulose II and amorphous cellulose	[23–27]
1370–1365	Δ C–H and δ CH ₃	Cellulose and hemicelluloses	[23–27]
1260–1235	Elongation vibration of the acetyl bond	Lignin e hemicelluloses	[24–27, 29]
1160–1155	Asymmetric stretching C–O–C	Cellulose e hemicelluloses	[24–27, 29]
1110–1105	CH stretching vibrations	Different groups of lignin, cellulose and hemicelluloses	[23–27]
1035–1030	Skeletal vibration of the C–O–C polysaccharide ring	Cellulose and hemicelluloses	[24–28]
900–896	C–OH	β (1–4) glycosidic bond in cellulose and hemicelluloses	[24–27, 29]
835–830	Tertiary alkyl groups	Amorphous cellulose	[23–27]

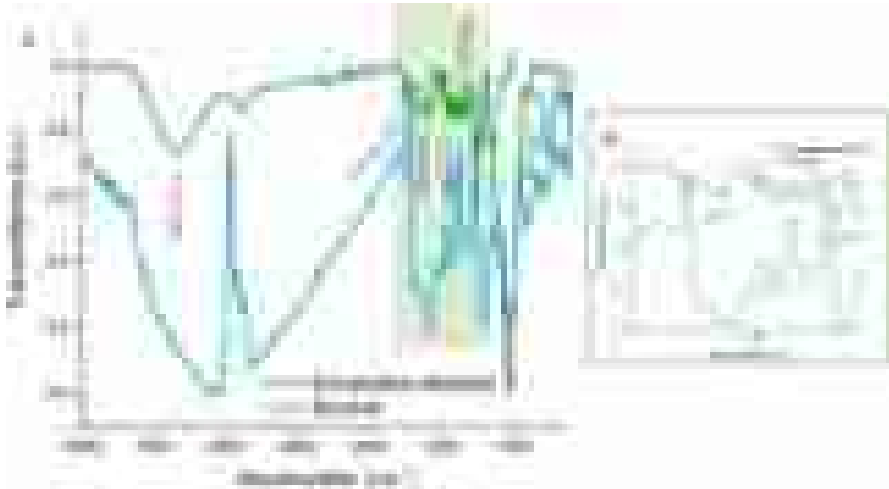


Fig. 2 **a** FTIR spectra of eucalyptus fibers before and after treatment with biochar, highlighting the main lignocellulosic peaks, **b** characteristic peaks of lignin impacted during the treatment with biochar

since most of the peaks related to cellulose and hemicellulose were not identified in the FTIR spectrum of the fiber subjected to this chemical treatment.

SEM

The micrographs that present the eucalyptus fiber sawdust and lignin biochar are presented in Fig. 3. An interesting aspect observed in the microstructure of the fiber after treatment with sulfuric acid was the appearance of pores on its surface, making it rough and porous. This porosity can be explained by the cellulosic degradation capacity of the method since, as observed through the FTIR analysis, several

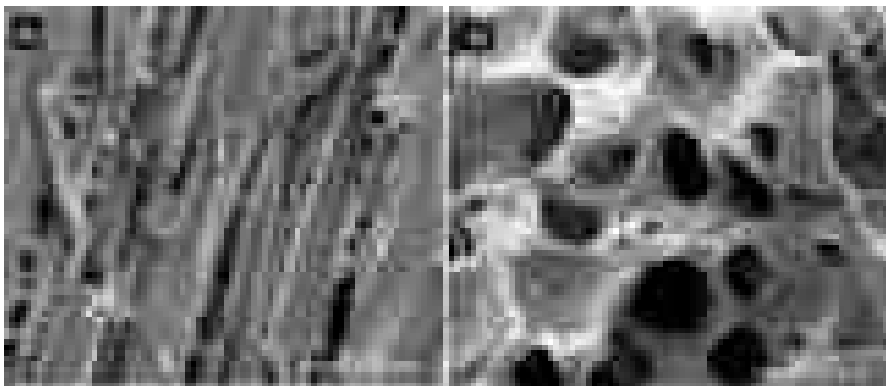


Fig. 3 Micrographs obtained by SEM: **a** eucalyptus sawdust and **b** biochar

characteristic peaks related to cellulose and hemicellulose were not detected in the post-treatment biochar, as well as some peaks related to lignin. Therefore, their respective chemical structures probably underwent important changes, resulting in the appearance of pores in the fiber surface area. There is a possibility that an activated lignin biochar was created due to this porosity [32].

Biochar is a solid carbon-rich product obtained through the pyrolysis of lignocellulosic materials from plant residues. It is black and similar to natural coal, both physically and chemically, presenting high carbon content, low nutrient content, large surface area, and good cation exchange capacity compared to in-natura biomass [33]. Literature results indicate that the morphological structure of biochar is essentially porous, due to water losses in the dehydration process and the release of volatile constituents from the carbon matrix [32–34]. The amount of pores and their size are directly linked to the origin of the biomass used in the biochar production process [32].

There is a wide range of possible applications, such as carbon sequestration from soils, absorption of contaminants and nutrients, improvement in soil fertility, among others [33]. Therefore, creating an activated biochar proved to be an interesting application of the lignin extractive process through the use of biochar.

Thermal stability

TGA of the samples allows obtaining information related to the loss of mass with the progressive increase in temperature, and from this information, it is possible to carry out a qualitative analysis of the constituents of the eucalyptus fiber. The first derivative of the TGA curve (DTG) allows for a better observation of mass decreases, as its signal causes noticeable and easily visualized changes [35].

Figure 4 shows the TGA/DTG curves for eucalyptus sawdust that underwent chemical treatment with biochar. As shown in the literature, three main ranges of thermal degradation are observed. However, unlike what was shown by Lopes (2018), these bands are much smoother, making it difficult to identify them. The first range is related to the dehydration process of the material, the second to the thermal degradation of hemicelluloses, and to a lesser extent, of lignin and the third to the degradation of lignin. According to Lopes (2018), the T_{MAX} for lignin obtained through this method is approximately 425 °C, a value very close to that obtained experimentally (432.2 °C) and which can be observed in Fig. 4.

Tejado and collaborators showed that using lignin in the production of phenol–formaldehyde (PF) resins increased the temperatures for the thermal decomposition of the samples, expanding the thermal range of application of these modified samples [36]. This result indicates that lignin needs more energy to be volatilized than cellulose and hemicellulose due to its strongly condensed aromatic structures. Therefore, T_{MAX} is higher for samples that contain large amounts of lignin, which is in agreement with what was found in the literature.

The biochar presented TGA/DTG curves different from eucalyptus sawdust. T_{MAX} underwent a large increase, which indicates the higher presence of lignin in the samples and suggests cellulose and hemicellulose degradation during treatment since lignin has a higher maximum degradation temperature, around 370–400 °C.

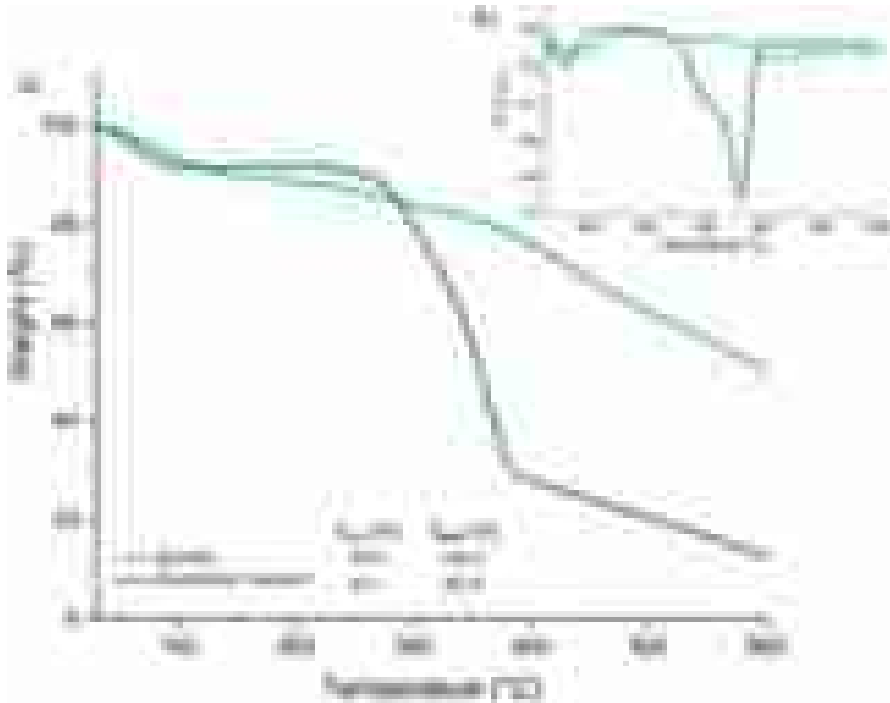


Fig. 4 **a** Thermal behavior of eucalyptus sawdust fiber samples before and after treatment with biochar, with $T_{10\%}$ and T_{MAX} values highlighted, **b** inserts are corresponding DTG curves

These results confirm the success of the work’s first stage, related to removing cellulose and hemicellulose in residual forest biomass to produce biochar based on lignin.

Cellulose hydrogels containing biochar

FTIR

FTIR analysis was performed to compare the composition of cellulose hydrogels with and without biochar (Bc) to identify vibrational modes of bonds, chemical groups, and material modifications. The spectra of all samples showed great similarity, as seen in Fig. 5. The band 3338 cm^{-1} was found for all hydrogel samples and is related to hydroxyl groups O–H characteristic of polysaccharides [37, 38]. As these bonds are commonly found in the crystalline structure of cellulose, it can be said that the appearance of this peak indicates its presence in the three-dimensional structure of hydrogels. The bands 2916 cm^{-1} , 2887 cm^{-1} , and 2848 cm^{-1} (Fig. 5b) are related to the presence of C–H bonds, which are also commonly found in polysaccharides, related to the cellulose structure.

Figure 5c shows a series of bands typically associated with cellulose present in the region between the peaks 1650 cm^{-1} and 890 cm^{-1} . The peaks 1644 cm^{-1} ,

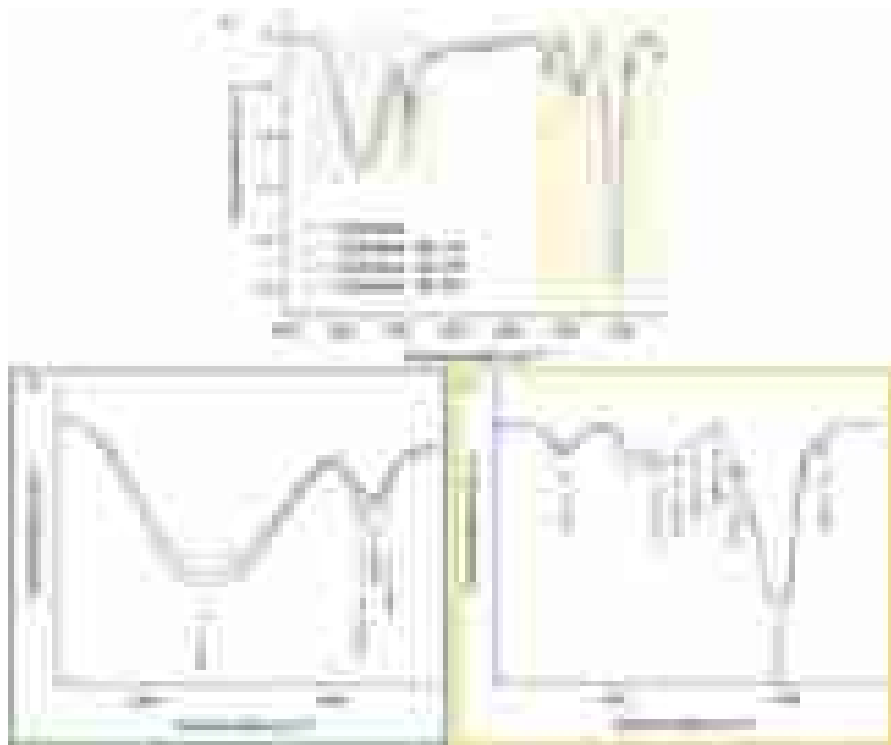


Fig. 5 a Spectra of hydrogel samples. Characteristic peaks found in the regions: b 3500–2800 cm^{-1} and c 1650–890 cm^{-1}

1370 cm^{-1} , 1315 cm^{-1} , 1265 cm^{-1} , 1200 cm^{-1} , 1154 cm^{-1} , 1020 cm^{-1} , and 896 cm^{-1} correspond to the stretching and bending vibrations of $-\text{CH}_2$ and $-\text{CH}$, $-\text{OH}$, and $\text{C}-\text{O}$ bonds of cellulose [38–40]. Therefore, the spectra of the hydrogels were similar, without significant chemical changes related to the inclusion of Bc, not compromising the hydrogel crosslinking process. Moreover, no characteristic peak from biochar was observed, possibly due to the low concentration and overlapping with peaks observed on pure cellulose hydrogel. Therefore, the inclusion of biochar in the hydrogel structure will probably impact the water absorption and interaction with target contaminants due to the functional groups present in biochar and its higher porosity [41].

SEM/EDS

The micrograph obtained for the pure sample (Fig. 6a), without adding Bc, showed a smooth surface, without particle deposition, with some wrinkles, and with the presence of some pores, not very well defined. On the other hand, the micrographs obtained for the samples with the presence of Bc (Fig. 6b–d) showed microstructures with more irregular, rough, and porous surfaces, desirable characteristics for the

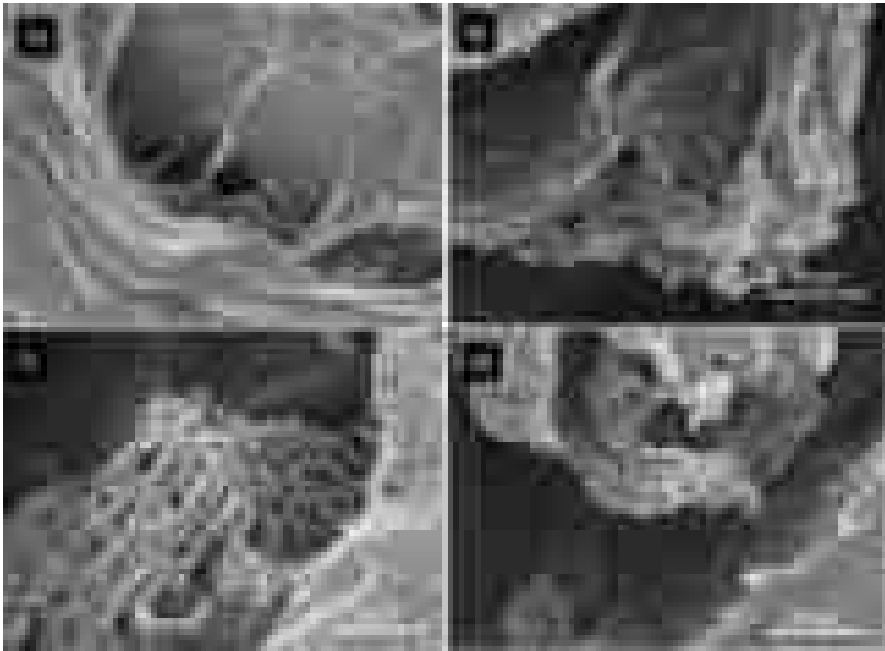


Fig. 6 Micrographs obtained by SEM of hydrogel samples: **a** cellulose, **b** cellulose-Bc—1 wt%, **c** cellulose-Bc—3 wt% and **d** cellulose-Bc—5 wt%

adsorption of heavy metals since the presence of pores and irregular regions favor the diffusion of ions to their internal regions [42]. Akl, Zaki, and ElSaeed observed similar microstructural characteristics for hydrogel composites with the addition of biochar, with favorable results for uranium adsorption by these materials [38].

For the cellulose-Bc 3% sample (Fig. 6c), the presence of pores is more evident, with many cavities. For the cellulose-Bc 1% and 5% hydrogels, on the other hand, the presence of porous regions is less evident, with the appearance of some small cavities dispersed on the surface of the material. In addition to the appearance of pores, it is possible to notice in the samples with the addition of Bc the deposition and dispersion of this material on the surface of the hydrogels since there is the presence of small particles observable in their micrographs (Fig. 8b–d). The dispersed presence of these particles may indicate a better adsorption capacity for these hydrogels since the greater presence of active sites on the material's surface is positive for the removal of metal ions [42].

The EDS spectra were obtained to identify the chemical composition on the biochar, neat hydrogel, and its hydrogel composites, before and after heavy metals sorption (Fig. 7). According to the EDS technique, all samples before sorption showed only carbon and oxygen with element percentage of 54.54 and 45.46%, 59.40 and 40.60%, and 72.02 and 27.98% for cellulose, cellulose-Bc 5%, and Biochar, respectively. Furthermore, gold was detected in the chemical composition of the samples, due to the pre-treatment that the materials are subjected to for SEM/EDS analyses. The chlorine element was not detected in the hydrogel spectrum, which indicates

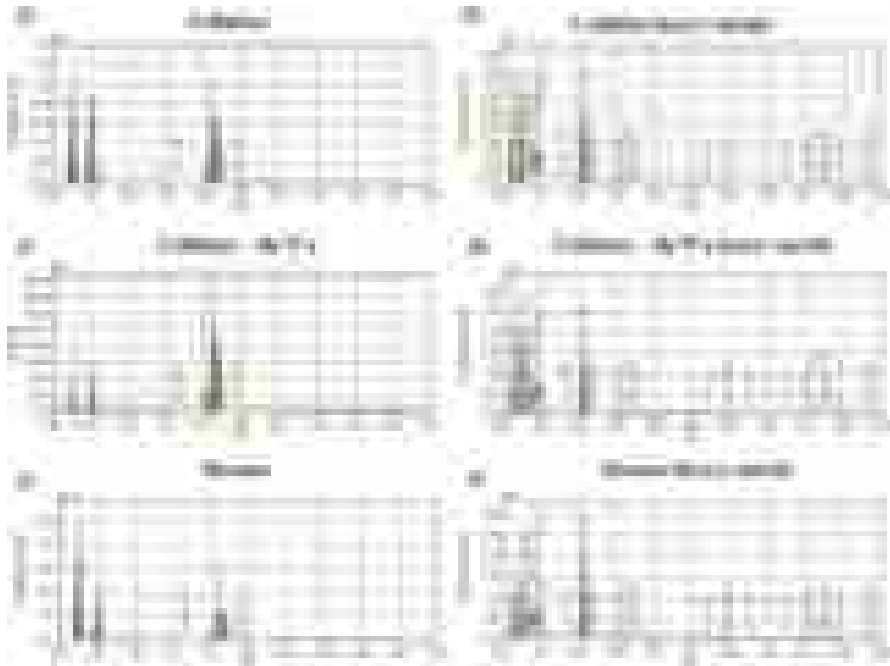


Fig. 7 EDS spectra of neat hydrogel, biochar, and its composite hydrogel before and after sorption of heavy metals at 1500 \times magnification

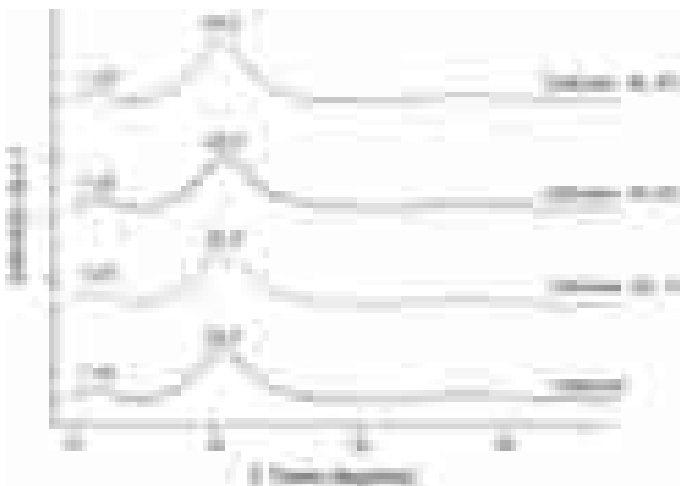


Fig. 8 Hydrogel diffractograms of cellulose hydrogel containing lignin biochar

that washing them after crosslinking with epichlorohydrin removed the reaction residues. After sorption, copper, nickel, zinc, manganese, cadmium, chromium, besides carbon and oxygen, were verified on the materials surface. This confirms that the metals were adsorbed on the surface of the materials.

XRD

Figure 8 presents the diffractograms obtained for the hydrogels. It is possible to observe very similar patterns for all samples, indicating the non-appearance of significant changes in the materials' crystalline structures after adding Bc. Two clear peaks were identified: one of greater intensity at 20.2° and one of lesser intensity at 11.6° . The peak at 20.2° is possibly related to the amorphous phase of cellulose present in the structure of hydrogels [39, 43, 44]. The peak located at 11.6° is also related to crystalline planes associated with cellulose, as indicated by literature [45]. Thus, the limited number of peaks and the presence of amorphous phases associated with cellulose and wider bands may indicate a relatively poor crystallinity of the materials [2].

Furthermore, the non-appearance and non-disappearance of peaks after Bc addition may be related to good dispersion of this material in the three-dimensional (3D) structure of the hydrogels [39], probably because the fillers were well mixed and adhered to the cellulose chains, indicating that the biochar particles were well trapped within the hydrogel network [46]. This hypothesis would also support the non-observance of Bc peaks in FTIR analysis.

BET

Figure 9 displays the nitrogen adsorption–desorption isotherms for three selected samples based on their removal efficiency: lignin biochar, pure cellulose hydrogel without dispersed phase incorporation, and cellulose hydrogel with the addition of 5 wt% biochar. According to the International Union of Pure and Applied Chemistry (IUPAC) classification, these isotherms can be categorized as Type IV, due to the presence of a hysteresis loop within the partial pressure range of 0.1–0.99. This indicates that the materials exhibit mesoporous characteristics, with pore sizes ranging from 2 to 50 nm [47]. The shape of the hysteresis loop aligns with the IUPAC H3 classification, which is associated with materials featuring slit-shaped pores. Since there is no defined capillary mechanism, the desorption curve does not fully close the loop, leaving it open at the upper end [48].

Table 2 presents the values of surface area and micro- and mesopore volumes estimated from the analysis. It can be observed that lignin biochar exhibited the highest specific surface area ($9.634 \text{ m}^2/\text{g}$), followed by pure cellulose hydrogel ($8.168 \text{ m}^2/\text{g}$) and the cellulose hydrogel with biochar addition ($6.630 \text{ m}^2/\text{g}$). The biochar showed a relatively small surface area compared to other results reported in the literature, which may be attributed to the relatively low temperature used in its synthesis process [49, 50]. However, for the specific application of removing potentially toxic metal ions, not only the specific surface area contributes to the

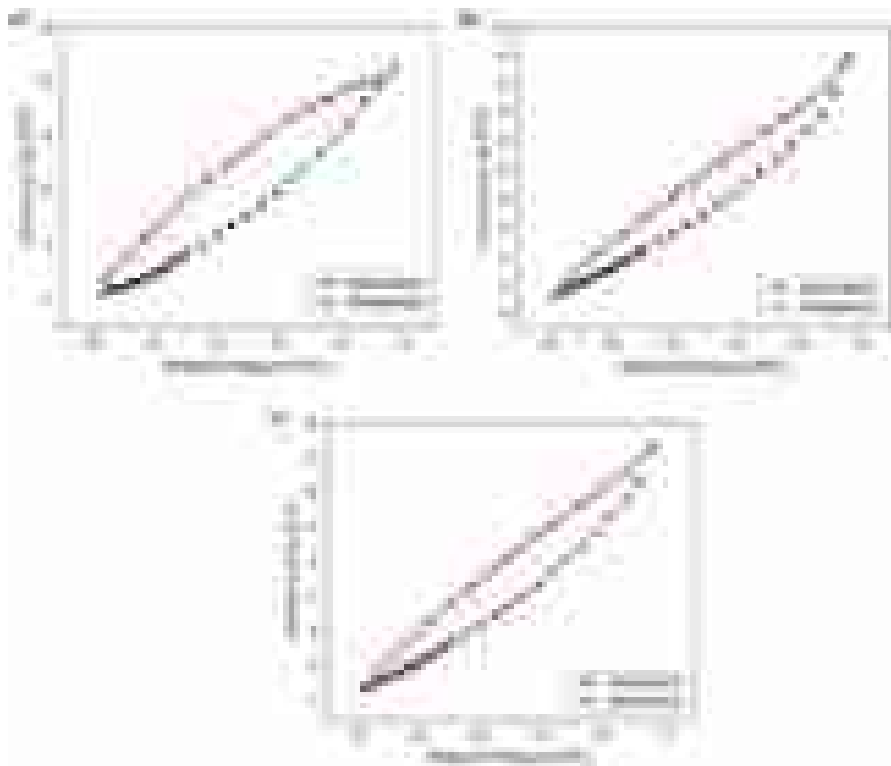


Fig. 9 Adsorption and desorption isotherms curves for the following samples: biochar (a), cellulose (b) and cellulose-Bc—5 wt% (c)

adsorption process but also other critical factors such as the availability of functional groups on the surface that can interact with the contaminants [50].

The decrease in specific surface area from the pure hydrogel to the hydrogel with biochar addition can be explained by the potential filling or blocking of the material's pores caused by the incorporation of the dispersed phase [49]. The high mesopore volume in the biochar indicates that this material is predominantly mesoporous, exhibiting a more open and porous structure compared to the pure cellulose hydrogel. In contrast, cellulose hydrogels displayed a higher volume of micropores (smaller than 2 nm), which were partially filled upon the addition of biochar.

Table 2 Specific surface area (S_{BET}), micropore volume (V_{mi}) and mesopore volume (V_{me}) of prepared samples

Samples	Isotherm type	S_{BET} (m^2/g)	V_{mi} (cm^3/g)	V_{me} (cm^3/g)
Biochar	IV	9.634	0.062	0.889
Cellulose	IV	8.168	0.099	0.700
Cellulose-Bc 5%	IV	6.630	0.065	0.587

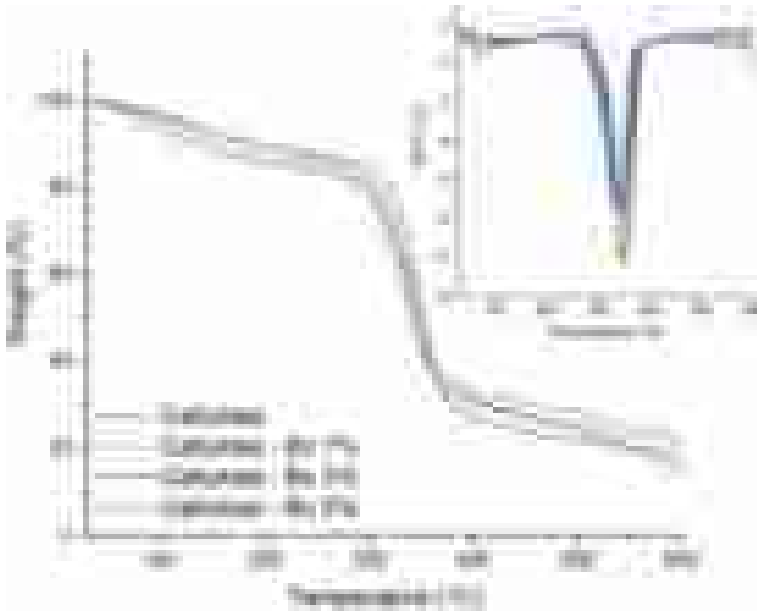


Fig. 10 Thermal behavior of hydrogel samples. The inserts are corresponding DTG curves

Thermal stability

The thermal behavior presented by the hydrogels (Fig. 10) was similar for all samples. A distinct mass loss event was observed around 100 °C, where water evaporation events due to hydrogen bond breakage are usually located [6, 51]. This event was evident for the cellulose-Bc—3% hydrogel, with a clear mass variation in this region, while for the other samples, it was almost imperceptible, with a much smaller mass variation. This observed difference endorses the hypothesis of a higher water concentration in this sample.

A considerable weight loss event could be observed for the hydrogels at T_{MAX} , where the decomposition rate is maximum, related to the total breakage of the main chain and the crosslinked matrix [6]. T_{MAX} values were similar for all samples in Table 3, found in the 334.7–349.3 °C range. This result may indicate that adding Bc did not significantly alter the thermal stability of the hydrogels, keeping T_{MAX} values close. However, it can be seen that the presence of Bc causes a gradual decrease in T_{MAX} . Therefore, for higher concentrations of Bc, the temperature required to degrade the samples is lower.

Water absorption

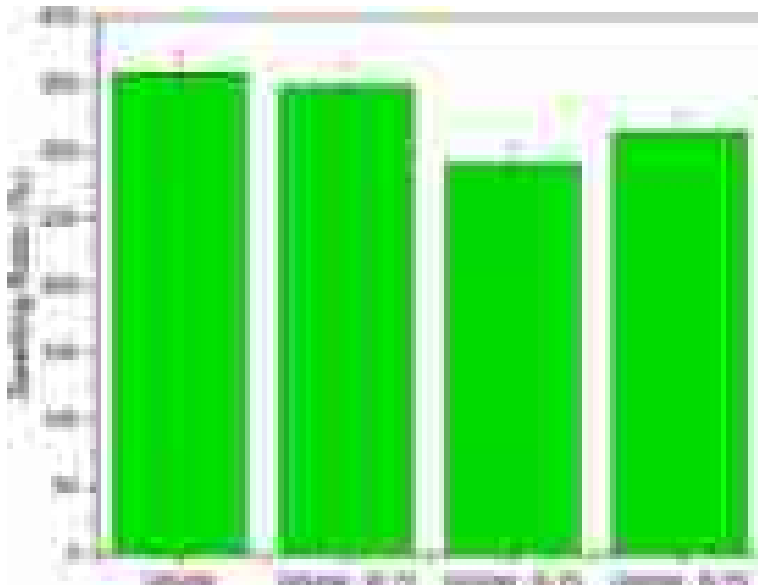
The water absorption capacity of hydrogels is one of the main characteristics of this type of material, allowing a wide range of applications in various areas of

Table 3 Temperatures after initial decrease of 10% by mass and maximum temperatures for sample degradation

Samples	$T_{10\%}$ (°C)	T_{MAX} (°C)
Cellulose	193.8	349.3
Cellulose-Bc 1%	169.9	343.6
Cellulose-Bc 3%	135.2	342.6
Cellulose-Bc 5%	196.6	334.7

engineering, such as biomedical applications, development of intelligent materials, advances in hygiene and health products, and improvements in agricultural production [2, 52]. Because they have a three-dimensional (3D) polymer structure with crosslinked hydrophilic chains, when in contact with water, instead of dissolving, the hydrogels swell and absorb the liquid, keeping it in their structure [53].

This behavior can be explained by the presence of functional groups such as $-NH_2$, $-OH$, $-COOH$, $-SO_3H$ in its structure, which when undergoing a crosslinking reaction, ensure stability and prevent dissolution [52]. Furthermore, due to the porous structure, the osmotic pressure induces water diffusion into the material, where water-binding molecules can perform polar or hydrophilic interactions with the polymer chains [52, 54]. The swelling ratio (SR) determines a material's ability to absorb a certain amount of solvent over time by analyzing the increase in its volume [53]. It is possible to observe in Fig. 11 the swelling ratio for the hydrogels produced, highlighting the pure hydrogel, with a higher absorption capacity of 357.9%. The hydrogel with the addition of 1% Bc showed a SR very close to the

**Fig. 11** Swelling ratios of the cellulose hydrogels containing different contents of lignin biochar

pure hydrogel, of 348.4%, while the other hydrogels with higher percentages of Bc, 3 wt% and 5 wt%, showed lower SR values, 290.7% and 314.2%, respectively.

Cellulose and cellulose-Bc 1% hydrogels presented a SR difference of 9.5%, while cellulose-Bc 3% and 5% hydrogels showed a difference from pure cellulose hydrogel of 67.2% and 43.7%, respectively. One hypothesis is that adding filler generally reduces the material's elasticity and increases its stiffness, resulting in lower water absorption values [55]. That is directly related to the degree of crosslinking of the hydrogel, a parameter responsible for providing information about the stability between the chains of the hydrogel's polymeric network, and consequently, the material's mechanical properties, such as hardness [56]. Salmaso et al. [57] studied the relationship between the concentration of hexamethylated cyclodextrins (CD) as a crosslinking agent and the degree of intumescence of hydrogels and found that for higher concentrations of CD, the stiffness of the material increased, and the degree of intumescence decreased.

In addition, the decreased absorption capacity may be related to the possible presence of hydrophobic groups in the structure of Bc, responsible for repelling the diffusion of water into the material. According to Mao, Zhang, and Chen, producing biochar at lower temperatures may increase the presence of aliphatic groups in the biochar's pores by increasing the material's hydrophobicity [58]. However, it should be noted that even with a decrease in the absorptive capacity of the hydrogels with the presence of Bc, the SR achieved by these materials were relevant and indicated a good absorptive capacity.

Heavy metals adsorption

The adsorption method is widely used to remove heavy metal ions from wastewater since this process has numerous advantages compared to other techniques, such as simplicity, low cost, flexibility, and operational convenience [42, 59]. The use of biochar as an adsorbent has been widely studied due to active sites favorable to the adsorption process in its structure that enable ion exchange, such as hydroxyl, carboxyl, and amino functional groups. Biochar can be obtained from different materials, such as bamboo, rice straw, and sugarcane bagasse, and its adsorption capacity varies according to the source and its active groups [60]. Sadeghi et al. [37] developed polyacrylamide-rice husk biochar composite hydrogels and evaluated their role in removing phenols from contaminated water. The results obtained indicated excellent adsorption for phenol and p-nitrophenol. Another research related to the adsorptive behavior of biochar was conducted by Li and Chen, in which the adsorption of cadmium from contaminated water by polyacrylamide-biochar composite hydrogels was studied. The results were positive, with higher cadmium concentrations retained by the hydrogels with higher concentrations of biochar [40]. The binding of heavy metal ions to the adsorbent surface may occur due to a physical (physical adsorption) or chemical (ion exchange, coordination and/or electrostatic) interaction [58].

Like biochar, hydrogels have an excellent adsorption capacity due to the presence of hydrophilic chains, which can act as complexing agents for removing metal ions, the presence of active sites and porosity in their structure [42]. Thus,

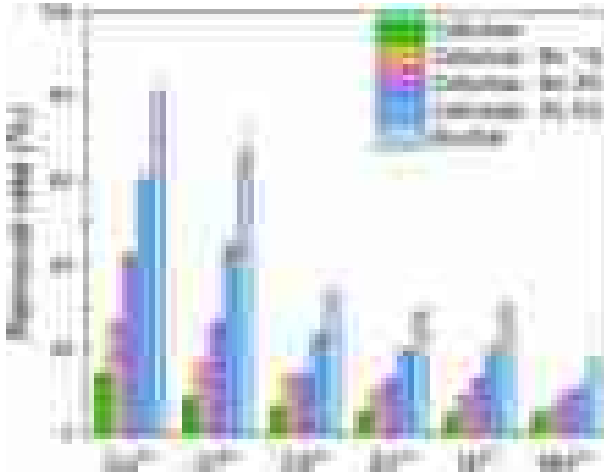


Fig. 12 Adsorption of heavy metals (Cr^{6+} , Cd^{2+} , Ni^{2+} , Mn^{2+} , Zn^{2+} , and Cu^{2+}) by biochar, neat hydrogel, and hydrogel composites ($C_0=0.052\pm 0.011$ mmol/L of each, dosage of 1.0 g/L, pH 4.0–4.5, and $T\sim 25^\circ\text{C}$)

the formulation of a composite material using hydrogel as a polymeric matrix for the dispersion of biochar appears as a potential alternative to increase the sorption capacity of metal ions since there is an increase in sorption sites on the surface of the structure [42]. To evaluate the adsorption potential of the hydrogels produced, a selectivity test was performed using solutions with the presence of heavy metals, among them chromium hexavalent, a highly toxic, mutagenic, and carcinogenic metal [61].

Cr^{6+} , Cd^{2+} , Ni^{2+} , Mn^{2+} , Zn^{2+} , and Cu^{2+} ions adsorption efficiencies by neat hydrogel, hydrogel composites, and biochar are shown in Fig. 12. It is interesting to note that proposed hydrogel composites exhibited an increase in removal efficiency for Cu^{2+} (14.25% for cellulose to 60.57% for cellulose-Bc 5 wt%) and Cr^{6+} (8.48% for cellulose to 44.99% for cellulose-Bc 5 wt%). In comparison, biochar showed removal efficiency of 80.57 and 67.31% for Cu^{2+} and Cr^{6+} , respectively, under the same operational conditions. Regarding divalent cations (Zn^{2+} , Cd^{2+} , Ni^{2+} , and Mn^{2+}) uptake, a lower removal efficiency (lower than 20%) was obtained for developed hydrogel composites, while for biochar there was a low removal percentage for Cd^{2+} (33.49%), followed by Zn^{2+} (28.99%), Ni^{2+} (27.73%), and Mn^{2+} (17.62%). This result shows that adding biochar to the cellulose hydrogel improved the removal of heavy metals, mainly Cu^{2+} and Cr^{6+} . Li and Chen [60] also showed that the addition of biochar at mass concentrations of 1, 3, and 5 wt% in the structure of polyacrylamide hydrogels increased their adsorption capacity by 23.9%, 139.5%, and 157.2%, respectively, values much higher than those achieved by the samples of cellulose hydrogels with the addition of Bc. Another important fact was the observation that for larger amounts of Bc in the hydrogels, the sorption capacity increases, indicating important participation of Bc in the adsorption process.

The high removal of Cu^{2+} and Cr^{6+} by biochar and hydrogel composites may be related to the combined mechanism of electrostatic interactions or electrostatic interactions followed by reduction [62]. In this mechanism, the oxyanions of Cr^{6+} (CrO_4^{2-} , $\text{Cr}_2\text{O}_7^{2-}$, or HCrO_4^-) are reduced to Cr^{3+} trivalent cation due to electron donor groups present in the structure of biochar and hydrogel composites [63]. This chemical species with less toxic potential, in turn, competes with the divalent cations (Cd^{2+} , Ni^{2+} , Mn^{2+} , Zn^{2+} , and Cu^{2+}) in solution for the active groups of biochar and hydrogel composites. The greater removal rate of Cu^{2+} concerning the other metal cations can be explained by the binding strength parameters (e.g., electronegativity and covalent character), favoring the coordination of the complexes formed between the functional groups of biochar-hydrogel composites and Cu^{2+} [64, 65].

Finally, to optimize this process, one of the alternatives is the chemical modification of the functional groups present in the biochar, improving the interaction capacity between its surface and the metallic ions [59]. Furthermore, in future studies, it is suggested to adjust the test conditions such as pH, temperature, metal ions concentration, and contact time, to obtain better adsorption results and to know the necessary parameters for the process viability in scale-up [39].

Conclusions

The extraction method, with an emphasis on lignin biochar production, showed promising results, allowing the obtainment of a porous and highly stable material with the potential to adsorb heavy metal ions from water. The material's surface area is relatively large ($9.634 \text{ m}^2/\text{g}$), which can provide more functional groups for interaction with metal ions. Incorporating biochar into cellulose hydrogels resulted in a material with a greater presence of pores, as observed from the BET characterization, while maintaining a water absorption capacity similar to that of pure cellulose hydrogel. The potential for removing Cu^{2+} and Cr^{6+} oxyanions was demonstrated, with higher biochar content leading to greater removal capacity. Therefore, the results highlight a new application of eucalyptus residues for developing materials that can potentially mitigate the environmental impact of toxic elements. Moreover, using biopolymers is advantageous due to their abundance, low cost, and functionalization possibilities, enabling the development of highly efficient and environmentally friendly materials.

Author contribution LRG and RRF contributed to conceptualization, data curation, formal analysis, investigation, methodology, validation, roles/writing—original draft, writing—review and editing. AGS helped in data curation, formal analysis, investigation, methodology, validation, roles/writing—original draft, writing—review and editing. RFSB and TBdAC helped in data curation, formal analysis, investigation, roles/writing—original draft. DdSR contributed to conceptualization, funding acquisition, methodology, project administration, resources, supervision, writing—review and editing.

Funding This research was funded by CNPq (#308053/2021-4 and #403934/2021-4) and LRG acknowledges CNPq for the Grant #132681/2024-2; RRF acknowledges FAPESP for Grants # 2022/01382-3 and # 2024/08105-0; RFSB thanks FAPESP for the Grant ##2021/08296-2; TBdAC acknowledges FAPESP

for Grants #2022/11133-0 and #2023/11783-8; and DSR thanks FAPESP for Grants #2020/13703-3 and #2021/14714-1.

Data availability No datasets were generated or analyzed during the current study.

Declarations

Conflict of interest The authors declare no competing interests.

References

1. Tanan W, Panichpakdee J, Saengsuwan S (2019) Novel biodegradable hydrogel based on natural polymers: synthesis, characterization, swelling/reswelling and biodegradability. *Eur Polym J* 112:678–687. <https://doi.org/10.1016/j.eurpolymj.2018.10.033>
2. Marciano JS, Ferreira RR, de Souza AG et al (2021) Biodegradable gelatin composite hydrogels filled with cellulose for chromium (VI) adsorption from contaminated water. *Int J Biol Macromol* 181:112–124. <https://doi.org/10.1016/j.ijbiomac.2021.03.117>
3. Dai Y, Sun Q, Wang W et al (2018) Utilizations of agricultural waste as adsorbent for the removal of contaminants: a review. *Chemosphere* 211:235–253. <https://doi.org/10.1016/j.chemosphere.2018.06.179>
4. Das S, Chakraborty P, Ghosh R et al (2017) Folic acid-polyaniline hybrid hydrogel for adsorption/reduction of chromium(VI) and selective adsorption of anionic dye from water. *ACS Sustain Chem Eng* 5:9325–9337. <https://doi.org/10.1021/acssuschemeng.7b02342>
5. Rossi T, Silva PMS, De Moura LF et al (2017) Waste from eucalyptus wood steaming as a natural dye source for textile fibers. *J Clean Prod* 143:303–310. <https://doi.org/10.1016/j.jclepro.2016.12.109>
6. Ferreira RR, Souza AG, Nunes LL et al (2020) Use of ball mill to prepare nanocellulose from eucalyptus biomass: challenges and process optimization by combined method. *Mater Today Commun* 22:100755. <https://doi.org/10.1016/j.mtcomm.2019.100755>
7. Uma Maheswari R, Mavukkandy MO, Adhikari U et al (2020) Synergistic effect of humic acid on alkali pretreatment of sugarcane bagasse for the recovery of lignin with phenomenal properties. *Biomass Bioenergy* 134:105486. <https://doi.org/10.1016/j.biombioe.2020.105486>
8. Suopajarvi T, Ricci P, Karvonen V et al (2020) Acidic and alkaline deep eutectic solvents in delignification and nanofibrillation of corn stalk, wheat straw, and rapeseed stem residues. *Ind Crops Prod* 145:111956. <https://doi.org/10.1016/j.indcrop.2019.111956>
9. Hanif I (2018) Impact of fossil fuels energy consumption, energy policies, and urban sprawl on carbon emissions in East Asia and the Pacific: a panel investigation. *Energ Strat Rev* 21:16–24. <https://doi.org/10.1016/j.esr.2018.04.006>
10. Camani PH, Anholon BF, Toder RR, Rosa DS (2020) Microwave-assisted pretreatment of eucalyptus waste to obtain cellulose fibers. *Cellulose* 27:3591–3609. <https://doi.org/10.1007/s10570-020-03019-7>
11. El-saied HA, El-Fawal EM (2021) Green superabsorbent nanocomposite hydrogels for high-efficiency adsorption and photo-degradation/reduction of toxic pollutants from waste water. *Polym Test* 97:107134. <https://doi.org/10.1016/j.polymertesting.2021.107134>
12. Ling H, Shen Y, Xu L et al (2022) Preparation and characterization of dual-network interpenetrating structure hydrogels with shape memory and self-healing properties. *Colloids Surf A Physicochem Eng Asp* 636:128061. <https://doi.org/10.1016/j.colsurfa.2021.128061>
13. Kun D, Pukánszky B (2017) Polymer/lignin blends: interactions, properties, applications. *Eur Polym J* 93:618–641. <https://doi.org/10.1016/j.eurpolymj.2017.04.035>
14. Di Girolamo G, Bertin L, Capecchi L et al (2014) Mild alkaline pre-treatments loosen fibre structure enhancing methane production from biomass crops and residues. *Biomass Bioenergy* 71:318–329. <https://doi.org/10.1016/j.biombioe.2014.09.025>

15. Den W, Sharma VK, Lee M et al (2018) Lignocellulosic biomass transformations via greener oxidative pretreatment processes: access to energy and value-added chemicals. *Front Chem*. <https://doi.org/10.3389/fchem.2018.00141>
16. Liu XJ, Li MF, Singh SK (2021) Manganese-modified lignin biochar as adsorbent for removal of methylene blue. *J Market Res* 12:1434–1445. <https://doi.org/10.1016/j.jmrt.2021.03.076>
17. Li Y, Wang F, Miao Y et al (2020) A lignin-biochar with high oxygen-containing groups for adsorbing lead ion prepared by simultaneous oxidation and carbonization. *Bioresour Technol*. <https://doi.org/10.1016/j.biortech.2020.123165>
18. Tang M, Snoussi Y, Bhakta AK et al (2023) Unusual, hierarchically structured composite of sugarcane pulp bagasse biochar loaded with Cu/Ni bimetallic nanoparticles for dye removal. *Environ Res*. <https://doi.org/10.1016/j.envres.2023.116232>
19. Bayoka H, Snoussi Y, Bhakta AK et al (2023) Evidencing the synergistic effects of carbonization temperature, surface composition and structural properties on the catalytic activity of biochar/bimetallic composite. *J Anal Appl Pyrolysis*. <https://doi.org/10.1016/j.jaap.2023.106069>
20. Geça M, Khalil AM, Tang M et al (2023) Surface treatment of biochar—methods, surface analysis and potential applications: a comprehensive review. *Surfaces* 6:179–213
21. Segal L, Creely JJ, Martin AE, Conrad CM (1952) Opportunity for new developments in all phases of textile manufacturing. Literature cited an empirical method for estimating the degree of crystallinity of native cellulose using the X-ray diffractometer
22. Gañán-Gómez J, Macías-García A, Díaz-Díez MA et al (2006) Preparation and characterization of activated carbons from impregnation pitch by ZnCl₂. *Appl Surf Sci* 252:5976–5979. <https://doi.org/10.1016/j.apsusc.2005.11.011>
23. Boukir A, Fellak S, Doumenq P (2019) Structural characterization of *Argania spinosa* Moroccan wooden artifacts during natural degradation progress using infrared spectroscopy (ATR-FTIR) and X-Ray diffraction (XRD). *Heliyon* 5:e02477. <https://doi.org/10.1016/j.heliyon.2019.e02477>
24. Geminiani L, Campione FP, Corti C et al (2022) Differentiating between natural and modified cellulosic fibres using ATR-FTIR spectroscopy. *Heritage* 5:4114–4139. <https://doi.org/10.3390/heritage5040213>
25. Romruen O, Karbowiak T, Tongdeesontorn W et al (2022) Extraction and characterization of cellulose from agricultural by-products of Chiang Rai Province, Thailand. *Polymers (Basel)*. <https://doi.org/10.3390/polym14091830>
26. Cao W, Xu H, Zhang X et al (2023) Novel post-treatment of ultrasound assisting with acid washing enhance lignin-based biochar for CO₂ capture: adsorption performance and mechanism. *Chem Eng J*. <https://doi.org/10.1016/j.cej.2023.144523>
27. Kostryukov SG, Matyakubov HB, Masterova YY et al (2023) Determination of lignin, cellulose, and hemicellulose in plant materials by FTIR spectroscopy. *J Anal Chem* 78:718–727. <https://doi.org/10.1134/S1061934823040093>
28. Lun LW, Gunny AAN, Kasim FH, Arbain D (2017) Fourier transform infrared spectroscopy (FTIR) analysis of paddy straw pulp treated using deep eutectic solvent. *AIP Conf Proc*. <https://doi.org/10.1063/1.4981871>
29. Ikramullah RS, Thalib S, Huzni S (2018) Hemicellulose and lignin removal on typha fiber by alkali treatment. *IOP Conf Ser Mater Sci Eng* 352:012019. <https://doi.org/10.1088/1757-899X/352/1/012019>
30. Melikoğlu AY, Bilek SE, Cesur S (2019) Optimum alkaline treatment parameters for the extraction of cellulose and production of cellulose nanocrystals from apple pomace. *Carbohydr Polym* 215:330–337. <https://doi.org/10.1016/j.carbpol.2019.03.103>
31. Lun LW, Gunny AAN, Kasim FH, Arbain D (2017) Fourier transform infrared spectroscopy (FTIR) analysis of paddy straw pulp treated using deep eutectic solvent, p 020049
32. Ma X, Zhou B, Budai A et al (2016) Study of biochar properties by scanning electron microscope—energy dispersive X-ray spectroscopy (SEM-EDX). *Commun Soil Sci Plant Anal* 47:593–601. <https://doi.org/10.1080/00103624.2016.1146742>
33. Gondim RS, Muniz CR, Lima CEP, DOS Santos CLA (2018) Explaining the water-holding capacity of biochar by scanning electron microscope images. *Revista Caatinga* 31:972–979. <https://doi.org/10.1590/1983-21252018v31n420rc>
34. Hospodarova V, Singovszka E, Stevilova N (2018) Characterization of cellulosic fibers by FTIR spectroscopy for their further implementation to building materials. *Am J Analyt Chem* 09:303–310. <https://doi.org/10.4236/ajac.2018.96023>

35. Lühr C, Pecenka R (2020) Development of a model for the fast analysis of polymer mixtures based on cellulose, hemicellulose (xylan), lignin using thermogravimetric analysis and application of the model to poplar wood. *Fuel* 277:118169. <https://doi.org/10.1016/j.fuel.2020.118169>
36. Leng L, Xiong Q, Yang L et al (2021) An overview on engineering the surface area and porosity of biochar. *Sci Total Environ* 763:144204. <https://doi.org/10.1016/j.scitotenv.2020.144204>
37. Sadeghi Afjeh M, Bageri Marandi G, Zohuriaan- Mehr MJ (2021) Hydrogel-rice husk biochar composite as an adsorbent for the removal of phenol and PNP from aqueous solutions. *Sep Sci Technol* 56:1195–1210. <https://doi.org/10.1080/01496395.2020.1775254>
38. Akl ZF, Zaki EG, ElSaeed SM (2021) Green hydrogel-biochar composite for enhanced adsorption of uranium. *ACS Omega* 6:34193–34205. <https://doi.org/10.1021/acsomega.1c01559>
39. Domingues RR, Trugilho PF, Silva CA et al (2017) Properties of biochar derived from wood and high-nutrient biomasses with the aim of agronomic and environmental benefits. *PLoS ONE* 12:e0176884. <https://doi.org/10.1371/journal.pone.0176884>
40. Vilela PB, Matias CA, Dalalibera A et al (2019) Polyacrylic acid-based and chitosan-based hydrogels for adsorption of cadmium: Equilibrium isotherm, kinetic and thermodynamic studies. *J Environ Chem Eng* 7:103327. <https://doi.org/10.1016/j.jece.2019.103327>
41. Wu Y, Brickler C, Li S, Chen G (2021) Synthesis of microwave-mediated biochar-hydrogel composites for enhanced water absorbency and nitrogen release. *Polym Test* 93:106996. <https://doi.org/10.1016/j.polymertesting.2020.106996>
42. Kabir SMF, Sikdar PP, Haque B et al (2018) Cellulose-based hydrogel materials: chemistry, properties and their prospective applications. *Prog Biomater* 7:153–174. <https://doi.org/10.1007/s40204-018-0095-0>
43. Yang Z, Peng H, Wang W, Liu T (2010) Crystallization behavior of poly(ϵ -caprolactone)/layered double hydroxide nanocomposites. *J Appl Polym Sci*. <https://doi.org/10.1002/app.31787>
44. Gong J, Li J, Xu J et al (2017) Research on cellulose nanocrystals produced from cellulose sources with various polymorphs. *RSC Adv* 7:33486–33493. <https://doi.org/10.1039/C7RA06222B>
45. Ubaid M, Murtaza G (2018) Fabrication and characterization of genipin cross-linked chitosan/gelatin hydrogel for pH-sensitive, oral delivery of metformin with an application of response surface methodology. *Int J Biol Macromol* 114:1174–1185. <https://doi.org/10.1016/j.ijbiomac.2018.04.023>
46. Sanyang ML, Ghani WAWAK, Idris A, Bin AM (2016) Hydrogel biochar composite for arsenic removal from wastewater. *Desalin Water Treat* 57:3674–3688. <https://doi.org/10.1080/19443994.2014.989412>
47. Tam NTM, Liu YG, Bashir H et al (2020) Synthesis of porous biochar containing graphitic carbon derived from lignin content of forestry biomass and its application for the removal of diclofenac sodium from aqueous solution. *Front Chem*. <https://doi.org/10.3389/fchem.2020.00274>
48. Xu L, Zhang J, Ding J et al (2020) Pore structure and fractal characteristics of different shale lithofacies in the dalong formation in the western area of the lower yangtze platform. *Minerals*. <https://doi.org/10.3390/min10010072>
49. Shaaban A, Se SM, Mitani NMM, Dimin MF (2013) Characterization of biochar derived from rubber wood sawdust through slow pyrolysis on surface porosities and functional groups. In: *Procedia engineering*. Elsevier Ltd, pp 365–371
50. Liao W, Zhang X, Ke S et al (2022) Effect of different biomass species and pyrolysis temperatures on heavy metal adsorption, stability and economy of biochar. *Ind Crops Prod*. <https://doi.org/10.1016/j.indcrop.2022.115238>
51. Ju X, Bowden M, Brown EE, Zhang X (2015) An improved X-ray diffraction method for cellulose crystallinity measurement. *Carbohydr Polym* 123:476–481. <https://doi.org/10.1016/j.carbpol.2014.12.071>
52. Holback H, Yeo Y, Park K (2011) Hydrogel swelling behavior and its biomedical applications. In: *Biomedical hydrogels*. Elsevier, pp 3–24
53. Peppas NA, Hoffman AS (2020) Hydrogels. In: *Biomaterials science*. Elsevier, pp 153–166
54. Sarmah D, Karak N (2020) Biodegradable superabsorbent hydrogel for water holding in soil and controlled-release fertilizer. *J Appl Polym Sci* 137:48495. <https://doi.org/10.1002/app.48495>
55. Dias G, Santos SBF, Leal E, Costa ACFM Efeitos do grau de reticulação com genipina em hidrogéis à base de quitosana para possível uso como biomaterial
56. Salmasso S, Semenzato A, Bersani S et al (2007) Cyclodextrin/PEG based hydrogels for multi-drug delivery. *Int J Pharm* 345:42–50. <https://doi.org/10.1016/j.ijpharm.2007.05.035>

57. Mao J, Zhang K, Chen B (2019) Linking hydrophobicity of biochar to the water repellency and water holding capacity of biochar-amended soil. *Environ Pollut* 253:779–789. <https://doi.org/10.1016/j.envpol.2019.07.051>
58. Zhang M, Yin Q, Ji X et al (2020) High and fast adsorption of Cd(II) and Pb(II) ions from aqueous solutions by a waste biomass based hydrogel. *Sci Rep* 10:3285. <https://doi.org/10.1038/s41598-020-60160-w>
59. Wang J, Wang S (2019) Preparation, modification and environmental application of biochar: a review. *J Clean Prod* 227:1002–1022. <https://doi.org/10.1016/j.jclepro.2019.04.282>
60. Li S, Chen G (2018) Using hydrogel-biochar composites for enhanced cadmium removal from aqueous media. *Mater Sci Eng Int J*. <https://doi.org/10.15406/mseij.2018.02.00073>
61. Elgarahy AM, Elwakeel KZ, Mohammad SH, Elshoubaky GA (2021) A critical review of biosorption of dyes, heavy metals and metalloids from wastewater as an efficient and green process. *Clean Eng Technol* 4:100209. <https://doi.org/10.1016/j.clet.2021.100209>
62. Xu C, Xu Y, Zhong D et al (2023) Zr⁴⁺ and glutaraldehyde cross-linked polyethyleneimine functionalized chitosan composite: Synthesis, characterization, Cr(VI) adsorption performance, mechanism and regeneration. *Int J Biol Macromol* 239:124266. <https://doi.org/10.1016/j.ijbiomac.2023.124266>
63. Bertagnolli C, Uhart A, Dupin J-C et al (2014) Biosorption of chromium by alginate extraction products from *Sargassum filipendula*: investigation of adsorption mechanisms using X-ray photoelectron spectroscopy analysis. *Bioresour Technol* 164:264–269. <https://doi.org/10.1016/j.biortech.2014.04.103>
64. Cardoso SL, Costa CSD, Nishikawa E et al (2017) Biosorption of toxic metals using the alginate extraction residue from the brown algae *Sargassum filipendula* as a natural ion-exchanger. *J Clean Prod* 165:491–499. <https://doi.org/10.1016/j.jclepro.2017.07.114>
65. Zhao P, Geng T, Zhao Y et al (2021) Removal of Cu(II) ions from aqueous solution by a magnetic multi-wall carbon nanotube adsorbent. *Chem Eng J Adv* 8:100184. <https://doi.org/10.1016/j.ceja.2021.100184>

Publisher's Note Springer Nature remains neutral with regard to jurisdictional claims in published maps and institutional affiliations.

Springer Nature or its licensor (e.g. a society or other partner) holds exclusive rights to this article under a publishing agreement with the author(s) or other rightsholder(s); author self-archiving of the accepted manuscript version of this article is solely governed by the terms of such publishing agreement and applicable law.



Innovative pectin-based composite membranes: preparation, characterization and color pollutant separation from water

Ana Maria Tischer^{1,2} · Rafaela Reis Ferreira³ · Ionara de Fátima Ferreira¹ · Derval dos Santos Rosa³ · Alexandre Tadeu Paulino⁴

Received: 7 December 2024 / Revised: 22 February 2025 / Accepted: 3 March 2025 / Published online: 22 March 2025
© The Author(s), under exclusive licence to Springer Science+Business Media, LLC, part of Springer Nature 2025

Abstract

The aim of the present study was to synthesise and characterise innovative pectin/pine sawdust/magnetite composite membranes as potential sorbents for the purification of water contaminated with color pollutants. Methylene blue (MB) was employed as the pollutant model for sorption. Fourier-transform infrared spectroscopy (FTIR) was performed to analyse the formation of crosslinked membrane chains and confirm the sorption processes of the dye molecules. Thermogravimetry (TGA) and derivative thermogravimetry (DTG) indicated that the polymer matrix is stable at low temperatures and begins to degrade at temperatures above 250 °C, whereas X-Ray diffraction (XRD) patterns confirmed crystalline and amorphous regions. Mechanical assays confirmed an increase in the modulus of elasticity and tensile strength of the biopolymer membranes after incorporating PS. Moreover, a reduction in mechanical deformation was found after the incorporation of Fe₃O₄. Pollutant separation experiments were performed in a pH range from 3.0 to 10.0 with initial pollutant concentrations of 5 to 25 mg L⁻¹ and separation times from 1 to 3050 min. Higher sorption capacity was found after 1800 min with an initial pollutant concentration of 20 mg L⁻¹ and pH 10.0. The best isotherm fit was found using the Redlich-Peterson model, with fits using the Langmuir model depending on the experimental conditions. The best kinetic fit was found using the pseudo-first-order or pseudo-second-order models at pH 3.0, with differences in more alkaline solutions. The pectin-based composite membranes proved to be viable options for the purification of wastewater from industry using dye and could also be tested for the photodegradation of organic pollutants in water due to the presence of Fe₃O₄.

Keywords Membrane · Sorption · Separation · Pollutant · Color compounds · Composite

1 Introduction

The severe shortage of drinking water is one of the most significant global challenges of the 21st century [43, 71]. According to a World Health Organization (WHO) report, more than 50% of the world's population will live in areas with certain water scarcity by the year 2025, which constitutes a growing concern [9]. Moreover, population growth translates to high water consumption, and industrial/technological sectors release toxic compounds into the environment, such as dyes, metalloids (species with intermediate properties between typical metal and non-metal), and metals, such as arsenic and antimony [19], making access to clean water more difficult. Given this scenario, there is considerable worldwide concern about water quality and a need to develop strategies to remove pollutants from wastewater [11].

✉ Alexandre Tadeu Paulino
alexandre.paulino@udesc.br

¹ Department of Food and Chemical Engineering, Santa Catarina State University, Br 282, Km 574, Linha Santa Terezinha, Pinhalzinho, SC 89870-000, Brazil

² Department of Chemistry, Materials and Chemical Engineering “Giulio Natta” (DCMC), Politecnico di Milano, Piazza Leonardo da Vinci 32, Milan 20133, Italy

³ Engineering, Modeling and Applied Social Sciences Center (CECS), Federal University of ABC, Av dos Estados, 5001, Bairro Bangu, Santo André, SP 09210-580, Brazil

⁴ Department of Chemistry, Santa Catarina State University, Rua Paulo Malschitzki, 200, Zona Industrial Norte, Joinville, SC 89219-710, Brazil

Due to operational limitations, conventional wastewater treatment methods are inefficient in removing many types of organic pollutants from aqueous solutions [69]. Thus, the scientific and industrial communities have made efforts to develop alternative wastewater treatment methods and ensure the quality of the water consumed by humans and animals. Currently, the main conventional wastewater treatment methods are coagulation, flocculation [68], ion exchange [41], flotation [44], biological processes [2], and sorption [65]. Limitations for the large-scale applications of these methods include the high cost, low efficiency, the production of secondary waste, and environmental impacts [11]. Filtration processes using natural polysaccharide-based membranes or photodegradation processes using membranes containing photocatalysts are viable options for the treatment of wastewater with less environmental impact compared to conventional methods [60, 61]. Wastewater treatment with the use of membranes offers the advantages of energy efficiency, low cost, easy maintenance, compact construction, and high separation efficiency [63]. However, synthetic polymers, such as polysulfone, polyimide, nylon, polyacrylonitrile, and polyvinylidene fluoride [31, 43], are not renewable, biodegradable materials and generate secondary pollution after real-world applications [8]. Pectin-based membranes could overcome this problem, minimizing the environmental impact due to the fact that pectin is an environmentally friendly biopolymer [4].

Pectin is a structural acidic heteropolysaccharide obtained from the methylation of polygalacturonic acid, which has high gelation and expansion capacity. This polysaccharide is obtained from citrus peel extract and is widely employed in the food industry [29]. Pectin-based membranes are also effective at sorbing dyes and metal ions due to the single -COOH bonding groups and single -OH bonding groups [36]. Membranes were prepared by electrospinning with polyvinyl acetate as a supporting polymer and starch in a green solvent (water) and used to remove methylene blue (MB) from aqueous media. Due to its high stability (based on the tensile test), the manufactured membrane could be used as a filter for the rapid separation of MB (cationic dye) and methyl orange (anionic dye) [47]. A poly(vinyl alcohol)/carboxymethyl cellulose/halloysite membrane was developed for the effective sorption of cationic dyes. This membrane demonstrated excellent removal efficiency (99.5%) for MB under ideal conditions (nanoclay 6 wt %, initial dye concentration of 10 ppm, contact time of 240 min, pH 10, and temperature of 30 °C) [64]. It is important to highlight that pectin over other bio-based polymeric materials in dye removal is highly competitive [53]. Its high sorption efficiency, ease of process, and cost-effectiveness make it an advantageous choice [46]. Furthermore, according to Tischer et al., [78] its eco-friendly nature, derived from

renewable natural sources, and its capacity for extended useful life and recyclability highlight it as a sustainable solution for environmental pollution challenges [78].

The crosslinking of biopolymer-based membrane chains is an approach employed to improve the physical properties and mechanical stability of the membrane with the aim of preventing the disintegration of the polymeric matrix in aqueous media. The crosslinking of pectin with calcium ions leads to the formation of strong membrane chains that can absorb large amounts of water without dissolving [67]. Membranes crosslinked with calcium ions are efficiently synthesized using pectin with a low degree of esterification (DE) (lower than 50%), as pectin with esterification higher than 50% does not have enough acid groups to form a gel or precipitate with calcium ions [48]. Low DE pectin can be produced by de-esterification using ammonia in an alcoholic medium. The resulting pectin has amide groups that play an important role in gel formation, contributing to the texture and tensile strength of the final biomembrane [5]. Membranes must have good stability and reusability. Regeneration capacity is an important aspect to evaluate in reusing membranes in sorption processes. Membrane reutilization in different processes can be explored through sorption-desorption recycling experiments [88].

Composite membranes prepared by incorporating sorbent inorganic or organic nanomaterials into the membrane structure are alternative solid supports for removing pollutants from water [36]. For instance, the incorporation of natural nanofiber containing a high content of lignin, cellulose, and hemicellulose favors the crosslink density, pore size, sorption capacity, and mechanical resistance of the final biomembrane [75] due to higher reactive surface area [11], whereas the incorporation of metal oxide nanoparticles, such as magnetite (Fe₃O₄), favors the application of the final biomembrane in photodegradation studies [25].

In this study, we developed novel pectin-based composite membranes containing pine sawdust (PS) and Fe₃O₄, offering an innovative approach for removing pollutants from the wastewater of industries that employ dyes. PS was chosen because it is an abundant, low-cost, biodegradable byproduct with a large surface area, which enhances the chemical sorption capacity [20]. Fe₃O₄ was chosen because it imparts magnetic properties to the composite biomaterial, facilitating membrane recovery and reuse, in addition to aiding in pollutant removal via sorption [3]. To date, no author has carried out a study with this specific dye system, further emphasizing our research's uniqueness and originality. The MB pollutant model was used to evaluate the effectiveness of the membranes. We evaluated membranes' physicochemical, thermal, and mechanical properties with different PS/Fe₃O₄ contents. Furthermore, we consider the possibility of applying these membranes in the photodegradation

of pollutants in water due to the presence of Fe_3O_4 in their polymeric structure. The results indicate that composite membranes have the potential to be effective biomaterials for the purification of industrial wastewater contaminated with dyes. This promising approach opens new perspectives for developing sustainable and efficient solutions for the remediation of industrial effluents.

2 Experimental

2.1 Material

Citrus pectin (DE ranging from 70 to 85%) was purchased from Biotec[®], Brazil. PS was obtained from wood pallets used to transport industrial packaging. The preparation of PS (particle sizes around 850 μm) was performed following a method described elsewhere [36]. Fe_3O_4 with an average particle size of 50 nm were purchased from Fisher Scientific[®], USA. Calcium chloride dihydrate and ammonium hydroxide were purchased from Dinâmica[®], Brazil. Ethyl alcohol 99.5% (v/v) was purchased from inética[®], Brazil. MB ($\text{C}_{16}\text{H}_{18}\text{N}_3\text{SC}_{1.3}\text{H}_2\text{O}$) was purchased from LabSynth[®], Brazil. Glycerol and other chemical reagents were purchased from Sigma-Aldrich, Brazil.

2.2 De-esterification of pectin

2.0 g of raw pectin was dispersed in 100 mL of 65% (v/v) ethanol containing 2.3 g of ammonium hydroxide. The mixture was placed in a closed flask and left under magnetic stirring (IKA[®] C-Mag) at 900 rpm for 180 min at 25 °C. The solid/liquid mixture was then filtered with a filter paper (Whatman[®]) and the remaining solid residue was washed with 65% (v/v) ethanol to remove free ammonia. This solid was washed again with 99.5% (v/v) ethanol and dried in a vacuum desiccator (Sigma-Aldrich[®] Z740644) for 24 h at room temperature. The dried pectin was then ground using a knife mill (IKA[®] A11) prior to characterization and use.

2.3 Determination of degree of esterification

Potentiometric titration determined the DE of commercial pectin and de-esterified pectin. For such, 2.0 g of pectin was dispersed in 20 mL of distilled water. This solution was left under mechanical stirring at 900 rpm for 2 h. The pectin solution was then titrated with an aqueous solution of sodium hydroxide (NaOH) 0.1 mol L^{-1} in the presence of phenolphthalein as the acid-base indicator, and the results were recorded as initial titration (T_i). To saponify the esterified carboxyl groups of the polymer, 10 mL of an aqueous solution of NaOH 0.1 mol L^{-1} was added to the neutralized

pectin under constant stirring at 900 rpm for 2 h. Following saponification, 10 mL of an aqueous solution of hydrochloric acid (HCl) 0.1 mol L^{-1} was added, and the excess was titrated with an aqueous solution of NaOH 0.1 mol L^{-1} . The NaOH volume spent in this titration (T_f) and the number of esterified carboxyl groups was determined using Eq. (1):

$$\text{DE} (\%) = \frac{T_f}{T_i + T_f} \times 100 \quad (1)$$

in which DE is the degree of esterification, T_i is the NaOH volume used in the initial titration, and T_f is the NaOH volume spent in the final titration.

2.4 Membrane preparation

Esterified pectin-based membranes were synthesized, as shown in Fig. 1, following a method described elsewhere [90] with adaptation for pectin. Briefly, 6 g of esterified pectin was dissolved in 400 mL of distilled water. Next, 3.6 g of glycerol and known proportions of PS (1, 3, 5, or 10% w/w) were added. This mixture was heated to 70 °C. Pre-crosslinking was performed by adding 30 mL of a 1.0% CaCl_2 (w/v) solution under constant stirring at a flowrate of 1 mL min^{-1} manually controlled using a micropipette. Pre-crosslinking was conducted for 90 min. Known contents of Fe_3O_4 (1, 5, 10, or 15% w/w) were then added to the still-hot pre-crosslinked solution under constant magnetic stirring, and the mixture was transferred to Petri dishes. These systems were placed in a forced-air circulation oven (Famem[®] Orion 515) at 40 °C for 20 h. The formed membranes were immersed in 50 mL of 70% (v/v) ethanol solution containing 5% CaCl_2 (w/v) for 30 min for complete crosslinking, washed with distilled water, and dried in a forced-air circulation oven at 25 °C for 5 h. All membranes were stored in a vacuum desiccator for 72 h at 25 °C and low relative humidity. Different membrane compositions (Table 1) were studied to achieve satisfactory mechanical resistance for application in water and wastewater treatment.

2.5 Characterization of membranes

2.5.1 Fourier-transform infrared spectroscopy (FTIR)

FTIR spectra were recorded using a PerkinElmer Frontier spectrometer (Spectrum 100, Perkin Elmer[®], Inc. Massachusetts, USA) with attenuated total reflectance (ATR) operating in the wavenumber range from 500 to 4000 cm^{-1} with 32 scans per minute and resolution of 4 cm^{-1} .

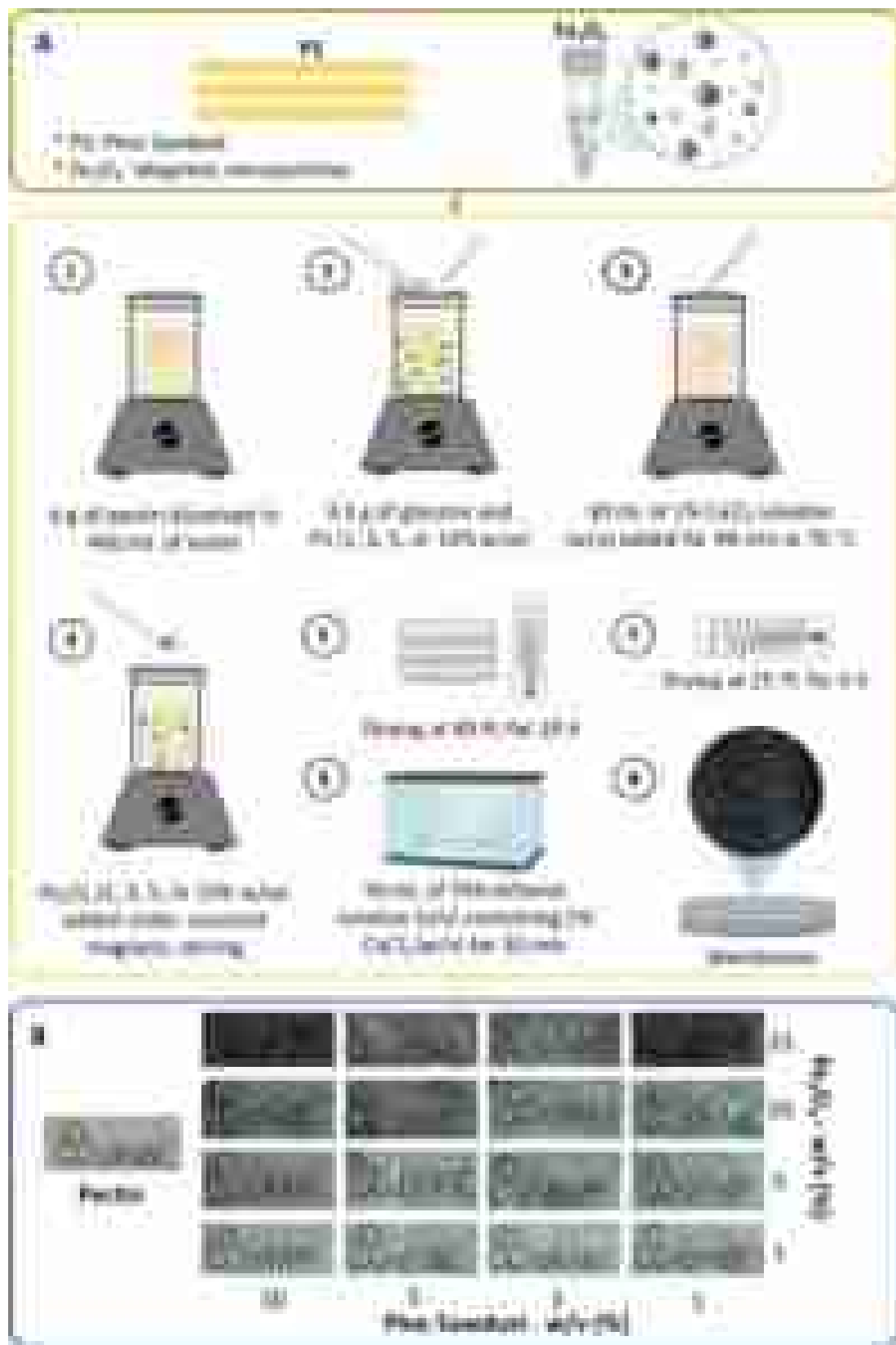


Fig. 1 Illustrative scheme of synthesis method for pectin-based composite membranes

Table 1 PS and Fe₃O₄ contents in different pectin-based membranes

Samples	PS (%)	Fe ₃ O ₄ (%)
ME0	0	0
ME1	1	1
ME2	1	5
ME3	1	10
ME4	1	15
ME5	3	1
ME6	3	5
ME7	3	10
ME8	3	15
ME9	5	1
ME10	5	5
ME11	5	10
ME12	5	15
ME13	10	1
ME14	10	5
ME15	10	10
ME16	10	15

2.5.2 Thermogravimetric analysis (TGA)

Thermal stability was tested using the PerkinElmer STA 6000 equipment. All samples were placed in alumina pans and heated from 30 to 600 °C at a rate of 10 °C min⁻¹ in a nitrogen atmosphere (20 mL min⁻¹).

2.5.3 Mechanical assays

Tensile strength tests were performed using the Norwood Instron 3367 (Instron Corporation, Norwood, MA) equipment at room temperature following the ASTM D638-14 standard. For such, a 50-N load cell, test speed of 25 mm min⁻¹, and film thickness of 0.15 ± 0.05 mm were employed.

2.5.4 X-ray diffraction (XRD)

XRD measurements were performed using a D8 Focus diffractometer (Bruker AXS Advanced X-ray Solutions GmbH, Karlsruhe, Germany), operating at 40 kV and 40 mA. Monochromatic CuKα1 radiation (λ = 1.54056 Å) at a step width of 0.01° and a counting time of 100 s at each 0.5°, from 2θ = 10–70°, were employed.

2.5.5 Degree of swelling (DS)

The DS was determined by immersing 150 mg of dried membrane pieces in 100 mL of distilled or drinking water at room temperature. The DS (g of water per g of the dried membrane [g g⁻¹]) was calculated using Eq. (2):

$$DS = \frac{m_s - m_d}{m_d} \quad (2)$$

in which m_s and m_d are the masses of the swollen and dried membranes.

2.6 Separation assays

MB separation experiments were performed by immersing 150 mg of dried membrane pieces in flasks containing 50 mL of dye solution with different initial concentrations (5, 10, 15, 20, and 25 mg L⁻¹) and different pH values (3.0, 4.0, 6.0, 8.0, and 10.0). Similar experiments were performed with pure Fe₃O₄ employed in the membrane synthesis, to evaluate the effects of magnetic material on the pollutant sorption. The remaining dye concentration in the solutions at specific time intervals was determined by UV-vis spectrophotometry (Spectroquant® Prove 600, Merck) at a wavelength of 664 nm. The dye sorption capacity (q_e , mg g⁻¹) of the membranes was calculated using Eq. (3):

$$q_e = \frac{C_0 - C_e}{m} \times V \quad (3)$$

in which m (g) is the mass of the dried membrane, C_0 and C_e (mg L⁻¹) are the initial and equilibrium concentrations of dye in the solution, and V (L) is the volume of the solution.

2.7 Sorption kinetics

MB sorption kinetics were studied using a dye concentration of 20 mg L⁻¹ and a membrane mass of 150 mg. The pseudo-first-order kinetic model was employed to determine whether the diffusion mechanism is dependent on dye concentration, whereas the pseudo-second-order kinetic model was employed to determine the occurrence of dependence between the amount of dye sorbed on the membrane surface and the amount of dye at equilibrium [87]. These models were selected due to their widespread acceptance and ability to provide insights into sorption mechanisms [30, 39]. The parameters of the non-linear pseudo-first and pseudo-second-order kinetic models were determined by Eqs. (4) and (5), respectively:

$$q_t = q_e(1 - e^{-k_1 t}) \quad (4)$$

$$q_t = \frac{q_e^2 k_2 t}{1 + q_e k_2 t} \quad (5)$$

in which, q_e (mg g⁻¹) is the sorption capacity of the membrane at equilibrium, q_t (mg g⁻¹) is the sorption capacity of the membrane at time t (min), k_1 and k_2 are the rate constants (g mg⁻¹ min⁻¹).

2.8 Sorption isotherms

The non-linear Langmuir, Freundlich, Sips, and Redlich-Peterson isotherm models were employed to predict the types of interactions between the membrane and dye. According to the Langmuir model [38, 85], the sorption mechanism occurs through the formation of a monolayer and ideal sorbate distribution on the sorbent surface. In this case, active sorption sites have equivalent energies on the sorbent surfaces. The non-linear Langmuir isotherm model is represented by Eq. (6):

$$q_e = \frac{q_m K_L C_e}{1 + K_L C_e} \quad (6)$$

in which, K_L ($L \text{ mg}^{-1}$) is the sorption/desorption rate, C_e (mg L^{-1}) is the equilibrium sorbate concentration, q_m (mg g^{-1}) is the maximum sorption capacity of the sorbent, and q_e (mg g^{-1}) is the equilibrium sorption capacity of the sorbent.

The non-linear Freundlich isotherm model [21, 85] is employed for describing sorption processes with multilayer formation and the non-uniform distribution of sorbates on sorbent surfaces. In this case, the sorption sites in the sorbent structures have different affinities. The non-linear Freundlich isotherm model is represented by Eq. (7):

$$q_e = K_F C_e^{1/n} \quad (7)$$

in which, K_F ($L^{1/n} \text{ mg}^{1-1/n} \text{ g}^{-1}$) is the Freundlich sorption constant, n is the number of active sites in/on sorbent structures, C_e (mg L^{-1}) is the equilibrium sorbate concentration, and q_e (mg g^{-1}) is the equilibrium sorption capacity.

The non-linear Sips isotherm model [74] is employed to overcome the limitations of the Langmuir and Freundlich isotherm models. This isotherm model is represented by Eq. (8):

$$q_e = \frac{q_{ms} K_s C_e^{n_s}}{1 + K_s C_e^{n_s}} \quad (8)$$

in which, q_{ms} (mg g^{-1}) is the maximum sorption capacity of the sorbate, K_s ($L^{n_s} \text{ mg}^{-n_s}$), n_s is Sips constant, and q_e (mg g^{-1}) is the equilibrium sorption capacity of the sorbent.

The non-linear Redlich-Peterson isotherm model [66] assumes that monolayer formation on sorbent surfaces and multisite interactions take place simultaneously during the sorption process. Thus, this model exhibits properties of the Langmuir and Freundlich models. The non-linear Redlich-Peterson isotherm model is represented by Eq. (9):

$$q_e = \frac{A C_e}{1 + B C_e^g} \quad (9)$$

in which, A ($L \text{ mg}^{-1}$) and B ($L \text{ mg}^{-1}$)^g are Redlich-Peterson constants, g is the Redlich-Peterson exponent, C_e (mg L^{-1}) is the equilibrium sorbate concentration, and q_e (mg g^{-1}) is the sorption capacity of the sorbent.

2.9 Error analysis

The reliability of the dye sorption results in the membrane structures were evaluated using the chi-square statistical test (χ^2), and coefficient of determination (R^2) [56, 57]. The best isotherm and kinetic fits were estimated by considering the lowest χ^2 value and highest R^2 value. The two error functions are represented by Eqs. (10) and (11), respectively:

$$\chi^2 = \sum_{i=1}^n \frac{(q_{e,\text{exp}} - q_{e,p})^2}{q_{e,p}} \quad (10)$$

$$R^2 = 1 - \frac{\sum (q_{e,\text{exp}} - q_{e,p})^2}{\sum (q_{e,\text{exp}} - q_{e,m})^2} \quad (11)$$

in which, $q_{e,\text{exp}}$ (mg g^{-1}) is the experimental equilibrium sorption capacity and $q_{e,p}$ (mg g^{-1}) is the equilibrium sorption capacity predicted from the model equations. $q_{e,m}$ is the average of $q_{e,\text{exp}}$.

3 Results and discussion

3.1 Membrane characterization

3.1.1 DE

The DE of the commercial pectin obtained by titration was 82.73%, confirming that this polysaccharide has high esterification ($DE > 50\%$). Hence, it does not have enough acid groups for crosslinking with calcium ions and solubilizes in water, hindering membrane/gel formation [48]. The yield of the de-esterification reaction was 66% with a DE of 46.33%, indicating a low DE polysaccharide. The de-esterified pectin was efficiently crosslinked in the presence of calcium ions during membrane synthesis, decreasing its solubility in water. This increased the mechanical and thermal resistance of the membranes, as observed in the mechanical and thermal assays.

3.1.2 FTIR

FTIR spectra recorded before (Fe_3O_4) and after ($\text{Fe}_3\text{O}_4 + \text{MB}$) sorption studies of MB in Fe_3O_4 can be seen in Fig. 2. Overall, Fe_3O_4 characteristic bands tend to appear at ~ 3000 , 1625, 1500, 1366, 1190, and 627 cm^{-1} , which are

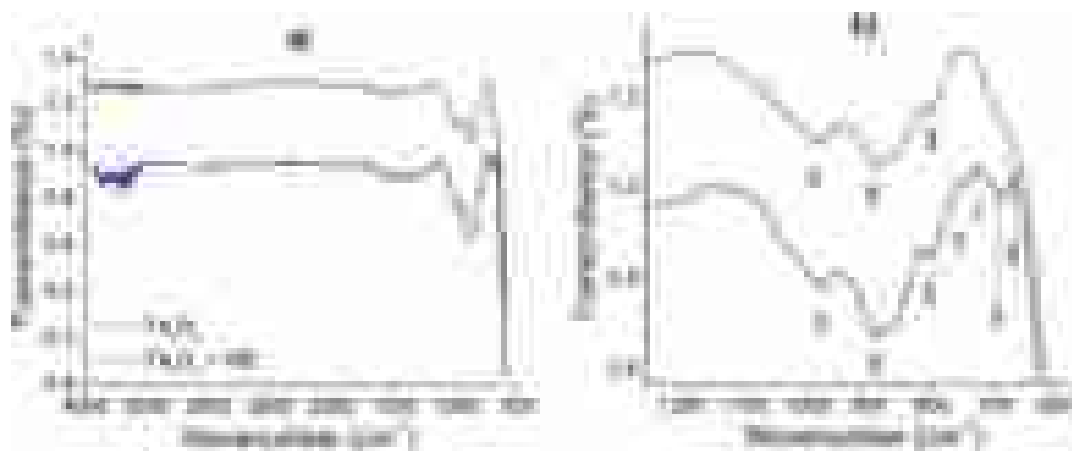


Fig. 2 FTIR spectra recorded before (Fe_3O_4) and after ($\text{Fe}_3\text{O}_4 + \text{MB}$) sorption studies of MB in pure Fe_3O_4

related to O–H or N–H, C=O, C=C, C–N, C–O or C–N and Fe–O groups, respectively [22]. By observing all experimental results at wavelengths between 600 and 1200 cm^{-1} (Fig. 2b), it is possible to identify small band shifts after sorption studies of MB, with the appearance of signals at ~ 784 , 721, 693, and 668 cm^{-1} . Moreover, pure Fe_3O_4 peaks shifted from 984.4 to 973.4, indicating intermolecular interaction between MB and Fe_3O_4 during sorption. This interaction was confirmed by the sorption capacity discussed throughout this manuscript.

Absorption bands found at ~ 3200 and 2950 cm^{-1} in Fig. 3 were associated with OH and C–H group stretching vibrations in the membrane structure [62]. The absorption band at 1730 cm^{-1} corresponded to carbonyl group stretching (C=O) from methyl ester and COOH contained in the pectin molecules [15]. The absorption band at 1149 cm^{-1} was assigned to COC vibrations from glycosidic rings, which are commonly found in polysaccharide macromolecular structures. The absorption bands at 1045 and 1076 cm^{-1} were assigned to the presence of arabinose, xylose, and galactose in the pectin-based polymer chains [12]. As pectin is a natural polysaccharide found in the walls of plant cells, it has homogalacturonan (HG), xylogalacturonan, rhamnogalacturonan type I (RGI), and rhamnogalacturonan type II (RGII) units [86]. This explains the strong absorption bands at 1022, 1106, and 1149 cm^{-1} due to CC, CO, CCH, and OCH group vibrations [13]. The absorption bands at 830 and 763 cm^{-1} suggest efficient crosslinking between pectin and calcium [15].

Slight shifts were observed in the FTIR spectra after adding PS and Fe_3O_4 to the pectin-based membrane structure due probably to disturbances taking place during the formation of new chemical bonds. An absorption band that appeared at 542 cm^{-1} was assigned to stretching vibrations due to presence of tetrahedral and octahedral Fe–O covalent bonds from Fe_3O_4 [1]. Moreover, PS increased the free

hydroxyl peak intensities between 3200 and 2950 cm^{-1} due to presence of water bound to either OH groups of the pectin or Fe_3O_4 molecules [1]. This behavior was also observed in the absorption band at ~ 1640 cm^{-1} . The slight influence of PS and Fe_3O_4 incorporated into the membrane chains was confirmed by recording non-bulky curves at wavenumbers ranging from 1700 to 1550 cm^{-1} , as shown in Figs. 1, 2, 3 and 4, S 5 (Supplementary Material). Overall, incorporating PS and Fe_3O_4 in the pectin-based polymer matrices altered the OH vibration intensities, resulting in modifications on the surfaces of lignocellulosic species. This, in turn, alters membrane hydrophobicity, pollutant sorption capacity, and electrical conductivity [40].

3.1.3 TGA and derivative thermogravimetry (DTG)

Thermal degradation of the membrane occurred in two main stages of mass loss (Fig. 4) – one from 30 to 100 $^{\circ}\text{C}$ due to the evaporation of physically adsorbed water [40] and the second from 250 to 300 $^{\circ}\text{C}$ due to the degradation of pectin macromolecules [17]. The pectin-based membrane thermogram (ME0) revealed that thermal degradation of 10% of the membrane chain ($T_{10\%}$, also the onset temperature) occurred at 97.2 $^{\circ}\text{C}$. The onset temperature after the addition of PS [1, 3, 5, and 10% (w/w)] and Fe_3O_4 [1, 5, 10, and 15% (w/w)] increased ~ 10 $^{\circ}\text{C}$ compared to the thermogram of the pectin-based membrane, indicating an increase in thermal stability after the anchoring of organic and inorganic species in the polymeric matrix. Similar results have previously been found for pectin-based hydrogels containing PS [15] and Fe_3O_4 [36]. A gain of ~ 20 $^{\circ}\text{C}$ was determined for T_{max} in the composite membranes, confirming the increase in thermal stability (Table 2). This new thermal pattern suggests that PS and Fe_3O_4 participate in crosslinking during membrane formation. The composite membrane's thermal

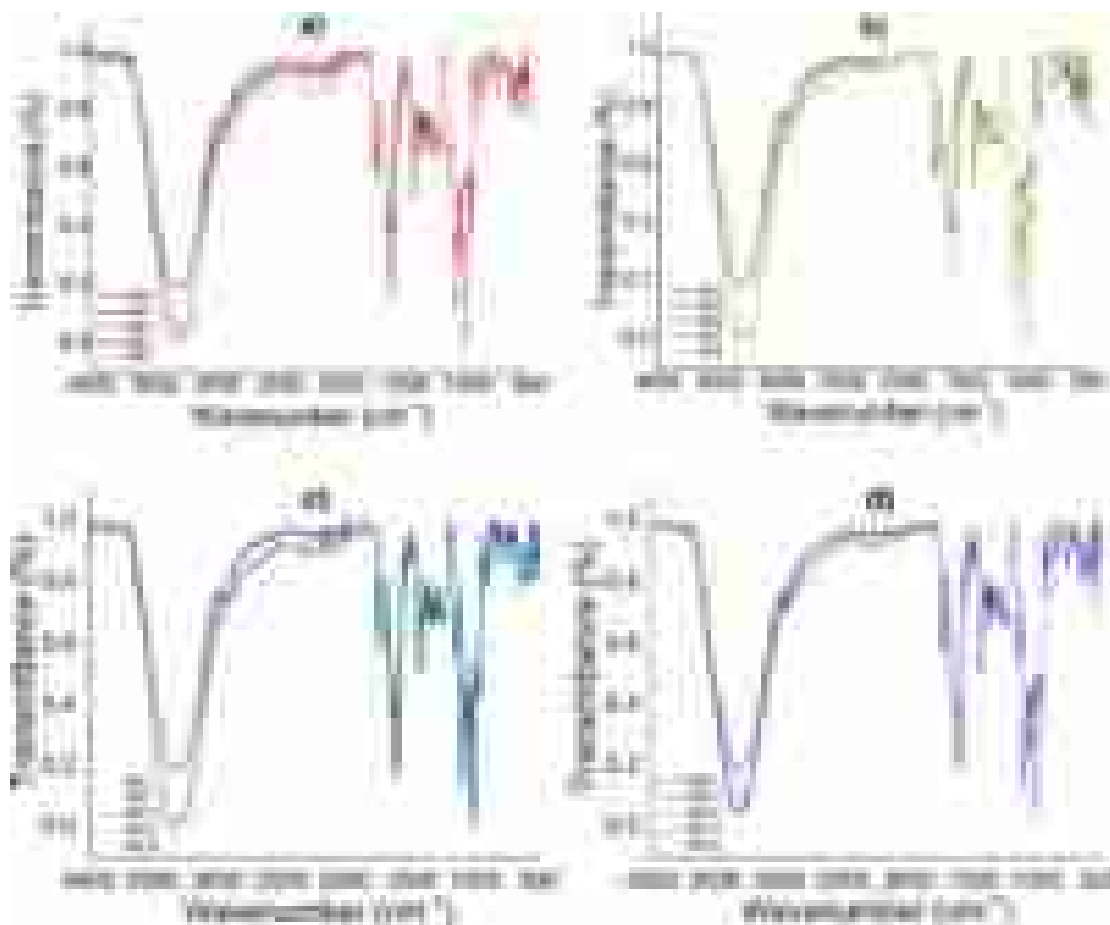


Fig. 3 **a** FTIR spectra for pectin-based membrane (ME0) and composite membranes containing 1% PS plus 1 (ME1), 5 (ME2), 10 (ME3), and 15% (w/w) (ME4) Fe_3O_4 . **b** FTIR spectra for composite membranes containing 3% PS plus 1 (ME5), 5 (ME6), 10 (ME7), and 15% (w/w) (ME8) Fe_3O_4 . **c** FTIR spectra for composite membranes con-

taining 5% PS plus 1 (ME9), 5 (ME10), 10 (ME11), and 15% (w/w) (ME12) Fe_3O_4 . **d** FTIR spectra for composite membranes containing 10% PS plus 1 (ME13), 5 (ME14), 10 (ME15), and 15% (w/w) (ME16) Fe_3O_4

properties are excellent for water and wastewater treatment applications.

3.1.4 Mechanical assays

The ME5 and ME9 membranes had tensile strengths of 126.7 and 337.2 MPa, whereas maximum deformations were 87.8 and 92.4%, respectively (Table 2; Fig. 5). Gains in the elasticity modulus were also found in these membranes, indicating that PS occupies empty spaces between pectin and Fe_3O_4 in the membrane structure, improving the filler dispersion capacity. The gains in E and σ_{\max} (Table 2) suggest possible physiochemical interactions among hydroxyl groups of the pectin macromolecules and active sites of the PS fibers. The formation of a percolated polymer chain is responsible for increasing the rigidity of the membrane [11, 15]. Higher Fe_3O_4 contents decreased the mechanical deformation of the polysaccharide membranes due possibly to nanoparticle aggregation, altering physiochemical

interaction intensity, particle size, particle distribution, and particle dispersion in the polymer chain. An improper membrane preparation method favors nanoparticle agglomeration, contributing to the rupture of the material structure [26]. Thus, inorganic nanoparticle dispersion in polymer networks is particularly important in improving mechanical resistance. This property is essential for applying polymer membranes in water filtration processes, mainly when the aim is to reuse the polymer material in successive filtration cycles with high water flow [11].

3.1.5 XRD

The crystallinity of Fe_3O_4 after sorption of MB ($\text{Fe}_3\text{O}_4 + \text{MB}$), and membranes was evaluated by X-ray diffractograms as shown in Fig. 6. All the crystalline planes [(220), (311), (400), (422), (511), (440)] in the 2θ values equal to 30.3, 35.6, 43.5, 53.5, 57.4, and 63.07° were assigned to the structure of Fe_3O_4 [79]. Even after the sorption of MB, all six

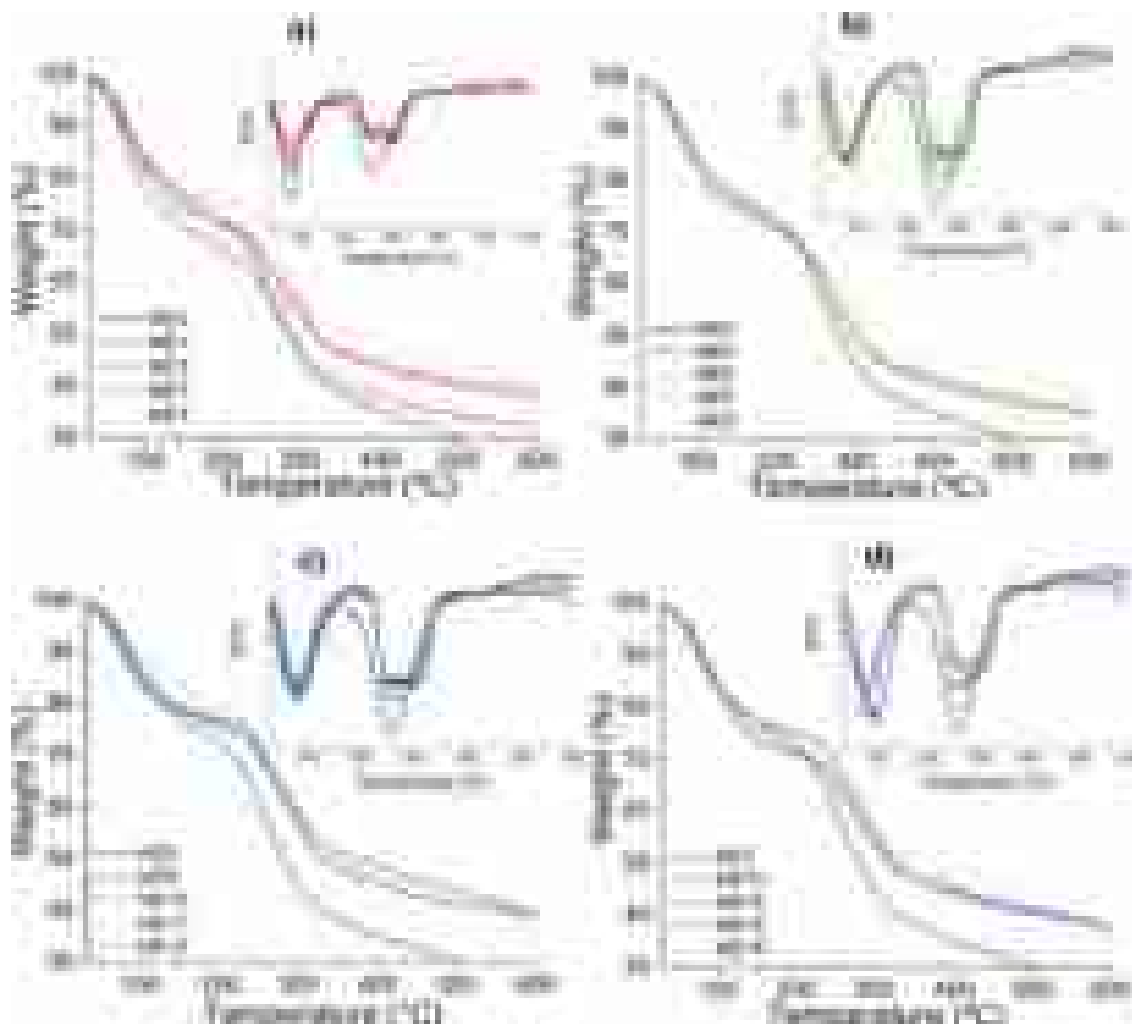


Fig. 4 **a** TGA and DTG curves for pectin-based membrane (ME0) and composite membranes containing 1% PS plus 1 (ME1), 5 (ME2), 10 (ME3), and 15% (w/w) (ME4) Fe_3O_4 . **b** Composite membranes containing 3% PS plus 1 (ME5), 5 (ME6), 10 (ME7), and 15% (w/w)

(ME8) Fe_3O_4 . **c** Composite membranes containing 5% PS plus 1 (ME9), 5 (ME10), 10 (ME11), and 15% (w/w) (ME12) Fe_3O_4 . **d** Composite membranes containing 10% PS plus 1 (ME13), 5 (ME14), 10 (ME15), and 15% (w/w) (ME16) Fe_3O_4

X-ray patterns did not change. Specific X-ray patterns were observed in the composite membrane after incorporating Fe_3O_4 and PS. In this case, the amorphous regions decreased compared to the membrane without Fe_3O_4 and PS. The final composite material can assess a synergy among magnetite, PS and polysaccharide chains.

3.2 Separation studies

3.2.1 Degree of swelling

Figure 7 shows the degree of swelling of the pectin-based composite membrane containing 3% (w/w) PS and 1% (w/w) Fe_3O_4 in distilled water and drinking water at room temperature. Swelling equilibrium occurred after 100 min in both aqueous media, determining a low degree of swelling. This indicates weak intermolecular interactions among

chemical groups and nonsignificant macromolecular relaxation of the polymeric structure of the membrane [16]. The degree of swelling of the composite membrane was 2.24 and 1.93 g of water per g of dried membrane in distilled water and drinking water, respectively. These values decreased significantly with composite membranes containing higher PS, different Fe_3O_4 contents, and specific pH values of the aqueous media (data not shown). This is due to the increase in the crosslinking density of the polymer chains and the presence of charged chemical species in aqueous media [27, 28]. The absence of salts in distilled water contributed to higher water absorption capacity, as Na^+ , Mg^{2+} , Ca^{2+} , H^+ , Na^+ , and K^+ ions interact with anionic groups of the membrane structure, decreasing electrostatic repulsion forces among adjacent ionic carboxylic groups [91]. A higher concentration of cations in an aqueous solution leads to a lower degree of swelling of the polymer membrane, as the amount

Table 2 Thermal and mechanical assay results for pectin-based membranes

Samples	Tensile strength (σ) (MPa)	Deformation (%)	Elastic modulus (E) (MPa)	T _{10%} (°C)	T _{max} (°C)
ME0	-	-	-	97.2	257.8
ME1	51.1 ± 1.6	166.7 ± 1.3	201.3 ± 1.5	70.6	283.0
ME2	195.4 ± 1.7	27.4 ± 1.1	447.4 ± 1.1	78.9	273.0
ME3	260.3 ± 1.9	40.6 ± 1.1	448.8 ± 1.6	76.9	286.0
ME4	178.1 ± 1.3	39.1 ± 1.4	445.2 ± 1.2	85.4	267.0
ME5	126.7 ± 1.2	87.8 ± 1.7	447.1 ± 1.4	77.6	298.0
ME6	53.4 ± 1.5	28.8 ± 1.7	488.3 ± 1.5	82.3	267.0
ME7	189.3 ± 1.6	47.8 ± 1.7	444.9 ± 1.3	83.5	268.0
ME8	203.8 ± 1.6	39.7 ± 1.6	548.2 ± 1.6	80.2	279.7
ME9	337.2 ± 1.4	92.4 ± 1.9	450.5 ± 1.8	84.6	290.8
ME10	91.8 ± 1.1	67.1 ± 1.3	439.2 ± 1.6	87.9	255.3
ME11	292.1 ± 1.5	57.0 ± 1.7	444.1 ± 1.6	95.2	278.1
ME12	171.1 ± 1.9	38.6 ± 1.6	412.3 ± 1.1	80.7	259.6
ME13	65.8 ± 1.4	40.4 ± 1.6	646.4 ± 1.3	79.0	254.8
ME14	159.1 ± 1.4	76.7 ± 1.2	718.0 ± 1.8	89.4	277.0
ME15	77.8 ± 1.8	36.9 ± 1.4	440.3 ± 1.3	84.2	284.0
ME16	160.6 ± 1.3	31.6 ± 1.5	445.8 ± 1.7	80.5	267.0

Maximum tensile strength (σ_{\max}), deformation (%), and elastic modulus (E)

of water absorbed depends on the amount of hydrophilic or hydrophobic groups and pores sizes in/on the sorbent material. This explains the low degree of swelling, especially in composite membranes with high amounts of PS and Fe₃O₄ [91]. Based on the characterization studies, pectin-based composite membranes are potential polymer matrices for water and wastewater treatment. Thus, due to its performance (Fig. 8), the pectin-based composite membrane containing 3% PS and 1 wt% Fe₃O₄ was tested as a model material for the sorption and removal of MB from water.

3.2.2 Dye separation assays

Figure 9 shows the MB sorption capacity of the control Fe₃O₄ and composite membrane containing 3% (w/w) PS and 1% (w/w) Fe₃O₄ as a function of time at pH 3.0, 4.0, 6.0, 8.0, and 10.0. The dye sorption capacity of the composite membrane increased rapidly from 0 to 500 min due to the high amount of available active sorption sites at the beginning of the process, followed by a slight increase from 500 to 1500 min (sorption equilibrium) at all pH values. The sorption rate decreases over time due to the saturation of the polymer membrane structure [24, 59]. Saturation occurs after the dye molecule is transferred from the aqueous solution to the boundary layer of the membrane and into the pores. Sorption processes take place on/in available active sites of solid sorbents due to interactions between positive and negative ionic groups in polymer materials [89]. The

sorption capacity of the polymeric membrane ranged from 0.88 to 1.18 mg of dye per g of dried membrane at pH from 3.0 to 10.0 after 2000 min. Some authors obtained a sorption capacity for MB dye of 0.75 mg g⁻¹ at pH 4 using a pectin membrane [29]. Low sorption capacity is commonly related to the amount of hydroxyl and carboxyl groups available in the sorbent structure [35, 89]. Slightly higher sorption capacities were found in aqueous media with alkaline pH due to the ionization of carboxyl groups [18].

Although the effect of different membrane dosages was not directly studied in this work, it is well established in the literature that increasing the sorbent dosage enhances the number of active sorption sites for interactions, thereby improving the removal efficiency of chemicals from solutions [6, 7, 45, 51, 72, 73, 77]. However, an increase in dosage can also reduce the sorption capacity per unit mass of membrane, as the available dye molecules in the solution become limited compared to the amount of sorbent material, leaving sorption sites unsaturated. Similar behavior has been reported for other sorbents, such as activated carbon [72, 73], clay minerals [7, 51, 77], and magnetic composites [6, 45].

Based on trends and the findings of the present study, one can infer that a membrane dosage of approximately 150 mg combined with an initial dye concentration of 20 mg L⁻¹ at pH 10.0 could offer optimal conditions for dye removal from contaminated water. This makes pectin-based composite membranes potential matrices for water filtration and the removal of dyes from textile wastewater, as textile effluents commonly have a high pH value (around 10), which varies with the source of pollution [55]. The sorption results of dye in Fe₃O₄ were similar to those found for membranes in an acid solution, with slightly higher values in an alkaline solution. Fe₃O₄ powder is a potential sorbent for removing dyes from aqueous solutions; however, it is improper for membrane-filtration processes. In view of this, Fe₃O₄ was incorporated into the membrane networks to achieve synergic effects during membrane filtration. Moreover, magnetic membranes can be recovered by applying an external magnetic field, as described elsewhere [58].

3.2.3 Sorption kinetics

Figure 10 shows the predicted and experimental non-linear kinetics for the sorption of the dye in the pectin-based composite membrane containing 3% (w/w) PS and 1% (w/w) Fe₃O₄ at pH 3.0 (a), 4.0 (b), 6.0 (c), 8.0 (d), and 10.0 (e). The kinetic parameters are shown in Table 3. Sorption kinetics of dye in pure Fe₃O₄ can be seen in supplementary materials (Fig. 6S and Table 1S). The pseudo-first-order kinetic model is typically applied to study the occupation rate of active sites during sorption assays. In this case, proportionality

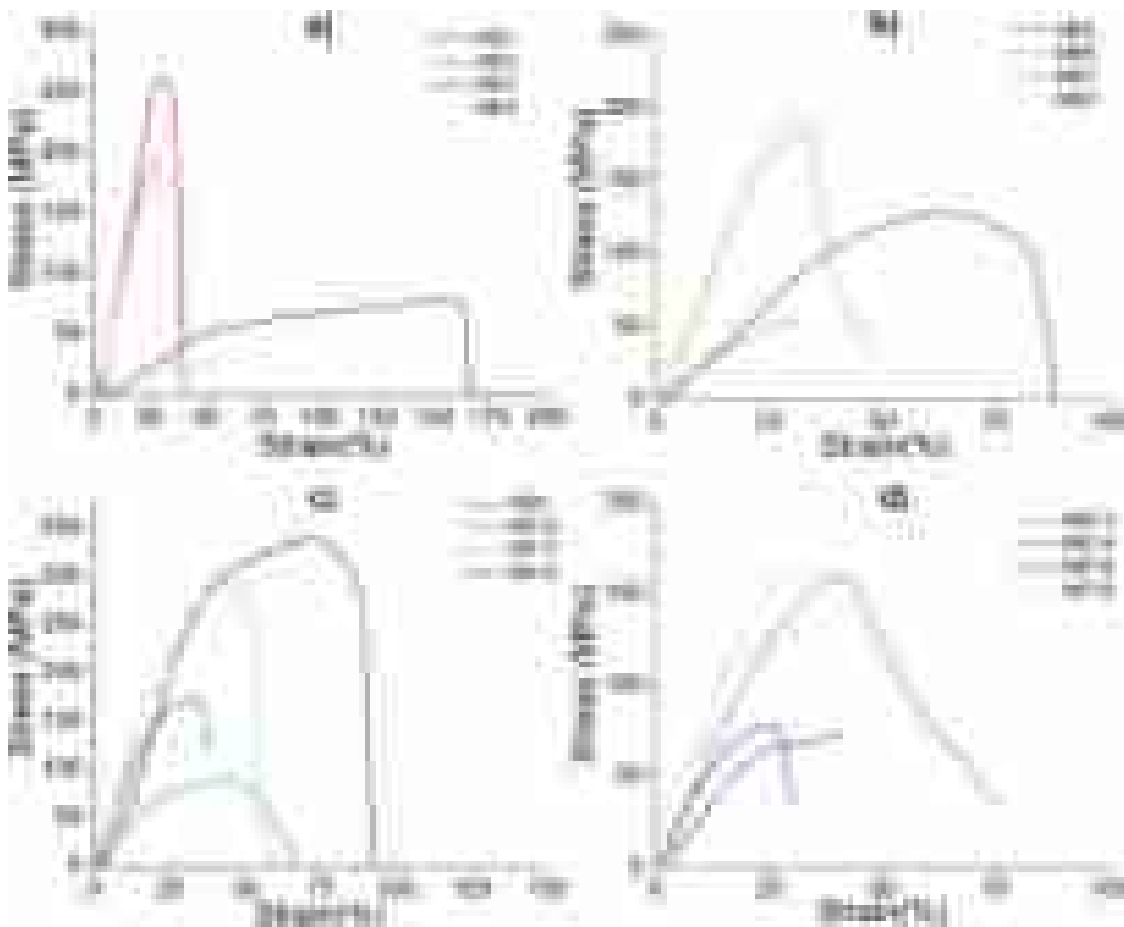


Fig. 5 Curves of strain versus stress for pectin-based composite membranes containing different PS and Fe₃O₄ contents. **a** 1% PS plus 1 (ME1), 5 (ME2), 10 (ME3), and 15% (w/w) (ME4) Fe₃O₄. **b** Results of mechanical assays for pectin-based composite membranes containing 3% PS plus 1 (ME5), 5 (ME6), 10 (ME7), and 15% (w/w) (ME8)

Fe₃O₄. **c** Results of mechanical assays for pectin-based composite membranes containing 5% PS plus 1 (ME9), 5 (ME10), 10 (ME11), and 15% (w/w) (ME12) Fe₃O₄. **d** Results of mechanical assays for pectin-based composite membranes containing 10% PS plus 1 (ME13), 5 (ME14), 10 (ME15), and 15% (w/w) (ME16) Fe₃O₄

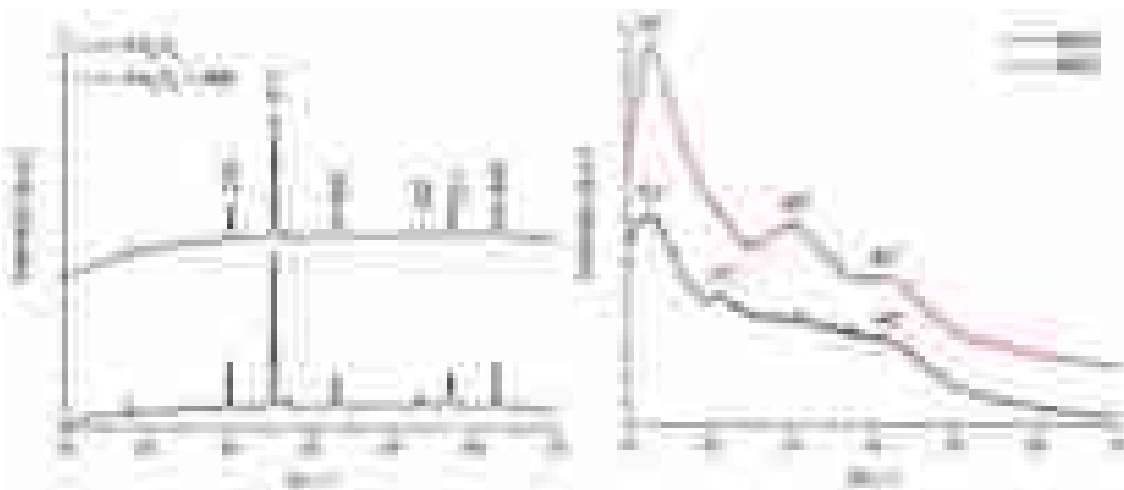


Fig. 6 XRD diffractograms for Fe₃O₄, after sorption of Fe₃O₄ + MB, membrane without Fe₃O₄ and PS (ME0), and composite membrane containing 3% (w/w) PS and 1% (w/w) Fe₃O₄ (ME5)

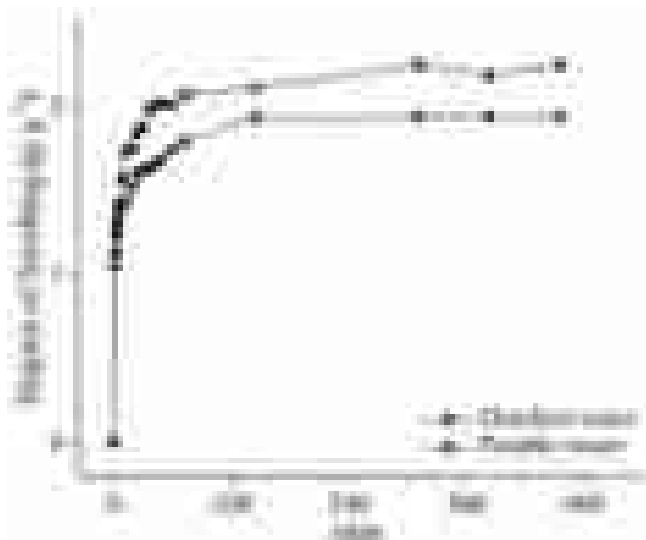


Fig. 7 Degree of swelling of pectin-based composite membrane containing 3% (w/w) PS and 1% (w/w) Fe_3O_4 in distilled water and drinking water at room temperature

occurs between occupied and unoccupied sites, suggesting a

sorption mechanism based on physical interactions between the sorbent and sorbate [83, 84]. On the other hand, the pseudo-second-order kinetic model assumes that the sorption rate is related to the square of the number of unoccupied sites, suggesting a sorption mechanism based on chemical interactions between the sorbent and sorbate. Both physical and chemical interactions are important when describing membrane filtration processes in water purification systems [87]. Many kinetic models are empirical and do not generate relevant information on mass transfer mechanisms, whereas the pseudo-first-order and pseudo-second-order kinetic models are useful for sorption processes. In view of our main aim, other kinetic models were considered irrelevant to our results. In this study, the kinetic fit at pH 3.0 could be explained by both pseudo-first-order and pseudo-second-order models due to the similar correlation coefficient (R^2) and chi-square test (χ^2) values. Thus, the best kinetic fit was defined based on predicted and experimental q_e values. As these values were similar using the pseudo-second-order kinetic model, this model represents the sorption kinetics of MB dye in pectin-based composite



Fig. 8 Scheme illustrating membrane with best performance



Fig. 9 MB sorption capacity of **a** control Fe_3O_4 and **b** composite membrane containing 3% (w/w) PS and 1% (w/w) Fe_3O_4 as a function of time at pH 3.0, 4.0, 6.0, 8.0, and 10.0. Experimental conditions: initial

dye concentration of 20 mg L^{-1} , membrane mass of 150 mg, and solution volume of 50 mL

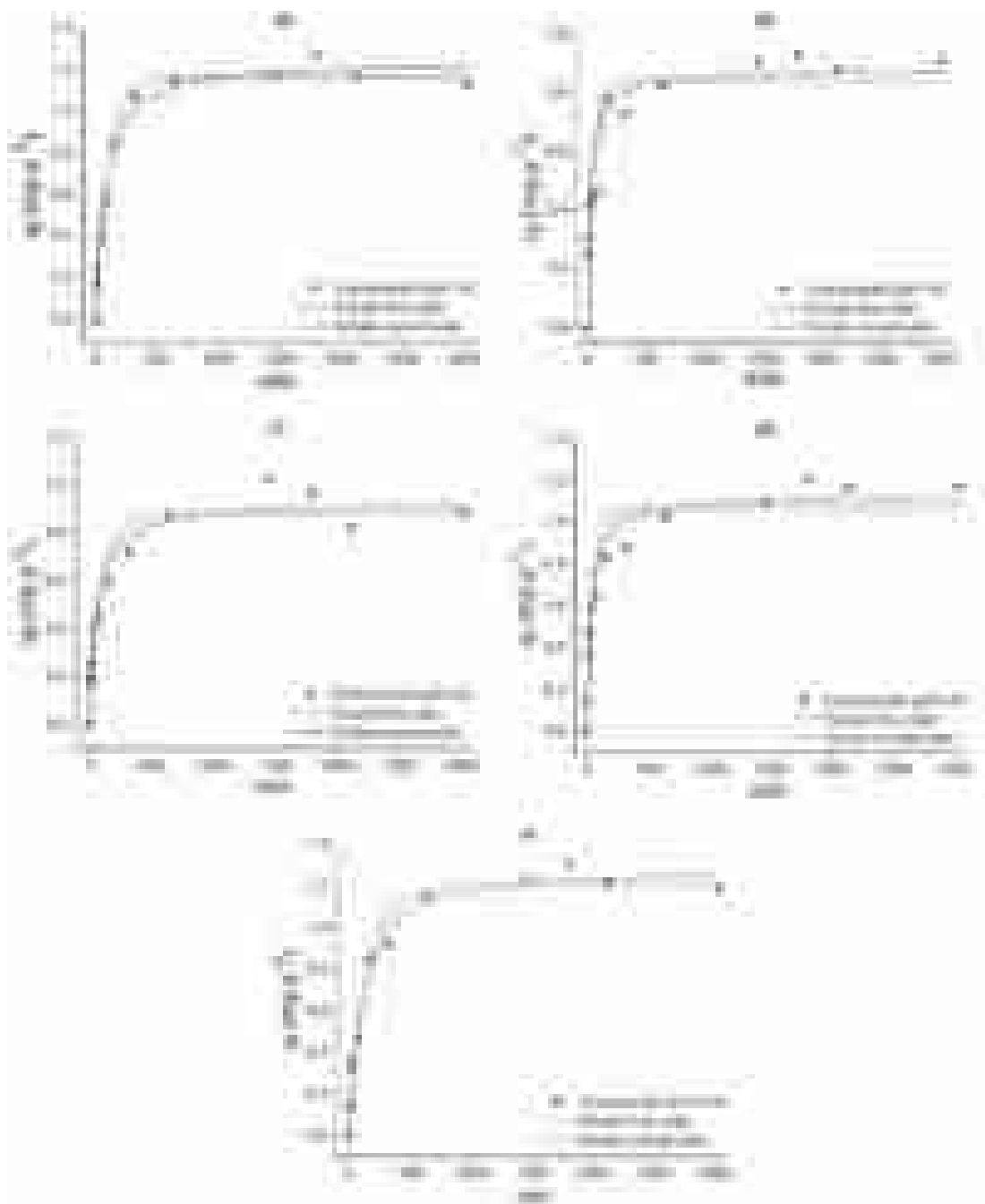


Fig. 10 Predicted and experimental non-linear kinetics for sorption of dye in pectin-based composite membrane containing 3% (w/w) PS and 1% (w/w) Fe_3O_4 at pH 3.0 (**a**), 4.0 (**b**), 6.0 (**c**), 8.0 (**d**), and 10.0

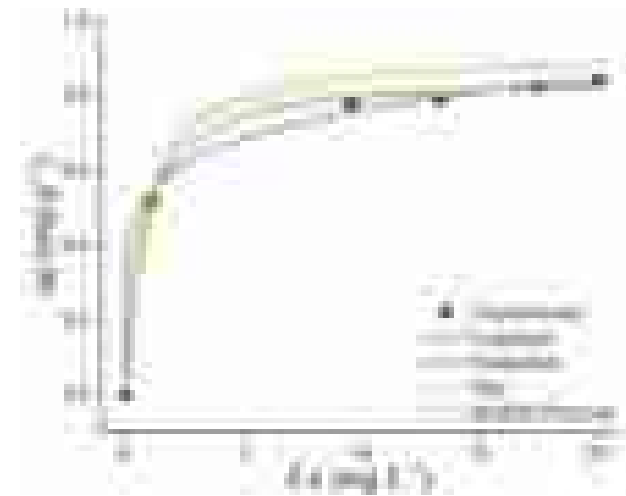
(**e**). Experimental conditions: initial dye concentration of 20.0 mg L^{-1} , solution volume of 50.0 mL, and room temperature

membranes containing PS and Fe_3O_4 . Other studies have reported pseudo-second-order kinetic models to describe the sorption of MB dye molecules [34, 42]. Different results were found at higher pH values due to changes in the charge in the polymeric structures. Changes in the pH values of aqueous solutions tend to disturb the reaction equilibrium, altering k_1 , and k_2 (sorption rates) values. This indicates that the sorption process is governed by the number of reactions

occurring between the sorbate and sorbent [52]. The sorption kinetics of MB in the pectin-based membranes following the pseudo-second-order model suggest that the sorption rate-limiting step is a chemical reaction [30]. Thus, the dye sorption was conducted by chemical reactions between the sorbate and surface sites through covalent bonding [70].

Table 3 Kinetic parameters for sorption of dye in pectin-based composite membrane containing 3% (w/w) PS and 1% (w/w) Fe₃O₄ at different pH values

Kinetic model	Parameters	pH				
		3.0	4.0	6.0	8.0	10.0
Pseudo-first-order model	k_1 (min ⁻¹)	0.0089	0.0194	0.0097	0.0179	0.0071
	q_e (mg g ⁻¹)	1.1809	0.8419	0.8827	1.0609	1.2014
	R^2	0.9898	0.8703	0.9113	0.9025	0.9677
	χ^2	0.0027	0.0131	0.0112	0.0175	0.0083
Pseudo-second-order model	k_2 (10 ⁻⁵ min ⁻¹)	0.0099	0.0368	0.0161	0.0228	0.0077
	q_e (mg g ⁻¹)	1.2621	0.8792	0.9343	1.1262	1.2920
	R^2	0.9891	0.9319	0.9448	0.9611	0.9817
	χ^2	0.0029	0.0069	0.0070	0.0070	0.0047

**Fig. 11** Non-linear Langmuir, Freundlich, Sips, and Redlich-Peterson isotherms for sorption of MB in pectin-based composite membrane containing 3% (w/w) PS and 1% (w/w) Fe₃O₄. Experimental conditions: sorption time of 2000 min, membrane mass of 150 mg, solution volume of 50.0 mL, and pH 8.0**Table 4** Parameters of non-linear Langmuir, Freundlich, sips, and Redlich-Peterson isotherms for sorption of MB using pectin-based composite membrane containing 3% (w/w) PS and 1% (w/w) Fe₃O₄

Isotherm model	Parameters	Isotherm model	Parameters
Langmuir	Q_m (mg g ⁻¹)	Freundlich	K_F (L mg ⁻¹)
	K_L (L mg ⁻¹)		n_F
	R^2		R^2
	χ^2		χ^2
Sips	Q_m (mg g ⁻¹)	Redlich-Peterson	A (mg ⁻¹)
	K_S (L mg ⁻¹)		B (L g ⁻¹)
	n_S		g
	R^2		R^2
	χ^2		χ^2

3.2.4 Sorption isotherms

Figure 11 shows the isotherms for the sorption of MB in the pectin-based composite membrane containing 3% (w/w) PS and 1% (w/w) Fe₃O₄. The isotherm parameters are shown in Table 4. Two-parameter isotherm models (e.g., Langmuir and Freundlich) and three-parameter isotherm models (e.g., Sips and Redlich-Peterson) are commonly applied to heterogeneous and homogeneous sorption processes, providing a comprehensive description of interactions between the sorbate and sorbent [80, 81]. Two-parameter isotherm models are simple and effective at describing sorption processes with fewer variables, but may be useful in complex systems with heterogeneous surfaces or varying sorption energies [80, 81]. The formation of a monolayer on the membrane surface was investigated using the Langmuir model, whereas surface heterogeneity and the type of interaction between neighboring sorption sites were considered with the Freundlich model. Three-parameter isotherm models are useful for describing sorption processes on heterogeneous surfaces with different sorption energies and sites. The Sips three-parameter isotherm model can be represented by the Langmuir two-parameter isotherm model at low sorbate concentrations, whereas the Redlich-Peterson three-parameter isotherm model combines properties of the Langmuir and Freundlich isotherms in a wide sorbate concentration range [50]. The Temkin and Dubinin-Radushkevich (D-R) isotherm models were initially tested in this work, but had poor fits, as determined by statistical assessment metrics, such as R^2 and χ^2 (data not shown). Therefore, these models were not employed to assess the results of this work. The sorption capacity increased with the increase in the initial dye concentration due to the increase in the driving force of the concentration gradient, which accelerates the diffusion of organic molecules from aqueous solutions to rigid solid surfaces [76]. The sorption capacity increased slightly to 0.788 mg g⁻¹ when the initial dye concentration increased to 15 mg L⁻¹, inferring the saturation of active sites of the membrane network. Isotherm parameters were determined using the optimization procedure employed by the solver

add-in functions as well as trial-and-error optimization in Microsoft Excel. Based on the R^2 and χ^2 values, the best isotherm fit was obtained using the Redlich-Peterson model, suggesting that the sorption process is governed mainly by multisite interactions [83, 84]. As the g value was 1, the Redlich-Peterson model behaves similarly to the Langmuir model [38]. Hence, monolayer formation occurs at low dye concentrations with no physiochemical interactions between the dye molecules sorbed at specific active sites and available neighboring active sites [18]. The maximum sorption capacity (q_{max}) of pectin-based membrane for MB dye is 0.86 mg g^{-1} at 298 K. This indicates that the pectin-based composite membrane containing PS and Fe_3O_4 is a promising matrix for the sorption of cationic textile dyes contained in wastewater. Thus, water treatment methods can be proposed using pectin-based composite membranes with the aim of purifying drinking water containing different types of organic pollutants, as represented in Fig. 12.

3.2.5 Biosorbent prospects for pollutant separation

Table 5 compares using pectin-based membranes for MB dye with other sorbents made from biomass materials and other applications. Several factors affect the sorption

capacity, including pH, temperature, dosage of adsorbents and their type, surface area, contact time, etc. The optimal parameters for each sorbent vary significantly, and optimizing each factor is important to large-scale industrial applications and understanding the sorption mechanism [82]. The introduction of Fe_3O_4 provided additional adsorptive sites, increasing the overall capacity, while PS contributed to the mechanical strength and stability of the adsorbent, which may allow the pectin-based membrane to tolerate diverse wastewater conditions.

Several studies have shown that adsorbents prepared from biomass materials are less expensive than conventional treatment technologies for pollutant removal, although they did not incorporate cost-benefit analysis in their study. A significant advantage of using biomass materials like pectin and PS is their low cost. The cost of forest wastes such as PS is only associated with the transport cost from the storage place to the site where they will be utilized [14]. The cost of pectin in the market is 12–21 \$ per kg [49]. In comparison, conventional starch sorbents such as insoluble starch xanthate and soluble starch xanthane have been reported at \$7.61/100 g and \$0.10/100 g respectively [10]. Fe_3O_4 , while not a biomass material, offers significant benefits in terms of sorption efficiency and recovery ease, despite its higher cost

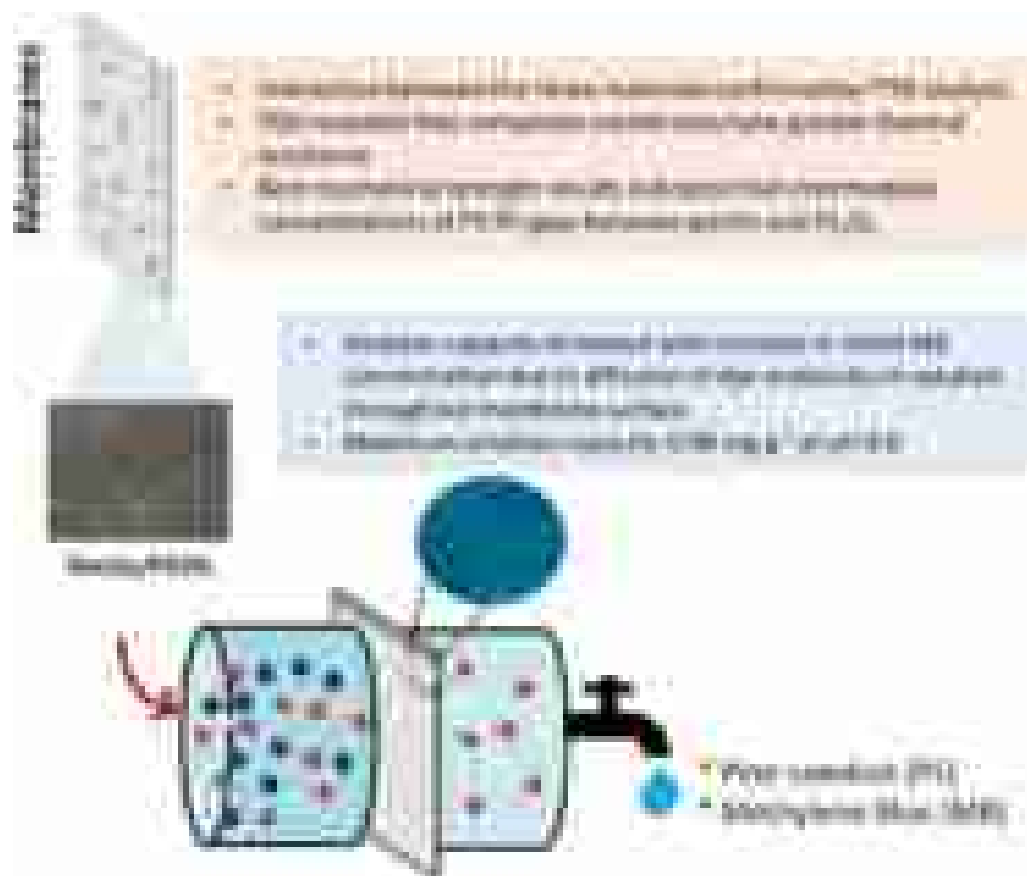


Fig. 12 Schematic of prepared membrane and simulation of application in drinking water purification

Table 5 Comparative of sorption capacities for removal of pollutants from water on different biomass materials (PSO: pseudo-second-order)

Sorbent type	Adsorbent dosage (g)	Surface area (m ² g ⁻¹)	Pollutant	Q _{max} (mg g ⁻¹) (T(°C)/pH)	Desorption capacity	Kinetic	Isotherm	Industrial application potential assessment	Advantages	Disadvantages	References
Pectin–pinus sawdust-iron oxide Fe ₃ O ₄ nanocomposite	0.15 g/50 mL	-	MB	0.86 (25/8)	-	PSO	Langmuir	Textile effluents	Low cost, environmentally friendly, Fe ₃ O ₄ presence may favor the application in photodegradation studies	Low adsorption capacity	This study
Acid factionalized Coconut shell	0.1 g/100 mL	1.137	MB	50.6 (30/8)	-	PSO	Freundlich	Textile effluents	Low cost, renewability, and environmentally friendly	Lack of desorption data	[33]
Sulphuric acid-modified bagasse	0.4 g/100 mL	-	MB	56.5 (27/9)	95.41%	PSO	Langmuir and Freundlich	Textile effluents	Low cost agricultural waste, highly adsorbing in terms of high percentage of color removal and chemical oxygen demand (COD) reduction		[42]
Pectin–iron oxide magnetic nanocomposite	20 mg/20 mL	67	Cu (II)	48.99 (25/5)	93.70%	PSO	Langmuir and Freundlich	Mining effluents	Low cost, adsorption properties of pectin and magnetic properties of iron oxide	Lack of stability and inconvenience to be separated from the aqueous solution	[23]
Groundnut seed cake powder	0.75 g/50 mL	470	Cu (II)	4.82 (40/5)	-	PSO	Langmuir	Pulp and paper mills, fertilizers, petroleum refineries, basic steel work foundries, non-ferrous metal works, motor vehicles, aircraft plating effluents	Low cost, agricultural waste		[37]
Sesame seed cake powder	1.0 g/50 mL	480		4.24 (40/5)							
Coconut cake powder	1.0 g/50 mL			4.32 (40/5)							
Hybrid pectin-agar	0.02 g/20 mL	-	Zn (II)	25 (22/4)	-	-	-	Anti-corrosive coatings, constructional materials, batteries, paints and cosmetics, as well as its presence in the mine waters	Low cost, pectin-based beads may be easily separated from purified solution	Lack of kinetics and desorption data	[32]
Coffee husks	1 g/150 mL	-	Cu(II), Cd(II) and Zn(II)	5.6 (25/4)	-	PSO	Langmuir and Freundlich	Industrial effluents	Low cost agricultural waste, widely availability	Difficulty of their separation from purified water	[54]

compared to purely biomass materials. Still, this contrasts sharply with the higher costs associated with conventional activated carbons (\$259.5 per kg) [14].

Our study aligns with environmental sustainability by utilizing waste materials and natural polymers. The composite nature of our adsorbent also suggests potential for multiple-cycle use, although reusability studies are yet to be conducted. Future work will focus on these aspects to ensure the adsorbent's practical application in industrial wastewater treatment is not only effective but also environmentally responsible.

4 Conclusion

A pectin-based composite membrane containing 3% (w/w) PS and 1% (w/w) Fe_3O_4 was efficiently synthesized and characterized for the purification of water containing organic pollutants. With the pectin de-esterification and crosslinking process of the polymer chain with calcium, it was possible to reduce the solubility of the membrane in water during application studies. FTIR, TGA, and mechanical assays confirmed the crosslinked membrane structure. The composite membranes containing either Fe_3O_4 or PS had higher thermal resistance than the pectin-based membrane alone due to greater amounts of crosslinking points among pectin, PS, and Fe_3O_4 in the polymeric structure. Higher mechanical resistance was also found for the composite membranes containing from 1 to 3% (w/w) Fe_3O_4 and 3 and 5% (w/w) of PS. The degree of swelling and dye sorption capacity of the membranes were affected by the pH of the aqueous solutions and salt concentrations. The dye sorption kinetics can be described by either the pseudo-first-order model or pseudo-second-order model at pH 3.0, with differences at more alkaline solutions. Lastly, either the non-linear Redlich-Peterson or Langmuir isotherm models can describe the sorption mechanism depending on the experimental conditions. Based on the present results, the proposed pectin/PS/ Fe_3O_4 composite membrane constitutes a novel approach for dye removal applications. The synthesized adsorbent using pectin, PS, and Fe_3O_4 presents a promising solution for dye removal in wastewater treatment, combining environmental sustainability with cost-efficiency. Future studies will further explore the scalability and reusability of this adsorbent to enhance its industrial application potential.

Supplementary Information The online version contains supplementary material available at <https://doi.org/10.1007/s10450-025-00619-2>.

Acknowledgements ATP thanks Fundação de Amparo à Pesquisa e Inovação do Estado de Santa Catarina (FAPESC, Brazil) for the financial support (Grant numbers: 2023/TR331 and 2024/TR002572) and Conselho Nacional de Desenvolvimento Científico e Tecnológico

(CNPq, Brazil) for the research productivity fellowship (Grant number: 313064/ 2022-9). DSR thanks CNPq (Grant number: 308053/ 2021-4 and 403934/ 2021-4) and Fundação de Amparo à Pesquisa do Estado de São Paulo (FAPESP, Brazil) for research support (Grant numbers: 2022/ 01382-3, 2021/ 14714-1, and 2020/ 13703-3). This work was partially supported by Brazilian agencies MCTIC/CNPq (Grant number: 406973/ 2022-9) and by Coordenação de Aperfeiçoamento de Pessoal de Nível Superior (CAPES, Brazil – Finance Code 001) and Multiuser Central Facilities (CEM - UFABC).

Author contributions Ana Maria Tischer: Data curation, formal analysis, roles/writing – original draft- Rafaela Reis Ferreira: Data curation, formal analysis, roles/writing – original draft- Ionara de Fátima Ferreira: Data curation, formal analysis- Derval dos Santos Rosa: Funding acquisition, Roles/writing – original draft- Alexandre Tadeu Paulino: Project administration, Data curation, Funding acquisition, resources, writing – review & editing.

Data availability No datasets were generated or analysed during the current study.

Declarations

Competing interests The authors declare no competing interests.

Ethical approval Not applicable.

Consent to participate Not applicable.

Consent to publish Not applicable.

References

- 1 Abbas, M., Parvatheeswara Rao, B., Naga, S.M., Takahashi, M., Kim, C.: Synthesis of high magnetization hydrophilic magnetite (Fe_3O_4) nanoparticles in single reaction—Surfactantless polyol process. *Ceram. Int.* **39**, 7605–7611 (2013). <https://doi.org/10.1016/j.ceramint.2013.03.015>
- 2 Abu Hasan, H., Muhammad, M.H., Ismail, N., 'Izzati: A review of biological drinking water treatment technologies for contaminants removal from polluted water resources. *J. Water Process. Eng.* **33**, 101035 (2020). <https://doi.org/10.1016/j.jwpe.2019.101035>
- 3 Abutaleb, A., Imran, M., Zouli, N., Khan, A.H., Hussain, S., Ali, M.A., Bakather, O., Gondal, M.A., Khan, N.A., Panchal, H., Zahmatkesh, S.: Fe_3O_4 -multiwalled carbon nanotubes-bentonite as adsorbent for removal of methylene blue from aqueous solutions. *Chemosphere.* **316**, 137824 (2023). <https://doi.org/10.1016/j.chemosphere.2023.137824>
- 4 Ahmad, S.I., Ahmad, R., Khan, M.S., Kant, R., Shahid, S., Gautam, L., Hasan, G.M., Hassan, M.I.: Chitin and its derivatives: Structural properties and biomedical applications. *Int. J. Biol. Macromol.* **164**, 526–539 (2020). <https://doi.org/10.1016/j.ijbiomac.2020.07.098>
- 5 Alemzadeh, I., Saifkordi, A.A., Kahforooshan, D., Nahid, P.: Production of low ester (LM) pectin by de-esterification of high ester (HM) Apple pectin. *Scientia Iranica.* **12**, 306–310 (2005)
- 6 Algethami, J.S., Alhamami, M.A.M., Alqadami, A.A., Melhi, S., Seliem, A.F.: Magnetic hydrochar grafted-chitosan for enhanced efficient adsorption of malachite green dye from aqueous solutions: Modeling, adsorption behavior, and mechanism analysis.

- Int. J. Biol. Macromol. **254**, 127767 (2024). <https://doi.org/10.1016/j.ijbiomac.2023.127767>
- 7 Aljeboree, A.M., Alkaim, A.F., Alsaltany, F.H., Issa, S.K.: Highly reusable nano adsorbent based on Clay-Incorporated hydrogel nanocomposite for cationic dye adsorption. *J. Inorg. Organomet. Polym. Mater.* (2024). <https://doi.org/10.1007/s10904-024-0334-4-5>
 - 8 Ao, C., Zhao, J., Li, Q., Zhang, J., Huang, B., Wang, Q., Gai, J., Chen, Z., Zhang, W., Lu, C.: Biodegradable all-cellulose composite membranes for simultaneous oil/water separation and dye removal from water. *Carbohydr. Polym.* **250**, 116872 (2020). <https://doi.org/10.1016/j.carbpol.2020.116872>
 - 9 Ávila, F.G., Cabrera-Sumba, J., Valdez-Pilataxi, S., Villalta-Chungata, J., Valdiviezo-Gonzales, L., Alegria-Arnedo, C.: Removal of heavy metals in industrial wastewater using adsorption technology: Efficiency and influencing factors. *Clean. Eng. Technol.* **24**, 100879 (2025). <https://doi.org/10.1016/j.clet.2025.100879>
 - 10 Bailey, S.E., Olin, T.J., Bricka, R.M., Adrian, D.D.: A review of potentially low-cost sorbents for heavy metals. *Water Res.* **33**, 2469–2479 (1999). [https://doi.org/10.1016/S0043-1354\(98\)00475-8](https://doi.org/10.1016/S0043-1354(98)00475-8)
 - 11 Barbosa, R.F.S., Souza, A.G., Maltez, H.F., Rosa, D.S.: Chromium removal from contaminated wastewaters using biodegradable membranes containing cellulose nanostructures. *Chem. Eng. J.* **395**, 125055 (2020). <https://doi.org/10.1016/j.cej.2020.125055>
 - 12 Baum, A., Dominiak, M., Vidal-Melgosa, S., Willats, W.G.T., Søndergaard, K.M., Hansen, P.W., Meyer, A.S., Mikkelsen, J.D.: Prediction of pectin yield and quality by FTIR and carbohydrate microarray analysis. *Food Bioproc Tech.* **10**, 143–154 (2017). <https://doi.org/10.1007/s11947-016-1802-2>
 - 13 Baum, A., Dominiak, M., Vidal-Melgosa, S., Willats, W.G.T., Søndergaard, K.M., Hansen, P.W., Meyer, A.S., Mikkelsen, J.D.: Prediction of pectin yield and quality by FTIR and carbohydrate microarray analysis. *Food Bioproc Tech.* **10**, 143–154 (2017). <https://doi.org/10.1007/s11947-016-1802-2>
 - 14 Bello, O.S., Adegoke, K.A., Fagbenro, S.O., Lameed, O.S.: Functionalized coconut husks for rhodamine-B dye sequestration. *Appl. Water Sci.* **9**, 189 (2019). <https://doi.org/10.1007/s13201-019-1051-4>
 - 15 Cargnin, M.A., de Souza, A.G., de Lima, G.F., Gasparin, B.C., dos Santos Rosa, D., Paulino, A.T.: Pinus residue/pectin-based composite hydrogels for the immobilization of β -D-galactosidase. *Int. J. Biol. Macromol.* **149**, 773–782 (2020). <https://doi.org/10.1016/j.ijbiomac.2020.01.280>
 - 16 da Cruz, L.F., Polizeli, A.G., Enzweiler, H., Paulino, A.T.: Chitosan-co-GLU/eucalyptus residue composite membrane for the stabilization of β -d-galactosidase in aqueous solutions. *Polym. Bull.* (2023). <https://doi.org/10.1007/s00289-023-05008-9>
 - 17 Dai, J., Wu, S., Jiang, W., Li, P., Chen, X., Liu, L., Liu, J., Sun, D., Chen, W., Chen, B., Li, F.: Facile synthesis of pectin coated Fe₃O₄ nanospheres by the sonochemical method. *J. Magn. Magn. Mater.* **331**, 62–66 (2013). <https://doi.org/10.1016/j.jmmm.2012.11.004>
 - 18 Dalalibera, A., Vilela, P.B., Vieira, T., Becegato, V.A., Paulino, A.T.: Removal and selective separation of synthetic dyes from water using a polyacrylic acid-based hydrogel: Characterization, isotherm, kinetic, and thermodynamic data. *J. Environ. Chem. Eng.* **8**, 104465 (2020). <https://doi.org/10.1016/j.jece.2020.104465>
 - 19 Dixit, R., Wasiullah, Malaviya, D., Pandiyan, K., Singh, U., Sahu, A., Shukla, R., Singh, B., Rai, J., Sharma, P., Lade, H., Paul, D.: Bioremediation of heavy metals from soil and aquatic environment: An overview of principles and criteria of fundamental processes. *Sustainability.* **7**, 2189–2212 (2015). <https://doi.org/10.3390/su7022189>
 - 20 Ferreira, R.R., Souza, A.G., Nunes, L.L., Shahi, N., Rangari, V.K., dos S. Rosa, D.: Use of ball mill to prepare nanocellulose from Eucalyptus biomass: Challenges and process optimization by combined method. *Mater. Today Commun.* **22**, 100755 (2020). <https://doi.org/10.1016/j.mtcomm.2019.100755>
 - 21 Freundlich, H.M.F.: Over the adsorption in solution. *J. Phys. Chem.* **57**, 385–471 (1906)
 - 22 Ghorbanizadeh, S., Karami, F., Delfani, S., Shakibaie, M., Razlansari, A., Rezaei, F.: Antibacterial effects and cellular mechanisms of iron oxide magnetic nanoparticles coated by piroctone olamine against some cariogenic bacteria. *Annals Med. Surg.* (2022). <https://doi.org/10.1016/j.amsu.2022.104291>
 - 23 Gong, J.L., Wang, X.Y., Zeng, G.M., Chen, L., Deng, J.H., Zhang, X.R., Niu, Q.Y.: Copper (II) removal by pectin-iron oxide magnetic nanocomposite adsorbent. *Chem. Eng. J.* 185–186 (2012). <https://doi.org/10.1016/j.cej.2012.01.050>
 - 24 Guilherme, M.R., Reis, A.V., Paulino, A.T., Moia, T.A., Mattoso, L.H.C., Tambourgi, E.B.: Pectin-based polymer hydrogel as a carrier for release of agricultural nutrients and removal of heavy metals from wastewater. *J. Appl. Polym. Sci.* **117**, 3146–3154 (2010). <https://doi.org/10.1002/app.32123>
 - 25 Gurung, K., Neibi, M.C., Sillanpää, M.: Removal and fate of emerging organic micropollutants (EOMs) in municipal wastewater by a pilot-scale membrane bioreactor (MBR) treatment under varying solid retention times. *Sci. Total Environ.* **667**, 671–680 (2019). <https://doi.org/10.1016/j.scitotenv.2019.02.308>
 - 26 Han, C., Cai, N., Chan, V., Liu, M., Feng, X., Yu, F.: Enhanced drug delivery, mechanical properties and antimicrobial activities in poly(lactic acid) nanofiber with mesoporous Fe₃O₄-COOH nanoparticles. *Colloids Surf. Physicochem Eng. Asp.* **559**, 104–114 (2018). <https://doi.org/10.1016/j.colsurfa.2018.09.012>
 - 27 Hanauer, D.C., Paulino, A.T.: Anchoring lactase in pectin-based hydrogels for lactose hydrolysis reactions. *Process Biochem.* **122**, 50–59 (2022). <https://doi.org/10.1016/j.procbio.2022.08.026>
 - 28 Hanauer, D.C., de Souza, A.G., Cargnin, M.A., Gasparin, B.C., Rosa, D.S., Paulino, A.T.: Pectin-based bihydrogels reinforced with Eucalyptus sawdust: Synthesis, characterization, β -D-Galactosidase immobilization and activity. *J. Ind. Eng. Chem.* **97**, 368–382 (2021). <https://doi.org/10.1016/j.jiec.2021.02.022>
 - 29 Hastuti, B., Nur Afifah, S., Mulyani, B., Susilowati, E.: Adsorption of methylene blue dyes using pectin membrane. *J. Phys. Conf. Ser.* **1503**, 012031 (2020). <https://doi.org/10.1088/1742-6596/1503/1/012031>
 - 30 Ho, Y.S., Ng, J.C.Y., McKay, G.: Kinetics of pollutant sorption by biosorbents: Review. *Sep. Purif. Methods.* **29**, 189–232 (2000). <https://doi.org/10.1081/SPM-100100009>
 - 31 Huang, Y., Huang, Q., Liu, H., Xiao, C., Sun, K.: A facile and environmental-friendly strategy for Preparation of Poly (tetrafluoroethylene-co-hexafluoropropylene) Hollow fiber membrane and its membrane emulsification performance. *Chem. Eng. J.* **384**, 123345 (2020). <https://doi.org/10.1016/j.cej.2019.123345>
 - 32 Jakóbcik-Kolon, A., Bok-Badura, J., Karoń, K., Mitko, A., Milewski, K.: Hybrid pectin-based biosorbents for zinc ions removal. *Carbohydr. Polym.* **169**, 213–219 (2017). <https://doi.org/10.1016/j.carbpol.2017.03.095>
 - 33 Jawad, A.H., Abdulhameed, A.S., Mastuli, M.S.: Acid-fractionalized biomass material for methylene blue dye removal: a comprehensive adsorption and mechanism study. *J. Taibah Univ. Sci.* **14**, 305–313 (2020). <https://doi.org/10.1080/16583655.2020.1736767>
 - 34 Jawad, A.H., Mamat, N.F.H., Hameed, B.H., Ismail, K.: Biofilm of cross-linked Chitosan-Ethylene glycol diglycidyl ether for removal of reactive red 120 and Methyl Orange: Adsorption and mechanism studies. *J. Environ. Chem. Eng.* **7**, 102965 (2019). <https://doi.org/10.1016/j.jece.2019.102965>

- 35 Khare, A.R., Peppas, N.A.: Swelling/deswelling of anionic copolymer gels. *Biomaterials*. **16**, 559–567 (1995). [https://doi.org/10.1016/0142-9612\(95\)91130-Q](https://doi.org/10.1016/0142-9612(95)91130-Q)
- 36 Kulal, P., Badalamoole, V.: Magnetite nanoparticle embedded Pectin-graft-poly(N-hydroxyethylacrylamide) hydrogel: Evaluation as adsorbent for dyes and heavy metal ions from waste water. *Int. J. Biol. Macromol.* **156**, 1408–1417 (2020). <https://doi.org/10.1016/j.ijbiomac.2019.11.181>
- 37 Kumar, P., Malla, K.A., Yerra, B., Srinivasa Rao, K.: Removal of Cu(II) using three low-cost adsorbents and prediction of adsorption using artificial neural networks. *Appl. Water Sci.* **9** (2019). <https://doi.org/10.1007/s13201-019-0924-x>
- 38 Langmuir, I.: Adsorption of gases on plain surfaces of glass mica platinum. *J. Am. Chem. Soc.* (1918). <https://doi.org/10.1006/ceps.2001.1094>
- 39 Lima, E.C., Adebayo, M.A., Machado, F.M.: Chap. 3 - Kinetic and equilibrium models of adsorption. *Carbon Nanomaterials as Adsorbents Environ. Biol. Appl.* (2015). <https://doi.org/10.1007/978-3-319-18875-1>
- 40 de Lima, G.F., de Souza, A.G., Rosa, D.S.: Effect of adsorption of polyethylene glycol (PEG), in aqueous media, to improve cellulose nanostructures stability. *J. Mol. Liq.* **268**, 415–424 (2018). <https://doi.org/10.1016/j.molliq.2018.07.080>
- 41 Liu, Z., Lompe, K.M., Mohseni, M., Bérubé, P.R., Sauvé, S., Barbeau, B.: Biological ion exchange as an alternative to biological activated carbon for drinking water treatment. *Water Res.* **168**, 115148 (2020). <https://doi.org/10.1016/j.watres.2019.115148>
- 42 Low, L.W., Teng, T.T., Ahmad, A., Morad, N., Wong, Y.S.: A novel pretreatment method of lignocellulosic material as adsorbent and kinetic study of dye waste adsorption. *Water Air Soil Pollut.* **218**, 293–306 (2011). <https://doi.org/10.1007/s11270-010-0642-3>
- 43 Ma, W., Li, Y., Zhang, M., Gao, S., Cui, J., Huang, C., Fu, G.: Biomimetic durable multifunctional Self-Cleaning nanofibrous membrane with outstanding oil/water separation, photodegradation of organic contaminants, and antibacterial performances. *ACS Appl. Mater. Interfaces.* **12**, 34999–35010 (2020). <https://doi.org/10.1021/acsami.0c09059>
- 44 Mao, Y., Bu, X., Peng, Y., Tian, F., Xie, G.: Effects of simultaneous ultrasonic treatment on the separation selectivity and flotation kinetics of high-ash lignite. *Fuel.* **259**, 116270 (2020). <https://doi.org/10.1016/j.fuel.2019.116270>
- 45 Mohammadi, M., Eivazzadeh-Keihan, R., Babamoradi, M., Maleki, A.: A magnetic and antibacterial nanocomposite based on graphene oxide nanosheets embedded with Zn-Fe layered double hydroxide as a novel and highly effective adsorbent for the removal of methylene blue dye. *Diam. Relat. Mater.* **144**, 111010 (2024). <https://doi.org/10.1016/j.diamond.2024.111010>
- 46 Mohrazi, A., Ghasemi-Fasaee, R.: Removal of methylene blue dye from aqueous solution using an efficient chitosan-pectin bio-adsorbent: Kinetics and isotherm studies. *Environ. Monit. Assess.* **195**, 339 (2023). <https://doi.org/10.1007/s10661-022-10900-4>
- 47 Moradi, E., Ebrahimzadeh, H., Mehrani, Z., Asgharinezhad, A.A.: The efficient removal of methylene blue from water samples using three-dimensional Poly (vinyl alcohol)/starch nanofiber membrane as a green nanosorbent. *Environ. Sci. Pollut. Res.* **26**, 35071–35081 (2019). <https://doi.org/10.1007/s11356-019-06400-7>
- 48 Morris, G., Foster, T.J., Harding, S.E.: The effect of the degree of esterification on the hydrodynamic properties of citrus pectin. *Food Hydrocoll.* **14**, 227–235 (2000). [https://doi.org/10.1016/S0268-005X\(00\)00007-2](https://doi.org/10.1016/S0268-005X(00)00007-2)
- 49 Moslemi, M.: Reviewing the recent advances in application of pectin for technical and health promotion purposes: From laboratory to market. *Carbohydr. Polym.* **254**, 117324 (2021). <https://doi.org/10.1016/j.carbpol.2020.117324>
- 50 Murphy, O.P., Vashishtha, M., Palanisamy, P., Kumar, K.V.: A review on the adsorption isotherms and design calculations for the optimization of adsorbent mass and contact time. *ACS Omega.* **8**, 17407–17430 (2023). <https://doi.org/10.1021/acsomega.2c08155>
- 51 Ngulube, T., Gumbo, J.R., Masindi, V., Maity, A.: Preparation and characterisation of high performing magnesite-halloysite nanocomposite and its application in the removal of methylene blue dye. *J. Mol. Struct.* **1184**, 389–399 (2019). <https://doi.org/10.1016/j.molstruc.2019.02.043>
- 52 Norouzi, S., Heidari, M., Alipour, V., Rahmanian, O., Fazlzadeh, M., Mohammadi-moghadam, F., Nourmoradi, H., Goudarzi, B., Dindarloo, K.: Preparation, characterization and Cr(VI) adsorption evaluation of NaOH-activated carbon produced from date press cake; an agro-industrial waste. *Bioresour. Technol.* (2018). <https://doi.org/10.1016/j.biortech.2018.02.106>
- 53 Nsom, M.V., Etape, E.P., Tendo, J.F., Namond, B.V., Chongwain, P.T., Yufanyi, M.D., William, N.: A green and facile approach for synthesis of Starch-Pectin magnetite nanoparticles and application by removal of methylene blue from textile effluent. *J. Nanomater.* **2019**, 1–12 (2019). <https://doi.org/10.1155/2019/4576135>
- 54 Oliveira, W.E., Franca, A.S., Oliveira, L.S., Rocha, S.D.: Untreated coffee husks as biosorbents for the removal of heavy metals from aqueous solutions. *J. Hazard. Mater.* **152**, 1073–1081 (2008). <https://doi.org/10.1016/j.jhazmat.2007.07.085>
- 55 Pal, P.: *Industry-Specific Water Treatment*. (2017)
- 56 Paulino, A.T., Belfiore, L.A., Kubota, L.T., Muniz, E.C., Almeida, V.C., Tambourgi, E.B.: Effect of magnetite on the adsorption behavior of Pb(II), Cd(II), and Cu(II) in chitosan-based hydrogels. *Desalination* **275**, 187–196 (2011). <https://doi.org/10.1016/j.desal.2011.02.056>
- 57 Paulino, A.T., Belfiore, L.A., Kubota, L.T., Muniz, E.C., Tambourgi, E.B.: Efficiency of hydrogels based on natural polysaccharides in the removal of Cd²⁺ ions from aqueous solutions. *Chem. Eng. J.* (2011). <https://doi.org/10.1016/j.cej.2010.12.037>
- 58 Paulino, A.T., Fajardo, A.R., Junior, A.P., Muniz, E.C., Tambourgi, E.B.: Two-step synthesis and properties of a magnetic-field-sensitive modified maltodextrin-based hydrogel. *Polym. Int.* **60**, 1324–1333 (2011). <https://doi.org/10.1002/pi.3084>
- 59 Paulino, A.T., Guilherme, M.R., Mattoso, L.H.C., Tambourgi, E.B.: Smart hydrogels based on modified gum arabic as a potential device for magnetic biomaterial. *Macromol. Chem. Phys.* (2010). <https://doi.org/10.1002/macp.200900657>
- 60 Paz, M.J., Serafini, S., Enzweiler, H., Visioli, L.J., Paulino, A.T.: Photodegradation of Emerging Pollutants Using Catalysts Supported in Organic and Inorganic Composite Materials. Presented at the (2022)
- 61 Paz, M.J., Vieira, T., Enzweiler, H., Paulino, A.T.: Chitosan/wood sawdust/magnetite composite membranes for the photodegradation of agrochemicals in water. *J. Environ. Chem. Eng.* **10**, 106967 (2022b). <https://doi.org/10.1016/j.jece.2021.106967>
- 62 Pereira, B.L.C., Carneiro, A.D.C.O., Carvalho, A.M.M.L., Colodette, J.L., Oliveira, A.C., Fontes, M.P.F.: Influence of Chemical Composition of Eucalyptus Wood on Gravimetric Yield and Charcoal Properties. *Bioresources* (2013). <https://doi.org/10.15376/biores.8.3.4574-4592>
- 63 Psaltou, S., Zouboulis, A.: Catalytic ozonation and membrane Contactors—A review concerning fouling occurrence and pollutant removal. *Water (Basel)*. **12**, 2964 (2020). <https://doi.org/10.3390/w12112964>
- 64 Radoor, S., Karayil, J., Parameswaranpillai, J., Siengchin, S.: Adsorption of methylene blue dye from aqueous solution by a novel PVA/CMC/halloysite nanoclay bio composite: Characterization, kinetics, isotherm and antibacterial properties. *J. Environ. Health Sci. Eng.* **18**, 1311–1327 (2020). <https://doi.org/10.1007/s40201-020-00549-x>

- 65 Rahman, M.M., Rimu, S.H.: Recent development in cellulose nanocrystal-based hydrogel for decolouration of methylene blue from aqueous solution: A review. *Int. J. Environ. Anal. Chem.* **102**, 6766–6783 (2022). <https://doi.org/10.1080/03067319.2020.1817424>
- 66 Redlich, O., Peterson, D.L.: A useful adsorption isotherm. *J. Phys. Chem.* **63**, 1024–1024 (1959). <https://doi.org/10.1021/j150576a611>
- 67 Rezvanian, M., Ahmad, N., Amin, M., Ng, M.C.I.: Optimization, characterization, and in vitro assessment of alginate-pectin ionic cross-linked hydrogel film for wound dressing applications. *Int. J. Biol. Macromol.* **97**, 131–140 (2017). <https://doi.org/10.1016/j.ijbiomac.2016.12.079>
- 68 Ribera-Pi, J., Badia-Fabregat, M., Arias, D., Gómez, V., Taberna, E., Sanz, J., Martínez-Lladó, X., Jubany, I.: Coagulation-flocculation and moving bed biofilm reactor as pre-treatment for water recycling in the petrochemical industry. *Sci. Total Environ.* **715**, 136800 (2020). <https://doi.org/10.1016/j.scitotenv.2020.136800>
- 69 Rojas, S., Horcajada, P.: Metal–Organic frameworks for the removal of emerging organic contaminants in water. *Chem. Rev.* **120**, 8378–8415 (2020). <https://doi.org/10.1021/acs.chemrev.9b00797>
- 70 Sahoo, T.R., Prelot, B.: Adsorption processes for the removal of contaminants from wastewater. In: Bonelli, B., Freyria, F.S., Rossetti, I., Sethi, R. (eds.) *Nanomaterials for the Detection and Removal of Wastewater Pollutants*, pp. 161–222. Elsevier (2020)
- 71 Sayed, E.T., Shehata, N., Abdelkareem, M.A., Atieh, M.A.: Recent progress in environmentally friendly bio-electrochemical devices for simultaneous water desalination and wastewater treatment. *Sci. Total Environ.* **748**, 141046 (2020). <https://doi.org/10.1016/j.scitotenv.2020.141046>
- 72 Sayed, N.S.M., Ahmed, A.S.A., Abdallah, M.H., Gouda, G.A.: ZnO@ activated carbon derived from wood sawdust as adsorbent for removal of Methyl red and Methyl orange from aqueous solutions. *Sci. Rep.* **14**, 5384 (2024). <https://doi.org/10.1038/s41598-024-55158-7>
- 73 Sharma, Y.C., Uma: Optimization of parameters for adsorption of methylene blue on a Low-Cost activated carbon. *J. Chem. Eng. Data.* **55**, 435–439 (2010). <https://doi.org/10.1021/je900408s>
- 74 Sips, R.: On the structure of a catalyst surface. *J. Chem. Phys.* **16**, 490–495 (1948). <https://doi.org/10.1063/1.1746922>
- 75 de Souza, A.G., Cesco, C.T., de Lima, G.F., Artifon, S.E.S., Rosa, D.S., Paulino, A.T.: Arabic gum-based composite hydrogels reinforced with Eucalyptus and Pinus residues for controlled phosphorus release. *Int. J. Biol. Macromol.* **140**, 33–42 (2019). <https://doi.org/10.1016/j.ijbiomac.2019.08.106>
- 76 Sun, G., Xu, X.: Sunflower stalks as adsorbents for color removal from textile wastewater. *Ind. Eng. Chem. Res.* **36**, 808–812 (1997). <https://doi.org/10.1021/ie9603833>
- 77 Tarekegn, M.M., Balakrishnan, R.M., Hiruy, A.M., Dekebo, A.H.: Removal of methylene blue dye using nano zerovalent iron, nanoclay and iron impregnated nanoclay– a comparative study. *RSC Adv.* **11**, 30109–30131 (2021). <https://doi.org/10.1039/D1R403918K>
- 78 Tischer, A.M., Ferreira, R.R., Ribeiro, J.G., dos Santos Rosa, D., Paulino, A.T.: Green synthesis of an advanced composite membrane for the purification of water contaminated with potentially toxic metals. *J. Water Process. Eng.* **61**, 105239 (2024). <https://doi.org/10.1016/j.jwpe.2024.105239>
- 79 Tripathy, S., Sahu, S., Patel, R.K., Panda, R.B., Kar, P.K.: Novel Fe₃O₄-Modified Biochar Derived from Citrus Bergamia Peel: A Green Synthesis Approach for Adsorptive Removal of Methylene Blue. *ChemistrySelect* (2022). <https://doi.org/10.1002/slct.202103595>
- 80 Vieira, T., Artifon, S.E.S., Cesco, C.T., Vilela, P.B., Becegato, V.A., Paulino, A.T.: Chitosan-based hydrogels for the sorption of metals and dyes in water: Isothermal, kinetic, and thermodynamic evaluations. *Colloid Polym. Sci.* **299**, 649–662 (2021). <https://doi.org/10.1007/s00396-020-04786-2>
- 81 Vieira, T., Becegato, V.A., Paulino, A.T.: Equilibrium Isotherms, Kinetics, and Thermodynamics of the Adsorption of 2,4-Dichlorophenoxyacetic Acid to Chitosan-Based Hydrogels. *Water Air Soil. Pollut.* (2021). <https://doi.org/10.1007/s11270-021-05021-6>
- 82 Vievard, J., Alem, A., Pantet, A., Ahfir, N.-D., Arellano-Sánchez, M.G., Devouge-Boyer, C., Mignot, M.: Bio-Based adsorption as ecofriendly method for wastewater decontamination: A review. *Toxics.* **11**, 404 (2023). <https://doi.org/10.3390/toxics11050404>
- 83 Vilela, P.B., Dalalibera, A., Duminelli, E.C., Becegato, V.A., Paulino, A.T.: Adsorption and removal of chromium (VI) contained in aqueous solutions using a chitosan-based hydrogel. *Environ. Sci. Pollut. Res.* **26**, 28481–28489 (2019). <https://doi.org/10.1007/s11356-018-3208-3>
- 84 Vilela, P.B., Matias, C.A., Dalalibera, A., Becegato, V.A., Paulino, A.T.: Polyacrylic acid-based and chitosan-based hydrogels for adsorption of cadmium: Equilibrium isotherm, kinetic and thermodynamic studies. *J. Environ. Chem. Eng.* **7**, 103327 (2019). <https://doi.org/10.1016/j.jece.2019.103327>
- 85 Vinhal-Freitas, I., Maldonado, A., Alvarenga, C., Camargo, R., Wendling, B.: Adsorção E Dessorção De Metais No Solo E Coeficientes De Isotermas De Freundlich E Langmuir. *Semantic Scholar* (2010)
- 86 Voragen, F., Beldman, G., Schools, H.: Chemistry and enzymology of pectins. In: McCleary, B.V., Prosky, L. (eds.) *Advanced Dietary Fibre Technology*, pp. 379–398. Wiley (2000)
- 87 Wang, J., Guo, X.: Adsorption kinetic models: Physical meanings, applications, and solving methods. *J. Hazard. Mater.* **390**, 122156 (2020). <https://doi.org/10.1016/j.jhazmat.2020.122156>
- 88 Wang, Q., Ju, J., Tan, Y., Hao, L., Ma, Y., Wu, Y., Zhang, H., Xia, Y., Sui, K.: Controlled synthesis of sodium alginate electrospun nanofiber membranes for multi-occasion adsorption and separation of methylene blue. *Carbohydr. Polym.* **205**, 125–134 (2019). <https://doi.org/10.1016/j.carbpol.2018.10.023>
- 89 Weber, W.J.: Adsorption processes. *Pure Appl. Chem.* **37**, 375–392 (1974). <https://doi.org/10.1351/pac197437030375>
- 90 Zactiti, E.M., Kieckbusch, T.G.: Potassium sorbate permeability in biodegradable alginate films: Effect of the antimicrobial agent concentration and crosslinking degree. *J. Food Eng.* **77**, 462–467 (2006). <https://doi.org/10.1016/j.jfoodeng.2005.07.015>
- 91 Zonatto, F., Muniz, E.C., Tambourgi, E.B., Paulino, A.T.: Adsorption and controlled release of potassium, phosphate and ammonia from modified Arabic gum-based hydrogel. *Int. J. Biol. Macromol.* **105**, 363–369 (2017). <https://doi.org/10.1016/j.ijbiomac.2017.07.051>

Publisher's note Springer Nature remains neutral with regard to jurisdictional claims in published maps and institutional affiliations.

Springer Nature or its licensor (e.g. a society or other partner) holds exclusive rights to this article under a publishing agreement with the author(s) or other rightsholder(s); author self-archiving of the accepted manuscript version of this article is solely governed by the terms of such publishing agreement and applicable law.



Innovative pectin-based composite membranes: preparation, characterization and color pollutant separation from water

Ana Maria Tischer^{1,2} · Rafaela Reis Ferreira³ · Ionara de Fátima Ferreira¹ · Derval dos Santos Rosa³ · Alexandre Tadeu Paulino⁴

Received: 7 December 2024 / Revised: 22 February 2025 / Accepted: 3 March 2025 / Published online: 22 March 2025
© The Author(s), under exclusive licence to Springer Science+Business Media, LLC, part of Springer Nature 2025

Abstract

The aim of the present study was to synthesise and characterise innovative pectin/pine sawdust/magnetite composite membranes as potential sorbents for the purification of water contaminated with color pollutants. Methylene blue (MB) was employed as the pollutant model for sorption. Fourier-transform infrared spectroscopy (FTIR) was performed to analyse the formation of crosslinked membrane chains and confirm the sorption processes of the dye molecules. Thermogravimetry (TGA) and derivative thermogravimetry (DTG) indicated that the polymer matrix is stable at low temperatures and begins to degrade at temperatures above 250 °C, whereas X-Ray diffraction (XRD) patterns confirmed crystalline and amorphous regions. Mechanical assays confirmed an increase in the modulus of elasticity and tensile strength of the biopolymer membranes after incorporating PS. Moreover, a reduction in mechanical deformation was found after the incorporation of Fe₃O₄. Pollutant separation experiments were performed in a pH range from 3.0 to 10.0 with initial pollutant concentrations of 5 to 25 mg L⁻¹ and separation times from 1 to 3050 min. Higher sorption capacity was found after 1800 min with an initial pollutant concentration of 20 mg L⁻¹ and pH 10.0. The best isotherm fit was found using the Redlich-Peterson model, with fits using the Langmuir model depending on the experimental conditions. The best kinetic fit was found using the pseudo-first-order or pseudo-second-order models at pH 3.0, with differences in more alkaline solutions. The pectin-based composite membranes proved to be viable options for the purification of wastewater from industry using dye and could also be tested for the photodegradation of organic pollutants in water due to the presence of Fe₃O₄.

Keywords Membrane · Sorption · Separation · Pollutant · Color compounds · Composite

1 Introduction

The severe shortage of drinking water is one of the most significant global challenges of the 21st century [43, 71]. According to a World Health Organization (WHO) report, more than 50% of the world's population will live in areas with certain water scarcity by the year 2025, which constitutes a growing concern [9]. Moreover, population growth translates to high water consumption, and industrial/technological sectors release toxic compounds into the environment, such as dyes, metalloids (species with intermediate properties between typical metal and non-metal), and metals, such as arsenic and antimony [19], making access to clean water more difficult. Given this scenario, there is considerable worldwide concern about water quality and a need to develop strategies to remove pollutants from wastewater [11].

✉ Alexandre Tadeu Paulino
alexandre.paulino@udesc.br

¹ Department of Food and Chemical Engineering, Santa Catarina State University, Br 282, Km 574, Linha Santa Terezinha, Pinhalzinho, SC 89870-000, Brazil

² Department of Chemistry, Materials and Chemical Engineering “Giulio Natta” (DCMC), Politecnico di Milano, Piazza Leonardo da Vinci 32, Milan 20133, Italy

³ Engineering, Modeling and Applied Social Sciences Center (CECS), Federal University of ABC, Av dos Estados, 5001, Bairro Bangu, Santo André, SP 09210-580, Brazil

⁴ Department of Chemistry, Santa Catarina State University, Rua Paulo Malschitzki, 200, Zona Industrial Norte, Joinville, SC 89219-710, Brazil

Due to operational limitations, conventional wastewater treatment methods are inefficient in removing many types of organic pollutants from aqueous solutions [69]. Thus, the scientific and industrial communities have made efforts to develop alternative wastewater treatment methods and ensure the quality of the water consumed by humans and animals. Currently, the main conventional wastewater treatment methods are coagulation, flocculation [68], ion exchange [41], flotation [44], biological processes [2], and sorption [65]. Limitations for the large-scale applications of these methods include the high cost, low efficiency, the production of secondary waste, and environmental impacts [11]. Filtration processes using natural polysaccharide-based membranes or photodegradation processes using membranes containing photocatalysts are viable options for the treatment of wastewater with less environmental impact compared to conventional methods [60, 61]. Wastewater treatment with the use of membranes offers the advantages of energy efficiency, low cost, easy maintenance, compact construction, and high separation efficiency [63]. However, synthetic polymers, such as polysulfone, polyimide, nylon, polyacrylonitrile, and polyvinylidene fluoride [31, 43], are not renewable, biodegradable materials and generate secondary pollution after real-world applications [8]. Pectin-based membranes could overcome this problem, minimizing the environmental impact due to the fact that pectin is an environmentally friendly biopolymer [4].

Pectin is a structural acidic heteropolysaccharide obtained from the methylation of polygalacturonic acid, which has high gelation and expansion capacity. This polysaccharide is obtained from citrus peel extract and is widely employed in the food industry [29]. Pectin-based membranes are also effective at sorbing dyes and metal ions due to the single -COOH bonding groups and single -OH bonding groups [36]. Membranes were prepared by electrospinning with polyvinyl acetate as a supporting polymer and starch in a green solvent (water) and used to remove methylene blue (MB) from aqueous media. Due to its high stability (based on the tensile test), the manufactured membrane could be used as a filter for the rapid separation of MB (cationic dye) and methyl orange (anionic dye) [47]. A poly(vinyl alcohol)/carboxymethyl cellulose/halloysite membrane was developed for the effective sorption of cationic dyes. This membrane demonstrated excellent removal efficiency (99.5%) for MB under ideal conditions (nanoclay 6 wt %, initial dye concentration of 10 ppm, contact time of 240 min, pH 10, and temperature of 30 °C) [64]. It is important to highlight that pectin over other bio-based polymeric materials in dye removal is highly competitive [53]. Its high sorption efficiency, ease of process, and cost-effectiveness make it an advantageous choice [46]. Furthermore, according to Tischer et al., [78] its eco-friendly nature, derived from

renewable natural sources, and its capacity for extended useful life and recyclability highlight it as a sustainable solution for environmental pollution challenges [78].

The crosslinking of biopolymer-based membrane chains is an approach employed to improve the physical properties and mechanical stability of the membrane with the aim of preventing the disintegration of the polymeric matrix in aqueous media. The crosslinking of pectin with calcium ions leads to the formation of strong membrane chains that can absorb large amounts of water without dissolving [67]. Membranes crosslinked with calcium ions are efficiently synthesized using pectin with a low degree of esterification (DE) (lower than 50%), as pectin with esterification higher than 50% does not have enough acid groups to form a gel or precipitate with calcium ions [48]. Low DE pectin can be produced by de-esterification using ammonia in an alcoholic medium. The resulting pectin has amide groups that play an important role in gel formation, contributing to the texture and tensile strength of the final biomembrane [5]. Membranes must have good stability and reusability. Regeneration capacity is an important aspect to evaluate in reusing membranes in sorption processes. Membrane reutilization in different processes can be explored through sorption-desorption recycling experiments [88].

Composite membranes prepared by incorporating sorbent inorganic or organic nanomaterials into the membrane structure are alternative solid supports for removing pollutants from water [36]. For instance, the incorporation of natural nanofiber containing a high content of lignin, cellulose, and hemicellulose favors the crosslink density, pore size, sorption capacity, and mechanical resistance of the final biomembrane [75] due to higher reactive surface area [11], whereas the incorporation of metal oxide nanoparticles, such as magnetite (Fe₃O₄), favors the application of the final biomembrane in photodegradation studies [25].

In this study, we developed novel pectin-based composite membranes containing pine sawdust (PS) and Fe₃O₄, offering an innovative approach for removing pollutants from the wastewater of industries that employ dyes. PS was chosen because it is an abundant, low-cost, biodegradable byproduct with a large surface area, which enhances the chemical sorption capacity [20]. Fe₃O₄ was chosen because it imparts magnetic properties to the composite biomaterial, facilitating membrane recovery and reuse, in addition to aiding in pollutant removal via sorption [3]. To date, no author has carried out a study with this specific dye system, further emphasizing our research's uniqueness and originality. The MB pollutant model was used to evaluate the effectiveness of the membranes. We evaluated membranes' physicochemical, thermal, and mechanical properties with different PS/Fe₃O₄ contents. Furthermore, we consider the possibility of applying these membranes in the photodegradation

of pollutants in water due to the presence of Fe_3O_4 in their polymeric structure. The results indicate that composite membranes have the potential to be effective biomaterials for the purification of industrial wastewater contaminated with dyes. This promising approach opens new perspectives for developing sustainable and efficient solutions for the remediation of industrial effluents.

2 Experimental

2.1 Material

Citrus pectin (DE ranging from 70 to 85%) was purchased from Biotec[®], Brazil. PS was obtained from wood pallets used to transport industrial packaging. The preparation of PS (particle sizes around 850 μm) was performed following a method described elsewhere [36]. Fe_3O_4 with an average particle size of 50 nm were purchased from Fisher Scientific[®], USA. Calcium chloride dihydrate and ammonium hydroxide were purchased from Dinâmica[®], Brazil. Ethyl alcohol 99.5% (v/v) was purchased from inética[®], Brazil. MB ($\text{C}_{16}\text{H}_{18}\text{N}_3\text{SC}_{1.3}\text{H}_2\text{O}$) was purchased from LabSynth[®], Brazil. Glycerol and other chemical reagents were purchased from Sigma-Aldrich, Brazil.

2.2 De-esterification of pectin

2.0 g of raw pectin was dispersed in 100 mL of 65% (v/v) ethanol containing 2.3 g of ammonium hydroxide. The mixture was placed in a closed flask and left under magnetic stirring (IKA[®] C-Mag) at 900 rpm for 180 min at 25 °C. The solid/liquid mixture was then filtered with a filter paper (Whatman[®]) and the remaining solid residue was washed with 65% (v/v) ethanol to remove free ammonia. This solid was washed again with 99.5% (v/v) ethanol and dried in a vacuum desiccator (Sigma-Aldrich[®] Z740644) for 24 h at room temperature. The dried pectin was then ground using a knife mill (IKA[®] A11) prior to characterization and use.

2.3 Determination of degree of esterification

Potentiometric titration determined the DE of commercial pectin and de-esterified pectin. For such, 2.0 g of pectin was dispersed in 20 mL of distilled water. This solution was left under mechanical stirring at 900 rpm for 2 h. The pectin solution was then titrated with an aqueous solution of sodium hydroxide (NaOH) 0.1 mol L^{-1} in the presence of phenolphthalein as the acid-base indicator, and the results were recorded as initial titration (T_i). To saponify the esterified carboxyl groups of the polymer, 10 mL of an aqueous solution of NaOH 0.1 mol L^{-1} was added to the neutralized

pectin under constant stirring at 900 rpm for 2 h. Following saponification, 10 mL of an aqueous solution of hydrochloric acid (HCl) 0.1 mol L^{-1} was added, and the excess was titrated with an aqueous solution of NaOH 0.1 mol L^{-1} . The NaOH volume spent in this titration (T_f) and the number of esterified carboxyl groups was determined using Eq. (1):

$$\text{DE} (\%) = \frac{T_f}{T_i + T_f} \times 100 \quad (1)$$

in which DE is the degree of esterification, T_i is the NaOH volume used in the initial titration, and T_f is the NaOH volume spent in the final titration.

2.4 Membrane preparation

Esterified pectin-based membranes were synthesized, as shown in Fig. 1, following a method described elsewhere [90] with adaptation for pectin. Briefly, 6 g of esterified pectin was dissolved in 400 mL of distilled water. Next, 3.6 g of glycerol and known proportions of PS (1, 3, 5, or 10% w/w) were added. This mixture was heated to 70 °C. Pre-crosslinking was performed by adding 30 mL of a 1.0% CaCl_2 (w/v) solution under constant stirring at a flowrate of 1 mL min^{-1} manually controlled using a micropipette. Pre-crosslinking was conducted for 90 min. Known contents of Fe_3O_4 (1, 5, 10, or 15% w/w) were then added to the still-hot pre-crosslinked solution under constant magnetic stirring, and the mixture was transferred to Petri dishes. These systems were placed in a forced-air circulation oven (Famem[®] Orion 515) at 40 °C for 20 h. The formed membranes were immersed in 50 mL of 70% (v/v) ethanol solution containing 5% CaCl_2 (w/v) for 30 min for complete crosslinking, washed with distilled water, and dried in a forced-air circulation oven at 25 °C for 5 h. All membranes were stored in a vacuum desiccator for 72 h at 25 °C and low relative humidity. Different membrane compositions (Table 1) were studied to achieve satisfactory mechanical resistance for application in water and wastewater treatment.

2.5 Characterization of membranes

2.5.1 Fourier-transform infrared spectroscopy (FTIR)

FTIR spectra were recorded using a PerkinElmer Frontier spectrometer (Spectrum 100, Perkin Elmer[®], Inc. Massachusetts, USA) with attenuated total reflectance (ATR) operating in the wavenumber range from 500 to 4000 cm^{-1} with 32 scans per minute and resolution of 4 cm^{-1} .

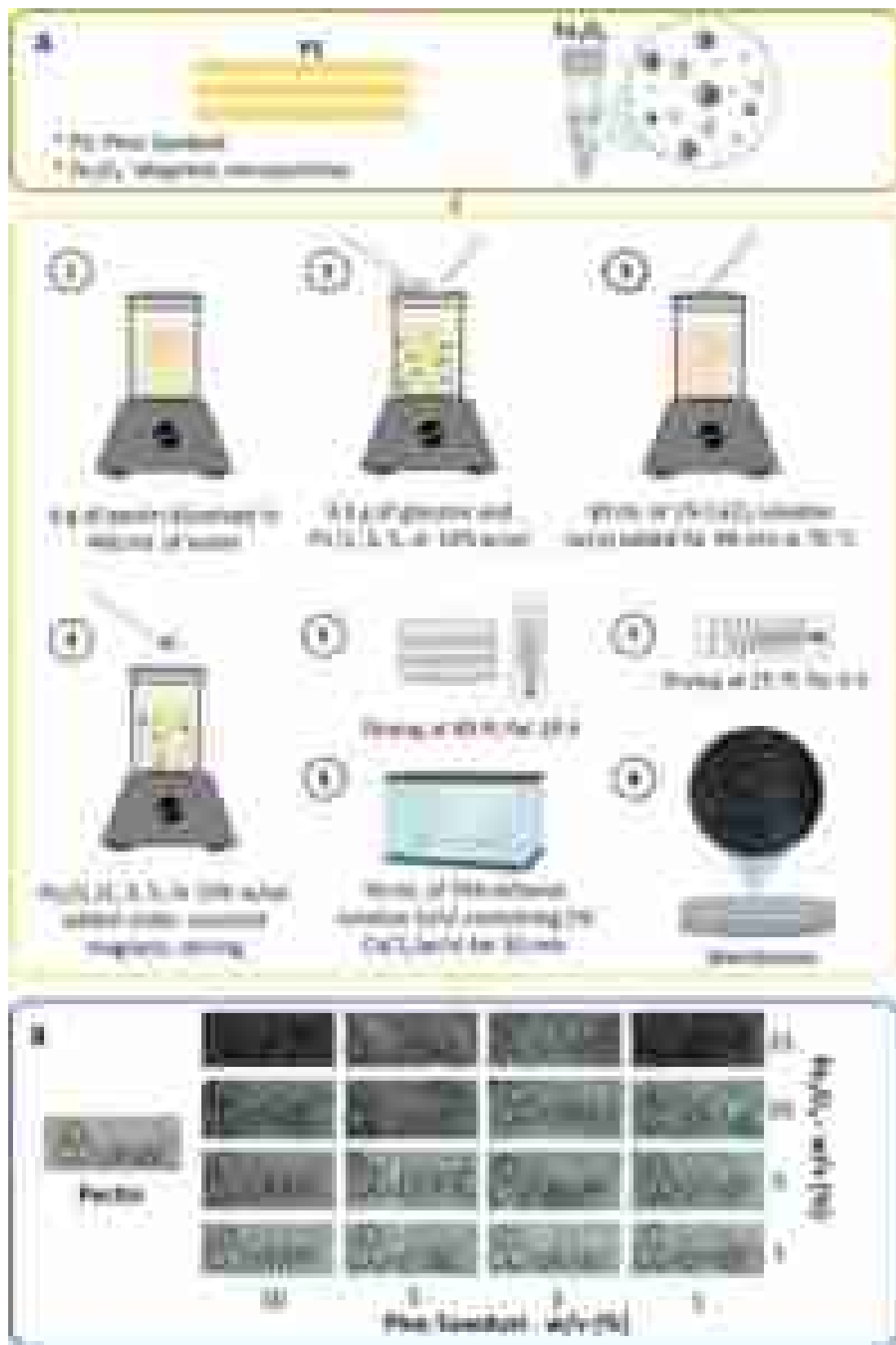


Fig. 1 Illustrative scheme of synthesis method for pectin-based composite membranes

Table 1 PS and Fe₃O₄ contents in different pectin-based membranes

Samples	PS (%)	Fe ₃ O ₄ (%)
ME0	0	0
ME1	1	1
ME2	1	5
ME3	1	10
ME4	1	15
ME5	3	1
ME6	3	5
ME7	3	10
ME8	3	15
ME9	5	1
ME10	5	5
ME11	5	10
ME12	5	15
ME13	10	1
ME14	10	5
ME15	10	10
ME16	10	15

2.5.2 Thermogravimetric analysis (TGA)

Thermal stability was tested using the PerkinElmer STA 6000 equipment. All samples were placed in alumina pans and heated from 30 to 600 °C at a rate of 10 °C min⁻¹ in a nitrogen atmosphere (20 mL min⁻¹).

2.5.3 Mechanical assays

Tensile strength tests were performed using the Norwood Instron 3367 (Instron Corporation, Norwood, MA) equipment at room temperature following the ASTM D638-14 standard. For such, a 50-N load cell, test speed of 25 mm min⁻¹, and film thickness of 0.15 ± 0.05 mm were employed.

2.5.4 X-ray diffraction (XRD)

XRD measurements were performed using a D8 Focus diffractometer (Bruker AXS Advanced X-ray Solutions GmbH, Karlsruhe, Germany), operating at 40 kV and 40 mA. Monochromatic CuKα1 radiation (λ = 1.54056 Å) at a step width of 0.01° and a counting time of 100 s at each 0.5°, from 2θ = 10–70°, were employed.

2.5.5 Degree of swelling (DS)

The DS was determined by immersing 150 mg of dried membrane pieces in 100 mL of distilled or drinking water at room temperature. The DS (g of water per g of the dried membrane [g g⁻¹]) was calculated using Eq. (2):

$$DS = \frac{m_s - m_d}{m_d} \quad (2)$$

in which *m_s* and *m_d* are the masses of the swollen and dried membranes.

2.6 Separation assays

MB separation experiments were performed by immersing 150 mg of dried membrane pieces in flasks containing 50 mL of dye solution with different initial concentrations (5, 10, 15, 20, and 25 mg L⁻¹) and different pH values (3.0, 4.0, 6.0, 8.0, and 10.0). Similar experiments were performed with pure Fe₃O₄ employed in the membrane synthesis, to evaluate the effects of magnetic material on the pollutant sorption. The remaining dye concentration in the solutions at specific time intervals was determined by UV-vis spectrophotometry (Spectroquant® Prove 600, Merck) at a wavelength of 664 nm. The dye sorption capacity (*q_e*, mg g⁻¹) of the membranes was calculated using Eq. (3):

$$q_e = \frac{C_0 - C_e}{m} \times V \quad (3)$$

in which *m* (g) is the mass of the dried membrane, *C₀* and *C_e* (mg L⁻¹) are the initial and equilibrium concentrations of dye in the solution, and *V* (L) is the volume of the solution.

2.7 Sorption kinetics

MB sorption kinetics were studied using a dye concentration of 20 mg L⁻¹ and a membrane mass of 150 mg. The pseudo-first-order kinetic model was employed to determine whether the diffusion mechanism is dependent on dye concentration, whereas the pseudo-second-order kinetic model was employed to determine the occurrence of dependence between the amount of dye sorbed on the membrane surface and the amount of dye at equilibrium [87]. These models were selected due to their widespread acceptance and ability to provide insights into sorption mechanisms [30, 39]. The parameters of the non-linear pseudo-first and pseudo-second-order kinetic models were determined by Eqs. (4) and (5), respectively:

$$q_t = q_e(1 - e^{-k_1 t}) \quad (4)$$

$$q_t = \frac{q_e^2 k_2 t}{1 + q_e k_2 t} \quad (5)$$

in which, *q_e* (mg g⁻¹) is the sorption capacity of the membrane at equilibrium, *q_t* (mg g⁻¹) is the sorption capacity of the membrane at time *t* (min), *k₁* and *k₂* are the rate constants (g mg⁻¹ min⁻¹).

2.8 Sorption isotherms

The non-linear Langmuir, Freundlich, Sips, and Redlich-Peterson isotherm models were employed to predict the types of interactions between the membrane and dye. According to the Langmuir model [38, 85], the sorption mechanism occurs through the formation of a monolayer and ideal sorbate distribution on the sorbent surface. In this case, active sorption sites have equivalent energies on the sorbent surfaces. The non-linear Langmuir isotherm model is represented by Eq. (6):

$$q_e = \frac{q_m K_L C_e}{1 + K_L C_e} \quad (6)$$

in which, K_L ($L \text{ mg}^{-1}$) is the sorption/desorption rate, C_e (mg L^{-1}) is the equilibrium sorbate concentration, q_m (mg g^{-1}) is the maximum sorption capacity of the sorbent, and q_e (mg g^{-1}) is the equilibrium sorption capacity of the sorbent.

The non-linear Freundlich isotherm model [21, 85] is employed for describing sorption processes with multilayer formation and the non-uniform distribution of sorbates on sorbent surfaces. In this case, the sorption sites in the sorbent structures have different affinities. The non-linear Freundlich isotherm model is represented by Eq. (7):

$$q_e = K_F C_e^{1/n} \quad (7)$$

in which, K_F ($L^{1/n} \text{ mg}^{1-1/n} \text{ g}^{-1}$) is the Freundlich sorption constant, n is the number of active sites in/on sorbent structures, C_e (mg L^{-1}) is the equilibrium sorbate concentration, and q_e (mg g^{-1}) is the equilibrium sorption capacity.

The non-linear Sips isotherm model [74] is employed to overcome the limitations of the Langmuir and Freundlich isotherm models. This isotherm model is represented by Eq. (8):

$$q_e = \frac{q_{ms} K_s C_e^{n_s}}{1 + K_s C_e^{n_s}} \quad (8)$$

in which, q_{ms} (mg g^{-1}) is the maximum sorption capacity of the sorbate, K_s ($L^{n_s} \text{ mg}^{-n_s}$), n_s is Sips constant, and q_e (mg g^{-1}) is the equilibrium sorption capacity of the sorbent.

The non-linear Redlich-Peterson isotherm model [66] assumes that monolayer formation on sorbent surfaces and multisite interactions take place simultaneously during the sorption process. Thus, this model exhibits properties of the Langmuir and Freundlich models. The non-linear Redlich-Peterson isotherm model is represented by Eq. (9):

$$q_e = \frac{A C_e}{1 + B C_e^g} \quad (9)$$

in which, A ($L \text{ mg}^{-1}$) and B ($L \text{ mg}^{-1}$)^g are Redlich-Peterson constants, g is the Redlich-Peterson exponent, C_e (mg L^{-1}) is the equilibrium sorbate concentration, and q_e (mg g^{-1}) is the sorption capacity of the sorbent.

2.9 Error analysis

The reliability of the dye sorption results in the membrane structures were evaluated using the chi-square statistical test (χ^2), and coefficient of determination (R^2) [56, 57]. The best isotherm and kinetic fits were estimated by considering the lowest χ^2 value and highest R^2 value. The two error functions are represented by Eqs. (10) and (11), respectively:

$$\chi^2 = \sum_{i=1}^n \frac{(q_{e,\text{exp}} - q_{e,p})^2}{q_{e,p}} \quad (10)$$

$$R^2 = 1 - \frac{\sum (q_{e,\text{exp}} - q_{e,p})^2}{\sum (q_{e,\text{exp}} - q_{e,m})^2} \quad (11)$$

in which, $q_{e,\text{exp}}$ (mg g^{-1}) is the experimental equilibrium sorption capacity and $q_{e,p}$ (mg g^{-1}) is the equilibrium sorption capacity predicted from the model equations. $q_{e,m}$ is the average of $q_{e,\text{exp}}$.

3 Results and discussion

3.1 Membrane characterization

3.1.1 DE

The DE of the commercial pectin obtained by titration was 82.73%, confirming that this polysaccharide has high esterification ($DE > 50\%$). Hence, it does not have enough acid groups for crosslinking with calcium ions and solubilizes in water, hindering membrane/gel formation [48]. The yield of the de-esterification reaction was 66% with a DE of 46.33%, indicating a low DE polysaccharide. The de-esterified pectin was efficiently crosslinked in the presence of calcium ions during membrane synthesis, decreasing its solubility in water. This increased the mechanical and thermal resistance of the membranes, as observed in the mechanical and thermal assays.

3.1.2 FTIR

FTIR spectra recorded before (Fe_3O_4) and after ($\text{Fe}_3\text{O}_4 + \text{MB}$) sorption studies of MB in Fe_3O_4 can be seen in Fig. 2. Overall, Fe_3O_4 characteristic bands tend to appear at ~ 3000 , 1625, 1500, 1366, 1190, and 627 cm^{-1} , which are

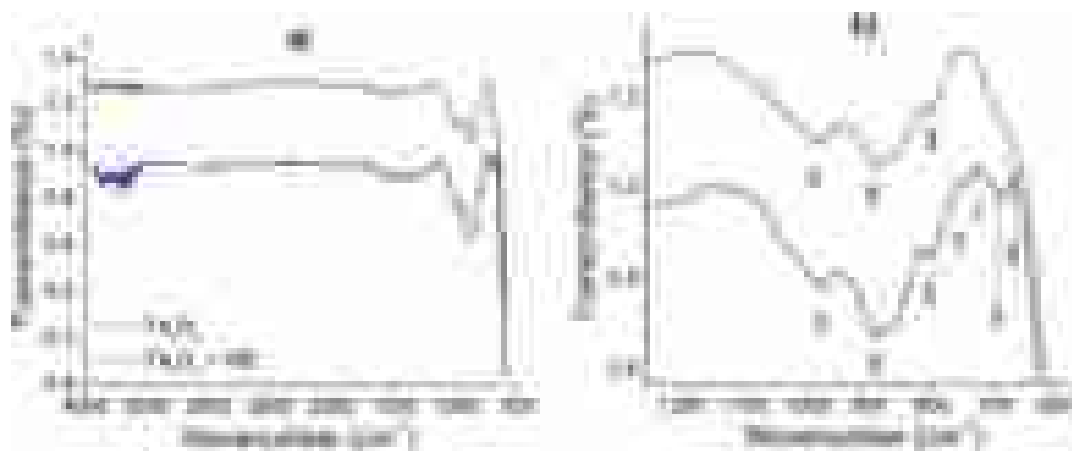


Fig. 2 FTIR spectra recorded before (Fe_3O_4) and after ($\text{Fe}_3\text{O}_4 + \text{MB}$) sorption studies of MB in pure Fe_3O_4

related to O–H or N–H, C=O, C=C, C–N, C–O or C–N and Fe–O groups, respectively [22]. By observing all experimental results at wavelengths between 600 and 1200 cm^{-1} (Fig. 2b), it is possible to identify small band shifts after sorption studies of MB, with the appearance of signals at ~ 784 , 721, 693, and 668 cm^{-1} . Moreover, pure Fe_3O_4 peaks shifted from 984.4 to 973.4, indicating intermolecular interaction between MB and Fe_3O_4 during sorption. This interaction was confirmed by the sorption capacity discussed throughout this manuscript.

Absorption bands found at ~ 3200 and 2950 cm^{-1} in Fig. 3 were associated with OH and C–H group stretching vibrations in the membrane structure [62]. The absorption band at 1730 cm^{-1} corresponded to carbonyl group stretching (C=O) from methyl ester and COOH contained in the pectin molecules [15]. The absorption band at 1149 cm^{-1} was assigned to COC vibrations from glycosidic rings, which are commonly found in polysaccharide macromolecular structures. The absorption bands at 1045 and 1076 cm^{-1} were assigned to the presence of arabinose, xylose, and galactose in the pectin-based polymer chains [12]. As pectin is a natural polysaccharide found in the walls of plant cells, it has homogalacturonan (HG), xylogalacturonan, rhamnogalacturonan type I (RGI), and rhamnogalacturonan type II (RGII) units [86]. This explains the strong absorption bands at 1022, 1106, and 1149 cm^{-1} due to CC, CO, CCH, and OCH group vibrations [13]. The absorption bands at 830 and 763 cm^{-1} suggest efficient crosslinking between pectin and calcium [15].

Slight shifts were observed in the FTIR spectra after adding PS and Fe_3O_4 to the pectin-based membrane structure due probably to disturbances taking place during the formation of new chemical bonds. An absorption band that appeared at 542 cm^{-1} was assigned to stretching vibrations due to presence of tetrahedral and octahedral Fe–O covalent bonds from Fe_3O_4 [1]. Moreover, PS increased the free

hydroxyl peak intensities between 3200 and 2950 cm^{-1} due to presence of water bound to either OH groups of the pectin or Fe_3O_4 molecules [1]. This behavior was also observed in the absorption band at ~ 1640 cm^{-1} . The slight influence of PS and Fe_3O_4 incorporated into the membrane chains was confirmed by recording non-bulky curves at wavenumbers ranging from 1700 to 1550 cm^{-1} , as shown in Figs. 1, 2, 3 and 4, S 5 (Supplementary Material). Overall, incorporating PS and Fe_3O_4 in the pectin-based polymer matrices altered the OH vibration intensities, resulting in modifications on the surfaces of lignocellulosic species. This, in turn, alters membrane hydrophobicity, pollutant sorption capacity, and electrical conductivity [40].

3.1.3 TGA and derivative thermogravimetry (DTG)

Thermal degradation of the membrane occurred in two main stages of mass loss (Fig. 4) – one from 30 to 100 $^{\circ}\text{C}$ due to the evaporation of physically adsorbed water [40] and the second from 250 to 300 $^{\circ}\text{C}$ due to the degradation of pectin macromolecules [17]. The pectin-based membrane thermogram (ME0) revealed that thermal degradation of 10% of the membrane chain ($T_{10\%}$, also the onset temperature) occurred at 97.2 $^{\circ}\text{C}$. The onset temperature after the addition of PS [1, 3, 5, and 10% (w/w)] and Fe_3O_4 [1, 5, 10, and 15% (w/w)] increased ~ 10 $^{\circ}\text{C}$ compared to the thermogram of the pectin-based membrane, indicating an increase in thermal stability after the anchoring of organic and inorganic species in the polymeric matrix. Similar results have previously been found for pectin-based hydrogels containing PS [15] and Fe_3O_4 [36]. A gain of ~ 20 $^{\circ}\text{C}$ was determined for T_{max} in the composite membranes, confirming the increase in thermal stability (Table 2). This new thermal pattern suggests that PS and Fe_3O_4 participate in crosslinking during membrane formation. The composite membrane's thermal

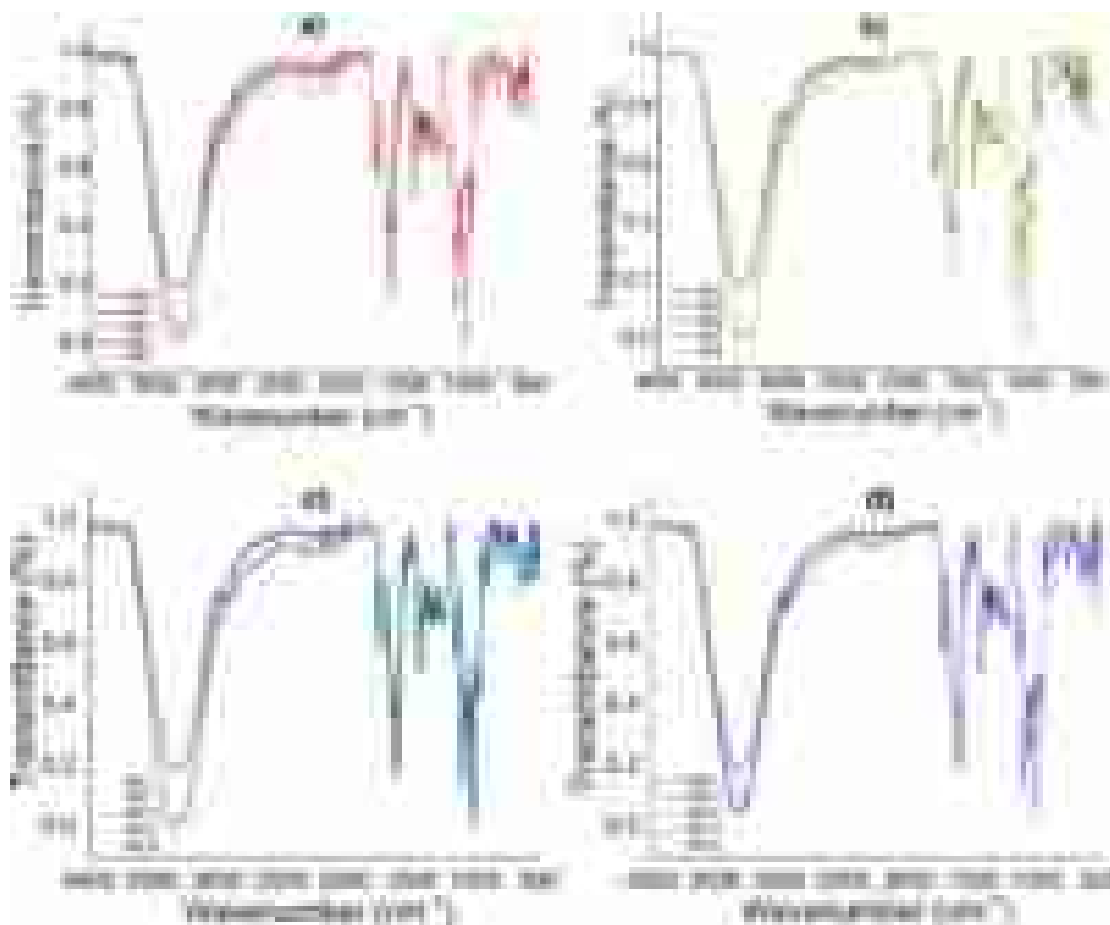


Fig. 3 **a** FTIR spectra for pectin-based membrane (ME0) and composite membranes containing 1% PS plus 1 (ME1), 5 (ME2), 10 (ME3), and 15% (w/w) (ME4) Fe_3O_4 . **b** FTIR spectra for composite membranes containing 3% PS plus 1 (ME5), 5 (ME6), 10 (ME7), and 15% (w/w) (ME8) Fe_3O_4 . **c** FTIR spectra for composite membranes con-

taining 5% PS plus 1 (ME9), 5 (ME10), 10 (ME11), and 15% (w/w) (ME12) Fe_3O_4 . **d** FTIR spectra for composite membranes containing 10% PS plus 1 (ME13), 5 (ME14), 10 (ME15), and 15% (w/w) (ME16) Fe_3O_4

properties are excellent for water and wastewater treatment applications.

3.1.4 Mechanical assays

The ME5 and ME9 membranes had tensile strengths of 126.7 and 337.2 MPa, whereas maximum deformations were 87.8 and 92.4%, respectively (Table 2; Fig. 5). Gains in the elasticity modulus were also found in these membranes, indicating that PS occupies empty spaces between pectin and Fe_3O_4 in the membrane structure, improving the filler dispersion capacity. The gains in E and σ_{\max} (Table 2) suggest possible physiochemical interactions among hydroxyl groups of the pectin macromolecules and active sites of the PS fibers. The formation of a percolated polymer chain is responsible for increasing the rigidity of the membrane [11, 15]. Higher Fe_3O_4 contents decreased the mechanical deformation of the polysaccharide membranes due possibly to nanoparticle aggregation, altering physiochemical

interaction intensity, particle size, particle distribution, and particle dispersion in the polymer chain. An improper membrane preparation method favors nanoparticle agglomeration, contributing to the rupture of the material structure [26]. Thus, inorganic nanoparticle dispersion in polymer networks is particularly important in improving mechanical resistance. This property is essential for applying polymer membranes in water filtration processes, mainly when the aim is to reuse the polymer material in successive filtration cycles with high water flow [11].

3.1.5 XRD

The crystallinity of Fe_3O_4 after sorption of MB ($\text{Fe}_3\text{O}_4 + \text{MB}$), and membranes was evaluated by X-ray diffractograms as shown in Fig. 6. All the crystalline planes [(220), (311), (400), (422), (511), (440)] in the 2θ values equal to 30.3, 35.6, 43.5, 53.5, 57.4, and 63.07° were assigned to the structure of Fe_3O_4 [79]. Even after the sorption of MB, all six

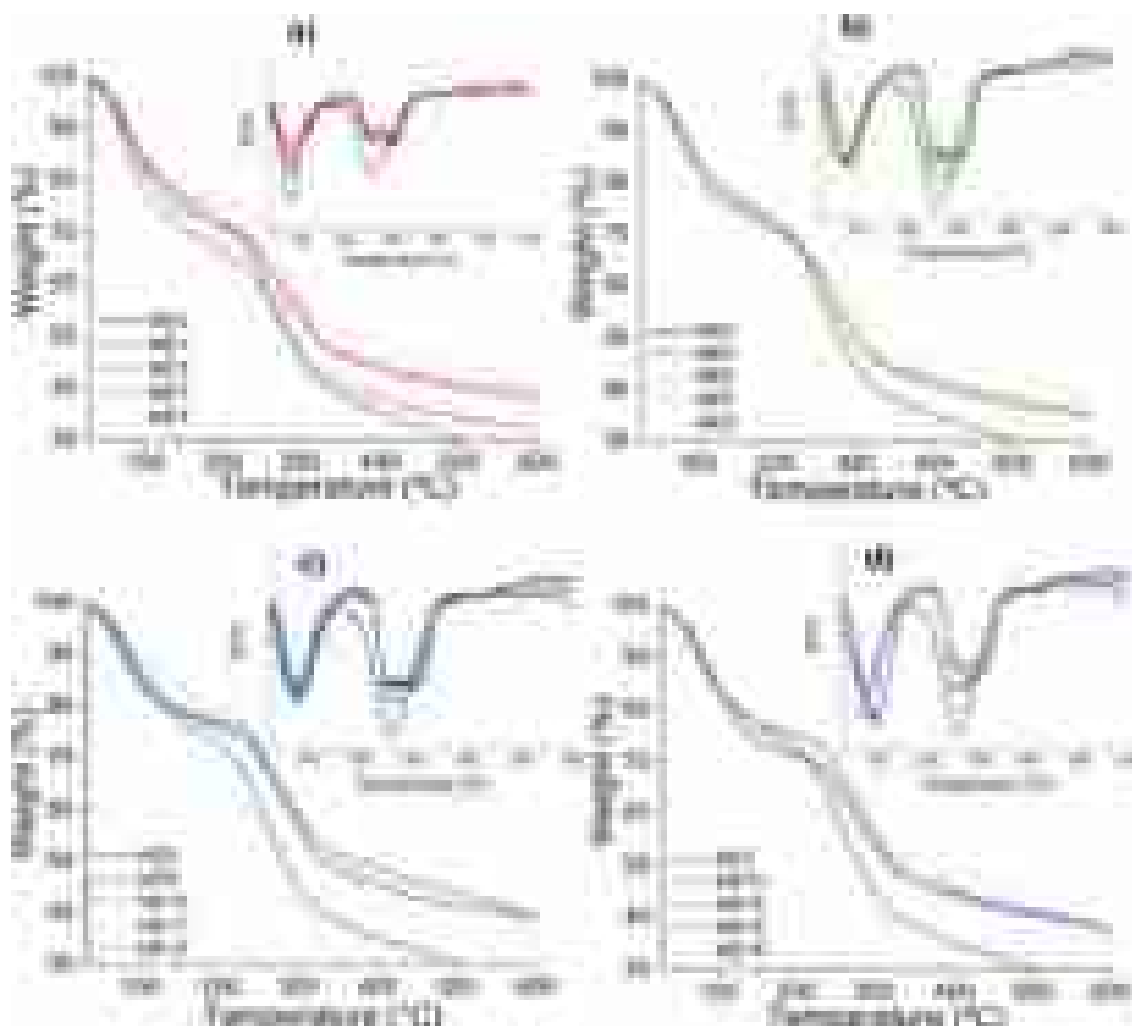


Fig. 4 **a** TGA and DTG curves for pectin-based membrane (ME0) and composite membranes containing 1% PS plus 1 (ME1), 5 (ME2), 10 (ME3), and 15% (w/w) (ME4) Fe_3O_4 . **b** Composite membranes containing 3% PS plus 1 (ME5), 5 (ME6), 10 (ME7), and 15% (w/w)

(ME8) Fe_3O_4 . **c** Composite membranes containing 5% PS plus 1 (ME9), 5 (ME10), 10 (ME11), and 15% (w/w) (ME12) Fe_3O_4 . **d** Composite membranes containing 10% PS plus 1 (ME13), 5 (ME14), 10 (ME15), and 15% (w/w) (ME16) Fe_3O_4

X-ray patterns did not change. Specific X-ray patterns were observed in the composite membrane after incorporating Fe_3O_4 and PS. In this case, the amorphous regions decreased compared to the membrane without Fe_3O_4 and PS. The final composite material can assess a synergy among magnetite, PS and polysaccharide chains.

3.2 Separation studies

3.2.1 Degree of swelling

Figure 7 shows the degree of swelling of the pectin-based composite membrane containing 3% (w/w) PS and 1% (w/w) Fe_3O_4 in distilled water and drinking water at room temperature. Swelling equilibrium occurred after 100 min in both aqueous media, determining a low degree of swelling. This indicates weak intermolecular interactions among

chemical groups and nonsignificant macromolecular relaxation of the polymeric structure of the membrane [16]. The degree of swelling of the composite membrane was 2.24 and 1.93 g of water per g of dried membrane in distilled water and drinking water, respectively. These values decreased significantly with composite membranes containing higher PS, different Fe_3O_4 contents, and specific pH values of the aqueous media (data not shown). This is due to the increase in the crosslinking density of the polymer chains and the presence of charged chemical species in aqueous media [27, 28]. The absence of salts in distilled water contributed to higher water absorption capacity, as Na^+ , Mg^{2+} , Ca^{2+} , H^+ , Na^+ , and K^+ ions interact with anionic groups of the membrane structure, decreasing electrostatic repulsion forces among adjacent ionic carboxylic groups [91]. A higher concentration of cations in an aqueous solution leads to a lower degree of swelling of the polymer membrane, as the amount

Table 2 Thermal and mechanical assay results for pectin-based membranes

Samples	Tensile strength (σ) (MPa)	Deformation (%)	Elastic modulus (E) (MPa)	T _{10%} (°C)	T _{max} (°C)
ME0	-	-	-	97.2	257.8
ME1	51.1 ± 1.6	166.7 ± 1.3	201.3 ± 1.5	70.6	283.0
ME2	195.4 ± 1.7	27.4 ± 1.1	447.4 ± 1.1	78.9	273.0
ME3	260.3 ± 1.9	40.6 ± 1.1	448.8 ± 1.6	76.9	286.0
ME4	178.1 ± 1.3	39.1 ± 1.4	445.2 ± 1.2	85.4	267.0
ME5	126.7 ± 1.2	87.8 ± 1.7	447.1 ± 1.4	77.6	298.0
ME6	53.4 ± 1.5	28.8 ± 1.7	488.3 ± 1.5	82.3	267.0
ME7	189.3 ± 1.6	47.8 ± 1.7	444.9 ± 1.3	83.5	268.0
ME8	203.8 ± 1.6	39.7 ± 1.6	548.2 ± 1.6	80.2	279.7
ME9	337.2 ± 1.4	92.4 ± 1.9	450.5 ± 1.8	84.6	290.8
ME10	91.8 ± 1.1	67.1 ± 1.3	439.2 ± 1.6	87.9	255.3
ME11	292.1 ± 1.5	57.0 ± 1.7	444.1 ± 1.6	95.2	278.1
ME12	171.1 ± 1.9	38.6 ± 1.6	412.3 ± 1.1	80.7	259.6
ME13	65.8 ± 1.4	40.4 ± 1.6	646.4 ± 1.3	79.0	254.8
ME14	159.1 ± 1.4	76.7 ± 1.2	718.0 ± 1.8	89.4	277.0
ME15	77.8 ± 1.8	36.9 ± 1.4	440.3 ± 1.3	84.2	284.0
ME16	160.6 ± 1.3	31.6 ± 1.5	445.8 ± 1.7	80.5	267.0

Maximum tensile strength (σ_{\max}), deformation (%), and elastic modulus (E)

of water absorbed depends on the amount of hydrophilic or hydrophobic groups and pores sizes in/on the sorbent material. This explains the low degree of swelling, especially in composite membranes with high amounts of PS and Fe₃O₄ [91]. Based on the characterization studies, pectin-based composite membranes are potential polymer matrices for water and wastewater treatment. Thus, due to its performance (Fig. 8), the pectin-based composite membrane containing 3% PS and 1 wt% Fe₃O₄ was tested as a model material for the sorption and removal of MB from water.

3.2.2 Dye separation assays

Figure 9 shows the MB sorption capacity of the control Fe₃O₄ and composite membrane containing 3% (w/w) PS and 1% (w/w) Fe₃O₄ as a function of time at pH 3.0, 4.0, 6.0, 8.0, and 10.0. The dye sorption capacity of the composite membrane increased rapidly from 0 to 500 min due to the high amount of available active sorption sites at the beginning of the process, followed by a slight increase from 500 to 1500 min (sorption equilibrium) at all pH values. The sorption rate decreases over time due to the saturation of the polymer membrane structure [24, 59]. Saturation occurs after the dye molecule is transferred from the aqueous solution to the boundary layer of the membrane and into the pores. Sorption processes take place on/in available active sites of solid sorbents due to interactions between positive and negative ionic groups in polymer materials [89]. The

sorption capacity of the polymeric membrane ranged from 0.88 to 1.18 mg of dye per g of dried membrane at pH from 3.0 to 10.0 after 2000 min. Some authors obtained a sorption capacity for MB dye of 0.75 mg g⁻¹ at pH 4 using a pectin membrane [29]. Low sorption capacity is commonly related to the amount of hydroxyl and carboxyl groups available in the sorbent structure [35, 89]. Slightly higher sorption capacities were found in aqueous media with alkaline pH due to the ionization of carboxyl groups [18].

Although the effect of different membrane dosages was not directly studied in this work, it is well established in the literature that increasing the sorbent dosage enhances the number of active sorption sites for interactions, thereby improving the removal efficiency of chemicals from solutions [6, 7, 45, 51, 72, 73, 77]. However, an increase in dosage can also reduce the sorption capacity per unit mass of membrane, as the available dye molecules in the solution become limited compared to the amount of sorbent material, leaving sorption sites unsaturated. Similar behavior has been reported for other sorbents, such as activated carbon [72, 73], clay minerals [7, 51, 77], and magnetic composites [6, 45].

Based on trends and the findings of the present study, one can infer that a membrane dosage of approximately 150 mg combined with an initial dye concentration of 20 mg L⁻¹ at pH 10.0 could offer optimal conditions for dye removal from contaminated water. This makes pectin-based composite membranes potential matrices for water filtration and the removal of dyes from textile wastewater, as textile effluents commonly have a high pH value (around 10), which varies with the source of pollution [55]. The sorption results of dye in Fe₃O₄ were similar to those found for membranes in an acid solution, with slightly higher values in an alkaline solution. Fe₃O₄ powder is a potential sorbent for removing dyes from aqueous solutions; however, it is improper for membrane-filtration processes. In view of this, Fe₃O₄ was incorporated into the membrane networks to achieve synergic effects during membrane filtration. Moreover, magnetic membranes can be recovered by applying an external magnetic field, as described elsewhere [58].

3.2.3 Sorption kinetics

Figure 10 shows the predicted and experimental non-linear kinetics for the sorption of the dye in the pectin-based composite membrane containing 3% (w/w) PS and 1% (w/w) Fe₃O₄ at pH 3.0 (a), 4.0 (b), 6.0 (c), 8.0 (d), and 10.0 (e). The kinetic parameters are shown in Table 3. Sorption kinetics of dye in pure Fe₃O₄ can be seen in supplementary materials (Fig. 6S and Table 1S). The pseudo-first-order kinetic model is typically applied to study the occupation rate of active sites during sorption assays. In this case, proportionality

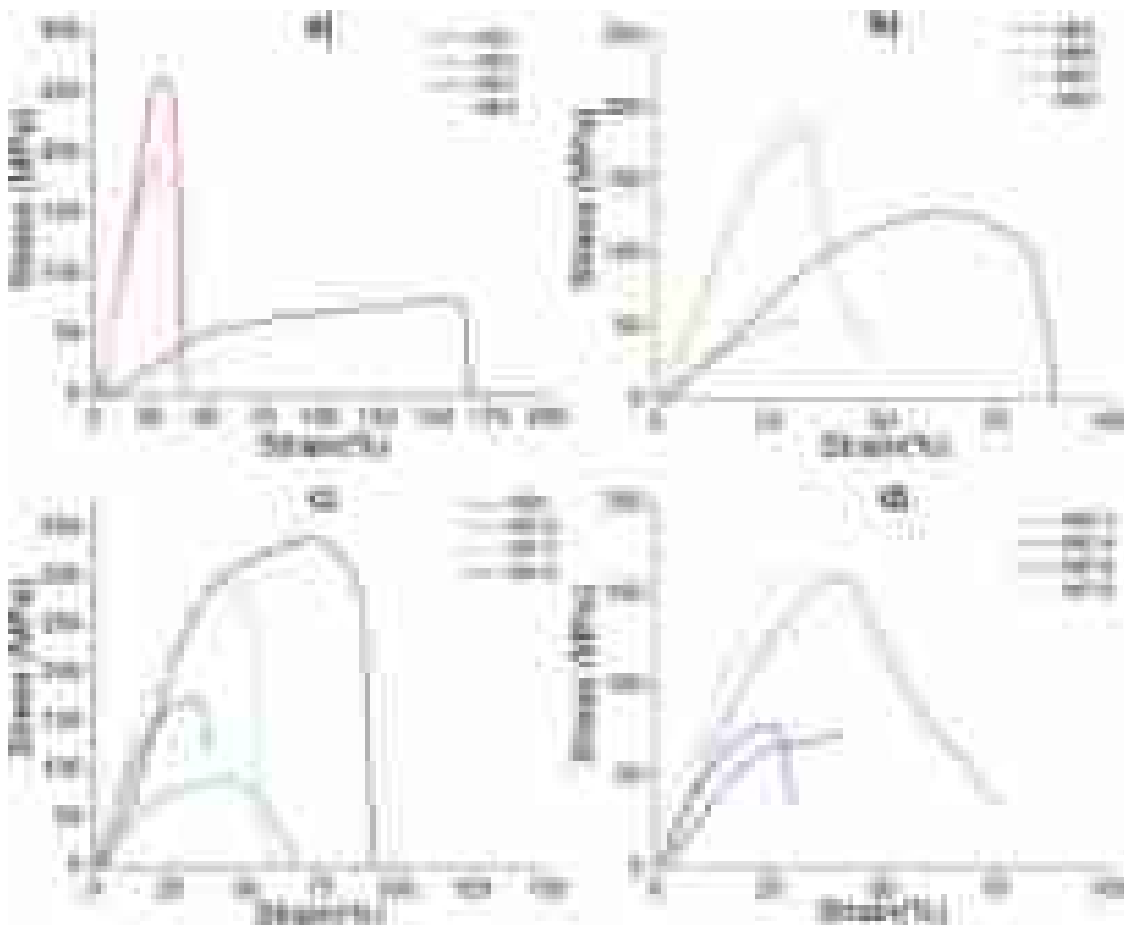


Fig. 5 Curves of strain versus stress for pectin-based composite membranes containing different PS and Fe₃O₄ contents. **a** 1% PS plus 1 (ME1), 5 (ME2), 10 (ME3), and 15% (w/w) (ME4) Fe₃O₄. **b** Results of mechanical assays for pectin-based composite membranes containing 3% PS plus 1 (ME5), 5 (ME6), 10 (ME7), and 15% (w/w) (ME8)

Fe₃O₄. **c** Results of mechanical assays for pectin-based composite membranes containing 5% PS plus 1 (ME9), 5 (ME10), 10 (ME11), and 15% (w/w) (ME12) Fe₃O₄. **d** Results of mechanical assays for pectin-based composite membranes containing 10% PS plus 1 (ME13), 5 (ME14), 10 (ME15), and 15% (w/w) (ME16) Fe₃O₄

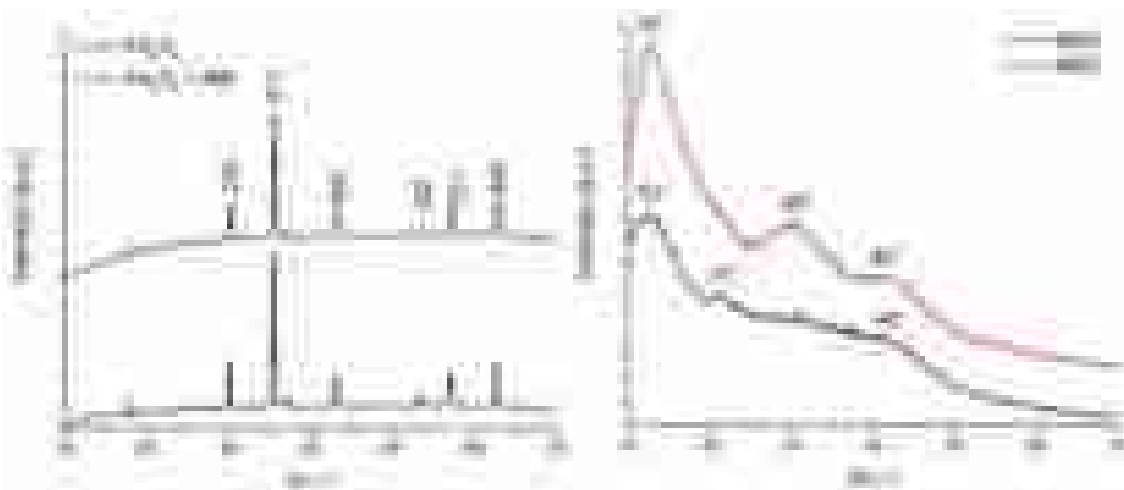


Fig. 6 XRD diffractograms for Fe₃O₄, after sorption of Fe₃O₄ + MB, membrane without Fe₃O₄ and PS (ME0), and composite membrane containing 3% (w/w) PS and 1% (w/w) Fe₃O₄ (ME5)

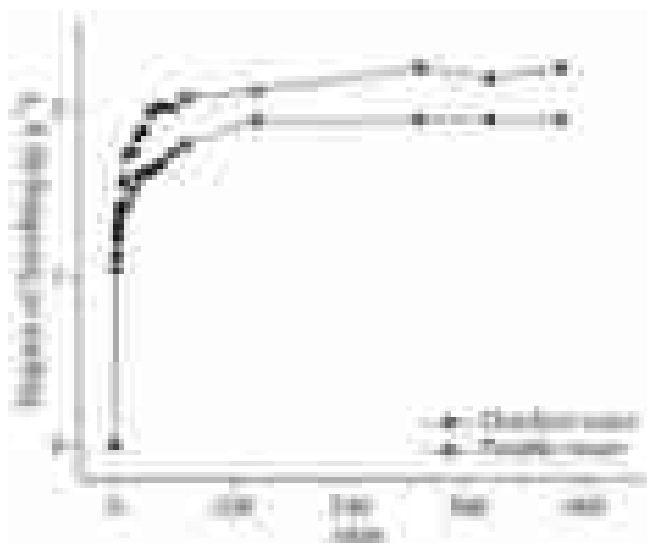


Fig. 7 Degree of swelling of pectin-based composite membrane containing 3% (w/w) PS and 1% (w/w) Fe₃O₄ in distilled water and drinking water at room temperature

occurs between occupied and unoccupied sites, suggesting a

sorption mechanism based on physical interactions between the sorbent and sorbate [83, 84]. On the other hand, the pseudo-second-order kinetic model assumes that the sorption rate is related to the square of the number of unoccupied sites, suggesting a sorption mechanism based on chemical interactions between the sorbent and sorbate. Both physical and chemical interactions are important when describing membrane filtration processes in water purification systems [87]. Many kinetic models are empirical and do not generate relevant information on mass transfer mechanisms, whereas the pseudo-first-order and pseudo-second-order kinetic models are useful for sorption processes. In view of our main aim, other kinetic models were considered irrelevant to our results. In this study, the kinetic fit at pH 3.0 could be explained by both pseudo-first-order and pseudo-second-order models due to the similar correlation coefficient (R^2) and chi-square test (χ^2) values. Thus, the best kinetic fit was defined based on predicted and experimental q_e values. As these values were similar using the pseudo-second-order kinetic model, this model represents the sorption kinetics of MB dye in pectin-based composite



Fig. 8 Scheme illustrating membrane with best performance

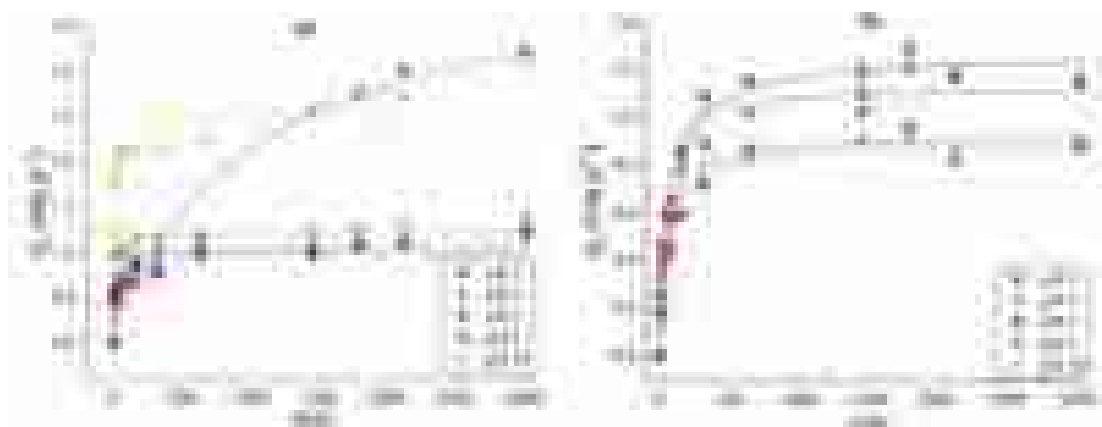


Fig. 9 MB sorption capacity of **a** control Fe₃O₄ and **b** composite membrane containing 3% (w/w) PS and 1% (w/w) Fe₃O₄ as a function of time at pH 3.0, 4.0, 6.0, 8.0, and 10.0. Experimental conditions: initial

dye concentration of 20 mg L⁻¹, membrane mass of 150 mg, and solution volume of 50 mL

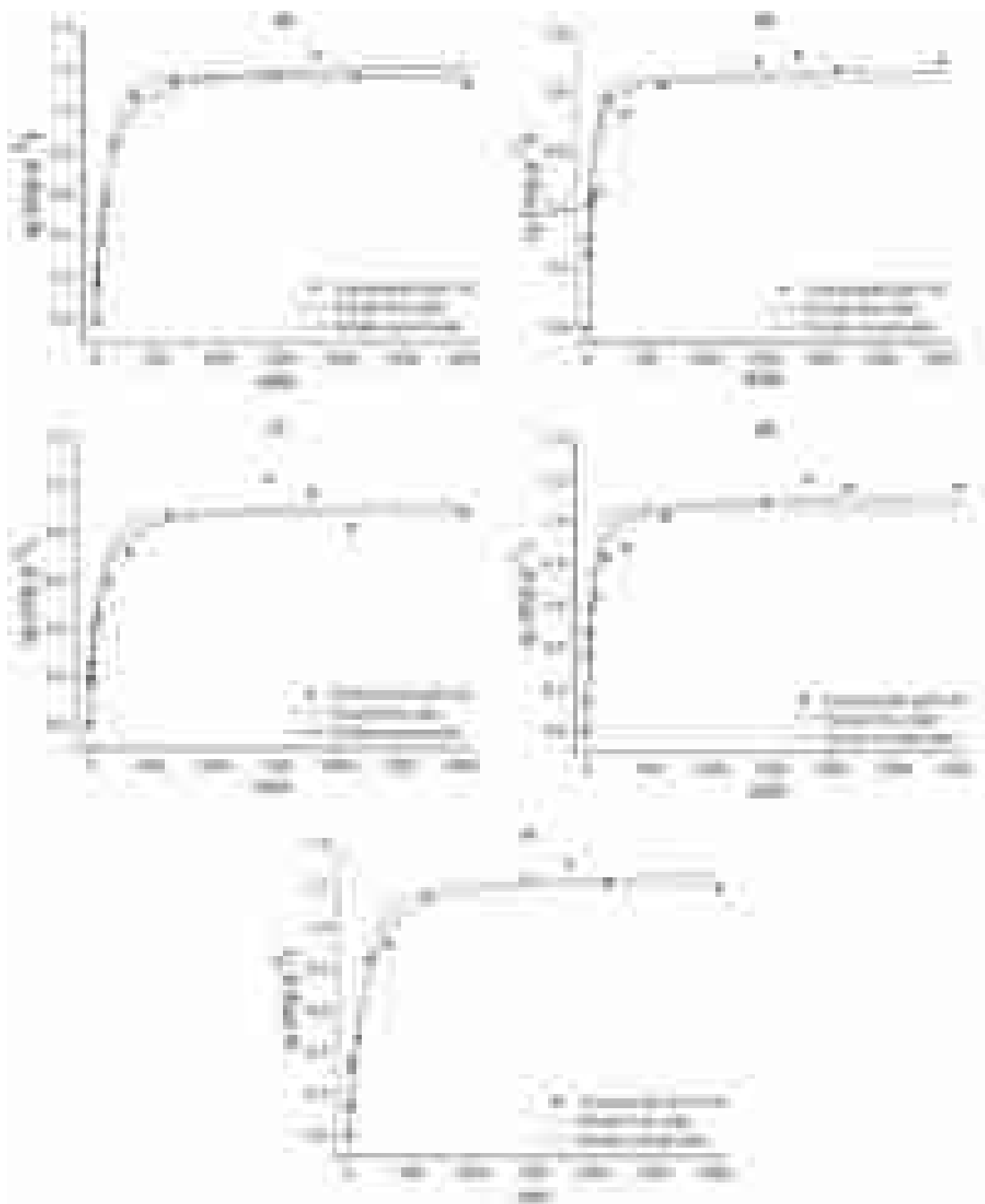


Fig. 10 Predicted and experimental non-linear kinetics for sorption of dye in pectin-based composite membrane containing 3% (w/w) PS and 1% (w/w) Fe_3O_4 at pH 3.0 (a), 4.0 (b), 6.0 (c), 8.0 (d), and 10.0

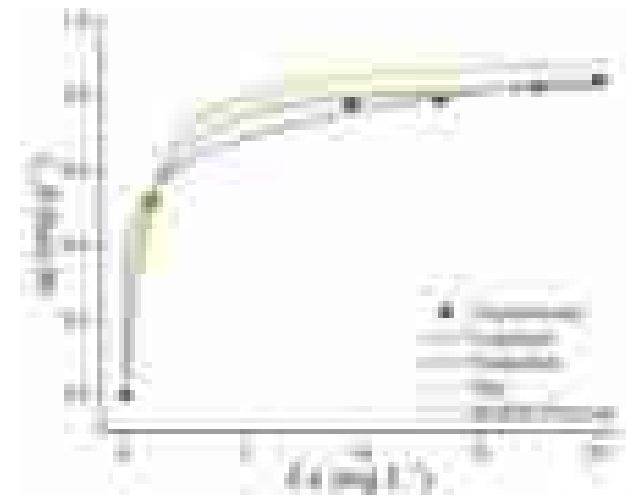
membranes containing PS and Fe_3O_4 . Other studies have reported pseudo-second-order kinetic models to describe the sorption of MB dye molecules [34, 42]. Different results were found at higher pH values due to changes in the charge in the polymeric structures. Changes in the pH values of aqueous solutions tend to disturb the reaction equilibrium, altering k_1 , and k_2 (sorption rates) values. This indicates that the sorption process is governed by the number of reactions

(e). Experimental conditions: initial dye concentration of 20.0 mg L^{-1} , solution volume of 50.0 mL, and room temperature

occurring between the sorbate and sorbent [52]. The sorption kinetics of MB in the pectin-based membranes following the pseudo-second-order model suggest that the sorption rate-limiting step is a chemical reaction [30]. Thus, the dye sorption was conducted by chemical reactions between the sorbate and surface sites through covalent bonding [70].

Table 3 Kinetic parameters for sorption of dye in pectin-based composite membrane containing 3% (w/w) PS and 1% (w/w) Fe₃O₄ at different pH values

Kinetic model	Parameters	pH				
		3.0	4.0	6.0	8.0	10.0
Pseudo-first-order model	k_1 (min ⁻¹)	0.0089	0.0194	0.0097	0.0179	0.0071
	q_e (mg g ⁻¹)	1.1809	0.8419	0.8827	1.0609	1.2014
	R^2	0.9898	0.8703	0.9113	0.9025	0.9677
	χ^2	0.0027	0.0131	0.0112	0.0175	0.0083
Pseudo-second-order model	k_2 (10 ⁻⁵ min ⁻¹)	0.0099	0.0368	0.0161	0.0228	0.0077
	q_e (mg g ⁻¹)	1.2621	0.8792	0.9343	1.1262	1.2920
	R^2	0.9891	0.9319	0.9448	0.9611	0.9817
	χ^2	0.0029	0.0069	0.0070	0.0070	0.0047

**Fig. 11** Non-linear Langmuir, Freundlich, Sips, and Redlich-Peterson isotherms for sorption of MB in pectin-based composite membrane containing 3% (w/w) PS and 1% (w/w) Fe₃O₄. Experimental conditions: sorption time of 2000 min, membrane mass of 150 mg, solution volume of 50.0 mL, and pH 8.0**Table 4** Parameters of non-linear Langmuir, Freundlich, sips, and Redlich-Peterson isotherms for sorption of MB using pectin-based composite membrane containing 3% (w/w) PS and 1% (w/w) Fe₃O₄

Isotherm model	Parameters	Isotherm model	Parameters
Langmuir	Q_m (mg g ⁻¹)	Freundlich	K_F (L mg ⁻¹)
	K_L (L mg ⁻¹)		n_F
	R^2		R^2
	χ^2		χ^2
Sips	Q_m (mg g ⁻¹)	Redlich-Peterson	A (mg ⁻¹)
	K_S (L mg ⁻¹)		B (L g ⁻¹)
	n_S		g
	R^2		R^2
	χ^2		χ^2

3.2.4 Sorption isotherms

Figure 11 shows the isotherms for the sorption of MB in the pectin-based composite membrane containing 3% (w/w) PS and 1% (w/w) Fe₃O₄. The isotherm parameters are shown in Table 4. Two-parameter isotherm models (e.g., Langmuir and Freundlich) and three-parameter isotherm models (e.g., Sips and Redlich-Peterson) are commonly applied to heterogeneous and homogeneous sorption processes, providing a comprehensive description of interactions between the sorbate and sorbent [80, 81]. Two-parameter isotherm models are simple and effective at describing sorption processes with fewer variables, but may be useful in complex systems with heterogeneous surfaces or varying sorption energies [80, 81]. The formation of a monolayer on the membrane surface was investigated using the Langmuir model, whereas surface heterogeneity and the type of interaction between neighboring sorption sites were considered with the Freundlich model. Three-parameter isotherm models are useful for describing sorption processes on heterogeneous surfaces with different sorption energies and sites. The Sips three-parameter isotherm model can be represented by the Langmuir two-parameter isotherm model at low sorbate concentrations, whereas the Redlich-Peterson three-parameter isotherm model combines properties of the Langmuir and Freundlich isotherms in a wide sorbate concentration range [50]. The Temkin and Dubinin-Radushkevich (D-R) isotherm models were initially tested in this work, but had poor fits, as determined by statistical assessment metrics, such as R^2 and χ^2 (data not shown). Therefore, these models were not employed to assess the results of this work. The sorption capacity increased with the increase in the initial dye concentration due to the increase in the driving force of the concentration gradient, which accelerates the diffusion of organic molecules from aqueous solutions to rigid solid surfaces [76]. The sorption capacity increased slightly to 0.788 mg g⁻¹ when the initial dye concentration increased to 15 mg L⁻¹, inferring the saturation of active sites of the membrane network. Isotherm parameters were determined using the optimization procedure employed by the solver

add-in functions as well as trial-and-error optimization in Microsoft Excel. Based on the R^2 and χ^2 values, the best isotherm fit was obtained using the Redlich-Peterson model, suggesting that the sorption process is governed mainly by multisite interactions [83, 84]. As the g value was 1, the Redlich-Peterson model behaves similarly to the Langmuir model [38]. Hence, monolayer formation occurs at low dye concentrations with no physiochemical interactions between the dye molecules sorbed at specific active sites and available neighboring active sites [18]. The maximum sorption capacity (q_{max}) of pectin-based membrane for MB dye is 0.86 mg g^{-1} at 298 K. This indicates that the pectin-based composite membrane containing PS and Fe_3O_4 is a promising matrix for the sorption of cationic textile dyes contained in wastewater. Thus, water treatment methods can be proposed using pectin-based composite membranes with the aim of purifying drinking water containing different types of organic pollutants, as represented in Fig. 12.

3.2.5 Biosorbent prospects for pollutant separation

Table 5 compares using pectin-based membranes for MB dye with other sorbents made from biomass materials and other applications. Several factors affect the sorption

capacity, including pH, temperature, dosage of adsorbents and their type, surface area, contact time, etc. The optimal parameters for each sorbent vary significantly, and optimizing each factor is important to large-scale industrial applications and understanding the sorption mechanism [82]. The introduction of Fe_3O_4 provided additional adsorptive sites, increasing the overall capacity, while PS contributed to the mechanical strength and stability of the adsorbent, which may allow the pectin-based membrane to tolerate diverse wastewater conditions.

Several studies have shown that adsorbents prepared from biomass materials are less expensive than conventional treatment technologies for pollutant removal, although they did not incorporate cost-benefit analysis in their study. A significant advantage of using biomass materials like pectin and PS is their low cost. The cost of forest wastes such as PS is only associated with the transport cost from the storage place to the site where they will be utilized [14]. The cost of pectin in the market is 12–21 \$ per kg [49]. In comparison, conventional starch sorbents such as insoluble starch xanthate and soluble starch xanthane have been reported at \$7.61/100 g and \$0.10/100 g respectively [10]. Fe_3O_4 , while not a biomass material, offers significant benefits in terms of sorption efficiency and recovery ease, despite its higher cost

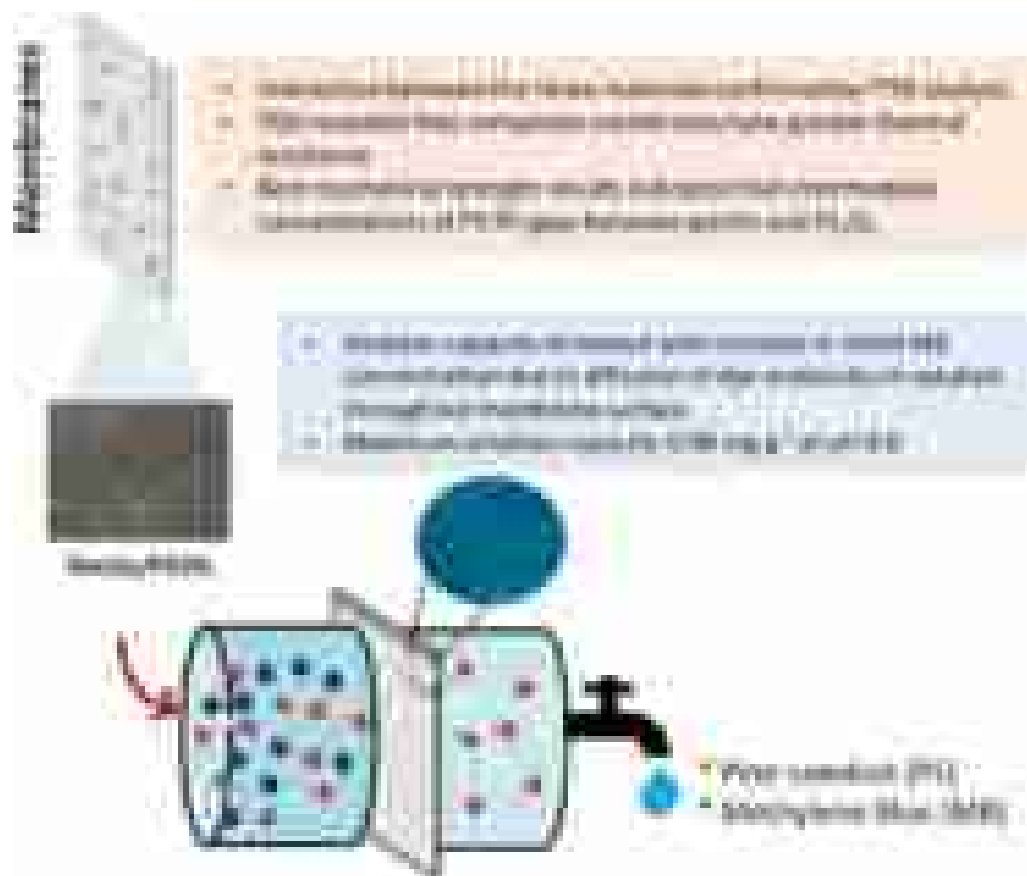


Fig. 12 Schematic of prepared membrane and simulation of application in drinking water purification

Table 5 Comparative of sorption capacities for removal of pollutants from water on different biomass materials (PSO: pseudo-second-order)

Sorbent type	Adsorbent dosage (g)	Surface area (m ² g ⁻¹)	Pollutant	Q _{max} (mg g ⁻¹) (T(°C)/pH)	Desorption capacity	Kinetic	Isotherm	Industrial application potential assessment	Advantages	Disadvantages	References
Pectin–pinus sawdust-iron oxide Fe ₃ O ₄ nanocomposite	0.15 g/50 mL	-	MB	0.86 (25/8)	-	PSO	Langmuir	Textile effluents	Low cost, environmentally friendly, Fe ₃ O ₄ presence may favor the application in photodegradation studies	Low adsorption capacity	This study
Acid factionalized Coconut shell	0.1 g/100 mL	1.137	MB	50.6 (30/8)	-	PSO	Freundlich	Textile effluents	Low cost, renewability, and environmentally friendly	Lack of desorption data	[33]
Sulphuric acid-modified bagasse	0.4 g/100 mL	-	MB	56.5 (27/9)	95.41%	PSO	Langmuir and Freundlich	Textile effluents	Low cost agricultural waste, highly adsorbing in terms of high percentage of color removal and chemical oxygen demand (COD) reduction		[42]
Pectin–iron oxide magnetic nanocomposite	20 mg/20 mL	67	Cu (II)	48.99 (25/5)	93.70%	PSO	Langmuir and Freundlich	Mining effluents	Low cost, adsorption properties of pectin and magnetic properties of iron oxide	Lack of stability and inconvenience to be separated from the aqueous solution	[23]
Groundnut seed cake powder	0.75 g/50 mL	470	Cu (II)	4.82 (40/5)	-	PSO	Langmuir	Pulp and paper mills, fertilizers, petroleum refineries, basic steel work foundries, non-ferrous metal works, motor vehicles, aircraft plating effluents	Low cost, agricultural waste		[37]
Sesame seed cake powder	1.0 g/50 mL	480		4.24 (40/5)							
Coconut cake powder	1.0 g/50 mL			4.32 (40/5)							
Hybrid pectin-agar	0.02 g/20 mL	-	Zn (II)	25 (22/4)	-	-	-	Anti-corrosive coatings, constructional materials, batteries, paints and cosmetics, as well as its presence in the mine waters	Low cost, pectin-based beads may be easily separated from purified solution	Lack of kinetics and desorption data	[32]
Coffee husks	1 g/150 mL	-	Cu(II), Cd(II) and Zn(II)	5.6 (25/4)	-	PSO	Langmuir and Freundlich	Industrial effluents	Low cost agricultural waste, widely availability	Difficulty of their separation from purified water	[54]

compared to purely biomass materials. Still, this contrasts sharply with the higher costs associated with conventional activated carbons (\$259.5 per kg) [14].

Our study aligns with environmental sustainability by utilizing waste materials and natural polymers. The composite nature of our adsorbent also suggests potential for multiple-cycle use, although reusability studies are yet to be conducted. Future work will focus on these aspects to ensure the adsorbent's practical application in industrial wastewater treatment is not only effective but also environmentally responsible.

4 Conclusion

A pectin-based composite membrane containing 3% (w/w) PS and 1% (w/w) Fe_3O_4 was efficiently synthesized and characterized for the purification of water containing organic pollutants. With the pectin de-esterification and crosslinking process of the polymer chain with calcium, it was possible to reduce the solubility of the membrane in water during application studies. FTIR, TGA, and mechanical assays confirmed the crosslinked membrane structure. The composite membranes containing either Fe_3O_4 or PS had higher thermal resistance than the pectin-based membrane alone due to greater amounts of crosslinking points among pectin, PS, and Fe_3O_4 in the polymeric structure. Higher mechanical resistance was also found for the composite membranes containing from 1 to 3% (w/w) Fe_3O_4 and 3 and 5% (w/w) of PS. The degree of swelling and dye sorption capacity of the membranes were affected by the pH of the aqueous solutions and salt concentrations. The dye sorption kinetics can be described by either the pseudo-first-order model or pseudo-second-order model at pH 3.0, with differences at more alkaline solutions. Lastly, either the non-linear Redlich-Peterson or Langmuir isotherm models can describe the sorption mechanism depending on the experimental conditions. Based on the present results, the proposed pectin/PS/ Fe_3O_4 composite membrane constitutes a novel approach for dye removal applications. The synthesized adsorbent using pectin, PS, and Fe_3O_4 presents a promising solution for dye removal in wastewater treatment, combining environmental sustainability with cost-efficiency. Future studies will further explore the scalability and reusability of this adsorbent to enhance its industrial application potential.

Supplementary Information The online version contains supplementary material available at <https://doi.org/10.1007/s10450-025-00619-2>.

Acknowledgements ATP thanks Fundação de Amparo à Pesquisa e Inovação do Estado de Santa Catarina (FAPESC, Brazil) for the financial support (Grant numbers: 2023/TR331 and 2024/TR002572) and Conselho Nacional de Desenvolvimento Científico e Tecnológico

(CNPq, Brazil) for the research productivity fellowship (Grant number: 313064/ 2022-9). DSR thanks CNPq (Grant number: 308053/ 2021-4 and 403934/ 2021-4) and Fundação de Amparo à Pesquisa do Estado de São Paulo (FAPESP, Brazil) for research support (Grant numbers: 2022/ 01382-3, 2021/ 14714-1, and 2020/ 13703-3). This work was partially supported by Brazilian agencies MCTIC/CNPq (Grant number: 406973/ 2022-9) and by Coordenação de Aperfeiçoamento de Pessoal de Nível Superior (CAPES, Brazil – Finance Code 001) and Multiuser Central Facilities (CEM - UFABC).

Author contributions Ana Maria Tischer: Data curation, formal analysis, roles/writing – original draft- Rafaela Reis Ferreira: Data curation, formal analysis, roles/writing – original draft- Ionara de Fátima Ferreira: Data curation, formal analysis- Derval dos Santos Rosa: Funding acquisition, Roles/writing – original draft- Alexandre Tadeu Paulino: Project administration, Data curation, Funding acquisition, resources, writing – review & editing.

Data availability No datasets were generated or analysed during the current study.

Declarations

Competing interests The authors declare no competing interests.

Ethical approval Not applicable.

Consent to participate Not applicable.

Consent to publish Not applicable.

References

- 1 Abbas, M., Parvatheeswara Rao, B., Naga, S.M., Takahashi, M., Kim, C.: Synthesis of high magnetization hydrophilic magnetite (Fe_3O_4) nanoparticles in single reaction—Surfactantless polyol process. *Ceram. Int.* **39**, 7605–7611 (2013). <https://doi.org/10.1016/j.ceramint.2013.03.015>
- 2 Abu Hasan, H., Muhammad, M.H., Ismail, N., 'Izzati: A review of biological drinking water treatment technologies for contaminants removal from polluted water resources. *J. Water Process. Eng.* **33**, 101035 (2020). <https://doi.org/10.1016/j.jwpe.2019.101035>
- 3 Abutaleb, A., Imran, M., Zouli, N., Khan, A.H., Hussain, S., Ali, M.A., Bakather, O., Gondal, M.A., Khan, N.A., Panchal, H., Zahmatkesh, S.: Fe_3O_4 -multiwalled carbon nanotubes-bentonite as adsorbent for removal of methylene blue from aqueous solutions. *Chemosphere.* **316**, 137824 (2023). <https://doi.org/10.1016/j.chemosphere.2023.137824>
- 4 Ahmad, S.I., Ahmad, R., Khan, M.S., Kant, R., Shahid, S., Gautam, L., Hasan, G.M., Hassan, M.I.: Chitin and its derivatives: Structural properties and biomedical applications. *Int. J. Biol. Macromol.* **164**, 526–539 (2020). <https://doi.org/10.1016/j.ijbiomac.2020.07.098>
- 5 Alemzadeh, I., Saifkordi, A.A., Kahforooshan, D., Nahid, P.: Production of low ester (LM) pectin by de-esterification of high ester (HM) Apple pectin. *Scientia Iranica.* **12**, 306–310 (2005)
- 6 Algethami, J.S., Alhamami, M.A.M., Alqadami, A.A., Melhi, S., Seliem, A.F.: Magnetic hydrochar grafted-chitosan for enhanced efficient adsorption of malachite green dye from aqueous solutions: Modeling, adsorption behavior, and mechanism analysis.

- Int. J. Biol. Macromol. **254**, 127767 (2024). <https://doi.org/10.1016/j.ijbiomac.2023.127767>
- 7 Aljeboree, A.M., Alkaim, A.F., Alsaltany, F.H., Issa, S.K.: Highly reusable nano adsorbent based on Clay-Incorporated hydrogel nanocomposite for cationic dye adsorption. *J. Inorg. Organomet. Polym. Mater.* (2024). <https://doi.org/10.1007/s10904-024-0334-4-5>
 - 8 Ao, C., Zhao, J., Li, Q., Zhang, J., Huang, B., Wang, Q., Gai, J., Chen, Z., Zhang, W., Lu, C.: Biodegradable all-cellulose composite membranes for simultaneous oil/water separation and dye removal from water. *Carbohydr. Polym.* **250**, 116872 (2020). <https://doi.org/10.1016/j.carbpol.2020.116872>
 - 9 Ávila, F.G., Cabrera-Sumba, J., Valdez-Pilataxi, S., Villalta-Chungata, J., Valdiviezo-Gonzales, L., Alegria-Arnedo, C.: Removal of heavy metals in industrial wastewater using adsorption technology: Efficiency and influencing factors. *Clean. Eng. Technol.* **24**, 100879 (2025). <https://doi.org/10.1016/j.clet.2025.100879>
 - 10 Bailey, S.E., Olin, T.J., Bricka, R.M., Adrian, D.D.: A review of potentially low-cost sorbents for heavy metals. *Water Res.* **33**, 2469–2479 (1999). [https://doi.org/10.1016/S0043-1354\(98\)00475-8](https://doi.org/10.1016/S0043-1354(98)00475-8)
 - 11 Barbosa, R.F.S., Souza, A.G., Maltez, H.F., Rosa, D.S.: Chromium removal from contaminated wastewaters using biodegradable membranes containing cellulose nanostructures. *Chem. Eng. J.* **395**, 125055 (2020). <https://doi.org/10.1016/j.cej.2020.125055>
 - 12 Baum, A., Dominiak, M., Vidal-Melgosa, S., Willats, W.G.T., Søndergaard, K.M., Hansen, P.W., Meyer, A.S., Mikkelsen, J.D.: Prediction of pectin yield and quality by FTIR and carbohydrate microarray analysis. *Food Bioproc Tech.* **10**, 143–154 (2017). <https://doi.org/10.1007/s11947-016-1802-2>
 - 13 Baum, A., Dominiak, M., Vidal-Melgosa, S., Willats, W.G.T., Søndergaard, K.M., Hansen, P.W., Meyer, A.S., Mikkelsen, J.D.: Prediction of pectin yield and quality by FTIR and carbohydrate microarray analysis. *Food Bioproc Tech.* **10**, 143–154 (2017). <https://doi.org/10.1007/s11947-016-1802-2>
 - 14 Bello, O.S., Adegoke, K.A., Fagbenro, S.O., Lameed, O.S.: Functionalized coconut husks for rhodamine-B dye sequestration. *Appl. Water Sci.* **9**, 189 (2019). <https://doi.org/10.1007/s13201-019-1051-4>
 - 15 Cargnin, M.A., de Souza, A.G., de Lima, G.F., Gasparin, B.C., dos Santos Rosa, D., Paulino, A.T.: Pinus residue/pectin-based composite hydrogels for the immobilization of β -D-galactosidase. *Int. J. Biol. Macromol.* **149**, 773–782 (2020). <https://doi.org/10.1016/j.ijbiomac.2020.01.280>
 - 16 da Cruz, L.F., Polizeli, A.G., Enzweiler, H., Paulino, A.T.: Chitosan-co-GLU/eucalyptus residue composite membrane for the stabilization of β -d-galactosidase in aqueous solutions. *Polym. Bull.* (2023). <https://doi.org/10.1007/s00289-023-05008-9>
 - 17 Dai, J., Wu, S., Jiang, W., Li, P., Chen, X., Liu, L., Liu, J., Sun, D., Chen, W., Chen, B., Li, F.: Facile synthesis of pectin coated Fe₃O₄ nanospheres by the sonochemical method. *J. Magn. Magn. Mater.* **331**, 62–66 (2013). <https://doi.org/10.1016/j.jmmm.2012.11.004>
 - 18 Dalalibera, A., Vilela, P.B., Vieira, T., Becegato, V.A., Paulino, A.T.: Removal and selective separation of synthetic dyes from water using a polyacrylic acid-based hydrogel: Characterization, isotherm, kinetic, and thermodynamic data. *J. Environ. Chem. Eng.* **8**, 104465 (2020). <https://doi.org/10.1016/j.jece.2020.104465>
 - 19 Dixit, R., Wasiullah, Malaviya, D., Pandiyan, K., Singh, U., Sahu, A., Shukla, R., Singh, B., Rai, J., Sharma, P., Lade, H., Paul, D.: Bioremediation of heavy metals from soil and aquatic environment: An overview of principles and criteria of fundamental processes. *Sustainability.* **7**, 2189–2212 (2015). <https://doi.org/10.3390/su7022189>
 - 20 Ferreira, R.R., Souza, A.G., Nunes, L.L., Shahi, N., Rangari, V.K., dos S. Rosa, D.: Use of ball mill to prepare nanocellulose from Eucalyptus biomass: Challenges and process optimization by combined method. *Mater. Today Commun.* **22**, 100755 (2020). <https://doi.org/10.1016/j.mtcomm.2019.100755>
 - 21 Freundlich, H.M.F.: Over the adsorption in solution. *J. Phys. Chem.* **57**, 385–471 (1906)
 - 22 Ghorbanizadeh, S., Karami, F., Delfani, S., Shakibaie, M., Razlansari, A., Rezaei, F.: Antibacterial effects and cellular mechanisms of iron oxide magnetic nanoparticles coated by piroctone olamine against some cariogenic bacteria. *Annals Med. Surg.* (2022). <https://doi.org/10.1016/j.amsu.2022.104291>
 - 23 Gong, J.L., Wang, X.Y., Zeng, G.M., Chen, L., Deng, J.H., Zhang, X.R., Niu, Q.Y.: Copper (II) removal by pectin-iron oxide magnetic nanocomposite adsorbent. *Chem. Eng. J.* 185–186 (2012). <https://doi.org/10.1016/j.cej.2012.01.050>
 - 24 Guilherme, M.R., Reis, A.V., Paulino, A.T., Moia, T.A., Mattoso, L.H.C., Tambourgi, E.B.: Pectin-based polymer hydrogel as a carrier for release of agricultural nutrients and removal of heavy metals from wastewater. *J. Appl. Polym. Sci.* **117**, 3146–3154 (2010). <https://doi.org/10.1002/app.32123>
 - 25 Gurung, K., Neibi, M.C., Sillanpää, M.: Removal and fate of emerging organic micropollutants (EOMs) in municipal wastewater by a pilot-scale membrane bioreactor (MBR) treatment under varying solid retention times. *Sci. Total Environ.* **667**, 671–680 (2019). <https://doi.org/10.1016/j.scitotenv.2019.02.308>
 - 26 Han, C., Cai, N., Chan, V., Liu, M., Feng, X., Yu, F.: Enhanced drug delivery, mechanical properties and antimicrobial activities in poly(lactic acid) nanofiber with mesoporous Fe₃O₄-COOH nanoparticles. *Colloids Surf. Physicochem Eng. Asp.* **559**, 104–114 (2018). <https://doi.org/10.1016/j.colsurfa.2018.09.012>
 - 27 Hanauer, D.C., Paulino, A.T.: Anchoring lactase in pectin-based hydrogels for lactose hydrolysis reactions. *Process Biochem.* **122**, 50–59 (2022). <https://doi.org/10.1016/j.procbio.2022.08.026>
 - 28 Hanauer, D.C., de Souza, A.G., Cargnin, M.A., Gasparin, B.C., Rosa, D.S., Paulino, A.T.: Pectin-based bihydrogels reinforced with Eucalyptus sawdust: Synthesis, characterization, β -D-Galactosidase immobilization and activity. *J. Ind. Eng. Chem.* **97**, 368–382 (2021). <https://doi.org/10.1016/j.jiec.2021.02.022>
 - 29 Hastuti, B., Nur Afifah, S., Mulyani, B., Susilowati, E.: Adsorption of methylene blue dyes using pectin membrane. *J. Phys. Conf. Ser.* **1503**, 012031 (2020). <https://doi.org/10.1088/1742-6596/1503/1/012031>
 - 30 Ho, Y.S., Ng, J.C.Y., McKay, G.: Kinetics of pollutant sorption by biosorbents: Review. *Sep. Purif. Methods.* **29**, 189–232 (2000). <https://doi.org/10.1081/SPM-100100009>
 - 31 Huang, Y., Huang, Q., Liu, H., Xiao, C., Sun, K.: A facile and environmental-friendly strategy for Preparation of Poly (tetrafluoroethylene-co-hexafluoropropylene) Hollow fiber membrane and its membrane emulsification performance. *Chem. Eng. J.* **384**, 123345 (2020). <https://doi.org/10.1016/j.cej.2019.123345>
 - 32 Jakóbcik-Kolon, A., Bok-Badura, J., Karoń, K., Mitko, A., Milewski, K.: Hybrid pectin-based biosorbents for zinc ions removal. *Carbohydr. Polym.* **169**, 213–219 (2017). <https://doi.org/10.1016/j.carbpol.2017.03.095>
 - 33 Jawad, A.H., Abdulhameed, A.S., Mastuli, M.S.: Acid-fractionalized biomass material for methylene blue dye removal: a comprehensive adsorption and mechanism study. *J. Taibah Univ. Sci.* **14**, 305–313 (2020). <https://doi.org/10.1080/16583655.2020.1736767>
 - 34 Jawad, A.H., Mamat, N.F.H., Hameed, B.H., Ismail, K.: Biofilm of cross-linked Chitosan-Ethylene glycol diglycidyl ether for removal of reactive red 120 and Methyl Orange: Adsorption and mechanism studies. *J. Environ. Chem. Eng.* **7**, 102965 (2019). <https://doi.org/10.1016/j.jece.2019.102965>

- 35 Khare, A.R., Peppas, N.A.: Swelling/deswelling of anionic copolymer gels. *Biomaterials*. **16**, 559–567 (1995). [https://doi.org/10.1016/0142-9612\(95\)91130-Q](https://doi.org/10.1016/0142-9612(95)91130-Q)
- 36 Kulal, P., Badalamoole, V.: Magnetite nanoparticle embedded Pectin-graft-poly(N-hydroxyethylacrylamide) hydrogel: Evaluation as adsorbent for dyes and heavy metal ions from waste water. *Int. J. Biol. Macromol.* **156**, 1408–1417 (2020). <https://doi.org/10.1016/j.ijbiomac.2019.11.181>
- 37 Kumar, P., Malla, K.A., Yerra, B., Srinivasa Rao, K.: Removal of Cu(II) using three low-cost adsorbents and prediction of adsorption using artificial neural networks. *Appl. Water Sci.* **9** (2019). <https://doi.org/10.1007/s13201-019-0924-x>
- 38 Langmuir, I.: Adsorption of gases on plain surfaces of glass mica platinum. *J. Am. Chem. Soc.* (1918). <https://doi.org/10.1006/ceps.2001.1094>
- 39 Lima, E.C., Adebayo, M.A., Machado, F.M.: Chap. 3 - Kinetic and equilibrium models of adsorption. *Carbon Nanomaterials as Adsorbents Environ. Biol. Appl.* (2015). <https://doi.org/10.1007/978-3-319-18875-1>
- 40 de Lima, G.F., de Souza, A.G., Rosa, D.S.: Effect of adsorption of polyethylene glycol (PEG), in aqueous media, to improve cellulose nanostructures stability. *J. Mol. Liq.* **268**, 415–424 (2018). <https://doi.org/10.1016/j.molliq.2018.07.080>
- 41 Liu, Z., Lompe, K.M., Mohseni, M., Bérubé, P.R., Sauvé, S., Barbeau, B.: Biological ion exchange as an alternative to biological activated carbon for drinking water treatment. *Water Res.* **168**, 115148 (2020). <https://doi.org/10.1016/j.watres.2019.115148>
- 42 Low, L.W., Teng, T.T., Ahmad, A., Morad, N., Wong, Y.S.: A novel pretreatment method of lignocellulosic material as adsorbent and kinetic study of dye waste adsorption. *Water Air Soil Pollut.* **218**, 293–306 (2011). <https://doi.org/10.1007/s11270-010-0642-3>
- 43 Ma, W., Li, Y., Zhang, M., Gao, S., Cui, J., Huang, C., Fu, G.: Biomimetic durable multifunctional Self-Cleaning nanofibrous membrane with outstanding oil/water separation, photodegradation of organic contaminants, and antibacterial performances. *ACS Appl. Mater. Interfaces.* **12**, 34999–35010 (2020). <https://doi.org/10.1021/acsami.0c09059>
- 44 Mao, Y., Bu, X., Peng, Y., Tian, F., Xie, G.: Effects of simultaneous ultrasonic treatment on the separation selectivity and flotation kinetics of high-ash lignite. *Fuel.* **259**, 116270 (2020). <https://doi.org/10.1016/j.fuel.2019.116270>
- 45 Mohammadi, M., Eivazzadeh-Keihan, R., Babamoradi, M., Maleki, A.: A magnetic and antibacterial nanocomposite based on graphene oxide nanosheets embedded with Zn-Fe layered double hydroxide as a novel and highly effective adsorbent for the removal of methylene blue dye. *Diam. Relat. Mater.* **144**, 111010 (2024). <https://doi.org/10.1016/j.diamond.2024.111010>
- 46 Mohrazi, A., Ghasemi-Fasaei, R.: Removal of methylene blue dye from aqueous solution using an efficient chitosan-pectin bio-adsorbent: Kinetics and isotherm studies. *Environ. Monit. Assess.* **195**, 339 (2023). <https://doi.org/10.1007/s10661-022-10900-4>
- 47 Moradi, E., Ebrahimzadeh, H., Mehrani, Z., Asgharinezhad, A.A.: The efficient removal of methylene blue from water samples using three-dimensional Poly (vinyl alcohol)/starch nanofiber membrane as a green nanosorbent. *Environ. Sci. Pollut. Res.* **26**, 35071–35081 (2019). <https://doi.org/10.1007/s11356-019-06400-7>
- 48 Morris, G., Foster, T.J., Harding, S.E.: The effect of the degree of esterification on the hydrodynamic properties of citrus pectin. *Food Hydrocoll.* **14**, 227–235 (2000). [https://doi.org/10.1016/S0268-005X\(00\)00007-2](https://doi.org/10.1016/S0268-005X(00)00007-2)
- 49 Moslemi, M.: Reviewing the recent advances in application of pectin for technical and health promotion purposes: From laboratory to market. *Carbohydr. Polym.* **254**, 117324 (2021). <https://doi.org/10.1016/j.carbpol.2020.117324>
- 50 Murphy, O.P., Vashishtha, M., Palanisamy, P., Kumar, K.V.: A review on the adsorption isotherms and design calculations for the optimization of adsorbent mass and contact time. *ACS Omega.* **8**, 17407–17430 (2023). <https://doi.org/10.1021/acsomega.2c08155>
- 51 Ngulube, T., Gumbo, J.R., Masindi, V., Maity, A.: Preparation and characterisation of high performing magnesite-halloysite nanocomposite and its application in the removal of methylene blue dye. *J. Mol. Struct.* **1184**, 389–399 (2019). <https://doi.org/10.1016/j.molstruc.2019.02.043>
- 52 Norouzi, S., Heidari, M., Alipour, V., Rahmanian, O., Fazlzadeh, M., Mohammadi-moghadam, F., Nourmoradi, H., Goudarzi, B., Dindarloo, K.: Preparation, characterization and Cr(VI) adsorption evaluation of NaOH-activated carbon produced from date press cake; an agro-industrial waste. *Bioresour. Technol.* (2018). <https://doi.org/10.1016/j.biortech.2018.02.106>
- 53 Nsom, M.V., Etape, E.P., Tendo, J.F., Namond, B.V., Chongwain, P.T., Yufanyi, M.D., William, N.: A green and facile approach for synthesis of Starch-Pectin magnetite nanoparticles and application by removal of methylene blue from textile effluent. *J. Nanomater.* **2019**, 1–12 (2019). <https://doi.org/10.1155/2019/4576135>
- 54 Oliveira, W.E., Franca, A.S., Oliveira, L.S., Rocha, S.D.: Untreated coffee husks as biosorbents for the removal of heavy metals from aqueous solutions. *J. Hazard. Mater.* **152**, 1073–1081 (2008). <https://doi.org/10.1016/j.jhazmat.2007.07.085>
- 55 Pal, P.: *Industry-Specific Water Treatment*. (2017)
- 56 Paulino, A.T., Belfiore, L.A., Kubota, L.T., Muniz, E.C., Almeida, V.C., Tambourgi, E.B.: Effect of magnetite on the adsorption behavior of Pb(II), Cd(II), and Cu(II) in chitosan-based hydrogels. *Desalination* **275**, 187–196 (2011). <https://doi.org/10.1016/j.desal.2011.02.056>
- 57 Paulino, A.T., Belfiore, L.A., Kubota, L.T., Muniz, E.C., Tambourgi, E.B.: Efficiency of hydrogels based on natural polysaccharides in the removal of Cd²⁺ ions from aqueous solutions. *Chem. Eng. J.* (2011). <https://doi.org/10.1016/j.cej.2010.12.037>
- 58 Paulino, A.T., Fajardo, A.R., Junior, A.P., Muniz, E.C., Tambourgi, E.B.: Two-step synthesis and properties of a magnetic-field-sensitive modified maltodextrin-based hydrogel. *Polym. Int.* **60**, 1324–1333 (2011). <https://doi.org/10.1002/pi.3084>
- 59 Paulino, A.T., Guilherme, M.R., Mattoso, L.H.C., Tambourgi, E.B.: Smart hydrogels based on modified gum arabic as a potential device for magnetic biomaterial. *Macromol. Chem. Phys.* (2010). <https://doi.org/10.1002/macp.200900657>
- 60 Paz, M.J., Serafini, S., Enzweiler, H., Visioli, L.J., Paulino, A.T.: Photodegradation of Emerging Pollutants Using Catalysts Supported in Organic and Inorganic Composite Materials. Presented at the (2022)
- 61 Paz, M.J., Vieira, T., Enzweiler, H., Paulino, A.T.: Chitosan/wood sawdust/magnetite composite membranes for the photodegradation of agrochemicals in water. *J. Environ. Chem. Eng.* **10**, 106967 (2022b). <https://doi.org/10.1016/j.jece.2021.106967>
- 62 Pereira, B.L.C., Carneiro, A.D.C.O., Carvalho, A.M.M.L., Colodette, J.L., Oliveira, A.C., Fontes, M.P.F.: Influence of Chemical Composition of Eucalyptus Wood on Gravimetric Yield and Charcoal Properties. *Bioresources* (2013). <https://doi.org/10.15376/biores.8.3.4574-4592>
- 63 Psaltou, S., Zouboulis, A.: Catalytic ozonation and membrane Contactors—A review concerning fouling occurrence and pollutant removal. *Water (Basel)*. **12**, 2964 (2020). <https://doi.org/10.3390/w12112964>
- 64 Radoor, S., Karayil, J., Parameswaranpillai, J., Siengchin, S.: Adsorption of methylene blue dye from aqueous solution by a novel PVA/CMC/halloysite nanoclay bio composite: Characterization, kinetics, isotherm and antibacterial properties. *J. Environ. Health Sci. Eng.* **18**, 1311–1327 (2020). <https://doi.org/10.1007/s40201-020-00549-x>

- 65 Rahman, M.M., Rimu, S.H.: Recent development in cellulose nanocrystal-based hydrogel for decolouration of methylene blue from aqueous solution: A review. *Int. J. Environ. Anal. Chem.* **102**, 6766–6783 (2022). <https://doi.org/10.1080/03067319.2020.1817424>
- 66 Redlich, O., Peterson, D.L.: A useful adsorption isotherm. *J. Phys. Chem.* **63**, 1024–1024 (1959). <https://doi.org/10.1021/j150576a611>
- 67 Rezvanian, M., Ahmad, N., Amin, M., Ng, M.C.I.: Optimization, characterization, and in vitro assessment of alginate-pectin ionic cross-linked hydrogel film for wound dressing applications. *Int. J. Biol. Macromol.* **97**, 131–140 (2017). <https://doi.org/10.1016/j.ijbiomac.2016.12.079>
- 68 Ribera-Pi, J., Badia-Fabregat, M., Arias, D., Gómez, V., Taberna, E., Sanz, J., Martínez-Lladó, X., Jubany, I.: Coagulation-flocculation and moving bed biofilm reactor as pre-treatment for water recycling in the petrochemical industry. *Sci. Total Environ.* **715**, 136800 (2020). <https://doi.org/10.1016/j.scitotenv.2020.136800>
- 69 Rojas, S., Horcajada, P.: Metal–Organic frameworks for the removal of emerging organic contaminants in water. *Chem. Rev.* **120**, 8378–8415 (2020). <https://doi.org/10.1021/acs.chemrev.9b00797>
- 70 Sahoo, T.R., Prelot, B.: Adsorption processes for the removal of contaminants from wastewater. In: Bonelli, B., Freyria, F.S., Rossetti, I., Sethi, R. (eds.) *Nanomaterials for the Detection and Removal of Wastewater Pollutants*, pp. 161–222. Elsevier (2020)
- 71 Sayed, E.T., Shehata, N., Abdelkareem, M.A., Atieh, M.A.: Recent progress in environmentally friendly bio-electrochemical devices for simultaneous water desalination and wastewater treatment. *Sci. Total Environ.* **748**, 141046 (2020). <https://doi.org/10.1016/j.scitotenv.2020.141046>
- 72 Sayed, N.S.M., Ahmed, A.S.A., Abdallah, M.H., Gouda, G.A.: ZnO@ activated carbon derived from wood sawdust as adsorbent for removal of Methyl red and Methyl orange from aqueous solutions. *Sci. Rep.* **14**, 5384 (2024). <https://doi.org/10.1038/s41598-024-55158-7>
- 73 Sharma, Y.C., Uma: Optimization of parameters for adsorption of methylene blue on a Low-Cost activated carbon. *J. Chem. Eng. Data.* **55**, 435–439 (2010). <https://doi.org/10.1021/jc900408s>
- 74 Sips, R.: On the structure of a catalyst surface. *J. Chem. Phys.* **16**, 490–495 (1948). <https://doi.org/10.1063/1.1746922>
- 75 de Souza, A.G., Cesco, C.T., de Lima, G.F., Artifon, S.E.S., Rosa, D.S., Paulino, A.T.: Arabic gum-based composite hydrogels reinforced with Eucalyptus and Pinus residues for controlled phosphorus release. *Int. J. Biol. Macromol.* **140**, 33–42 (2019). <https://doi.org/10.1016/j.ijbiomac.2019.08.106>
- 76 Sun, G., Xu, X.: Sunflower stalks as adsorbents for color removal from textile wastewater. *Ind. Eng. Chem. Res.* **36**, 808–812 (1997). <https://doi.org/10.1021/ie9603833>
- 77 Tarekegn, M.M., Balakrishnan, R.M., Hiruy, A.M., Dekebo, A.H.: Removal of methylene blue dye using nano zerovalent iron, nanoclay and iron impregnated nanoclay– a comparative study. *RSC Adv.* **11**, 30109–30131 (2021). <https://doi.org/10.1039/D1R403918K>
- 78 Tischer, A.M., Ferreira, R.R., Ribeiro, J.G., dos Santos Rosa, D., Paulino, A.T.: Green synthesis of an advanced composite membrane for the purification of water contaminated with potentially toxic metals. *J. Water Process. Eng.* **61**, 105239 (2024). <https://doi.org/10.1016/j.jwpe.2024.105239>
- 79 Tripathy, S., Sahu, S., Patel, R.K., Panda, R.B., Kar, P.K.: Novel Fe₃O₄-Modified Biochar Derived from Citrus Bergamia Peel: A Green Synthesis Approach for Adsorptive Removal of Methylene Blue. *ChemistrySelect* (2022). <https://doi.org/10.1002/slct.202103595>
- 80 Vieira, T., Artifon, S.E.S., Cesco, C.T., Vilela, P.B., Becegato, V.A., Paulino, A.T.: Chitosan-based hydrogels for the sorption of metals and dyes in water: Isothermal, kinetic, and thermodynamic evaluations. *Colloid Polym. Sci.* **299**, 649–662 (2021). <https://doi.org/10.1007/s00396-020-04786-2>
- 81 Vieira, T., Becegato, V.A., Paulino, A.T.: Equilibrium Isotherms, Kinetics, and Thermodynamics of the Adsorption of 2,4-Dichlorophenoxyacetic Acid to Chitosan-Based Hydrogels. *Water Air Soil. Pollut.* (2021). <https://doi.org/10.1007/s11270-021-05021-6>
- 82 Vievard, J., Alem, A., Pantet, A., Ahfir, N.-D., Arellano-Sánchez, M.G., Devouge-Boyer, C., Mignot, M.: Bio-Based adsorption as ecofriendly method for wastewater decontamination: A review. *Toxics.* **11**, 404 (2023). <https://doi.org/10.3390/toxics11050404>
- 83 Vilela, P.B., Dalalibera, A., Duminelli, E.C., Becegato, V.A., Paulino, A.T.: Adsorption and removal of chromium (VI) contained in aqueous solutions using a chitosan-based hydrogel. *Environ. Sci. Pollut. Res.* **26**, 28481–28489 (2019). <https://doi.org/10.1007/s11356-018-3208-3>
- 84 Vilela, P.B., Matias, C.A., Dalalibera, A., Becegato, V.A., Paulino, A.T.: Polyacrylic acid-based and chitosan-based hydrogels for adsorption of cadmium: Equilibrium isotherm, kinetic and thermodynamic studies. *J. Environ. Chem. Eng.* **7**, 103327 (2019). <https://doi.org/10.1016/j.jece.2019.103327>
- 85 Vinhal-Freitas, I., Maldonado, A., Alvarenga, C., Camargo, R., Wendling, B.: *Adsorção E Dessorção De Metais No Solo E Coeficientes De Isotermas De Freundlich E Langmuir*. Semantic Scholar (2010)
- 86 Voragen, F., Beldman, G., Schools, H.: Chemistry and enzymology of pectins. In: McCleary, B.V., Prosky, L. (eds.) *Advanced Dietary Fibre Technology*, pp. 379–398. Wiley (2000)
- 87 Wang, J., Guo, X.: Adsorption kinetic models: Physical meanings, applications, and solving methods. *J. Hazard. Mater.* **390**, 122156 (2020). <https://doi.org/10.1016/j.jhazmat.2020.122156>
- 88 Wang, Q., Ju, J., Tan, Y., Hao, L., Ma, Y., Wu, Y., Zhang, H., Xia, Y., Sui, K.: Controlled synthesis of sodium alginate electrospun nanofiber membranes for multi-occasion adsorption and separation of methylene blue. *Carbohydr. Polym.* **205**, 125–134 (2019). <https://doi.org/10.1016/j.carbpol.2018.10.023>
- 89 Weber, W.J.: Adsorption processes. *Pure Appl. Chem.* **37**, 375–392 (1974). <https://doi.org/10.1351/pac197437030375>
- 90 Zactiti, E.M., Kieckbusch, T.G.: Potassium sorbate permeability in biodegradable alginate films: Effect of the antimicrobial agent concentration and crosslinking degree. *J. Food Eng.* **77**, 462–467 (2006). <https://doi.org/10.1016/j.jfoodeng.2005.07.015>
- 91 Zonatto, F., Muniz, E.C., Tambourgi, E.B., Paulino, A.T.: Adsorption and controlled release of potassium, phosphate and ammonia from modified Arabic gum-based hydrogel. *Int. J. Biol. Macromol.* **105**, 363–369 (2017). <https://doi.org/10.1016/j.ijbiomac.2017.07.051>

Publisher's note Springer Nature remains neutral with regard to jurisdictional claims in published maps and institutional affiliations.

Springer Nature or its licensor (e.g. a society or other partner) holds exclusive rights to this article under a publishing agreement with the author(s) or other rightsholder(s); author self-archiving of the accepted manuscript version of this article is solely governed by the terms of such publishing agreement and applicable law.



Enhancing Corn Starch Hydrogels for Effective Sorption of Potentially Toxic Metals: The Role of Amylose and Amylopectin Content

Talles B. da Costa¹ · Paulo H. Camani¹ · Rafaela R. Ferreira¹ · Rennan F. S. Barbosa¹ · Derval dos S. Rosa¹

Accepted: 2 January 2025 / Published online: 25 January 2025

© The Author(s), under exclusive licence to Springer Science+Business Media, LLC, part of Springer Nature 2025

Abstract

This study evaluated the effect of corn starch's amylose/amylopectin content on the development of crosslinked hydrogels with trisodium citrate for the sorption of potentially toxic metals (PTMs). The results, obtained through a robust methodology, indicated a clear relation between the amylose content and crosslinking degree, thereby impacting the properties of the hydrogels. The hydrogel with high amylose (70 wt.%) and low amylopectin (30 wt.%) content (Hylon VII®) demonstrated a high crosslinking degree (0.297) and good thermal stability and water absorption (72.71%), with a semicrystalline structure. The hydrogel with low amylose (1.8 wt.%) and high amylopectin (98.2 wt.%) content (Amisol 4000®), on the other hand, showed the lowest degree of crosslinking (0.109), water absorption (49.77%), and high solubility (46%), which makes its applicability difficult due to its low stability in aqueous media. The influence of amylose (28 wt.%) and amylopectin (72 wt.%) content indicated that the Amisol 3408® hydrogel showed valuable properties, presenting a higher potential for PTMs sorption with the following affinity order: Cu^{2+} (68.62%) > Cd^{2+} (63.13%) > Mn^{2+} (37.36%) > Zn^{2+} (26.61%) > Cr^{6+} (16.80%). Besides, the possible sorption mechanism was ion exchange between $\text{Cu}^{2+}/\text{Cd}^{2+}/\text{Mn}^{2+}/\text{Zn}^{2+}$ and H^+ in the hydrogels. Thus, starch-based hydrogel is an alternative sorbent to remove and recover PTMs from wastewater.

Keywords Porous materials · Starch · Amylose/amylopectin structures · Covalent crosslinking · Toxic metals sorption

Introduction

According to the United Nations, worldwide, the use of water resources has grown twice as fast as population growth [1]. Ullah et al. [2] performed principal component analysis (PCA), whose 60.1% of the total variability revealed that the groundwater sources of the studied area are contaminated by geogenic sources (30.9%), anthropogenic sources (31.3%), and the mixed type (37.8%), including both geogenic and anthropogenic source of contamination. Pollution of water resources is caused by economic development, which is linked to population growth, which generates excessive use of water resources and destruction of existing vegetation, as well as environmental problems listed in inefficient urban surface water systems and agricultural discharges. Due to

water supply systems surrounding agricultural, domestic, or industrial environments, rapid urbanization in recent years has increased the contamination of natural ecosystems with PTMs [3].

The PTMs are pollutants that have concerned the technical-scientific community, especially As, Cd, Pb, Cr, Cu, Hg, and Ni, due to their presence in water in high concentrations and their highly harmful effects on health [4]. Thus, several removal technologies to mitigate these pollutants can be reported, highlighting conventional (bioremediation, phytoremediation, ion-exchange, adsorption, coagulation, flotation, membrane filtration, and chemical precipitation) emerging/current trends (activated carbon, use of carbon nanotubes, biochar) and miscellaneous approaches (biosorption, chemical-biological remediation methods, electrokinetic-microbial remediation approach, and electrokinetic-phytoremediation approach) [5]. However, promising attention has been given to technologies involving adsorption phenomena due to their high efficiency, simplicity, flexibility of operation, and pollutant removal at low concentrations [6, 7].

✉ Derval dos S. Rosa
derval.rosa@ufabc.edu.br

¹ Center for Engineering, Modeling, and Applied Social Sciences (CECS), Federal University of ABC (UFABC), Santo André, Brazil

In recent studies, starch-based adsorptive hydrogels were widely designed to remove heavy metals from effluents [8–10]. The literature survey shows that the grafted and crosslinking starch has suitable sorption characteristics towards PTMs [11]. Free radical graft polymerization of itaconic acid starch graft hydrogels for the sorption of divalent ions was investigated by Soto et al. [12]. The removal percentage was greater than 95% for the PTMs, while the sorption capacities followed the trend: $\text{Pb}^{2+} > \text{Ni}^{2+} > \text{Zn}^{2+} > \text{Cd}^{2+}$. Wang et al. [13] synthesized magnetic crosslinked starch-graft-poly-(acrylamide)-co-sodium xanthate to evaluate its behavior as an adsorbent for PTMs. About 78% and 63% removal of Pb^{2+} and Cu^{2+} were observed, respectively. The sorption capacity of Pb^{2+} using hydrolyzed starch graft poly-(acrylic acid) and starch graft (polyacrylonitrile) was investigated by Ekebafe et al. [14]. The maximum sorption capacities were 118.6 mg/g and 115.8 mg/g, respectively. Sorption of Co^{2+} using starch hydrogels prepared by radiation-induced grafting of copolymerization of dimethylaminoethyl methacrylate and 2-acrylamido-2-methylpropane-1-sulphonic acid was evaluated by Farag et al. [15]. The maximum sorption capacity was 350 mg/g. Corn starch was modified by grafting copolymerization of dibenzo-18-crown-6 in the presence of microwave radiation and was used as an adsorbent for Zn^{2+} , Cd^{2+} , Ni^{2+} , and Cu^{2+} [16]. The maximum sorption capacities were 28.1, 24.5, 30.8, and 17.9 mg/g for Zn^{2+} , Cd^{2+} , Ni^{2+} , and Cu^{2+} . Removal of divalent ions using starch-iron oxide nanocomposite was investigated by Mahmoud et al. [17]. The maximum sorption capacities were 200, 322, and 133 mg/g for Pb^{2+} , Cd^{2+} , and Hg^{2+} , respectively. The sorption capacity of Pb^{2+} using starch-modified montmorillonite was studied by Luu et al. [18]. Maximum sorption capacity was found to be 21.5 mg/g.

Currently, ongoing research focuses on synthesizing and studying new adsorbent materials that can be obtained by modifying traditional materials, functionalizing with functional groups, and using natural polymers, blends, and residues [19]. Among these natural polymers, starch is the primary storage polysaccharide in plants and exists in granular form. It is a mixture of two distinct entities: linear amylose and branched amylopectin, composed of anhydroglucose monomers. α -1,4 bonds link the linear amylose chains, whereas α -1,6 bonds link the branching points of amylopectin. Amylopectin usually is present in more significant amounts (70–80%) than amylose (20–30%), although these amounts vary based on the starch source and type [20, 21]. However, this polysaccharide does not have active functional groups capable of interacting with metal ions [22, 23]. By exposing the starch granules to sodium hydroxide (NaOH) solution, hydroxide ions (OH^-) can be more easily attracted by the starch, and the anions of the hydroxyl group can be ionized, leaving negative charges on the starch

molecules [6]. Therefore, the active sites become more reactive and can promote new reactions, like the crosslinking of the starch chain using a crosslinker agent responsible for including new functional groups in the structure. In addition, it is recommended to use a harmless crosslinker such as citric acid to carry out hydrogen crosslinking safely and efficiently, which also promotes a good affinity for metal ions [8].

In this study, we investigated and characterized the production of crosslinked hydrogels using corn starches from the same source, varying contents of amylose and amylopectin: 1.8 wt.% amylose/98.2 wt.% amylopectin (Amisol 4000®), 28 wt.% amylose/72 wt.% (Amisol 3408®), and 70 wt.% amylose/30 wt.% of amylopectin (Hylon VII®). We evaluated the produced hydrogels' chemical, thermal, and morphological properties and their performance in removing PTMs. Thus, this work primarily aimed to compare four types of hydrogels produced from different corn starches applied as efficient adsorbents to remove PTMs in an aqueous solution.

Materials and Methods

Materials and Reagents

Different corn starches were employed, such as Amisol 3408® containing 28 wt.% amylose and 72 wt.% amylopectin, Amisol 4000® containing 1.8 wt.% amylose and 98.2 wt.% amylopectin. In contrast, Hylon VII® contains 70 wt.% amylose and 30 wt.% amylopectin. Ingredient Company (São Paulo/Brazil) donated and supplied corn starches. Zinc nitrate hexahydrate ($\text{Zn}(\text{NO}_3)_2 \cdot 6\text{H}_2\text{O}$, 98%) and sodium hydroxide (NaOH, 98%) were obtained from Dynamics Contemporary Chemistry. Cadmium nitrate tetrahydrate ($\text{Cd}(\text{NO}_3)_2 \cdot 4\text{H}_2\text{O}$, 98%) and methyl alcohol (CH_3OH , 99%) were acquired from Neon Chemistry. Potassium dichromate ($\text{K}_2\text{Cr}_2\text{O}_7$, 99%) was obtained from ECIBRA Analytical Reagents. Copper nitrate trihydrate ($\text{Cu}(\text{NO}_3)_2 \cdot 3\text{H}_2\text{O}$, 99%), citric acid ($\text{C}_6\text{H}_8\text{O}_7$, 99.5%), nitric acid (HNO_3 , 65%), and sulfuric acid (H_2SO_4 , 95%) were acquired from Synth. Manganese nitrate tetrahydrate ($\text{Mn}(\text{NO}_3)_2 \cdot 4\text{H}_2\text{O}$, 98%), oxalic acid ($\text{C}_2\text{H}_2\text{O}_4$, 98%), ammonium hydroxide (NH_4OH , 30%), 2,6-Pyridinedicarboxylic acid ($\text{C}_7\text{H}_5\text{NO}_4$, 99%), 1,5-Diphenylcarbazide ($\text{C}_{13}\text{H}_{14}\text{N}_4\text{O}$, 99%), and sodium carbonate (Na_2CO_3 , 99%) were acquired from Sigma-Aldrich. The standard stock solutions of 1000 mg/L, 99.9% purity (hexavalent chromium, copper, cadmium, manganese, nickel, and zinc) were acquired from Specscol. Ultrapure water was used for solution formulation and was obtained by the system ARIUM® MINI (Sartorius, Germany).

Methods

Starch-Based Hydrogels Synthesis

The starch-based hydrogels were synthesized according to the methodologies proposed by Abhari et al. [24] and Camani et al. [22]. The hydrogels were prepared from starches from the same source (corn), with different amylose and amylopectin contents (Amisol 3408®, Amisol 4000®, and Hylon VII®). Corn starch was suspended in ultrapure water (40 °C at 70 g/L) in distinct lots. After dissolving corn starch, NaOH (13 g/L) was added, and the mixtures were maintained under mechanical agitation (713DS, Fisatom, UK) at 40 °C for three hours. In the case of Hylon VII® corn starch, this condition was adapted from previous studies that solubilized this starch granules under similar conditions [25, 26]. Then, citric acid ($C_6H_8O_7$) (19.4 g/L) was added to form the crosslinking agent (trisodium citrate, $Na_3C_6H_5O_7$), considering the reaction's stoichiometric balance. Chemical crosslinking occurred with the system under mechanical agitation at 40 °C for 17 h. The produced hydrogel was heated in a bath at 90 °C for 30 min, stabilized at room temperature (~25 °C) for 30 min, and dried in an oven at 60 °C for 48 h. Finally, the produced hydrogels were neutralized with HNO_3 (3.0 mol/L) and dried again in an oven at 60 °C for 48 h to avoid the collapse of the pores of the synthesized starch hydrogels, besides thermal degradation of the starch polymer chains [23, 27] (Fig. 1).

Hydrogels Characterization

The corn starch sources, and starch-based hydrogels developed were characterized using Fourier transform infrared spectroscopy (FTIR), X-ray diffraction (XRD), thermal analysis (TGA/DTG), and scanning electron microscopy (SEM) techniques. To perform the analyses, the samples were dried in an oven at 60 °C for 48 h.

Fourier Transform Infrared Spectroscopy (FTIR) The functional groups were obtained using the FTIR technique (Frontier 94.942, PerkinElmer, USA) in the operation mode with attenuated total reflectance (ATR), using a range of 4000–500 cm^{-1} , the spectral resolution of 4 cm^{-1} , and 32 scans.

X-ray Diffraction (XRD) The crystalline structure and its changes were obtained using the XRD technique (STADI-PS diffractometer, STOE & Cie GmbH, Germany). Analyses were performed using $CuK_{\alpha 1}$ radiation ($\lambda = 1.54060 \text{ \AA}$), a scan range of 10–80 °, a step of 0.015 °, a voltage of 40 kV, and a current of 40 mA. The relative crystallinity (RC) was calculated by Eq. (1).

$$RC = \frac{A_c}{(A_c + A_a)} \cdot 100 \quad (1)$$

wherein, A_c is the area of the crystalline region and A_a is the area of the amorphous region. For the calculation of RC of starches and starch hydrogels, the scan range was considered 10 to 40°.

Thermogravimetry Analysis (TGA) The thermal stability of the materials was obtained by thermogravimetry analysis (STA 6000, PerkinElmer, USA). Samples were heated from 30 to 600 °C, with a heating rate of 10 °C/min under an N_2 atmosphere (flow rate of 20 mL/min).

Scanning Electron Microscopy (SEM) Morphology, structure, and pore size were obtained by SEM technique (FEI Quanta 250, Thermo Fisher Scientific, USA). The materials were fractured in liquid N_2 to analyze the fracture region. Samples were covered with a thin layer of gold with a thickness of 25 nm (Sputtering Leica EM ACE200, Leica Microsystems, Germany). The micrographs were obtained under



Fig. 1 Schematic illustration of the production process of starch hydrogels presenting the starch chains (amylose and amylopectin) rearrangement during the crosslinking process

the conditions: current of 50 pA, voltage of 10 kV, and spot size of 4 nm. Pore size distribution of starch hydrogels was performed using ImageJ® software. Besides, pore size distribution was performed from the sample's triplicate, using ten SEM images, adopting the methodologies by Alves et al. [23] and Camani et al. (2021).

Water Uptake and Solubility Tests

The water absorption of the starch hydrogels was obtained by immersing 0.1 g of dry hydrogel pieces in 50 mL of ultrapure water. The assays were carried out at room temperature (~25 °C). Samples were collected periodically from 0 to 24 h to weigh the mass of swollen hydrogels. At the end of the assay, the hydrogel solubility was measured by taking the same sample and drying it until constant weight, and then comparing it with the initial hydrogel weight used during the water uptake test to determine the weight loss in an aqueous medium. The degree of swelling (DS) and solubility (%S) were calculated by Eqs. (2) and (3), respectively.

$$DS = \frac{(m_t - m_i)}{m_i} \cdot 100 \quad (2)$$

$$\%S = \frac{(m_i - m_f)}{m_i} \cdot 100 \quad (3)$$

wherein, m_i is the initial dry weight of hydrogels (g), m_t is the swollen weight of hydrogels at time t (g), and m_f is the final dry weight of hydrogels (g).

The water diffusion mechanism in the corn hydrogels network was determined by Fick diffusion model (Eq. 4).

$$\frac{m_t}{m_e} = k \cdot t^n \quad (4)$$

wherein, m_e is the swollen weight of hydrogels at equilibrium (g), k is the constant of the Fick diffusion model (dimensionless), and n is the parameter that describes the diffusion mechanism (dimensionless).

Metallic Speciation

Chemical equilibrium diagrams for PTMs (Cu, Zn, Cd, Mn, and Cr) were simulated using the Visual MINTEQ software with a 1.0 mmol/L concentration. The chemical equilibrium diagrams indicated that the pH range of 4.0–4.5 was adequate for the PTMs sorption experiments. Metallic speciation was performed considering the stoichiometric ratios of the PTM salts evaluated.

Sorption Assays in the Batch System: Hydrogel Affinity

The affinity of Amisol 3408®, Amisol 4000®, and Hylon VII® hydrogels for Cu^{2+} , Zn^{2+} , Cd^{2+} , Mn^{2+} , and Cr^{6+} was performed by adding 0.25 g of hydrogels and 25 mL of PTMs solution (0.2 mmol/L each) in Erlenmeyer flasks (125 mL). The pH control, defined by the chemical equilibrium diagrams (see Sect. "Metallic speciation"), was carried out with an HNO_3 solution (0.2 to 1.0 mol/L). The sorption affinity assays were conducted in a shaker incubator (SL-180/A, Solab, Brazil) under 200 rpm at room temperature (~25 °C). After 24 h, PTM concentrations were determined by ion chromatography (940 Professional IC Vario, Metrohm, Switzerland). The method quantification of transition metals was validated using $\text{C}_2\text{H}_2\text{O}_4$ solution (0.003 mol/L) as eluent and $\text{C}_7\text{H}_5\text{NO}_4$ (1.939×10^{-4} mol/L) as post-column reagent at a flow rate of 0.9 mL/min, Metrosep C4 column (250 mm × 4.0 mm), column temperature of 45 °C, injection volume of 20 μL , and UV–Vis detector. The method validated for hexavalent chromium used Na_2CO_3 solution (0.013 mol/L) as eluent and $\text{C}_{13}\text{H}_{14}\text{N}_4\text{O}$ solution (0.002 mol/L) as post-column reagent at a flow rate of 0.7 mL/min, Metrosep ASupp5 column (100 mm × 4.0 mm), column temperature of 45 °C, injection volume of 20 μL , and UV–Vis's detector. Removal efficiencies (%R) were determined by Eq. (5).

$$\%R = \frac{(C_0 - C_e)}{C_0} \cdot 100 \quad (5)$$

wherein, C_0 is the PTMs initial concentration (mmol/L) and C_e is the PTMs concentration at equilibrium (mmol/L).

Statistical Analysis

All experiments were performed in replicates, and standard deviations were calculated to measure mean dispersions. One-way analysis of variance (ANOVA) was applied to the data using Excel software and a 95% confidence level.

Characterizations after PTMs Uptake

After PTMs uptake from sorption batch experiments, the hydrogels submitted to 24 h of contact time with simulated water containing Cu^{2+} , Zn^{2+} , Cd^{2+} , Mn^{2+} , and Cr^{6+} in the concentration of 1.0 mmol/L (0.2 mmol/L for each metal ion), an adsorbent dose of 10.0 g/L, constant temperature, and pH of about 25 °C and 4.0–4.5, respectively. Then, the hydrogels were removed from the contaminated aqueous solution and dried in an oven at 60 °C for 24 h to perform FTIR and SEM–EDS. FTIR was used to monitor the changes after the sorption processes of metal ions. The same

conditions adopted before contamination were used to perform FTIR after contamination, using an FTIR spectrometer (Frontier 94.942, PerkinElmer, USA) in the operation mode with attenuated total reflectance (ATR), using a range of 4000–600 cm^{-1} , the spectral resolution of 4 cm^{-1} , and 32 scans. Samples were covered with a thin layer of gold with a thickness of 25 nm (Sputtering Leica EM ACE200, Leica Microsystems, Germany). SEM–EDS evaluated spectra of chemical elements using Compact Scanning Electron Microscope (JSM-6010LA, Jeol System Technology Co., LTD.) using the following conditions: current of 50 pA, voltage of 15 kV, and spot size of 50 nm.

Results and Discussion

Characterizations of the Corn Starches and Starch-Based Hydrogels

Fourier Transform Infrared Spectroscopy (FTIR)

FTIR analysis evaluated the hydrogel formation and the effect of crosslinking degree for hydrogel structures prepared from different starch sources containing various amount of amylose and amylopectin. Their spectra are presented in Fig. 2. The bands at 3284 cm^{-1} (–OH stretching), 2924 cm^{-1} (–CH asymmetric stretching), 1637 cm^{-1} (–OH bending), 1460 cm^{-1} (–CH₂ twisting), 1412 cm^{-1} (–CH₂ scissoring), 1337 cm^{-1} (–CH₂ twisting), 1150 cm^{-1} (–CO stretching), 997 and 928 cm^{-1} (–C–O–C group, from anhydroglucose ring), and 845 and 760 cm^{-1} (–CH bending) were found in all corn starch spectra. These vibrational

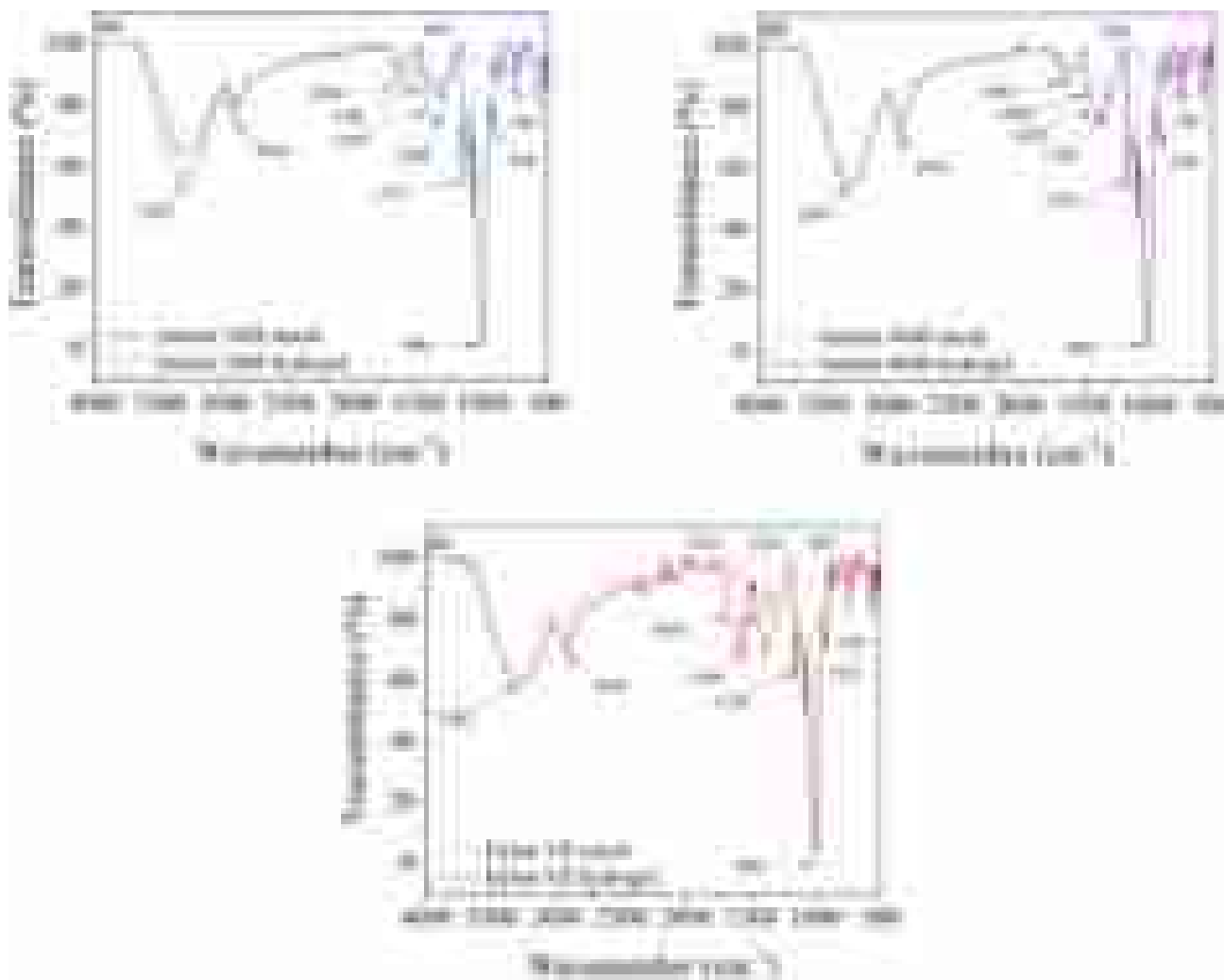


Fig. 2 FTIR spectra for corn starches and starch-based hydrogels with different contents of amylose and amylopectin: **a** Amisol 3408®, **b** Amisol 4000®, and **c** Hylon VII®

mode signatures are predominantly characteristic of corn starch structures [28–30].

For starch-based hydrogels, some changes were observed in the spectra of Fig. 2. The peak around 3284 cm^{-1} showed a slight shifting to 3300 cm^{-1} (Amisol 3408® hydrogel), 3312 cm^{-1} (Amisol 4000® hydrogel), and 3287 cm^{-1} (Hylon VII® hydrogel) compared to pure starches. Therefore, this displacement can be associated hydroxyl stretching and bending. This shifting is an indicative of retrogradation process due to the formation of the intermolecular hydrogen bonds and the rearrangement of the molecules in the retrogradation process and the crosslinking of the gel generated by heat, followed by cooling and storage of gelatinized starch [31]. Yang et al. [32] observed a similar shifting band $3000\text{--}3700\text{ cm}^{-1}$ for high wavenumbers related to the starch recrystallization during the retrogradation and formation of a gel.

Another change was observed in the spectrum region between 1750 and 1250 cm^{-1} , which can be attributed to aliphatic bonds, indicating conformational changes of the carbon–carbon bonds resulting from the crosslinking process, correlating with the retrogradation and reorganization of the amylose to amylopectin chains [33, 34]. Besides, the peaks close to 960 , 1060 , and 1150 cm^{-1} showed similar behavior, indicating that the chemical structure of pure starches was not modified during covalent crosslinking [22]. Besides, the band at 928 cm^{-1} present in all starches was slightly shifted to 933 cm^{-1} for all hydrogels. According to Camani et al. [22] and Wang et al. [28], this band shift is regarded as a crosslinking agent, which interacts with hydroxyl groups, generating crosslinks and forming interconnected 3D networks.

According to Camani et al. [22], the regions between 1750 and 1500 cm^{-1} and 1060 and 960 cm^{-1} were deconvoluted to investigate the crosslinking process of starch hydrogels, evaluating different starch hydrogels prepared from the different amylose and amylopectin contents. The region between 1750 and 1500 cm^{-1} was chosen due to the appearance of the new peak at 1580 cm^{-1} , which is associated with the stretching vibration of $\text{C}=\text{O}$ of the trisodium citrate carboxyl group. Subsequently, as 1060 and 960 cm^{-1} did not present modifications before and after crosslinking, this region was chosen as a non-changing pattern to perform the ratio of $1582/995\text{ cm}^{-1}$ peaks area to estimate the crosslinking degree [22, 31]. Other authors discussed the ratio between peaks obtained from deconvoluted peak areas linked to the ether bond signals for dried hydrogels synthesized from hydroxypropyl- β -cyclodextrin crosslinked with ethyleneglycol diglycidylether in the absence or presence of hydroxypropylmethylcellulose (HPMC) to apply them as carriers of amphiphilic drugs. This investigation of the ratio between peaks studied the crosslinking process

of these hydrogels [35]. Figure 3 and Table 1 show each region's deconvoluted FTIR spectra and peak area values, respectively.

Evaluating the deconvoluted spectra in the region from 1750 to 1500 cm^{-1} (Fig. 3 on the left), the pure starches only showed a peak close to 1630 cm^{-1} , while the hydrogels, regardless of the amylose and amylopectin content, showed between two to three peaks close to 1580 cm^{-1} . According to Ghorpade et al. [36], these new peaks can be associated with the stretching vibration of the $\text{C}=\text{O}$ groups, present in the carboxyl group of the trisodium citrate crosslinking agent. Corroborating with this observation, Abhari et al. [24] and Abhari et al. [31] suggested a possible crosslinking mechanism involving starch, sodium hydroxide, and citric acid. They reported that could have been a nucleophilic replacement, in which the two or more deprotonated carbon of carboxyl groups (COO^-) of citric acid are attacked by alkoxides (as alkali starch, mentioned previously), forming an intra/intermolecular crosslinking, occurring more easily for amylose structure. As a crosslinking agent, trisodium citrate creates the crosslinks between starch molecules during the reaction. This crosslinking increased the strength of the material due to the 3D-interconnected network structure.

The region from 1060 to 950 cm^{-1} (Fig. 3 on the right) shows the characteristic peaks of the chemical structure of starch in hydrogels, which shows a similar curve for the Amisol 3408® and Amisol 4000® hydrogels, but with changes in the individual peaks compared to pure starches. A different behavior was observed regarding Hylon VII®, whose characteristic peak of the chemical structure of native starch and hydrogel presented similar behavior. This behavior may have occurred due to the process of starch retrogradation and molecular rearrangement promoted by the action of the crosslinking agent and the different levels of amylose and amylopectin in the starches [22].

Evaluating the ratio of $1580/995\text{ cm}^{-1}$ peaks area, values of 0.109 , 0.182 , and 0.297 were found for hydrogels of Amisol 4000®, Amisol 3408®, and Hylon VII®, respectively. Thus, the ratio between the peak area of the starch hydrogels with different amylose and amylopectin contents increased by 67% (comparing the samples Amisol 4000® and Amisol 3408®) and increased by 172% (comparing the samples Amisol 4000® and Hylon VII®). Therefore, the increase in the amylose content of the Hylon VII® hydrogel ($70\text{ wt.}\%$) allowed more crosslinks between the linear structures of the starch, possibly due to the less steric hindrance observed in these types of starch since they possess less amylopectin content ($30\text{ wt.}\%$). This behavior may have promoted greater crosslinking with trisodium citrate and a consequent increase in the degree of crosslinking of this hydrogel. The polyhydroxy groups in the polysaccharide structure bond to the citric acid molecule, forming ester bindings [37, 38].

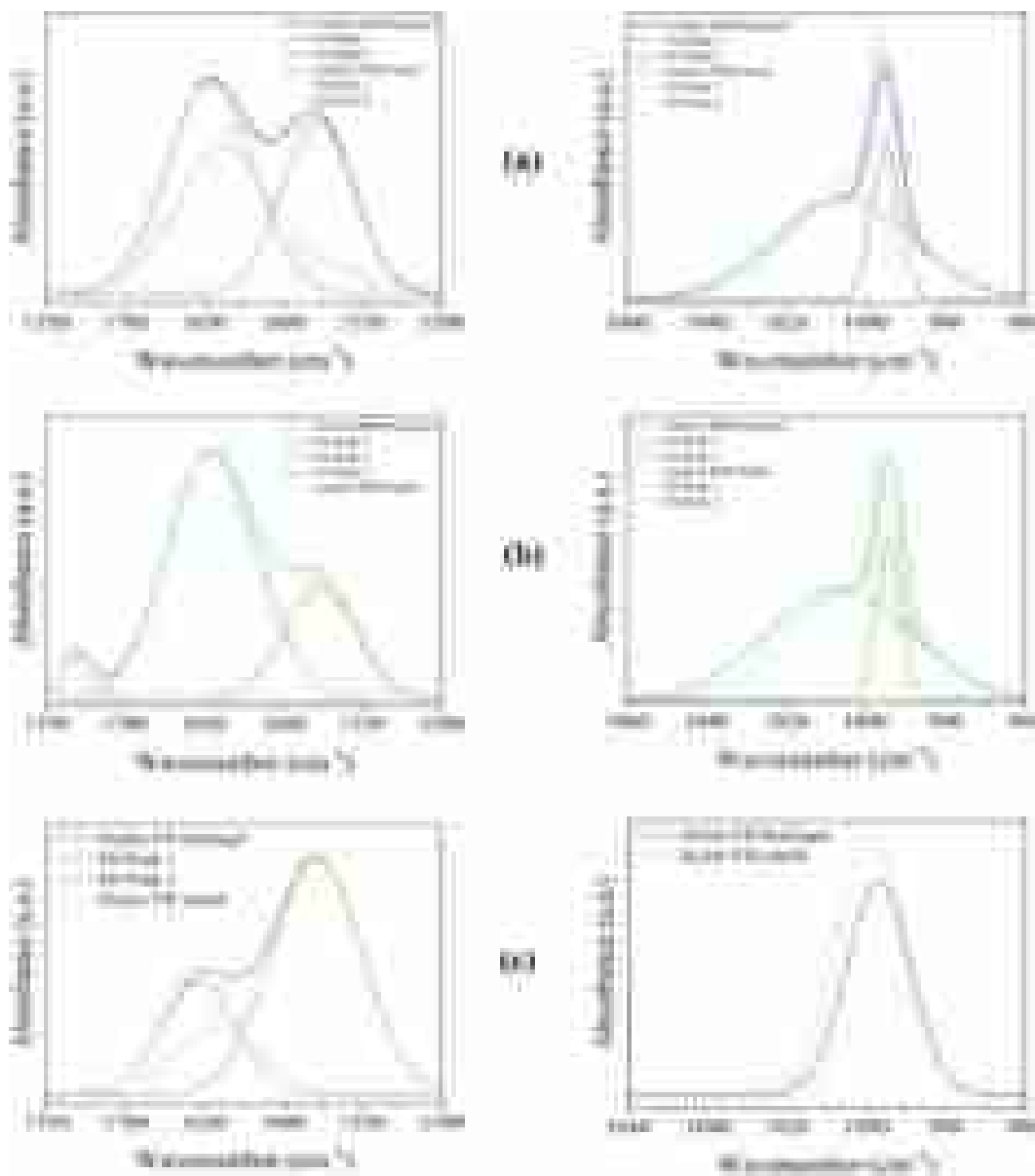


Fig. 3 Deconvoluted FTIR spectra where left represents the region between 1750–1500 cm^{-1} and right represents the region between 1060–960 cm^{-1} : **a** Amisol 3408®, **b** Amisol 4000®, and **c** Hylon VII®

Thus, crosslinking plays a crucial role in the hydrogels' morphological, chemical, and swelling properties [39].

Furthermore, the conformation of the starch chains with medium amylose content (Amisol 3408®) may have influenced the crosslinking degree of this hydrogel. However,

this value was lower than the Hylon VII® hydrogel found, which may indicate that not all chemical groups were impacted during crosslinking. This behavior positively impacts the sorption properties (see Sect. "Affinity tests"). Thus, intermediate levels of crosslinking are interesting

Table 1 Peak areas from deconvoluted FTIR spectra for regions in 1580 cm^{-1} and 995 cm^{-1}

Samples	Peak area 1580 cm^{-1}	Peak area 995 cm^{-1}	Cross-linking degree
Amisol 3408® hydrogel	2.738	15.017	0.182
Amisol 4000® hydrogel	1.525	13.952	0.109
Hylon VII® hydrogel	10.956	36.847	0.297

because they may allow the formation of a stable hydrogel structure, but with the availability of chemical groups for interaction with the PTMs. Besides, the formation of a stable hydrogel is confirmed by water absorption (Sect. "Water absorption"), which crosslinked structure allows the hydrogel swelling due to less molecular chain mobility, diffusivity, water retention within the pores, and increase in the hydrogel volume [23].

X-ray Diffraction (XRD)

X-ray diffraction (XRD) was used to characterize the alterations of the crystalline structure of the samples (Fig. 4a) between range from 10 to 80° , and amplification of the crystalline region between 10 – 40° (Fig. 4b) [40].

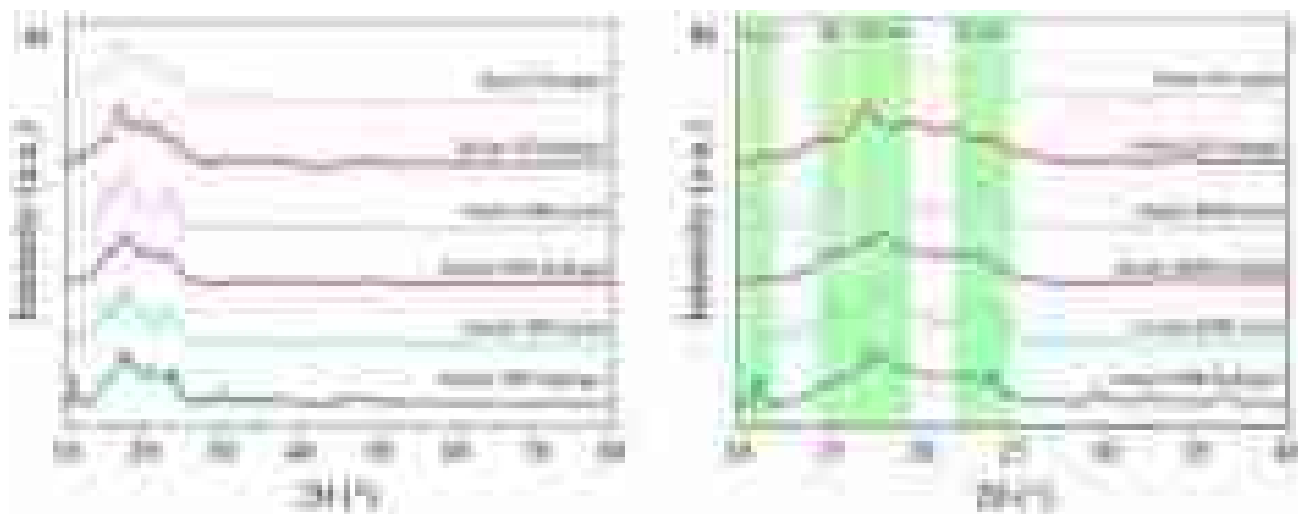
Native corn starches Amisol 3408® and 4000® showed a typical type A diffraction pattern, characterized by strong diffraction peaks (2θ) at 15° , 17° , 18° , and 23° , respectively [41]. In turn, Hylon VII® is a native corn starch type B, unmodified, and derived from corn with a high amylose content ($\sim 70\%$ amylose) and has diffraction peaks at 5.5° , 15° , 17° , 19° , 22° , and 23° [42]. However, the main peaks linked to B-type crystalline structure of this native corn starch are found at (2θ) = 17° and 20° [43].

Despite the similarities in the diffractograms of the samples, some differences are notable after the hydrogel formation process. Firstly, a new peak located at approximately

11.3° was found for Amisol 3408® and Hylon VII® hydrogels, in contrast of the Amisol 4000® hydrogel. He et al. [44] observed an appearance of characteristic peak located at $2\theta \sim 12.7^\circ$. This diffraction peak can be associated with crystalline pattern of V_H -type structure, consisting of a complex crystalline structure of the single-helix format. On the other hand, during retrogradation and gelatinization of the starch chains, a destruction of the single helix structure of starch (native corn starch type B), followed by the rearrangement of amylose chains, and the formation of V_H -type crystalline structure. Besides, according to Alves et al. [23] and Camani et al. [22], this peak was verified for starch gels (hydrogels and aerogels) and is correlated to the retrogradation of amylose and amylopectin to form crosslinked hydrogel structure. The non-appearance of this peak for Amisol 4000® can be correlated with less intensity of the crosslinking reaction discussed previously in the FTIR section.

Hydrogels showed slight changes in the intensities and shifts of XRD signals, with an increase in the intensity of peaks at 18 and 23° compared to native starches. He et al. [44] and Alula Gebresas, Szabó, and Marossy [45] reported that crosslinking process generates an increase of amorphous phase, maintaining crystalline structure of the starch. However, Kou et al. [46] justified this slight alteration of diffraction peaks due to partial gelatinization of the structural rearrangement of the alkali media promoted by crosslinking process.

For this reason, the relative crystallinity (%) of the starches were 25.54, 35.04, and 22.34% for Amisol 3408®, Amisol 4000®, Hylon VII®, respectively. In contrast, hydrogels presented some differences between raw materials and among themselves, achieving the relative crystallinity (%) around 21.35, 11.95, and 29.53% for hydrogels prepared from Amisol 3408®, Amisol 4000®, Hylon VII®,

**Fig. 4** XRD diffractograms for corn starches and starch-based hydrogels with different contents of amylose and amylopectin

respectively. Comparing each starch and respective their hydrogels.

Analyzing the relative crystallinity of the different starches and hydrogels, Amisol 3408® and Amisol 4000® hydrogels presented a reduction of these values. It can be related to the presence of citric acid avoids the retrogradation process of amylose chains. A mechanical mixture plus citric acid decreased crystallinity by forming diester bridges, preventing crystallization but not avoiding the retrogradation process of the amylose chains [22, 47]. Lipatova and Yusova [48] corroborated with the same conclusion, which crosslinked starch films presented a reduction of crystallinity with citric acid. Besides, Amisol 4000® presented a drastic reduction in relative crystallinity. On the other hand, increasing the amylopectin content, the crystallization peak of the gel weakens, possibly making the structure amorphous and poorly crosslinked, as seen in Koev et al. [49].

In counterpart of Amisol' hydrogels, Hylon VII® hydrogel had an increase in relative crystallinity. This increase can be explained due to high amount of amylose, facilitating the formation of crystallites of amylose complexes [50]. Other aspect that can correlate this increase was the high formation of the crosslinks due to the excessive crosslinking process, as seen from FTIR discussion previously. Camani et al. [22] observed the same result for increase of crosslinking agent proportion, that increased crosslinking process, resulting in high relative crystallinity. Therefore, depending on the type of starch and percentage of amylose and amylopectin, this difference can affect the formation of the crystalline structure after crosslinking.

Thermogravimetry Analysis (TGA)

Thermal decomposition and weight loss events are shown in Fig. 1S (see Supplementary Material). Two main thermal events of weight loss are observed from the TGA curves, which are confirmed by two peaks observed in the DTG curves. The first thermal weight loss event occurred between 60–120 °C. According to Liu et al. [51], weight loss in this temperature range occurs due to water loss. Pan et al. [52] also observed the same thermal event related to

dehydration due to the evaporation of residual water in the bulk of the material. The second thermal weight loss event occurred between 200–400 °C. This thermal event may be related to the thermal degradation or pyrolysis of the cross-linked chains of amylose and amylopectin derived from starch [52].

Table 2 presents the $T_{10\%}$ and T_{MAX} for the corn starches and starch hydrogel samples with different amylose and amylopectin contents to understand the thermal effect of crosslinking. From the results observed in Table 2, about $T_{10\%}$, there was a slight increase in the hydrogel samples regarding the pure starches. It may have occurred due to the increased crosslinking degree of the hydrogels (see FTIR analysis). On the other hand, all hydrogel samples showed lower T_{MAX} than their raw material, which, according to Pan et al. [52], may have occurred due to the semicrystalline structure of starch, which in its *in natura* form is organized within the granules (before starch retrogradation). Despite this, the weight loss at 600 °C decreased for all samples, indicating that the hydrogels presented higher thermal stability at elevated temperatures with no sudden change in the pyrolysis of the hydrogels with different amylose and amylopectin contents.

Scanning Electron Microscopy (SEM)

SEM images for corn starch granules with different amylose and amylopectin contents are shown in Fig. 5. The shape of the starch grains varied depending on the amylose and amylopectin content. Amisol 3408® and Amisol 4000® presented granules with polygonal structures due to low amylose contents (indicated by ampliation and blue and pink circles in Fig. 5a and b, respectively). However, the most part of particles have had a spherical format and some rod/filamentous granules were found for Hylon VII® (indicated by ampliation and red circles in Fig. 5c). Lv et al. [53] reported the same trends, evaluating the granules' morphology of different starches. These results were also corroborated by Jiang et al. [54], indicating that high amylose percentages promote spherical granules and rod/filamentous granules. As for the particle sizes of the different corn starches, there was no apparent difference in the average size of the starch granules, having an average size range between 9.21 to 12.77 μm and a monomodal distribution of average particle size, consistent with literature reports [55].

Morphologically, hydrogels from different corn starches presented highly porous structures but with some differences (Fig. 6). Amisol 3408® [Fig. 6a (low magnification) and 6.b (high magnification)] had irregular pore shapes and closed-cell walls. Sringam et al. [56] also showed a porous structure with irregular pores and closed-cell walls. Biduski et al. [57] obtained hydrogels prepared from low and medium

Table 2 TGA ($T_{10\%}$) and DTG (T_{MAX}) of the corn starches and starch-based hydrogels

Samples		$T_{10\%}$ (°C)	T_{MAX} (°C)
Amisol 3408®	Starch	90.9	326.3
	Hydrogel	98.3	286.7
Amisol 4000®	Starch	90.4	327.3
	Hydrogel	98.4	285.8
Hylon VII®	Starch	91.0	324.4
	Hydrogel	98.5	290.6

$T_{10\%}$: temperature at which the weight loss was 10% and T_{MAX} : temperature at which the weight loss was maximum

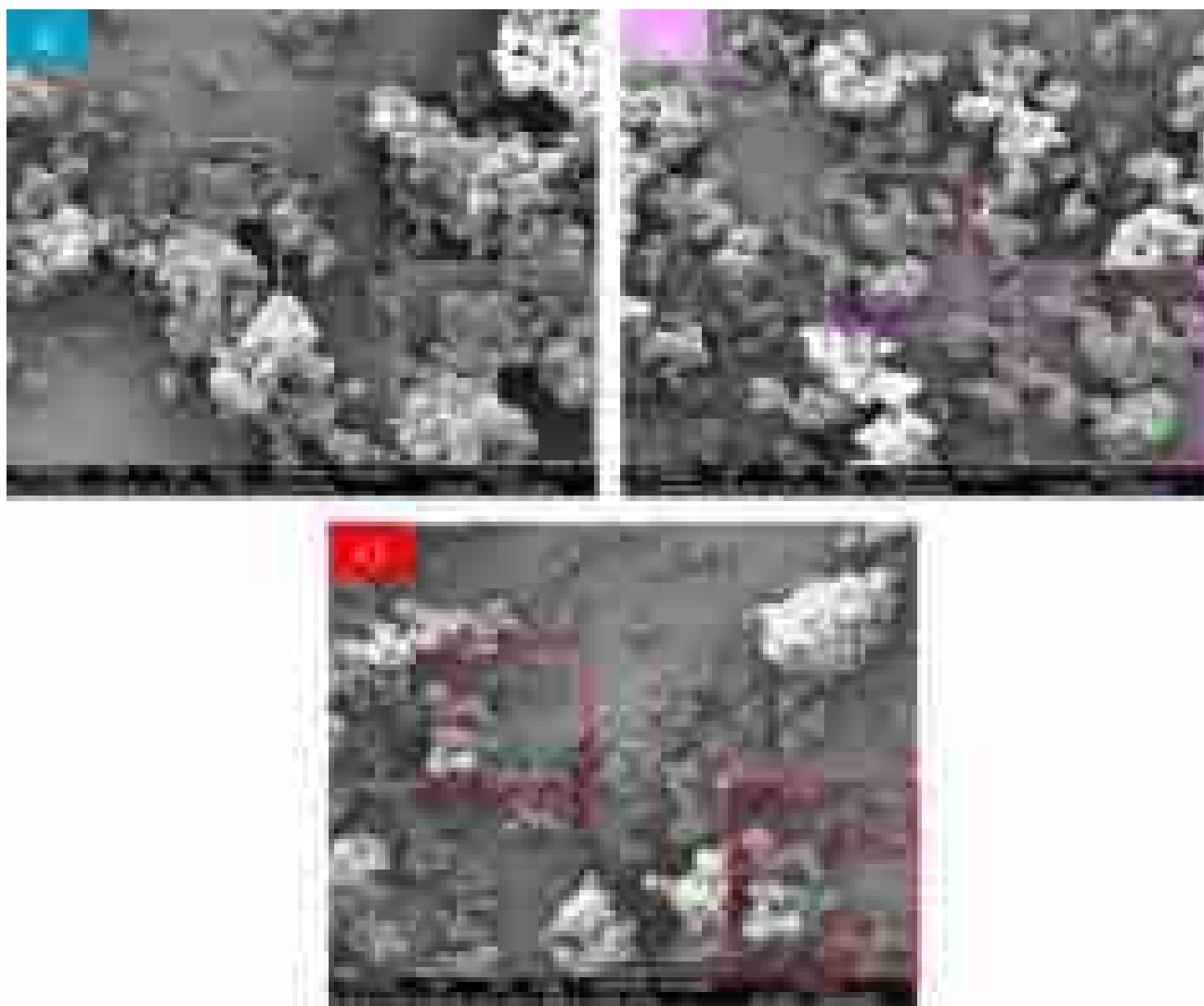


Fig. 5 SEM images for different starch grains: **a** Amisol 3408®, **b** Amisol 4000®, and **c** Hylon VII®

amylose contents, presenting heterogeneous pore structures and highlighting micropores within the large pores. Amisol 4000® [Fig. 6c (low magnification) and 6.d (high magnification)] presented the highest porous structure due to this starch's high amylopectin percentage, allowing regular pore formation [58]. Besides, Sangseethong et al. [59] obtained no difference in hydrogel morphology, even if hydrogels are prepared from rice starches (Glutinous rice, Jasmine rice, and Normal rice starches) containing 6.52%, 18.10%, and 29.60% of amylose, respectively.

Moreover, for high amylose-containing starch hydrogel, Hylon VII® hydrogel [Fig. 6e (low magnification) and 6.f (high magnification)] had very few pores in the cross-section of the synthesized hydrogel. This low number of pores of the Hylon VII® starch hydrogel has a tendency contrary to hydrogels with medium and low percentages of amylose. Due to Hylon VII® being a starch-containing

a high percentage of amylose, as reported by Biduski et al. [57], they hypothesized that the starch hydrogel with a high percentage of amylose did not produce pores in the internal structure due to the inhibiting action of amylose organization during hydrogel production. Luo et al. [58] also observed that high amylose percentage did not produce enough porous structure, affecting the gel formation. It is consistent with FTIR results, indicating that Hylon VII® hydrogel presented a higher crosslinking degree.

Pore sizes for all hydrogels were measured from SEM images. As hydrogels presented heterogeneous pore sizes, two different ranges were considered: large pore sizes (<20 μm) and small pore sizes (>20 μm). Thus, Fig. 2S and 3S (see Supplementary File) present histograms of large and small pore sizes, respectively. Table 3 shows average pore sizes for small and large pore sizes, including the pore density for each hydrogel.

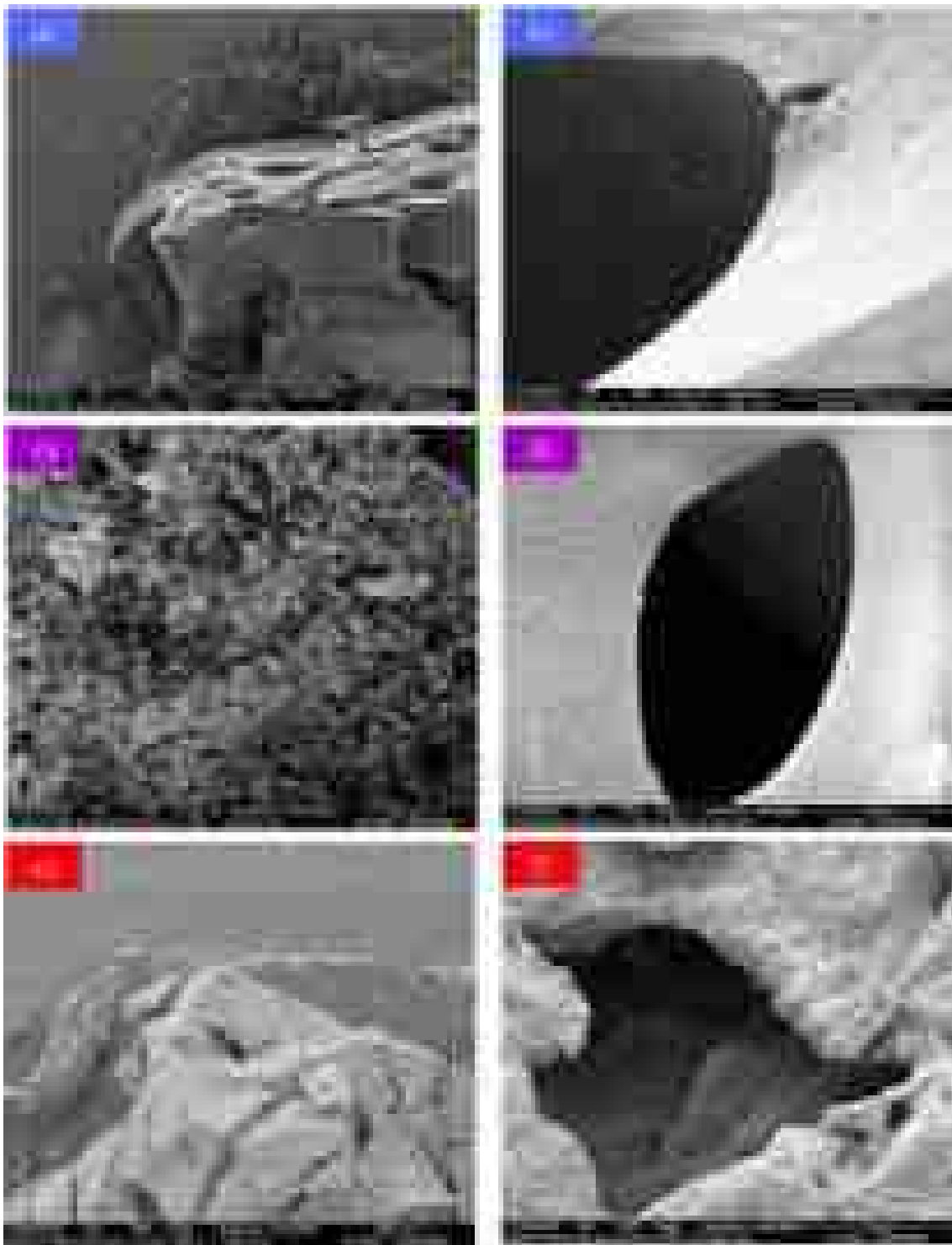


Fig. 6 SEM images of two magnification times of $100\times$ and $10,000\times$ for hydrogels prepared from **a** and **b** Amisol 3408®, **c** and **d** Amisol 4000®, and **e** and **f** Hylon VII®, respectively

Analyzing the data from Table 3, all average pore sizes of hydrogels are classified as macropores due to pore size being more significant than 50 nm [22]. However, differences were observed depending on the starch type used to

prepare hydrogels. Regarding small pore sizes, Hylon VII® hydrogel resulted in smaller pore sizes than others. As for the larger pores, Amisol 4000® and Hylon VII® hydrogels presented small pore sizes. Konstantakos et al. [60] also

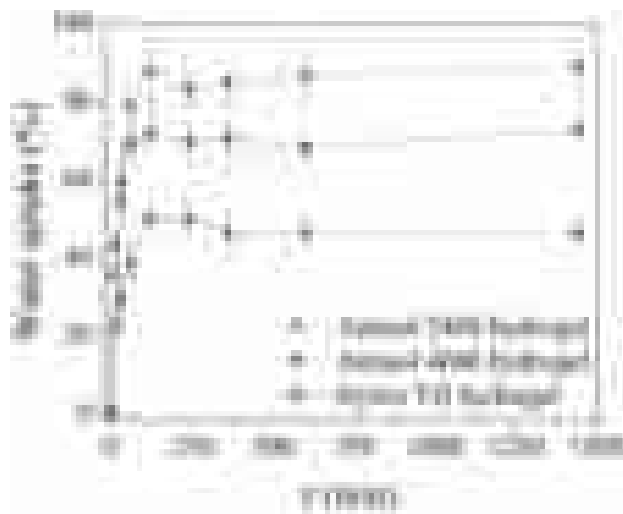
Table 3 Average pore size (μm) for all hydrogels prepared from different starch

Samples	Average pore size (μm)	Average pore size (μm)	Pore density (cont. mm^{-1})
	Small pores	Large pores	
Amisol 3408®	22.3 \pm 7.8	137.0 \pm 23.3	32.00 \pm 7.6
Amisol 4000®	37.0 \pm 7.3	62.1 \pm 9.0	126.6 \pm 25.0
Hylon VII®	4.2 \pm 2.0	42.0 \pm 9.0	11.50 \pm 1.0

observed these two pore sizes distribution, obtaining pore sizes around 50 to 250 μm and tiny pores between \sim 5 to 50 μm .

ANOVA statistical analysis (Table 1S, see Supplementary File) was employed to understand the difference in pore size distribution further, considering a 95% level of confidence, whose p -value $>$ 0.05 is statistically equal (=) and p -value $<$ 0.05 is statistically different. After evaluating the large and small pore sizes, statistical differences were verified between all hydrogels. One hypothesis is that the statistical difference may have occurred due to the amylose and amylopectin percentages from starches of the same source (corn) being different. Camani et al. [22] observed that aerogels synthesized by Amidex 3001® and crosslinking using trisodium citrate also obtained large and small pore sizes due to higher crosslinking degrees for high crosslinking agent concentration. Besides, high amylose contents of these starches may promote higher crosslinking, which decreases small pore size [61]. However, other works showed that high amylopectin content provides a crosslinking ratio of gel, which resulted in high porosity [58], corroborating with the high pore density observed by Amisol 4000® hydrogel. Furthermore, Luo et al. [58] reported that increasing the amylopectin content above 70% generates high porosity and smaller pores; however, the small amount of amylose present interferes with the crosslinking process, making the main structure of amylopectin ineffective in building a three-dimensional network structure, justifying weight loss and possible solubilization of the hydrogel structure. This behavior will be discussed later (see Sect. "Water absorption").

Therefore, hydrogels prepared from Hylon VII® and Amisol 4000® had smaller pore sizes, considering both size ranges. Besides, the excess of amylopectin in Amisol 4000® generated high pore density among the synthesized hydrogels. In contrast, the hydrogels prepared with Hylon VII® obtained a small pore size but a very low pore density due to the excess amylose in the structure.

**Fig. 7** Water uptake (%) of corn starch hydrogels with different amylose and amylopectin contents

Analysis of Specific Properties of Hydrogels

Water Absorption

Water absorption and structural integrity are essential properties that define the end-use applications of hydrogels. Figure 7 presents the kinetic curves of the starch hydrogels' water uptake, showing that all hydrogels showed considerable water uptake during the first hour of immersion. After reaching the equilibrium time (\sim 1 h), it was verified that each starch hydrogel presented a different absorption degree in the following order: Amisol 3408® (88.82%) $>$ Hylon VII® (72.71%) $>$ Amisol 4000® (49.77%). Starch hydrogel with medium amylose content (Amisol 3408®) showed higher water absorption capacity. The lowest water absorption rate was obtained by Amisol 4000® hydrogel, which had low amylose and high amylopectin content. The high molecular weight and branched structure of amylopectin can reduce the mobility of the polymer chains and interfere with any tendency for them to become oriented closely enough to permit significant levels of hydrogen bonding [62, 63]. The low crosslinking degree of Amisol 4000® hydrogel verified in the deconvoluted FTIR spectra corroborates this hypothesis. Furthermore, amylopectin's rigid and branched structure hinders water movement in the hydrogel, resulting in lower water absorption.

Regarding the Hylon VII® hydrogel, there was a reduction of water absorption by up to 18%, which indicates that the higher amylose content probably increased the rigidity conformation of the hydrogel. This behavior resulted in less molecular chain mobility, diffusivity, water retention within the pores, and hydrogel volume. This result is consistent with the deconvoluted FTIR spectra that showed

a high crosslinking degree in the Hylon VII® hydrogel, which reveals that the increase in amylose content may have promoted more connections between structures in the crosslinking of this starch. Biduski et al. [57] evaluated the influence of the amylose content and gelatinization method on producing rice-starch hydrogels. They found that the starch sample with high amylose content had low water absorption due to the greater stiffness of the hydrogel structure that resisted swelling.

Additionally, the Amisol 4000® hydrogel was observed to have high solubility in the aqueous medium (close to 46%). The hydrogels with high (Hylon VII®) and medium (Amisol 3408®) amylose content showed low water solubility (close to 15%, 25%, and 27%), respectively. Indeed, the leaching of the amylose can increase hydrogel solubility. However, increased interaction between amylose/amylose and amylose/amylopectin during crosslinking can reduce starch chain leaching. As observed in the FTIR analysis, the Amisol 4000® hydrogel presented the lowest crosslinking degree, which explains its higher solubility. This behavior may explain the water solubility characteristics of hydrogel starches with medium and high amylose content and their relationship with the crosslinking process [64]. Besides, the starch retrogradation can also affect the solubility of starch hydrogels. According to Liu et al. [65], the retrogradation process is influenced by amylose content and length of polymer chains. The low retrogradation tendency may fragment and solubilize the hydrogels, such as occurred to the starch hydrogel with high amylopectin content (Amisol 4000®).

In addition to water absorption, understanding the hydrogel structure's swelling process is essential. Table 4 presents the fit parameters of the Fick diffusion model to the experimental data of water absorption inside the starch hydrogels. The R^2 values were above 0.9, indicating a good fit by the Fick diffusion model. According to the literature, n values ≤ 0.45 indicate that the water transport in the polymer network of the hydrogel is Fickian. For n values between $0.45 < n < 0.89$, the water transport is governed by non-Fickian diffusion, in which the intra-pore diffusion and macromolecular relaxation occur simultaneously. For n values ≥ 0.89 , the water transport is governed by the relaxation of polymer chains [66, 67]. The n values ranged from 0.194 to 0.409 by varying the amylose and amylopectin content of the corn starch hydrogels, indicating that the Fickian process controlled the diffusion mechanism and hydrogel swelling.

Table 4 Fick diffusion parameters for corn starch-based hydrogels

Samples	Parameters		
	k	n	R^2
Amisol 3408® hydrogel	0.500	0.409	0.956
Amisol 4000® hydrogel	0.624	0.280	0.951
Hylon VII® hydrogel	0.711	0.212	0.993

In some applications (e.g., the sorption process), a high-water absorption-insoluble hydrogel is required. Therefore, corn starch-based hydrogels with medium amylose content play an important role in maintaining the hydrogel's network structure and present satisfactory physical performance for application in sorption tests.

Metallic Speciation

Chemical equilibrium diagrams were simulated to evaluate the proper pH (1–14) condition para sorption of PTMs by corn starch-based hydrogels. Figure 8 presents the chemical speciation diagrams for the PTMs (Cr, Zn, Cd, Mn, and Cu) at 0.2 mmol/L concentrations.

Figure 8a–d present PTMs (Cu, Zn, Cd, and Mn) in their soluble divalent ionic form (Cu^{2+} , Zn^{2+} , Cd^{2+} , and Mn^{2+}) specifically at lower pH. As the pH increases, each metal can suffer hydrolysis or chemical precipitation, forming different chemical species, such as $[\text{Cu}(\text{OH})_2]$, $[\text{Cu}(\text{OH})_3]^-$, $[\text{Cu}(\text{OH})_4]^{2-}$, $[\text{Cu}_2(\text{OH})_2]^{2+}$, $[\text{Cu}_3(\text{OH})_4]^{2+}$, $[\text{CuOH}]^+$, $[\text{Zn}(\text{OH})_2]$, $[\text{Zn}(\text{OH})_3]^-$, $[\text{Zn}(\text{OH})_4]^{2-}$, $[\text{ZnOH}]^+$, $[\text{Cd}(\text{OH})_2]$, $[\text{Cd}(\text{OH})_3]^-$, $[\text{Cd}(\text{OH})_4]^{2-}$, $[\text{CdOH}]^+$, $[\text{Mn}(\text{OH})_4]^{2-}$, $[\text{Mn}_2(\text{OH})_3]^+$, and $[\text{MnOH}]^+$. A previous study by da Costa et al. [68] observed the range $3.0 \leq \text{pH} \leq 3.5$, with hydrolysis or precipitation above pH 3.5, for sorption of Cr^{3+} , Al^{3+} , Cu^{2+} , Pb^{2+} , Cd^{2+} , Zn^{2+} , and Ni^{2+} by sericin/alginate/poly(vinyl alcohol) beads. Cardoso et al. [69] observed the Ag^+ , Ni^{2+} , Cu^{2+} , Zn^{2+} , and Cd^{2+} as dominant species in the pH range of 1–8, while Pozdniakova et al. [70] reported the pH range of 1–7.5 for Zn^{2+} . Sheng et al. [71] evaluated the pH effect on the sorption of Cu^{2+} , Zn^{2+} , Cd^{2+} , Ni^{2+} , and Pb^{2+} by *Sargassum* biomass and found that there was an increase in the removal rate of PTMs with increasing pH (2–6).

For hexavalent chromium (Cr^{6+}), its soluble ionic forms typically exist in the form of oxyanions ($[\text{CrO}_4]^{2-}$, $[\text{Cr}_2\text{O}_7]^{2-}$, $[\text{H}_2\text{CrO}_4]$, and $[\text{HCrO}_4]^-$), depending on the solution pH. According to Fig. 8e, the $[\text{HCrO}_4]^-$ oxyanion remains dominant at $\text{pH} < 4.5$ and drops rapidly as pH increases, reaching about 50% at pH 6.5, while the formation of $[\text{CrO}_4]^{2-}$ oxyanion starts at $\text{pH} > 4.5$. Studies on removing Cr^{6+} generally show greater removal capacities under acidic pH conditions [72]. This behavior has been verified in the removal of Cr^{6+} by activated red mud [73], *Pinus sylvestris* biomass [74], activated rice husk carbon and activated alumina [75], *Tamarindus indica* seeds [76], residue of alginate extraction from *Sargassum filipendula* [77], sericin/alginate beads [78], Jute fiber (PANI-Jute) [79], and chitosan Fe° Nanoparticles [80]. High Cr^{6+} removals in the acidic pH range can be associated with its reduction to Cr^{3+} since Cr^{6+} is a strong oxidant [81]. Equations (6) and (7) present the reduction reactions of Cr^{6+} species at low and moderate pH values, respectively [69, 72].

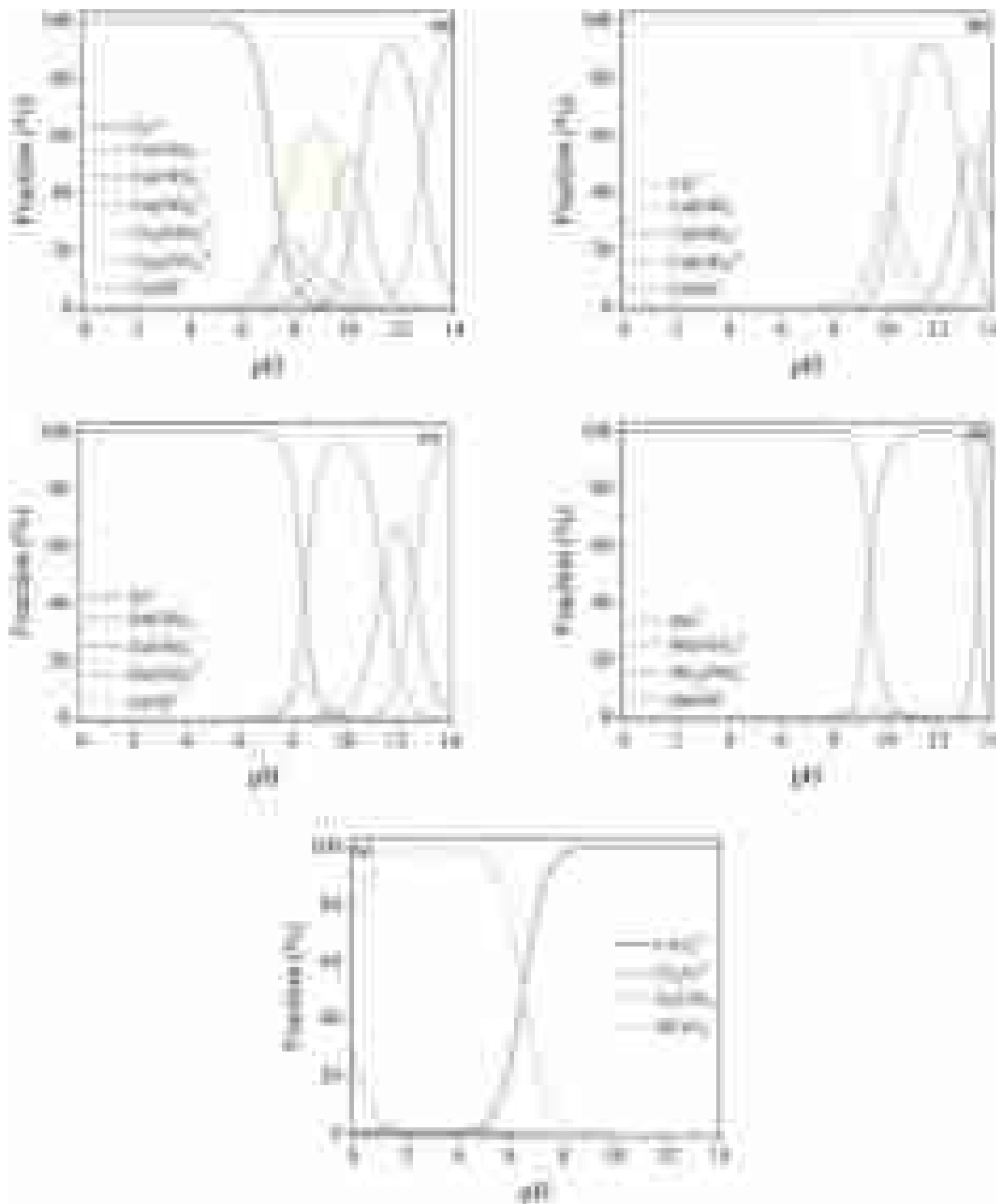
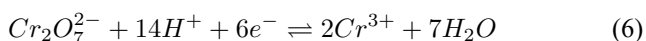


Fig. 8 Chemical equilibrium diagrams of PTMs simulated using Visual MINTEQ® 3.0 software ($C_0=0.2$ mmol/L each, pH 1–14, and $T=25$ °C) a Cu, b Cd, c Zn, d Mn, e Cr



Therefore, the range $4.0 \leq \text{pH} \leq 4.5$ was defined to investigate the sorptive affinity of the corn starch-based hydrogels on the PTMs uptake, avoiding the precipitation/hydrolysis of metal species in an aqueous medium. Although the sorption capacity of Cr^{6+} is higher at low pH values, the affinity assays were conducted at pH 4.0–4.5, as this pH range better reflects the pH of drinking water and wastewater.

Affinity Tests

The affinity between the adsorbate/adsorbent predicts the sorption efficiency. In the case of PTMs, this affinity has been strongly associated with experimental conditions, specific surface area, and functional groups on the adsorbent [82, 83]. Affinity assays were performed to evaluate the sorption potential of the corn starch-based hydrogels by PTMs (Cu^{2+} , Cd^{2+} , Mn^{2+} , Zn^{2+} , and Cr^{6+}) (Fig. 9).

From Fig. 9, Amisol 3408® hydrogel showed greater sorptive affinity by PTMs ions, followed by the Amisol 4000® and Hylon VII® hydrogels. The greater removal efficiency achieved by Amisol 3408® hydrogel indicates that corn starch with medium amylose content has better sorption characteristics for metallic contaminants. Corroborating with FTIR results, the high crosslinking degree of the high amylose content hydrogel (Hylon VII®, 0.297) may have reduced the number of sites available for PTMs sorption. On the other hand, the high removal achieved by the Amisol 4000® hydrogel (high amylopectin content) may be related to its high solubility in water (close to 46%), which

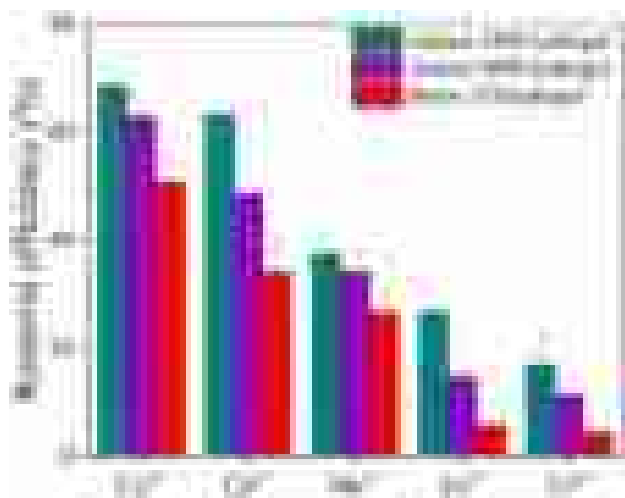


Fig. 9 Sorption affinity of PTMs ions (Cu^{2+} , Cd^{2+} , Mn^{2+} , Zn^{2+} , and Cr^{6+}) by corn starch-based hydrogels ($C_0=0.2$ mmol/L each, pH 4.0–4.5, and $T \sim 25$ °C)

may have caused an increase in its specific surface area and number of sites available for sorption.

The sorption affinity of the corn starch-based hydrogels among PTMs ions follows the order: Cu^{2+} (68.62 to 50.63%) > Cd^{2+} (63.13 to 33.99%) > Mn^{2+} (37.36 to 26.54%) > Zn^{2+} (26.61 to 5.63%) > Cr^{6+} (16.80 to 4.38%), which is consistent with the sequence of hydrated ionic radius sizes and electronegativity of PTMs [84, 85]. In general, PTMs with higher valence can be exchanged more easily for sorption by ion exchange because the affinity between adsorbent/adsorbate tightly depends on the metal ions' hydrated ionic radius size and electronic structure [86, 87]. Therefore, towards divalent cations, these corn starch hydrogels show better affinity towards Cu^{2+} and Cd^{2+} . Wang et al. [88] synthesized magnetic starch-graft-poly-(acrylamide)-co-sodium xanthate to evaluate its behavior as an adsorbent for PTMs and found 78 and 63% removal efficiencies of Pb^{2+} and Cu^{2+} , respectively. Mahmoud et al. [17] investigated the sorption of divalent PTMs (Pb^{2+} , Cd^{2+} , and Hg^{2+}) by starch-iron oxide composite and found a maximum removal efficiency in the range of 70–94, 76–93, and 93–97% for the Hg^{2+} , Cd^{2+} , and Pb^{2+} , respectively.

On the other hand, Cr^{6+} can hardly be sorbed, which further suggests the ion exchange mechanism is due to the presence of oxyanions in an aqueous medium. According to the metallic speciation diagram (Fig. 8e), Cr^{6+} typically exists in the forms $[CrO_4]^{2-}$, $[Cr_2O_7]^{2-}$, $[H_2CrO_4]$, and $[HCrO_4]^-$, depending on the pH, while their negative charges and large hydrated ionic radius weaken their affinity to the functional groups present in the hydrogels' structure. Finally, the results showed a greater sorption affinity between Amisol 3408® hydrogel and PTMs ions Cu^{2+} and Cd^{2+} . Therefore, further studies of kinetic, equilibrium, thermodynamic, desorption/reuse, and fixed-bed columns for scale-up are strongly recommended to understand the sorption process deeply.

Characterizations after PTMs Uptake

To better understand the interactions between PTMs/adsorbents, Amisol 3408®, Amisol 4000®, and Hylon VII® hydrogels, before and after PTMs sorption, were analyzed using SEM/EDS and FTIR techniques. The hydrogels were saturated with Cu^{2+} , Cd^{2+} , Mn^{2+} , Zn^{2+} , and Cr^{6+} in sorption tests under the following experimental conditions: PTMs load of 0.2 mmol/L each, a dose of 10.0 g/L, $T \sim 25$ °C, and pH 4.0–4.5. Micrographs of hydrogels and hydrogels/PTMs were obtained using the SEM technique, as illustrated in Fig. 4S (see Supplementary Material).

From the surface micrograph of the starch hydrogels at $500\times$ magnification, it is possible to observe that the adsorbents had a homogeneous composition with few pores, with Hylon VII® hydrogel presenting a surface with greater

roughness. The surface roughness can be attributed to stirring with HNO_3 (3.0 mol/L) to neutralize the hydrogel's surface. The drying process of the hydrogels also contributes to the formation of the rough surface, as the volume of the hydrogels decreases with drying. Silva et al. [89] also reported surface roughness and homogeneity in the composition of the beads produced from the crosslinked sericin/alginate blend. After the sorption of PTMs, there were a few changes in the hydrogel morphology, which presented an irregular shape and some cracks on their surface. These fractures are probably related to the drying process at 60 °C to which the hydrogels were subjected after the sorption experiment and characterization analyses.

The EDS technique, coupled with the SEM technique, was performed to identify the chemical elements on the starch hydrogel's surface. The spectra obtained for the starch hydrogels, before and after PTMs sorption, are shown in Fig. 10. According to the EDS technique, all hydrogels showed the elements carbon and oxygen in their chemical composition. Starch hydrogels were prepared by adding

NaOH in different batches when opening the starch grains. However, the element sodium was not detected in the starch hydrogels, indicating that there was leaching of sodium ions on the surface of the adsorbents, resulting from the neutralization step with HNO_3 (3.0 mol/L) of the synthesized starch hydrogels. After sorption, PTMs, besides carbon and oxygen, were verified. Possibly, H^+ present on the starch hydrogels surface was exchanged for Cu^{2+} , Cd^{2+} , Mn^{2+} , and Zn^{2+} during the sorption process, which highlights the mechanism of ion exchange between $\text{Cu}^{2+}/\text{Cd}^{2+}/\text{Mn}^{2+}/\text{Zn}^{2+}$ and H^+ in the starch hydrogels.

FTIR analysis was performed to compare the starch hydrogels before and after PTM capture (Fig. 11). Comparison between hydrogels spectra before and after (yellow curves in Fig. 11) capture of PTMs was also performed to identify the bonds and chemical groups of the adsorbents involved in sorption. The spectra of all samples in natura and loaded with PTMs (yellow curves of Fig. 11) showed great similarity. However, there were changes in the different peaks of the hydrogels after sorption, including the

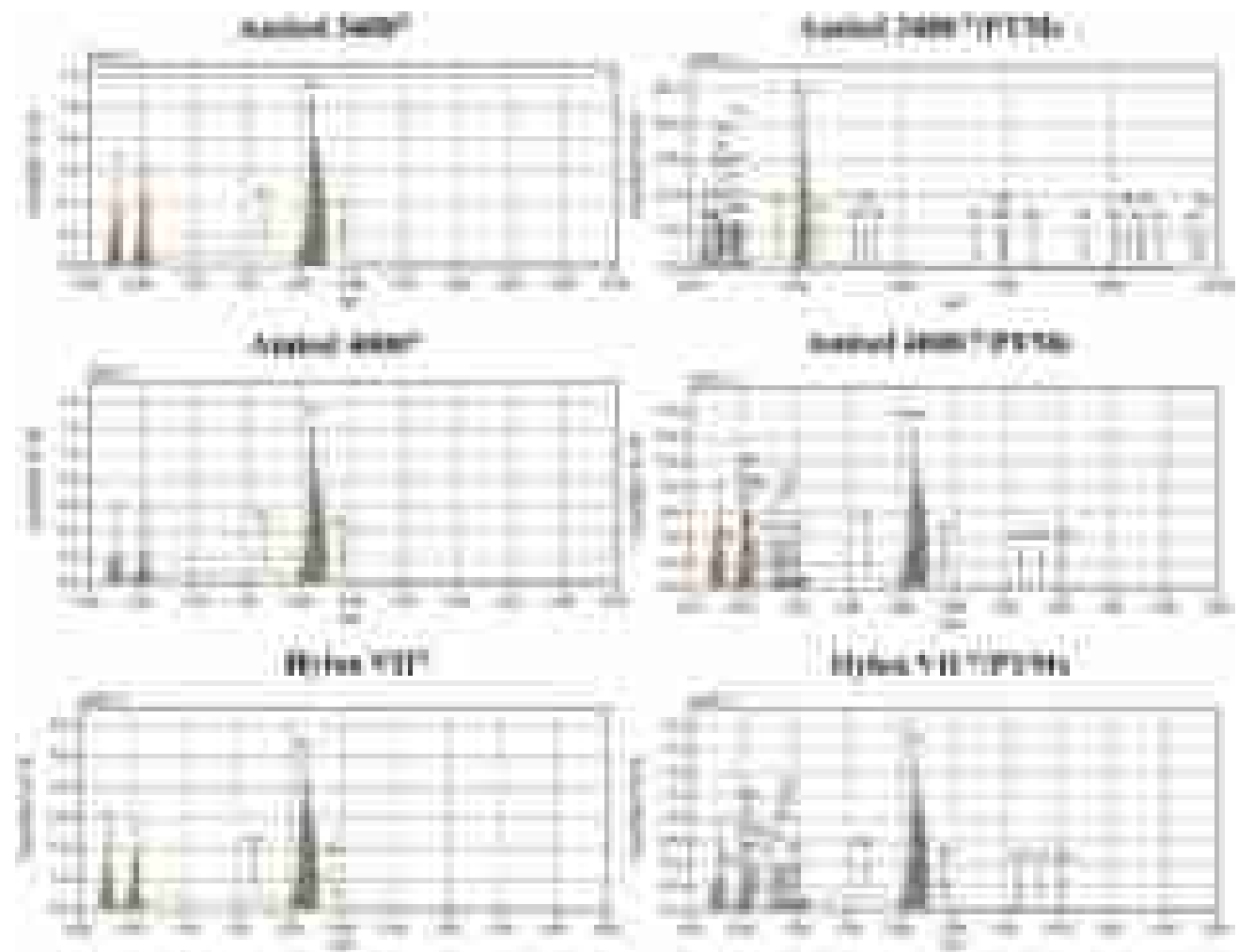


Fig. 10 EDS spectra of starch hydrogels and starch hydrogels/PTMs at 1500× magnification

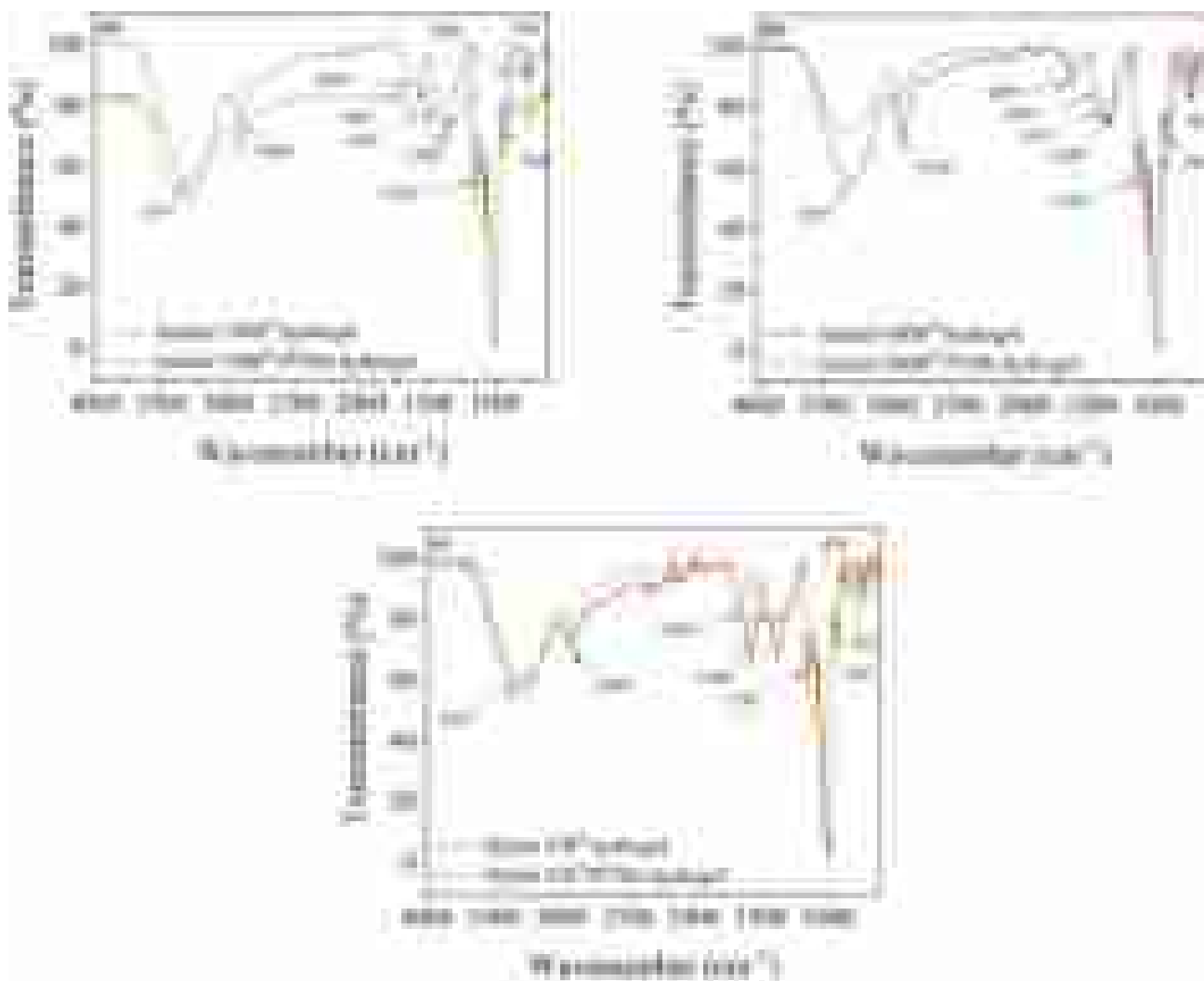
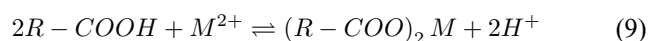
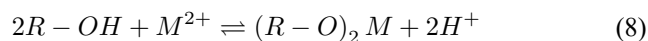


Fig. 11 FTIR spectra for starch hydrogels and starch hydrogels/PTMs

peaks corresponding to the $-\text{OH}$ groups and $-\text{C}=\text{O}$ in $-\text{COOH}$ groups, which implies the participation of these groups in the sorption of PTMs. The stretching vibrations $-\text{C}=\text{O}$ in $-\text{COOH}$ appeared in the spectra of hydrogels, which showed that free $-\text{COOH}$ functional groups were transformed into $-\text{COONa}$ groups during covalent crosslinking with trisodium citrate to form the starch hydrogels. These stretching vibrations are not present in the spectrum of starch hydrogels without acid leaching [23]. After leaching the beads with HNO_3 (3.0 mol/L), the $-\text{COO}^-$ groups were changed to $-\text{COOH}$. Thus, a new functional group ($-\text{C}=\text{O}$ in $-\text{COOH}$) was introduced into the structure to improve interactions with a divalent cations target [90]. FTIR analysis further proves that interactions with hydroxyl/carboxyl groups control divalent cations captured by starch hydrogels. Equations (8)–(9) present the possible mechanisms proposed for the sorption of PTMs by starch hydrogels [91, 92].



Conclusions

This study proposes the development of starch-based hydrogels containing different amylose/amylopectin content and investigating their properties to remove PTMs. FTIR analysis indicated that hydrogel crosslinking was directly affected by amylose content, for which the higher amount of amylose was related to a higher crosslinking degree. Importantly, all starch-based hydrogels displayed low crystalline domains and excellent thermal stability, irrespective of amylose and amylopectin content. On the other hand, the hydrogels' porous structure, water uptake capacity, and solubility were directly influenced by the amylose and amylopectin content,

which could be associated with the crosslinking degree and the availability of functional groups. Higher amylose content had a detrimental effect on the porous structure of the hydrogels, exhibiting low pore density and limited water absorption.

In contrast, the hydrogel with medium amylose content (Amisol 3408®) demonstrated an improved porous structure and greater water uptake capacity. The hydrogel solubility was also affected, showing that the hydrogels with low amylose presented lower water holding capacity, while other compositions presented higher stability. Simulated metallic speciation diagrams showed that the pH range of 4.0–4.5 is optimal for capturing PTMs while avoiding precipitation or hydrolysis of metal species in aqueous media. Among the hydrogels, Amisol 3408® exhibited the highest removal efficiency for metallic contaminants, particularly Cu^{2+} (68.62%) and Cd^{2+} (63.13%). This finding highlights the superior sorption characteristics of corn starch with medium amylose content, especially for Amisol 3408®. Besides, SEM–EDS and FTIR revealed interactions with hydroxyl/carboxyl groups control divalent cations captured by starch hydrogels. This understanding opens new possibilities for utilizing this renewable polysaccharide in applications such as removing PTMs from wastewater.

Supplementary Information The online version contains supplementary material available at <https://doi.org/10.1007/s10924-025-03495-7>.

Acknowledgements This study was financed, in part, by Fundação de Amparo à Pesquisa do Estado de São Paulo (FAPESP), Brazil, Process Numbers #2019/16301-6, #2020/13703-3, #2021/08296-2, #2022/11133-0, #2022/01382-3, #2023/11783-8, #2023/11229-0, #2024/08105-0, and #2024/15696-5; Conselho Nacional de Desenvolvimento Científico e Tecnológico (CNPq), Brazil, Process Numbers #308053/2021-4 and #403934/2021-4; Coordenação de Aperfeiçoamento de Pessoal de Nível Superior (CAPES), Brazil, Finance Code 001. The authors thank the technical support of the Multiuser Experimental Center of UFABC (CEM-UFABC), CECS (UFABC), and REVALORES for assistance. The authors also thank Ingredion Company for donation of the corn starches.

Author Contribution T.B.C. Conceptualization; Methodology; Investigation; Data Curation; Writing—Original Draft; Writing—Review & Editing; Preparation; Visualization; Validation; Formal Analysis. P.H.C. Investigation; Validation; Data curation; Writing—Original Draft; Writing—Review & Editing; Preparation; Validation; Visualization; Formal Analysis. R.R.F. Investigation; Writing—Original Draft; Data Curation; Visualization; Preparation; Validation. R.F.S.B. Investigation; Validation; Data curation; Writing—Review & Editing; Preparation; Validation; Visualization. D.S.R. Supervision; Resources; Writing—Review & Editing; Project administration; Funding acquisition.

Funding Fundação de Amparo à Pesquisa do Estado de São Paulo (#2019/16301-6, #2020/13703-3, #2021/08296-2, #2022/11133-0, #2022/01382-3, #2023/11783-8, #2023/11229-0, #2024/08105-0, and #2024/15696-5); Conselho Nacional de Desenvolvimento Científico e Tecnológico (#308053/2021-4, #403934/2021-4); Coordenação de

Aperfeiçoamento de Pessoal de Nível Superior (Finance Code 001).

Data Availability No datasets were generated or analysed during the current study.

Declarations

Competing Interests The authors declare no competing interests.

References

- Mishra B, Kumar P, Saraswat C et al (2021) Water security in a changing environment: concept. *Chall Solut Water* 13:490. <https://doi.org/10.3390/w13040490>
- Ullah Z, Rashid A, Ghani J et al (2022) Groundwater contamination through potentially harmful metals and its implications in groundwater management. *Front Environ Sci*. <https://doi.org/10.3389/fenvs.2022.1021596>
- Gao S, Wu Q, Li F et al (2023) Dissolved potentially toxic elements in the megacity river network of Shanghai, China. *ACS Earth Sp Chem* 7:589–596. <https://doi.org/10.1021/acsearthspacchem.2c00356>
- Ungureanu EL, Soare AD, Mocanu AL et al (2022) Occurrence of potentially toxic elements in bottled drinking water—carcinogenic and non-carcinogenic risks assessment in adults via ingestion. *Foods* 11:1407. <https://doi.org/10.3390/foods11101407>
- Singh A, Chauhan S, Varjani S et al (2022) Integrated approaches to mitigate threats from emerging potentially toxic elements: a way forward for sustainable environmental management. *Environ Res* 209:112844. <https://doi.org/10.1016/j.envres.2022.112844>
- Chen L, Zhu Y, Cui Y et al (2021) Fabrication of starch-based high-performance adsorptive hydrogels using a novel effective pretreatment and adsorption for cationic methylene blue dye: behavior and mechanism. *Chem Eng J* 405:126953. <https://doi.org/10.1016/j.cej.2020.126953>
- da Costa TB, da Silva MGC, Vieira MGA (2020) Recovery of rare-earth metals from aqueous solutions by bio/adsorption using non-conventional materials: a review with recent studies and promising approaches in column applications. *J Rare Earths* 38:339–355
- Keirudin AA, Zainuddin N, Yusof NA (2020) Crosslinked carboxymethyl sago starch/citric acid hydrogel for sorption of Pb^{2+} , Cu^{2+} , Ni^{2+} and Zn^{2+} from aqueous solution. *Polymers (Basel)* 12:2465. <https://doi.org/10.3390/polym12112465>
- Haq F, Mehmood S, Haroon M et al (2022) Role of starch based materials as a bio-sorbents for the removal of dyes and heavy metals from wastewater. *J Polym Environ* 30:1730–1748. <https://doi.org/10.1007/s10924-021-02337-6>
- Sarmah D, Karak N (2022) Starch based mechanically tough hydrogel for effective removal of toxic metal ions from wastewater. *J Clean Prod* 344:131074. <https://doi.org/10.1016/j.jclepro.2022.131074>
- Gupta AD, Rawat KP, Bhadauria V, Singh H (2021) Recent trends in the application of modified starch in the adsorption of heavy metals from water: a review. *Carbohydr Polym* 269:117763. <https://doi.org/10.1016/j.carbpol.2021.117763>
- Soto D, Urdaneta J, Pernia K et al (2016) Itaconic acid grafted starch hydrogels as metal remover: capacity, selectivity and adsorption kinetics. *J Polym Environ* 24:343–355. <https://doi.org/10.1007/s10924-016-0780-9>
- Wang Z, Zhang X, Wu X et al (2017) Soluble starch functionalized graphene oxide as an efficient adsorbent for aqueous removal of Cd(II): the adsorption thermodynamic, kinetics and isotherms.

- J Sol-Gel Sci Technol 82:440–449. <https://doi.org/10.1007/s10971-017-4313-3>
14. Ekebafé LO, Ogbeifun DE, Okieimen FE (2018) Equilibrium, kinetic and thermodynamic studies of lead (II) sorption on hydrolyzed starch graft copolymers. *J Polym Environ* 26:807–818. <https://doi.org/10.1007/s10924-017-0949-x>
 15. Farag AM, Sokker HH, Zayed EM et al (2018) Removal of hazardous pollutants using bifunctional hydrogel obtained from modified starch by grafting copolymerization. *Int J Biol Macromol* 120:2188–2199. <https://doi.org/10.1016/j.ijbiomac.2018.06.171>
 16. Ibrahim BM, Fakhre NA (2019) Crown ether modification of starch for adsorption of heavy metals from synthetic wastewater. *Int J Biol Macromol* 123:70–80. <https://doi.org/10.1016/j.ijbiomac.2018.11.058>
 17. Mahmoud ME, Nabil GM, Zaki MM, Saleh MM (2019) Starch functionalization of iron oxide by-product from steel industry as a sustainable low cost nanocomposite for removal of divalent toxic metal ions from water. *Int J Biol Macromol* 137:455–468. <https://doi.org/10.1016/j.ijbiomac.2019.06.170>
 18. Luu TH, Nguyen HV, Ha NTC, Vo KND (2019) Synthesis of starch modified montmorillonite as an effective adsorbent for Pb (II) removal from water. *Vietnam J Sci Technol* 57:94. <https://doi.org/10.15625/2525-2518/57/3A/13952>
 19. Banta S (2023) How a protein differentiates between rare-earth elements. *Nature* 618:35–36. <https://doi.org/10.1038/d41586-023-01739-x>
 20. Duquette D, Nzediegwu C, Portillo-Perez G et al (2020) Eco-friendly synthesis of hydrogels from starch, citric acid, and itaconic acid: swelling capacity and metal chelation properties. *Starch - Stärke* 72:1900008. <https://doi.org/10.1002/star.201900008>
 21. Cui C, Jia Y, Sun Q et al (2022) Recent advances in the preparation, characterization, and food application of starch-based hydrogels. *Carbohydr Polym* 291:119624. <https://doi.org/10.1016/j.carbpol.2022.119624>
 22. Camani PH, Gonçalves MGM, Barbosa RFS, Rosa DS (2021) Comprehensive insight of crosslinking agent concentration influence on starch-based aerogels porous structure. *J Appl Polym Sci* 138:50863. <https://doi.org/10.1002/app.50863>
 23. Alves DF, Camani PH, Souza AG, Rosa DS (2023) A novel sustainable composite hydrogel containing nanocellulose to remove potentially toxic metals from contaminated water. *Polym Bull.* <https://doi.org/10.1007/s00289-023-04986-0>
 24. Abhari N, Madadlou A, Dini A (2017) Structure of starch aerogel as affected by crosslinking and feasibility assessment of the aerogel for an anti-fungal volatile release. *Food Chem* 221:147–152. <https://doi.org/10.1016/j.foodchem.2016.10.072>
 25. Fang J (2004) The chemical modification of a range of starches under aqueous reaction conditions. *Carbohydr Polym* 55:283–289. <https://doi.org/10.1016/j.carbpol.2003.10.003>
 26. Sadeghi R, Daniella Z, Uzun S, Kokini J (2017) Effects of starch composition and type of non-solvent on the formation of starch nanoparticles and improvement of curcumin stability in aqueous media. *J Cereal Sci* 76:122–130. <https://doi.org/10.1016/j.jcs.2017.05.020>
 27. Marciano JS, Ferreira RR, de Souza AG et al (2021) Biodegradable gelatin composite hydrogels filled with cellulose for chromium (VI) adsorption from contaminated water. *Int J Biol Macromol* 181:112–124. <https://doi.org/10.1016/j.ijbiomac.2021.03.117>
 28. Wang L, Sánchez-Soto M, Abt T et al (2016) Microwave-cross-linked bio-based starch/clay aerogels. *Polym Int* 65:899–904. <https://doi.org/10.1002/pi.5104>
 29. Bakierska M, Chojnacka A, Świętosławski M et al (2017) Multifunctional carbon aerogels derived by sol-gel process of natural polysaccharides of different botanical origin. *Materials (Basel)* 10:1336. <https://doi.org/10.3390/ma10111336>
 30. Kovačević S, Schwarz I, Đorđević S, Đorđević D (2020) Synthesis of corn starch derivatives and their application in yarn sizing. *Polymers (Basel)* 12:1251. <https://doi.org/10.3390/polym12061251>
 31. Abhari N, Madadlou A, Dini A, Hosseini naveh O, (2017) Textural and cargo release attributes of trisodium citrate cross-linked starch hydrogel. *Food Chem* 214:16–24. <https://doi.org/10.1016/j.foodchem.2016.07.042>
 32. Yang S, Dhital S, Shan C-S et al (2021) Ordered structural changes of retrograded starch gel over long-term storage in wet starch noodles. *Carbohydr Polym* 270:118367. <https://doi.org/10.1016/j.carbpol.2021.118367>
 33. Gonenc I, Us F (2019) Effect of glutaraldehyde crosslinking on degree of substitution, thermal, structural, and physicochemical properties of corn starch. *Starch - Stärke* 71:1800046. <https://doi.org/10.1002/star.201800046>
 34. Mohammadi A, MOGHADDAS J, (2020) Mesoporous starch aerogels production as drug delivery matrices: synthesis optimization, ibuprofen loading, and release property. *TURKISH J Chem* 44:614–633. <https://doi.org/10.3906/kim-1912-18>
 35. Rodriguez-Tenreiro C, Alvarez-Lorenzo C, Rodriguez-Perez A et al (2006) New cyclodextrin hydrogels cross-linked with diglycidylethers with a high drug loading and controlled release ability. *Pharm Res* 23:121–130. <https://doi.org/10.1007/s11095-005-8924-y>
 36. Ghorpade VS, Dias RJ, Mali KK, Mulla SI (2019) Citric acid crosslinked carboxymethylcellulose-polyvinyl alcohol hydrogel films for extended release of water soluble basic drugs. *J Drug Deliv Sci Technol* 52:421–430. <https://doi.org/10.1016/j.jddst.2019.05.013>
 37. Kaya M (2017) Super absorbent, light, and highly flame retardant cellulose-based aerogel crosslinked with citric acid. *J Appl Polym Sci.* <https://doi.org/10.1002/app.45315>
 38. Ruccia MG, Alvarez-Perez MA, Demitri C et al (2015) Effect of citric acid crosslinking cellulose-based hydrogels on osteogenic differentiation. *J Biomed Mater Res Part A* 103:2045–2056. <https://doi.org/10.1002/jbm.a.35343>
 39. Rizwan M, Rubina Gilani S, Iqbal Durani A, Naseem S (2021) Materials diversity of hydrogel: Synthesis, polymerization process and soil conditioning properties in agricultural field. *J Adv Res* 33:15–40. <https://doi.org/10.1016/j.jare.2021.03.007>
 40. Al-Aidy H, Amdeha E (2021) Green adsorbents based on polyacrylic acid-acrylamide grafted starch hydrogels: the new approach for enhanced adsorption of malachite green dye from aqueous solution. *Int J Environ Anal Chem* 101:2796–2816. <https://doi.org/10.1080/03067319.2020.1711896>
 41. Wang J, Ren F, Yu J et al (2019) Toward a better understanding of different dissolution behavior of starches in aqueous ionic liquids at room temperature. *ACS Omega* 4:11312–11319. <https://doi.org/10.1021/acsomega.9b00962>
 42. Ferreira RR, Souza AG, Quispe YM, Rosa DS (2021) Essential oils loaded-chitosan nanocapsules incorporation in biodegradable starch films: a strategy to improve fruits shelf life. *Int J Biol Macromol* 188:628–638. <https://doi.org/10.1016/j.ijbiomac.2021.08.046>
 43. Apostolidis E, Kioupis D, Kakali G et al (2021) Effect of starch concentration and resistant starch filler addition on the physical properties of starch hydrogels. *J Food Sci* 86:5340–5352. <https://doi.org/10.1111/1750-3841.15954>
 44. He Z, Woo MW, Shan Z et al (2022) Preparation and characterization of crosslinked starch films pretreated with sodium hydroxide/amide/water solvent system. *Colloids Surfaces A Physicochem Eng Asp* 650:129544. <https://doi.org/10.1016/j.colsurfa.2022.129544>
 45. Gebresas GA, Szabó T, Marossy K (2023) A comparative study of carboxylic acids on the cross-linking potential of corn starch

- films. *J Mol Struct* 1277:134886. <https://doi.org/10.1016/j.molstruc.2022.134886>
46. Kou T, Song J, Liu M, Fang G (2022) Effect of amylose and crystallinity pattern on the gelatinization behavior of cross-linked starches. *Polymers (Basel)* 14:2870. <https://doi.org/10.3390/polym14142870>
 47. Minhas MU, Ahmad M, Ali L, Sohail M (2013) Synthesis of chemically cross-linked polyvinyl alcohol-co-poly (methacrylic acid) hydrogels by copolymerization; a potential graft-polymeric carrier for oral delivery of 5-fluorouracil. *J Pharm Sci* 21:44. <https://doi.org/10.1186/2008-2231-21-44>
 48. Lipatova IM, Yusova AA (2021) Effect of mechanical activation on starch crosslinking with citric acid. *Int J Biol Macromol* 185:688–695. <https://doi.org/10.1016/j.ijbiomac.2021.06.139>
 49. Koev TT, Muñoz-García JC, Iuga D et al (2020) Structural heterogeneities in starch hydrogels. *Carbohydr Polym* 249:116834. <https://doi.org/10.1016/j.carbpol.2020.116834>
 50. Marinopoulou A, Papastergiadis E, Raphaelides SN (2016) An investigation into the structure, morphology and thermal properties of amylo maize starch-fatty acid complexes prepared at different temperatures. *Food Res Int* 90:111–120. <https://doi.org/10.1016/j.foodres.2016.10.035>
 51. Liu X, Lan C, Al A et al (2016) Preparation of cross-linked high amylose corn-starch and its effects on self-reinforced starch films. *Int J Food Eng* 12:673–680. <https://doi.org/10.1515/ijfe-2015-0139>
 52. Pan J, Li M, Zhang S et al (2019) Effect of epigallocatechin gallate on the gelatinisation and retrogradation of wheat starch. *Food Chem* 294:209–215. <https://doi.org/10.1016/j.foodchem.2019.05.048>
 53. Lv X, Hong Y, Zhou Q, Jiang C (2021) Structural features and digestibility of corn starch with different amylose content. *Front Nutr*. <https://doi.org/10.3389/fnut.2021.692673>
 54. Jiang H, Campbell M, Blanco M, Jane J-L (2010) Characterization of maize amylose-extender (ae) mutant starches: Part II. Structures and properties of starch residues remaining after enzymatic hydrolysis at boiling-water temperature. *Carbohydr Polym* 80:1–12. <https://doi.org/10.1016/j.carbpol.2009.10.060>
 55. Fan X, Zhu J, Dong W et al (2019) Comparison of pasting properties measured from the whole grain flour and extracted starch in barley (*Hordeum vulgare* L.). *PLoS ONE* 14:e0216978. <https://doi.org/10.1371/journal.pone.0216978>
 56. Sringam J, Pankongadisak P, Trongsatitkul T, Suppakarn N (2022) Improving mechanical properties of starch-based hydrogels using double network strategy. *Polymers (Basel)* 14:3552. <https://doi.org/10.3390/polym14173552>
 57. Biduski B, da Silva WMF, Colussi R et al (2018) Starch hydrogels: the influence of the amylose content and gelatinization method. *Int J Biol Macromol* 113:443–449. <https://doi.org/10.1016/j.ijbiomac.2018.02.144>
 58. Luo H, Dong F, Wang Q et al (2021) Construction of porous starch-based hydrogel via regulating the ratio of amylopectin/amylose for enhanced water-retention. *Molecules* 26:3999. <https://doi.org/10.3390/molecules26133999>
 59. Sangseethong K, Chatakanonda P, Sriroth K (2018) Superabsorbent hydrogels from rice starches with different amylose contents. *Starch - Stärke* 70:1700244. <https://doi.org/10.1002/star.201700244>
 60. Konstantakos S, Marinopoulou A, Papaemmanouil S et al (2019) Preparation of model starch complex hydrogels. *Food Hydrocoll* 96:365–372. <https://doi.org/10.1016/j.foodhyd.2019.05.046>
 61. Xiao X, Yu L, Xie F et al (2017) One-step method to prepare starch-based superabsorbent polymer for slow release of fertilizer. *Chem Eng J* 309:607–616. <https://doi.org/10.1016/j.cej.2016.10.101>
 62. Zhou J, Zhang J, Ma Y, Tong J (2008) Surface photo-crosslinking of corn starch sheets. *Carbohydr Polym* 74:405–410. <https://doi.org/10.1016/j.carbpol.2008.03.006>
 63. Zou W, Yu L, Liu X et al (2012) Effects of amylose/amylopectin ratio on starch-based superabsorbent polymers. *Carbohydr Polym* 87:1583–1588. <https://doi.org/10.1016/j.carbpol.2011.09.060>
 64. Klein B, Pinto VZ, Vanier NL et al (2013) Effect of single and dual heat–moisture treatments on properties of rice, cassava, and pinhao starches. *Carbohydr Polym* 98:1578–1584. <https://doi.org/10.1016/j.carbpol.2013.07.036>
 65. Liu J, Wang B, Lin L et al (2014) Functional, physicochemical properties and structure of cross-linked oxidized maize starch. *Food Hydrocoll* 36:45–52. <https://doi.org/10.1016/j.foodhyd.2013.08.013>
 66. Gürkan Polat T, Duman O, Tuğç S (2020) Preparation and characterization of environmentally friendly agar/κ-carrageenan/montmorillonite nanocomposite hydrogels. *Colloids Surfaces A Physicochem Eng Asp* 602:124987. <https://doi.org/10.1016/j.colsurfa.2020.124987>
 67. Carginin MA, de Souza AG, de Lima GF et al (2020) Pinus residue/pectin-based composite hydrogels for the immobilization of β-D-galactosidase. *Int J Biol Macromol* 149:773–782. <https://doi.org/10.1016/j.ijbiomac.2020.01.280>
 68. da Costa TB, da Silva MGC, Vieira MGA (2021) Biosorption of rare-earth and toxic metals from aqueous medium using different alternative biosorbents: evaluation of metallic affinity. *Environ Sci Pollut Res*. <https://doi.org/10.1007/s11356-021-16506-6>
 69. Cardoso SL, Costa CSD, Nishikawa E et al (2017) Biosorption of toxic metals using the alginate extraction residue from the brown algae *Sargassum filipendula* as a natural ion-exchanger. *J Clean Prod* 165:491–499. <https://doi.org/10.1016/j.jclepro.2017.07.114>
 70. Pozdniakova TA, Mazur LP, Boaventura RAR, Vilar VJP (2016) Brown macro-algae as natural cation exchangers for the treatment of zinc containing wastewaters generated in the galvanizing process. *J Clean Prod* 119:38–49. <https://doi.org/10.1016/j.jclepro.2016.02.003>
 71. Sheng PX, Ting YP, Chen JP, Hong L (2004) Sorption of lead, copper, cadmium, zinc, and nickel by marine algal biomass: characterization of biosorptive capacity and investigation of mechanisms. *J Colloid Interface Sci* 275:131–141. <https://doi.org/10.1016/j.jcis.2004.01.036>
 72. Alvarez-Galvan Y, Minofar B, Futera Z et al (2022) Adsorption of hexavalent chromium using activated carbon produced from *Sargassum* spp.: comparison between lab experiments and molecular dynamics simulations. *Molecules* 27:6040. <https://doi.org/10.3390/molecules27186040>
 73. Gupta VK, Gupta M, Sharma S (2001) Process development for the removal of lead and chromium from aqueous solutions using red mud—an aluminium industry waste. *Water Res* 35:1125–1134. [https://doi.org/10.1016/S0043-1354\(00\)00389-4](https://doi.org/10.1016/S0043-1354(00)00389-4)
 74. Ucin H, Bayhan YK, Kaya Y et al (2002) Biosorption of chromium(VI) from aqueous solution by cone biomass of *Pinus sylvestris*. *Bioresour Technol* 85:155–158. [https://doi.org/10.1016/S0960-8524\(02\)00086-X](https://doi.org/10.1016/S0960-8524(02)00086-X)
 75. Bishnoi NR, Bajaj M, Sharma N, Gupta A (2004) Adsorption of Cr(VI) on activated rice husk carbon and activated alumina. *Bioresour Technol* 91:305–307. [https://doi.org/10.1016/S0960-8524\(03\)00204-9](https://doi.org/10.1016/S0960-8524(03)00204-9)
 76. Agarwal GS, Bhuptawat HK, Chaudhari S (2006) Biosorption of aqueous chromium(VI) by *Tamarindus indica* seeds. *Bioresour Technol* 97:949–956. <https://doi.org/10.1016/j.biortech.2005.04.030>
 77. Bertagnolli C, da Silva MGC, Guibal E (2014) Chromium biosorption using the residue of alginate extraction from *Sargassum filipendula*. *Chem Eng J* 237:362–371. <https://doi.org/10.1016/j.cej.2013.10.024>

78. de Andrade JR, da Silva MGC, Gimenes ML, Vieira MGA (2018) Bioadsorption of trivalent and hexavalent chromium from aqueous solutions by sericin-alginate particles produced from *Bombyx mori* cocoons. *Environ Sci Pollut Res* 25:25967–25982. <https://doi.org/10.1007/s11356-018-2651-5>
79. Tejada-Tovar C, Gonzalez-Delgado AD, Villabona-Ortiz A (2019) Characterization of residual biomasses and its application for the removal of lead ions from aqueous solution. *Appl Sci* 9:4486. <https://doi.org/10.3390/app9214486>
80. Nag S, Bar N, Das SK (2020) Cr(VI) removal from aqueous solution using green adsorbents in continuous bed column– statistical and GA-ANN hybrid modelling. *Chem Eng Sci* 226:115904. <https://doi.org/10.1016/j.ces.2020.115904>
81. Gallios GP, Vaclavikova M (2008) Removal of chromium (VI) from water streams: a thermodynamic study. *Environ Chem Lett* 6:235–240. <https://doi.org/10.1007/s10311-007-0128-8>
82. Diniz V, Volesky B (2005) Effect of counterions on lanthanum biosorption by *Sargassum polycystum*. *Water Res* 39:2229–2236. <https://doi.org/10.1016/j.watres.2005.04.004>
83. de Freitas GR, da Silva MGC, Vieira MGA (2019) Biosorption technology for removal of toxic metals: a review of commercial biosorbents and patents. *Environ Sci Pollut Res* 26:19097–19118. <https://doi.org/10.1007/s11356-019-05330-8>
84. Jeon C, Nah IW, Hwang KY (2007) Adsorption of heavy metals using magnetically modified alginic acid. *Hydrometallurgy* 86:140–146. <https://doi.org/10.1016/j.hydromet.2006.11.010>
85. Wang F, Zhao J, Wei X et al (2014) Adsorption of rare earths (III) by calcium alginate-poly glutamic acid hybrid gels. *J Chem Technol Biotechnol* 89:969–977. <https://doi.org/10.1002/jctb.4186>
86. Wang F, Zhao J, Pan F et al (2013) Adsorption properties toward trivalent rare earths by alginate beads doping with silica. *Ind Eng Chem Res* 52:3453–3461. <https://doi.org/10.1021/ie302753q>
87. da Costa TB, da Silva MGC, Vieira MGA (2022) Effective recovery of ytterbium through biosorption using crosslinked sericin-alginate beads: a complete continuous packed-bed column study. *J Hazard Mater* 421:126742. <https://doi.org/10.1016/j.jhazmat.2021.126742>
88. Wang S, Zhang C, Chang Q (2017) Synthesis of magnetic cross-linked starch-graft-poly(acrylamide)-co-sodium xanthate and its application in removing heavy metal ions. *J Exp Nanosci* 12:270–284. <https://doi.org/10.1080/17458080.2017.1321793>
89. da Silva TL, da Silva MGC, Vieira MGA (2021) Palladium adsorption on natural polymeric sericin-alginate particles cross-linked by polyethylene glycol diglycidyl ether. *J Environ Chem Eng* 9:105617. <https://doi.org/10.1016/j.jece.2021.105617>
90. da Costa TB, da Silva TL, da Silva MGC, Vieira MGA (2023) Efficient recovery of europium by biosorption and desorption using beads developed from sericin residues from silk yarns processing, sodium alginate and poly(ethylene glycol) diglycidyl ether. *J Environ Chem Eng* 11:109222. <https://doi.org/10.1016/j.jece.2022.109222>
91. Gok C (2014) Neodymium and samarium recovery by magnetic nano-hydroxyapatite. *J Radioanal Nucl Chem* 301:641–651. <https://doi.org/10.1007/s10967-014-3193-z>
92. Zhang Q, He M, Chen B, Hu B (2016) Preparation, characterization and application of *Saussurea tridactyla* Sch-Bip as green adsorbents for preconcentration of rare earth elements in environmental water samples. *Spectrochim Acta - Part B At Spectrosc* 121:1–10. <https://doi.org/10.1016/j.sab.2016.04.005>

Publisher's Note Springer Nature remains neutral with regard to jurisdictional claims in published maps and institutional affiliations.

Springer Nature or its licensor (e.g. a society or other partner) holds exclusive rights to this article under a publishing agreement with the author(s) or other rightsholder(s); author self-archiving of the accepted manuscript version of this article is solely governed by the terms of such publishing agreement and applicable law.



Electrospun adsorbent membrane of PLA containing chitosan for toxic metal ions removal from aqueous solution: Effect of chitosan incorporation

Henrique Borba Modolon^{a,b,*}, Luyza Bortolotto Teixeira^a, Luciana Prazeres Mazur^c, Pedro Henrique Santos^d, Paulo Henrique Camani^c, Lucia Helena Innocentini Mei^c, Tiago Bender Wermuth^{a,b}, Oscar Rubem Klegues Montedo^{a,b}, Matheus V.G. Zimmermann^b, Sabrina Arcaro^{a,b}, Derval dos Santos Rosa^d

^a Laboratório de cerâmica técnica (CerTec), grupo de pesquisa em biomateriais e materiais nanoestruturados, Universidade do Extremo Sul Catarinense (UNESC), Criciúma, Santa Catarina, Brazil

^b Programa de Pós-Graduação em Ciência e Engenharia de Materiais (PPGCEM), Universidade do Extremo Sul Catarinense (UNESC), Criciúma, Santa Catarina, Brazil

^c State University of Campinas (Unicamp), School of Chemical Engineering, Department of Materials Engineering and Bioprocess, Cidade Universitária Zeferino Vaz, Campinas, SP, Brazil

^d Center for Engineering, Modeling, and Applied Sciences (CECS), Federal University of ABC (UFABC), São Paulo 09210-580, Brazil

ARTICLE INFO

Keywords:

Membranes
Electrospinning
Poly(lactic acid)
Chitosan
Metal ion removal

ABSTRACT

The scarcity of water resources and their pollution are vital to modern civilization. Thus, adsorptive membranes are promising candidates to be applied in the filtration systems to improve the water quality. In summary, this study investigated the effect of chitosan (CS) in the morphological, chemical, and physical aspects of PLA-based membranes incorporating chitosan obtained by electrospinning process, their adsorption behavior in multielement aqueous systems containing Cr^{6+} , Cu^{2+} , Zn^{2+} , Mn^{2+} , Ni^{2+} , and Cd^{2+} in pH 4, and the possible removal mechanism on the composite electrospun membrane's surface. The addition of chitosan within the PLA matrix reduced the diameters and porosity of the fibers and pores, resulting in an improvement in the modulus of elasticity and tensile strength until rupture, reaching values around 346.4 ± 61.4 MPa and 4.57 ± 0.69 MPa for mechanical tests carried out in the alignment of fibers with the highest percentage of CS. Besides, the contact angle varied between $70 \pm 5^\circ$ and $114 \pm 3^\circ$, depending on side of membrane's surface (smoother or rougher). For removal efficiency of six metal ions in multielement aqueous systems, the best results were verified for Cr^{6+} (40 up to 100 %). The adsorption efficiency did not significantly change when the chitosan content increased, but the value increased for Cr^{6+} percentage drastically. From SEM-EDS and XPS, indicatives of possible adsorption mechanism showed the contribution of amino groups and oxygen-rich functional groups of chitosan (especially oxyanion chromium); the PLA chain ends (active $-\text{COO}^-$ sites) for divalent metal ions removal, and the lowest ionic radius of chromium, that facilitate its removal. Thus, PLA membranes containing chitosan are a promising candidate with excellent mechanical and adsorptive properties for environmental remediation.

1. Introduction

Heavy metals from industrial and agricultural activities can pollute the soil and water, entering the human food chain and accumulating over the years, becoming toxic for living beings and resulting in serious and chronic diseases. In the rest of the world, studies reported that in

some places, such as the Patna community, Bihar, India, a flood event generated a loss of water quality, whose high values of total dissolved solids, total hardness, total alkalinity were found, achieving values around 1120 mg/L, 575 mg/L, and 3516.75 mg/L, respectively. Besides, 60 % of samples presented high amounts of Mg^+ and Cl^- , and traces of As (0.0516 mg/L) [1]. In Brazil, other environmental disasters have

* Corresponding author at: Laboratório de cerâmica técnica (CerTec), grupo de pesquisa em biomateriais e materiais nanoestruturados, Universidade do Extremo Sul Catarinense (UNESC), Criciúma, Santa Catarina, Brazil.

E-mail addresses: henrique.modolon@gmail.com (H.B. Modolon), lmazur@unicamp.br (L.P. Mazur), henrique.p@ufabc.edu.br (P.H. Santos), pcamani@unicamp.br (P.H. Camani), lumeibit@unicamp.br (L.H.I. Mei), tbw@unesc.net (T.B. Wermuth), okm@unesc.net (O.R.K. Montedo), matheus.vgz@unesc.net (M.V.G. Zimmermann), sarcaro@unesc.net (S. Arcaro), derval.rosa@ufabc.edu.br (D. dos Santos Rosa).

<https://doi.org/10.1016/j.ijbiomac.2024.139435>

Received 31 July 2024; Received in revised form 9 December 2024; Accepted 31 December 2024

Available online 3 January 2025

0141-8130/© 2024 Published by Elsevier B.V.

caused great socio-environmental damages, as in the Doce River basin, where the Fundão dam ruptured. This rupture released high concentrations of pollutants of Fe and Mn, around 32.36 mg/L and 936 mg/L, respectively [2].

The toxicity and human diseases generated by contamination concern the world population. Depending on their oxidation states, metal ions act in the human body distinctly [3]. Cr^{6+} can cause skin allergies to cancer (in the digestive and/or respiratory system) in small and high quantities, respectively [4]. Zn^{2+} and Cu^{2+} accumulation can result in gastrointestinal distress and diarrhea and Wilson disease, metabolic disorders and even death [5,6]. Cd^{2+} can cause pulmonary edema, osteomalacia, damage to the hematopoietic system, even so cancer [7].

For removing these heavy metals from nature, there are several processes that can be applied, and the most currently is the adsorption process due to this simplicity methodology and low cost. Combining these aspects of adsorption with highly selective and adsorptive membranes improves the performance of the contaminant removal process and reduces membrane fouling [8]. Among several adsorbents, there are the conventional and unconventional adsorbents [9]. Carbon-based adsorbents are the major material type used for this application, and usually, surface modification processes, such as nitrogenation, oxidation, or sulfuration, are applied to improve the performance [10–12].

Chitosan is a natural polymer highly used to obtain adsorbents to heavy metal removal from wastes, especially water, due to its amino ($-\text{NH}_2$) and hydroxyl ($-\text{OH}$) groups presented on composition. However, some negative points are the low porosity and surface area, and usually there is need to combine this polymer with another one to reach high values for ion removal and adequate mechanical properties (Bruno [12,13]). Another biopolymer that has properties like those verified in petroleum-based polymers is the poly(acid lactic) (PLA). It presents biodegradability, biocompatibility and its production is relatively eco-friendly with low cost. Besides, this biopolymer is widely applied to produce membranes for water purification [14]. These two polymers have good biocompatibility and are adequate to obtain membranes for different uses, such as filtration, heavy metal removal and bio applications [15,16]. Furthermore, other characteristic of these membranes applied to heavy metal removal is the presence of specific functional groups, such as hydroxyl ($-\text{OH}$), carboxyl ($-\text{COOH}$), epoxy ($-\text{COC}-$), amine ($-\text{NH}_2$), and carbonyl ($-\text{C}=\text{O}$) that promote high removal of these contaminants (Bruno [13,17,18]).

To fabricate the filtration membranes, there are several papers describing different methods to synthesize them using different sources, such as emulsification, electrospinning and freeze-casting, aiming the application of the metal ion removal [19–21]. Among these fabrication methods, electrospinning is a technique used to produce ultrathin fibers from polymer solutions, using an electric field, that poses high surface-volume relation qualifying them to applications like tissue engineering, fluid filtration and heavy metals filtration/capture. The suspension is ejected through a capillary and attracted to the collector due to the potential gap between these sides. Some parameters can affect the thickness of the fibers, highlighting the viscosity and pH of the polymeric solution, distance between collector and capillary, voltage, humidity and temperature [22,23].

Due to the difficult to produce pure chitosan membranes by electrospinning process, another polymer is added to the composition to facilitate the fibrous structure formation. One of the difficulties to form fibers is due to the high viscosity, polycationic properties, and strong intramolecular forces of the chitosan polymer solution, even low concentrations of chitosan from electrospinning process. Thus, the blending of the chitosan with other polymers such as [polyethylene oxide (PEO), polyvinyl alcohol (PVA), poly(lactic acid) (PLA), and polycaprolactone (PCL) is another route to prepare electrospun fibers [24,25]. However, only three works were published in the current literature from the research performed on the Web of Science platform preparing poly(lactic acid)-based membranes containing chitosan [26–28]. However,

the joining of a simple fabrication to prepare membranes and the study about the possible adsorption mechanism of the metal ion was not studied from multicomponent aqueous systems. Therefore, the aim of the research paper is to evaluate the effect of chitosan addition (CS) (0–20 wt%) in the morphology, microstructure, chemical composition, and physical properties of PLA-based membranes obtained by electrospinning. These composite electrospun membranes were applied as possible candidates to remove metal ions from contaminated aqueous systems (Cr^{6+} , Cu^{2+} , Ni^{2+} , Zn^{2+} , Mn^{2+} , and Cd^{2+}), and the possible removal mechanism of the metal ions.

2. Materials and methods

2.1. Materials

Poly(lactic acid) pellets (PLA, National 3D), chloroform (CHCl_3 , 99 %, Synth), Chitosan ($\text{C}_{18}\text{H}_{35}\text{N}_3\text{O}_{13}$, 93 %, Exodo Científica®), absolute alcohol ($\text{C}_2\text{H}_6\text{O}$, 99 %, Dynamics Contemporary Chemistry), acetic acid (CH_3COOH , 99 %, Dynamics Contemporary Chemistry) were used to produce the membranes. Zinc nitrate hexahydrate ($\text{Zn}(\text{NO}_3)_2 \cdot 6\text{H}_2\text{O}$, 98 %, Dynamics Contemporary Chemistry), nickel nitrate hexahydrate ($\text{Ni}(\text{NO}_3)_2 \cdot 6\text{H}_2\text{O}$, 98 %, Dynamics Contemporary Chemistry), cadmium nitrate tetrahydrate ($\text{Cd}(\text{NO}_3)_2 \cdot 4\text{H}_2\text{O}$, 98 %, Neon Chemistry), potassium dichromate ($\text{K}_2\text{Cr}_2\text{O}_7$, 99 %, ECIBRA Analytical Reagents), copper nitrate trihydrate ($\text{Cu}(\text{NO}_3)_2 \cdot 3\text{H}_2\text{O}$, 99 %, Synth), and manganese nitrate tetrahydrate ($\text{Mn}(\text{NO}_3)_2 \cdot 4\text{H}_2\text{O}$, 98 %, Sigma-Aldrich) were used to prepare the multi-metal solution. The standard stock solutions of 1000 mg/L, 99.9 % purity (hexavalent chromium, copper, cadmium, manganese, nickel, and zinc) were acquired from Specscol. HNO_3 (65 %) provided by Sigma-Aldrich was used for pH adjustment.

2.2. Methods

2.2.1. Preparation of the polymer solutions and electrospinning

Initially, a 10 % (w/v) polylactic acid (PLA) solution was prepared using chloroform as the solvent. The solution was homogenized for 24 h at 25 °C and 300 rpm in a magnetic stirrer (Fisatom 753 A). Subsequently, a 2 % (w/v) chitosan solution was prepared using acetic acid and absolute alcohol as solvents in a ratio of 9:1, respectively, and then magnetically stirred at 25 °C and 300 rpm for 24 h. To prepare the PLA/chitosan solutions, the chitosan solution was added drop by drop to the PLA solution until the final solutions contained 10 % and 20 % (v/v) of the chitosan solution, and they were stirred on a magnetic stirrer at 25 °C, 300 rpm for 24 h.

For electrospun membrane preparation, the solutions were inserted into 10 mL plastic luer slip syringes equipped with a 25 × 0.7 mm metal needle (Descarpack Brasil). These solutions were then subjected to the electrospinning process (DBM Eletrotech, Brasil), using a voltage of 15 kV, a distance of 15 cm to the collector, a flow rate of 0.15 mL/min. The membranes were collected on an aluminum foil-covered rotating drum bulkhead with a rotation of 150 rpm and left to dry in a desiccator for a minimum of 24 h at 25 °C to remove any residual solvents. The acronyms of the membranes were PLA (membrane without chitosan), and membranes containing chitosan at 10 wt% (PLA CS 90–10) and 20 wt% (PLA CS 80–20). Thus, Fig. 1 illustrates the polymer solubilization, the addition of CS and the electrospinning approach to prepare electrospun membranes.

2.2.2. Electrospun membranes characterization

2.2.2.1. Field emission gun – scanning electron microscope (FEG-SEM).

The morphology of the adsorptive membrane samples was analyzed by Field Emission Gun – Scanning Electron Microscope (FEG-SEM). FEG-SEM using high resolution (Schottky) scanning electron microscope (Thermofisher - Quattro S) and was performed in the Biomass



Fig. 1. Illustrative scheme of polymer solubilization and preparation of membranes by electrospinning.

Characterization Laboratory, Analytical and Calibration Resources (LRAC) at the Faculty of Chemical Engineering at UNICAMP. The membranes were kept at room temperature for 24 h in a vacuum desiccator to remove moisture. The dried samples were mounted on a slab covered with carbon conductive tape before coating with a thin layer of Au to make them conductive. The working voltage was 15 kV and the current 55 pA (Spot Size: 3.0). The average fiber diameters were determined by randomly measuring 100 individual fibers from the SEM images using a commercially available image analysis program (Image J software).

To determine the membrane porosity. The membranes were cut into 1 cm² squares, the dimensions were measured using a caliper (Mitutoyo, IP67), the thickness was measured using a micrometer (Mitutoyo, IP6), the samples were weighted in a precision balance (Shimadzu, AUY220), the apparent density was then obtained by the Eq. (1):

$$D_{ap} = m \times v \quad (1)$$

In which: m is mass, and v is the volume.

The true density of each sample was determined using helium gas pycnometry (AccuPyc 1340, Micromeritics, USA). Porosity was then calculated by relating the apparent and true density measurements of the samples by the Eq. (2):

$$p = (1 - D_{ap} \times D_{true}) \times 100 \quad (2)$$

In which: D_{ap} is apparent density, and D_{true} is the true density of the membrane.

2.2.2.2. Fourier transform infrared spectroscopy (FTIR). Fourier transform infrared spectroscopy (FTIR) with attenuated total reflectance (ATR-FTIR, Tensor II model, Bruker) was utilized to identify the functional groups in the membranes. The spectroscopy was conducted at wavelengths ranging from 2000 to 400 cm⁻¹ with 200 scans and was verified on the smooth and rough surface.

2.2.2.3. Water contact angle (WCA). The wettability of each membrane was determined in its both sides using a WCA analyzer (Phoenix 300, SEO, South Korea). A sample of the polymeric membrane (1.2 cm × 2 cm × 0.1 mm) was attached to the rectangular platform of the equipment and then 20 µL water droplets were inserted under the sample and immediately measured. The final contact angle was performed in triplicate.

2.2.2.4. Tensile mechanical performance. The mechanical tensile strength analysis was carried out in accordance with ASTM D882 standard with a universal testing machine (EMIC, DL10000). Test specimens, measuring 100 × 10 mm and a grip distance of 50 mm, were employed for the evaluation. The testing apparatus maintained a

constant speed of 5 mm/min and included a set of 7 specimens per sample. The mechanical analysis was performed in both fiber alignment and transverse directions.

2.2.2.5. Adsorption experiments. The adsorption experiments were conducted in 125 mL Erlenmeyer flasks, containing 25 mL of a multi-metal solution (Cr⁶⁺, Cu²⁺, Ni²⁺, Zn²⁺, Mn²⁺, and Cd²⁺) with a total initial concentration of 1.2 mmol/L. To ensure an equal number of molecules available for adsorption sites, the multi-metal solution comprised of 0.2 mmol/L of each metal ion. The pH solution was set at 4.0 using HNO₃, and approximately 0.13 g of the adsorbent membrane (adsorbent dose of 5 g/L) was added. This pH was chosen due to previous works present good removal of the metal ions between pH 3–5 in the literature [29–31]. Each test was performed in duplicate, and the suspension was agitated in an orbital shaker incubator at 180 rpm and 25 °C for 24 h, allowing sufficient time for equilibrium to be reached. Following the designated time, the samples were filtered using 0.45 µm cellulose acetate filters. The pH was measured, and the remaining metal concentration was analyzed. Cationic metals and hexavalent chromium were analyzed using an Ion Chromatography system (940 Professional IC Vario, Metrohm, Switzerland). The cationic metals were analyzed with a Metrosep C4 column (250 mm × 4.0 mm) at a column temperature of 45 °C, and an injection volume of 20 µL. The total chromium concentration was determined using Atomic Absorption Spectrometry (AAS) (AA-6300, Shimadzu). The removal efficiency (RE) was determined by Eq. (3), as described by Costa and co-workers [32].

$$RE (\%) = \frac{C_0 - C_e}{C_0} \times 100 \quad (3)$$

where C_0 is the initial concentration of metal in the solution (mmol/L), and C_e is the concentration of metal at the equilibrium (mmol/L).

2.2.2.6. High-resolution scanning electron microscopy and energy-dispersive spectroscopy (SEM-EDS). The samples were fixed in the specimen holder with double-sided carbon adhesive tape and coated with a thin layer of gold (20 nm) using Sputter Coater (K450, Emitech, Kent, United Kingdom). The samples were analyzed using a high-resolution scanning electron microscope (Quattro S., Termo Fisher Scientific), equipped with a chemical microanalysis module (EDS) (ANAX-60P-B, Thermo Scientific UltraDry, Brno, Czech Republic) using a working distance of 20 mm, voltage of 20 kV, current of 64 pA, spot size of 3.0, and magnifications of 1000×. The analysis was performed to evaluate the elements C, O, Si, Cl, Cr, Ca, Mg, Al, and Fe. This technique was available in Biomass Characterization Laboratory, Analytical and Calibration Resources (LRAC) at the Faculty of Chemical Engineering at UNICAMP.

2.2.2.7. X-ray photoelectron spectroscopy (XPS). The chemical structure of the PLA and PLA CS fiber membranes before (BS) and after (AS) metal ion sorption was analyzed using X-Ray Photoelectron Spectroscopy (XPS). The samples before adsorption were performed in the rough (the surface in contact with the tip of the needle) and the smoother (the surface in direct contact with the collector) surface of the membranes. Using an Al K X-ray source, the XPS spectra were obtained with a K-ALPHA (Al) (Thermo Scientific) spectrometer. The binding energies of the existing elements in the sample were determined using the survey spectra and components as the C1s and O1s region.

3. Results and discussions

3.1. Electrospun membranes characterization

3.1.1. Scanning electron microscopy

Firstly, SEM images of PLA, PLA CS 90–10 and PLA CS 80–20 are presented in Fig. 2. Besides, from SEM images, the values of fiber and pore diameters were fitted in a gaussian curve and plotted, being presented in Fig. 2.

In general, all membranes obtained a highly fibrous structure, that is an inherent aspect of electrospun membranes [33]. PLA membranes exhibited an average fiber diameter and pore diameter around $5.98 \pm 0.06 \mu\text{m}$ and $18.81 \pm 0.58 \mu\text{m}$, respectively. According to Huang and Thomas, PLA membranes prepared from chloroform promotes surface

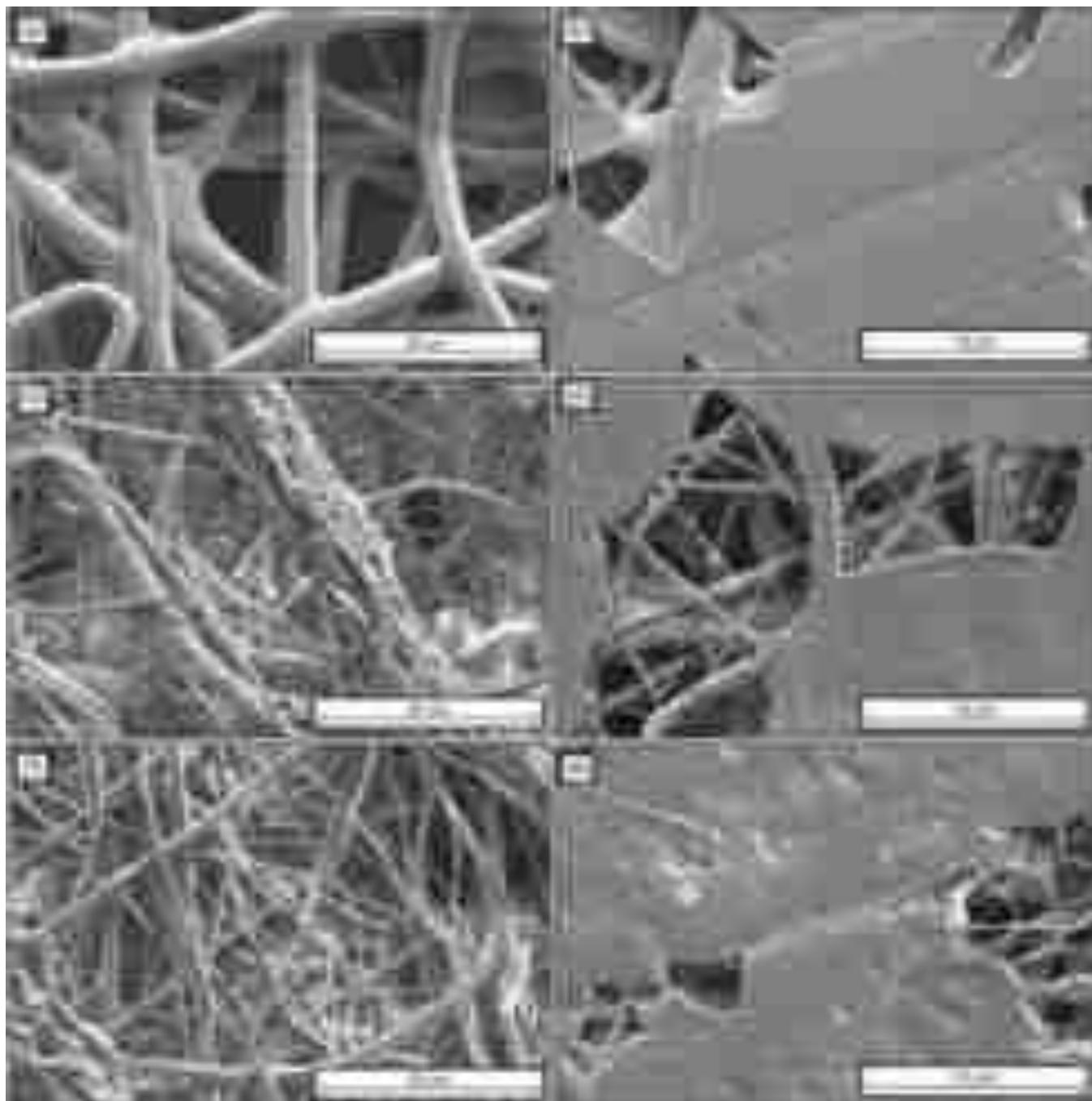


Fig. 2. SEM images showing both sides of the membranes, (a) and (b) PLA, (c) and (d) PLA CS 90–10, and (e) and (f) PLA CS 80–20.

roughness of electrospun fiber, ranging from few nanometers to 10 μm [34]. Also, the PLA nanofibers presented themselves highly porous, increasing the total porosity of the whole membrane, what is a positive result for an adsorption system since the total area for adsorption increases. The enhance in fiber porosity was attributed to the effect of humidity, according to Casper and co-workers, who showed that increasing in the environment humidity during electrospinning may cause circular pores formation in the nanofibers due to the evaporation of the solvent during the solution direction to the collector [35,36].

As CS was incorporated into the PLA membrane structure by electrospinning, the average size to fiber diameter decreased, ranging the values of 38.80 % and 77.93 % for CS 10 and 20 wt%, respectively, with left-dislocate narrow gaussian curves verified in every different composition. Regarding the pore diameter of the membranes, the average values also decreased, presenting a decline of 14.72 % and 54.12 % for CS 10 and 20 wt%, respectively. Analyzing these two values, they decreased as the chitosan content increased in formulation. In this parameter, left-dislocated large gaussian curves were verified with different compositions. Similar tendency was verified by Thomas and co-workers, in which the authors obtained PLA/chitosan (0.2–0.8 wt%) membranes by electrospinning method [37]. Other authors also observed the same trend. Guo and co-workers reported a decrease in the fiber diameter as CS increases for membranes prepared from a blend of poly(butylene carbonate)/poly(lactic acid)/chitosan (CS) by electrospinning [38]. Thomas and co-workers also observed a reduction of fiber diameter and pore size as nanochitosan was added into poly(lactic acid) (PLA) synthesized from electrospinning process to remove Cd^{2+} from

water [39] (Fig. 3).

Corroborating with SEM discussion, Table 1 presents the porosity values for membranes.

From the porosity percentage values found in Table 1, it was verified a decrease as the chitosan content increased, what is in accordance with those presented on Fig. 2. Besides it can also be noted a decrease in fiber diameter as the chitosan increase. Thomas and co-workers observed a decrease in porosity attributed to increase of chitosan percentage [16]. In addition to this affirmative, the decreasing in nanofibers diameter as function of chitosan level in the mixture of PLA/Chitosan may be explained by the enhanced charge density that is positioned on the surface of the solution jet that causes certain repulsion and stretching of the fibers on the way to the collector. This was verified in previous research that showed a smaller average fiber diameter when incorporating more chitosan into the mixture [40–43].

3.1.2. Fourier transform infrared spectroscopy (FTIR)

Fig. 4 shows the FTIR spectra of raw materials and membranes with different compositions and different analyzed surfaces. In general, the

Table 1
Porosity values of the membranes.

Sample	Porosity (%)
PLA	82,36
PLA CS 90–10	77,71
PLA CS 80–20	71,51

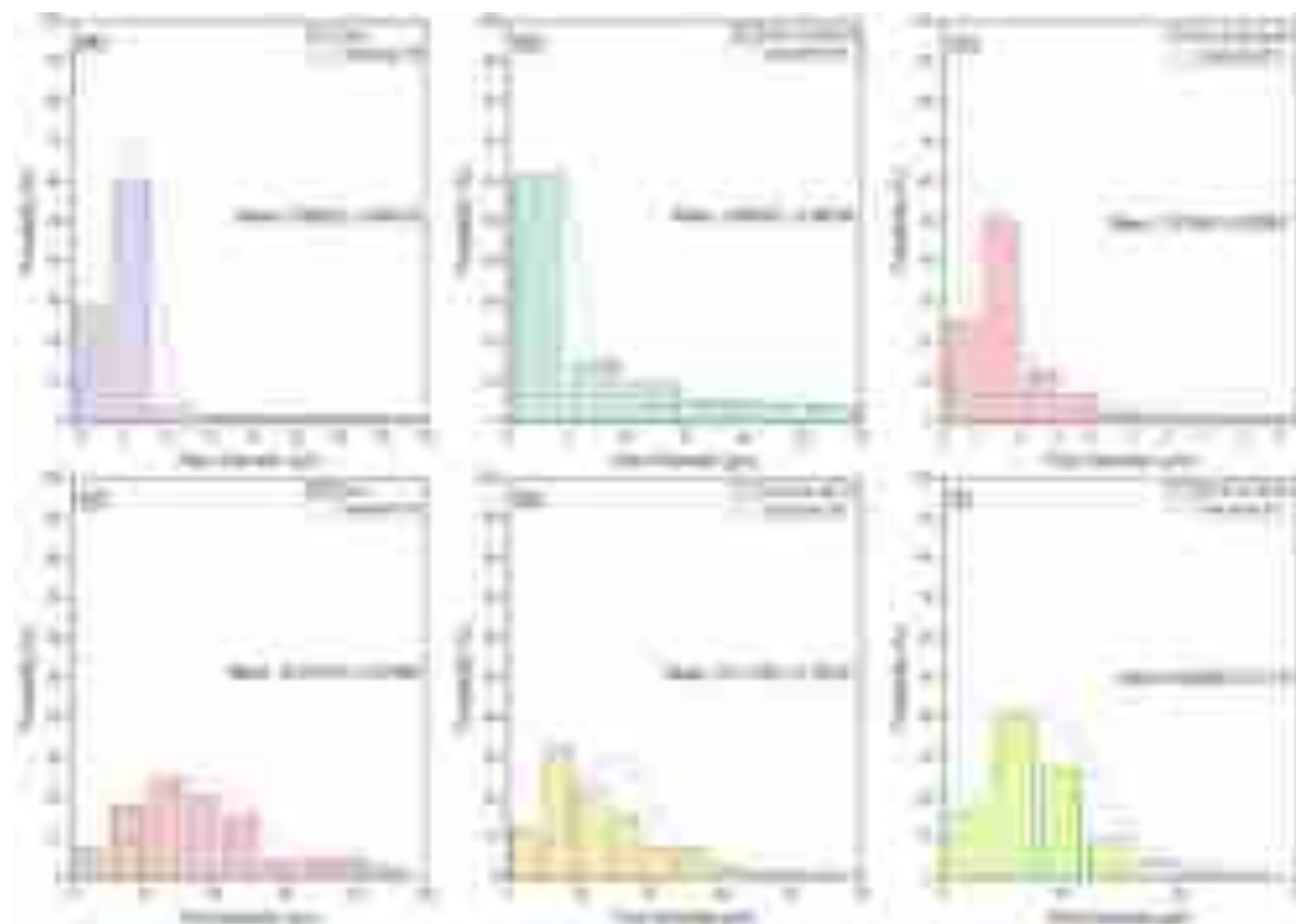


Fig. 3. Probability plots for fiber diameter where, (a) PLA, (b) PLA CS 90–10, (c) PLA CS 80–20, and pore diameter for, (d) PLA, (e) PLA CS 90–10 and (f) PLA CS 80–20.

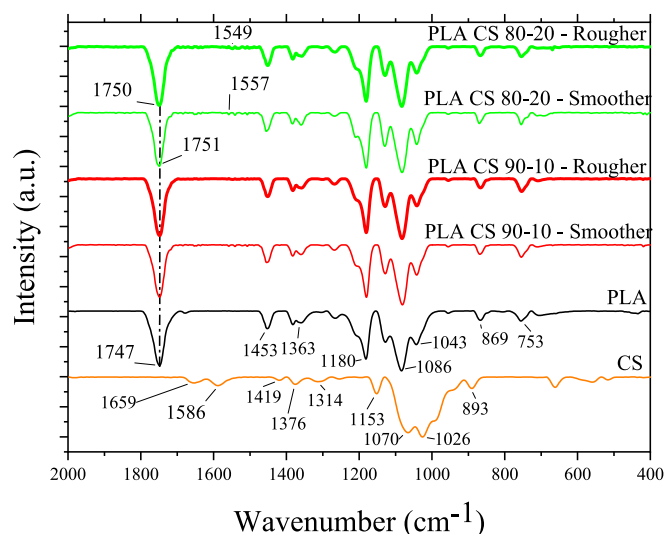


Fig. 4. FTIR spectra for raw materials, PLA membrane, and PLA membranes containing different CS percentages obtained with different sides of membranes (smoother and rougher surface).

curves present the same bands, with different intensities, and the curves from rough surfaces present more noise than the smooth surfaces.

Evaluating the CS spectra, several characteristic peaks are found. Firstly, peaks located in 1659 cm^{-1} , 1586 cm^{-1} , 1419 cm^{-1} , 1376 cm^{-1} , and 1153 cm^{-1} corresponds to -C-O group in primary amides, secondary amides, -CH₂ bending, CH₃ symmetrical deformation, and antisymmetric stretch C-O-C and C-N stretch are some typical peaks found in the chitosan macromolecular chains. Other peaks verified in 1070 cm^{-1} , 1026 cm^{-1} , and 893 cm^{-1} are attributed to asymmetric -C-OH stretching, C-O stretching, and C-N bonds [13,44,45].

From PLA spectra, the characteristics peaks were found at 1747 cm^{-1} related to -C=O stretching in ester band, 1453 and 1363 cm^{-1} regarding to -CH₃ angular deformation, 1180 cm^{-1} and 1086 cm^{-1} related to C-O-C symmetric and asymmetric stretching, respectively, and 1043 cm^{-1} corresponding to -C-O- stretching [46,47]. These peaks are like those obtained on Chitosan/PVA/PLA films, prepared by emulsion and conformed by casting [46]. Besides, peaks located at 869 cm^{-1} and 753 cm^{-1} are associated with -C-O- deforming and O-H bending, respectively [48].

One first slight difference detected especially for PLA CS 80-20 (containing higher CS percentage) was the slight shift of peak found at 1747 cm^{-1} for 1751 cm^{-1} and 1750 cm^{-1} increasing the CS percentage. Mollah and co-workers developed colored films composed on starch and chitosan by using *Acacia catechu*. They reported that shifting of this peak can be correlated with reaction between starch chains and amide group of chitosan, or also the formation of hydrogen bonds of these compounds [49]. In addition, in the 10-20 wt% CS percentage, there was not much of a change when compared to PLA spectra. From the spectra of starch/chitosan films for food packaging, Mutmainna and co-workers claimed that above 35 wt% CS, there were spectral changes observed and at 65 wt% CS, there was no interaction between the starch chains and chitosan [50]. Lastly, other peaks at 1549 cm^{-1} and 1557 cm^{-1} for PLA CS 90-10 and PLA CS 80-20 appeared due to the higher concentration of CS inside the PLA matrix. As previously mentioned, this peak is correlated to N-H bending, indicating the presence of chitosan in the blend membrane [51].

3.1.3. Water contact angle (WCA)

The electrospinning process provided membranes with distinct characteristics on their two faces: the surface that was in direct contact with the collector surface was smoother, while the outside surface was rough. Thus, wettability was evaluated for both sides of the membranes,

whose water contact angle values are presented in Fig. 5, with (a), (b), and (c), corresponding to the smooth surface of PLA, PLA CS 90-10, and PLA, PLA CS 80-20, respectively. In contrast, (d), (e), and (f) refer to rough surface of the PLA, PLA CS 90-10, and PLA, PLA CS 80-20.

The water drops profiles on smooth surfaces (Fig. 5(a), (b), and (c)) revealed differences in drop spreading. Specifically, the sample that exhibited the highest chitosan content (PLA CS 80-20), demonstrated a greater drop spreading. Fig. 5.c indicated its superior hydrophilic nature. In contrast, the sample composed solely of polylactic acid (pure PLA) exhibits a higher drop height, accompanied by an increased contact angle, which indicated a reduced interaction with the membrane. Similar findings in PLA/chitosan membranes were reported by Wu and co-workers [52], where the authors reported a reduction from 67.73° to 61.31° on contact angle values of PLA and PLA/chitosan membranes, respectively [52], and by Tighzert and co-workers on nanofibers based on PLA and chitosan blends by electrospinning [53].

In contrast, the contact angle measurements on rough surfaces revealed an opposite behavior. As depicted in Fig. 5(d), (e), and (f), the pure PLA sample showed hydrophobic behavior, with a contact angle of 99.4° . However, the addition of chitosan at 10 wt% (PLA CS 90-10) and 20 wt% (PLA CS 80-20) further increased the hydrophobicity of the surface, with contact angles of 110.3° and 114.0° , respectively, highlighting the low affinity of this surface with water. Similar findings were reported by Thomas and co-workers, where the authors reported an increase in the contact angle of the PLA membrane with the addition of different fractions of chitosan [37].

Based on these findings, definitive confirmation regarding the impact of enhanced chitosan concentration and the level of wettability caused in the electrospun membranes surface morphology could be verified. Nevertheless, the formation of two surfaces with distinct wettability characteristics was evident: a smooth surface demonstrating higher hydrophilicity and wetting properties ($\theta < 90^\circ$), and a rough surface displaying increased hydrophobicity and reduced wettability ($\theta > 90^\circ$). This structural difference between two surfaces of the same electrospun membrane has already been reported in the literature. Liu and co-workers developed PLA microfiltration membranes using chitosan acetic acid solution as the coagulation bath plus glutaraldehyde as the crosslinking agent by the non-solvent phase inversion (NIPS) method and, in addition to observing higher water flux through the membrane with an increase in chitosan concentration, they also noticed two distinct surfaces: one rougher and the other smoother, as observed in the present work [54].

Besides polarity, some structural characteristics, such as average diameter, pore diameter distribution and structural form of the membranes, are also directly related to the wettability of electrospun membranes [55,56]; therefore, its determination could be of great value for further elucidating the different wettability characteristics observed on each surface. One hypothesis for the difference between the sides of the membranes is due to the availability of polar functional groups of the chitosan molecules, which resulted in a higher wettability for smooth surface than rough surface.

3.1.4. Tensile mechanical performance

Table 2 presents the results from the tensile strength of the membranes, in which the tensile was applied in different fiber directions (fiber alignment and transverse section).

Evaluating the mechanical properties of PLA membrane, the elastic modulus, tensile strength at break, and strain were $73.76 \pm 12.03\text{ MPa}$, $2.06 \pm 0.19\text{ MPa}$, and $40.80 \pm 5.30\%$, respectively. Ghafari and co-workers reported the development of electrospun membranes based on poly(lactic acid), polyethylene oxide and enzymatic cellulose nanofibers using three different solvent mixtures. They obtained elastic modulus, tensile strength, and elongation at break around $60 \pm 8\text{ MPa}$, $2.55 \pm 0.03\text{ MPa}$, and $40 \pm 8\%$, respectively [57], proving the similarity with the values obtained by tensile test on the fiber alignment.

As chitosan was added inside the PLA matrix, both tension directions



Fig. 5. WCA images on membranes of (a) PLA (smooth surface), (b) PLA CS 90–10 (smooth surface), (c) PLA CS 80–20 (smooth surface), (d) PLA (rough surface), (e) PLA CS 90–10 (rough surface), (f) PLA CS 80–20 (rough surface).

Table 2

Tensile property values for PLA and PLA containing CS in 10 wt% and 20 wt%, considering different directions for tension application.

Sample	Elastic Modulus (MPa)	Tensile strength at break (MPa)	Strain (%)
Tension direction: Fiber alignment			
PLA	73.76 ± 12.03	2.06 ± 0.19	40.80 ± 5.30
PLA CS 90–10	236.70 ± 74.90	3.87 ± 0.74	4.51 ± 1.60
PLA CS 80–20	346.40 ± 61.40	4.57 ± 0.69	2.43 ± 0.70
Tension direction: transverse			
PLA	56.90 ± 20.30	1.36 ± 0.29	6.94 ± 2.30
PLA CS 90–10	144.50 ± 33.20	2.23 ± 0.60	3.20 ± 0.90
PLA CS 80–20	167.40 ± 23.20	2.31 ± 0.38	1.61 ± 0.80

had a drastic increase of elastic modulus and tensile strength, and subsequently decrease of strain were verified. Besides, the increase of chitosan provided an increase of mechanical performance. These results are promising because they confirmed that the addition of chitosan to PLA membranes enhances the mechanical resistance of the system as desired. Kasirajan and co-workers reported the same trend of an increase in mechanical properties of biodegradable packaging of PLA containing chitosan [58]. Momtaz and co-workers developed nanocomposite films of gelatin/chitosan incorporating different contents of nickel oxide nanoparticles by casting. They verified that the addition of chitosan increases the tensile strength due to good interaction between gelatin and chitosan [59]. Besides, another aspect observed was the decrease in fiber diameter generating higher mechanical performance. Thomas and co-workers observed the same trend as nano-chitosan was filled into the PLA matrix to remove Cd^{2+} from the contaminated water. They reported that high tensile strength can be attributed to low fiber diameter since it was observed after the addition of nano-chitosan inside PLA polymer matrix [39]. Finally, the strain values are inversely proportional to the other values (tensile strength at break and elastic modulus). The values of tension and strain obtained were higher than those verified for other biopolymer systems as Chitosan/PEO membranes [47] or polymer films with Chitosan/PVA/PLA in 1–2–2 and 6–1–1 proportions [46].

Considering only the tension direction, mechanical characterization presents higher results (tensile strength at break and elastic modulus) in

the vertical direction of the fiber alignment than in the transversal direction as expected. This is probably due to the additional secondary forces acting among the polymer chains after their alignment under tension, offering more resistance to the applied tension. In the similar work with biopolymers, Zhang and co-workers reported the mechanical performance in two tensile directions of microfibrillar poly(lactic acid)/polyethyleneglycol membranes, varying PEG percentage from an *in situ* drafting-assisted melt-blowing process for application in skin contactors. They always found superior mechanical performance values (tensile strength and elastic modulus) for machine direction than transverse direction [60]. It can be an indicative of the main orientation of electrospun fibers of PLA and PLA containing CS, that is favorable on fiber alignment, as seen by Zhang and co-workers if the fiber alignment was in the same machine direction.

3.2. Adsorption experiments

The removal efficiency of metals in a multi-elemental solution of Cr^{6+} , Cu^{2+} , Ni^{2+} , Zn^{2+} , Mn^{2+} , and Cd^{2+} by the PLA, PLA CS 90–10, and PLA CS 80–20 electrospun membranes can be seen in Fig. 6.

From the results of removal efficiency in Fig. 6, it is possible to

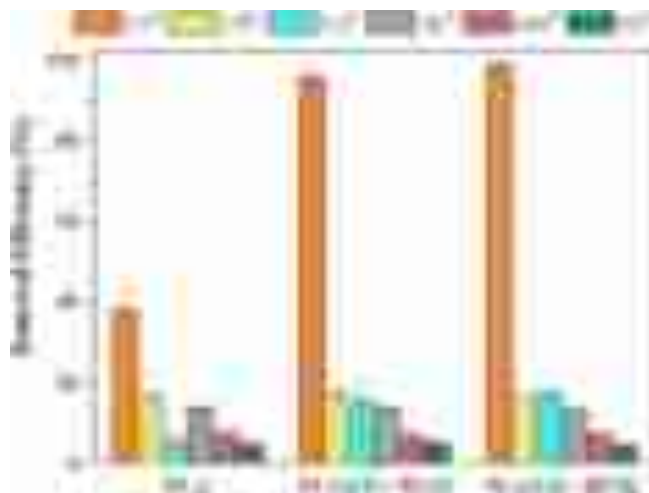


Fig. 6. Removal efficiency of Cr^{6+} , Cu^{2+} , Cd^{2+} , Zn^{2+} , Ni^{2+} , and Mn^{2+} ions present in a multi-metal solution in pH of 4.0 for different adsorbent membranes. Experimental conditions: Total initial concentration of 1.2 mmol/L, 5 g/L of adsorbent, and 180 rpm of orbital stirring at 25 °C for 24 h.

observe two different adsorption profiles, one for cationic species and another for hexavalent chromium (oxyanion). Firstly, the adsorption efficiency of cationic species did not change significantly with the presence and/or increase in the amount of CS. Xiong et al. [31] synthesized cellulose acetate/chitosan electrospun fibers. They obtained an increase in adsorption capacity due to the high chitosan percentage of 50 wt%. However, a slight decrease of thermal stability and appearance of shrinkage were observed for this chitosan percentage [31]. Therefore, as the aiming was obtaining a high performance electrospun membrane, percentages of 10 and 20 wt% was more available chosen, presenting higher adsorption efficiency than neat electrospun membrane and maintaining intrinsic properties without great losses. Besides, the lack of adsorption capacity of chitosan can be attributed to the absence of interactions between the cations (Cd^{2+} , Cu^{2+} , Zn^{2+} , Ni^{2+} , and Mn^{2+} ions) and the CS polymer chains in lower pH values. On the other hand, the extent of protonation of the amino group ($-\text{NH}^+$) increased, generating an electrostatic repulsion between $-\text{NH}^{3+}$ and cationic metal ions [61,62]. So, the cation adsorption capacity of the membrane can be attributed only to the presence of functional groups on the PLA surface. Polylactic acid possesses terminal groups of $-\text{OH}$ and $-\text{COOH}$, which acts as adsorption sites that vary in quantity depending on the molecular weight of the polymer and the pH values. Nevertheless, the impact of these end groups can be negligible in high-molecular-weight polymers, as their presence is practically insignificant [63]. However, the influence of these end groups can be noteworthy in the case of lower molecular weight polymers, as they increase considerably. It is important to note that at low pH values, carboxylic acids dissociate into carbonyl anions, which increase in abundance as polymer chain degradation takes place. This results in increased availability of active $-\text{COO}^-$ sites for the complexation of transition metal ions. Therefore, it is possible to observe that within the investigated pH range of 4.0, the adsorption of cations was attributed to the higher concentration of carboxylic acid present at the polymer chain ends, which is promoted by the hydrolysis of the polymer under these pH conditions.

The maximum cation efficiency removal was 17 % for Cd^{2+} and Cu^{2+} by PLA membranes containing 10 and 20 wt% of CS, respectively. Similar efficiency removal (15 %) for Cd^{2+} at pH 4.0 was obtained by Karim and co-workers, when they evaluated the pH effect (ranging from 2.0 to 10.0) on Pb^{2+} and Cd^{2+} adsorption efficiency by fabricated poly(vinyl alcohol)/chitosan nanofibers membranes [64]. Furthermore, the authors concluded that the removal of Cd^{2+} increased with the increasing the solution pH from 2.0 to 8.0, however high pH values should be avoided to prevent metal ions precipitation [65]. Refaat Alawady and co-workers reported that in alkali conditions, chitosan chains became more flexible, allowing more active sites to be provided, resulting in an increase of adsorption capacity of the membranes for divalent ions (cations), such as Co^{2+} , Ni^{2+} , Cu^{2+} , Cd^{2+} , and Pb^{2+} . In contrast, between pH 6–8 and below these values, there is a competition of the divalent metal ions to be removed [66]. Moreover, it can be found that the adsorption efficiency of the PLA membranes containing 10 and 20 % of CS increases as follows: $\text{Cd}^{2+} \equiv \text{Cu}^{2+} \equiv \text{Zn}^{2+} > \text{Mn}^{2+} \equiv \text{Ni}^{2+}$. This trend was also found by Sahebamee and co-workers, that adsorbed $\text{Cd}^{2+} > \text{Cu}^{2+} > \text{Ni}^{2+}$ using chitosan/polyvinyl alcohol adsorptive membranes containing 0.5 wt% polyethyleneimine [67].

Additionally, the adsorption efficiency of hexavalent chromium species was substantially affected by the presence of the CS, increasing from 38 % to the pure PLA membrane, to 96 and 99 % to the PLA membranes containing 10 and 20 % of CS, respectively. This phenomenon can be attributed to the electrostatic attraction between Cr(VI) ions and protonated amino groups and hydroxyl ($\text{O}-\text{H}$) of electrospun membranes, since between pH 2 and 6, the predominant hexavalent chromium species in aqueous solution are hydrogen chromate (HCrO_4^-) and dichromate ($\text{Cr}_2\text{O}_7^{2-}$) negative ions [68,69]. Billah and co-workers reported that chitosan in acid pH protonated $-\text{NH}_3^+$ groups of chitosan, promoting the hexavalent chromium removal of aqueous solution [70]. Besides, Wang et al. [30] reported that low pH media increased

adsorption capacity due to the protonation of the NH_3^+ and OH_2^+ of the amino and hydroxyl groups and strong attraction between HCrO_4^- and protonated groups on the chitosan surface [30], meanwhile, pH 2 is not available to remove HCrO_4^- due to the elevated protonation of amine groups ($-\text{NH}_2$) employing high acid conditions [29]. In addition to these works, Xiong et al. [31] obtained the best adsorption capacity at pH 3, with a slight decrease from this pH. However, pH 4 presented a slight decrease of 11.52 %, but a higher adsorption capacity was maintained compared to high pH media values [31].

Moreover, the adsorption increases with the increase in the CS content, due to the increased availability of active sites within the fiber, enabling a greater number of interactions with chromium ions. Consequently, as reported by Zhang and co-workers [71], a higher extent of mutual reaction occurs between the chitosan and chromium ions. Besides, according to Mohammed and co-workers, physical (mainly through electrostatic interactions) and chemical (controlled by the mechanisms of chelation, and ion exchange) adsorption are involved in the Cr(VI) interactions with the functional groups on the fibrous membrane surface [72]. Functional groups such as amino groups possess lone pair electrons, which exhibit a strong electron-donating capability, allowing them to be used to reduce Cr(VI) to Cr(III) ions, that can be thereafter adsorbed, even in preference of divalent cations [72,73]. Li and co-workers found through XPS analysis Cr(III) species in chitosan membranes after the Cr(VI) adsorption, proving that Cr(VI) reduction to Cr(III) is also participating in the removal mechanism of this metal [74]. This phenomenon cannot be observed in our results with CS since there was no difference between the total and hexavalent chromium concentration in the solutions after contact with the membranes containing 10 and 20 % of CS, indicating that these membranes can completely remove all the chromium species. However, despite being able to remove 38 % of the Cr(VI) ions, the PLA membrane alone is not able to remove the total chromium species. The total chromium concentration in solution after the contact with the PLA membranes was 0.19 mmol/L, in contrast with the initial concentration of 0.2 mmol/L. These results indicate that the Cr(VI) removal by the PLA mats is attributed to its reduction to Cr(III) species, however, these species remain in the solution. This further emphasizes the significance of incorporating CS into the membranes, imparting them with desirable adsorptive properties.

3.2.1. SEM-EDS

The EDS patterns of each membrane before and after adsorption, without and containing chitosan and their chemical surface composition are verified on Fig. 2S and Table 3. Besides, Fig. 1S presents the images of each side of the membrane's surface before and after adsorption that was analyzed by SEM-EDS.

Table 3 presents the results for chemical composition of the membranes, before and after adsorption experiments. Comparing the PLA compositions there was a decrease in C and Si content and an increase in O content. Besides, it is verified some change on the other elements, which were Mg, Al and Fe before adsorption and only Cl after adsorption. The metals applied on adsorption tests (Cd, Cu, Zn, Mn and Ni) were not detected in the membranes, with exception of a small amount of Cr,

Table 3
Chemical composition of the membranes before and after adsorption.

Element (wt%)	Before adsorption		After adsorption	
	PLA	PLA	PLA CS 90–10	PLA CS 80–20
C	43.70	40.43	39.22	38.60
O	51.07	58.30	59.28	59.73
Si	3.37	0.90	0.85	1.02
Cl	–	0.36	0.35	0.18
Cr	–	–	0.30	0.38
Ca	–	–	–	0.08
Mg	0.15	–	–	–
Al	1.25	–	–	–
Fe	0.45	–	–	–

that was verified in membranes with chitosan.

Table 3 presents the EDS measures of membranes before and after adsorption experiments, corroborating with Fig. 1S (patterns of SEM-EDS). For every condition, the major elements verified were C and O and Cr also appears in membranes after adsorption. In PLA membranes, small peaks of Si and Cl were verified, both before and after adsorption. In membranes with PLA and chitosan, small peaks of Si, Cl and Cr were observed. Other alkaline elements, as Na, K and Ca were verified in PLA CS 90–10 membranes before adsorption experiments. These other small peaks can be negligible of the EDS spectra, being associated with some impurities or peak detection error [75,76].

Analyzing the weight percentage of elements C and O in Table 3, there was a slight reduction of the carbon percentage comparing samples before and after metal ion removal; however, oxygen obtained a considerable increase. The same tendency was found by Kong and co-workers, that adsorbed Cd²⁺ using a thiol-functional Cd²⁺-imprinted silica-based polymer [77]. This result corroborates with the participation of oxygen functional groups in the metal ion removal, that it will be approached by XPS. Another characteristic observed by element percentage was the appearance of small percentage of chromium, that slightly increased according to the increase of chitosan content into the PLA matrix. This appearance of Cr element after sorption is an indicative to high adsorption of Cr⁶⁺ on the polymer membrane containing chitosan [78–80]. In addition, among all of metal ions studied, Cr(VI) presents 44 pm ionic radius, that is the lowest ionic radius among all metal ions studied. Its low ionic radius possibly facilitated the interaction with the membrane's surface, on the other hand, it is another factor corroborates with the metal ion removal of hexavalent chromium [81,82].

3.2.2. X-ray photoelectron spectroscopy

XPS was used to determine the possible mechanism to understand the metal ion removal for PLA and PLA containing CS in 10 and 20 wt%. The electrospinning process has generated membranes with distinct characteristics on their two surfaces: a smoother surface (direct contact with the collector) and a rough surface (contact with the jet created by the tip of the needle). Firstly, an analysis of the atomic concentration (%) obtained from Survey spectra (Fig. 5S) in the surface was performed before (BS) and after multi-elemental sorption (AS) of six metal ions (Cr⁶⁺, Cu²⁺, Cd²⁺, Zn²⁺, Ni²⁺, and Mn²⁺ ions) (Table 4).

Evaluating both sides of the membrane (rough and smoother), no tendency of the data is found. A high atomic concentration was observed for the elements such as C1s, O1s, Si2p, and N1s. Adding the chitosan inside the PLA membrane promoted the appearance of N1s located at 400.34 eV. Da Silva and co-workers reported an appearance of N1s peak at 401 eV, corresponding to the C–NH–C bonds linked to the addition of chitosan nanocapsules on the cotton fabrics' surface [83]. It proved a

possible interaction and effective production of composite membranes based on PLA, containing chitosan, to improve the adsorbent effect of the PLA matrix.

However, other elements with low atomic percentages have also been found, such as Cl2p, Na 1 s, and Ca 2p, located at 199.67 eV, 1072.30 eV, 348.22 eV, respectively. These other elements presented a low atomic concentration; thus, this discussion did not consider these peaks. Gorzalski, Danley, and Coronell presented that XPS does not provide reliable detection of significant elements in depth-heterogeneous samples, being considered non-effective when the sample presents a heterogeneity of structure; on the other hand, these membranes have a heterogeneity inherent in their structures [84].

After metal ion sorption, the signatures of N1s disappeared. Wei and co-workers reported that the Ca²⁺ ion removal caused a decrease in the intensity of N1s peaks due to the binding with Ca²⁺ [85]. Chitosan molecules contain amine groups strongly reactive to remove metal ions, especially Cr⁶⁺. Amine functional groups are protonated in low pH; thus, they are more reactive when interacting with oxyanions. In low pH, hexavalent chromium ion behaves like an anion in an aqueous medium, presenting them in the form of ([CrO₄]²⁻, [Cr₂O₇]²⁻, [H₂CrO₄], and [HCrO₄]⁻) (Bruno [13]). Besides, chromium signature was not observed after sorption. One hypothesis is the multielement removal tests were performed at a total concentration of 1.2 mmol/L and 0.2 mmol/L for each ion. Correspondingly, 0.2 mmol/L is equivalent to 10.4 mg/L for hexavalent chromium. According to the XPS analysis, this concentration is below the equipment's detection limit, which is <1.0 % (w/w). Corroborating with the current literature, Da Costa et al. [86] studied the adsorption of multicomponent systems containing lanthanum and ytterbium ions using modified sericin/alginate/poly(vinyl alcohol) beads as adsorbents. They conducted their adsorption experiments evaluating XPS spectra of beads before and after adsorption from contaminated bead with 5.0 mmol/L of each rare earth metal ion. However, even at high ion concentrations, their adsorbed ion percentage were about 0.04 and 2.50 % for lanthanum and ytterbium ions, respectively [86]. It can be proved from XPS spectra after sorption (AS) comparing three XPS spectra of electrospun membranes (Fig. 2S), which there was not a surface appearance of Cr⁶⁺ peaks between 571 and 596 eV, that corresponding to the Cr2p [87,88].

Moreover, from the survey spectra of each membrane before and after sorption, C1s and O1s were obtained. These XPS spectra are presented in Fig. 5s (C1s spectra) and Fig. 6S (O1s spectra), aiming to point out the binding energy of functional groups containing carbon and oxygen elements before and after sorption. Besides, Table 5 presents the peak area (%) of each deconvoluted curve of the C1s and O1s spectra for PLA membranes before and after sorption and their composite membranes containing two distinct CS percentages (10 and 20 wt%).

In the first step, from the deconvolution of C1s spectra, some curves

Table 4

Atomic concentration (%) of elements present in the membrane's surface before sorption (rough and smoother of membrane's surface) and after metal ions sorption for PLA membrane and membranes containing 10 and 20 wt% CS.

Sample	Si 2p 103.375 (eV)	Cl 2p 199.67 (eV)	C 1s 286.05 (eV)	N 1s 400.34 (eV)	O 1s 533.82 (eV)	Na 1s 1072.30 (eV)	Ca 2p 348.22 (eV)
Before sorption – rough							
PLA	3.00 ± 0.88	0.19 ± 0.08	67.88 ± 1.66	0.70 ± 0.21	27.16 ± 0.57	0.94 ± 0.13	0.30 ± 0
PLA CS 90–10	3.19 ± 0.30	0	64.03 ± 1.94	0.37 ± 0	32.47 ± 2.09	0.25 ± 0	0
PLA CS 80–20	3.15 ± 0.14	0	66.24 ± 1.92	0	30.04 ± 1.85	0	0.57 ± 0.07
Before sorption – smooth							
PLA	4.09 ± 0.62	0.08 ± 0	64.64 ± 3.52	0.56 ± 0	30.62 ± 3.83	0.29 ± 0	0.37 ± 0
PLA CS 90–10	2.57 ± 0.99	0	68.30 ± 4.46	0.56 ± 0.32	28.01 ± 4.07	0.15 ± 0.05	0.43 ± 0.21
PLA CS 80–20	3.28 ± 0.13	0	65.07 ± 0.10	0.74 ± 0	30.91 ± 0.47	0.07 ± 0	0.34 ± 0.07
After sorption							
PLA	3.93 ± 0	0	71.69 ± 0	0	24.38 ± 0	0	0
PLA CS 90–10	2.48 ± 0	0	62.45 ± 0	0	35.06 ± 0	0	0
PLA CS 80–20	4.07 ± 0	0	58.61 ± 0	0	37.32 ± 0	0	0

Table 5

Peak's area (%) of each deconvoluted curve of the C1s and O1s on the membrane's surface before sorption (rough and smoother of membrane's surface) and after metal ions sorption for PLA membrane and membranes containing 10 and 20 wt% CS.

Sample	C1 (285.0 eV)	C2 (286.6 eV)	C3 (287.6 eV)	C4 (289.2 eV)	O3 (532.7 eV)	O4 (533.8 eV)
Before sorption – rough (%)						
PLA	64.21	3.28	16.48	16.03	77.04	22.96
PLA CS 90–10	54.35	14.97	7.08	23.61	52.12	47.88
PLA CS 80–20	64.24	3.56	10.94	21.26	45.13	54.87
Before sorption – smoother (%)						
PLA	57.08	5.05	16.20	21.67	59.55	40.45
PLA CS 90–10	59.31	0.97	20.74	18.98	63.84	36.16
PLA CS 80–20	56.32	0.27	23.12	20.29	55.73	44.27
After sorption (%)						
PLA	64.65	17.96	6.77	10.61	100.00	0.00
PLA CS 90–10	46.46	21.79	3.49	28.27	40.92	59.08
PLA CS 80–20	45.04	25.13	17.90	11.93	18.47	81.53

of types of the binding energy of chemical linkages of carbon element are C1 at 285 eV (C – C and C – H), C2 at 286.6 eV (C – O of alcohols and ethers), C3 at 287.6 eV (O – C – O and C=O), and C4 at 289.2 eV (O – C – O of esters groups) [7,89,90]. For the deconvolution of O1s spectra, some curves were provided, highlighting the prominent peaks at 532.7 eV and 533.8 eV, corresponding to the O3 and O4 linkages of C – O and O – H from chemisorbed water molecules [91,92].

PLA showed a peak of the methyl group with the binding energy at 285 eV, followed by a peak at 286.9 eV associated with α -carbon of ester groups, and two other peaks at 287.6 eV and 289.2 eV of carbon of ethers and carbonyl groups and esters [93]. Incorporating CS inside the membrane structure, a few changes in the peak's area were verified. Besides, comparing the top and bottom of the membrane's surface, no difference was observed for the peak areas of components of the C1s spectra. Kormunda and co-workers observed this pattern because independent of the membrane's side; the samples presented the same groups of C1s spectra of the polyamide 6 (PA6) [94]. However, as the O1s is evaluated, the addition of the chitosan promotes the increase of O4 binding energy's peak of the rough surface of composite membranes, with a peak area of O1s spectra around 47.88 % and 54.87 % according to an increase of CS percentage. Bandara, Nadres, and Rodrigues also observed an increase of C and O elements that can be linked to the multiple functional groups with oxygen, such as carboxylic, hydroxyls, and carbonyl groups [95].

After multi-elemental sorption, the drastic decrease in the O3 peak's area and a drastic increase in the O4 peak's area were verified. It may be linked to the interaction between oxygen-rich functional groups and metal ions, especially Cr (VI). Ouyang and co-workers observed the same trend: an intensity alteration was verified for oxygen groups after sorption [96]. Besides, the slight participation of N1s, which generated the disappearance of signals of the XPS spectra after sorption from survey spectra, shows the interference of $-\text{NH}_2$ of chitosan in this metal ion removal process [97]. Li and co-workers observed a similar trend: the peak area of 532.0 eV (O3 in this paper) decreased from 86.08 % to 57.88 %. It indicates the influence of oxygen functional groups to capture metal ions [98]. Besides, evaluating the percentage of peak's area for C1 at 285 eV and C2 at 286.6 eV, after sorption, C1 percentage decreased, and C2 increased their percentages, indicating the contribution of functional groups containing oxygen elements (C–O of alcohols and ethers) in the removal of metal ions [98]. These indications of the adsorption mechanism gave rise to the schematic illustration in Fig. 7.

Fig. 7 presents the possible mechanisms proposed for removing ions using PLA membranes containing CS. In contrast to the XPS spectra results, SEM-EDS obtained a low percentage of chromium on the electrospun membranes surface, proving the presence and interaction of the hexavalent chromium ion on the membrane's surface. Therefore,

observing the appearance of the chromium peak in the EDS spectra of the membranes containing chitosan and the alterations between XPS spectra before and after sorption of C1s and O1s, the possible mechanism elucidated in Fig. 7 were: 1) the interaction of amine groups ($-\text{NH}_2$) originating from the chitosan chain, 2) the presence of oxygen-rich groups (such as $-\text{C} - \text{O}$ and $-\text{COO}$) present in both chitosan and PLA (due to PLA's polymer chain ends), and 3) the smaller ionic radius of Cr^{6+} , which generated greater removal compared to other divalent ions. This conclusion was obtained from two complementary analyses.

4. Conclusions

The electrospinning method was employed to produce poly(lactic acid) (PLA) membranes with the addition of chitosan (CS), evaluating the effect of chitosan addition on their intrinsic properties of these electrospun membranes, their application as adsorptive membranes, and the possible removal mechanism to capture metal ion. The membranes exhibited distinct surface characteristics, including a smoother texture when in direct contact with the smooth surface of the collector, and a rougher texture on the opposite side. Structurally, the addition of CS into PLA matrix decreased the average fiber diameter, covering values around 38.80 % and 77.93 % and the average pore diameter also decreased, presenting a decline of 14.72 % and 54.12 % for PLA CS 90–10 and PLA CS 80–20, respectively. Besides, the porosity of membranes containing chitosan decreased slightly. It was demonstrated that the addition of chitosan resulted in a decrease in fiber diameter and porosity of the membranes. The water contact angle of the membranes exhibited distinct behaviors. The smoother surface demonstrated hydrophilic characteristics with values ranging from 70 to 78°, whereas the rougher surface exhibited hydrophobic behavior with values ranging from 99 to 114°. It was demonstrated that the increase in chitosan content had a minimal effect on the contact angle of the membranes. However, comparing PLA and PLA containing CS, aspects of membranes such as average diameter, pore diameter distribution and structural form affected the wettability. Besides, the incorporation of CS generated a drastic higher elastic modulus and tensile strength at break and lower strain than neat PLA membrane. It was due to the reduction of fiber and pore diameter, that provided more resistance of the membranes. In addition, these mechanical properties increased with the increase of the chitosan content. If evaluated the tension direction, the elastic modulus and tensile strength at break increased in the fiber alignment direction compared to transversal direction. This behavior is generally attributed to many fibrous systems whose secondary interaction forces among the chemical groups in the fibers surface, mainly hydrogen bonds, increase the tension necessary to break the chains.

In the adsorption aspect, the adsorption efficiency of the membranes was evaluated in pH 4. The membranes demonstrated removal efficiency



Fig. 7. Illustrative scheme of the proposed adsorption mechanism from PLA membrane containing CS.

values ranging from 5 to 17 % for Cd^{2+} , Cu^{2+} , Zn^{2+} , Mn^{2+} , and Ni^{2+} . On the other hand, the affinity of the metal ions according to the increase of Cs followed as $\text{Cd}^{2+} \equiv \text{Cu}^{2+} \equiv \text{Zn}^{2+} > \text{Mn}^{2+} \equiv \text{Ni}^{2+}$. Possibly, divalent ions had the great affinity with polymer PLA chain ends, more especially, by the interaction of $-\text{OH}$ and $-\text{COOH}$ functional groups of PLA. Notably, the membranes with chitosan exhibited high removal efficiency for Cr^{6+} , with values ranging from 38 % for the pure PLA membrane to 96 % for the PLA CS 90–10 and 99 % for the PLA CS 80–20 membranes. This high adsorption efficiency of Cr^{6+} can be evidenced by the presence of chromium content of 0.38 % wt., seen by SEM-EDS. Besides, as Cr^{6+} has the lowest ionic radius than other metals studied, its interaction of membrane 1s surface is favored. The XPS analysis revealed that no statistically significant differences were observed in terms of chemical composition on the rough or smooth surfaces of the membranes prior to adsorption. After adsorption, nitrogen concentration disappeared due to possible interaction of the metal ions with amino groups. Concomitantly, a reduction in the O3 peak and an increase in the O4 peak were observed. These changes were attributed to the strong interaction between oxygen-rich functional groups present in the chitosan and Cr^{6+} . These results indicate that the PLA CS electrospun membranes have a high potential to be used as an adsorptive membrane for Cr^{6+} in specific condition of the pH 4 in the aqueous media.

Future works to enhance PLA chitosan electrospun membranes should focus on optimizing functional groups to improve selectivity, incorporating additional materials to enhance mechanical and adsorption properties, and expanding performance studies under diverse pH and environmental conditions. Lastly a comprehensive lifecycle assessment will ensure these membranes are sustainable and economically viable for large-scale applications.

CRedit authorship contribution statement

Henrique Borba Modolon: Writing – review & editing, Writing – original draft, Validation, Supervision, Resources, Project administration, Methodology, Investigation, Funding acquisition, Formal analysis, Data curation, Conceptualization. **Luyza Bortolotto Teixeira:** Writing – original draft, Methodology, Formal analysis, Conceptualization. **Luciana Prazeres Mazur:** Methodology, Formal analysis. **Pedro Henrique Santos:** Methodology, Formal analysis. **Paulo Henrique Camani:** Writing – original draft, Methodology, Formal analysis. **Lucia Helena**

Innocentini Mei: Writing – original draft, Methodology, Formal analysis. **Tiago Bender Wermuth:** Writing – original draft, Methodology, Investigation. **Oscar Rubem Klegues Montedo:** Writing – original draft, Formal analysis. **Matheus V.G. Zimmermann:** Writing – original draft, Formal analysis. **Sabrina Arcaro:** Writing – review & editing, Writing – original draft, Validation, Supervision, Resources, Project administration, Methodology, Investigation, Funding acquisition, Formal analysis, Data curation, Conceptualization. **Derval dos Santos Rosa:** Writing – review & editing, Writing – original draft, Validation, Supervision, Resources, Project administration, Methodology, Investigation, Funding acquisition, Formal analysis, Data curation, Conceptualization.

Declaration of competing interest

The authors declare that they have no known competing financial interests or personal relationships that could have appeared to influence the work reported in this paper.

Acknowledgments

This study was financed by the São Paulo Research Foundation (FAPESP), Project number 2020/13703-3 and Coordenação de Aperfeiçoamento de Pessoal de Nível Superior (CAPES) – Projeto CAPES-Epidemias, Process number 88887.715335/2022-00. The authors thank the BIOMAT-UNICAMP, UFABC and CerTec-UNESC. The also authors acknowledge FAPESP and CAPES for the scholarships (L.P. Mazur: 2022/06829-6, P.H. Santos: 88887.715335/2022-00, P. H. Camani: 2023/11229-0).

Appendix A. Supplementary data

Supplementary data to this article can be found online at <https://doi.org/10.1016/j.ijbiomac.2024.139435>.

References

- [1] K. Ravindra, N. Vig, K. Chhoden, R. Singh, K. Kishor, N.S. Maurya, S. Narayan, S. Mor, Impact of massive flood on drinking water quality and community health risk assessment in Patna, Bihar, India, *Sustain. Water Resour. Manag.* 10 (2024) 104, <https://doi.org/10.1007/s40899-024-01052-z>.

- [2] A.K.S. Macêdo, T. de C.M. de Oliveira, L.S. Brighenti, H.B. dos Santos, R.G. Thomé, Socio-environmental impacts on the Doce River basin, Brazil: a review from historic pollution to large disaster events, *Int. J. Environ. Sci. Technol.* 21 (2024) 2339–2356, <https://doi.org/10.1007/s13762-023-05350-5>.
- [3] R. Parui, G.S. Nongthombam, M. Hossain, L.R. Adil, R. Gogoi, S. Bhowmik, D. Barman, P.K. Iyer, Impact of heavy metals on human health, in: *Remediation of Heavy Metals*, Wiley, 2024, pp. 47–81, <https://doi.org/10.1002/9781119853589.ch4>.
- [4] Md.M. Islam, A.A. Mohana, Md.A. Rahman, M. Rahman, R. Naidu, M.M. Rahman, A comprehensive review of the current progress of chromium removal methods from aqueous solution, *Toxics* 11 (2023) 252, <https://doi.org/10.3390/toxics11030252>.
- [5] D. Chauhan, A. Kumar, S.G. Warkar, An efficient adsorbent for the removal of Zn²⁺ + Cd²⁺ and Hg²⁺ from the real industrial effluents, *International Journal of Environmental Science and Technology* 19 (2022) 1483–1494, <https://doi.org/10.1007/s13762-021-03615-5>.
- [6] Noelle C. Zanini, Rennan F.S. Barbosa, Alana G. de Souza, Rafaela R. Ferreira, Paulo H. Camani, Sueli A. Oliveira, Daniella R. Mulinari, Derval S. Rosa, Enhancing the Cu (II) removal in water using functional hybrid membranes, *Sustainable Chemical Engineering* 299–319 (2024), <https://doi.org/10.37256/sce.5220244351>.
- [7] P.H. Camani, C.D. Midhun Dominic, D.F. Parra, H.F. Maltez, D.S. Rosa, Divalent metal ion removal from simulated water using sustainable starch aerogels: effect of crosslinking agent concentration and sorption conditions, *Int. J. Biol. Macromol.* 226 (2023), <https://doi.org/10.1016/j.ijbiomac.2022.11.308>.
- [8] S. Kim, S.-N. Nam, A. Jang, M. Jang, C.M. Park, A. Son, N. Her, J. Heo, Y. Yoon, Review of adsorption–membrane hybrid systems for water and wastewater treatment, *Chemosphere* 286 (2022) 131916, <https://doi.org/10.1016/j.chemosphere.2021.131916>.
- [9] G. Crini, E. Lichtfouse, L.D. Wilson, N. Morin-Crini, Conventional and non-conventional adsorbents for wastewater treatment, *Environ. Chem. Lett.* 17 (2019) 195–213, <https://doi.org/10.1007/s10311-018-0786-8>.
- [10] M. Ahmad, J. Wang, J. Xu, Q. Zhang, B. Zhang, Magnetic tubular carbon nanofibers as efficient Cu(II) ion adsorbent from wastewater, *J. Clean. Prod.* 252 (2020) 119825, <https://doi.org/10.1016/j.jclepro.2019.119825>.
- [11] F. Chen, S. Guo, Y. Wang, L. Ma, B. Li, Z. Song, L. Huang, W. Zhang, Concurrent adsorption and reduction of chromium(VI) to chromium(III) using nitrogen-doped porous carbon adsorbent derived from loofah sponge, *Front. Environ. Sci. Eng.* 16 (2022) 57, <https://doi.org/10.1007/s11783-021-1491-6>.
- [12] N.A.A. Qasem, R.H. Mohammed, D.U. Lawal, Removal of heavy metal ions from wastewater: a comprehensive and critical review, *NPJ Clean Water* 4 (2021) 36, <https://doi.org/10.1038/s41545-021-00127-0>.
- [13] Bruno de Oliveira, M. Silva, T. Barcelos da Costa, P.H. Camani, D. dos Santos Rosa, Chitosan-based foam composites for hexavalent chromium remediation: effect of microcellulose and crosslinking agent content, *Int. J. Biol. Macromol.* 264 (2024) 130446, <https://doi.org/10.1016/j.ijbiomac.2024.130446>.
- [14] N. More, M. Avhad, S. Utekar, A. More, Poly(lactic acid) (PLA) membrane—significance, synthesis, and applications: a review, *Polym. Bull.* 80 (2023) 1117–1153, <https://doi.org/10.1007/s00289-022-04135-z>.
- [15] S. Banehali, H. Sanaeepur, A. Ebadi Amooghini, S. Shirazian, S. Ramakrishna, Biodegradable polymers for membrane separation, *Sep. Purif. Technol.* 269 (2021) 118731, <https://doi.org/10.1016/j.seppur.2021.118731>.
- [16] M.S. Thomas, P.K.S. Pillai, M. Faria, N. Cordeiro, H. Barud, S. Thomas, L.A. Pothén, Electrospun poly(lactic acid)-chitosan composite: a bio-based alternative for inorganic composites for advanced application, *J. Mater. Sci. Mater. Med.* 29 (2018) 1–12, <https://doi.org/10.1007/S10856-018-6146-1/FIGURES/9>.
- [17] Y. Cai, M. Fang, X. Tan, B. Hu, X. Wang, Highly efficient selective elimination of heavy metals from solutions by different strategies, *Sep. Purif. Technol.* 350 (2024) 127975, <https://doi.org/10.1016/j.seppur.2024.127975>.
- [18] L. Nassar, H.M. Hegab, H. Khalil, V.S. Wadi, V. Naddeo, F. Banat, S.W. Hasan, Development of green poly(lactic acid) asymmetric ultrafiltration membranes for nutrient removal, *Sci. Total Environ.* 824 (2022) 153869, <https://doi.org/10.1016/j.scitotenv.2022.153869>.
- [19] K. He, J. Tang, H. Weng, G. Chen, Z. Wu, M. Lin, Efficient extraction of precious metal ions by a membrane emulsification circulation extractor, *Sep. Purif. Technol.* 213 (2019) 93–100, <https://doi.org/10.1016/j.seppur.2018.12.024>.
- [20] B.-S. Liaw, T.-T. Chang, H.-K. Chang, W.-K. Liu, P.-Y. Chen, Fish scale-extracted hydroxyapatite/chitosan composite scaffolds fabricated by freeze casting—An innovative strategy for water treatment, *J. Hazard. Mater.* 382 (2020) 121082, <https://doi.org/10.1016/j.jhazmat.2019.121082>.
- [21] L. Prazeres Mazur, R. Reis Ferreira, R. Felix da Silva Barbosa, P. Henrique Santos, T. Barcelos da Costa, M. Gurgel Adeodato Vieira, A. da Silva, D. dos Santos Rosa, L. Helena Innocentini Mei, Development of novel biopolymer membranes by electrospinning as potential adsorbents for toxic metal ions removal from aqueous solution, *J. Mol. Liq.* 395 (2024) 123782, <https://doi.org/10.1016/j.molliq.2023.123782>.
- [22] K.C. de Castro, J.M. Costa, L.H.I. Mei, Advances in electrospinning technique in the manufacturing process of nanofibrous materials, in: *Electrospun Materials and Their Allied Applications*, Wiley, 2020, pp. 379–399, <https://doi.org/10.1002/9781119655039.ch13>.
- [23] L. Wei, Electrospinning Theory, in: *Electrospinning*, Wiley, 2024, pp. 1–13, <https://doi.org/10.1002/9783527841479.ch1>.
- [24] E. Antaby, K. Klinkhammer, L. Sabantina, Electrospinning of chitosan for antibacterial applications—current trends, *Appl. Sci.* 11 (2021) 11937, <https://doi.org/10.3390/app112411937>.
- [25] C. Cui, S. Sun, S. Wu, S. Chen, J. Ma, F. Zhou, Electrospun chitosan nanofibers for wound healing application, *Engineered Regeneration* 2 (2021) 82–90, <https://doi.org/10.1016/j.engreg.2021.08.001>.
- [26] R.R. Gadhari, S.W. Ali, A. Das, R. Alagirusamy, Silver nanowires embedded chitosan/poly-lactic acid electrospun nanocomposite web based nanofibrous multifunctional membrane for safe water purification, *Adv. Sustain. Syst.* 6 (2022), <https://doi.org/10.1002/adsu.202100360>.
- [27] Y. Ren, L. Mei, Y. Gu, N. Zhao, Y. Wang, R. Fan, A. Tong, H. Chen, H. Yang, B. Han, G. Guo, Stereocomplex crystallite-based eco-friendly nanofiber membranes for removal of Cr(VI) and antibacterial effects, *ACS Sustain. Chem. Eng.* 7 (2019) 16072–16083, <https://doi.org/10.1021/acssuschemeng.9b02828>.
- [28] Q. Zia, M. Tabassum, J. Meng, Z. Xin, H. Gong, J. Li, Polydopamine-assisted grafting of chitosan on porous poly(L-lactic acid) electrospun membranes for adsorption of heavy metal ions, *Int. J. Biol. Macromol.* 167 (2021) 1479–1490, <https://doi.org/10.1016/j.ijbiomac.2020.11.101>.
- [29] Z. Li, T. Li, L. An, P. Fu, C. Gao, Z. Zhang, Highly efficient chromium(VI) adsorption with nanofibrous filter paper prepared through electrospinning chitosan/poly(methylmethacrylate) composite, *Carbohydr. Polym.* 137 (2016) 119–126, <https://doi.org/10.1016/j.carbpol.2015.10.059>.
- [30] P. Wang, L. Wang, S. Dong, G. Zhang, X. Shi, C. Xiang, L. Li, Adsorption of hexavalent chromium by novel chitosan/poly(ethylene oxide)/permuit electrospun nanofibers, *New J. Chem.* 42 (2018) 17740–17749, <https://doi.org/10.1039/C8NJ03899F>.
- [31] J. Xiong, Q. Hu, J. Wu, Z. Jia, S. Ge, Y. Cao, J. Zhou, Y. Wang, J. Yan, L. Xie, X. Chai, L. Zhang, G. Du, S. Wang, K. Xu, Structurally stable electrospun nanofibrous cellulose acetate/chitosan biocomposite membranes for the removal of chromium ions from the polluted water, *Adv. Compos. Hybrid Mater.* 6 (2023) 99, <https://doi.org/10.1007/s42114-023-00680-x>.
- [32] T.B. da Costa, T.L. da Silva, M.G.C. da Silva, M.G.A. Vieira, Biosorption of europium and erbium from aqueous solutions using crosslinked sericin-alginate beads, *Environ. Sci. Pollut. Res.* (2023), <https://doi.org/10.1007/s11356-023-31427-2>.
- [33] M.S. Thomas, P.K.S. Pillai, M. Faria, N. Cordeiro, L. Kailas, N. Kalarikkal, S. Thomas, L.A. Pothén, Poly(lactic acid)/nano chitosan composite fibers and their morphological, physical characterization for the removal of cadmium(II) from water, *J. Appl. Polym. Sci.* 137 (2020), <https://doi.org/10.1002/app.48993>.
- [34] C. Huang, N.L. Thomas, Fabricating porous poly(lactic acid) fibres via electrospinning, *Eur. Polym. J.* 99 (2018) 464–476, <https://doi.org/10.1016/j.eurpolymj.2017.12.025>.
- [35] C.L. Casper, J.S. Stephens, N.G. Tassi, D.B. Chase, J.F. Rabolt, Controlling surface morphology of electrospun polystyrene fibers: effect of humidity and molecular weight in the electrospinning process, *Macromolecules* 37 (2004) 573–578, <https://doi.org/10.1021/ma0351975>.
- [36] M.S. Islam, B.C. Ang, A. Andriyana, A.M. Affi, A review on fabrication of nanofibers via electrospinning and their applications, *SN Appl. Sci.* 1 (2019) 1248, <https://doi.org/10.1007/s42452-019-1288-4>.
- [37] M.S. Thomas, P.K.S. Pillai, M. Faria, N. Cordeiro, H. Barud, S. Thomas, L.A. Pothén, Electrospun poly(lactic acid)-chitosan composite: a bio-based alternative for inorganic composites for advanced application, *J. Mater. Sci. Mater. Med.* 29 (2018) 1–12, <https://doi.org/10.1007/S10856-018-6146-1/FIGURES/9>.
- [38] X. Gu, R. Cao, Y. Li, S. Liu, Z. Wang, S. Feng, F. Li, S. Lyu, Three-component antibacterial membrane of poly(butylene carbonate), poly(lactic acid) and chitosan prepared by electrospinning, *Mater. Technol.* 34 (2019) 463–470, <https://doi.org/10.1080/10667857.2019.1576822>.
- [39] M.S. Thomas, P.K.S. Pillai, M. Faria, N. Cordeiro, L. Kailas, N. Kalarikkal, S. Thomas, L.A. Pothén, Poly(lactic acid)/nano chitosan composite fibers and their morphological, physical characterization for the removal of cadmium(II) from water, *J. Appl. Polym. Sci.* 137 (2020), <https://doi.org/10.1002/app.48993>.
- [40] H.T. Au, L.N. Pham, T.H.T. Vu, J.S. Park, Fabrication of an antibacterial non-woven mat of poly(lactic acid)/chitosan blend by electrospinning, *Macromol. Res.* 20 (2012) 51–58, <https://doi.org/10.1007/s13233-012-0010-9>.
- [41] D. Bahati, M. Bricha, A. Semlali, K. El Mabrouk, Preparation and characterization of poly(lactic acid)-chitosan blend fibrous electrospun membrane loaded with bioactive glass nanoparticles for guided bone/tissue regeneration, *Mater. Chem. Phys.* 323 (2024) 129637, <https://doi.org/10.1016/j.matchemphys.2024.129637>.
- [42] Y. Li, F. Chen, J. Nie, D. Yang, Electrospun poly(lactic acid)/chitosan core-shell structure nanofibers from homogeneous solution, *Carbohydr. Polym.* 90 (2012) 1445–1451, <https://doi.org/10.1016/j.carbpol.2012.07.013>.
- [43] T.T.T. Nguyen, O.H. Chung, J.S. Park, Coaxial electrospun poly(lactic acid)/chitosan (core/shell) composite nanofibers and their antibacterial activity, *Carbohydr. Polym.* 86 (2011) 1799–1806, <https://doi.org/10.1016/j.carbpol.2011.07.014>.
- [44] G. Lawrie, I. Keen, B. Drew, A. Chandler-Temple, L. Rintoul, P. Fredericks, L. Gröndahl, Interactions between alginate and chitosan biopolymers characterized using FTIR and XPS, *Biomacromolecules* 8 (2007) 2533–2541, <https://doi.org/10.1021/BM070014Y/ASSET/IMAGES/LARGE/BM070014YF00009.JPEG>.
- [45] M.B. de O. Silva, S.A. de Oliveira, D. dos S. Rosa, Comparative study on microwave-assisted and conventional chitosan production from shrimp shell: process optimization, characterization, and environmental impacts, *J. Clean. Prod.* 440 (2024) 140726, <https://doi.org/10.1016/j.jclepro.2024.140726>.
- [46] R. Grande, A.J.F. Carvalho, Compatible ternary blends of chitosan/poly(vinyl alcohol)/poly(lactic acid) produced by oil-in-water emulsion processing, *Biomacromolecules* 12 (2011) 907–914, https://doi.org/10.1021/BM101227Q/ASSET/IMAGES/LARGE/BM-2010-011227Q_0011.JPEG.
- [47] M.I. Shariful, S. Bin Sharif, J.J.L. Lee, U. Habiba, B.C. Ang, M.A. Amalina, Adsorption of divalent heavy metal ion by mesoporous-high surface area chitosan/

- poly (ethylene oxide) nanofibrous membrane, *Carbohydr. Polym.* 157 (2017) 57–64, <https://doi.org/10.1016/j.carbpol.2016.09.063>.
- [48] P.A.L. Campini, É.R. de Oliveira, P.H. Camani, C.G. da Silva, E.D.C. Yudice, S.A. de Oliveira, D. dos S. Rosa, Assessing the efficiency of essential oil and active compounds/poly (lactic acid) microcapsules against common foodborne pathogens, *Int. J. Biol. Macromol.* 186 (2021) 702–713, <https://doi.org/10.1016/j.ijbiomac.2021.07.071>.
- [49] M.Z.I. Mollah, N. Akter, F.B. Quader, S. Sultana, R.A. Khan, Biodegradable colour polymeric film (starch-chitosan) development: characterization for packaging materials, *Open Journal of Organic Polymer Materials* 06 (2016) 11–24, <https://doi.org/10.4236/ojopm.2016.61002>.
- [50] I. Mutmainna, D. Tahir, P. Lobo Gareso, S. Ilyas, Synthesis composite starch-chitosan as biodegradable plastic for food packaging, *J. Phys. Conf. Ser.* 1317 (2019) 012053, <https://doi.org/10.1088/1742-6596/1317/1/012053>.
- [51] L. Gao, T. Zhu, F. He, Z. Ou, J. Xu, L. Ren, Preparation and characterization of functional films based on chitosan and corn starch incorporated tea polyphenols, *Coatings* 11 (2021) 817, <https://doi.org/10.3390/coatings11070817>.
- [52] Y. Wu, Y. Ma, Y. Gao, Y. Liu, C. Gao, Poly (lactic acid)-based pH responsive membrane combined with chitosan and alizarin for food packaging, *Int. J. Biol. Macromol.* 214 (2022) 348–359, <https://doi.org/10.1016/j.ijbiomac.2022.06.039>.
- [53] W. Tighzert, A. Habi, A. Aji, T. Sadoun, F.B.-O. Daoud, Fabrication and characterization of nanofibers based on poly(lactic acid)/chitosan blends by electrospinning and their functionalization with phospholipase A1, *Fibers and Polymers* 18 (2017) 514–524, <https://doi.org/10.1007/s12221-017-6953-x>.
- [54] F. Liu, B. Li, D. Sun, F. Li, X. Pei, The effect of chitosan (CS) coagulation bath on structure and performance of polylactic acid (PLA) microfiltration membrane, *Korean J. Chem. Eng.* 39 (2022) 1307–1315, <https://doi.org/10.1007/s11814-021-0992-0>.
- [55] J. Bae, H. Kim, K.S. Kim, H. Choi, Effect of asymmetric wettability in nanofiber membrane by electrospinning technique on separation of oil/water emulsion, *Chemosphere* 204 (2018) 235–242, <https://doi.org/10.1016/j.chemosphere.2018.04.003>.
- [56] B. Machado, S. Roberto, E. Bonafé, S. Camargo, C. Camargo, K. Popat, M. Kipper, A. Martins, Chitosan imparts better biological properties for poly(ϵ -caprolactone) electrospun membranes than dexamethasone, *J. Braz. Chem. Soc.* (2019), <https://doi.org/10.21577/0103-5053.20190077>.
- [57] R. Ghafari, R. Scaffaro, A. Maio, E.F. Gulino, G. Lo Re, M. Jonoobi, Processing-structure-property relationships of electrospun PLA-PEO membranes reinforced with enzymatic cellulose nanofibers, *Polym. Test.* 81 (2020) 106182, <https://doi.org/10.1016/j.polymertesting.2019.106182>.
- [58] S. Kasirajan, D. Umaphathy, C. Chandrasekar, V. Aafrin, M. Jenitapeter, L. Udhayasoorian, A.S.B. Packirisamy, S. Muthusamy, Preparation of poly(lactic acid) from *Prosopis juliflora* and incorporation of chitosan for packaging applications, *J. Biosci. Bioeng.* 128 (2019) 323–331, <https://doi.org/10.1016/j.jbiosc.2019.02.013>.
- [59] M. Momtaz, E. Momtaz, M.A. Mehrgardi, F. Momtaz, T. Narimani, F. Poursina, Preparation and characterization of gelatin/chitosan nanocomposite reinforced by NiO nanoparticles as an active food packaging, *Sci. Rep.* 14 (2024) 519, <https://doi.org/10.1038/s41598-023-50260-8>.
- [60] H. Zhang, Q. Zhen, Y. Cao, Y. Gan, Z. Yang, X. Qian, Soft, strong, and breathable poly(lactic acid)/poly(ethylene glycol) microfibrillar membranes with a fluffy alignment structure for skin contactor, *Text. Res. J.* 93 (2023) 4372–4382, <https://doi.org/10.1177/00405175231173156>.
- [61] M. Agostini de Moraes, D.S. Coceniza, F. da Cruz Vasconcellos, L.F. Fraceto, M. M. Beppu, Chitosan and alginate biopolymer membranes for remediation of contaminated water with herbicides, *J. Environ. Manage.* 131 (2013) 222–227, <https://doi.org/10.1016/j.jenvman.2013.09.028>.
- [62] D. Yang, L. Li, B. Chen, S. Shi, J. Nie, G. Ma, Functionalized chitosan electrospun nanofiber membranes for heavy-metal removal, *Polymer (Guildf)* 163 (2019) 74–85, <https://doi.org/10.1016/j.polymer.2018.12.046>.
- [63] B. Kost, M. Basko, M. Bednarek, M. Socka, B. Kopka, G. Łapienis, T. Biela, P. Kubisa, M. Brzeziński, The influence of the functional end groups on the properties of polylactide-based materials, *Prog. Polym. Sci.* 130 (2022) 101556, <https://doi.org/10.1016/j.progpolymsci.2022.101556>.
- [64] M.R. Karim, M.O. Ajiaz, N.H. Alharth, H.F. Alharbi, F.S. Al-Mubaddel, M.R. Awual, Composite nanofibers membranes of poly(vinyl alcohol)/chitosan for selective lead (II) and cadmium(II) ions removal from wastewater, *Ecotoxicol. Environ. Saf.* 169 (2019) 479–486, <https://doi.org/10.1016/j.ecoenv.2018.11.049>.
- [65] L.P. Mazur, M.A.P. Cechinel, S.M.A.G.U. de Souza, R.A.R. Boaventura, V.J.P. Vilar, Brown marine macroalgae as natural cation exchangers for toxic metal removal from industrial wastewaters: a review, *J. Environ. Manage.* 223 (2018) 215–253, <https://doi.org/10.1016/j.jenvman.2018.05.086>.
- [66] A. Refaat Alawady, A. Ali Alshahrani, T. Ali Aouak, N. Mohamed Alandis, Polysulfone membranes with CNTs/chitosan biopolymer nanocomposite as selective layer for remarkable heavy metal ions rejection capacity, *Chem. Eng. J.* 388 (2020) 124267, <https://doi.org/10.1016/j.cej.2020.124267>.
- [67] N. Sahebamee, M. Soltanieh, S.M. Mousavi, A. Heydarinasab, Removal of Cu²⁺, Cd²⁺ and Ni²⁺ ions from aqueous solution using a novel chitosan/poly(vinyl alcohol) adsorptive membrane, *Carbohydr. Polym.* 210 (2019) 264–273, <https://doi.org/10.1016/j.carbpol.2019.01.074>.
- [68] Q.H. Li, M. Dong, R. Li, Y.Q. Cui, G.X. Xie, X.X. Wang, Y.Z. Long, Enhancement of Cr(VI) removal efficiency via adsorption/photocatalysis synergy using electrospun chitosan/g-C₃N₄/TiO₂ nanofibers, *Carbohydr. Polym.* 253 (2021) 117200, <https://doi.org/10.1016/j.carbpol.2020.117200>.
- [69] L. Ma, X. Shi, X. Zhang, S. Dong, L. Li, Electrospun Cellulose Acetate-Polycaprolactone/Chitosan Core-Shell Nanofibers for the Removal of Cr (VI), *Phys. Status Solidi A* 216 (2019) 1900379, <https://doi.org/10.1002/PSSA.201900379>.
- [70] R.E.K. Billah, M.A. Khan, Y.-K. Park, A. AM, H. Majdoubi, Y. Haddaji, B.-H. Jeon, A comparative study on hexavalent chromium adsorption onto chitosan and chitosan-based composites, *Polymers (Basel)* 13 (2021) 3427, <https://doi.org/10.3390/polym13193427>.
- [71] S. Zhang, Y. Zhang, L. Fu, M. Jing, A chitosan fiber as green material for removing Cr(VI) ions and Cu(II) ions pollutants, *Scientific Reports* (2021) 1–9, <https://doi.org/10.1038/s41598-021-02399-5>, 2021 11:1 11.
- [72] A.M. Mohammed, M.R. Thalji, S.A. Yasin, J.J. Shim, K.F. Chong, A.A. Guda, G.A. M. Ali, Recent advances in electrospun fibrous membranes for effective chromium (VI) removal from water, *J. Mol. Liq.* 383 (2023) 122110, <https://doi.org/10.1016/j.molliq.2023.122110>.
- [73] L.P. Mazur, T.A. Pozdniakova, D.A. Mayer, S.M.A.G.U. de Souza, R.A. R. Boaventura, V.J.P. Vilar, Cation exchange prediction model for copper binding onto raw brown marine macro-algae *Ascophyllum nodosum*: batch and fixed-bed studies, *Chem. Eng. J.* 316 (2017) 255–276, <https://doi.org/10.1016/j.cej.2017.01.080>.
- [74] L. Li, Y. Li, L. Cao, C. Yang, Enhanced chromium (VI) adsorption using nanosized chitosan fibers tailored by electrospinning, *Carbohydr. Polym.* 125 (2015) 206–213, <https://doi.org/10.1016/j.carbpol.2015.02.037>.
- [75] P.N. Gamaletos, A. Godelitsas, T. Kasama, A. Kuzmin, M. Lagos, T.J. Mertzimekis, J. Göttlicher, R. Steininger, S. Xanthos, Y. Pontikes, G.N. Angelopoulos, C. Zarkadas, A. Komelkov, E. Tzamos, A. Filippidis, The role of nano-perovskite in the negligible thorium release in seawater from Greek bauxite residue (red mud), *Sci. Rep.* 6 (2016) 21737, <https://doi.org/10.1038/srep21737>.
- [76] V.C. Saha, M.M.A. Sabuj, P. Shams, S. Rahman, M.R. Qadir, M.R. Islam, F. Gulshan, Synthesis and characterization of reduced graphene oxide reinforced polymer matrix composite, *IOP Conf. Ser. Mater. Sci. Eng.* 438 (2018) 012008, <https://doi.org/10.1088/1757-899X/438/1/012008>.
- [77] Q. Kong, B. Xie, S. Preis, Y. Hu, H. Wu, C. Wei, Adsorption of Cd²⁺ by an ion-imprinted thiol-functionalized polymer in competition with heavy metal ions and organic acids, *RSC Adv.* 8 (2018) 8950–8960, <https://doi.org/10.1039/C7RA11811B>.
- [78] L. Chen, C. Wang, S. Liu, L. Zhu, Investigation of adsorption/desorption behavior of Cr(VI) at the presence of inorganic and organic substance in membrane capacitive deionization (MCDI), *J. Environ. Sci.* 78 (2019) 303–314, <https://doi.org/10.1016/j.jes.2018.11.005>.
- [79] X.-L. Chen, F. Li, X.J. Xie, Z. Li, L. Chen, Nanoscale zero-valent iron and chitosan functionalized *Eichhornia crassipes* biochar for efficient hexavalent chromium removal, *Int. J. Environ. Res. Public Health* 16 (2019) 3046, <https://doi.org/10.3390/ijerph16173046>.
- [80] A.B.V. de Farias, T.B. da Costa, M.G.C. da Silva, M.G.A. Vieira, Cerium biosorption onto alginate/vermiculite-based particles functionalized with ionic imprinting: kinetics, equilibrium, thermodynamic, and reuse studies, *Int. J. Biol. Macromol.* 241 (2023) 124542, <https://doi.org/10.1016/j.ijbiomac.2023.124542>.
- [81] X. Feng, R. Long, L. Wang, C. Liu, Z. Bai, X. Liu, A review on heavy metal ions adsorption from water by layered double hydroxide and its composites, *Sep. Purif. Technol.* 284 (2022) 120099, <https://doi.org/10.1016/j.seppur.2021.120099>.
- [82] U. Zulfikar, F.U. Haider, M. Ahmad, S. Hussain, M.F. Maqsood, M. Ishaq, B. Shahzad, M.M. Waqas, B. Ali, M.N. Tayyab, S.A. Ahmad, I. Khan, S.M. Eldin, Chromium toxicity, speciation, and remediation strategies in soil-plant interface: a critical review, *Front. Plant Sci.* 13 (2023), <https://doi.org/10.3389/fpls.2022.1081624>.
- [83] D.J. da Silva, R.R. Ferreira, G. Da S. Ferreira, R.F.S. Barbosa, J.S. Marciano, P. H. Camani, A.G. Souza, D.S. Rosa, Multifunctional cotton fabrics with novel antibacterial coatings based on chitosan nanocapsules and polyacrylate, *J. Coat. Technol. Res.* 20 (2023) 1541–1555, <https://doi.org/10.1007/s11998-023-00761-y>.
- [84] A.S. Gorzalski, C. Donley, O. Coronell, Elemental composition of membrane foulant layers using EDS, XPS, and RBS, *J. Memb. Sci.* 522 (2017) 31–44, <https://doi.org/10.1016/j.memsci.2016.08.055>.
- [85] X. Wei, S. Chen, J. Rong, Z. Sui, S. Wang, Y. Lin, J. Xiao, D. Huang, Improving the Ca(II) adsorption of chitosan via physical and chemical modifications and characterizing the structures of the calcified complexes, *Polym. Test.* 98 (2021) 107192, <https://doi.org/10.1016/j.polymertesting.2021.107192>.
- [86] T.B. da Costa, T.L. da Silva, M.G.C. da Silva, M.G.A. Vieira, Selectivity of lanthanum and ytterbium in binary and multi-component system by modified sericin/alginate/poly (vinyl alcohol) adsorbent beads, *J. Environ. Chem. Eng.* 12 (2024) 112329, <https://doi.org/10.1016/j.jece.2024.112329>.
- [87] J. Geng, L. Lin, F. Gu, J. Chang, Adsorption of Cr(VI) and dyes by plant leaves: effect of extraction by ethanol, relationship with element contents and adsorption mechanism, *Ind. Crop. Prod.* 177 (2022) 114522, <https://doi.org/10.1016/j.indcrop.2022.114522>.
- [88] D. Qiu, Y. Geng, J. Geng, H. Du, J. Chang, Removal of dyes from wastewater using Eucalyptus wood fiber loaded nanoscale zero-valent iron: characterization and removal mechanism, *Int. J. Biol. Macromol.* 266 (2024) 131141, <https://doi.org/10.1016/j.ijbiomac.2024.131141>.
- [89] P.H. Camani, A.G. de Souza, D. dos S. Rosa, Electrostatic or steric stabilization of the cellulose nanostructures using different modifying agents, *Macromol. Symp.* 394 (2020), <https://doi.org/10.1002/masy.202000110>.
- [90] T.R. Gengenbach, G.H. Major, M.R. Linford, C.D. Easton, Practical guides for x-ray photoelectron spectroscopy (XPS): interpreting the carbon 1s spectrum, *J. Vac. Sci. Technol. A* 39 (2021), <https://doi.org/10.1116/6.0000682>.
- [91] C. Kalogirou, O. Höfft, A. Gödde, N. Papadimitriou, P.K. Pandis, C. Argiris, G. Sourkouni, Assessing the time dependence of AOPs on the surface properties of

- polylactic acid, *J. Polym. Environ.* 31 (2023) 345–357, <https://doi.org/10.1007/s10924-022-02608-w>.
- [92] A. Koterwa, I. Kaczmarzyk, S. Mania, M. Cieslik, R. Tylingo, T. Ossowski, R. Bogdanowicz, P. Niedziałkowski, J. Ryl, The role of electrolysis and enzymatic hydrolysis treatment in the enhancement of the electrochemical properties of 3D-printed carbon black/poly(lactic acid) structures, *Appl. Surf. Sci.* 574 (2022) 151587, <https://doi.org/10.1016/j.apsusc.2021.151587>.
- [93] L. Ribba, L. Tamayo, M. Flores, A. Riveros, M.J. Kogan, E. Cerda, S. Goyanes, Asymmetric biphasic hydrophobic/hydrophilic poly(lactic acid)–polyvinyl alcohol meshes with moisture control and noncytotoxic effects for wound dressing applications, *J. Appl. Polym. Sci.* 136 (2019), <https://doi.org/10.1002/app.47369>.
- [94] M. Kormunda, P. Ryšánek, O. Kylián, M. Benkocká, P. Čapková, Hydrophobisation of electrospun nanofiber membranes by plasma deposited CF coating, *Surfaces and Interfaces* 26 (2021) 101333, <https://doi.org/10.1016/j.surfin.2021.101333>.
- [95] P.C. Bandara, E.T. Nades, D.F. Rodrigues, Use of response surface methodology to develop and optimize the composition of a chitosan–polyethyleneimine–graphene oxide nanocomposite membrane coating to more effectively remove Cr(VI) and Cu (II) from water, *ACS Appl. Mater. Interfaces* 11 (2019) 17784–17795, <https://doi.org/10.1021/acsami.9b03601>.
- [96] J. Ouyang, Y. Wang, T. Li, L. Zhou, Z. Liu, Immobilization of carboxyl-modified multiwalled carbon nanotubes in chitosan-based composite membranes for U(VI) sorption, *J. Radioanal. Nucl. Chem.* 317 (2018) 1419–1428, <https://doi.org/10.1007/s10967-018-5993-z>.
- [97] Y. Liu, H. Shan, C. Zeng, H. Zhan, Y. Pang, Removal of Cr(VI) from wastewater using graphene oxide chitosan microspheres modified with α -FeO(OH), *Materials* 15 (2022) 4909, <https://doi.org/10.3390/ma15144909>.
- [98] L. Li, Q. Liao, B. Hou, C. He, J. Liu, B. Li, M. Yu, Y. Liu, B. Lai, B. Yang, Synchronous reduction and removal of hexavalent chromium from wastewater by modified magnetic chitosan beads, *Sep. Purif. Technol.* 304 (2023) 122363, <https://doi.org/10.1016/J.SEPPUR.2022.122363>.



Sustainable starch–microcellulose composite hydrogels for efficient removal of heavy metals from water

Talles B. da Costa^a, Paulo H. Camani^b, Rafaela R. Ferreira^a, Alana G. Souza^a,
Melissa G.A. Vieira^c, Derval dos S. Rosa^{a,*}

^a Center for Engineering, Modeling, and Applied Social Sciences, Federal University of ABC (UFABC), dos Estados Avenue, 09280-560 Santo André, Brazil

^b School of Chemical Engineering, Department of Materials Engineering and Bioprocess, University of Campinas (UNICAMP), Albert Einstein Avenue, 13083-852 Campinas, Brazil

^c School of Chemical Engineering, Department of Process and Products Design, University of Campinas (UNICAMP), Albert Einstein Avenue, 13083-852 Campinas, Brazil

ARTICLE INFO

Keywords:

Hydrogels
Cellulose microstructures
Sorption
Potentially toxic metals

ABSTRACT

This work investigates the development of sustainable composite hydrogels based on corn starch and microfibrillated cellulose (MFC) derived from eucalyptus sawdust for the removal of copper from aqueous environments. The incorporation of MFC into the starch matrix reduced solubility from 55.2 % to 36.4 %, increased true density from 1.466 to 1.525 g/cm³, and decreased surface area with increasing MFC content (from 4.010 to 1.814 m²/g). The MFC presented the following metallic affinity order: Cu²⁺ > Mn³⁺ > Ni²⁺ > Zn²⁺ > Cd²⁺ > Cr⁶⁺. Adsorption experiments showed enhanced Cu²⁺ removal with increasing MFC content, with the Starch/MFC-5 % hydrogel achieving a maximum removal efficiency of 52.4 % and sorption capacity of 0.258 mmol/g. Langmuir isotherms provided the best fit to the equilibrium data ($R^2 = 0.998$), and the Dubinin–Radushkevich analysis indicated a shift from physisorption ($E = 2.42$ kJ/mol) to chemisorption ($E = 8.11$ kJ/mol). Kinetics equilibrium time was reached between 480 and 780 min, with best description by pseudo second-order model. The reuse of hydrogel was achieved for up to four sorption/desorption cycles. The mechanisms of Cu²⁺ sorption involved interactions with the functional groups present on the materials and cation exchange. These results confirm that starch/MFC hydrogels are promising, low-cost, and biodegradable materials for the efficient removal of metal ions from contaminated water.

1. Introduction

Aquatic ecosystems are an essential part of the biosphere and evolve in harmony with chemical elements and the environment in a synergistic manner [1]. However, with the swift advancements in industry and human activities, inappropriate waste disposal can contaminate natural environments with toxic compounds, representing a serious threat to the balance of biota and the environment [2,3]. Worldwide, 1.7 million deaths happen each year linked to water contamination, raising significant environmental and public health concerns [4]. Besides, urban centers hold 55 % of the world's population, forecasting an increase to 68 % by 2050 (i.e., 9.9 billion people), whose uncontrolled population growth accelerates water contamination due to the demand for consumption [5–9].

Nickel (Ni), copper (Cu), chromium (Cr), manganese (Mn), cadmium (Cd), and zinc (Zn) are common metallic contaminants in industrial

waste from the processing, electroplating, alloys, and metallurgy, manufacturing of electronic components, and recycling of electronic waste, being capable of causing several serious toxicological effects to humans [1,10–13]. Considering the high industrial demand for these metals, the recovery of PTMs from secondary sources is an environmental and economic interest from the perspective of the circular economy, through the reuse of resources already extracted in a new production cycle [14,15]. Thus, due to the accumulation of PTMs in aquatic biota and their market demand, the development of efficient technologies for the removal and recovery of these metals from secondary sources has become increasingly important [16].

Several methods can be used to remediate water pollution, including oxidative treatment, ion exchange, precipitation, ultrafiltration membrane, and reverse osmosis [102,103]. Among the several available methodologies, sorption is considered more effective and low-cost for removing PTMs than other treatments due to the use of adsorbent

* Corresponding author.

E-mail address: derval.rosa@ufabc.edu.br (D.S. Rosa).

<https://doi.org/10.1016/j.ijbiomac.2025.144710>

Received 2 April 2025; Received in revised form 19 May 2025; Accepted 26 May 2025

Available online 28 May 2025

0141-8130/© 2025 Elsevier B.V. All rights are reserved, including those for text and data mining, AI training, and similar technologies.

materials with high adsorption capacity from renewable biomass sources, such as polysaccharides [17]. The sorbents market size was estimated at USD 5.90 billion in 2024, with expected growth to USD 6.10 billion in 2025 and USD 8.31 billion in 2034. Besides, there is a focus on the development of recycled or renewable materials for the sorbents. In this way, adsorbents can be produced from biomass waste (e.g., crustacean shells, wood, and other lignocellulosic waste), enabling reuse in a sustainable and economically viable way [18–20].

Hydrogels are a three-dimensional solid structure formed by highly porous cross-linked polymeric networks with a high specific surface area and hydrophilicity, with the ability to absorb large amounts of water [21–23]. Furthermore, its surface characteristics can be modified to control the diffusion process and sorption kinetics [24]. Hydrogels can be produced by natural macromolecules from natural biomass, presenting adequate stability, effectiveness, reusability, and biodegradability to act as an environmentally friendly adsorbent for removing PTMs in contaminated waters [25,26].

Among natural polymeric adsorbents, cellulose and starch are considered abundant, renewable, biodegradable, and low-cost polysaccharides [27,28]. A biopolymer's chemical structure presents different functional groups (e.g., hydroxyls, carboxyl, carbonyls) that guarantee the starch/cellulose hydrogel the ability to remove metal ions [29]. In fact, cellulose and starch-based materials have shown good sorption capacity for different PTMs and reuse after successive cycles [30–32]. For example, Tan et al. [105] developed a starch-composite magnetic material modified with polyethyleneimine for efficient removal of diclofenac sodium, methyl orange, Amaranth, and Cr^{6+} . Al-Aidy and Amdehab [106] reported on a starch-g-poly(acrylic acid) hydrogel that exhibited high adsorption capacities for malachite green. Pereira et al. [107] developed a lignin-functionalized starch hydrogel for the efficient removal of PTMs and dyes, achieving an adsorption capacity of 99.4 mg/g for methylene blue. Similarly, Costa et al. [108] reviewed recent advances in starch-based adsorbents for the removal of heavy metals and emerging pollutants, emphasizing the importance of chemical modifications to improve adsorption performance.

However, starch hydrogels for application in sorption/desorption have some disadvantages, such as low mechanical resistance, low thermal stability, and low stability in acidic media [33,34]. Furthermore, although starch hydrogels have hydroxyl groups, there is a need to enhance the sorption capacity of these materials for their effective application in the removal of different PTMs in contaminated water [35]. In this sense, the incorporation of micro/nanostructures into hydrogels can improve the properties of these materials and their sorption capacity [36–38]. However, as described by Ioelovich et al., using nanocellulose to prepare composite materials can show the high cost of production because nanostructures are advanced materials prepared by several steps with high cost. Comparing the benefit-cost, an estimative of \$17 per kg DM is used to extract cellulose nanofibers (CNFs). Meanwhile, the CNCs production cost can reach \$30–40 per kg DM, covering costs such as the isolation, equipment depreciation, salary, overhead costs, and other costs. Thus, cellulose microfibrils (MFC) have an inferior cost and promising properties [39].

MFCs are cellulose structures available on the market, presenting a fibrous format with a micrometer-scale diameter, good surface area, excellent mechanical properties, and low production cost, in addition to being biocompatible and biodegradable [40–43]. A search conducted on the Web of Science platform in March 2025 using the keywords 'hydrogel,' 'starch,' 'cellulose,' 'removal,' and 'metal ion' retrieved 27 published papers. However, none of these studies explored the incorporation of MFC into starch-based hydrogels for metal ion removal. This gap highlights the innovative nature of our approach, which leverages a low-cost, sustainable material as an efficient adsorbent.

This study evaluates the efficiency of starch-based hydrogels reinforced with MFC derived from eucalyptus waste in treating water contaminated with potentially toxic metals (Cu^{2+} , Mn^{3+} , Ni^{2+} , Zn^{2+} , Cd^{2+} , and Cr^{6+}), with a particular focus on Cu^{2+} removal. The research

introduces an eco-friendly hydrogel formulation that incorporates MFCs upcycled from eucalyptus residues, reinforcing its role as a sustainable material for water treatment. Furthermore, the study examines how variations in MFC concentration influence both the sorption capacity and structural properties of the hydrogels. Despite its potential, the effect of MFC content on the availability of functional groups within starch hydrogels remains scarcely explored, making this investigation particularly relevant. In this context, the main novelty is the compatibilization of natural biopolymer with a MFC waste from eucalyptus sawdust, which is an approach that has still been underexplored to date.

2. Materials and methods

2.1. Materials

For microfibrillated cellulose (MFC) preparation, Eucalyptus wastes (*Eucalyptus citriodora*) were collected post-harvest and logging activities in Mato Grosso, Brazil. Sodium chlorite (NaClO_2 , 99 %) was purchased by Sigma-Aldrich (Brazil), and sodium hydroxide (NaOH , 95 %) and potassium hydroxide (KOH , 98 %) were purchased from Synth. The corn starch was kindly donated by Ingredion Company (São Paulo/Brazil) - Amisol 3408® containing 28 wt% amylose and 72 wt% amylopectin. Citric acid ($\text{C}_6\text{H}_8\text{O}_7$, 99.5 %), nitric acid (HNO_3 , 65 %), and sodium hydroxide (NaOH , 95 %) were acquired from Synth. Distilled water was used to prepare corn-starch hydrogels.

Zinc nitrate hexahydrate ($\text{Zn}(\text{NO}_3)_2 \cdot 6\text{H}_2\text{O}$, 98 %) and sodium hydroxide (NaOH , 98 %) were obtained from Dynamics Contemporary Chemistry (São Paulo, Brazil). Cadmium nitrate tetrahydrate ($\text{Cd}(\text{NO}_3)_2 \cdot 4\text{H}_2\text{O}$, 98 %) was acquired from Neon Chemistry (São Paulo, Brazil). Potassium dichromate ($\text{K}_2\text{Cr}_2\text{O}_7$, 99 %) was obtained from ECIBRA Analytical Reagents (São Paulo, Brazil). Copper nitrate trihydrate ($\text{Cu}(\text{NO}_3)_2 \cdot 3\text{H}_2\text{O}$, 99 %) and manganese nitrate tetrahydrate ($\text{Mn}(\text{NO}_3)_2 \cdot 4\text{H}_2\text{O}$, 98 %) were acquired from Sigma-Aldrich. The standard stock solutions of 1000 $\text{mg} \cdot \text{L}^{-1}$, 99.9 % purity (hexavalent chromium, copper, cadmium, manganese, nickel, and zinc) were acquired from Specsol (São Paulo, Brazil). Ultrapure water was used for solution formulation and was obtained by the system ARIUM® MINI (Sartorius, Germany).

2.2. Methods

2.2.1. Microfibrillated cellulose (MFC) extraction

Microfibrillated cellulose was extracted following a well-described methodology previously published by Ferreira et al. [44], and de Souza et al. [45], with some adaptations. The eucalyptus waste was dried for 24 h and then treated in a solution of 3.2 % w/v sodium chlorite at 70 °C for 2 h. After washing, the sample was subjected to an aqueous solution of 10 % w/v sodium hydroxide and 10 % w/v potassium hydroxide at 25 °C for 2 h. The obtained material was washed until neutral pH, and to isolate the MFC, the sample was ground in an aqueous medium at 5 wt%, using a conventional blender for 30 min. Finally, it was combined with high-intensity ultrasound for 20 min, in pulses of 30 s with 5 s intervals in an ice bath. This grinding and ultrasonication to decrease the fiber's size was based on Silva et al. [18]. This methodology is illustrated in Fig. 1a.

2.2.2. Starch-based composite hydrogel synthesis

The starch-based hydrogels were synthesized according to the methodology proposed by Camani et al. [46]. Corn starch was dissolved in ultrapure water, and then sodium hydroxide was added. The mixture was maintained under mechanical agitation at 40 °C for 3 h. Then, citric acid was added to crosslinking at 40 °C for 17 h. The produced hydrogel was heated in a bath (Final Treatment), stabilized at room temperature, and dried at 60 °C for 48 h. For the composite hydrogels, MFC was added during the starch solubilization in the concentrations of 1.0, 3.0, and 5.0 wt% (Starch/MFC-1 %, Starch/MFC-3 %, and Starch/MFC-5 %). Finally,



Fig. 1. Schematic illustration of the a) MFC extraction, and b) synthesis of composite hydrogels containing MFC.

the produced hydrogels were neutralized and dried again at 60 °C for 48 h (Fig. 1b).

2.3. Characterization

2.3.1. Laser diffraction spectroscopy (BetterSize)

A BetterSize ST equipment (Bettersize Instruments, China) was used to evaluate the MFC particle size within a measurement range of 0.10 to 1000 μm in triplicate. MFC was dispersed in distilled water with continuous stirring (1600 rpm) and subjected to ultrasound for 3 min.

2.3.2. Fourier transform infrared spectroscopy (FTIR)

The functional groups were identified using the FTIR technique (Frontier 94.942, PerkinElmer, USA) in attenuated total reflectance (ATR) mode, with a spectral range of 4000–500 cm^{-1} , a spectral resolution of 4 cm^{-1} , and 32 scans.

2.3.3. X-ray diffraction (XRD)

The crystalline structure was obtained using the XRD technique (STADI-PS diffractometer, STOE & Cie GmbH, Germany). Analyses were performed using $\text{CuK}\alpha 1$ radiation ($\lambda = 1.54060 \text{ \AA}$), a scan range of 10–80°, a step of 0.015°, a voltage of 40 kV, and a current of 40 mA.

MFC crystallinity was calculated using Eq. (1) developed by Segal et al. [47,48], where I_{200} represents the peak intensity corresponding to the (200) plane ($\sim 2\theta = 22.5^\circ$), while I_{am} represents the valley intensity between the (200) and (110) planes ($\sim 2\theta = 18^\circ$).

$$RC = \frac{(I_{200} - I_{am})}{I_{200}} \cdot 100 \quad (1)$$

For the composite hydrogels, the relative crystallinity (RC) was calculated using Eq. (2), as described by Alves et al. [49], where A_c is the crystalline region area and A_a is the amorphous region area. For the calculation of RC of starches and starch hydrogels, the scan range was 10–40°.

$$RC = \frac{A_c}{(A_c + A_a)} \cdot 100 \quad (2)$$

2.3.4. Scanning electron microscopy (SEM) and energy dispersive X-ray spectroscopy (EDS)

Morphology was obtained using the SEM technique with a FEI Quanta 250 (Thermo Fisher Scientific, USA). The sample was coated

with a thin layer of gold, 25 nm thick (Sputtering Leica EM ACE200, Leica Microsystems, Germany). The micrographs were obtained under the conditions: 50 pA current, 10 kV voltage, and 4 nm spot size. Samples were also investigated before and after Cu^{2+} capture by SEM-EDS to evaluate the spectra of chemical elements using Compact Scanning Electron Microscope (JSM-6010LA, Jeol System Technology Co., LTD.) using the following conditions: current of 50 pA, voltage of 15 kV, and spot size of 50 nm.

2.3.5. Thermogravimetry analysis (TGA)

The thermal stability was obtained by thermogravimetry analysis (STA 6000, PerkinElmer, USA). Samples were heated from 30 to 600 °C at a heating rate of 10 °C/min under a N_2 atmosphere (flow rate of 20 mL/min).

2.3.6. Brunauer-Emmett-teller (BET)

The specific surface area (S_{BET}) analysis was performed using the BET technique (Quantachrome, NOVA1200e model, Germany). Samples were heat-treated under a vacuum at 70 °C for 24 h to ensure the absence of water in the pores of the materials. The complete isotherm for nitrogen adsorption/desorption was obtained by varying the relative pressure (P/P_0) from 0.1 to 0.99 at -196°C .

2.3.7. Mercury intrusion porosimetry

Mercury intrusion porosimetry analysis was performed at low to high pressure levels using a Micromeritics AutoPore IV 9510 model (USA). At the low-pressure level (0.03 to 2.41 bar), a vacuum is performed to introduce mercury into the system (penetrometer + samples set). After mercury intrusion, the systems are placed at the high-pressure level (2.41 to 4136.85 bar) to obtain the apparent density ($\rho_{apparent}$) and pore size distribution of the materials. This equipment covers a pore diameter range of approximately 0.003 to 360 μm .

2.3.8. Helium pycnometry

The true density (ρ_{true}) was measured by helium pycnometry (Micromeritics, Accupyc II 1340 model, USA) under pressure of 1.33 bar with an equilibrium rate of 0.00034 bar/min. The materials porosity (ϵ) was calculated by Eq. (3).

$$\epsilon = \left(1 - \frac{\rho_{apparent}}{\rho_{true}}\right) \cdot 100 \quad (3)$$

2.3.9. Water uptake and solubility tests

The hydrogels water absorption was obtained by immersing 0.1 g of dry hydrogel in 50 mL of ultrapure water. Samples were collected periodically from 0 to 24 h to weigh the swollen hydrogels mass. At the end of the assay, the hydrogel solubility was measured to determine the weight loss. The degree of swelling (DS) was calculated by Eqs. (4), where m_i is the initial dry weight of hydrogels (g), m_t is the swollen weight of hydrogels at time t (g), and m_f is the final dry weight of hydrogels (g).

$$DS = \frac{(m_t - m_i)}{m_i} \cdot 100 \quad (4)$$

2.3.10. Sorption assays: MFC and composite hydrogels affinity

The affinity of MFC for Cu^{2+} , Zn^{2+} , Ni^{2+} , Cd^{2+} , Mn^{2+} , Cr^{6+} (0.17 mmol. L⁻¹ each) and starch-based composite hydrogels for Cu^{2+} (1.0 mmol. L⁻¹) were performed using a dosage of 10.0 g. L⁻¹. The sorption affinity assays were conducted in a shaker incubator, under 200 rpm at 25 to 55 °C, and pH between 4.0 and 4.5. After 24 h, PTMs concentrations were determined by ion chromatography, IC (940 Professional IC Vario, Metrohm, Switzerland). Removal efficiencies ($R\%$) were determined by Eq. (5), where C_0 is the PTMs initial concentration (mmol/L) and C_e is the PTMs concentration at equilibrium (mmol/L).

$$R\% = \frac{(C_0 - C_e)}{C_0} \cdot 100 \quad (5)$$

2.3.11. Equilibrium isotherms and kinetics sorption

Sorption isotherms of composite hydrogels (dosage of 10.0 g. L⁻¹) were carried out with Cu^{2+} initial concentrations ranging from 0.011 to 7.526 mmol. L⁻¹ for 24 h at 25 °C under continuous stirring (200 rpm). The kinetics assays were carried out under magnetic stirring (~200 rpm and 25 °C), with a dose of 10.0 g.L⁻¹, and Cu^{2+} initial load of 0.584 mmol.L⁻¹ at different time intervals between 0 and 1320 min. Cu^{2+} sorption capacity at equilibrium (q_e) was calculated by Eq. (6), where C_0 is the Cu^{2+} initial concentration (mmol.L⁻¹) and C_e is the Cu^{2+} concentration at equilibrium (mmol.L⁻¹), m is the composite hydrogel mass (g), and V is the volume of Cu^{2+} solution (L).

$$q_e = \frac{(C_0 - C_e)}{m} \cdot V \quad (6)$$

Non-linear models (Eqs. 7–13) were fitted to the isotherm or kinetics experimental profiles through the *OriginPro®2024b* software (Table 1), where q_e is the sorption capacity at equilibrium (mmol.g⁻¹), q_{max} is the maximum sorption capacity (mmol.g⁻¹), K_L is the Langmuir equilibrium constant (L.mmol⁻¹), R_L is the separation factor or equilibrium parameter (dimensionless), K_F is the Freundlich constant [(mmol/g)/(l/mmol) 1/n], n is the empirical constant related to the sorption intensity (dimensionless), K_{DR} is the constant related to sorption energy (mol²).

Table 1
Isotherm and kinetics models of Cu^{2+} sorption.

Mathematical models	Equations	References
Langmuir	$q_e = \frac{q_{max} \cdot K_L \cdot C_e}{(1 + K_L \cdot C_e)}$	(7) [50]
	$R_L = \frac{1}{(1 + K_L \cdot C_0)}$	(8)
Freundlich	$q_e = K_F \cdot C_e^{1/n}$	(9) [51]
Dubinin-Radushkevich	$q_e = q_{max} \cdot \exp \left[-K_{DR} \cdot \left(R \cdot T \cdot \ln \left(1 + \frac{1}{C_e} \right) \right)^2 \right]$	(10) [52]
	$E = \frac{1}{\sqrt{2 \cdot K_{DR}}}$	(11)
PFO	$q_t = q_e (1 - e^{-k_1 t})$	(12) [18]
PSO	$q_t = \frac{k_2 q_e^2 t}{1 + k_2 q_e t}$	(13) [88]

J^{-2}), T is the temperature (K), R is the ideal gas constant (8.314 J.(mol. K)⁻¹), E is the mean free energy of sorption (J/mol), q_t is the sorption capacity at time t (mmol.L⁻¹), k_1 is the PFO sorption rate constant (min⁻¹), and k_2 is the PSO sorption rate constant (g.mmol⁻¹.min⁻¹).

The simplified batch design can be used to estimate the composite hydrogels mass required to achieve Cu^{2+} removal efficiencies of 30 to 90 % for the volume ranging from 1 to 1000 L Cu^{2+} at an initial concentration of 1.0 mmol.L⁻¹. The operation line comes from the mass balance for a batch system with its outputs and inputs (Fig. 1S - Supplementary Material). The material balance from Eq. (6) results in Eq. (14). Langmuir parameters were established by the 25 °C isotherms to perform the design.

$$m = \frac{V \cdot (C_0 - C_e)}{\frac{q_{max} \cdot K_L \cdot C_e}{(1 + K_L \cdot C_e)}} \quad (14)$$

2.3.12. Statistical analysis

The fit of the models applied to the experimental profiles was evaluated considering determination coefficient (R^2) and corrected Akaike information criteria (AIC_c), calculated by Eqs. (15) and (16), respectively [53].

$$R^2 = 1 - \frac{\sum_{i=1}^N (q_{exp} - q_{calc})^2}{\sum_{i=1}^N (q_{exp} - \bar{q})^2} \quad (15)$$

$$AIC_c = N \cdot \ln \left[\frac{\sum_{i=1}^N (q_{exp} - q_{calc})^2}{N} \right] + 2p + \frac{2p(p+1)}{N-p-1} \quad (16)$$

wherein, N is the number of observations, q_{exp} is the experimental sorption capacity (mmol/g), q_{calc} is the sorption capacity calculated by the model (mmol/g), \bar{q} is the overall average of the experimental values (mmol/g), and p is the number of model parameters.

All experiments were performed in replicate, and the standard deviations were calculated to measure the average spreads.

2.3.13. Desorption and reusability

In each reuse cycle, 50 mL of Cu^{2+} solution (0.511 mmol.L⁻¹) was stirred with 0.5 g of Starch/MFC-5 % hydrogel (dose of 10.0 g.L⁻¹) for 24 h under stirring magnetic. Then, the hydrogel loaded with Cu^{2+} was dried at 60 °C. The hydrogel loaded with Cu^{2+} (0.5 g) was desorbed in 25 mL of HNO_3 solution (0.1 mol L⁻¹) (dosage of 20.0 g.L⁻¹) for 6 h under magnetic stirring. Before the next reuse cycle, the regenerated hydrogel was washed with ultrapure water until pH neutralization and dried at 60 °C. At the end, samples were filtered and the Cu^{2+} concentration was determined by IC. The desorption capacity (q_{el} , mmol.g⁻¹) and recovery percentages ($D\%$) in each cycle were calculated by Eqs. (17) and (18), respectively.

$$q_{el} = \left(\frac{C_{el}}{m} \right) \cdot V_{el} \quad (17)$$

$$D\% = \left(\frac{q_{el}}{q_e} \right) \cdot 100 \quad (18)$$

wherein, C_{el} is the concentration of Cu^{2+} in the eluent (mmol.L⁻¹), V_{el} is the volume of eluent (L), and q_e is the sorption capacity at equilibrium (mmol.g⁻¹).

3. Results and discussion

The characterizations of the MFC (particle size distribution obtained by BetterSize analysis, FTIR spectrum, diffractogram, photomicrograph, TGA/DTG curves, and nitrogen physisorption isotherms) and the discussions are presented in Fig. 2S (please, see Supplementary Material).

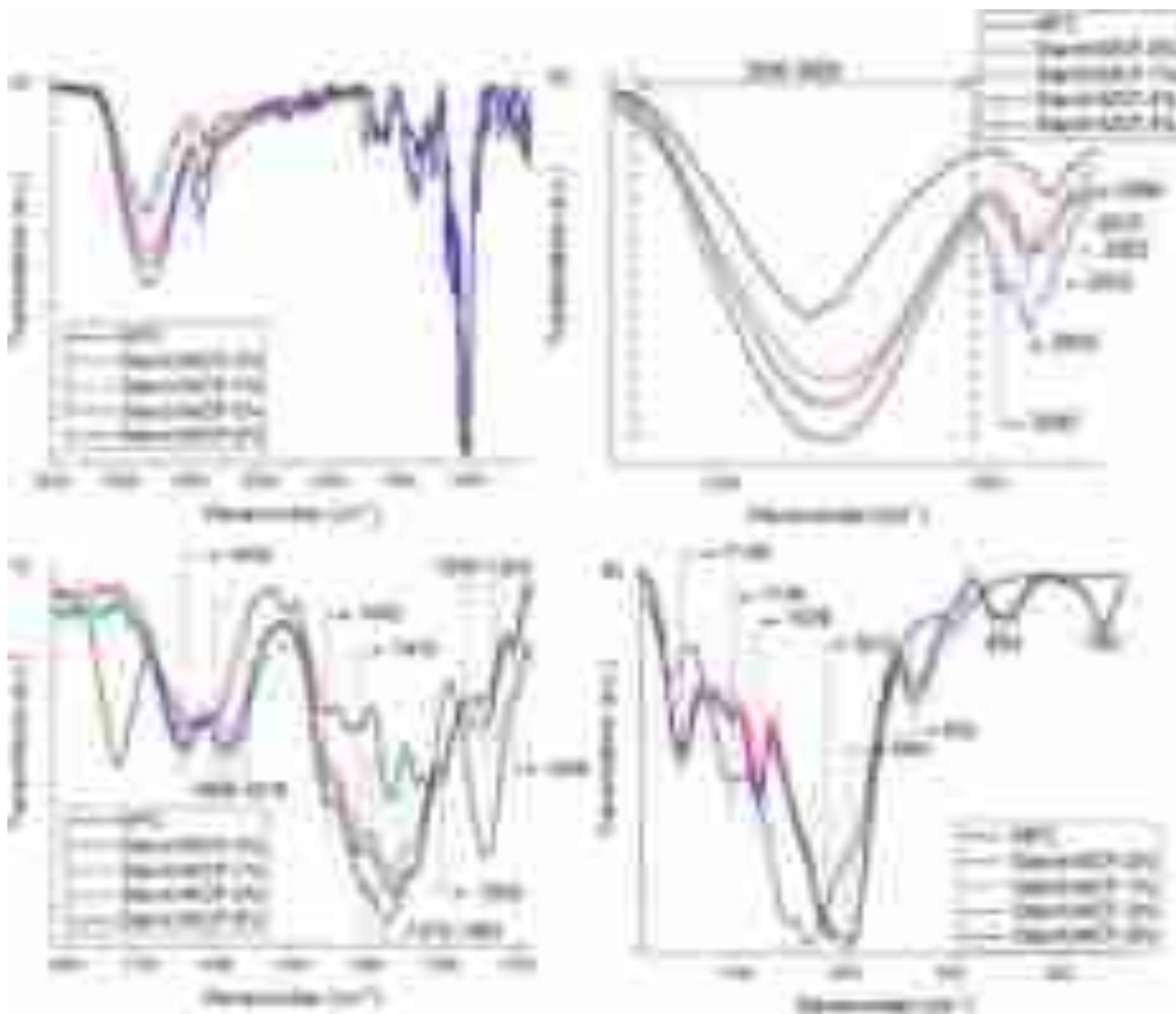


Fig. 2. FTIR spectra of microfibrillar cellulose and starch hydrogels a) full spectra and zoom in the regions b) 3800–2800 cm^{-1} , c) 1800–1200 cm^{-1} , and d) 1200–8500 cm^{-1} .

3.1. Characterizations of the composite hydrogels

3.1.1. Fourier transform infrared spectroscopy (FTIR)

Fig. 2 illustrates the FTIR graphs of the developed hydrogels, and Fig. 2a shows the full spectra. The band between 3500 and 3000 cm^{-1} (Fig. 2b) is attributed to OH- stretching, and 2900–2850 cm^{-1} is assigned to methyl groups C–H stretching, and both bands are commonly found in both cellulose and starch characteristic graphs. The increase in intensity in 3500–3000 cm^{-1} occurred in a growing manner for hydrogels from 0 to 5 %, indicating that the higher the MFC concentration, the greater the amount of available hydroxyl groups [54]. This result indicates that the addition of cellulose to the hydrogel increased the amount of available reactive groups, which was expected and desired to maximize contaminant adsorption. Additionally, shifts were observed in the band at 2890 cm^{-1} after the MCF incorporation, indicating changes in C–H vibrations, that are sensible to the chemical environment and intermolecular interactions [55]. In starch/MCF-0 %, the peak at 2890 cm^{-1} is associated with the C–H stretching vibrations of the glucose units. The introduction of CMF can form new hydrogen bonds between the starch chains and the cellulose fibers. These bonds can alter the electronic environment of the C–H groups, resulting in a shift of the C–H stretching peaks to higher frequencies, and the CMF concentration influences the interactions extension [56].

Other characteristic peaks (Fig. 2c-d) were observed at 1642 cm^{-1} (C–O bending associated with OH group) [57], 1594 and 1452 cm^{-1} (C–H bending vibration), 1410 and 1368 cm^{-1} (C–H bending vibrations), 1300 cm^{-1} (O–C–H, C–C–H, and C–O–H bending modes) [58], 1246 cm^{-1} (-OH vibrations), 1205 cm^{-1} (CH_2 stretching vibration), 1149 cm^{-1} (C–O bending vibrations), 1104 cm^{-1} (C–O–C asymmetric stretching) [59], 1076 and 1012 cm^{-1} (associated with starch structures) [60], 994, 932, 854, and 760 cm^{-1} (O–H stretching and bending vibrations, and C–O stretching) [61]. Similar to that observed at higher wavenumbers, shifts indicative of molecular alterations were observed between 1589 and 1579 cm^{-1} , 1372–1363 cm^{-1} , and 1250–1242 cm^{-1} . The first shift is associated with the C=O or C=C band in modified polysaccharides [104], and the introduction of cellulose can alter the chemical environment of these groups, especially through hydrogen bonds, which modifies the polarization of the bonds and shifts the band [62]. The vibrations between 1372 and 1363 cm^{-1} are attributed to CH_2 and CH_3 stretching, which can be a result from secondary reactions between cellulose hydroxyl and starch functional groups, altering the polymeric structure conformation [63,64].

Finally, there are shifts between 1250 and 1242 cm^{-1} (C–O–C or C–OH stretching vibration in polysaccharides). This range is related to the stretching vibrations of the C–O–C groups of the glycosidic bond and C–OH of the hydroxyls present in starch and cellulose [65]. The

displacement suggests changes in the electronic environment of the oxygen atoms, possibly due to the formation of more intense hydrogen bonds between the polymers. Since cellulose is rich in hydroxyl groups, its incorporation can alter the hydrogen bond network of the hydrogel, modifying the energy required for the vibrational transitions of the C-OH and C-O-C groups [66,67].

3.1.2. X-ray diffraction (XRD)

Fig. 3a-b shows the diffractograms of native starch, neat hydrogel, and composite hydrogels containing MFC. Fig. 3a shows the characteristic peaks of native starch and neat hydrogel at $2\theta = 15^\circ$ and a double peak at $2\theta = 17$ and 18° , and 23.1° . According to Camani et al. [68] and Abhari et al. [69], these peaks are associated with the crystalline structure of starch. After the crosslinking, the peak at 15.2° (101

crystalline plan) disappeared, and a new peak emerged at 11.5° , associated with retrogradation of amylose and amylopectin chains in the gel structure [49,68,70]. These peaks' changes indicate molecular rearrangement within the hydrogel.

Furthermore, the broad band between 17 and 18° resulted in more defined peaks, and the peak at 23.1° also showed an increase in definition with a narrowing of the width. The well-defined peaks in the hydrogel diffractogram can be correlated to the crystalline structure of corn starch type B, which is due to the recrystallization of gelatinized starch [71]. The relative crystallinity values (RC) of native starch and neat hydrogels (Starch/MFC-0 %), were calculated as 70.1 and 74.0 %, which can be explained by the action of MFC as a nucleating agent, since cellulose restricts molecular mobility, leading to more structured microcrystalline regions, influencing starch recrystallization and

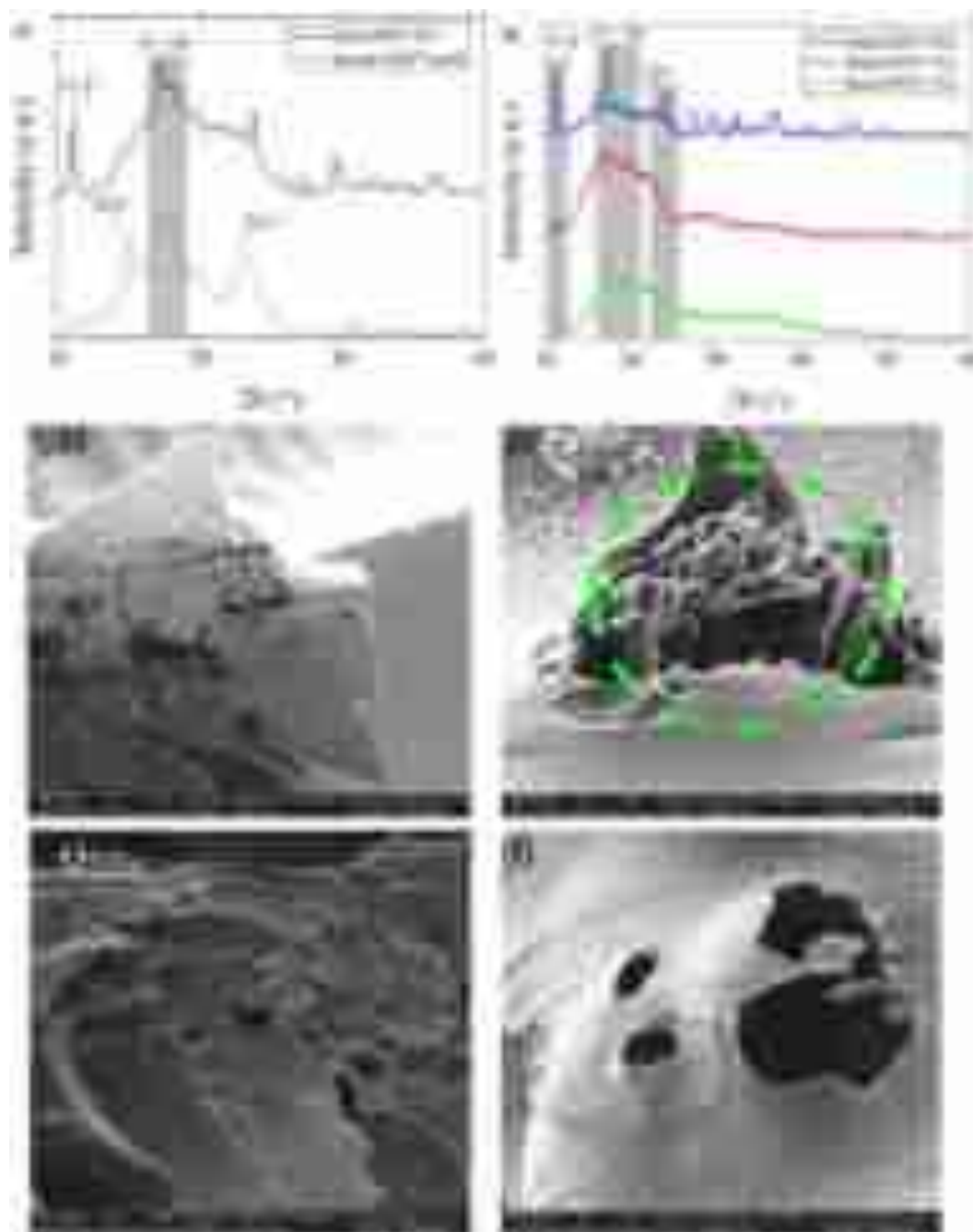


Fig. 3. Diffractograms of a) native starch and corn starch-based hydrogel, b) and hydrogels containing different MFC concentrations (1.0, 3.0, and 5.0 wt%), and Micrographs of c) corn starch-based hydrogel and hydrogels containing different MFC concentrations d) 1.0, e) 3.0, and f) 5.0 wt%.

promoting a better-organized crystalline structure [72]. A similar trend was also observed by Alves et al. [49], due to the crosslinking process of starch chains to form hydrogels.

Starch/MFC hydrogels exhibited a more defined peak at 23°, particularly for Starch/MFC-5 % (the highest MFC percentage), indicating the presence of MFC within the hydrogel structure. The presence of this peak was observed by Thinkohkaew et al. [73], who correlated this appearance with the increase in the peak's intensity and the high percentage of cellulose fiber in the PVA hydrogel. In composite hydrogels, the relative crystallinity was 67.5, 66.2, and 68.0 % for samples containing 1, 3, and 5 wt%, respectively. Compared to neat hydrogel (Starch/MFC-0 %), a slight decrease in relative crystallinity was observed (~10 %), result of the native crystalline starch structure disruption by crosslinking and the partial inhibition of molecular rearrangement due to increased amorphous regions introduced by MFC [74]. This aligns with findings from previous studies on cellulose-reinforced polymeric hydrogels, where an increase in fiber content led to enhanced local crystallinity but slightly reduced global crystallinity due to structural heterogeneity [75,76].

3.1.3. Scanning electron microscopy (SEM)

Figs. 4c-f present the morphology of hydrogel without and containing MFC in different percentages. The morphology of all hydrogels is highly porous, presenting pores with different sizes. The porous surface of the hydrogels is one of the characteristics generated from the crosslinking reaction between the crosslinking agent and starch chains (amylose and amylopectin) [49]. According to Keirudin et al. [77], this porous structure occurred due to the starch chains and citric acid esterification under alkali medium. However, in contrast to aerogels or cryogels, ambient pressure drying (employed to prepare these hydrogels) can collapse the pore structure, resulting in a structure with high density and low porosity [78].

With the addition of microfibrillated cellulose (MFC), cellulose fibers were observed within the polymer matrix, as highlighted in Fig. 3b. This presence in the cryo-fractured region of the MFC-containing samples suggests strong adhesion between starch and cellulose chains, likely facilitated by hydrogen bonding interactions between hydroxyl groups of both polysaccharides [79]. The ability of MFC to act as a reinforcing agent within the starch network is supported by previous studies, where the incorporation of cellulosic microstructures improved mechanical stability, water retention, and porosity control in hydrogel-based materials. Interestingly, this fiber distribution was more prominent in the hydrogel containing 1 wt% MFC, whereas samples with higher MFC concentrations (3 and 5 wt%) exhibited a greater incidence of porosity and an apparent change in structural uniformity [49]. This trend suggests that at lower concentrations, MFC fibers act primarily as structural reinforcements, facilitating polymer chain entanglements, whereas at higher concentrations, phase separation or fiber aggregation may lead to increased pore formation [80,81].

Additionally, composite hydrogels demonstrated a more uniform porous structure compared to neat hydrogels. This is in line with previous reports showing that cellulose-based fillers can modulate the hydrogel network morphology, enhancing interfacial interactions and reducing phase separation [69]. However, these findings differ from those of Spagnol et al. [82], who synthesized chitosan-graft-poly(acrylic acid)/cellulose nanofibril composite hydrogels. Their study suggested that nanocellulose, due to its higher surface area and strong interaction with the polymer matrix, led to irregular pore formation and reduced structural uniformity. In contrast, the cellulose fibers used in this study (MFC) exhibited a different interaction mechanism with the corn starch matrix, leading to a more regular porous architecture [83,84]. This difference may be attributed to the scale of the cellulose structure, as microfibrillated cellulose retains a larger fiber diameter compared to nanocellulose, potentially preventing excessive entanglements and

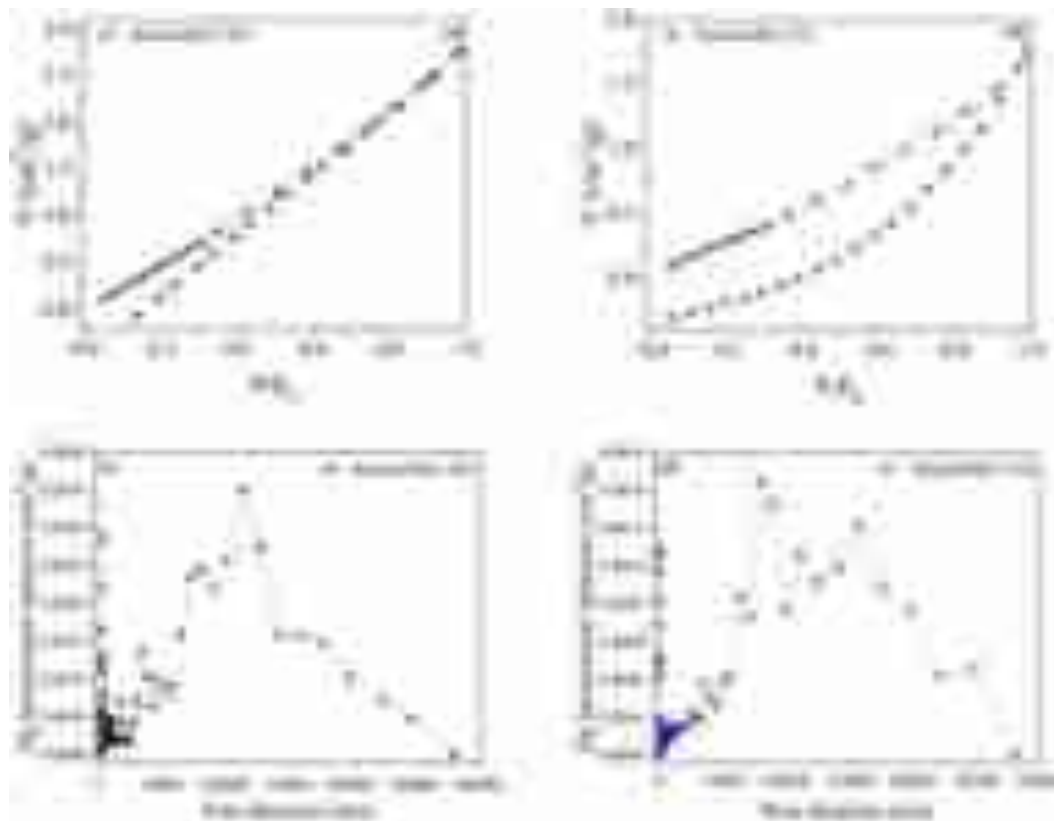


Fig. 4. Nitrogen physisorption isotherms (a, b) and Profiles of mercury intrusion increment versus pore diameter (c, d) for Starch/MFC-0 % and Starch/MFC-5 % hydrogels, respectively.

ensuring better phase distribution within the hydrogel matrix [85].

3.1.4. Thermogravimetry analysis (TGA)

To evaluate the thermal stability of the hydrogels, TGA was performed. Fig. 3S (please, see supplementary material) shows the TGA graphs and the discussion, and Table 1S shows the main thermal parameters reported for each sample.

3.1.5. Brunauer-Emmett-teller (BET), mercury intrusion porosimetry, and helium pycnometry

The pore size and specific surface area of Starch/MFC-0 % and Starch/MFC-5 % were analyzed using BET, and Fig. 4a-b shows the adsorption-desorption isotherms. Fig. 4c-d presents the mercury intrusion increment versus pore diameter profiles, and Table 2 presents the specific surface area, mercury porosimetry analysis (apparent density), and helium gas pycnometry (real density) of all developed samples. Microfibrillated cellulose presented the lowest specific surface area value ($1.210 \text{ m}^2 \cdot \text{g}^{-1}$), which is expected due to its compact and less porous fibrous structure compared to hydrogels. Kumar et al. [86] reported $1.023 \text{ m}^2 \cdot \text{g}^{-1}$ values for cellulose and described its modification with graphene to improve surface area and remove phenol from aqueous solution. Starch/MFC-0 % showed the highest surface area ($4.010 \text{ m}^2 \cdot \text{g}^{-1}$), indicating a highly porous structure that reflects the formation of an expanded polymer network with a greater surface area available for interaction with liquids or contaminants.

After MFC incorporation, cellulose increase resulted in a progressive decrease in the specific surface area, suggesting that MFC influences the hydrogel porosity by filling micropores within the starch matrix, reducing available pore volume, restricting polymer network expansion, leading to fewer accessible cavities, and increasing matrix compaction, particularly at higher MFC concentrations. Besides, the MFC addition resulted in higher hysteresis (Fig. 4a-b) in the adsorption-desorption isotherms, suggesting the presence of mesopores (pores with diameters between 2 and 50 nm) and capillary condensation effects [87]. Mesoporosity is important for water retention, contaminant diffusion, and adsorption performance as it increases the available surface area for interactions.

The BET results were complemented by mercury intrusion porosimetry (MIP) and helium pycnometry (HP). The MIP results material and information on the pore size distribution and accessible pore volume, while the HP data provides the density of the material, excluding open pores. According to Costa et al. [88], the true density is obtained by the ratio of mass to true volume without considering empty pore volume. Apparent density is calculated based on the relationship between mass and total volume of the solid, i.e., the true volume of the material added to the volume occupied by mercury filling the pores of the solid. Starch/MFC-5 % showed higher true density than Starch/MFC-0 % (1.525 versus $1.466 \text{ g} \cdot \text{cm}^{-3}$) due to the presence of MFC structures – which corroborates the BET results. This increase in density is associated with the characteristics of MFC, which are dense and rigid when compared to hydrated starch. In addition, the incorporation results in the occupation of spaces within the polymer network, reducing the voids and the expansion of the starch matrix. It is worth noting that the specific surface area of porous materials is proportional to materials porosity.

Table 2
Textural properties of MFC, Starch/MFC-0 %, Starch/MFC-1 %, Starch/MFC-3 %, and Starch/MFC-5 %.

Property	MFC	Starch/ MFC-0 %	Starch/ MFC-1 %	Starch/ MFC-3 %	Starch/ MFC-5 %
S_{BET} (m^2/g)	1.21	4.01	3.99	2.29	1.81
ρ_{apparent} (g/cm^3)	1.66	1.01	1.11	1.20	1.29
ρ_{true} (g/cm^3)	1.77	1.47	1.49	1.51	1.52
ϵ (%)	6.51	30.8	25.7	20.6	15.6

Mercury intrusion porosimetry was used to evaluate the pore size distribution (Fig. 4c-d). In both samples, a predominance of pores with diameters $>50 \text{ nm}$ was observed, indicating a macroporous structure, even after MFC incorporation. According to the IUPAC classification [89], pores larger than 50 nm fall within the macroporous range, and their presence suggests that the hydrogel matrix retains relatively open channels regardless of filler content. These findings were further supported by nitrogen adsorption-desorption isotherms (Fig. 4c-d), which exhibited Type II isotherms with visible hysteresis loops. This type of isotherm is typically associated with macroporous or non-porous materials with unrestricted monolayer-multilayer adsorption [90]. The hysteresis observed suggests capillary condensation within pore networks, confirming the presence of a well-defined porous architecture with interconnected macropores. While both techniques confirm the macroporous nature of the hydrogels, the addition of MFC influenced key structural parameters. BET analysis showed a significant decrease in specific surface area from $4.010 \text{ m}^2/\text{g}$ (Starch/MFC-0 %) to $1.814 \text{ m}^2/\text{g}$ (Starch/MFC-5 %), indicating a reduction in the accessible surface likely due to partial pore blockage or compaction of the polymeric network. This is further corroborated by the increase in true density (from 1.466 to $1.525 \text{ g}/\text{cm}^3$) and reduction in total porosity (ϵ) from 30.82% to 15.65% , reflecting a denser and more compact internal structure with fewer available voids, even though the overall pore size remained in the macroporous range. The results indicate that MFC incorporation does not alter the macroporous classification of hydrogels but rather modifies the internal architecture by reducing pore volume and surface area, potentially altering adsorption capacity and transport properties.

3.2. Analysis of specific properties of composite hydrogels

3.2.1. Water absorption

From the observed water absorption results (Fig. 5a), all hydrogels showed a considerable degree of swelling (DS) during the test. The pure starch composition exhibited 89% of DS capacity, and the addition of MFC decreased absorption by up to 24% , indicating that the microfibers likely increased the rigidity of the hydrogel's conformation. This result corroborates the expected lower molecular chain mobility, diffusivity, and water retention within the pores and hydrogel volume. Additionally, during the water absorption tests, the hydrogel samples had high solubility in the aqueous medium without MFC (close to 30.1%), reflecting a non-satisfactory physical performance for application in sorption tests. Adding MFC to the starch hydrogel reduced the solubility in aqueous media to about 5% .

3.2.2. Affinity tests

The sorption efficiency of MFC for different metal ions (Cu^{2+} , Cd^{2+} , Mn^{2+} , Zn^{2+} , and Cr^{6+}) was evaluated, as shown in Fig. 5b. The sorption efficiency of MFC for various metal ions (Cu^{2+} , Cd^{2+} , Mn^{2+} , Zn^{2+} , and Cr^{6+}) is presented in Fig. 5b. The results demonstrate a markedly higher adsorption capacity for divalent metal cations such as Cu^{2+} , Mn^{2+} , Ni^{2+} , Zn^{2+} , and Cd^{2+} , in contrast with the significantly lower removal of Cr^{6+} (approximately 30%) under the same conditions [91]. This disparity is attributed to the chemical nature of Cr^{6+} in aqueous media. Unlike transition metal ions that exist as positively charged divalent cations, Cr^{6+} predominantly occurs in the form of oxyanions (e.g., CrO_4^{2-} , HCrO_4^- , $\text{Cr}_2\text{O}_7^{2-}$), depending on the pH of the solution [92]. These negatively charged species experience electrostatic repulsion from the typically negatively charged surface of MFC at neutral to slightly alkaline pH values, where the hydroxyl groups on the cellulose fibers are deprotonated. Moreover, Cr^{6+} removal is further hindered by its high hydration energy and lower affinity for neutral or slightly negatively charged adsorbents [93]. Thus, Cu^{2+} ions were evaluated for sorption on starch-containing MFC-based hydrogels. Although the other divalent cations (Ni^{2+} , Cd^{2+} , Zn^{2+} , Mn^{2+}) are also very common and can be found alongside copper in polluted sites, the choice of Cu^{2+} is due to its wide use in industrial activities and presence in wastewater that is

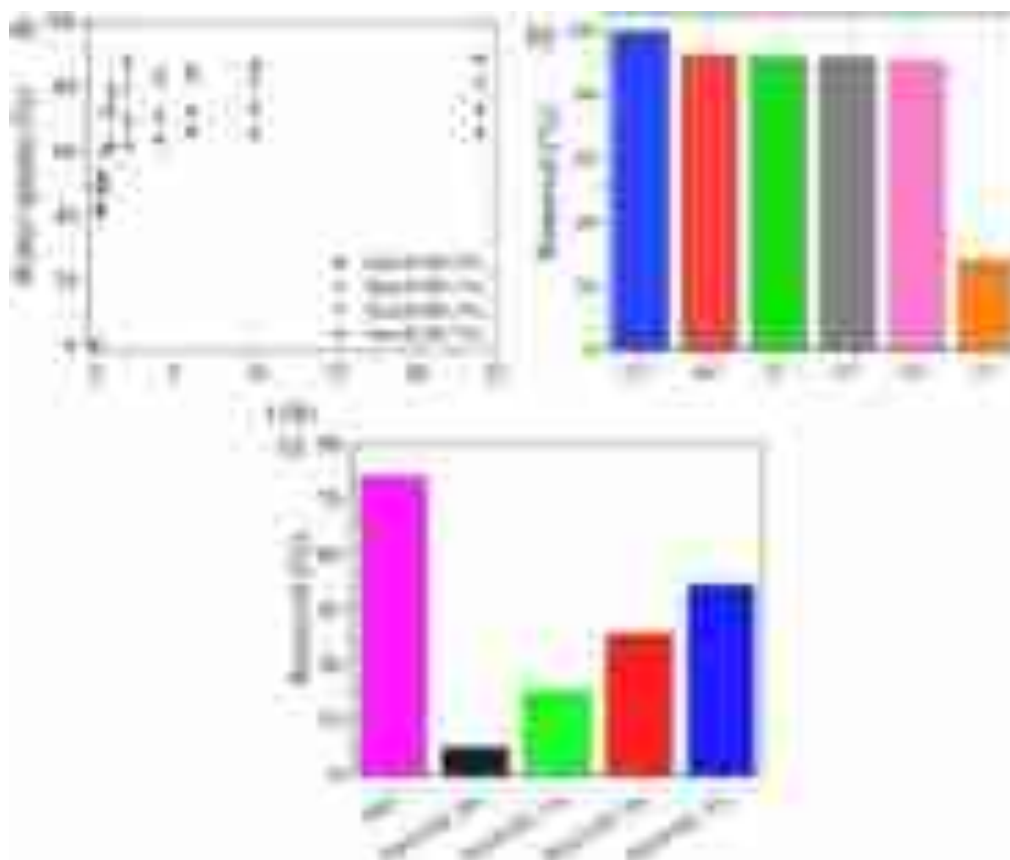


Fig. 5. a) Water uptake (%) for MFC hydrogels containing different MFC concentrations (1.0, 3.0, and 5.0 wt%), b) Sorption affinity of PTMs ions (Cu^{2+} , Cd^{2+} , Mn^{2+} , Zn^{2+} , and Cr^{6+}) by MFC, and c) removal efficiency of Cu^{2+} for MFC, corn starch-based hydrogel, hydrogels containing different MFC concentrations (1.0, 3.0, and 5.0 wt%).

generated in large volumes every day.

The starch-based hydrogel showed an increase in Cu^{2+} sorption (Fig. 5c). Specifically, the Starch/MFC-5 % hydrogel achieved a maximum Cu^{2+} removal of approximately 52 %, whereas the starch-only hydrogel (Starch/MFC-0 %) showed limited performance. These findings indicate that native starch has a low affinity for Cu^{2+} ions, likely due to the absence of sufficient functional groups or accessible surface area required for effective binding [94,95]. The progressive enhancement of metal removal with increasing MFC content underscores a synergistic interaction between MFC and the starch-based hydrogel matrix. The MFC introduces additional active sites for metal ion coordination, particularly through hydroxyl groups that can participate in complexation or electrostatic interactions [96]. This result also shows that the dose of fillers with high sorption capacity is a fundamental factor in improving the removal potential of the polymeric matrix. In this study, MFC loads between 1, 3 and 5 wt% were anchored, in which the MFC dose was 0.1, 0.3 and 0.5 $\text{g}\cdot\text{L}^{-1}$, respectively. These values are 100, 33 and 20 times lower than the dose used in the test with pure MFC (10.0 $\text{g}\cdot\text{L}^{-1}$). Besides that, the cellulose can modulate the internal structure of the hydrogels, as discussed before, influencing porosity, ion accessibility, and diffusion pathways [97]. The effect of temperature on Cu^{2+} sorption by MFC and its starch hydrogels was also investigated in the range of 25 to 55 °C (Fig. 4S - Supplementary Material). There were no significant changes in the removal efficiency with increasing temperature. Therefore, the temperature condition of 25 °C was maintained for performing the sorption kinetics and equilibrium isotherms.

3.2.3. Equilibrium sorption and simplified batch design

Fig. 6 (a) shows the sorption equilibrium isotherms of Cu^{2+} on starch/MFC-1 % (a), starch/MFC-3 % (b), and starch/MFC-5 % (c) at

25 °C, which showed a similar favorable behavior at the three MFC-added loads. Additionally, the maximum sorption capacity of Cu^{2+} increased in the following order: starch/MFC-5 % (0.258 mmol/g) > starch/MFC-3 % (0.105 mmol/g) > starch/MFC-1 % (0.037 mmol/g). Cheng et al. [4,98] employed $\text{SiO}_2/\text{Na}_2\text{O}$ geopolymer and obtained a lower Cu^{2+} sorption capacity of 0.057 mmol/g at equilibrium, which is five times lower than starch/MFC-5 %. Dang et al. [99] evaluated the Cu^{2+} sorption by wheat straw and reported a sorption capacity of 0.180 mmol/g for Cu^{2+} . Silva et al. [100] also found lower Cu^{2+} sorption capacities for sericin/alginate beads (0.090 mmol/g). Almeida Neto et al. [101] found a maximum sorption capacity of Cu^{2+} of 0.075 and 0.060 mmol/g for Bofe and Verde-lodo bentonite clays, respectively. These comparisons highlight the high affinity and efficiency of starch/MFC hydrogels, particularly at higher MFC content, for Cu^{2+} removal. This superior performance is attributed to the synergistic combination of the polymeric hydrogel network with the surface functionality and structural reinforcement provided by MFC, offering a promising, low-cost, and biodegradable alternative for heavy metal adsorption in water treatment applications.

Table 3 shows the values of statistical parameters (R^2 and $AICc$) and parameters obtained by models fitting (Langmuir, Freundlich, and Dubinin-Radushkevich). The non-linear fit of the isotherms is shown in Fig. 6a. The experimental maximum sorption capacities increased progressively with MFC content: 0.037 mmol/g (1.0 wt%), 0.105 mmol/g (3.0 wt%), and 0.258 mmol/g (5.0 wt%), confirming the beneficial role of MFC in enhancing metal ion binding.

The Langmuir model provided the best fit to the experimental data, with $R^2 \sim 0.99$ and the lowest Akaike Information Criterion ($AICc$) values for all samples, suggesting monolayer adsorption on a homogeneous surface with a finite number of identical sites. The Langmuir

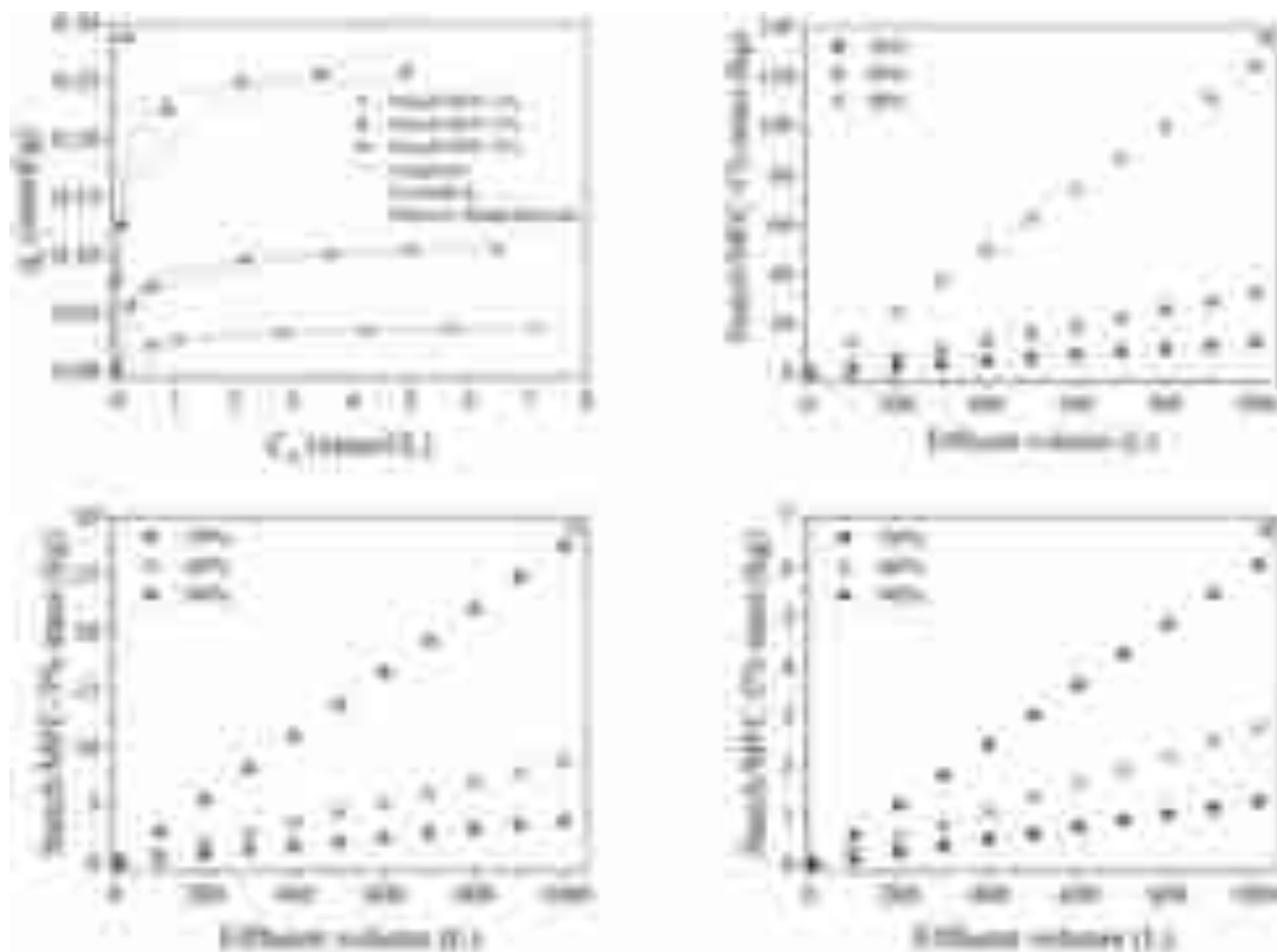


Fig. 6. Equilibrium isotherms for Cu²⁺ at 25 °C (a) and simplified batch adsorption design (b, c, d) for the Starch/MFC-1 %, Starch/MFC-3 %, and Starch/MFC-5 % systems.

Table 3

Fitting parameters of the isothermal and kinetics models of Cu²⁺ sorption by Starch/MFC composites.

		Parameters	Starch/ MFC-1 %	Starch/ MFC-3 %	Starch/ MFC-5 %	
Isothermal models	Experimental	q_{max} (mmol/g)	0.037	0.105	0.258	
		Langmuir	q_{max} (mmol/g)	0.039	0.108	0.257
		K_L (L/mmol)	2.283	4.334	13.733	
		R_L	0.055	0.030	0.010	
		R^2	0.998	0.995	0.940	
		AICc	-90.539	-68.371	-36.653	
		Freundlich	K_F (mmol/g).(L/mmol) ^{1/n}	0.026	0.077	0.205
		n	4.686	4.908	5.053	
		R^2	0.976	0.971	0.918	
		AICc	-72.099	-55.670	-34.449	
		Dubinin-Radushkevich	q_{max} (mmol/g)	0.036	0.102	0.245
		$K_{DR} \times 10^{-8}$ (mol ² /J ²)	8.521	3.456	0.760	
		E (kJ/mol)	2.422	3.804	8.113	
		R^2	0.995	0.986	0.933	
	AICc	-82.853	-60.786	-35.794		
Kinetics models	Experimental	q_e (mmol/g)	0.026	0.046	0.067	
		PFO	q_e (mmol/g)	0.034	0.058	0.080
		k_1 (1/min)	0.003	0.005	0.007	
		R^2	0.993	0.985	0.983	
		AICc	-248.784	-211.772	-195.882	
		PSO	q_e (mmol/g)	0.026	0.048	0.069
		k_2 (g/mmol.min)	0.091	0.085	0.103	
		R^2	0.997	0.987	0.998	
		AICc	-261.529	-214.626	-231.485	

separation factor was below 0.1 for all hydrogels, indicating highly favorable adsorption. Additionally, the Langmuir affinity constant increased substantially with MFC content—from 2.283 to 13.733 L/mmol—supporting the argument that MFC not only introduces more sorption sites but also enhances their affinity for Cu^{2+} .

The Freundlich model also described the data adequately ($R^2 > 0.91$), not as good as the Langmuir, especially for lower MFC contents. The Freundlich constant n (4.7–5.1) was >1 for all formulations, indicating favorable multilayer sorption on a heterogeneous surface. However, the higher AIC_c values and slightly lower R^2 compared to Langmuir suggest that monolayer adsorption is more dominant in these systems, particularly at higher MFC loadings. The D–R model estimated q_{\max} values close to the experimental results, confirming its suitability. The mean sorption energy (E) increased significantly with MFC content—from 2.4 to 8.1 kJ/mol, suggesting a transition from physisorption ($E < 8$ kJ/mol) at low MFC content to chemisorption ($E > 8$ kJ/mol) for starch/MFC-5 % hydrogel. This result reinforces the hypothesis that MFC contributes active functional groups capable of forming stronger, possibly specific interactions with Cu^{2+} ions (e.g., complexation with hydroxyls).

Fig. 6 b-d shows the minimum composite hydrogel mass needed to achieve removal efficiencies of 30–90 % for different volumes (1–1000L) of Cu^{2+} solutions (1.0 mmol/L). The effluent volume and composite hydrogels mass are linearly correlated for all investigated removal efficiencies. The greater the volume of Cu^{2+} solution to be treated, the greater the hydrogel mass to achieve a given removal efficiency. For the uptake of 90 % of Cu^{2+} in 1000 L of effluent with 1.0 mmol/L Cu^{2+} , about 124 kg of starch/MFC-1 %, 27 kg of starch/MFC-3 %, and 6 kg of starch/MFC-5 % are required. The lower mass of starch/MFC-5 % needed for Cu^{2+} uptake under the same experimental conditions is in line with the maximum sorption capacity of Cu^{2+} at equilibrium (0.258 mmol/g for starch/MFC-5 %) in relation to the other composite hydrogels (0.105 mmol/g for starch/MFC-3 % and 0.037 mmol/g for starch/MFC-1 %). This is evidence of the good potential of starch/MFC-5 % for Cu^{2+} sorption. Finally, considering that MFC-based materials (e.g. starch/MFC composite hydrogel) are abundant and low-

cost, the MFC can be a promising alternative as an additive in polymeric architectures of advanced porous materials (e.g., aerogels, hydrogels, or membranes) for the treatment of large volumes of wastewater contaminated with toxic metals, such as Cu^{2+} .

3.2.4. Kinetics sorption

The kinetic profiles (Fig. 5S) showed that there was a reduction in equilibration times with increasing MFC loads (1, 3, and 5 wt%): 780 min (Starch/MFC-1 %) $>$ 660 min (Starch/MFC-3 %) $>$ 480 min (Starch/MFC-5 %). This behavior is due to the reduction in the resistance to Cu^{2+} mass transfer in the external film by the increase in MFC loads anchored in the hydrogel matrix, increasing the contact with the MFC active sites in the starch hydrogel. The experimental data of the Cu^{2+} sorption by the three materials were also modeled using PFO and PSO kinetic models (Table 3 and Fig. 5S). Higher R^2 values and lower AIC_c values were observed for the fits of PSO model, suggesting that surface reactions govern Cu^{2+} sorption processes.

3.2.5. SEM-EDS after Cu^{2+} uptake

To better understand the interactions between Cu^{2+} and MFC and its Starch/MFC-5 % hydrogel, the materials were evaluated, before and after sorption, using SEM/EDS analysis (Fig. 7). The materials were saturated with Cu^{2+} in sorption tests under the following experimental conditions: Cu^{2+} load of 1.0 mmol.L⁻¹, dose of 10.0 g.L⁻¹, $T \sim 25$ °C, and pH 4.5. The SEM micrographs at 50 \times magnification showed that MFC showed a homogeneous and fibrous morphology. After the addition of MFC to form Starch/MFC-5 % hydrogel, it was observed a good anchoring and dispersion of MFC, since an MFC-like morphology was identified across the smooth surface of the hydrogel. After Cu^{2+} sorption, a reduction of empty pores was observed for both the MFC and the Starch/MFC-5 %, indicating their occupancy by Cu^{2+} . Furthermore, the SEM-EDS surface mapping confirmed the presence of Cu^{2+} homogeneously distributed and sorbed over the materials surface.

The EDS technique was performed to identify the chemical elements on the MFC and Starch/MFC-5 % surface before and after Cu^{2+} sorption (Fig. 7). According to the EDS technique, MFC showed carbon (50.79 %)

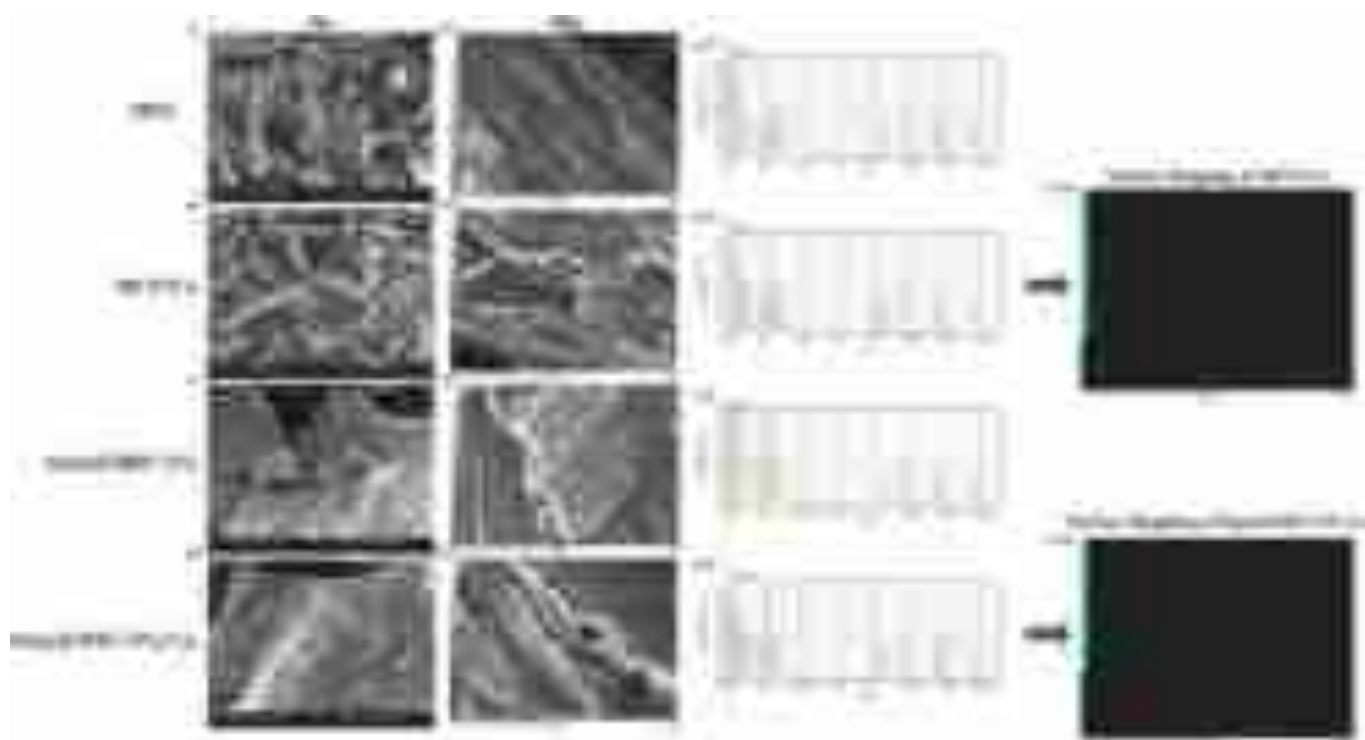


Fig. 7. SEM/EDS micrographs of MFC (a, b) and Starch/MFC-5 % hydrogel (c, d), with a 50 \times and 500 \times magnification; and surface mapping of Cu^{2+} .

and oxygen (46.50 %) elements in their chemical composition and gold (due to the pre-treatment of the samples for the SEM-EDS analyses). Besides these elements, the MFC presented sodium (1.42 %) and chlorine (1.30 %) on its surface. The presence of sodium and chlorine comes from the eucalyptus waste treatment step with sodium chlorite. After anchoring MFC into the Starch/MFC-5 % hydrogel, besides carbon (49.77 %) and oxygen (49.27 %) elements, sodium (0.84 %) and chlorine (0.12 %) were also detected, confirming the presence of MFC on the hydrogel matrix.

After Cu^{2+} sorption, a reduction in sodium content was observed in MFC/Cu (0.14 %) and Starch/MFC-5 %/Cu (0.05 %) surfaces, indicating the involvement of this element in the sorption mechanism. Possibly, Na^+ present on the materials may have been exchanged for Cu^{2+} during the sorption process, which highlights the ion exchange mechanism in the adsorbents. Fig. 8 describes the possible sorption mechanisms of Cu^{2+} by starch-MFC hydrogels, highlighting the expansion of adsorption sites and the chemical interaction with hydroxyl groups and citric acid.

3.2.6. Hydrogel reusability

Due to the more significant sorption potential of Cu^{2+} by Starch/MFC-5 % hydrogel, this system was selected to evaluate Cu^{2+} desorption and hydrogel reusability. The reuse of Cu^{2+} -loaded Starch/MFC-5 % hydrogel was carried out for up to four cycles employing HNO_3 (0.1 mol. L^{-1}) as eluent (Fig. 9). Cu^{2+} removal by Starch/MFC-5 % hydrogel was >95 % for the first sorption cycle and decreased by the fourth cycle to about 70 %. The reduction in the sorption potential of the hydrogel may have occurred due to the hydraulic shear force, which damages the hydrogels and reduces the number of available active sites. The desorption cycles also showed that Cu^{2+} recovery was affected throughout the reuse cycles. The system was able to recover Cu^{2+} at rates of around 97 % in the first desorption cycle. In the remaining cycles, the Cu^{2+} recovery fell to around 63 %. This indicates that the active sites of the hydrogel were not completely released throughout the elution cycles, which also contributed to the reduction of active sites

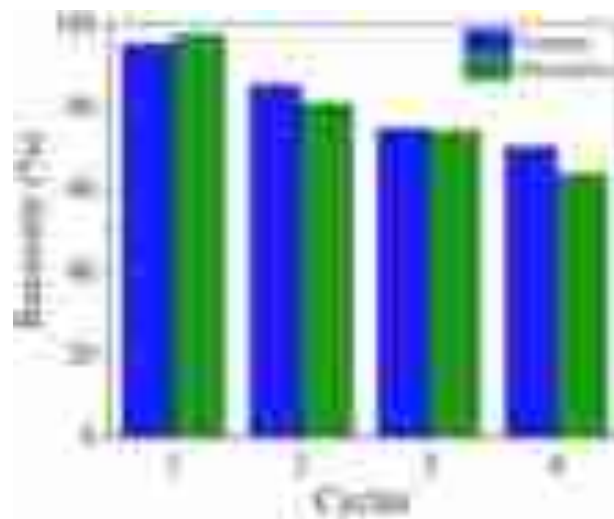


Fig. 9. Removal and recovery of Cu^{2+} by Starch/MFC-5 % hydrogel in reuse cycles (sorption: dose of 10.0 g L^{-1} , $C_0 = 0.511 \text{ mmol/L}$, pH 4.5, and $T = \sim 25 \text{ }^\circ\text{C}$) (desorption: dose of 20.0 g L^{-1} , $T = \sim 25 \text{ }^\circ\text{C}$, and $0.1 \text{ mol L}^{-1} \text{ HNO}_3$ as eluent).

available for Cu^{2+} sorption.

3.2.7. Limitations, challenges, and future research perspectives

Due to the current scenario, the recovery of PTMs, such as copper, from effluents is a matter of extreme importance for technological and environmental purposes. In this work, starch/MFC-based composite hydrogels were examined for the removal/recovery of copper from aqueous medium. The use of starch-based composite hydrogels loaded with microfibrillated cellulose (MFC) contributes to the cellulose and paper farming activity chain, since a new application is being proposed

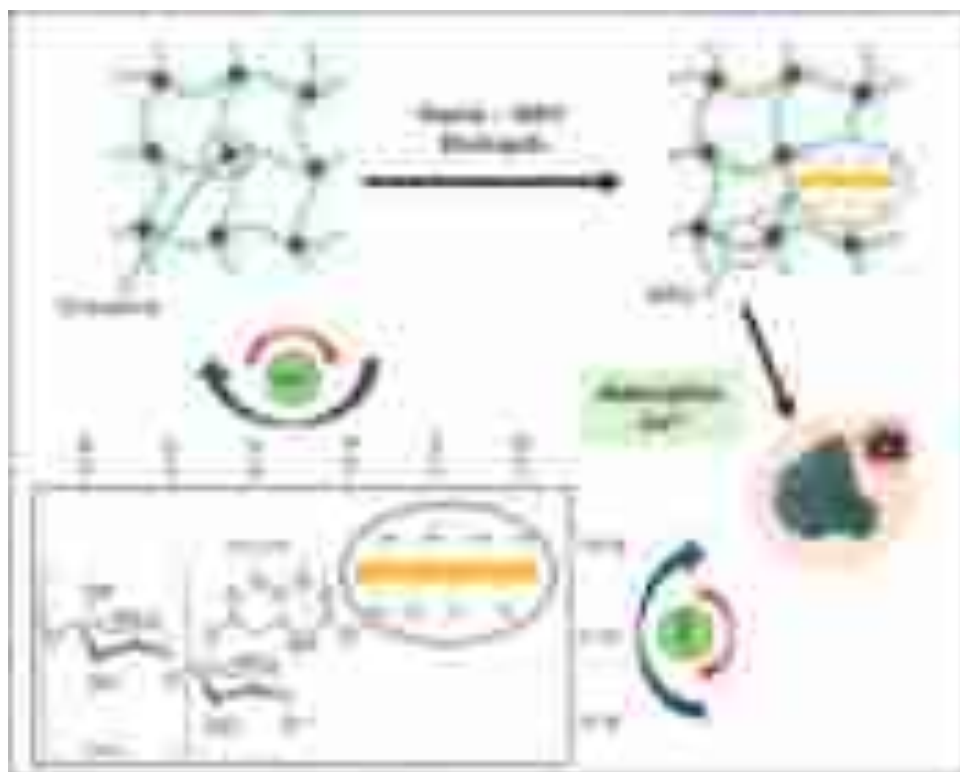


Fig. 8. Mechanism of Cu^{2+} adsorption by starch-MFC hydrogels, highlighting the expansion of adsorption sites and the chemical interaction with hydroxyl groups and citric acid.

for microcellulose, an abundant biopolymer extracted from eucalyptus sawdust wastes, joining the use of corn starch as a biodegradable matrix, thus producing a green composite adsorbent.

The results of this work show that besides all the advantages, the commercial application of starch/MFC-based composite hydrogels for removal/recovery of copper is also faced with several challenges that need to be addressed before scaling up this technology. Copper removal from aqueous medium by starch/MFC-based hydrogels is limited in successive regeneration cycles and selective sorption of copper. Therefore, to improve reuse, selectivity, and sorption capacity of this system, techniques for the functionalization and modification of the microstructures/hydrogels are necessary. These techniques include organic and inorganic modifications or thermal treatments to obtain adsorbents with greater sorption capacity, selectivity, and stability for reuse. In addition, continuous sorption tests on a fixed-bed column and Life Cycle Assessment are important to investigate the environmental performance for scale-up. Finally, future studies should be focused on investigation of the potential of hydrogels toward copper and other PTMs removal from real effluents.

4. Conclusions

This study demonstrated the potential of corn starch-based composite hydrogels reinforced with microfibrillated cellulose (MFC) derived from eucalyptus residues as sustainable and efficient biosorbents for removing potentially toxic metals, particularly Cu^{2+} , from aqueous solutions. The incorporation of MFC improved the hydrogel's physicochemical properties, including a decrease in solubility from 55.2 % (Starch/MFC-0 %) to 36.4 % (Starch/MFC-5 %) and an increase in true density from 1.466 to 1.525 g/cm^3 . Mercury intrusion porosimetry and nitrogen physisorption confirmed the presence of macroporosity (pores >50 nm), and BET analysis showed a reduction in surface area with MFC addition (from 4.010 to 1.814 m^2/g), attributed to structural compaction. Adsorption tests revealed that Cu^{2+} removal increased from 9.2 % (Starch/MFC-0 %) to 52.4 % (Starch/MFC-5 %), with maximum sorption capacities rising from 0.037 to 0.258 mmol/g . Langmuir isotherm modeling confirmed monolayer adsorption with high correlation ($R^2 = 0.998$), while Dubinin–Radushkevich analysis indicated a transition from physisorption ($E = 2.42$ kJ/mol) to chemisorption ($E = 8.11$ kJ/mol) with increasing MFC content. Regarding kinetics sorption, the equilibrium time ranged from 480 to 780 min, and the PSO model best represented the kinetics data. In addition, Starch/MFC-5 % showed satisfactory regeneration results and can be reused for up to four cycles. These findings emphasize the synergistic role of MFC in enhancing the hydrogel's structural and functional performance and highlight the material's promise as a biodegradable, low-cost platform for metal ion removal in water treatment applications.

CRediT authorship contribution statement

Talles B. da Costa: Writing – review & editing, Writing – original draft, Visualization, Validation, Methodology, Investigation, Formal analysis, Data curation, Conceptualization. **Paulo H. Camani:** Writing – review & editing, Writing – original draft, Methodology, Formal analysis, Data curation. **Rafaela R. Ferreira:** Writing – review & editing, Writing – original draft, Investigation, Formal analysis, Data curation. **Alana G. Souza:** Writing – review & editing, Writing – original draft, Investigation, Formal analysis, Data curation. **Melissa G.A. Vieira:** Writing – review & editing, Validation, Resources. **Derval dos S. Rosa:** Writing – review & editing, Validation, Supervision, Resources, Project administration, Conceptualization.

Declaration of competing interest

The authors declare that they have no known competing financial interests or personal relationships that could have appeared to influence

the work reported in this paper.

Acknowledgments

This study was financed, in part, by Fundação de Amparo à Pesquisa do Estado de São Paulo (FAPESP) (#2019/16301-6, #2020/13703-3, #2021/08296-2, #2022/11133-0, #2022/01382-3, #2023/11783-8, #2023/11229-0, #2024/08105-0, #2024/15696-5), Conselho Nacional de Desenvolvimento Científico e Tecnológico (CNPq) (#308053/2021-4, #403934/2021-4), and Coordenação de Aperfeiçoamento de Pessoal de Nível Superior (CAPES) (Finance Code 001). The authors thank the technical support of the Multiuser Experimental Center of UFABC (CEM-UFABC), CECS (UFABC), and REVALORES for assistance.

Appendix A. Supplementary data

Supplementary data to this article can be found online at <https://doi.org/10.1016/j.ijbiomac.2025.144710>.

Data availability

Data will be made available on request.

References

- [1] L. Zhang, M. Qiao, H. Zheng, T. Vancov, V. Antoniadis, S.M. Shaheen, S. Joseph, C. Chen, S. Shan, H. Chen, H. Wang, Integrating spectroscopic analysis and theoretical calculations to elucidate the adsorption efficiency and mechanisms of Cd, Pb, and Cu using novel carboxymethyl cellulose/pectin-based hydrogel beads, *Int J Biol Macromol* 305 (2025) 141028, <https://doi.org/10.1016/j.ijbiomac.2025.141028>.
- [2] C.M. Justus, A. Pasini, J.A. Raminelli, L.S.A. Gonçalves, A. Celligoi, Chemical elements in the water of the São Pedro river basin, Faxinal - Paraná, *Semin Cienc Agrar* 41 (2020) 743, <https://doi.org/10.5433/1679-0359.2020v41n3p743>.
- [3] Y. Zhang, X. Qi, Q. Ma, J. Li, X. Guo, J. Qiao, Y. Wu, Fluorescent β -cyclodextrin-based hydrogel for enhanced adsorption and fluorescence detection of malachite green, *Sep. Purif. Technol.* 363 (2025) 132065, <https://doi.org/10.1016/j.seppur.2025.132065>.
- [4] M.D. Sharma, P. Gupta, S. Chauhan, R. Panwar, S. Singh, P. Kumar, S. Kulshrestha, Seasonal impact on microbiological quality of drinking water in Solan City of Himachal Pradesh, India, *Environ Monit Assess* 195 (2023) 930, <https://doi.org/10.1007/s10661-023-11510-4>.
- [5] M. Hachaichi, J. Egieya, Water-food-energy Nexus in global cities: addressing complex urban interdependencies, *Water Resour. Manag.* 37 (2023) 1811–1825, <https://doi.org/10.1007/s11269-023-03455-7>.
- [6] I. Farid, M. Abbas, M. Bassouny, A. Gameel, H. Abbas, Indirect impacts of irrigation with low quality water on the environmental safety, *Egypt. J. Soil Sci.* 0 (0) (2019), <https://doi.org/10.21608/ejss.2019.15434.1294>.
- [7] L.A. Savassi, A.L. Paschoalini, F.P. Arantes, E. Rizzo, N. Bazzoli, Heavy metal contamination in a highly consumed Brazilian fish: immunohistochemical and histopathological assessments, *Environ. Monit. Assess.* 192 (2020) 542, <https://doi.org/10.1007/s10661-020-08515-8>.
- [8] N. Morin-Crini, E. Lichtfouse, G. Liu, V. Balaran, A.R.L. Ribeiro, Z. Lu, F. Stock, E. Carmona, M.R. Teixeira, L.A. Picos-Corralles, J.C. Moreno-Piraján, L. Giraldo, C. Li, A. Pandey, D. Hocquet, G. Torri, G. Crini, Worldwide cases of water pollution by emerging contaminants: a review, *Environ. Chem. Lett.* 20 (2022) 2311–2338, <https://doi.org/10.1007/s10311-022-01447-4>.
- [9] M. Liu, L. Zhang, M. Wang, X. Wang, H. Cui, J. Wei, X. Li, The role of metal-organic frameworks in removing emerging contaminants in wastewater, *J. Clean. Prod.* 429 (2023) 139526, <https://doi.org/10.1016/j.jclepro.2023.139526>.
- [10] T.O.M. Lopes, L.S. Passos, L.V. Vieira, E. Pinto, F. Dorr, R. Scherer, N. de Andrade Salustriano, M.T.W.D. Carneiro, L.F. Postay, L.C. Gomes, Metals, arsenic, pesticides, and microcystins in tilapia (*Oreochromis niloticus*) from aquaculture parks in Brazil, *Environ. Sci. Pollut. Res.* 27 (2020) 20187–20200, <https://doi.org/10.1007/s11356-020-08493-x>.
- [11] B.G.K. Steiger, Z. Zhou, Y.A. Anisimov, R.W. Evitts, L.D. Wilson, Valorization of agro-waste biomass as composite adsorbents for sustainable wastewater treatment, *Ind. Crop. Prod.* 191 (2023) 115913, <https://doi.org/10.1016/j.indcrop.2022.115913>.
- [12] G. Li, R. Du, Z. Cao, C. Li, J. Xue, X. Ma, S. Wang, Research Progress in graphene-based adsorbents for wastewater treatment: preparation, adsorption properties and mechanisms for inorganic and organic pollutants, *C (Basel)* 10 (2024) 78, <https://doi.org/10.3390/c10030078>.
- [13] Y. Guo, M. Li, T. Zhou, Q. Wu, C. Liu, S. Li, Q. Feng, H. Wang, Z. Li, Environmentally friendly bacterial cellulose hydrogel-derived aerogel and membrane for efficient water purification, *J. Environ. Chem. Eng.* 13 (2025) 116023, <https://doi.org/10.1016/j.jece.2025.116023>.

- [14] Ó. Barros, L. Costa, F. Costa, A. Lago, V. Rocha, Z. Vipotnik, B. Silva, T. Tavares, Recovery of rare earth elements from wastewater towards a circular economy, *Molecules* 24 (2019) 1–25, <https://doi.org/10.3390/molecules24061005>.
- [15] T. Joensuu, H. Edelman, A. Saari, Circular economy practices in the built environment, *J. Clean. Prod.* 276 (2020) 124215, <https://doi.org/10.1016/j.jclepro.2020.124215>.
- [16] J. Chen, W. Luo, A. Guo, T. Luo, C. Lin, H. Li, L. Jing, Preparation of a novel carboxylate-rich palygorskite as an adsorbent for Ce³⁺ from aqueous solution, *J. Colloid Interface Sci.* 512 (2018) 657–664, <https://doi.org/10.1016/j.jcis.2017.09.107>.
- [17] D.J. da Silva, D.S. Rosa, Chromium removal capability, water resistance and mechanical behavior of foams based on cellulose nanofibrils with citric acid, *Polymer* 253 (2022) 125023, <https://doi.org/10.1016/j.polymer.2022.125023>.
- [18] M.B. de Oliveira Silva, T. B.s da Costa, P.H. Camani, D. dos S. Rosa, Chitosan-based foam composites for hexavalent chromium remediation: effect of microcellulose and crosslinking agent content, *Int. J. Biol. Macromol.* 264 (2024) 130446, <https://doi.org/10.1016/j.ijbiomac.2024.130446>.
- [19] Md.N. Hasan, M.A. Shenashen, Md.M. Hasan, H. Znad, Md.R. Awual, Assessing of cesium removal from wastewater using functionalized wood cellulosic adsorbent, *Chemosphere* 270 (2021) 128668, <https://doi.org/10.1016/j.chemosphere.2020.128668>.
- [20] O. Ogunlalu, I.P. Oyekunle, K.O. Iwuozor, A.D. Aderibigbe, E.C. Emenike, Trends in the mitigation of heavy metal ions from aqueous solutions using unmodified and chemically-modified agricultural waste adsorbents, *Current Research in Green and Sustainable Chemistry* 4 (2021) 100188, <https://doi.org/10.1016/j.crgsc.2021.100188>.
- [21] L.-Y. Long, Y.-X. Weng, Y.-Z. Wang, Cellulose aerogels: synthesis, applications, and prospects, *Polymers (Basel)* 10 (2018) 623, <https://doi.org/10.3390/polym10060623>.
- [22] Y. Guo, J. Bae, Z. Fang, P. Li, F. Zhao, G. Yu, Hydrogels and hydrogel-derived materials for energy and water sustainability, *Chem. Rev.* 120 (2020) 7642–7707, <https://doi.org/10.1021/acs.chemrev.0c00345>.
- [23] P.H. Camani, C.D. Midhun Dominic, D.F. Parra, H.F. Maltez, D.S. Rosa, Divalent metal ion removal from simulated water using sustainable starch aerogels: effect of crosslinking agent concentration and sorption conditions, *Int. J. Biol. Macromol.* 226 (2023) 628–645, <https://doi.org/10.1016/j.ijbiomac.2022.11.308>.
- [24] L. Weerasundara, B. Gabriele, A. Figoli, Y.-S. Ok, J. Bundschuh, Hydrogels: novel materials for contaminant removal in water—a review, *Crit. Rev. Environ. Sci. Technol.* 51 (2021) 1970–2014, <https://doi.org/10.1080/10643389.2020.1776055>.
- [25] Z. Al-Qodah, M.A. Yahya, M. Al-Shannag, On the performance of bioadsorption processes for heavy metal ions removal by low-cost agricultural and natural by-products bioadsorbent: a review, *Desalination. Water Treat.* 85 (2017) 339–357, <https://doi.org/10.5004/dwt.2017.21256>.
- [26] M. Yalpani, *Polysaccharides: syntheses, modifications and structure/property relations*, First edition, 1988. Senneville, Quebec, Canada.
- [27] F.I. Chowdhury, M.R. Rahman, J. Islam, Cellulose-based foaming materials, in: *Fundamentals and Recent Advances in Nanocomposites Based on Polymers and Nanocellulose*, Elsevier, 2022, pp. 207–242, <https://doi.org/10.1016/B978-0-323-85771-0.00002-6>.
- [28] L. Costes, F. Laoutid, S. Brohez, P. Dubois, Bio-based flame retardants: when nature meets fire protection, *Mater. Sci. Eng. R. Rep.* 117 (2017) 1–25, <https://doi.org/10.1016/j.mser.2017.04.001>.
- [29] U. Upadhyay, I. Sreedhar, S.A. Singh, C.M. Patel, K.L. Anitha, Recent advances in heavy metal removal by chitosan-based adsorbents, *Carbohydr. Polym.* 251 (2021) 117000, <https://doi.org/10.1016/j.carbpol.2020.117000>.
- [30] H. Kargazadeh, M. Mariano, D. Gopakumar, I. Ahmad, S. Thomas, A. Dufresne, J. Huang, N. Lin, Advances in cellulose nanomaterials, *Cellulose* 25 (2018) 2151–2189, <https://doi.org/10.1007/s10570-018-1723-5>.
- [31] X. Luo, J. Zeng, S. Liu, L. Zhang, An effective and recyclable adsorbent for the removal of heavy metal ions from aqueous system: magnetic chitosan/cellulose microspheres, *Bioresour. Technol.* 194 (2015) 403–406, <https://doi.org/10.1016/j.biortech.2015.07.044>.
- [32] R. Reshmy, E. Philip, A. Madhavan, A. Pugazhendhi, R. Sindhu, R. Sirohi, M. K. Awasthi, A. Pandey, P. Binod, Nanocellulose as green material for remediation of hazardous heavy metal contaminants, *J. Hazard. Mater.* 424 (2022) 127516, <https://doi.org/10.1016/j.jhazmat.2021.127516>.
- [33] A.A. Salehi, M. Ghannadi-Maragheh, M. Torab-Mostaedi, R. Torkaman, M. Asadolahzadeh, Hydrogel materials as an emerging platform for desalination and the production of purified water, *Sep. Purif. Rev.* 50 (2021) 380–399, <https://doi.org/10.1080/15422119.2020.1789659>.
- [34] I.H. Alsohaimi, M.S. Alhumaimess, H.M.A. Hassan, M. Reda, A.M. Aldawsari, Q. Chen, M.A. Kariri, Chitosan polymer functionalized-activated carbon/montmorillonite composite for the potential removal of Lead ions from wastewater, *Polymers (Basel)* 15 (2023) 2188, <https://doi.org/10.3390/polym15092188>.
- [35] A.D. Gupta, K.P. Rawat, V. Bhaduria, H. Singh, Recent trends in the application of modified starch in the adsorption of heavy metals from water: a review, *Carbohydr. Polym.* 269 (2021) 117763, <https://doi.org/10.1016/j.carbpol.2021.117763>.
- [36] L. Joseph, B.-M. Jun, J.R.V. Flora, C.M. Park, Y. Yoon, Removal of heavy metals from water sources in the developing world using low-cost materials: a review, *Chemosphere* 229 (2019) 142–159, <https://doi.org/10.1016/j.chemosphere.2019.04.198>.
- [37] J. Xu, X. Tan, L. Chen, X. Li, F. Xie, Starch/microcrystalline cellulose hybrid gels as gastric-floating drug delivery systems, *Carbohydr. Polym.* 215 (2019) 151–159, <https://doi.org/10.1016/j.carbpol.2019.03.078>.
- [38] S.C. Mamah, P.S. Goh, B.C. Ng, M.S. Abdullah, A.F. Ismail, Z. Samavati, N. A. Ahmad, Y.O. Raji, The utilization of chitin and chitosan as green modifiers in nanocomposite membrane for water treatment, *Journal of Water Process Engineering* 62 (2024) 105394, <https://doi.org/10.1016/j.jwpe.2024.105394>.
- [39] Michael Jacob Ioelovich, Microcellulose Vs Nanocellulose – A Review, *World Journal of Advanced Engineering Technology and Sciences* 5 (2022) 001–015, <https://doi.org/10.30574/wjaets.2022.5.2.0037>.
- [40] A.A.B. Omran, A.A.B.A. Mohammed, S.M. Sapuan, R.A. Ilyas, M.R.M. Asyraf, S. S. Rahimian Koloor, M. Petrù, Micro- and nanocellulose in polymer composite materials: a review, *Polymers (Basel)* 13 (2021) 231, <https://doi.org/10.3390/polym13020231>.
- [41] A. Sharma, M. Thakur, M. Bhattacharya, T. Mandal, S. Goswami, Commercial application of cellulose nano-composites – a review, *Biotechnology Reports* 21 (2019) e00316, <https://doi.org/10.1016/j.btre.2019.e00316>.
- [42] S.S. Ahankari, A.R. Subhedar, S.S. Bhaduria, A. Dufresne, Nanocellulose in food packaging: a review, *Carbohydr. Polym.* 255 (2021) 117479, <https://doi.org/10.1016/j.carbpol.2020.117479>.
- [43] I.O. Saheed, W. Da Oh, F.B.M. Suah, Chitosan modifications for adsorption of pollutants – a review, *J. Hazard. Mater.* 408 (2021) 124889, <https://doi.org/10.1016/j.jhazmat.2020.124889>.
- [44] R.R. Ferreira, A.G. Souza, L.L. Nunes, N. Shahi, V.K. Rangari, D. dos S. Rosa, Use of ball mill to prepare nanocellulose from eucalyptus biomass: challenges and process optimization by combined method, *Mater. Today Commun.* 22 (2020) 100755, <https://doi.org/10.1016/j.mtcomm.2019.100755>.
- [45] A.G. de Souza, M.T. Junqueira, G.F. de Lima, V.K. Rangari, D.S. Rosa, A new proposal of preparation of different polymorphs of Nanocellulose from Eucalyptus citriodora, *J. Polym. Environ.* 28 (2020) 1150–1159, <https://doi.org/10.1007/s10924-020-01672-4>.
- [46] P.H. Camani, M.G.M. Gonçalo, R.F.S. Barbosa, D.S. Rosa, Comprehensive insight of crosslinking agent concentration influence on starch-based aerogels porous structure, *J. Appl. Polym. Sci.* 138 (2021) 50863, <https://doi.org/10.1002/app.50863>.
- [47] G.M. Baggio, P.H. Camani, D.S. Rosa, Concentration and carbon chain length effects of cationic surfactant in enzymatic production of cellulose nanostructures, *J. Mol. Liq.* 346 (2022) 118231, <https://doi.org/10.1016/j.molliq.2021.118231>.
- [48] L. Segal, J.J. Creely, A.E. Martin, C.M. Conrad, An empirical method for estimating the degree of crystallinity of native cellulose using the X-ray diffractometer, *Text. Res. J.* 29 (1959) 786–794, <https://doi.org/10.1177/004051755902901003>.
- [49] D.F. Alves, P.H. Camani, A.G. Souza, D.S. Rosa, A novel sustainable composite hydrogel containing nanocellulose to remove potentially toxic metals from contaminated water, *Polym. Bull.* (2023), <https://doi.org/10.1007/s00289-023-04986-0>.
- [50] I. Langmuir, The adsorption of gases on plane surfaces of glass, mica and platinum, *J. Am. Chem. Soc.* 40 (1918) 1361–1403, <https://doi.org/10.1021/ja02242a004>.
- [51] H.M.F. Freundlich, Over the adsorption in solution, *J. Phys. Chem.* 57 (1906) 385–471.
- [52] M.M. Dubinin, L.V. Radushkevich, Equation of the characteristic curve of activated charcoal, *Proc. Acad. Sci. USSR, Phys. Chem. Sect.* 55 (1947) 331–333.
- [53] P. Bonate, J.-L. Steimer, *Pharmacokinetics pharmacodynamics modeling simulation*, Springer, San Antonio, Texas, TX, USA, 2011.
- [54] J. Zhang, B. Liu, Y. Wang, P. Pan, S. Song, L. Yu, Effect of cellulose fibers on the structure, rheological and 3D printing properties of corn starch-based hydrogel ink, *Int. J. Biol. Macromol.* 306 (2025) 141443, <https://doi.org/10.1016/j.ijbiomac.2025.141443>.
- [55] L.B. dos Santos, T.A. Moreira, C.J. Dalmaschio, M.A. Machado, Preparação de biocompósito à base de amido termoplástico reforçado com fibras de eucalipto: avaliação do efeito do tamanho das fibras nas propriedades mecânicas e de sorção, *Quim Nova* (2024), <https://doi.org/10.21577/0100-4042.20240074>.
- [56] T. Hong, J.-Y. Yin, S.-P. Nie, M.-Y. Xie, Applications of infrared spectroscopy in polysaccharide structural analysis: Progress, challenge and perspective, *Food Chem X* 12 (2021) 100168, <https://doi.org/10.1016/j.fochx.2021.100168>.
- [57] F. Mohammadzadeh, M. Golshan, V. Haddadi-Asl, M. Salami-Kalajahi, Adsorption kinetics of methylene blue from wastewater using pH-sensitive starch-based hydrogels, *Sci. Rep.* 13 (2023) 11900, <https://doi.org/10.1038/s41598-023-39241-z>.
- [58] I.M. Lipatova, A.A. Yusova, Effect of mechanical activation on starch crosslinking with citric acid, *Int. J. Biol. Macromol.* 185 (2021) 688–695, <https://doi.org/10.1016/j.ijbiomac.2021.06.139>.
- [59] P. Sánchez-Cid, G. González-Ulloa, M. Alonso-González, M. Jiménez-Rosado, M. Rafii-El-Idrissi Benhnia, A. Romero, F.J. Ostos, V.M. Perez-Puyana, Influence of natural Crosslinkers on chitosan hydrogels for potential biomedical applications, *Macromol. Mater. Eng.* 308 (2023), <https://doi.org/10.1002/mame.202300195>.
- [60] Y. Xie, M.-N. Li, H.-Q. Chen, B. Zhang, Effects of the combination of repeated heat-moisture treatment and compound enzymatic hydrolysis on the structural and physicochemical properties of porous wheat starch, *Food Chem.* 274 (2019) 351–359, <https://doi.org/10.1016/j.foodchem.2018.09.034>.
- [61] M.I. Cruz-Balaz, M.F. Bósquez-Cáceres, A.D. Delgado, N. Arjona, V. Morera Córdova, L. Álvarez-Contreras, J.P. Tafur, Green energy storage: chitosan-avocado starch hydrogels for a novel generation of zinc battery electrolytes, *Polymers (Basel)* 15 (2023) 4398, <https://doi.org/10.3390/polym15224398>.

- [62] M. Szymańska-Chargot, J. Cybulska, A. Zdunek, Sensing the structural differences in cellulose from apple and bacterial Cell Wall materials by Raman and FT-IR spectroscopy, *Sensors* 11 (2011) 5543–5560, <https://doi.org/10.3390/s110605543>.
- [63] H. Liu, F. Xie, L. Yu, L. Chen, L. Li, Thermal processing of starch-based polymers, *Prog. Polym. Sci.* 34 (2009) 1348–1368, <https://doi.org/10.1016/j.progpolymsci.2009.07.001>.
- [64] G. Kowalski, P. Ptaszek, E. Luterasiński, Swelling of hydrogels based on Carboxymethylated starch and poly(acrylic acid): nonlinear rheological approach, *Polymers (Basel)* 12 (2020) 2564, <https://doi.org/10.3390/polym12112564>.
- [65] G. Lozano-Vazquez, J. Alvarez-Ramirez, C. Lobato-Calleros, E.J. Vernon-Carter, N.Y. Hernández-Marín, Characterization of corn starch-calcium alginate Xerogels by microscopy, thermal, XRD, and FTIR analyses, *Starch - Stärke* 73 (2021), <https://doi.org/10.1002/star.202000282>.
- [66] A. Bora, D. Sarmah, N. Karak, Cellulosic wastepaper modified starch/ itaconic acid/ acrylic acid-based biodegradable hydrogel as a sustain release of NPK fertilizer vehicle for agricultural applications, *Int. J. Biol. Macromol.* 253 (2023) 126555, <https://doi.org/10.1016/j.ijbiomac.2023.126555>.
- [67] A. Bora, D. Sarmah, M.A. Rather, M. Mandal, N. Karak, Nanocomposite of starch, gelatin and itaconic acid-based biodegradable hydrogel and ZnO/cellulose nanofiber: a pH-sensitive sustained drug delivery vehicle, *Int. J. Biol. Macromol.* 256 (2024) 128253, <https://doi.org/10.1016/j.ijbiomac.2023.128253>.
- [68] P.H. Camani, M.G.M. Gonçalves, R.F.S. Barbosa, D.S. Rosa, Comprehensive insight of crosslinking agent concentration influence on starch-based aerogels porous structure, *J. Appl. Polym. Sci.* 138 (2021) 50863, <https://doi.org/10.1002/app.50863>.
- [69] N. Abhari, A. Madadiou, A. Dini, Structure of starch aerogel as affected by crosslinking and feasibility assessment of the aerogel for an anti-fungal volatile release, *Food Chem.* 221 (2017) 147–152, <https://doi.org/10.1016/j.foodchem.2016.10.072>.
- [70] A. Olad, F. Doustdar, H. Gharekhani, Fabrication and characterization of a starch-based superabsorbent hydrogel composite reinforced with cellulose nanocrystals from potato peel waste, *Colloids Surf. A Physicochem. Eng. Asp.* 601 (2020) 124962, <https://doi.org/10.1016/j.colsurfa.2020.124962>.
- [71] A.G. Souza, R.R. Ferreira, L.C. Paula, S.K. Mitra, D.S. Rosa, Starch-based films enriched with nanocellulose-stabilized Pickering emulsions containing different essential oils for possible applications in food packaging, *Food Packag. Shelf Life* 27 (2021) 100615, <https://doi.org/10.1016/j.fpsl.2020.100615>.
- [72] M.M. González-Pérez, M.G. Lomeli-Ramírez, J.R. Robledo-Ortiz, J.A. Silva-Guzmán, R. Manríquez-González, Biodegradable biocomposite of starch films cross-linked with polyethylene glycol Diglycidyl ether and reinforced by microfibrillated cellulose, *Polymers (Basel)* 16 (2024) 1290, <https://doi.org/10.3390/polym16091290>.
- [73] K. Thinkohkaew, N. Rodthongkum, S. Ummartyotin, Coconut husk (Cocos nucifera) cellulose reinforced poly vinyl alcohol-based hydrogel composite with control-release behavior of methylene blue, *J. Mater. Res. Technol.* 9 (2020) 6602–6611, <https://doi.org/10.1016/j.jmrt.2020.04.051>.
- [74] G.G. de Lima, B.D. Ferreira, M. Matos, B.L.D. Nugent, F.A. Hansel, W.L.E. Magalhães, Effect of cellulose size-concentration on the structure of polyvinyl alcohol hydrogels, *Carbohydr. Polym.* 245 (2020) 116612, <https://doi.org/10.1016/j.carbpol.2020.116612>.
- [75] K. Hu, P. He, Z. Zhao, L. Huang, K. Liu, S. Lin, M. Zhang, H. Wu, L. Chen, Y. Ni, Nature-inspired self-powered cellulose nanofibrils hydrogels with high sensitivity and mechanical adaptability, *Carbohydr. Polym.* 264 (2021) 117995, <https://doi.org/10.1016/j.carbpol.2021.117995>.
- [76] J.Q. Pereira, A. Ambrosini, L.M.P. Passaglia, A. Brandelli, A new cold-adapted serine peptidase from Antarctic *Lysobacter* sp. A03: insights about enzyme activity at low temperatures, *Int. J. Biol. Macromol.* 103 (2017) 854–862, <https://doi.org/10.1016/j.ijbiomac.2017.05.142>.
- [77] A.A. Keirudin, N. Zainuddin, N.A. Yusof, Crosslinked Carboxymethyl sago starch/ citric acid hydrogel for sorption of Pb²⁺, Cu²⁺, Ni²⁺ and Zn²⁺ from aqueous solution, *Polymers (Basel)* 12 (2020) 2465, <https://doi.org/10.3390/polym12112465>.
- [78] C. Chartier, S. Buwalda, H. Van Den Bergh, B. Nottelet, T. Budtova, Tuning the properties of porous chitosan: aerogels and cryogels, *Int. J. Biol. Macromol.* 202 (2022) 215–223, <https://doi.org/10.1016/j.ijbiomac.2022.01.042>.
- [79] X. Zhang, W. Megone, T. Peijs, J.E. Gautrot, Functionalization of electrospun PLA fibers using amphiphilic block copolymers for use in carboxy-methyl-cellulose hydrogel composites, *Nanocomposites* 6 (2020) 85–98, <https://doi.org/10.1080/20550324.2020.1784600>.
- [80] M. Aliabadi, B.S. Chee, M. Matos, Y.J. Cortese, M.J.D. Nugent, T.A.M. de Lima, W. L.E. Magalhães, G.G. de Lima, Yerba mate extract in microfibrillated cellulose and corn starch films as a potential wound healing bandage, *Polymers (Basel)* 12 (2020) 2807, <https://doi.org/10.3390/polym12122807>.
- [81] C. Chen, L. Zong, J. Wang, J. Xie, Microfibrillated cellulose reinforced starch/ polyvinyl alcohol antimicrobial active films with controlled release behavior of cinnamaldehyde, *Carbohydr. Polym.* 272 (2021) 118448, <https://doi.org/10.1016/j.carbpol.2021.118448>.
- [82] C. Spagnol, F.H.A. Rodrigues, A.G.B. Pereira, A.R. Fajardo, A.F. Rubira, E. C. Muniz, Superabsorbent hydrogel composite made of cellulose nanofibrils and chitosan-graft-poly(acrylic acid), *Carbohydr. Polym.* 87 (2012) 2038–2045, <https://doi.org/10.1016/j.carbpol.2011.10.017>.
- [83] I.A. Duceac, L. Verestiuc, C.D. Dimitriu, V. Maier, S. Coseri, Design and preparation of new multifunctional hydrogels based on chitosan/acrylic polymers for drug delivery and wound dressing applications, *Polymers (Basel)* 12 (2020) 1473, <https://doi.org/10.3390/polym12071473>.
- [84] C. Ma, F. Xie, L. Wei, C. Zheng, X. Liu, L. Wang, P. Liu, All-starch-based hydrogel for flexible electronics: strain-sensitive batteries and self-powered sensors, *ACS Sustain. Chem. Eng.* 10 (2022) 6724–6735, <https://doi.org/10.1021/acssuschemeng.2c00872>.
- [85] F.H.A. Rodrigues, C. Spagnol, A.G.B. Pereira, A.F. Martins, A.R. Fajardo, A. F. Rubira, E.C. Muniz, Superabsorbent hydrogel composites with a focus on hydrogels containing nanofibers or nanowhiskers of cellulose and chitin, *J. Appl. Polym. Sci.* 131 (2014), <https://doi.org/10.1002/app.39725>.
- [86] N. Kumar, B. Kumar, H. Gupta, A. Kumar, Development and evaluation of cellulose/graphene-oxide based composite for removing phenol from aqueous solutions, *Polymers (Basel)* 15 (2023) 572, <https://doi.org/10.3390/polym15030572>.
- [87] Y. Feng, J. Yin, S. Liu, Y. Wang, B. Li, T. Jiao, Facile synthesis of ag/Pd nanoparticle - loaded poly(ethylene imine) composite hydrogels with highly efficient catalytic reduction of 4-Nitrophenol, *ACS Omega* 5 (2020) 3725–3733, <https://doi.org/10.1021/acsomega.9b04408>.
- [88] T.B. Costa, M.G.C. Silva, M.G.A. Vieira, Development of a natural polymeric bioadsorbent based on sericin, alginate and poly(vinyl alcohol) for the recovery of ytterbium from aqueous solutions, *J. Clean. Prod.* 279 (2021) 123555, <https://doi.org/10.1016/j.jclepro.2020.123555>.
- [89] K.S.W. Sing, Reporting physisorption data for gas/solid systems with special reference to the determination of surface area and porosity (recommendations 1984), *Pure Appl. Chem.* 57 (1985) 603–619, <https://doi.org/10.1351/pac198557040603>.
- [90] M. Thommes, K. Kaneko, A.V. Neimark, J.P. Olivier, F. Rodriguez-Reinoso, J. Rouquerol, K.S.W. Sing, Physisorption of gases, with special reference to the evaluation of surface area and pore size distribution (IUPAC technical report), *Pure Appl. Chem.* 87 (2015) 1051–1069, <https://doi.org/10.1515/pac-2014-1117>.
- [91] J. Wang, C. Chen, Biosorbents for heavy metals removal and their future, *Biotechnol. Adv.* 27 (2009) 195–226, <https://doi.org/10.1016/j.biotechadv.2008.11.002>.
- [92] V.K. Gupta, A. Rastogi, Biosorption of hexavalent chromium by raw and acid-treated green alga *Oedogonium* hatei from aqueous solutions, *J. Hazard. Mater.* 163 (2009) 396–402, <https://doi.org/10.1016/j.jhazmat.2008.06.104>.
- [93] A.Z.M. Badruddoza, Z.B.Z. Shawon, W.J.D. Tay, K. Hidajat, M.S. Uddin, Fe3O4/cyclodextrin polymer nanocomposites for selective heavy metals removal from industrial wastewater, *Carbohydr. Polym.* 91 (2013) 322–332, <https://doi.org/10.1016/j.carbpol.2012.08.030>.
- [94] C. Zhu, I. Dobryden, J. Rydén, S. Öberg, A. Holmgren, A.P. Mathew, Adsorption behavior of cellulose and its derivatives toward ag(I) in aqueous medium: an AFM, spectroscopic, and DFT study, *Langmuir* 31 (2015) 12390–12400, <https://doi.org/10.1021/acs.langmuir.5b03228>.
- [95] L. Gao, H. Luo, Q. Wang, G. Hu, Y. Xiong, Synergistic effect of hydrogen bonds and chemical bonds to construct a starch-based water-absorbing/retaining hydrogel composite reinforced with cellulose and poly(ethylene glycol), *ACS Omega* 6 (2021) 35039–35049, <https://doi.org/10.1021/acsomega.1c05614>.
- [96] M. Akter, M. Bhattacharjee, A.K. Dhar, F.B.A. Rahman, S. Haque, T.U. Rashid, S. M.F. Kabir, Cellulose-based hydrogels for wastewater treatment: a concise review, *Gels* 7 (2021) 30, <https://doi.org/10.3390/gels7010030>.
- [97] A. Daochalermwong, N. Chanka, K. Songsrirrote, P. Dittanet, C. Niamnyu, A. Seubsai, Removal of heavy metal ions using modified celluloses prepared from pineapple leaf Fiber, *ACS Omega* 5 (2020) 5285–5296, <https://doi.org/10.1021/acsomega.9b04326>.
- [98] T.W. Cheng, M.L. Lee, M.S. Ko, T.H. Ueng, S.F. Yang, The heavy metal adsorption characteristics on metakaolin-based geopolymer, *Appl. Clay Sci.* 56 (2012) 90–96, <https://doi.org/10.1016/j.clay.2011.11.027>.
- [99] V.B.H. Dang, H.D. Doan, T. Dang-Vu, A. Lohi, Equilibrium and kinetics of biosorption of cadmium(II) and copper(II) ions by wheat straw, *Bioresour. Technol.* 100 (2009) 211–219, <https://doi.org/10.1016/j.biortech.2008.05.031>.
- [100] T.L. da Silva, A.C. da Silva, M.G.A. Vieira, M.L. Gimenes, M.G.C. da Silva, Biosorption study of copper and zinc by particles produced from silk sericin – alginate blend: evaluation of blend proportion and thermal cross-linking process in particles production, *J. Clean. Prod.* 137 (2016) 1470–1478, <https://doi.org/10.1016/j.jclepro.2015.05.067>.
- [101] A.F. de Almeida Neto, M.G.A. Vieira, M.G.C. da Silva, Cu(II) adsorption on modified bentonitic clays: different isotherm behaviors in static and dynamic systems, *Mater. Res.* 15 (2011) 114–124, <https://doi.org/10.1590/S1516-14392011005000089>.
- [102] I.H. Alshohaimi, A.N. Alrashidi, H.M.A. Hassan, Q. Chen, Highly efficient ultrafiltration membrane performance of PES@microcrystalline cellulose extracted from waste fruits for the removal of BrO₃⁻ from drinking water samples, *Colloid Interface Sci. Commun.* 54 (2023) 100718, <https://doi.org/10.1016/j.colcom.2023.100718>.
- [103] I.H. Alshohaimi, M.S. Alhumaimess, H.M.A. Hassan, M. Reda, A.M. Aldawsari, Q. Chen, M.A. Kariri, Chitosan polymer functionalized-activated carbon/montmorillonite composite for the potential removal of Lead ions from wastewater, *Polymers* 15 (2023) 2188, <https://doi.org/10.3390/polym15092188>.
- [104] T.B. da Costa, P.H. Camani, R.R. Ferreira, R.F.S. Barbosa, D.S. Rosa, Enhancing corn starch hydrogels for effective sorption of potentially toxic metals: the role of amylose and amylopectin content, *J. Polym. Environ.* 33 (2025) 1615–1635, <https://doi.org/10.1007/s10924-025-03495-7>.

- [105] J. Tan, L. Kong, J. Fang, X. Liang, Y. Yin, Synthesis of a starch-composite magnetic material modified with polyethyleneimine for enhanced adsorption of diclofenac sodium, methyl orange, Amaranth, and hexavalent chromium, *Environmental Advances* 15 (2024) 100489, <https://doi.org/10.1016/j.envadv.2024.100489>.
- [106] H. Al-Aidy, E. Amdeha, Green adsorbents based on polyacrylic acid-acrylamide grafted starch hydrogels: the new approach for enhanced adsorption of malachite green dye from aqueous solution, *Int. J. Environ. Anal. Chem.* 101 (2021) 2796–2816, <https://doi.org/10.1080/03067319.2020.1711896>.
- [107] P.H.F. Pereira, A.I.C. da Silva, R.F.S. Barbosa, V. Arantes, D.R. Mulinari, D. S. Rosa, Insights in the adsorption of eco-friendly starch hydrogel, *Adsorption* 30 (2024) 1685–1702, <https://doi.org/10.1007/s10450-024-00509-z>.
- [108] T.B. Costa, P.M.C. Matias, M. Sharma, D. Murtinho, D.S. Rosa, A.J.M. Valente, Recent advances on starch-based adsorbents for heavy metal and emerging pollutant remediation, *Polymers* 17 (2025) 15, <https://doi.org/10.3390/polym17010015>.



Deconstruction of sisal lignocellulosic fibers by cupriethylenediamine hydroxide: creating hydrogels from cellulose, hemicelluloses, and lignin to assess their potential for heavy metal sorption

Giani de Vargas Brião^a, Bianca Groner Queiroz^a, Rafaela Reis Ferreira^b,
Derval dos Santos Rosa^b, Elisabete Frollini^{a,*}

^a Macromolecular Materials and Lignocellulosic Fibers Group, Center for Research on Science and Technology of BioResources, São Carlos Institute of Chemistry, University of São Paulo (USP), São Carlos 13566-590, Brazil

^b Center for Engineering, Modeling, and Applied Social Sciences - CECS, Federal University of ABC (UFABC), Santo André 09210-580, Brazil

ARTICLE INFO

Keywords:

CUEN deconstructing lignocellulosic fibers
Sisal lignocellulosic hydrogel
Water sorption
Heavy metal sorption

ABSTRACT

Developing bio-based hydrogels offers a sustainable alternative to traditional fossil-based materials in wastewater treatment, particularly for absorbing heavy metals. This study focused on creating hydrogels from the components of sisal fibers, specifically cellulose (around 59 %), hemicelluloses (29 %), and lignin (12 %), through a deconstruction process using cupriethylenediamine hydroxide (CUEN) as the solvent and water as the coagulation medium. CUEN deconstructed 1 g and 2 g of sisal fibers; in total mass, the dissolution efficiency achieved was 73.7 % (cellulose and hemicelluloses) and 52.4 %, respectively. Lignin remained suspended in the medium alongside fractions of hemicelluloses and cellulose. Macromolecules dissolved and suspended in the medium were incorporated into the hydrogels. The hydrogel made from 1 g of sisal showed a higher water sorption capacity (5076.4 %). Meanwhile, the one created using 2 g of sisal demonstrated superior crystallinity, compression, and rheological properties, with a compressive elastic modulus of 62.4 kPa and a shear storage modulus of 416.8 kPa. Sisal_2_hydro also presented higher BET surface area and pore volume, enabling them to reach sorption capacities of up to 0.41 mmol/g for heavy metals, specifically Cu(II), Ni(II), Zn(II), Cd(II), Mn(II), and Cr(VI). The deconstruction of sisal fibers successfully produced hydrogels that demonstrated potential for sorbing heavy metals.

1. Introduction

Developing and implementing efficient wastewater treatment technologies is crucial for addressing this issue and protecting public health and environmental integrity. The current focus is on cutting-edge technologies and materials, including photocatalysis, electro dialysis, and innovative biosorbents [1–3]. Sorption has been extensively researched due to its cost-effectiveness, high efficiency, ease of implementation and operation, utilization of various sorbent materials, and the potential for recovering both the sorbent and the sorbate. In recent decades, extensive research has focused on various sorbents for removing metals from industrial wastewater. These include zeolites, clays, metal-organic frameworks, carbon-based sorbents such as graphene, graphene oxide, carbon nanotubes, activated carbon, magnetic nanoparticles, and biosorbents.

Biosorbents, including materials such as algae (both freshwater and marine types), fungi, bacteria, industrial and agricultural waste, and plant polysaccharides, have garnered attention for their sustainability and their role in enhancing biomasses within a zero-waste and closed carbon loop framework. This holds significant implications for waste management and environmental sustainability [4,5]. These biosorbents have been proposed to address key issues in the sorption of toxic metals, including sustainability, selectivity towards target high-valued metals, and stability, thereby promoting the cyclic use of the sorbents [6,7]. Additionally, they presented an inherent challenge for the adsorption field related to overall economics, as the cost of adsorbent accounts for approximately 70 % of the total cost [8].

In a circular bioeconomy scenario, there are significant opportunities for exploration and innovation, particularly with plant-based biopolymer sorbents. Among bio-based products, hydrogels -

* Corresponding author.

E-mail address: elisabete@iqsc.usp.br (E. Frollini).

<https://doi.org/10.1016/j.ijbiomac.2025.146480>

Received 22 March 2025; Received in revised form 20 July 2025; Accepted 30 July 2025

Available online 31 July 2025

0141-8130/© 2025 Elsevier B.V. All rights reserved, including those for text and data mining, AI training, and similar technologies.

hydrophilic 3D polymer networks capable of retaining large amounts of water [9,10] - have garnered significant attention across various applications, including wastewater remediation [11,12]. These materials are valued for their physicochemical properties, flexibility, softness, biodegradability, and biocompatibility [13]. Additionally, bio-based hydrogels, incorporating cellulose, lignin, starch, alginate, and similar components, offer the advantage of accelerated biodegradation compared to synthetic alternatives [14,15]. Despite all these advantages of using bio-based hydrogels, their application as biosorbents still needs some enhancement in their properties, such as mechanical stability. [16,17].

Cellulose-based hydrogels offer exceptional potential due to the widespread availability of this polysaccharide, the most abundant naturally occurring glucose polymer in plants and their fibers [18,19]. Lignocellulosic biomasses, particularly non-woody ones [20], provide cost-effective raw materials from agriculture that can sustainably fulfill the global demand for cellulose [17]. Non-woody biomasses such as flax, hemp, jute, sisal, kenaf, and coir exemplify plant fibers with significant exploitable potential [21]. However, cellulose-based hydrogels have usually been done using commercial cellulose, *i.e.*, cellulose with a high level of purity, refined and separated from hemicelluloses and lignin, which means higher cost of production, higher consumption of chemicals, and higher generation of waste and effluents than the use of lignocellulosic biomass as a direct source of cellulose, especially if all the macromolecules that compose it are integrated into the hydrogel [17,20,22].

Sisal, scientifically known as *Agave sisalana* (Fig. 1), is a resilient plant well-suited to hot and arid environments. It can be harvested approximately two years after planting and has a productive lifespan of up to 10 years [23]. According to the Food and Agriculture Organization (FAO), global sisal production in 2022 was reported to be 239.5 thousand tons [24]. Sisal is inedible [25] and is distinguished from many lignocellulosic fibers by having a high cellulose content, estimated at around 60 % [26].

Despite the widespread availability and affordability of cellulose-rich sources, integrating cellulose into hydrogel production poses challenges due to the inherent difficulty of its dissolution. Cellulose, a biopolymer consisting of D-glucose monomers linked by β -1,4-glycosidic bonds [27], is rich in hydroxyl groups that establish both inter- and intramolecular hydrogen bonds as well as van der Waals interactions [28]. This robust network confers cellulose's strong stability and low solubility in water and many other solvents.

In the field of sisal fiber cellulosic pulps, various solvents have been utilized to improve the dissolution of cellulose after the removal of lignin and hemicelluloses. Notable examples of these solvents include lithium chloride combined with N,N dimethylacetamide (LiCl/DMAC)

[29,30], dimethyl sulfoxide/tetrabutylammonium fluoride [31], NaOH/thiourea [32,33], and ionic liquids [34,35]. Besides the mentioned solvents, there is also a class of solvents comprising aqueous solutions of metal complexes, in which cupriethylenediamine hydroxide (CUEN) is a non-derivatizing solvent widely recognized for its application in determining cellulose's average viscometric molar mass [36].

The creation of lignocellulose-based hydrogels directly from biomass, rather than analytical-grade cellulose or lignin, is scarce. Consequently, the use of these hydrogels for recovering heavy metals remains at the forefront of knowledge. Thus, the present study focused on deconstructing lignocellulosic sisal fibers using CUEN, on the formation of a hydrogel from all the macromolecular components of lignocellulosic sisal fibers (Fig. 1), and its application for the removal of toxic metals.

This study aimed to promote the value of an alternative non-woody biomass, using a non-derivatizing solvent in a direct method for sisal deconstruction, and preparing lignocellulosic hydrogels through a simple solvent inversion process. It also highlights the potential of an innovative material, a lignocellulosic hydrogel, as a biosorbent for treating toxic metal-contaminated wastewater. As far as is known, this investigation employed an approach that sets it apart from others reported.

2. Materials and methods

2.1. Materials

2.1.1. Hydrogel formation

Sisal Sul Indústria e Comércio Ltda (São Paulo, SP, Brazil) supplied sisal fibers composed of cellulose ($58.7 \pm 1.5\%$), hemicelluloses ($29.0 \pm 0.7\%$), lignin ($12.0 \pm 0.4\%$), ash ($1.2 \pm 0.0\%$), and moisture ($8.7 \pm 0.2\%$) [26,37]. For the deconstruction of the sisal fiber, the solvent was bis(ethylenediamine)copper(II) hydroxide solution (CUEN) (1 M, Êxodo Científica, Sumaré, SP, Brazil). The fibers and CUEN were used as received. Templates used to create hydrogels consisted of polystyrene 24-well plates with flat bottoms (Nest Biotechnology Co., Ltd.).

2.1.2. Sorption analysis

Hydrochloric acid (P.A. - ACS) was from Synth, Brazil. The salts used for the stock solutions of the toxic metals are zinc nitrate hexahydrate ($\text{Zn}(\text{NO}_3)_2 \cdot 6\text{H}_2\text{O}$, 98 %, Dinâmica Química Contemporânea® Ltda, Brazil), nickel nitrate hexahydrate ($\text{Ni}(\text{NO}_3)_2 \cdot 6\text{H}_2\text{O}$, 98 %, Dinâmica Química Contemporânea® Ltda, Brazil), cadmium nitrate tetrahydrate ($\text{Cd}(\text{NO}_3)_2 \cdot 4\text{H}_2\text{O}$, 98 %, Neon Chemistry), potassium dichromate ($\text{K}_2\text{Cr}_2\text{O}_7$, 99 %, ECIBRA Analytical Reagents), copper nitrate trihydrate ($\text{Cu}(\text{NO}_3)_2 \cdot 3\text{H}_2\text{O}$, 99 %, Synth), and manganese nitrate tetrahydrate (Mn

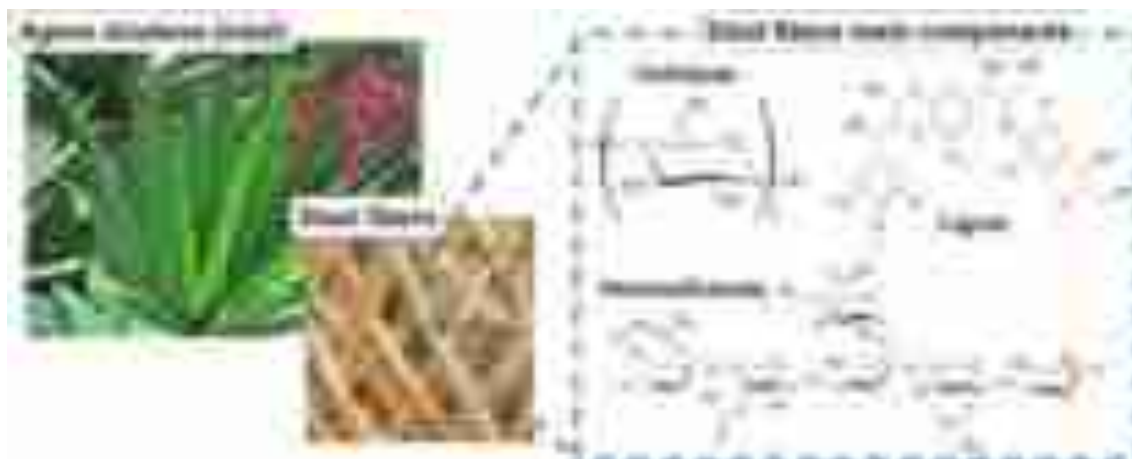


Fig. 1. Sisal fibers: source and main composition.

(NO_3)₂·4H₂O, 98 %, Sigma-Aldrich). The standard stock solutions of 1000 mg/L with 99.9 % purity (hexavalent chromium, copper, cadmium, manganese, nickel, and zinc) were obtained from Specsol, Brazil. They were all used as received.

2.2. Methods

2.2.1. Lignocellulosic hydrogel from sisal fibers

This section outlines the methodology employed for the deconstruction of fibers and the formation of hydrogels. Fig. 2(a) illustrates the process of generating a hydrogel from sisal fibers, which involves their deconstruction in CUEN, Fig. 2(b), followed by the coagulation of the resulting medium in distilled water.

2.2.1.1. Sisal fibers deconstruction. The fibers, as received, were ground in a knife mill (MA048, Marconi, Brazil) and ball mill (MM400, Retsch, Germany). The powder was sieved, and the fraction smaller than 0.149 mm (#100 mesh) was collected. Lastly, it was dried at 105 °C in an air circulation oven.

The deconstruction of sisal fiber in 1 M CUEN solution was carried out by mixing 1 g or 2 g of ground sisal fiber in 25 mL of distilled water, followed by adding 25 mL of CUEN. The viscous suspensions produced from the sisal deconstruction were labeled **sisal_1_CUEN** or **sisal_2_CUEN**, depending on the amount of sisal used in the deconstruction step. The system was then exposed to a flow of N₂ for 1 min. to remove air and prevent oxidation reactions. The mixture was stirred at room

temperature (about 25 °C) for 2 h; a viscous suspension formed afterward (Fig. 2(a)). The dissolution efficiency and rheology analysis were conducted to assess the fiber deconstruction and dissolution process. (see 2.2.2).

2.2.1.2. Hydrogel formation. The viscous dispersion was placed into a 50 mL syringe, and approximately 2 mL was injected into each cylindrical template (well), Fig. 2(a). The templates were then immersed in distilled water (10 mL of water/1 mL of gel) at room temperature (\cong 25 °C) and left for 96 h in the case of **sisal_1_CUEN** and 48 h for **sisal_2_CUEN** to ensure complete coagulation of the hydrogel. The cylinder-shaped hydrogels were carefully lifted from the templates using a spatula and placed into a vessel. They were then washed with distilled water while being agitated on a shaker maintained at room temperature and 200 rpm (MA-832, Marconi, Piracicaba, SP, Brazil). The hydrogel samples were named '**sisal_1_hydro**' and '**sisal_2_hydro**,' matching the initial mass of the sisal (1 g and 2 g, respectively).

2.2.2. Characterization of sisal fiber deconstruction

The CUEN medium, derived from the deconstruction of sisal fibers, was investigated to assess its effectiveness in dissolving cellulose and hemicelluloses. Rheological properties were also examined, with a focus on amplitude and frequency sweeps.

2.2.2.1. Dissolution efficiency. Aliquots of the viscous suspension formed were vacuum-filtered using a sintered glass filter #2 to measure

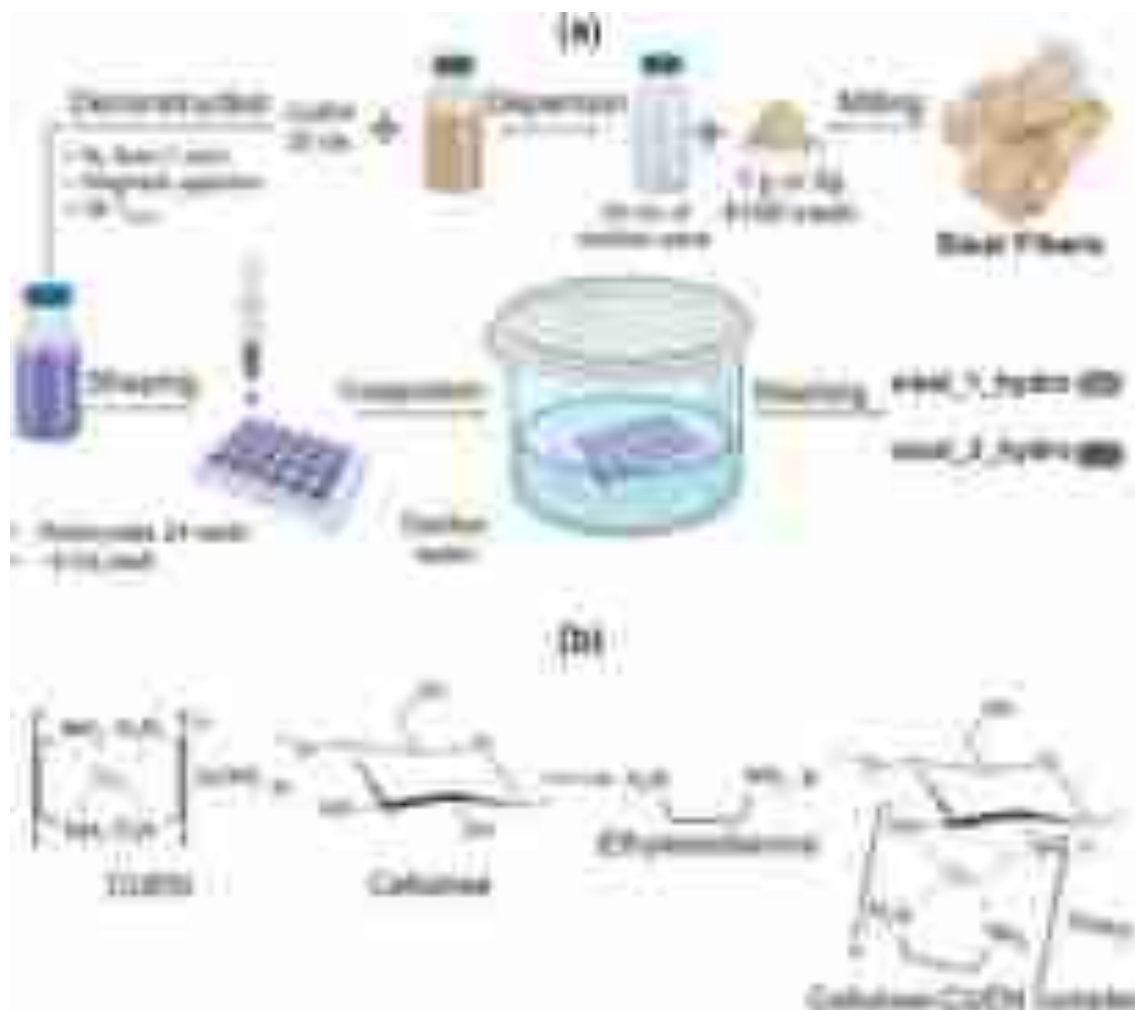


Fig. 2. Schematic representation of hydrogels formed from sisal fibers (a) and an illustration of the interaction of CUEN with a ring of the cellulose chain(b).

the solid content and calculate the dissolution efficiency (DE, %; Eq. 1).

$$DE = \frac{m_1 - m_2}{m_1} 100 \quad (1)$$

m_1 and m_2 are the initial sisal mass (g) and the final solid content (g) after the fiber's deconstruction.

2.2.2.2. Rheological properties of the solutions with suspended material.

The viscous suspensions obtained from sisal deconstruction were assessed by rheology (Discovery HR-2 rotational rheometer, TA Instruments, New Castle, DE, USA) at 25 °C using a cone/plate measuring module (plate diameter: 40 mm, cone/plate angle: 2°). The suspension was homogenized by ultrasound (USC 1400, Unique, ultrasonic Frequency: 40 kHz, ultrasonic power: 81 W) for 5 min before each measurement.

An amplitude sweep test was conducted to assess the viscoelastic properties of the suspensions. The storage and loss moduli were evaluated to characterize the samples' deformation behavior within the non-destructive range, defined as the linear-viscoelastic range [38].

After the preliminary amplitude sweep, the frequency dependencies of storage and loss moduli were measured in the linear viscoelastic region (strain at 1.0 %) by varying the angular frequency in the range of 0.0628–628 rad·s⁻¹. For the flow sweep test, rotational steady shear was performed to measure the flow behavior of the fluid gels and the viscosity as a function of the shear rate, increasing the shear rate from 0.001 s⁻¹ to 100 s⁻¹ [39]. All rheological measurements were done in triplicate.

2.2.3. Characterization of the hydrogels

As-prepared swollen hydrogels were analyzed in terms of shear stress to understand the viscoelastic behavior of the hydrogel. The hydrogels were then frozen at -80 °C for 24 h and lyophilized until complete drying (Freeze-dryer L 101, Liobras, Brazil). The dried hydrogel samples and milled sisal fibers were characterized using Fourier-transform infrared (FT-IR) spectroscopy, Raman spectroscopy, and X-ray diffraction (XRD). The dried hydrogels were characterized by water swellability test, scanning electron microscopy (SEM), accelerated surface area and porosimetry analysis (ASAP), and thermogravimetry analysis (TGA). Both swollen, dried, and rehydrated samples (24 h in water) were subjected to compression tests.

2.2.3.1. Fourier-transform infrared and Raman spectroscopy. Freeze-dried hydrogels and ground sisal fiber were analyzed using Fourier-transform infrared spectroscopy and Raman spectroscopy.

The analysis was performed using Fourier-transform infrared spectroscopy on a Tensor 27 spectrophotometer (Bruker, USA) equipped with an ATR (Attenuated Total Reflectance) cell.

Raman spectroscopy was carried out using a Horiba spectrometer (LabRam HR Evolution). The excitation source was a 785 nm laser, which reduces fluorescence issues, with an intensity of 30 mW. For the hydrogels, the exposure time was 90 s, with four scans accumulated, and an objective lens of 50× magnification. For the fibers, the exposure time was 25 s, and the accumulation of 8 scans, using the same objective lens.

2.2.3.2. X-ray diffraction. The crystallinity of milled sisal fibers and the lyophilized hydrogels was determined using X-ray diffraction (XRD) and a position-sensitive detector (PSD), model LynxEye. Analyses were performed with a Bruker D8 Advance diffractometer equipped with Cu K α radiation ($\lambda = 1.5418 \text{ \AA}$). Diffractograms were collected in the range of 5 to 60° (2 θ), with a step size of 0.02°, and diffraction intensities were recorded for 0.5 s at each step. To calculate the percentage of non-crystalline domains, the total area was determined by summing the areas of the peaks and the halo corresponding to non-crystalline domains (%; Eq. 2). This total area was then subtracted from the area of the peaks, and the resulting value was divided by the total area. The result

was multiplied by 100 to obtain the percentage of non-crystalline domains. The percentage of crystalline domains (%; Eq. 3) was calculated by subtracting the percentage of non-crystalline domains from 100.

$$\text{Non-crystalline domains} = \frac{\text{Total area} - \text{Peaks area}}{\text{Total area}} 100 \quad (2)$$

$$\text{Crystalline domains} = 100 - (\text{Non-crystalline domains}) \quad (3)$$

2.2.3.3. Swelling test. The mass of the hydrogel was measured after the water absorption during the coagulation step and following the freeze-drying process to determine the initial water content of the water-swollen hydrogels produced.

The dried hydrogels were subsequently immersed in water to assess water absorption over time, thereby enabling the examination of swellability. The solid/liquid ratio was 1 g/L. This experiment was done in triplicate.

2.2.3.4. Scanning Electron Microscopy. Scanning electron microscopies (SEM) of the sectional areas of the dried samples were done using a 400 Leo/Zeiss DMS instrument (Jena, Germany). The samples were coated with a thin layer of gold (Baltec Med 020, Liechtenstein).

2.2.3.5. Surface area and porosimetry. Isotherms of adsorption and desorption of N₂ were performed at Brazilian Agricultural Research Corporation – Instrumentation (Embrapa, São Carlos, São Paulo, Brazil) using an accelerated surface area and porosimetry analyzer (ASAP 2020, Micrometrics). The degassing process was done at 120 °C for 12 h. The isotherms were done at 77 K.

2.2.3.6. Thermogravimetric analysis. The lyophilized hydrogels, sisal_1_hydro and sisal_2_hydro, were individually ground in a mortar before being subjected to thermogravimetric analysis. The analysis was conducted using a TGA-50 (Shimadzu, Japan) in an inert nitrogen atmosphere at a flow rate of 50 mL/min and a heating rate of 10 °C/min from 25 to 700 °C.

2.2.3.7. Dynamic mechanical analysis (compressive and shear). The hydrogels were assessed using a dynamic mechanical analyzer (DMA, TA 800, USA). The DMA measurements were taken in quintuplicate.

The compression test evaluated the compression elastic modulus of the cylinder-type hydrogels. The typical compression test increased the applied force to the instrument limit, *i.e.*, 18 N.

Moreover, the viscoelastic behavior in steady mode was determined by the shear-sandwich test, in which an amplitude test determined the linear viscoelastic region and a frequency sweep was conducted from 1 to 10 Hz (6.28 to 63 rad/s) to verify the G' and G'' according to the frequency. For this purpose, the hydrogel cylindrical samples were sliced at a thickness of around 3.0 ± 0.2 mm and cut into a square form ($\cong 1 \text{ cm} \times 1 \text{ cm}$), which is suitable for the shear-sandwich specimen holder of the DMA [40].

2.2.4. Heavy metal sorption

For the sorption essays of heavy metals, the hydrogels were shaped/coagulated in a 96-well plate (instead of a 24-well plate, Fig. 2). This resulted in the formation of smaller cylinders (diameter $\cong 6.9 \text{ mm}$ and maximum height $\cong 10.9 \text{ mm}$). These hydrogels were also frozen at -80 °C for 24 h and lyophilized until completely dry.

The heavy metal sorption essays were performed in batch mode, in which a sorbent dosage of 1 g/L was used to remove metals from an equimolar solution of 0.17 mmol/L of each metal (Cu(II), Ni(II), Zn(II), Cd(II), Mn (II), and Cr(VI)).

The equimolar solution was prepared by diluting stock metal solutions in deionized water. The stock solutions were made by dissolving metal salts, including zinc nitrate hexahydrate, nickel nitrate hexahydrate, cadmium nitrate tetrahydrate, potassium dichromate, copper

nitrate trihydrate, and manganese nitrate tetrahydrate, which were used to create the multi-metal solution. The standard stock solutions of 1000 mg/L, 99.9 % purity (hexavalent chromium, copper, cadmium, manganese, nickel, and zinc), were used to calibrate the measurements in the ion chromatograph.

To prevent metal precipitation, drops of hydrochloric acid (0.025 M) were added to maintain the pH at 4.5. This adjustment was guided by simulations of metal species in relation to pH, conducted using Visual Minteq software. Fig. 3 shows that HCrO_4^- precipitates at pH values above 4.5, Cu^{2+} at values above 6.0, and others at pH levels above 8.0.

The contact time was 24 h; after that, the samples were filtered using a syringe filter (K18–230, KASVI). The system agitation was done in an incubator shaker at 25 °C at 250 rpm (MA-832, Marconi, Piracicaba, SP, Brazil). The experiments were done in duplicate. Samples before and after were subjected to ion chromatography (940 Professional IC Vario, Metrohm, Herisau, Switzerland) to measure the metal concentration and determine the sorption capacity (Eq. 4).

$$q = \frac{(C_0 - C)}{S} \quad (4)$$

Where q is the sorption capacity (mmol/g), C_0 and C are the initial and final concentrations (mmol/L), and S is the sorbent dosage (g/L).

3. Results and discussion

3.1. Sisal deconstruction

Fig. 2(b) demonstrates the interaction of CUEN with the hydroxyl groups present in glycosidic rings, facilitating the disruption of hydrogen bonds between adjacent chains, which in turn promotes the dissolution of cellulose. Comparable interactions may occur with the various sugar units that constitute hemicelluloses, resulting in the dissolution of this heteropolysaccharide as well. This property of CUEN allows for the deconstruction of lignocellulosic fibers, releasing their components—cellulose, hemicelluloses, and lignin—into the medium. Cellulose and hemicelluloses are dissolved, either fully or partially, depending on the conditions, while lignin remains suspended in the CUEN medium.

3.1.1. Solid content and efficiency

Table 1 presents the efficacy of the CUEN in deconstructing sisal fibers and dissolving their components, which was assessed by analyzing the residual filtered solid from the viscous suspension. For this mass balance, the main composition of the sisal was considered to estimate the masses of cellulose, hemicelluloses, and lignin in the starting

Table 1

Efficiency of the sisal fibers deconstruction and dissolution using CUEN.

Sample	Sisal mass (g)	DE (%)	Solid concentration ^a (g/mL)	
			Dissolved ^b	Suspended ^c
Sisal_1_CUEN	1.0	73.7 ± 0.25	0.015	0.005
Sisal_2_CUEN	2.0	52.4 ± 2.46	0.021	0.019

^a Volume of 50 mL of suspension.

^b Solubilized fraction composed of cellulose and hemicelluloses (sisal_1_CUEN) or primarily cellulose (sisal_2_CUEN).

^c Solid suspended constituted primarily by lignin (sisal_1_CUEN) or lignin plus hemicelluloses (sisal_2_CUEN).

material (sisal fibers). The primary constituents of sisal fibers comprise approximately 59 % cellulose, 29 % hemicelluloses, 12 % lignin, and 1.2 % ash, along with an 8.7 % moisture content. The total percentage exceeds 100 % due to measurement errors (± 1.5 %, ± 0.7 %, ± 0.4 %, ± 0.0 %, ± 0.2 %, respectively) [26]. The percentage of crystalline regions in the sisal fibers was evaluated (subsection 3.2.3) and determined to be 55 %. This result aligns with the naturally occurring cellulose content in these fibers (59 %), as cellulose is the component responsible for forming the crystalline regions.

When employing a ratio of 1 g/50 mL, 73.7 ± 0.25 % of the fiber components were successfully dissolved. The soluble fraction is composed of cellulose and hemicellulose macromolecules (Table 1). CUEN serves as an effective solvent for cellulose; however, in this case, the cellulose is embedded within a lignocellulosic fiber matrix. The non-crystalline regions of cellulose are more accessible to CUEN than the crystalline regions. Hemicelluloses, which are also dissolvable in CUEN, are in the non-crystalline regions and, to some extent, form complexes with lignin [41], a component that remains insoluble in this solvent. Therefore, it can be considered that the non-crystalline regions of cellulose are the most readily soluble, followed by hemicelluloses, and then the crystalline regions of cellulose. The results indicate that approximately 26 % of the solid material remained undissolved during the fiber deconstruction process. This observation indicates that lignin, along with parts of hemicelluloses and possibly some fractions of cellulose from crystalline regions, remained undissolved. The suspension was left unfiltered, enabling the insoluble fraction to be subsequently incorporated into the hydrogel.

When the sisal ratio was increased to 2 g per 50 mL, 52.4 ± 2.46 % of the fiber components dissolved (Table 1), while approximately 48 % of the solid material remained suspended. These results indicated that, compared to sisal_1_CUEN, for sisal_2_CUEN, in addition to all lignin, a larger fraction of hemicelluloses, as well as some cellulose from the crystalline regions, remained insoluble. It is essential to recognize that suspended solids can be advantageous, as employing this approach to integrate suspended insoluble materials into hydrogels can result in a composite exhibiting enhanced mechanical properties. The inclusion of these insoluble components not only strengthens the hydrogel matrix but also contributes to its overall structural integrity [26,42,43].

The dissolution efficiency was higher when a smaller amount of sisal was used (1 g/50 mL). The sisal_1_CUEN suspension exhibited a holocellulose (cellulose plus hemicelluloses) concentration of 0.015 g/mL, which is lower than that of the sisal_2_CUEN at 0.021 g/mL, as shown in Table 1. This difference is due to the higher initial content of holocellulose when 2 g of sisal is used. Consequently, although increasing the sisal mass decreases dissolution efficiency, it simultaneously raises the concentration of cellulose and hemicelluloses dissolved, as well as the solid content within the suspension.

A previous investigation found that using a LiCl/DMAc solvent system with a ratio of 1 g of sisal fibers to 50 mL of solvent dissolved approximately 40 % of the fibrous components after deconstruction [26]. In contrast, the current study demonstrated that CUEN dissolved about 74 % of the components, indicating greater efficiency than LiCl/DMAc. Additionally, even when the initial fiber mass was increased to 2

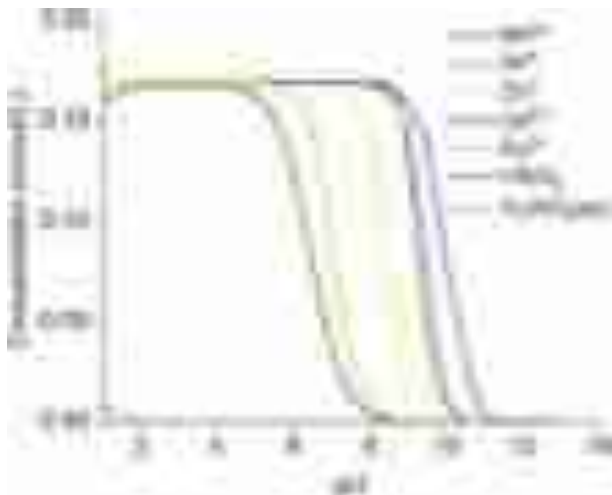


Fig. 3. Concentration of metallic species as a function of pH.

g per 50 mL, approximately 52 % of the fiber components still dissolved (Table 1).

3.1.2. Rheological properties of the lignocellulosic suspensions

The viscous medium obtained after the deconstruction of sisal fibers and dissolving some of their components into the medium, while the rest remained dispersed in CUEN, was assessed for its rheological properties, namely, the dependence of the viscosity (η) on the shear rate (Fig. 4(a)), and of the storage (G') and loss (G'') moduli on the angular frequency (ω) (Fig. 4(b)). These properties may contribute to a better understanding of the gelation process.

Fig. 4(a) shows the shear rate influence on the viscosity of the suspensions sisal_1_CUEN and sisal_2_CUEN. Both suspensions can be considered non-Newtonian fluids for shear rates higher than 0.01 1/s, a range in which their viscosities depend on shear rate. Additionally, they are shear-thinning or pseudoplastic fluids, as their viscosity decreases with increasing shear [44]. The decrease is more pronounced for the solution containing a higher suspended solids concentration (sisal_2_CUEN). This may occur due to the disentanglement of high-molar-mass polymers when subjected to sufficient shear, resulting in a subsequent decrease in viscosity [44]. Additionally, in the current study, the suspended macromolecules may have formed networks that were disrupted

under shear stress, leading to shear-thinning behavior [45]. This phenomenon may be more pronounced at elevated solid concentrations, as evidenced by sisal_2_CUEN. The viscosity characteristics of the sisal_1_CUEN suspension, which contains lower levels of dissolved cellulose and hemicelluloses as well as suspended lignin compared to the sisal_2_CUEN suspension, reveal that at low shear rates, up to approximately 0.01 1/s, the suspension exhibits a relatively high and stable viscosity, signifying resistance to flow under minimal stress conditions [46]. As the shear rate increases up to 0.1 1/s, there is a marked decrease in viscosity, suggesting that the previously mentioned phenomena have reduced internal friction, thereby facilitating flow. At even higher shear rates, beyond 0.1 1/s, the decline in viscosity becomes somewhat smoother, indicating that the disentanglement of polymer chains and the breakdown of potential networks formed by suspended macromolecules occurred extensively in the earlier phase. Consequently, further increases in shear rate result in a less pronounced reduction in viscosity.

Fig. 4(b) demonstrates that for sisal_2_CUEN, at angular frequencies up to approximately 15 rad/s, the storage modulus (G') is slightly lower but closely aligned with the loss modulus (G''). In a solution containing both dissolved and undissolved macromolecules, such as suspended solids, as in the present study, interactions can occur among these components. Such interactions may help establish a balance between liquid-like (viscous) and solid-like (elastic) behaviors. Up to around 15 rad/s, sisal_2_CUEN shows a slight inclination towards viscous behavior, with several overlapping data points sustained until 15.78 rad/s, where the two moduli intersect, marking the gelation point. Beyond this frequency, a mild predominance of elastic behavior is noted. In the case of sisal_1_CUEN, which had a lower suspended solids content than sisal_2_CUEN, a more pronounced tendency towards viscous behavior is noted, extending up to the gelation point at 62.8 rad/s. From there, a more pronounced predominance of elastic behavior is also observed compared to sisal_2_CUEN.

The gelation points of the suspensions, at 62.8 rad/s (sisal_1_CUEN) and 15.78 rad/s (sisal_2_CUEN) indicate that the viscoelastic relaxation of the macromolecular network shifts to the low-frequency region as the concentration of the macromolecules is increased, *i.e.*, more time was needed to reorganize the system to form a well-defined network [46]. Thus, when the initial sisal concentration increased, the crossover frequency reduced, which indicates that sisal_2_CUEN suspension would form a hydrogel with higher viscoelasticity than sisal_1_CUEN.

3.2. Characterization of the lignocellulosic-based hydrogels

This section discusses the morphology, structure, thermal decomposition, as well as the compression and shear resistance, and water absorption of sisal hydrogels.gels.

3.2.1. Digital Images

Fig. 5 shows digital images of the hydrogels sisal_1_hydro and sisal_2_hydro before and after lyophilization, as well as after 24 h of water immersion. In Fig. 5(a-1) and Fig. 5(b-1), the swollen hydrogels are displayed. The sisal_1_hydro has a greenish tint and looks more translucent at the edges compared to sisal_2_hydro, which has a darker hue. A close examination of the samples showed that sisal_2_hydro has sharper edges than sisal_1_hydro while still maintaining the shape of the template. The lyophilized samples, shown in Fig. 5(a-2) and Fig. 5(b-2), indicate that the hydrogel's original cylindrical shape was slightly deformed during freeze-drying, resulting in wrinkled surfaces.

The rehydrated samples, which are lyophilized samples exposed to water for 24 h, slightly altered their structure during swelling. However, sisal_2_hydro (Fig. 5(b-3)) maintained its shape better than sisal_1_hydro (Fig. 5(a-3)).

3.2.2. Fourier transform infrared and Raman spectroscopy analysis

The FTIR spectra of the samples (Fig. 6) presented the same behavior, with the sisal_2_hydro having slightly more intense peaks. The band

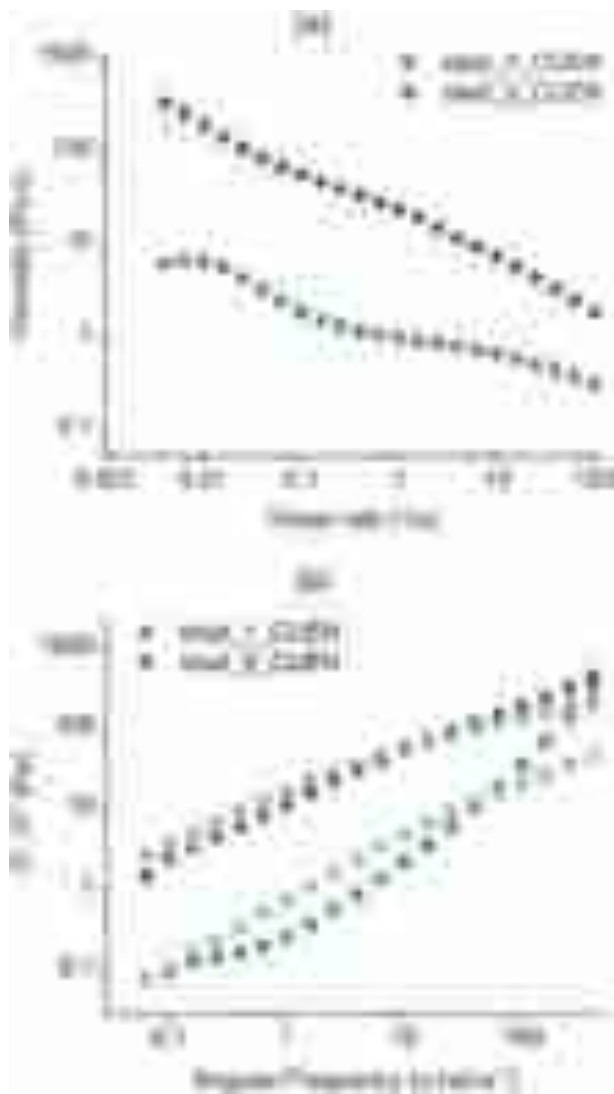


Fig. 4. Rheology of the viscous suspensions obtained from sisal deconstruction: flow sweep (a) and oscillatory frequency sweep (b) at 25 °C and 1 % strain. Empty symbols: loss modulus (G''); Filled symbols: storage modulus (G').



Fig. 5. Sisal lignocellulosic hydrogels from the deconstruction of fibers using CUEN: sisal_1_hydro (a), and sisal_2_hydro (b), swollen (a-1, b-1), lyophilized (a-2, b-2), and rehydrated after 24 h of water immersion (a-3, b-3).

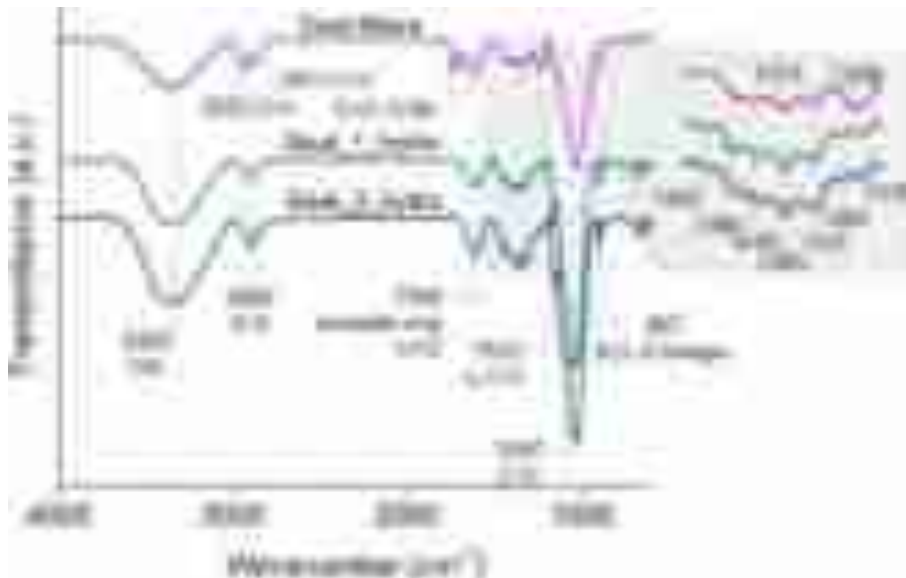


Fig. 6. FTIR spectra of sisal fibers, sisal_1_hydro, and sisal_2_hydro.

around 3302 cm^{-1} refers to the stretching of the H—O bond and can be mainly attributed to the polysaccharide fraction. The bands at 2923 cm^{-1} , 2893 cm^{-1} , and 2871 cm^{-1} are attributed to symmetric stretching in methylene groups.

The band at 1740 cm^{-1} (stretching vibrations of C=O) present in the sisal fiber spectrum disappeared in the hydrogel spectra [47]. This band is related to the ester bond between the ferulic acid of lignin and the hemicelluloses in the fiber's cell wall, and its disappearance in the hydrogels corroborates the cleavage of this lignin-carbohydrate complex

[48,49].

The band at 1599 cm^{-1} refers to aromatic ring vibration and C=O stretching [50]. The band at 1502 cm^{-1} indicates aromatic skeletal vibration. The band at 1460 cm^{-1} corresponds to the CH₂ of the pyran ring symmetric scissoring and OH plane deformation. The band at 1418 cm^{-1} is the aromatic skeletal vibration combined with C—H in-plane deformation, and at 1373 cm^{-1} (fiber) and 1365 cm^{-1} (hydrogel) represents the phenolic OH stretching of lignin (see magnification, Fig. 6). The signal at 1315 cm^{-1} refers to the C—O stretching of the aromatic ring in

the syringyl unit of lignin. The band at 1267 cm^{-1} means the guaiacyl ring plus C=O stretching, and 1240 cm^{-1} and 1234 cm^{-1} are related to the C–O stretching of the acetyl ester unit in hemicelluloses [51]. Bands at 1153 cm^{-1} correspond to the C–C ring stretching [52]. The band at 1047 cm^{-1} regards a complex vibration associated with C–O stretching in polysaccharides. C–O–C stretching in β -glycosidic bonds in cellulose and hemicelluloses was also observed at 897 cm^{-1} [53].

Raman spectra of sisal fibers and hydrogels are shown in Fig. 7, in which the most prominent peaks are highlighted. The peaks at 394 cm^{-1} and 412 cm^{-1} are typically attributed to C-C-C bending, C–O, C-C-O, and ring deformation, which are characteristic of the cellulose structure [54,55]. The peaks at 635 and 842 cm^{-1} are associated with ring and skeletal deformation, respectively. Both signals corroborate the lignin content [54]. The peak at 865 cm^{-1} means C-C-H and C-O-C bending [56]. The typical peak of CH_2 was shown at 998 cm^{-1} , and carbonyl stretching vibrations at 1774 cm^{-1} [54,55]. Regarding hemicelluloses, their structural similarity to cellulose causes a significant overlap in their Raman signals. This makes it difficult to distinguish the specific contributions of hemicelluloses within the spectrum [57].

FTIR and Raman spectra analysis confirmed that the hydrogels, formed by deconstructing sisal using CUEN solvent and subsequent coagulation with water, successfully preserved the cellulose, hemicelluloses, and lignin from the original sisal fibers. Incorporating the solid phase, especially lignin, into the gel can greatly improve properties such as mechanical strength, biocompatibility, biodegradability, and the ability to inhibit cellular and microbial growth [26,58,59]. These attributes are very beneficial for creating environmentally sustainable sorbents.

3.2.3. X-ray diffraction

The deconstruction of sisal fibers resulted in the release of cellulose chains into the solvent medium. The primary objective of the X-ray diffraction analysis was to evaluate the organizational potential of such chain segments during the hydrogel formation process, thereby facilitating the development of crystalline domains. The X-ray diffractograms of sisal fibers showed peaks at 16.0° , 22.3° , and 34.6° , Fig. 8, which are assigned to $(10\bar{1})$, (002) , and (040) reflection planes of the cellulose I structure [60].

The crystallinity is due to the arrangement of segments from previously dissolved cellulose chains, leading to the creation of crystalline regions within the hydrogels. Furthermore, it is plausible that a certain cellulose fraction with inherent crystallinity did not completely dissolve, remaining suspended within the CUEN medium, and may have integrated into the hydrogels, thus contributing to their crystallinity. In both scenarios, these components were subjected to the alkaline conditions of

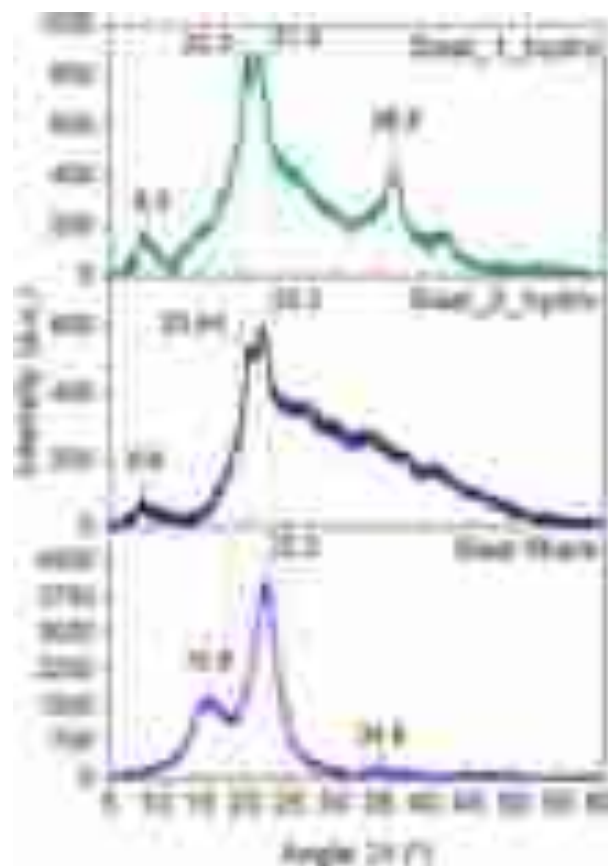


Fig. 8. X-ray diffractograms of sisal fibers, sisal_1_hydro, and sisal_2_hydro hydrogels.

the CUEN medium, which breaks hydrogen bonds in cellulose I (chains arranged in a parallel configuration) facilitating the transformation of cellulose I, present in the sisal fibers, into cellulose II (chains rearranged into an antiparallel configuration), a characteristic of the hydrogels (Fig. 8). The peaks for cellulose II polymorph are usually located at $2\theta \cong 12^\circ$, 20° and 22° , which correspond to the diffraction of (101) , $(10\bar{1})$ and (002) crystallographic plane reflection [61]. Peak positions may vary depending on factors such as the specific sample preparation method, variations in crystallite size, and the compressive forces within the crystal structure. The diffractogram of sisal_1_hydro shows peaks at 8.5° , 20.3° , and 21.4° , and that of sisal_2_hydro at 8.6° , 20.4° , and 22.2° (Fig. 8), which may be attributed to the diffractions mentioned for cellulose II. The peak at 36.8° (sisal_1_hydro) may tentatively be attributed to some cellulose I that has not been transformed into cellulose II.

The crystallinity of the milled sisal fibers, sisal_1_hydro and sisal_2_hydro is approximately 55 %, 26 % and 17 %, respectively. As expected, the crystallinity of the hydrogels was lower than that of the native cellulose in the sisal fibers because the rearrangement of cellulose chain segments during hydrogel formation was hindered by the presence of hemicellulose and lignin fractions, among other factors. This effect was more pronounced for sisal_2_hydro due to its higher insoluble content (Table 1), which resulted in lower crystallinity compared to sisal_1_hydro. It is important to note that low crystallinity can enhance the sorption capacity of hydrogels. This may occur because the interaction and diffusion of the substances to be sorbed are facilitated in non-crystalline regions. The greater distance between neighboring segments in these regions, as compared to crystalline ones, allows for more effortless movement and accessibility of the adsorbates involved.

3.2.4. Water uptake

Fig. 9 presents the original water content of the hydrogels, *i.e.*, the

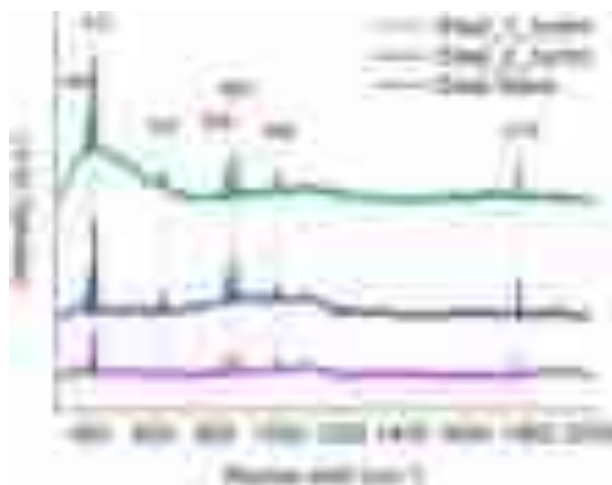


Fig. 7. Raman spectra of sisal fibers, sisal_1_hydro, and sisal_2_hydro.

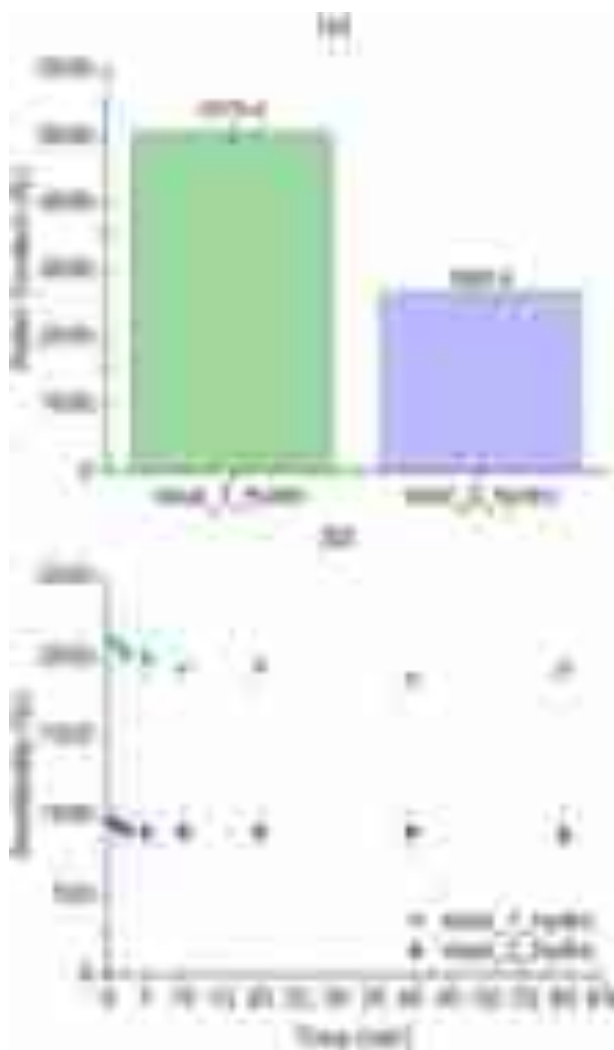


Fig. 9. Water absorption by the hydrogel during the coagulation step (a) and water reabsorption over time (water absorption by freeze-dried hydrogels) (b) of sisal_1_hydro and sisal_2_hydro.

water absorption during the coagulation step, and the reabsorbed water by the lyophilized hydrogels. The capacity to retain water is a crucial criterion for defining a material as a hydrogel (> 90 %) [62–64].

Fig. 9(a) indicates that sisal_1_hydro and sisal_2_hydro retained large amounts of water as they were produced. However, sisal_1_hydro has a higher water content (5076.4 %) than sisal_2_hydro (2685.8 %), which is inversely proportional to the solid fraction contained in each hydrogel. This appears to compensate for the fact that sisal_2_hydro has lower crystallinity than sisal_1_hydro, which could enhance water sorption. The hydrogel sisal_1_hydro was created from a suspension containing approximately 26 % solids, while the suspension that produced sisal_2_hydro had around 48 % solids, Table 1. Most suspended solids were likely integrated into the hydrogel network, as demonstrated by the subsequent SEM micrographs, which do not show any apparent free particulate matter within the hydrogels. However, mainly in the case of sisal_2_hydro, it is possible that some solids remained firmly adhered to the pore walls, thereby restricting the available space for water absorption. The fraction of suspended polysaccharides was likely incorporated into the holocellulose network formed by the soluble fraction, while the solids that adhered to the walls may primarily have consisted of lignin.

Fig. 9(b) shows the swelling of the freeze-dried samples over time. The swelling is rapid for both samples, achieving a maximum in the first

minute of contact with water. After this overshooting, the water absorption stabilized, with sisal_1_hydro achieving a maximum of approximately 1918 % and sisal_2_hydro at 880 %. This overshooting phenomenon may be related to the relaxation process of the macromolecular chains because of the spontaneous rearrangement of the gel structure on dynamic swelling [65,66].

The overshooting was slightly more pronounced for sisal_1_hydro than for sisal_2_hydro (Fig. 9), which may be related to the strength of the physical crosslinking in the gels. According to Kowasli et al. [65], the overshooting effect in the water absorption tends to be greater for weakly crosslinked samples. As the hydrogels were produced by physical coagulation, it is expected that sisal_1_hydro, a hydrogel made with a lower density of macromolecular content than sisal_2_hydro, has the lowest crosslinking degree. Because of that, sisal_1_hydro has a structure more susceptible to the relaxation chain effect, which could have intensified the overshooting phenomenon in water absorption.

Table 2 compares the swellability of dried cellulose-based hydrogels produced using different methods and biomasses. It also summarizes the cellulose sources and solvents used, as well as the hydrogel production methods from the literature.

Table 2 shows the results for rice, oats, wheat straw, sugarcane bagasse, recycled old corrugated containers, and sisal fibers as sources of cellulose. These non-wood biomasses have higher cellulose content and shorter harvest periods than wood resources [17]. As a result, these materials are considered more suitable for producing bio-based products than traditional wood sources. Besides differences in biomass, various methods exist for producing cellulose-based hydrogels, which directly impact the materials' water retention capabilities.

Oliveira et al. [67] conducted a study that blended cellulose fibers derived from rice and oat husks with polyvinyl alcohol (PVA) and crosslinked the resultant hydrogel using a physical freezing-thawing method. Compared to the alternatives in Table 2, these hydrogels exhibited intermediary water swellability levels of 392.1 % for rice husks and 254.3 % for oat husks.

Shan et al. [68] proposed the formation of hydrogels by free radical polymerization of acrylic acid blended with lignin, cellulose, and hemicelluloses from wheat straw. This method conferred great swellability, reaching approximately 3010 % water absorption. It is worth noting that this study reported the grafting of polyacrylic acid onto lignin, hemicellulose, and cellulose macromolecules through a radical reaction involving their hydroxyl groups. It is assumed that, including for reasons of steric repulsion, some of the carboxylic groups of polyacrylic acid remained unreacted, *i.e.*, they did not participate in the crosslinking reaction that followed the grafting step. In this context, these highly hydrophilic groups also contributed to the reported result. In the present study, only the hydrophilic functional groups in the macromolecules of lignin, cellulose, and hemicelluloses, primarily hydroxyl groups, participated in water sorption.

Ban et al. [69] and Queiroz et al. [26] utilized different biomass sources and cellulose solvents, but followed similar techniques for coagulating the hydrogels using ethanol, as shown in Table 2. Notably, the resulting materials' swellability varied significantly, likely due to the differences in drying methods [69]. Lyophilization tends to preserve the porous structure of hydrogels more effectively than air drying at room temperature [26]. When comparing the hydrogel produced in this study with that formulated by Queiroz et al. [26], both sourced from deconstructed sisal fibers, sisal_1_hydro demonstrates greater water absorption capacity, 1918.5 %, Table 2. This result can be attributed to the higher polysaccharide dissolution efficiency of the CUEN (74 %) compared to LiCl/DMAc (40 %), which led to a hydrogel with a higher content of hydrophilic components (cellulose and hemicelluloses).

Sangtarashani et al. [70] used water coagulation to create the hydrogel. The original water content of the hydrogel was 4700 %, and the water reabsorption of the freeze-dried hydrogel reached 2400 % after 24 h of immersion in water (Table 2). The same trend was observed in the survey by Queiroz et al. [26], where the water absorption capacity

Table 2
Comparison of the water retention capability of dried cellulose-based hydrogels.

Hydrogel	Cellulose Source	Solvent for cellulose extraction/ dissolution	Method for hydrogel production/ shaping	Swellability (%)	Reference
Cellulose fibers dispersed in PVA ^a	Rice husks	NaOH solution	Freeze-thaw	392.1	[67]
	Oat husks	NaOH solution	Freeze-thaw	254.3	
Lignocellulose and polyacrylic acid hydrogel	Wheat straw	H ₂ O ₂ /NaOH	Free-radical polymerization (KPS ^b , AA ^c , MBA ^d)	~3010	[68]
Regenerated cellulose	Sugarcane bagasse	ZnCl ₂ /CaCl ₂	Ethanol coagulation	52	[69]
Lignocellulose-based hydrogel	Sisal fibers	LiCl/DMAc	Ethanol coagulation	1091	[26]
Lignocellulosic hydrogel	Recycled old corrugated container	BMIMCl ^e	Water coagulation	2400	[70]
Lignocellulose-based hydrogel	Sisal fibers	CUEN	Water coagulation	1918	This study

^a Poly(vinyl alcohol);

^b Potassium persulfate;

^c Acrylic acid;

^d N,N'-methylenebisacrylamide;

^e 1-Butyl-3-methyl-imidazolium chloride;

decreased from 1936 % to 1091 %, and in the present study, where the capacity decreased from 5076 % to 1918 % (after freeze-drying). Sangtarashani et al. reported that the lignocellulosic biomass they used contained 6 % lignin, which is its most hydrophobic component. In contrast, the biomass used in the current study had an approximate lignin content of 12 %, making it less hydrophilic. However, a detailed comparative analysis of the hydrophilic properties of the freeze-dried hydrogels produced by Sangtarashani et al. and those formed in this study would require additional information, such as the surface areas and pore size distribution.

3.2.5. Scanning electron microscopy

Fig. 10 presents the SEM images of the transversal sections for sisal_1_hydro (a) and sisal_2_hydro (b). Micrographs Figs. 10(a-1) and 10(b-1), which correspond to the lyophilized hydrogels after swelling during the water coagulation step in their creation, demonstrate that sisal_1_hydro contains smaller pores than sisal_2_hydro. Furthermore, Figs. 10(a-2) and 10(b-2) illustrate that sisal_1_hydro possesses more pores than sisal_2_hydro, but with smaller sizes. This finding aligns with expectations, as sisal_2_hydro was formulated with double the macromolecular content within the same template volume as sisal_1_hydro.

The porosity and pore size of hydrogels were generated during freeze-drying by removing crystallized water through sublimation [71]. Sisal_1_hydro had a higher water content than sisal_2_hydro (Fig. 10), and sisal_2_hydro had double macromolecule content for the same volume (denser scaffold). The highly concentrated hydrogel (sisal_2_hydro) has lower water content to lose and a more intrigued, interconnected, and compacted 3D network. Thus, the water in the sisal_2_hydro was not dispersed throughout the entire hydrogel but was entrapped within the strongly crosslinked hydrogel, which conferred higher porosity to sisal_2_hydro.

Fig. 10 illustrates the absence of fiber fragments within the hydrogels, indicating that CUEN has effectively deconstructed the sisal fibers.

The SEM images of the lyophilized samples after rehydration, 24 h immersed in water, Fig. 10 (a-3, a-4), and Fig. 10 (b-3, b-4), show that the pore size of the samples changed after the water swelling, especially for sisal_2_hydro. It is evident in the comparison of Fig. 10 (b-2) to Fig. 10 (b-4) that the structure of swollen sisal_2_hydro had a wider range of pore sizes after the water reabsorption. The swelling of the hydrogel within the pore space altered the morphology of the porous media, and the crystals formed during freezing also created new pores [72,73].

The more pronounced impact of swelling and freeze-drying on the porous structure of sisal_2_hydro may be attributed to ice growth during the lyophilization process. Stronger crosslinked gels tend to form larger ice crystals within their micro-network [74]. This phenomenon may occur because the rigid network becomes brittle when subjected to the advancing ice fronts, resulting in the fragmentation of the hydrogel

walls and an increase in pore size. In contrast, the more flexible gel network of sisal_1_hydro may have exhibited greater resistance to the propagation of ice fronts owing to its superior stretchability.

3.2.6. Surface area and porosimetry

The N₂ adsorption and desorption isotherms, as well as the pore size distribution curves, of the dried sisal_1_hydro and sisal_2_hydro samples are presented in Fig. 11.

The shape of the isotherm shown in Fig. 11(a) can be classified as Type II with H3 hysteresis, according to the IUPAC classification. [75]. This type of isotherm and hysteresis indicates the presence of macropores, where the pore network is not filled with the condensate gas. Fig. 11(b) specified that the pore size range varied from 2.5 to 160 nm, where the major adsorbed volumes were achieved at pores in the macropore range (> 50 nm). During desorption, the pore diameter range is reduced because some of the condensate gas may be entrapped in the pores, with the most significant pore size being around 40 nm.

Table 3 summarizes the Brunauer–Emmett–Teller (BET) surface area and Barrett–Joyner–Halenda (BJH) pore volume of the sisal-based hydrogels. The surface area of the hydrogels is 26.2 and 34.7 m²/g, for sisal_1_hydro and sisal_2_hydro, respectively. The pore volume of the samples had the most distinct values, where sisal_2_hydro had a pore volume 65 % higher than sisal_1_hydro.

Hydrogels from different lignocellulosic matrices had surface area in a similar magnitude order of the sisal-based hydrogels, such as those based on poplar cellulose (9.96 m²/g) [76], physically crosslinked ionic liquid lignocellulose hydrogels (75.2 m²/g) [77], hydrogel based on nanocellulose from coconut husk fibers (26 m²/g) [78], bacterial cellulose and gelatin hydrogel (35 m²/g) [79], cellulose acetate nanofiber hydrogels (56 m²/g) [80]. Thus, the sisal-based hydrogels proposed in this study have a surface area comparable to that of other lignocellulosic freeze-dried hydrogels. It was also demonstrated that increasing the sisal mass in the hydrogels yields scaffolds with a higher surface area and pore volume, which is beneficial for sorption applications.

3.2.7. Thermogravimetric analysis

Fig. 12 shows that the thermal decomposition of the hydrogels occurs similarly, with the sisal_1_hydro exhibiting a slightly lower mass loss in the applied temperature range (up to 700 °C). The TG curves indicate that water volatilization from residual moisture occurred up to approximately 100 °C, resulting in an approximate weight loss of 8 %. The thermal decomposition of the fiber components resulted in a weight loss of roughly 65 % for sisal_1_hydro and 68 % for sisal_2_hydro. Cumulatively, sisal_1_hydro exhibited a total weight loss of approximately 76 % when heated to 700 °C, while sisal_2_hydro experienced a total weight loss of 80 %. As previously hypothesized (3.2.3), the solids adhering to the sisal_2_hydro walls may predominantly comprise lignin. In this context, the sisal_2_hydro mass analyzed using TGA may possess a

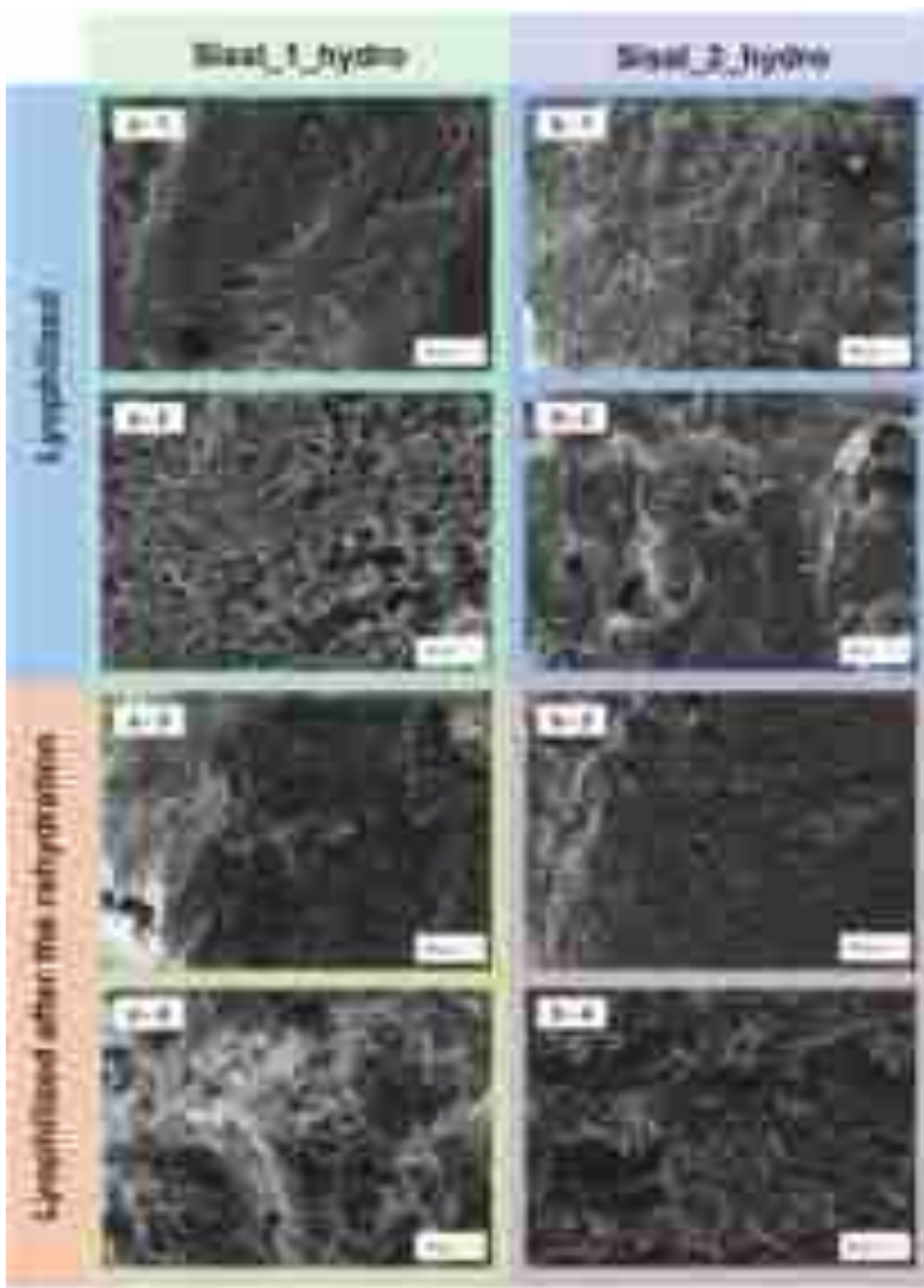


Fig. 10. Transactional SEM images and pore size distribution of sisal_1_hydro (a) and sisal_2_hydro (b), lyophilized (1,2) and after the rehydration and lyophilization (3,4) at a magnification of 100 and 500 times.

marginally elevated concentration of lignin, a compound characterized by a high carbon content, which could have influenced the observed results.

Hemicelluloses decomposed earlier than the other components of sisal fiber, starting at 160 °C (Fig. 12). The significant mass loss

primarily occurred within the 200 °C – 300 °C temperature range. The decomposition of hemicelluloses displayed a peak around 220 °C and a shoulder at approximately 300 °C, which can be attributed to the breaking of glycosidic bonds and the depolymerization of polysaccharide units [81].

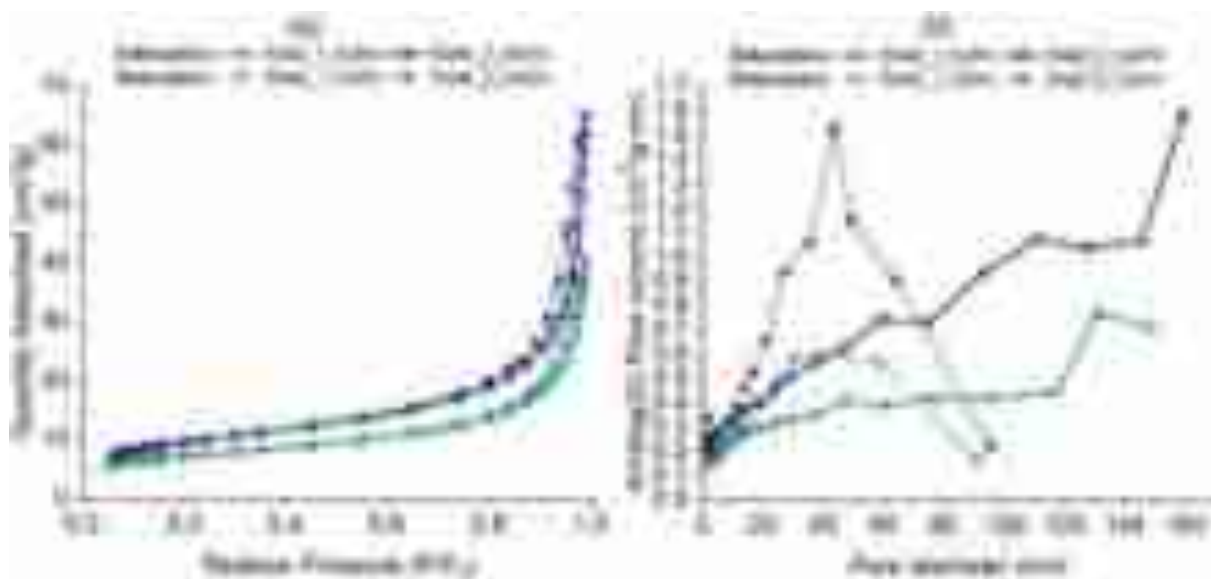


Fig. 11. N_2 adsorption and desorption isotherms (a) and BJH size distribution for the sisal-based hydrogels(b).

Table 3

BET surface area and BJH pore volume.

Sample	BET Surface Area (m^2/g)	BJH Total Pore Volume (cm^3/g)
Sisal_1_hydro	26.2	0.058
Sisal_2_hydro	34.7	0.096

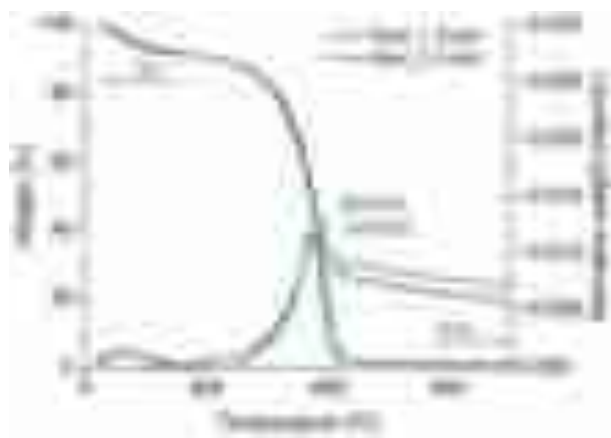


Fig. 12. TGA and DTG curves of the dried sisal_1_hydro and sisal_2_hydro. N_2 flow of 50 mL/min and a 10 °C/min heating rate.

The intense peak around 370 °C is attributed to cellulose (Fig. 12), the primary component of sisal fibers. Cellulose decomposes through a rapid depolymerization process by decomposing the glycosyl units to 1,6-anhydro-b-D-glucopyranose [82]. The DTG curves indicate a minor reduction in the intensity of the peak associated with sisal_2_hydro when compared to sisal_1_hydro. This supports the hypothesis that the first sample would have a marginally higher percentage of lignin, which may correlate with a comparatively lower percentage of cellulose.

Lignin typically shows a more pronounced thermal decomposition around the 400 °C range; in the TG curve, a gradual change starts at 400 °C (Fig. 12). However, since the change is gradual and the initial biomass has a low lignin content (about 12 %), no peak is observed in the DTG curve. Lignin's thermal decomposition disrupts the hydroxyl group connected to β - or γ -carbon in aliphatic and alkyl side chains [83]. However, the primary step in lignin thermal decomposition involves

breakages through C—C and β -scission or aryl-ether cleavage [82].

3.2.8. Dynamic mechanical analyses

3.2.8.1. Compression essays. Fig. 13 displays the stress-strain curves for the swollen (Fig. 13(a)), freeze-dried (Fig. 13(b)), and rehydrated (Fig. 13(c)) hydrogels, along with the compressive moduli of the samples (Fig. 13(d)). None of the samples failed until the applied force reached 18 N, which was the maximum force applied. Fig. 13(a) shows that at 18 N, the swollen sisal_1_hydro had the highest strength against compression up to 103.2 kPa at a strain of 86.7 %, while sisal_2_hydro achieved a lower maximum stress (84.0 kPa) at a compression strain of 75.1 %. At a strain of 75.1 % (the highest for sisal_2_hydro), sisal_1_hydro exhibited a stress of 44.1 kPa, which is significantly lower than the stress recorded for sisal_2_hydro, at 84.0 kPa. Neither sample achieved the stress breaking at the highest force applied, and both hydrogels could be compressed to strains higher than 70 %, indicating excellent load-bearing ability [84].

Fig. 13(b) shows that the lyophilized samples exhibited typical compressive stress-strain curves characteristic of foams. These curves have three regions: linear elastic, cell collapse, and plastic stiffening [85,86]. It is observable that sisal_2_hydro withstands more stress at lower strains than sisal_1_hydro within the same force range (<18 N). For sisal_1_hydro, the compression stress was 117.7 kPa at 72.4 % strain; for sisal_2_hydro, it was 120.2 kPa at 54.7 %. The superior mechanical properties of the freeze-dried sisal_2_hydro compared to sisal_1_hydro may be due to the higher concentration of macromolecules [87], *i.e.*, cellulose and hemicellulose, and its greater insoluble fraction.

Fig. 13(c) indicates that the rehydrated samples exhibit the same compressive behavior as the hydrogel. The compressive stress of sisal_1_hydro and sisal_2_hydro was 193.2 kPa at 88.1 % and 118.3 kPa at 79.9 %, respectively.

The compressive stress-strain behavior of the swollen and rehydrated hydrogels (Fig. 13(a) and Fig. 13(c)) indicates that sisal_1_hydro deformed more than sisal_2_hydro, *i.e.*, it reached higher strains (> 86 %). This means that the less massive hydrogel has a more flexible structure. The rehydrated sisal_1_hydrogel also exhibited a higher deformation compared to the as-formed swollen hydrogel.

Fig. 13(d) shows the compressive elastic moduli (Young's) of the samples. The swollen hydrogels, sisal_1_hydro and sisal_2_hydro, exhibited compressive elastic moduli of 29.7 and 62.4 kPa, respectively. Thus, the sisal_2_hydro had the double sisal_1_hydro modulus,

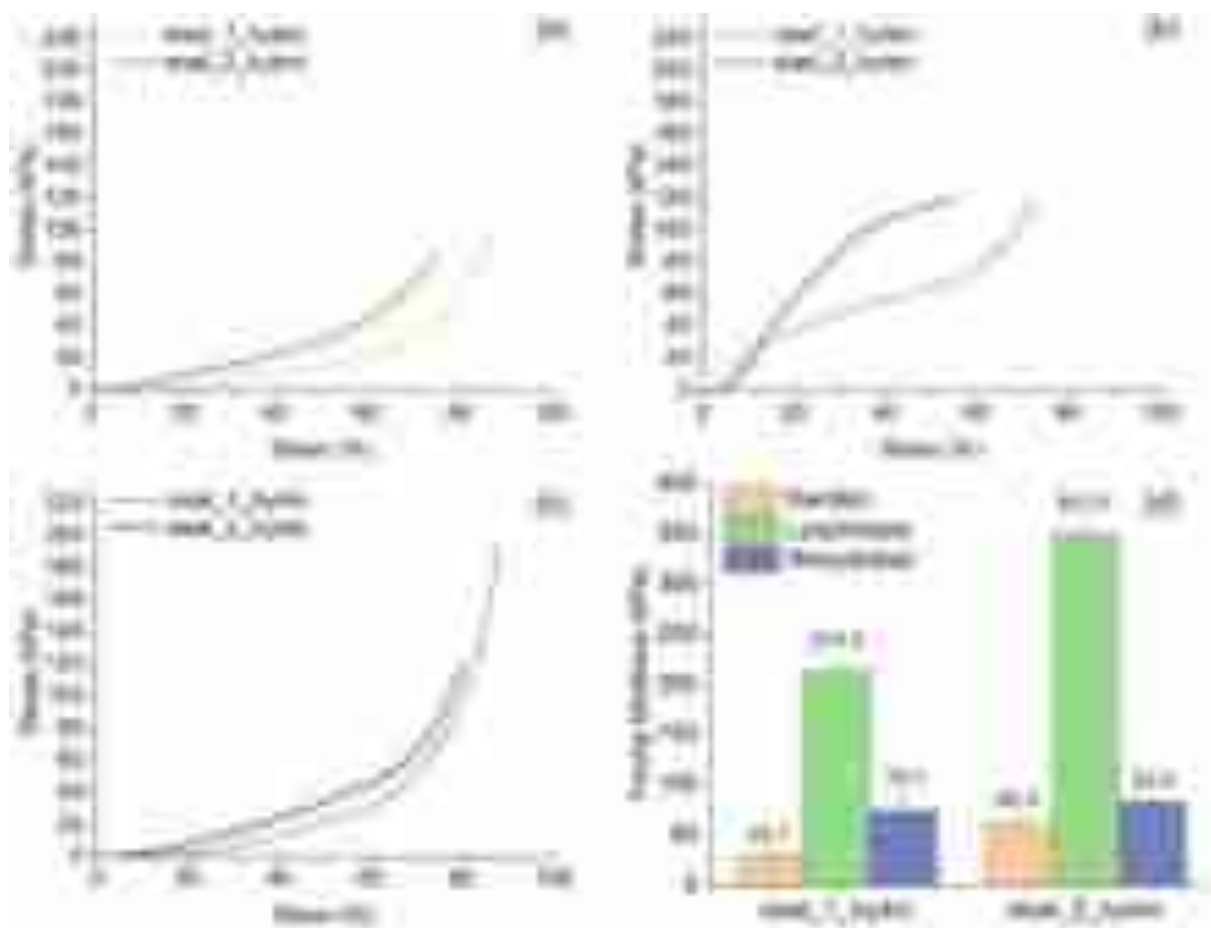


Fig. 13. Compressive stress-strain curves of swollen during coagulation (a), lyophilized (b), and rehydrated (c) samples; and compressive elastic moduli of the samples (d), obtained from the initial linear slope of the curves. Data collected with the applied force reaching a maximum of 18 N. Test temperature: 25 °C.

approximately, indicating a direct proportional relationship between the initial sisal mass deconstructed and dissolved and the compression resistance of the material.

Queiroz et al. [26] reached elastic moduli of 23 kPa and 73 kPa for the hydrogels made from sisal fibers without and with lignin content, respectively. It is worth noting that our results have a similar magnitude to those of Queiroz et al. [26], which is expected since both used sisal as the source of lignocellulose.

Fig. 13(d) also showed that the swollen *sisal_1_hydro* and *sisal_2_hydro* had the lowest Young's moduli compared to the lyophilized and rehydrated ones. The elastic moduli of the dried samples were 214.3 and 351 kPa, significantly higher than those of the swollen samples. The rehydrated samples, in turn, achieved intermediate elastic moduli of 75.1 kPa and 83.4 kPa.

The direct relationship between the initial sisal content and the moduli obtained by the swollen hydrogels was not observed for the lyophilized and rehydrated samples. In this case, the 100 % improvement in the sisal amount during hydrogel creation resulted in a 64 % and 10.7 % increase in compression moduli for lyophilized and rehydrated samples, respectively. *Sisal_2_hydro* had higher Young's moduli than *sisal_1_hydro*, corroborating that compressive modulus increases with the hydrogel concentration [87].

In Table 4, the compressive Young's moduli of various bio-based hydrogels are presented in their swollen, lyophilized, and rehydrated states, compared with the findings of the current study. The swollen biopolymeric hydrogels showed moduli ranging from 62.4 kPa (*sisal_2_hydro*) to 225 kPa (agar-based hydrogel). This variation may be due to the superior gelation properties of agar compared to cellulose [88]. Lyophilized and rehydrated *sisal_2_hydro* samples, on the

Table 4
Compressive Young's Modulus of different bio-based hydrogels.

Hydrogel	Condition	Young's Modulus (kPa)	Ref.
Agar-based hydrogel	Swollen	225*	[89]
Lignocellulose-based hydrogel	Swollen	73	[26]
<i>Sisal_2_hydro</i>	Swollen	62.4	This study
Nanocellulose-based hydrogel	Lyophilized	50*	[90]
Cellulose hydrogels	Lyophilized	150	[91]
Silk Fibroin Cryogel	Lyophilized	90	[92]
<i>Sisal_2_hydro</i>	Lyophilized	351.0	This study
Macroporous Poly(isocyanopeptide) cryogel	Rehydrated	7*	[93]
Hybrid starch-poly(acrylamide-co-itaconic acid)/ZnO hydrogel	Rehydrated	9.35	[94]
<i>Sisal_2_hydro</i>	Rehydrated	83.4	This study

* Proximate value extracted from graphs.

contrary, had the highest modulus, compared to other cellulose, starch, and amino acid-based hydrogels. This superior compression resistance may be attributed to the known filler effect of lignin particles [42,43].

3.2.8.2. Shear essays. Fig. 14 shows the viscoelastic properties of the hydrogels when subjected to shear stress. Fig. 14 (a) shows that the amplitude increases from 0.1 to 50 μ m, corresponding to a strain range of 0.02 % to 1.0 %. The storage modulus remains nearly constant across the assessed range, with only a slight deviation noted at higher

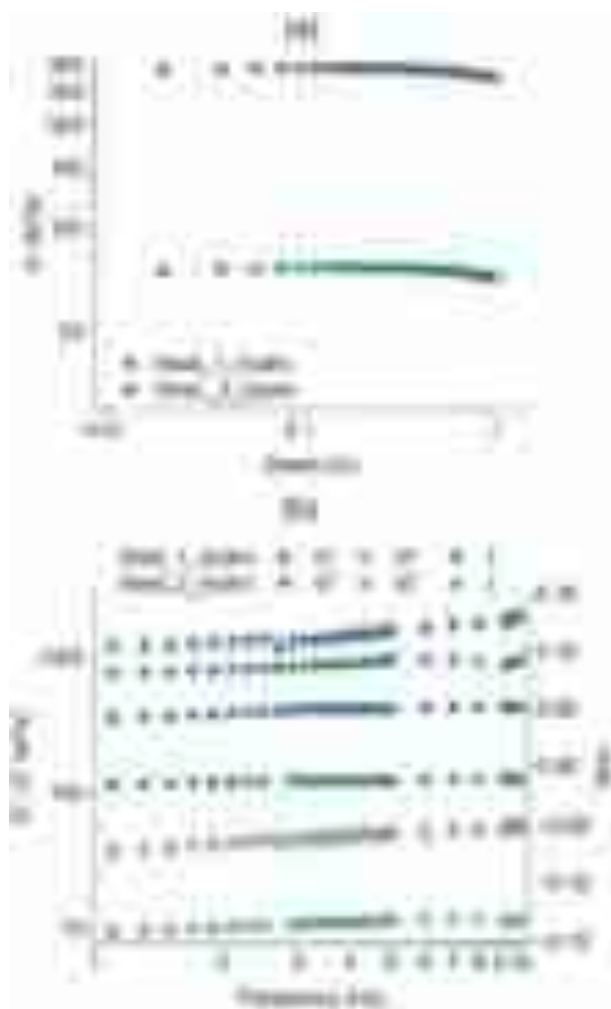


Fig. 14. Shear stress-strain curves of swollen hydro₁sisal and hydro₂sisal. Amplitude sweep (a) expresses the storage modulus in the function of the strain (%); frequency sweep (b) indicates the effect of the frequency over the storage, loss moduli, and tan δ . Test temperature: 25 °C.

amplitudes. Given a maximum deviation of 5 %, all measurements fall within the linear viscoelastic region (LVR).

A hydrogel's LVR is the range in which the material's viscoelastic properties remain stable and unaffected by the applied stress. Within this region, the hydrogel's structural integrity is preserved, enabling an accurate characterization of its mechanical properties, including the storage (G') and loss modulus (G'') [95]. As a result, the frequency sweep was performed at a strain of 0.2 % (equivalent to an amplitude of 10 μm) to ensure operation within the LVR, thereby maintaining sample stability under these conditions and complying with the equipment specifications, which recommend amplitudes between 10 and 20 μm .

Fig. 14(b) illustrates that for both hydrogels, the storage modulus (G') consistently exceeds the loss modulus (G'') across the entire applied frequency range. This results in a tangent delta ($\tan\delta = G''/G'$) value that remains below one, indicating a predominance of elastic behavior over viscous behavior in the material [96]. The tan delta value of sisal₁-hydro is lower than that of sisal₂-hydro, indicating that the former has greater elasticity.

The hydrogels were created from the polysaccharide fraction, which comprises cellulose and hemicelluloses, which are characterized by cyclic structures containing hydroxyl groups. Additionally, lignin, a macromolecule composed of aromatic rings with hydroxyl groups and other functional groups (Fig. 1), was incorporated into the composition. This combination resulted in hydrogels exhibiting a network

architecture predominantly formed by these cyclic compounds, with hydrogen bonding as the primary intermolecular force within this structural framework. The nearly independent relationship between G' and the oscillatory frequency across a wide range, as shown in Fig. 14 (b), defines both samples as "strong gels," primarily due to the chemical structure and intermolecular interactions of the components that make up the network. The average storage moduli for the hydrogels were 123.8 ± 2.84 kPa for sisal₁-hydro and 416.8 ± 23.0 kPa for sisal₂-hydro. This difference indicates that the viscoelastic properties of the hydrogels were significantly impacted by the suspended solid content in the CUEN medium, which played a crucial role in forming the network of the solidified gel [97].

3.3. Heavy metal sorption

Fig. 15 shows the sorption capacity of heavy metals by the hydrogels from a multi-component solution. The sisal₂-hydro achieved higher sorption capacities for each metal and total compared to sisal₁-hydro. This improved performance may be attributed to the larger pore volume and surface area of sisal₂-hydro (Table 3), which offers more sites for metal sorption compared to sisal₁-hydro. Furthermore, the lower crystallinity of this hydrogel (17 %) versus sisal₁-hydro (26 %) may also have played a role. Sisal₁-hydro removed preferably the metals in the following order: Cu(II) > Ni(II) > Cd(II) > Zn(II) > Mn(II) > Cr(VI), while the sisal₂-hydro sorbed the metals in this order: Cu(II) > Cd(II) > Ni(II) > Zn(II) > Mn(II) > Cr(VI). The lower selectivity towards chromium may be related to the fact that it is present as an oxyanion species HCrO_4^- at pH 4.5, while the other metals are completely dissociated as bivalent cations in the solution (Fig. 3). Except for cadmium, these affinity orders between the bivalent metals are inversely proportional to the improvement in ionic radii and coordination number (CN). Since the ionic radii order is: Cu(II) (CN 4.57 pm), Ni(II) (CN 6.69 pm), Zn(II) (CN 6.74 pm), Mn(II) (CN 6.83 pm), Cd(II) (CN 6.95 pm) [98].

The intermediary sorption capacity of cadmium on the hydrogels may not be ruled by the ion radii as the other metals but by the hydration energy. The bivalent cadmium cation has the lowest molar Gibbs energies of hydration (-1755 kJ/mol) [99], which means that the coordinated water can be more easily removed from the coordination shell, allowing cadmium to bond to the sorbent by inner-sphere interactions [100].

Cadmium was also more preferentially sorbed on sisal₂-hydro, likely due to the larger pores of this ion compared to sisal₁-hydro.

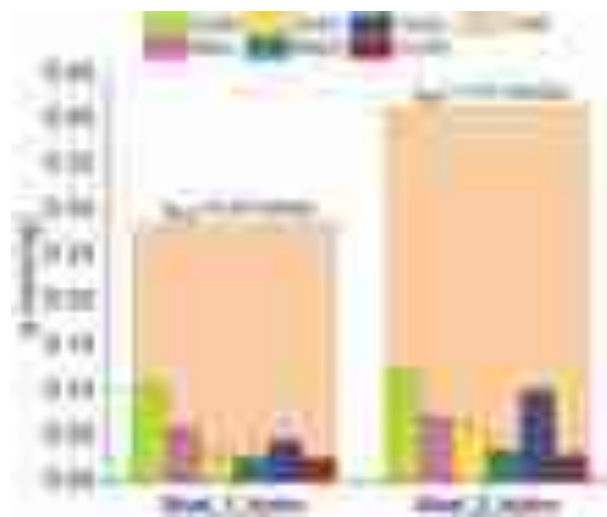


Fig. 15. Sorption capacity of the hydrogels towards the heavy metals. Experimental conditions: pH 4.5, 25 °C, 250 rpm, 24 h, $S = 1$ g/L, $C_0 = 0.17$ mmol/L (each).

Because of its radius and molar mass (112.41 u), cadmium has the least favorable diffusion into the pores. Thus, large pores could facilitate cadmium diffusion to the sorption sites of the hydrogels.

Table 5 presents recent findings on heavy metal sorption using lignocellulose-based hydrogels as sorbents, where tobacco straw, soybean residue, *Tectona grandis* sawdust, and sisal (this work) are used as lignocellulose sources to produce the hydrogel sorbents. Using biomass, especially non-woody types like those listed in Table 5, as a direct source of macromolecules is beneficial. This approach aligns with lean manufacturing principles, encourages recycling and upcycling materials, and seeks innovative ways to reduce or eliminate waste in the production process [101].

These hydrogels (Table 5) had different sorptive responses towards heavy metals. Those made by polymerizing pretreated wastes (tobacco straw or soybean residue) with acrylic acid/potassium acrylate by UV radiation initiation [102,103] achieved the highest sorption capacities. The enhanced performance results from the presence of carboxyl groups, which attract and bind metals because of their negative charge.

The findings achieved in this work were comparable, *i.e.*, sorption capacities in the same magnitude order, with the results obtained by Das et al. [104], Table 5. In their work, lignin was extracted from sawdust using sulfuric acid and added to a sodium alginate solution. The clay montmorillonite was also dispersed into the mixture. Unlike the methodology of Zhang et al. [102,103], Das et al. [104] prepared the hydrogel through copolymerization of acrylic acid without UV initiation. The authors confirmed that the heavy metal sorption mechanism is related to ion exchange and chelation.

4. Conclusions

This study investigated the creation of hydrogels using all components of sisal fibers, achieved through direct dissolution with CUEN, followed by coagulation in a water bath. Additionally, their effectiveness in recovering heavy metals from aqueous solutions was evaluated.

CUEN demonstrated the ability to effectively deconstruct sisal fibers, achieving dissolution efficiencies of 73.7 % (sisal_1_hydro) and 52.4 % (sisal_2_hydro), resulting in a viscous suspension. Rheological analysis of the hydrogels confirmed their gel-like characteristics, showing that their

viscoelastic properties were greatly affected by the solid content concentration suspended in the solution that made up the hydrogels.

The hydrogels exhibited high water sorption rates, specifically 5076.4 % and 2685.8 % for sisal_1_hydro and sisal_2_hydro, respectively. Water reabsorption after freeze-drying of water-swollen hydrogels was significantly lower than in the original hydrogel. This aspect should be further investigated in subsequent steps of this study to identify conditions that have a lesser impact on water absorption capacity.

The enhanced water absorption capacity of sisal_1_hydro can be attributed to its lower degree of physical cross-linking compared to sisal_2_hydro. This characteristic renders it more flexible and better equipped for internal reorganization, while also promoting the accessibility of hydrophilic groups. In contrast, the greater concentration of sisal components in the CUEN solution that produced sisal_2_hydro contributed to enhanced material crystallinity and mechanical strength, as evidenced by the increase in compressive elastic moduli, rising from 29.7 kPa for sisal_1_hydro to 62.4 kPa for sisal_2_hydro. Sisal_2_hydro also presented higher BET surface area and pore volume than sisal_1_hydro.

The physical hydrogels, produced through a straightforward solvent inversion methodology utilizing water as a non-solvent, demonstrated heavy metals sorption capacities of 0.29 and 0.41 mmol/g for sisal_1_hydro and sisal_2_hydro, respectively. The observed difference in sorption capacity can be attributed to factors such as surface area, pore size and volume, diffusion of the sorbate into the pores, and the availability of sorption sites within each material. These hydrogels exhibited sorption capacities comparable to those reported in the literature for other hydrogel materials, indicating their potential usefulness for wastewater treatment. The findings presented and analyzed align with the predictions established for the respective stage of the investigation. Future endeavors should focus on an in-depth examination of the sorption mechanism to clarify the interactions between the sorbent and the metal ions involved.

The findings reveal a promising method for water purification using hydrogels made from lignocellulosic sisal fibers, demonstrating their effectiveness in removing toxic metals from water. This could lead to the development of sustainable solutions for water contamination problems.

Table 5
Comparison of heavy metal sorption capacity of cellulose-based hydrogels from biomass.

Hydrogel	Experimental Conditions	Metal	q (mmol/g)	Ref.
Tobacco straw-based poly(acrylic acid) hydrogels	$C_0 = 4$ mmol/L	Pb(II)	1.49	[102]
	pH 6.0	Cd(II)	1.02	
	$S = 0.86$ g/L	Hg(II)	0.94	
	200 rpm			
Soybean residue-poly(acrylic acid) hydrogel	25 °C, 2 h	Pb(II)	2.03	[103]
	$C_0 = 2.5$ mmol/L			
	pH 6.0			
	$S = 0.6$ g/L	Cd(II)	1.43	
Alginate@Lignin–Montmorillonite Hydrogel Composite from <i>Tectona grandis</i> Sawdust	200 rpm			[104]
	25 °C, 2 h			
	$C_0 = 10$ ppm	Pb(II)	0.06	
	pH 8.0	Cd(II)	0.10	
Sisal_1_hydro	$S = 1.25$ g/L	Hg(II)	0.06	This study
	30 °C	As(II)	0.15	
	50 rpm, 4 h			
	$C_0 = 0.2$ mmol/L	Cu(II)	0.10	
	pH 4.5	Cd(II)	0.04	
	$S = 1$ g/L	Mn(II)	0.03	
	25 °C	Zn(II)	0.03	
	250 rpm, 24 h	Ni(II)	0.06	
Sisal_2_hydro		Cr(VI)	0.03	This study
	$C_0 = 0.2$ mmol/L	Cu(II)	0.12	
	pH 4.5	Cd(II)	0.10	
	$S = 1$ g/L	Mn(II)	0.03	
	25 °C	Zn(II)	0.06	
	250 rpm, 24 h	Ni(II)	0.07	
		Cr(VI)	0.03	

However, future research should aim to increase the swelling of dry hydrogels. Additionally, sorption properties should be assessed based on sorbent dosage, as well as pH and temperature levels typical of wastewater contaminated with heavy metals.

This study suggests a potential scalability of the process, indicating that further research could potentially increase its growth potential. Additionally, an upcoming investigation into the desorption of metals from hydrogels, as well as the subsequent reuse of both the extracted metals and the biomass comprising the hydrogels, will reinforce the principles of circular bioeconomy.

The methodology employed initiates with sisal fibers as the primary raw material and is based on fiber deconstruction, given that CUEN has the capability to dissolve both cellulose and hemicelluloses. Consequently, this approach applies to a wide range of lignocellulosic fibers, significantly broadening its potential global applications.

CRedit authorship contribution statement

Giani de Vargas Brião: Writing – review & editing, Writing – original draft, Visualization, Validation, Software, Methodology, Investigation, Formal analysis, Data curation, Conceptualization. **Bianca Groner Queiroz:** Visualization, Validation, Methodology, Investigation, Data curation, Conceptualization. **Rafaela Reis Ferreira:** Writing – review & editing, Visualization, Investigation, Formal analysis. **Derval dos Santos Rosa:** Writing – review & editing, Visualization, Validation, Methodology, Funding acquisition, Data curation, Conceptualization. **Elisabete Frollini:** Writing – review & editing, Writing – original draft, Visualization, Validation, Supervision, Project administration, Methodology, Investigation, Formal analysis, Data curation, Conceptualization.

Funding

This work was supported by FAPESP, São Paulo Research Foundation (grant #2020/13703–3 and grant #2023/07447–2).

Declaration of competing interest

The authors declare that they have no known competing financial interests or personal relationships that could have appeared to influence the work reported in this paper.

Data availability

Data will be made available on request.

References

- [1] R. Shrestha, S. Ban, S. Devkota, S. Sharma, R. Joshi, A.P. Tiwari, H.Y. Kim, M. K. Joshi, Technological trends in heavy metals removal from industrial wastewater: A review, *J. Environ. Chem. Eng.* 9 (2021) 105688, <https://doi.org/10.1016/j.jece.2021.105688>.
- [2] M.J. Sharifi, A. Nouralishahi, A. Hallajisani, Fe3O4-chitosan nanocomposite as a magnetic biosorbent for removal of nickel and cobalt heavy metals from polluted water, *Int. J. Biol. Macromol.* 248 (2023) 125984, <https://doi.org/10.1016/j.ijbiomac.2023.125984>.
- [3] Q. Hu, D. Tang, Y. Xiang, X. Chen, J. Lin, Q. Zhou, Magnetic ion-imprinted polyacrylonitrile-chitosan electro-spun nanofibrous membrane as recyclable adsorbent with selective heavy metal removal and antibacterial fouling in water treatment, *Int. J. Biol. Macromol.* 241 (2023) 124620, <https://doi.org/10.1016/j.ijbiomac.2023.124620>.
- [4] A. Agarwal, U. Upadhyay, I. Sreedhar, S.A. Singh, C.M. Patel, A review on valorization of biomass in heavy metal removal from wastewater, *J. Water Process Eng.* 38 (2020) 101602, <https://doi.org/10.1016/j.jwpe.2020.101602>.
- [5] K. Vijayaraghavan, R. Balasubramanian, Is biosorption suitable for decontamination of metal-bearing wastewaters? A critical review on the state-of-the-art of biosorption processes and future directions, *J. Environ. Manage.* 160 (2015) 283–296, <https://doi.org/10.1016/j.jenvman.2015.06.030>.
- [6] U.M. Ismail, M.S. Vohra, S.A. Onaizi, Adsorptive removal of heavy metals from aqueous solutions: Progress of adsorbents development and their effectiveness, *Environ. Res.* 251 (2024) 118562, <https://doi.org/10.1016/j.envres.2024.118562>.
- [7] J. Bayuo, M.J. Rwiza, J.W. Choi, K.M. Mtei, A. Hosseini-Bandegharai, M. Sillanpää, Adsorption and desorption processes of toxic heavy metals, regeneration and reusability of spent adsorbents: Economic and environmental sustainability approach, *Adv. Colloid Interf. Sci.* 329 (2024) 103196, <https://doi.org/10.1016/j.cis.2024.103196>.
- [8] G.L. Dotto, G. McKay, Current scenario and challenges in adsorption for water treatment, *J. Environ. Chem. Eng.* 8 (2020) 103988, <https://doi.org/10.1016/j.jece.2020.103988>.
- [9] Z. Tariq, D.N. Iqbal, M. Rizwan, M. Ahmad, M. Faheem, M. Ahmed, Significance of biopolymer-based hydrogels and their applications in agriculture: a review in perspective of synthesis and their degree of swelling for water holding, *Res. Adv.* 13 (2023) 24731–24754, <https://doi.org/10.1039/d3ra03472k>.
- [10] J.V. Alemán, A.V. Chadwick, J. He, M. Hess, K. Horie, R.G. Jones, P. Kratochvíl, I. Meisel, I. Mita, G. Moad, S. Penczek, R.F.T. Stepto, Definitions of terms relating to the structure and processing of sols, gels, networks, and inorganic-organic hybrid materials (IUPAC Recommendations 2007), *Pure Appl. Chem.* 79 (2007) 1801–1829, <https://doi.org/10.1351/pac200779101801>.
- [11] L.S. Maia, P.H.F. Pereira, A.I.C. da Silva, T.B. da Costa, D.R. Mulinari, D. dos S. Rosa, A novel starch-based composite hydrogel enhanced by activated charcoal from the banana peel for water decontamination, *J. Appl. Polym. Sci.* 141 (2024), <https://doi.org/10.1002/app.55685>.
- [12] J.G. Ribeiro, R.M. Raimondi, A.G. de Souza, D. dos Santos Rosa, A.T. Paulino, An ecofriendly pectin-co-montmorillonite composite hydrogel for the separation of contaminant metal ions from water, *Journal of Water, Process. Eng.* 69 (2025) 106629, <https://doi.org/10.1016/j.jwpe.2024.106629>.
- [13] A. Mahmood, D. Patel, B. Hickson, J. DesRochers, X. Hu, Recent Progress in Biopolymer-Based Hydrogel Materials for Biomedical Applications, *Int. J. Mol. Sci.* 23 (2022) 1415, <https://doi.org/10.3390/ijms23031415>.
- [14] T.A. Adjuik, S.E. Nokes, M.D. Montross, Biodegradability of bio-based and synthetic hydrogels as sustainable soil amendments: A review, *J. Appl. Polym. Sci.* 140 (2023), <https://doi.org/10.1002/app.53655>.
- [15] F. Sang, C. Liu, J. Yan, J. Su, S. Niu, S. Wang, Y. Zhao, Q. Dang, Polysaccharide- and protein-based hydrogel dressings that enhance wound healing: A review, *Int. J. Biol. Macromol.* 280 (2024) 135482, <https://doi.org/10.1016/j.ijbiomac.2024.135482>.
- [16] R. Zhou, R. Cai, Y. Chen, J. Qiao, K. Ding, X. Tan, M. Ding, Y. Chen, Research progress on the application of hydrogel adsorbent materials in wastewater treatment: A review, *Chem. Eng. Res. Des.* 216 (2025) 1–24, <https://doi.org/10.1016/j.cherd.2025.02.025>.
- [17] L.C. Wong, C.P. Leh, C.F. Goh, Designing cellulose hydrogels from non-woody biomass, *Carbohydr. Polym.* 264 (2021) 118036, <https://doi.org/10.1016/j.carbpol.2021.118036>.
- [18] S.M.F. Kabir, P.P. Sikdar, B. Haque, M.A.R. Bhuiyan, A. Ali, M.N. Islam, Cellulose-based hydrogel materials: chemistry, properties and their prospective applications, *Prog. Biomater.* 7 (2018) 153–174, <https://doi.org/10.1007/s40204-018-0095-0>.
- [19] J. Gong, L. Hou, Y.C. Ching, K.Y. Ching, N.D. Hai, C.H. Chuah, A review of recent advances of cellulose-based intelligent-responsive hydrogels as vehicles for controllable drug delivery system, *Int. J. Biol. Macromol.* 264 (2024) 130525, <https://doi.org/10.1016/j.ijbiomac.2024.130525>.
- [20] G. de V. Brião, D.S. Rosa, E. Frollini, Hydrogels from non-woody lignocellulosic biomass for toxic metal uptake from wastewater: a brief overview, *Cellulose* (2024), <https://doi.org/10.1007/s10570-024-06321-w>.
- [21] A. Karimah, M.R. Ridho, S.S. Munawar, D.S. Adi, R. Ismadi, B. Damayanti, W. Subiyanto, A. Fudholi Fatriasari, A review on natural fibers for development of eco-friendly bio-composite: characteristics, and utilizations, *J. Mater. Res. Technol.* 13 (2021) 2442–2458, <https://doi.org/10.1016/j.jmrt.2021.06.014>.
- [22] R.S. Abolore, S. Jaiswal, A.K. Jaiswal, Green and sustainable pretreatment methods for cellulose extraction from lignocellulosic biomass and its applications: A review, *Carbohydr. Polym. Technol. Appl.* 7 (2024), <https://doi.org/10.1016/j.carpta.2023.100396>.
- [23] A. Cantalino, E.A. Torres, M.S. Silva, Sustainability of Sisal Cultivation in Brazil Using Co-Products and Wastes, *J. Agric. Sci.* 7 (2015), <https://doi.org/10.5539/jas.v7n7p64>.
- [24] FAO, Jute, kenaf, sisal, abaca, coir and allied fibres, Rome, 2024, <https://openknowledge.fao.org/items/c079df05-113b-4fa8-9fbf-b80df6b8f826>, 2023. (Accessed 12 January 2025).
- [25] Y. Vasconcellos, Fiber of the future, *Revista FAPESP* (2009). <https://revistas.fapesp.br/en/fiber-of-the-future/> (accessed May 2, 2024).
- [26] B.G. Queiroz, H. Ciol, N.M. Inada, E. Frollini, Hydrogel from all in all lignocellulosic sisal fibers macromolecular components, *Int. J. Biol. Macromol.* 181 (2021) 978–989, <https://doi.org/10.1016/j.ijbiomac.2021.04.088>.
- [27] H. Yadav, C. Karthikeyan, Natural polysaccharides: Structural features and properties, in: *Polysaccharide Carriers for Drug Delivery*, Elsevier, 2019, pp. 1–17, <https://doi.org/10.1016/B978-0-08-102553-6.00001-5>.
- [28] M. Przyypis, A. Wawoczny, D. Gillner, Biomass and Cellulose Dissolution—The Important Issue in Renewable Materials Treatment, *Appl. Sci.* 13 (2023) 1055, <https://doi.org/10.3390/app13021055>.
- [29] B.V.M. Rodrigues, E. Heikkilä, E. Frollini, P. Fardim, Multi-technique surface characterization of bio-based films from sisal cellulose and its esters: A FE-SEM, μ -XPS and ToF-SIMS approach, *Cellulose* 21 (2014) 1289–1303, <https://doi.org/10.1007/s10570-014-0216-4>.
- [30] Y.-Y. Ma, Z.-L. Lu, Y.-Z. Xing, W.-S. Zheng, C.-G. Liu, A fresh perspective on dissociation mechanism of cellulose in DMAc/LiCl system based on Li bond

- theory, *Int. J. Biol. Macromol.* 268 (2024) 131729, <https://doi.org/10.1016/j.ijbiomac.2024.131729>.
- [31] L.A. Ramos, E. Frollini, Th. Heinze, Carboxymethylation of cellulose in the new solvent dimethyl sulfoxide/tetrabutylammonium fluoride, *Carbohydr. Polym.* 60 (2005) 259–267, <https://doi.org/10.1016/j.carbpol.2005.01.010>.
- [32] E.V.R. Almeida, E. Frollini, A. Castellan, V. Coma, Chitosan, sisal cellulose, and biocomposite chitosan/sisal cellulose films prepared from thiourea/NaOH aqueous solution, *Carbohydr. Polym.* 80 (2010) 655–664, <https://doi.org/10.1016/j.carbpol.2009.10.039>.
- [33] Z. Hu, Q. Liu, Q. Zhang, J. Zhang, L. Chen, S. Xu, Facile fabrication of regenerated cellulose-based separators for high-performance lithium-ion batteries by regulating degrees of polymerization, *Int. J. Biol. Macromol.* 268 (2024) 131854, <https://doi.org/10.1016/j.ijbiomac.2024.131854>.
- [34] M. Kostag, K. Jedvert, O.A. El Seoud, Engineering of sustainable biomaterial composites from cellulose and silk fibroin: Fundamentals and applications, *Int. J. Biol. Macromol.* 167 (2021) 687–718, <https://doi.org/10.1016/j.ijbiomac.2020.11.151>.
- [35] N. Keppeler, P.A.R. Pires, J.L.S. de Freitas, N.I. Malek, E. Frollini, O.A. El Seoud, Cellulose acetylation in ionic liquid-molecular solvent mixtures: influence of the biopolymer-induced preferential solvation on its dissolution and reactivity, *Cellulose* 31 (2024) 9043–9055, <https://doi.org/10.1007/s10570-024-06014-4>.
- [36] D.S. Porto, A. Cassales, H. Ciol, N.M. Inada, E. Frollini, Cellulose as a polyol in the synthesis of bio-based polyurethanes with simultaneous film formation, *Cellulose* 29 (2022) 6301–6322, <https://doi.org/10.1007/s10570-022-04662-y>.
- [37] B.G. Queiroz, H. Ciol, N.M. Inada, E. Frollini, Cross-linked bio-based hydrogels generated from solutions derived from the deconstruction of sisal fibers, *J. Mol. Liq.* 369 (2023) 120876, <https://doi.org/10.1016/j.molliq.2022.120876>.
- [38] J.P. Varela, A. Lamy-Mendes, L. Durães, A reconsideration on the definition of the term aerogel based on current drying trends, *Microporous Mesoporous Mater.* 258 (2018) 211–216, <https://doi.org/10.1016/j.micromeso.2017.09.016>.
- [39] S.O. Ilyin, A.V. Kostyuk, T.S. Anokhina, V.Y. Melekchina, D.S. Bakhtin, S. V. Antonov, A.V. Volkov, The Effect of Non-Solvent Nature on the Rheological Properties of Cellulose Solution in Diluted Ionic Liquid and Performance of Nanofiltration Membranes, *Int. J. Mol. Sci.* 24 (2023) 8057, <https://doi.org/10.3390/ijms24098057>.
- [40] M. Wortmann, P. Krieger, N. Frese, E. Moritzer, B. Hüsgen, Effect of Isocyanate Absorption on the Mechanical Properties of Silicone Elastomers in Polyurethane Vacuum Casting, *ACS Omega* 6 (2021) 4687–4695, <https://doi.org/10.1021/acsomega.0c05436>.
- [41] D. Tarasov, M. Leitch, P. Fatehi, Lignin-carbohydrate complexes: properties, applications, analyses, and methods of extraction: a review, *Biotechnol. Biofuels* 11 (2018) 269, <https://doi.org/10.1186/s13068-018-1262-1>.
- [42] K. Nakasone, T. Kobayashi, Cytocompatible cellulose hydrogels containing trace lignin, *Mater. Sci. Eng. C* 64 (2016) 269–277, <https://doi.org/10.1016/j.msec.2016.03.108>.
- [43] R.M. Kalinoski, J. Shi, Hydrogels derived from lignocellulosic compounds: Evaluation of the compositional, structural, mechanical and antimicrobial properties, *Ind. Crop. Prod.* 128 (2019) 323–330, <https://doi.org/10.1016/j.indcrop.2018.11.002>.
- [44] H. Ramli, N.F.A. Zainal, M. Hess, C.H. Chan, Basic principle and good practices of rheology for polymers for teachers and beginners, *Chemistry Teacher, International* 4 (2022) 307–326, <https://doi.org/10.1515/cti-2022-0010>.
- [45] D.B. Braun, M.R. Rosen, *Practical Rheology, in: Rheology Modifiers Handbook*, Elsevier, 1999, pp. 1–69, <https://doi.org/10.1016/B978-0-8155-1441-1.50006-1>.
- [46] R. Masrat, M. Maswal, O.A. Chat, G.M. Rather, A.A. Dar, A rheological investigation of sol-gel transition of hydroxypropyl cellulose with nonionic surfactant sorbitan monopalmitate: Modulation of gel strength by UV irradiation, *Colloids Surf. A Physicochem. Eng. Asp.* 489 (2016) 113–121, <https://doi.org/10.1016/j.colsurfa.2015.10.012>.
- [47] R.R.M. de Freitas, K.P. do Carmo, J. de Souza Rodrigues, V.H. de Lima, J. Osmari da Silva, V.R. Botaro, Influence of alkaline treatment on sisal fibre applied as reinforcement agent in composites of corn starch and cellulose acetate matrices, *Plast., Rubber Compos.* 50 (2021) 9–17, <https://doi.org/10.1080/14658011.2020.1816119>.
- [48] Y. Lu, Q. He, G. Fan, Q. Cheng, G. Song, Extraction and modification of hemicellulose from lignocellulosic biomass: A review, *Green Processes Synth.* 10 (2021) 779–804, <https://doi.org/10.1515/gps-2021-0065>.
- [49] S.-F. Sun, H.-Y. Yang, J. Yang, Z.-J. Shi, The effect of alkaline extraction of hemicellulose on cocksfoot grass enzymatic hydrolysis recalcitrance, *Ind. Crop. Prod.* 178 (2022) 114654, <https://doi.org/10.1016/j.indcrop.2022.114654>.
- [50] F. Xu, J. Yu, T. Tesso, F. Dowell, D. Wang, Qualitative and quantitative analysis of lignocellulosic biomass using infrared techniques: A mini-review, *Appl. Energy* 104 (2013) 801–809, <https://doi.org/10.1016/j.apenergy.2012.12.019>.
- [51] W. Wang, C. Wang, Zahoor, X. Chen, Q. Yu, Z. Wang, X. Zhuang, Z. Yuan, Effect of a Nonionic Surfactant on Enzymatic Hydrolysis of Lignocellulose Based on Lignocellulosic Features and Enzyme Adsorption, *ACS Omega* 5 (2020) 15812–15820, <https://doi.org/10.1021/acsomega.0c00526>.
- [52] B. Soni, E.B. Hassan, B. Mahmoud, Chemical isolation and characterization of different cellulose nanofibers from cotton stalks, *Carbohydr. Polym.* 134 (2015) 581–589, <https://doi.org/10.1016/j.carbpol.2015.08.031>.
- [53] J. Coates, *Encyclopedia of Analytical Chemistry - Interpretation of Infrared Spectra, A Practical Approach*, *Encycl. Anal. Chem.* (2004) 1–23. <http://www3.uma.pt/jrodrigues/disciplinas/QINO-II/Teoria/IR.pdf>.
- [54] J.S. Lupoi, E. Gjersing, M.F. Davis, Evaluating Lignocellulosic Biomass, Its Derivatives, and Downstream Products with Raman Spectroscopy, *Front. Bioeng. Biotechnol.* 3 (2015), <https://doi.org/10.3389/fbioe.2015.00050>.
- [55] K. Kavkler, A. Demšar, Examination of cellulose textile fibres in historical objects by micro-Raman spectroscopy, *Spectrochim. Acta A Mol. Biomol. Spectrosc.* 78 (2011) 740–746, <https://doi.org/10.1016/j.saa.2010.12.006>.
- [56] M.R. Almeida, R.S. Alves, L.B.L.R. Nascimben, R. Stephani, R.J. Poppi, L.F.C. de Oliveira, Determination of amylose content in starch using Raman spectroscopy and multivariate calibration analysis, *Anal. Bioanal. Chem.* 397 (2010) 2693–2701, <https://doi.org/10.1007/s00216-010-3566-2>.
- [57] X. Zhang, S. Chen, S. Ramaswamy, Y.S. Kim, F. Xu, Obtaining pure spectra of hemicellulose and cellulose from poplar cell wall Raman imaging data, *Cellulose* 24 (2017) 4671–4682, <https://doi.org/10.1007/s10570-017-1486-4>.
- [58] S. Barzegar, M.H. Aryaie Monfared, M.A. Hubbe, Cellulose and lignin as propitious candidates for preparation of hydrogels for pharmaceutical applications, *Mater Today Commun* 33 (2022) 104617, <https://doi.org/10.1016/j.mtcomm.2022.104617>.
- [59] L. Qin, Y. Zhu, H. Zhang, H. Ren, H. Zhai, Lignin-modified cellulose nanofibers hydrogel under adjustable binary solvent systems with excellent adhesion, self-healing and anti-freeze properties, *Int. J. Biol. Macromol.* 279 (2024) 135559, <https://doi.org/10.1016/j.ijbiomac.2024.135559>.
- [60] P. Krishnaiah, C.T. Ratnam, S. Manickam, Enhancements in crystallinity, thermal stability, tensile modulus and strength of sisal fibres and their PP composites induced by the synergistic effects of alkali and high intensity ultrasound (HIU) treatments, *Ultrason. Sonochem.* 34 (2017) 729–742, <https://doi.org/10.1016/j.ultsonch.2016.07.008>.
- [61] P.K. Gupta, V. Uniyal, S. Naithani, Polymorphic transformation of cellulose I to cellulose II by alkali pretreatment and urea as an additive, *Carbohydr. Polym.* 94 (2013) 843–849, <https://doi.org/10.1016/j.carbpol.2013.02.012>.
- [62] H. Cao, L. Duan, Y. Zhang, J. Cao, K. Zhang, Current hydrogel advances in physicochemical and biological response-driven biomedical application diversity, *Signal Transduct. Target. Ther.* 6 (2021), <https://doi.org/10.1038/s41392-021-00830-x>.
- [63] V. Gounden, M. Singh, Hydrogels and Wound Healing: Current and Future Prospects, *Gels* 10 (2024), <https://doi.org/10.3390/gels10010043>.
- [64] J. Xiang, L. Shen, Y. Hong, Status and future scope of hydrogels in wound healing: Synthesis, materials and evaluation, *Eur. Polym. J.* 130 (2020), <https://doi.org/10.1016/j.eurpolymj.2020.109609>.
- [65] G. Kowalski, M. Witczak, L. Kuterasiński, Structure Effects on Swelling Properties of Hydrogels Based on Sodium Alginate and Acrylic Polymers, *Molecules* 29 (2024), <https://doi.org/10.3390/molecules29091937>.
- [66] E. Díez-Peña, I. Quijada-Garrido, J.M. Barrales-Rienda, Analysis of the swelling dynamics of cross-linked P(N-iPAAm-co-MAA) copolymers and their homopolymers under acidic medium. A kinetics interpretation of the overshooting effect, *Macromolecules* 36 (2003) 2475–2483, <https://doi.org/10.1021/ma021469c>.
- [67] J.P. de Oliveira, G.P. Bruni, K.O. Lima, S.L.M. El Halal, G.S. da Rosa, A.R.G. Dias, E. da R. Zavareze, Cellulose fibers extracted from rice and oat husks and their application in hydrogel, *Food Chem.* 221 (2017) 153–160, <https://doi.org/10.1016/j.foodchem.2016.10.048>.
- [68] S. Shan, X.F. Sun, Y. Xie, W. Li, T. Ji, High-performance hydrogel adsorbent based on cellulose, hemicellulose, and lignin for copper(II) ion removal, *Polymers (Basel)* 13 (2021), <https://doi.org/10.3390/polym13183063>.
- [69] M.T. Ban, N. Mahadin, K.J. Abd Karim, Synthesis of hydrogel from sugarcane bagasse extracted cellulose for swelling properties study, *Mater Today Proc* 50 (2022) 2567–2575, <https://doi.org/10.1016/j.matpr.2021.08.342>.
- [70] S.M.H. Sangtarashani, M. Rahmani, R. Behrooz, A. Khosravi, Lignocellulosic hydrogel from recycled old corrugated container resources using ionic liquid as a green solvent, *J. Environ. Manag.* 270 (2020) 110853, <https://doi.org/10.1016/j.jenvman.2020.110853>.
- [71] R. Foudazi, R. Zowada, I. Manas-Zloczower, D.L. Feke, Porous Hydrogels: Present Challenges and Future Opportunities, *Langmuir* 39 (2023) 2092–2111, <https://doi.org/10.1021/acs.langmuir.2c02253>.
- [72] M. Sauerwein, H. Steeb, Modeling of dynamic hydrogel swelling within the pore space of a porous medium, *Int. J. Eng. Sci.* 155 (2020), <https://doi.org/10.1016/j.ijengsci.2020.103353>.
- [73] W.X. Waresindo, H.R. Luthfianty, A. Priyanto, D.A. Hapidin, D. Edikresna, A. H. Aimon, T. Suciati, K. Khairurrijal, Freeze-thaw hydrogel fabrication method: basic principles, synthesis parameters, properties, and biomedical applications, *Mater Res Express* 10 (2023), <https://doi.org/10.1088/2053-1591/acb98e>.
- [74] S. Feng, J. Yi, Y. Ma, J. Bi, Study on the ice crystals growth under pectin gels with different crosslinking strengths by modulating the degree of amidation in HG domain, *Food Chem.* 428 (2023) 136758, <https://doi.org/10.1016/j.foodchem.2023.136758>.
- [75] M. Thommes, K. Kaneko, A.V. Neimark, J.P. Olivier, F. Rodriguez-Reinoso, J. Rouquerol, K.S.W. Sing, Physisorption of gases, with special reference to the evaluation of surface area and pore size distribution (IUPAC Technical Report), *Pure Appl. Chem.* 87 (2015) 1051–1069, <https://doi.org/10.1515/pac-2014-1117>.
- [76] F. Zhang, C. Zhang, J. Teng, D. Han, L. Wu, W. Hou, Preparation of hydrogels based on poplar cellulose and their removal efficiency of Cd(II) from aqueous solutions, *J. Water Health* 21 (2023) 676–686, <https://doi.org/10.2166/wh.2023.252>.
- [77] I.C. Roata, C. Croitoru, A. Pascu, E.M. Stanciu, Characterization of physically crosslinked ionic liquid-lignocellulose hydrogels, *Bioresources* 13 (2018) 6110–6121, <https://doi.org/10.15376/biores.13.3.6110-6121>.
- [78] C. Poornachandhra, R.M. Jayabalakrishnan, M. Prasanthrajan, G. Balasubramanian, A. Lakshmanan, S. Selvakumar, J.E. John, Cellulose-based hydrogel for adsorptive removal of cationic dyes from aqueous solution:

- isotherms and kinetics, RSC Adv. 13 (2023) 4757–4774, <https://doi.org/10.1039/D2RA08283G>.
- [79] W. Treesuppharath, P. Rojanapanthu, C. Siangsanoh, H. Manuspiya, S. Ummartyotin, Synthesis and characterization of bacterial cellulose and gelatin-based hydrogel composites for drug-delivery systems, Biotechnol. Rep. 15 (2017) 84–91, <https://doi.org/10.1016/j.btre.2017.07.002>.
- [80] L. Jiang, X. Huang, C. Tian, Y. Zhong, M. Yan, C. Miao, T. Wu, X. Zhou, Preparation and Characterization of Porous Cellulose Acetate Nanofiber Hydrogels, Gels 9 (2023) 484, <https://doi.org/10.3390/gels9060484>.
- [81] Y.M. Faleeva, V.A. Lavrenov, V.M. Zaichenko, Investigation of plant biomass two-stage pyrolysis based on three major components: cellulose, hemicellulose, and lignin, Biomass Convers. Biorefinery (2022), <https://doi.org/10.1007/s13399-022-03385-1>.
- [82] G. Dorez, L. Ferry, R. Sonnier, A. Taguet, J.-M. Lopez-Cuesta, J.-M. Lopez, L. Ferry, R. Sonnier, J.-M. Lopez-Cuesta, Effect of cellulose, hemicellulose and lignin contents on pyrolysis and combustion of natural fibers, J. Anal. Appl. Pyrolysis (2014) 107, <https://doi.org/10.1016/j.jaap.2014.03.017>.
- [83] H. Li, Y. Qu, J. Xu, Microwave-Assisted Conversion of Lignin, 2015, pp. 61–82, https://doi.org/10.1007/978-94-017-9612-5_4.
- [84] L. Li, K. Zhang, T. Wang, P. Wang, B. Xue, Y. Cao, L. Zhu, Q. Jiang, Biofabrication of a biomimetic supramolecular-polymer double network hydrogel for cartilage regeneration, Mater. Des. 189 (2020), <https://doi.org/10.1016/j.matdes.2020.108492>.
- [85] Y. Li, B. Wang, X. Sui, H. Xu, L. Zhang, Y. Zhong, Z. Mao, Facile synthesis of microfibrillated cellulose/organosilicon/polydopamine composite sponges with flame retardant properties, Cellulose 24 (2017) 3815–3823, <https://doi.org/10.1007/s10570-017-1373-z>.
- [86] M. Sadighi, S.J. Salami, An investigation on low-velocity impact response of elastomeric & crushable foams, Central European, J. Eng. 2 (2012) 627–637, <https://doi.org/10.2478/s13531-012-0026-0>.
- [87] N. Buchtová, C. Pradille, J.-L. Bouvard, T. Budtova, Mechanical properties of cellulose aerogels and cryogels, Soft Matter 15 (2019) 7901–7908, <https://doi.org/10.1039/c9sm01028a>.
- [88] P. Sacco, F. Piazza, E. Marsich, M. Abrami, M. Grassi, I. Donati, Ionic Strength Impacts the Physical Properties of Agarose Hydrogels, Gels 10 (2024) 94, <https://doi.org/10.3390/gels10020094>.
- [89] B.R. Thompson, T.S. Horozov, S.D. Stoyanov, V.N. Paunov, An ultra melt-resistant hydrogel from food grade carbohydrates, RSC Adv. 7 (2017) 45535–45544, <https://doi.org/10.1039/C7RA08590G>.
- [90] L. Hossain, V.S. Raghuvanshi, J. Tanner, G. Garnier, Modulating nanocellulose hydrogels and cryogels strength by crosslinking and blending, Colloids Surf. A Physicochem. Eng. Asp. 630 (2021) 127608, <https://doi.org/10.1016/j.colsurfa.2021.127608>.
- [91] Y. Zhang, K. Kobayashi, M. Wada, Comparative analysis of the structures and properties of cellulose hydrogels prepared using different solvent systems, Cellulose 32 (2025) 2337–2351, <https://doi.org/10.1007/s10570-025-06437-7>.
- [92] B. Yetiskin, O. Okay, Silk Fibroin Cryogel Building Adaptive Organohydrogels with Switching Mechanics and Viscoelasticity, ACS Appl. Polym. Mater. 4 (2022) 5234–5245, <https://doi.org/10.1021/acsapm.2c00741>.
- [93] L. Gerrits, B. Bakker, L.D. Hendriks, S. Engels, R. Hammink, P.H.J. Kouwer, Tailoring of Physical Properties in Macroporous Poly(isocyanopeptide) Cryogels, Biomacromolecules 25 (2024) 3464–3474, <https://doi.org/10.1021/acs.biomac.4c00086>.
- [94] S. Ciftbudak, N. Orakdogan, Anionic starch-based hybrid cryogel-embedded ZnO nanoparticles: tuning the elasticity and pH-functionality of biocomposites with dicarboxylic acid units, Soft Matter 20 (2024) 4434–4455, <https://doi.org/10.1039/D4SM00136B>.
- [95] X. Zhang, X. Zhang, P. Wang, X. Wang, L. Zhong, S. Ma, W. Xu, Study on viscoelasticity and damping properties of OSA/PAAM hydrogel, J. Polym. Res. 31 (2024) 63, <https://doi.org/10.1007/s10965-024-03913-9>.
- [96] T.G. Mezger, The Rheology Handbook: For Users of Rotational and Oscillation Rheometers, 2nd ed, Vincentz, 2006.
- [97] T. Hajidariyori, N. Nuntawad, P. Somsaen, R. Prukdamrongchai, H. Cherdchoo, P. Posoknistakul, P. Khemthong, W. Wanmolee, P. Arjfuak, P. Pongchaikul, N. Laosiripojana, K.C.W. Wu, C. Sakdaronnarong, Cryo-Induced Cellulose-Based Nanogel from *Elaeis guineensis* for Antibiotic Delivery Platform, Int. J. Mol. Sci. 24 (2023), <https://doi.org/10.3390/ijms24021230>.
- [98] R.D. Shannon, ***Ionic radii***, Acta Cryst. A32 (1976) 751–767, <https://doi.org/10.1038/nchem.2370>.
- [99] Y. Marcus, Thermodynamics of solvation of ions. Part 5. - Gibbs free energy of hydration at 298.15 K, J. Chem. Soc. Faraday Trans. 87 (1991) 2995–2999, <https://doi.org/10.1039/FT9918702995>.
- [100] G. de V. Brião, C.B. Lopes, T. Trindade, C.M. Silva, M.G.C. da Silva, M.G.A. Vieira, NdFeB magnet scrap valorization by leaching and recovery of rare earth metals by sorption on low-cost expanded clay, J. Ind. Eng. Chem. 131 (2024) 558–568, <https://doi.org/10.1016/j.jiec.2023.10.060>.
- [101] U.S. EPA, Lean Manufacturing and the Environment. <https://www.epa.gov/sustainability/lean-manufacturing-and-environment>, 2023. (Accessed 27 June 2024).
- [102] M. Zhang, Y. Zhou, F. Wang, Z. Chen, X. Zhao, W. Duan, G. Yin, X. Yang, J. Li, Q. Yin, M. Zhao, Preparation of biomass-based hydrogels and their efficient heavy metal removal from aqueous solution, Front. Chem. 10 (2022) 1–15, <https://doi.org/10.3389/fchem.2022.1054286>.
- [103] M. Zhang, Q. Yin, X. Ji, F. Wang, X. Gao, M. Zhao, High and fast adsorption of Cd (II) and Pb(II) ions from aqueous solutions by a waste biomass based hydrogel, Sci. Rep. 10 (2020) 3285, <https://doi.org/10.1038/s41598-020-60160-w>.
- [104] T. Das, A. Kumar, J. Saji, A. Pandey, D.K. Patel, Remediation of Trace Metals from Aqueous Solution Using a Novel Lignin–Montmorillonite Hydrogel Composite Prepared from *Tectona grandis* Sawdust Derived Lignin, ACS Sustain. Resour. Manag. 1 (2024) 141–153, <https://doi.org/10.1021/acssusresmg.3c00077>.